NASA TECHNICAL NOTE

NASA TN D-8057

NASA TN D-8057

AERODYNAMIC CHARACTERISTICS OF A POWERED, EXTERNALLY BLOWN FLAP STOL TRANSPORT MODEL WITH TWO ENGINE SIMULATOR SIZES

William G. Johnson, Jr.

Langley Research Center
Hampton, Va. 23665

NATIONAL AERONAUTICS AND SPACE ADMINISTRATION • WASHINGTON, D. C. • NOVEMBER 1975

1. Report No. NASA TN D-8057	2. Government Accession No.	3. Recipient's Catalog No.
4. Title and Subtitle AERODYNAMIC CHARACTERISTICS OF A POWERED, EXTERNALLY BLOWN FLAP STOL TRANSPORT MODEL WITH TWO ENGINE SIMULATOR SIZES		5. Report Date November 1975 6. Performing Organization Code
7. Author(s) William G. Johnson, Jr.		8. Performing Organization Report No. L-10129 10. Work Unit No. 505-10-41-03
9. Performing Organization Name and Address NASA Langley Research Center Hampton, Va. 23665		11. Contract or Grant No. 13. Type of Report and Period Covered Technical Note
12. Sponsoring Agency Name and Address National Aeronautics and Space Administration Washington, D.C. 20546		14. Sponsoring Agency Code

15. Supplementary Notes

16. Abstract

The present investigation was made to determine the low-speed aerodynamic characteristics of a general research model – a swept-wing, jet-powered STOL transport with externally blown flaps. The model was tested with four-engine simulators mounted on pylons under the 9.3-percent-thick supercritical airfoil wing. Two sets of air ejectors were used to provide data with large and small engines. Tests were conducted in the Langley V/STOL tunnel over an angle-of-attack range of -4° to 22° and a thrust-coefficient range from 0 to approximately 4. Described in this report are the effects of power, wing leading-edge slat configuration, T-tail and low horizontal-tail positions, and double-slotted flap deflection. Additional untrimmed and trimmed engine-out data and tail-body data are included.

17. Key Words (Suggested by Author(s)) Externally blown flap STOL Powered lift	18. Distribution Statement Unclassified – Unlimited Subject Category 02		
19. Security Classif. (of this report) Unclassified	20. Security Classif. (of this page) Unclassified	21. No. of Pages 291	22. Price* $8.75

*For sale by the National Technical Information Service, Springfield, Virginia 22161

AERODYNAMIC CHARACTERISTICS OF A POWERED, EXTERNALLY BLOWN FLAP STOL TRANSPORT MODEL WITH TWO ENGINE SIMULATOR SIZES

William G. Johnson, Jr.
Langley Research Center

SUMMARY

An investigation has been conducted in the Langley V/STOL tunnel to determine the low-speed aerodynamic characteristics of a general research model – a swept-wing, jet-powered STOL transport with externally blown flaps. The model was tested with four-engine simulators mounted on pylons under the 9.3-percent-thick supercritical airfoil wing. Two sets of ejectors were used to provide data with large and small engines, where the size was based on the ratio of thrust area per engine to wing area. Tests were conducted over an angle-of-attack range of -4° to 22° and a thrust-coefficient range from 0 to approximately 4.

This report describes data with the two-engine simulator sizes showing the effects of power (increasing thrust coefficient), wing leading-edge slat configuration, T-tail and low horizontal-tail positions, and double-slotted flap deflection. Untrimmed and trimmed engine-out data are included. Analysis of these data shows that with the larger engine simulators, the maximum untrimmed lift coefficients were about 0.8 less for the take-off configuration and 0.5 less for the landing configuration than with the smaller engine simulators. The engine-out rolling moments for most of the conditions tested were trimmed by a spoiler, and the loss in lift resulting from increasing spoiler projection became smaller with increasing engine thrust. The use of a "power recovery" from an inboard engine-out configuration restored the lift loss and trimmed the engine-out rolling and yawing moments.

INTRODUCTION

In the development of a jet-powered STOL transport aircraft, the externally blown flap has received serious consideration as a means of producing the high lift required for STOL operations. The cruise aerodynamic characteristics of the supercritical airfoil made the use of a supercritical wing desirable in a STOL transport configuration. The results from an investigation reported in reference 1 indicated that high-lift flap systems

could be developed using a supercritical-airfoil wing to produce an effective externally blown flap high-lift configuration.

The present investigation was made to determine the low-speed aerodynamic characteristics of a general research model – a swept-wing, jet-powered STOL transport with externally blown flaps. The model was one in a series of four model configurations studied in an aerodynamic comparison of several powered high-lift concepts on models of the same size and planform. (See refs. 2 and 3.) The model was tested with four engine simulators mounted on pylons under the 9.3-percent-thick supercritical airfoil wing. Two sets of ejectors were used to provide data with large and small engines, where the size was based on the ratio of thrust area per engine to wing area S_T/S. Tests were conducted in the Langley V/STOL tunnel over an angle-of-attack range of -4^o to 22^o and a gross thrust-coefficient range from 0 to approximately 4.

Described in this report are data with the two-engine simulator sizes showing the effects of power, wing leading-edge slat configuration, T-tail and low horizontal-tail positions, and double-slotted flap deflection. Additional untrimmed and trimmed engine-out data and tail-body data are included.

SYMBOLS

The measurements of this investigation are presented in the International System of Units (SI) with the U.S. Customary Units being indicated in parentheses. The measurements and calculations were made in the U.S. Customary Units.

A sketch of the axis system used in this investigation is presented in figure 1. This sketch shows the positive directions of forces, moments, and angles. The forces and moments are referred to the stability-axis system. The origin of the axis is a point in the plane of symmetry which corresponds to the longitudinal location of the 40-percent point of the mean geometric chord. The vertical location of the origin is 3.48 cm (1.37 in.) above the fuselage center line for the bypass-ratio-6.2 engine configuration. It is relocated to 2.84 cm (1.12 in.) above the fuselage center line for the bypass-ratio-10.0 engine configuration to keep the axis system on the thrust axis.

A	aspect ratio
b	wing span, m (ft)
C_D	drag coefficient, $\text{Drag}/q_\infty S$
C_L	lift coefficient, $\text{Lift}/q_\infty S$

$C_{L,t}$ lift coefficient of horizontal tail, Tail lift/$q_\infty S_t$

C_l rolling-moment coefficient, $M_{X,s}/q_\infty Sb$

C_m pitching-moment coefficient, $M_{Y,s}/q_\infty Sc$

C_n yawing-moment coefficient, $M_{Z,s}/q_\infty Sb$

C_T total engine gross thrust coefficient, $T/q_\infty S$

c wing reference chord, m (ft)

c_{HT} horizontal-tail chord measured in m (ft)

c_s leading-edge slat chord measured in percent wing chord c_w

c_w local wing chord, m (ft)

F_A axial force, N (lb)

F_N normal force, N (lb)

i_t incidence of horizontal tail with respect to fuselage, positive when tail trailing edge is down, deg

$M_{X,s}$ rolling moment, m-N (in-lb)

$M_{Y,s}$ pitching moment, m-N (in-lb)

$M_{Z,s}$ yawing moment, m-N (in-lb)

q_∞ free-stream dynamic pressure, N/m^2 (lb/ft^2)

S wing area, m^2 (ft^2)

S_T thrust area per engine, m^2 (ft^2)

S_t horizontal-tail area, m^2 (ft^2)

T gross thrust, N (lb)

X,Y,Z model body axis (see fig. 1)

X_s,Y_s,Z_s model stability axis (see fig. 1)

α angle of attack of wing chord line (also fuselage center line), deg

α_t angle of attack of horizontal tail, $\alpha_t = -(\alpha + i_t)$, deg

δ_f flap deflection (deflection of three flap segments given in order from outboard to inboard on figures and in text) referenced to wing-chord line, positive when trailing edge is down, deg

δ_j jet or thrust deflection angle, $\arctan \frac{F_N}{F_A}$, deg

δ_s leading-edge slat deflection with respect to wing chord line (positive when nose is down), deg

δ_{sp} spoiler projection, height above surface of wing, percent c_w

η thrust recovery factor, $\frac{\sqrt{F_A^2 + F_N^2}}{T}$

Other notation:

BPR bypass ratio

MGC mean geometric chord

MODEL AND APPARATUS

The investigation was conducted with a general research model of a four-engine, externally blown flap airplane. A three-view drawing of the model is shown in figure 2, and a photograph of the model in a cruise configuration is shown in figure 3. Additional dimensions of the model are presented in table I.

The model had a 9.3-percent-thick supercritical airfoil wing with a nominal 30^o quarter-chord sweep. Flap, vane, and leading-edge slat details are shown schematically in figure 4 with related photographs in figure 5. The 35-percent wing chord double-slotted

flap system was deflected full span or partial span (out to 0.71b/2) to 35° and 65° from the flap zero position by use of fixed-angle flap brackets. Three leading-edge slat systems with chord lengths of 15-, 20-, and 25-percent wing chord were tested at deflections of 40° or 50°. It should be noted that the wing leading-edge-slat configurations ($c_s = 0.20c_w$ and $c_s = 0.25c_w$) used a 15-percent-chord slat from the fuselage to the outboard engine pylon with the 20- or 25-percent-chord slat deployed along the outboard portion of the wing span (0.43b/2 to the wing tip).

The variable-incidence horizontal tail had an 11.0-percent-thick symmetrical supercritical airfoil and was investigated in both a T-tail and low-tail position. Details of the 15-percent-chord inverted leading-edge slat and constant-chord elevators (used for most of the tests) are shown in figure 6. Also shown in figure 6 are the locations of the quarter-chord mean geometric chord for the vertical and horizontal tails. These locations are shown for the T-tail and low-tail positions. Photographs of these two tail positions are shown in figure 7.

Air-ejector engine simulators, shown schematically in figure 8(a) were used to simulate the jet propulsion system. Each engine simulator was a two-part ejector with individual air supply lines and control valves to provide the exhaust-flow characteristics of the fan and gas generator. Two separate sets of simulators were used to represent fan-jet engines with thrust area to wing area ratios $S_T/S = 0.0074$ and $S_T/S = 0.0115$, bypass ratios of 6.2 and 10.0, respectively, where bypass ratio is defined as the ratio of total fan exit flow to total gas-generator exit flow. The sizes and positions of the simulators are shown in figure 8(b). Photographs of the two sets of simulators installed on the model are shown in figure 9.

The right wing was fitted with the $0.15c_w$ full-span spoilers shown schematically in figure 10 and in the photograph in figure 11. Four spoiler projections, $\delta_{sp} = 2.5$, 5.0, 7.5, and 10.0 percent c_w, were provided.

TESTS AND PROCEDURES

Tests were conducted in the Langley V/STOL tunnel where the test-section dimensions are 4.42 m (14.5 ft) by 6.63 m (21.75 ft). Most of the tests were conducted at a free-stream dynamic pressure of 814 N/m^2 (17 lb/ft^2) for a Reynolds number of 0.676×10^6 based on the wing reference chord of 26.97 cm (10.62 in.). A 0.25-cm-wide (0.1-in.) strip of No. 60 carborundum was located on the surfaces of the wing, vertical tail, and horizontal tail at a point 4.29 cm (1.69 in.) aft of the leading edge measured along the surface. The transition strip was used for all tests. Most of the tests were made over an angle-of-attack range of -4° to 22° and a total gross thrust-coefficient range up to about 4.0 for a free-stream dynamic pressure of 814 N/m^2 (17 lb/ft^2).

The model was tested with full and partial span flap deflections of 35° and 65° with leading-edge slat deflections of 40° and 50°. Tests were made with the tail off and with the T-tail and low tail at various horizontal-tail incidence angles with the elevators off or deflected. Data were obtained with two sizes of engine simulators, $S_T/S = 0.0074$ and $S_T/S = 0.0115$, with which engine bypass ratios (BPR) of 6.2 and 10.0, respectively, were simulated. For convenience, the simulators are referred to by their BPR.

In preparation for the present tests, single-engine static thrust calibrations were made to determine the gross thrust and primary mass flows for each engine section as functions of the section plenum pressure. (See ref. 4.) The results from these calibrations are shown in figure 12. Individual valves in the air supply line to each engine section provided the control of the mass flows required to simulate the desired BPR. The solid symbols in figure 12 represent the pressure settings used in the tests for the specific BPR noted and the resultant mass flows and thrust. The accuracy of the thrust calibrations is indicated in figure 13 where the measured resultant forces are compared with the calculated thrust values (based on individual section calibrations) for a configuration thrust buildup from one engine section up to four complete engines. The data show the computed totals to be within about 1 percent of the total measured value.

PRESENTATION OF RESULTS

The data are presented in the following figures:

DISCUSSION OF RESULTS

An initial indication of the effectiveness of an externally blown flap configuration can be obtained from a plot of static turning angles and thrust recovery efficiencies. Such a plot is shown in figure 14 where the normal force divided by the static thrust is plotted against the longitudinal force divided by the static thrust for the several major configurations of the tests. These data show that for the take-off and landing flap deflections, the use of the BPR 6.2 engine results in approximately 10° higher jet turning (δ_j) than the BPR 10.0 engine; however, this higher turning results in about 5 percent lower thrust recovery (η). The use of these parameters as an aid in the analysis of powered-lift aerodynamic data is discussed in references 1, 3, 5, and 6. A comparison of δ_j and η values obtained at static conditions with similar variable values obtained from forward-speed wake-survey measurements is presented in reference 7, wherein good agreement from static to forward-speed conditions was obtained for only the values of η.

Longitudinal Aerodynamic Characteristics

Wind-tunnel wall corrections based on reference 8 were applied to a sample case of data to determine the effect on the basic longitudinal aerodynamic data (fig. 15). Because

of the small size of the model relative to the tunnel, these corrections resulted in no significant change in the values of C_L and C_m, and resulted in less than 1^o change in angle of attack at the highest value of C_T. Since these corrections are so small, the data are presented in the uncorrected form.

The effect of increasing thrust coefficient on the longitudinal aerodynamic characteristics is presented for the BPR 6.2 $\left(S_T/S = 0.0074\right)$ configurations in figures 16 to 19, and for the BPR 10.0 $\left(S_T/S = 0.0115\right)$ configurations in figures 20 to 24. The data are presented in plots of C_m against α and C_L against α, C_D, and C_m. In some cases, double curves are presented to show repeatability of the data taken from two different tunnel entries. In most cases, the repeatability is good. In general, the expected thrust-coefficient effects, such as higher lift-curve slopes and maximum-lift values, occur with increasing thrust coefficient. The severity of the stall lessens with increasing thrust coefficient for both the take-off and landing flap configurations. Maximum untrimmed lift coefficients obtained were about 7.4 for the take-off configuration and 8.6 for the landing configuration with BPR 6.2 engine simulators. With the BPR 10.0 engine simulators the maximum untrimmed lift coefficients obtained were about 6.6 for the take-off configuration and 8.1 for the landing configuration. Power-off lift and drag data show essentially no change resulting from the change in engine simulators.

The pitching-moment data show the expected slight decrease in instability with increasing thrust coefficient for all the configurations except the take-off flaps with the BPR 10.0 engine simulators. The plots of C_m against α show that of the four basic configurations – landing and take-off flaps with each of the two engine simulators – the take-off flaps with the BPR 10.0 engine simulators are the only combination which do not exhibit a change in C_m as a function of power after a power-on condition has been established. This result suggests for this combination, a balancing effect of the shift in the center of pressure on the wing due to the increasing supercirculation contribution to lift with the change in deflected thrust contribution to the pitching moment.

The effects of flap span (partial or full) are basically unchanged by an increase in thrust. The partial-span flap configurations produce the same maximum lift coefficients as the respective full-span configurations, but the partial-span configurations generally have a lower lift coefficient at zero angle of attack. The full-span flap configurations exhibit a more negative pitching moment at the lower angles of attack.

Thrust-Removed Lift-Drag Polars

References 1 and 7 described a procedure whereby the direct deflected thrust components of lift and drag could be removed from the total force data. The remaining data might be referred to as circulation lift and drag. This procedure was applied to the force data of figures 16 to 24. The resulting thrust-removed lift-drag polars are shown in fig-

ures 25 to 33. The data are plotted as thrust-removed lift (total measured lift minus thrust contribution to lift) as a function of the thrust-removed drag (total measured drag minus thrust contribution to drag). On all these figures, the broken line represents the drag polar determined from

$$C_D = C_{D,o} + \frac{C_L^2}{\pi Ae}$$

where the values of the Oswald wing efficiency factor e was set equal to 1 and the power-off values of the profile drag coefficient $C_{D,o}$ were found to be 0.102 for the take-off flap setting and 0.223 for the landing flap setting.

In general, the thrust-removed data for any given BPR 6.2 configuration form a single, well-defined polar with characteristics similar to the drag polar described previously. The exceptions occur with the combination of the highly deflected outboard flap element and higher engine thrust level such as figures 26(d), 27(d), and 28(d). Most of the BPR 10.0 configurations show an increment of thrust-removed drag in the power-on data that prevents correlation of the data to a single polar as shown earlier. A second point of interest on the BPR 10.0 configuration in that the slope of the thrust-removed polar for the partial- and full-span landing flaps (parts (c) and (d) of figs. 30 to 33) is greater than the slope for the reference drag polar. Other than possible forward-speed effects on the parameters that make up the deflected-thrust component of the total lift, there is no consistent explanation for the lack of correlation of these excepted data to a single polar as expected.

Wing Leading-Edge Slat Effects

Several leading-edge slat configurations were tested during this investigation. Slat chord lengths included 0.15, 0.20, and $0.25c_w$ with deflections of 40^o or 50^o. These data are presented in figures 34 to 41 to show the effect of wing leading-edge slat configuration on the longitudinal aerodynamic characteristics. The data show the expected increase in the stall angle of attack and in the maximum lift coefficient as the slat configuration is changed by increasing the slat deflection or slat chord. In general, the data show a slight increase in the lift-curve slope as the slat deflection is increased from 40^o to 50^o. Changes in the slat configuration do not cause any significant change in the trim requirements.

Longitudinal Stability Characteristics

The results of tests to determine the lift characteristics of the horizontal tail are shown in figure 42. The open and solid symbols represent data from model upright and model inverted tests, respectively, which were used to establish the complete lift curve.

The data show that the basic tail had a maximum lift coefficient of about 0.81. The addition of a leading-edge slat increased the lift coefficient of the tail to at least 1.57; however, physical limitations in the test setup prevented tests at angles of attack high enough to determine the maximum lift coefficient. The addition of a leading-edge slat and a constant-chord elevator increased the maximum lift coefficient of the tail to about 2.40. The lift coefficients noted are based on the horizontal-tail (elevator-off) reference area of 0.156 m^2 (1.682 ft^2). One significant point noted at the negative angles of attack is that the leading-edge slat caused a sharp decrease in the lift-curve slope of the tail which indicates flow separation on the bottom surface of the tail. This behavior is similar to that of other inverted high-lift T-tail configurations such as reported in reference 9. The suspected flow separation on the bottom surface of the tail can substantially affect the stability and control of the airplane configuration as shown by the nonlinear stability curves and sudden loss of tail effectiveness on many of the T-tail configurations discussed in this section.

The effects of horizontal-tail incidence angle were investigated for both the T-tail and the low-tail configurations. All the moment data are presented about a point in the plane of symmetry which corresponds to the longitudinal location of 40 percent of the wing mean geometric chord. The vertical location of the moment reference center is 3.48 cm (1.37 in.) above the fuselage center line for the bypass ratio 6.2 engine configuration and 2.84 cm (1.12 in.) above the fuselage center line for the bypass ratio 10.0 engine center line. The T-tail data in figure 43 show that the BPR 6.2 cruise configuration with flaps retracted and clean horizontal tail (elevator off) is basically stable up to stall with trim capability through the range of thrust coefficient and angle of attack. The low-tail data in figure 44 show generally neutrally stable characteristics for power-off and increasing stability with increasing power. These data also indicate trim capability for the cruise configuration with the clean tail. For the partial-span take-off and landing flap configurations, figures 45 and 46, respectively, the T-tail with leading-edge slat provides a stable, trimmable configuration through most of the angle-of-attack range up to the maximum lift. This tail configuration, however, requires a large negative tail incidence for the trim. The low-tail configuration for similar flap settings (figs. 47 and 48) results in a generally unstable design. Since the low-tail, high-lift configurations were generally unstable, only T-tail data are presented for the remaining configurations. The data in figures 49 to 54 show the effect of the horizontal-tail incidence angles on BPR 6.2 configurations with partial- or full-span landing or take-off flaps with various leading-edge deflections. The tail configuration for these data included a constant-chord elevator to improve the horizontal-tail effectiveness. These configurations are shown to be stable and can be trimmed, at all coefficients of thrust tested, by moderate incidence angles through the angle-of-attack range up to the maximum lift coefficients obtained for the particular high-lift configuration.

The data from the tests of the BPR 10.0 cruise and high-lift configurations are shown in figures 55 to 61. These data show stability and trim characteristics for the BPR 10.0 configurations to be similar to those of the BPR 6.2 configurations.

Longitudinal and Lateral Characteristics With Asymmetric Thrust

The basic longitudinal data and the rolling-moment and yawing-moment coefficients for two BPR 10.0 configurations are shown in figures 62 $\left(\delta_f = 0^o/35^o/35^o\right)$ and 63 $\left(\delta_f = 0^o/65^o/65^o\right)$ to compare the effects of thrust loss (engine out) from either the left outboard engine (engine 1) or the left inboard engine (engine 2). The most significant effects on the longitudinal data are the 0.2 loss in untrimmed lift coefficient for the take-off configuration and the 0.35 loss in untrimmed lift coefficient for the landing configuration when the left inboard engine (engine 2) is out. For the take-off configuration at high thrust (fig. 63(c)), the engine-1-out case, when compared with the engine-2-out case, results in an approximate 16 percent higher rolling moment at the higher angles of attack with a 20-percent increase in the yawing-moment coefficient at the low angles of attack. For the landing configuration at high thrust (fig. 64(c)), the engine-1-out case results in a generally constant 25 percent higher rolling moment and a 100-percent increase in the yawing moment. In general, the landing-flap, engine-1-out configuration results in a 50-percent increase in maximum rolling-moment coefficient and a 30-percent decrease in maximum yawing-moment coefficient when compared with the take-off flap, engine-1-out configuration.

Effect of Spoiler Projection

A schematic and photograph of the spoiler configurations tested are shown in figures 10 and 11, respectively. The tests were made with the spoiler projected on the right wing. The effects of spoiler projection on the longitudinal and lateral aerodynamic characteristics of several BPR 6.2 configurations and of several BPR 10.0 configurations are shown in figures 64 to 67 and in figures 68 to 73, respectively. The data for the BPR 6.2 take-off and landing flap configurations are presented for the left outboard engine (engine 1) out and the left inboard engine (engine 2) out conditions. The data for the BPR 10.0 take-off and landing flap configurations are presented for symmetrical power, left outboard engine (engine 1) out, and left inboard engine (engine 2) out conditions. Summary plots showing the variation of rolling- and yawing-moment coefficients with spoiler projection at an angle of attack of 8^o for several thrust coefficients are presented in figures 74 to 83 for the configurations presented in figures 64 to 73.

For all the configurations, the data show the expected decrease in lift with increasing spoiler projection. This decrease in lift becomes smaller with increasing engine thrust. This result indicates that a spoiler can become less effective with increased thrust than might be expected on certain powered-lift configurations such as the externally blown flap

and some internally blown flap designs since much of the lift is generated directly on the flap system aft of the spoiler. The roll effectiveness of the spoiler on the landing flap configuration is about twice that of the take-off flap configurations. This increased roll effectiveness is characteristic of all the symmetric and asymmetric thrust conditions of the tests. A comparison of the data for an engine-off, spoiler-off configuration with an engine-off, spoiler-on configuration (figs. 63(c) and 72(c), for example) shows the spoiler roll effectiveness to be sufficient to trim the engine-out rolling moments for most of the conditions. No attempt was made to define the yawing-moment trim requirements.

Power Recovery From Engine Out

Most normal flight conditions require engine throttle settings to be considerably less than full throttle. Therefore, the use of a "power recovery" from an engine-out condition – that is, increasing the power on the remaining good engine on the wing having the failed engine – is feasible. This approach was investigated for the case of the four engines initially at half thrust and after engine failure, the thrust on the remaining good engine was doubled to balance the thrust on both wings. The resulting longitudinal and lateral data are shown in figures 84 to 87. The data are presented for four cases; either the left outboard engine out, or the left inboard engine out for both the take-off and the landing flap configurations. These data show that doubling the power from the good engine on the engine-out wing restores the lift lost because of the failed engine in three of the four configurations tested. The exception is the left inboard engine out on the take-off flap configuration. One explanation for the inability to recover the lost lift with this configuration is the lower deflection of a shorter chord flap behind the outboard engine which is unable to capture and turn the exhaust flow of the outboard engine as effectively as the longer chord inboard flap or the highly deflected landing flaps. The lateral data show that the power recovery generally trims the engine-out yawing moment and the engine-out rolling moment on the inboard-engine-out configurations. Since the outboard-engine-out rolling moments are larger because of large moment arms for that engine, the increase in power on the inboard engines operates on a shorter moment arm and does not produce the required moment to trim.

SUMMARY OF RESULTS

An analysis of the results from this investigation has produced the following conclusions:

1. The expected power effects such as higher lift-curve slopes and maximum lift values occur with increasing thrust coefficient. With the larger $\left(S_T/S = 0.0115\right)$ engine simulators the maximum untrimmed lift coefficients were about 0.8 less for the take-off

configuration and 0.5 less for the landing configuration than with the smaller $(S_T/S = 0.0074)$ engine simulators. $(S_T$ denotes thrust area and S denotes wing area.)

2. Increasing the slat deflection or slat chord outboard of the engine nacelles resulted in significant increases in the stall angle of attack and the maximum lift coefficient.

3. The low-tail, high-lift configurations tested were generally unstable. The T-tail with slat and elevator provided stable configurations trimmable by moderate tail incidence angles at all thrust coefficients tested through the angle-of-attack range up to the maximum lift coefficients obtained.

4. The loss in lift resulting from increasing spoiler projection becomes smaller with increasing engine thrust.

5. The spoiler is shown to be sufficient to trim the engine-out rolling moments for most of the test conditions.

6. For initial engine conditions of half thrust, a "power recovery" will, in general, restore the lift lost because of a failed engine. For the inboard-engine-out configurations, the engine-out rolling and yawing moments are trimmed. For the outboard-engine-out configurations, the adverse moments are larger, and an increase in power on the inboard engine does not produce the required moments to trim.

Langley Research Center
National Aeronautics and Space Administration
Hampton, Va. 23665
August 20, 1975

REFERENCES

1. Johnson, William G., Jr.: Longitudinal Aerodynamic Characteristics of a Wing-Body Combination Having a Rectangular, Aspect-Ratio-6, Slotted Supercritical Wing With Externally Blown Flaps. NASA TM X-2388, 1971.

2. Hoad, Danny R.: Longitudinal Aerodynamic Characteristics of a Deflected-Thrust Propulsive-Lift Transport Model. NASA TM X-3234, 1975.

3. Sleeman, William C., Jr.; and Hohlweg, William C.: Low-Speed Wind-Tunnel Investigation of a Four-Engine Upper Surface Blown Model Having a Swept Wing and Rectangular and D-Shaped Exhaust Nozzles. NASA TN D-8061, 1975.

4. Hammond, Alexander D.; and Johnson, William G., Jr.: Development of Wind-Tunnel Test Techniques for Propulsion System Simulators for Use in Small-Scale V/STOL Models. NASA paper presented at ASME Joint Conference of Gas Turbine Division and Fluids Engineering Division (San Francisco), Mar. 26-30, 1972.

5. Hoad, Danny R.: Longitudinal Aerodynamic Characteristics of an Externally Blown Flap Powered-Lift Model With Several Propulsive System Simulators. NASA TN D-7670, 1974.

6. Johnson, William G., Jr.: Aerodynamic and Performance Characteristics of Externally Blown Flap Configurations. STOL Technology, NASA SP-320, 1972, pp. 43-54.

7. Johnson, William G., Jr.; and Kardas, Gerald E.: A Wind-Tunnel Investigation of the Wake Near the Trailing Edge of a Deflected Externally Blown Flap. NASA TM X-3079, 1974.

8. Heyson, Harry H.: Rapid Estimation of Wind-Tunnel Corrections With Application to Wind-Tunnel and Model Design. NASA TN D-6416, 1971.

9. Parlett, Lysle P.; Freeman, Delma C., Jr.; and Smith, Charles C., Jr.: Wind-Tunnel Investigation of a Jet Transport Airplane Configuration With High Thrust-Weight Ratio and an External-Flow Jet Flap. NASA TN D-6058, 1970.

TABLE I.- DIMENSIONS OF MODEL

Wing:		
Area, m^2 (ft^2)	0.4833	(5.202)
Span, m (ft)	1.902	(6.24)
Aspect ratio	7.48	
Airfoil section	9.3-percent-thick supercritical	
Length of mean geometric chord, m (ft)	0.2899	(0.951)
Length of wing reference chord, m (ft)	0.2697	(0.885)
Distances from nose of model to quarter-chord point of mean aerodynamic chord, cm (in.)	100.10	(39.41)
Spanwise station of mean aerodynamic chord, cm (in.)	37.36	(14.71)
Root chord (fuselage center line), cm (in.)	44.42	(17.49)
Tip chord, cm (in.)	10.97	(4.32)
Break-station chord, cm (in.)	25.93	(10.21)
Spanwise station of break, cm (in.)	39.62	(15.60)
Sweep of quarter-chord line:		
Inboard panel, deg	28.9	
Outboard panel, deg	31.1	
Dihedral of quarter-chord line:		
Inboard panel, deg	0.0	
Outboard panel, deg	0.0	
Incidence of mean aerodynamic chord, deg	0.0	
Incidence of root chord, deg	0.0	
Geometric twist:		
Root, deg	0.0	
Break station, deg	0.0	
Tip, deg	0.0	
Vertical tail:		
Area, m^2 (ft^2)	0.1382	(1.488)
Span, m (ft)	0.4877	(1.60)
Airfoil section	11-percent-thick symmetrical supercritical	
Sweep angles:		
Leading edge, deg	25.0	
Trailing edge, deg	4.5	
Root chord, cm (in.)	37.80	(14.88)
Tip chord, cm (in.)	18.90	(7.44)
Horizontal tail:		
Area, m^2 (ft^2)	0.156	(1.682)
Span, m (ft)	0.7964	(2.613)
Aspect ratio	4.06	
Airfoil section	11-percent-thick symmetrical supercritical	
Length of mean aerodynamic chord, m (ft)	0.213	(0.699)
Incidence	Variable	
Engines:		
Spanwise location of inboard engines, cm (in.)	24.18	(9.52)
Spanwise location of outboard engines, cm (in.)	39.62	(15.60)
Incidence of all engine center lines relative to waterline, deg	0.0	
Bypass ratio	6.2 and 10.0	
Moment reference:		
Longitudinal location, distance from nose of model, cm (in.)	100.10	(39.41)
Vertical location, distance from top of fuselage at wing, cm (in.):		
BPR 6.2 engine installation	8.41	(3.31)
BPR 10.0 engine installation	9.04	(3.56)

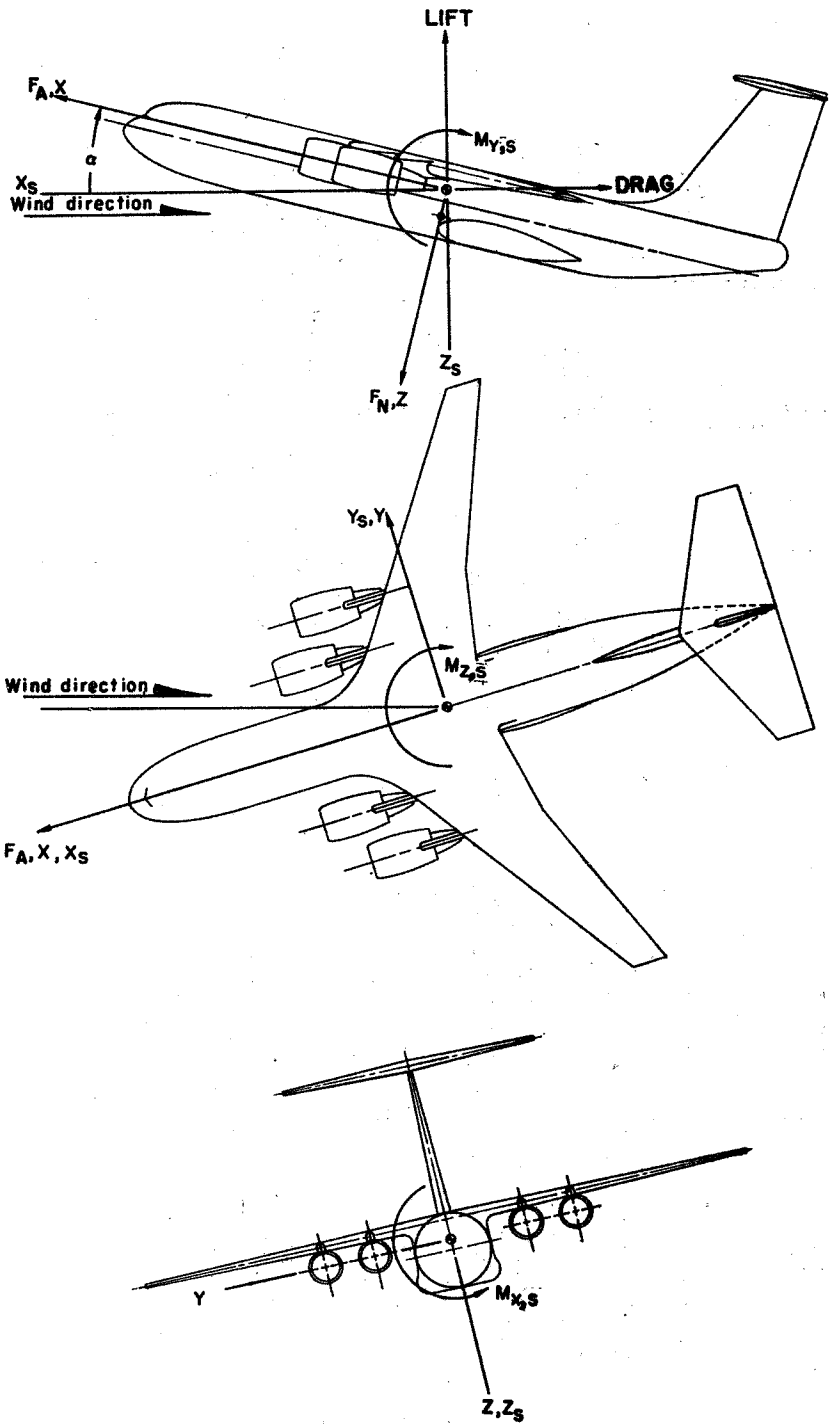

Figure 1.- System of axes. Positive direction of forces, moments, and angles are indicated.

Wing:	
Airfoil section: 9.3% thick supercritical	
Area, sq m, (sq ft)	.483 (5.202)
Wing reference chord, m (ft)	.270 (.885)
Span, m (ft)	1.902 (6.240)
Aspect ratio	7.48
Horizontal tail:	
Airfoil section: 11.0% thick supercritical	
Area, sq m (sq ft)	.156 (1.682)
Reference chord, m (ft)	.213 (.699)
Span, m (ft)	.796 (2.613)
Aspect ratio	4.06
Vertical tail:	
Airfoil section: 11.0% thick supercritical	
Area, sq m (sq ft)	.138 (1488)
Reference chord, m (ft)	.294 (.964)
Span, m (ft)	488 (1.600)

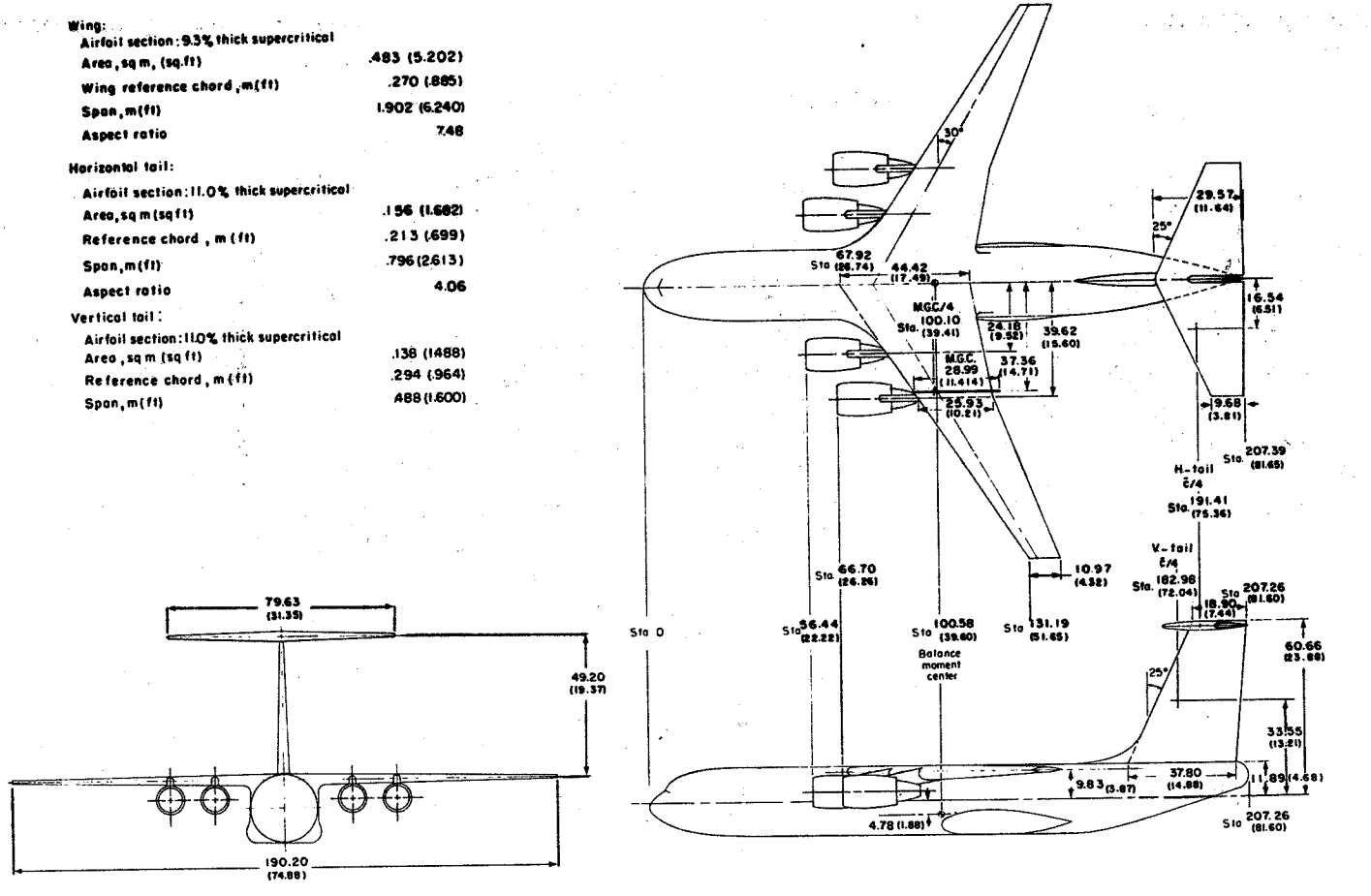

Figure 2.- Three-view drawing of model. All dimensions are in centimeters; parenthetical values are in inches.

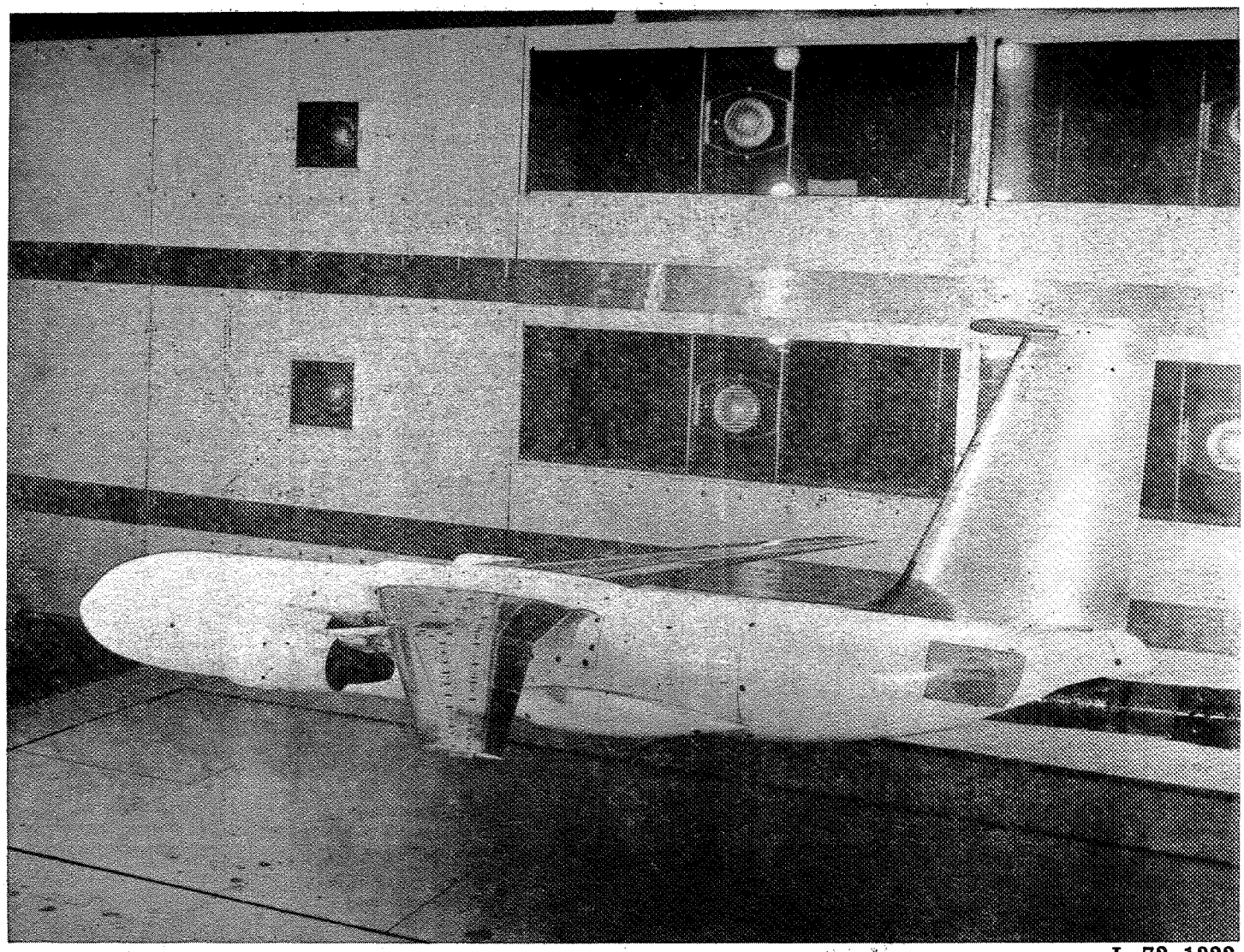

L-72-1322

Figure 3.- Photograph of model in cruise configuration in the Langley V/STOL tunnel.

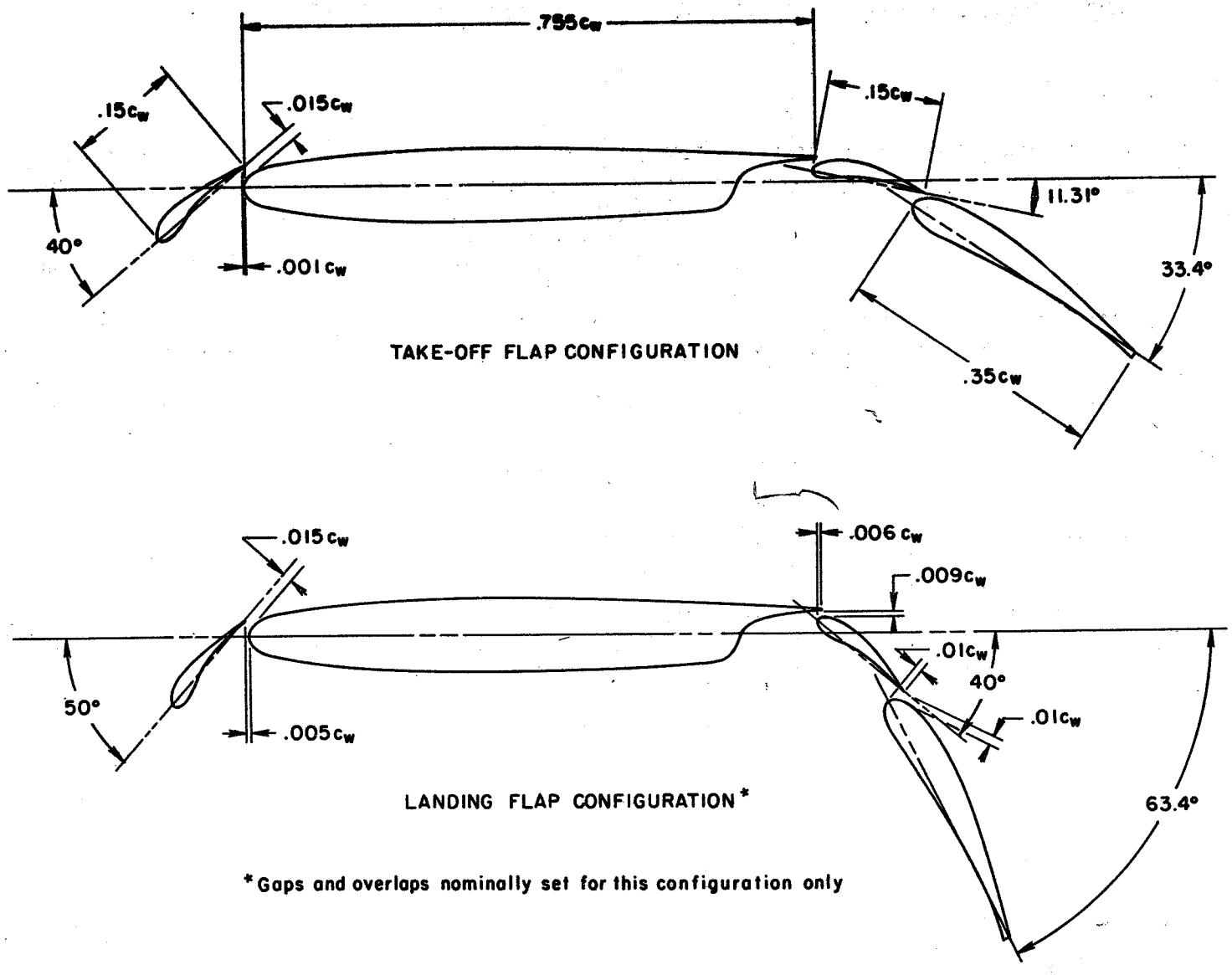

Figure 4.- Positioning details for flap, vane, and leading-edge slot.

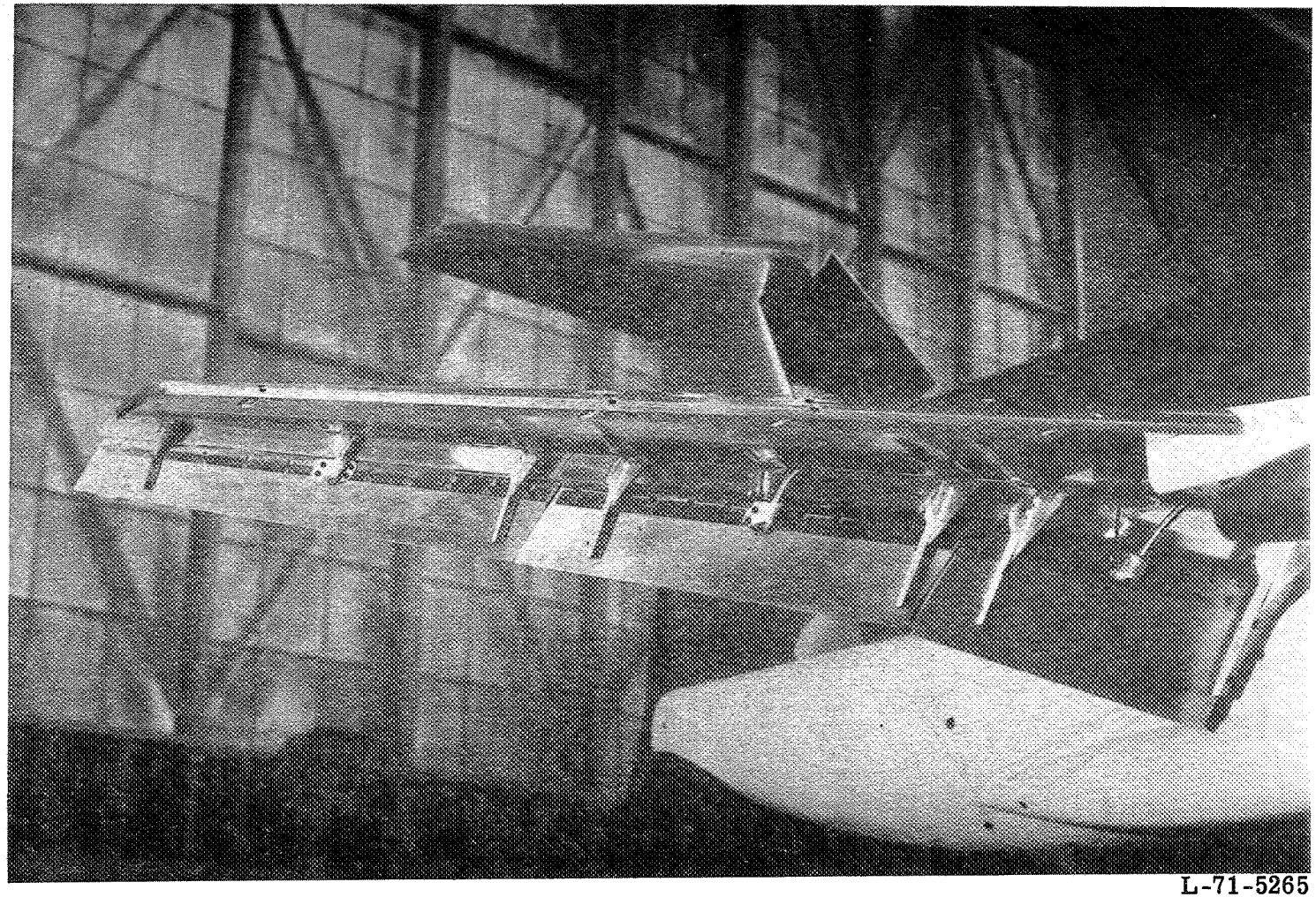

L-71-5265

(a) $\delta_f = 65^o/65^o/65^o$; $\delta_s = 50^o$; $c_s = 0.15c_w$.

Figure 5.- Photographs of deployed flap system.

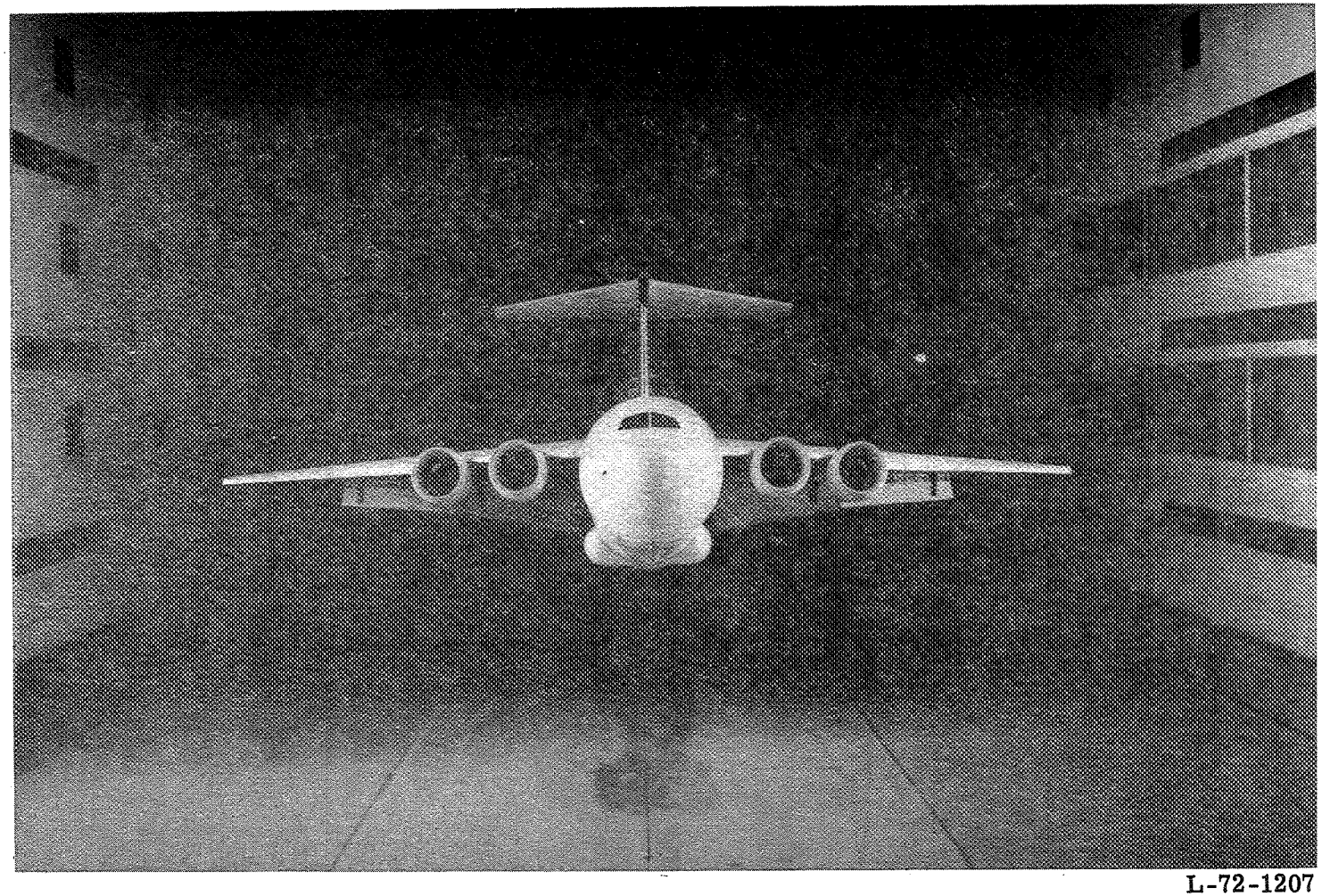

L-72-1207

(b) $\delta_f = 0^o/65^o/65^o$; $\delta_s = 50^o$; $c_s = 0.25c_w$.

Figure 5.- Concluded.

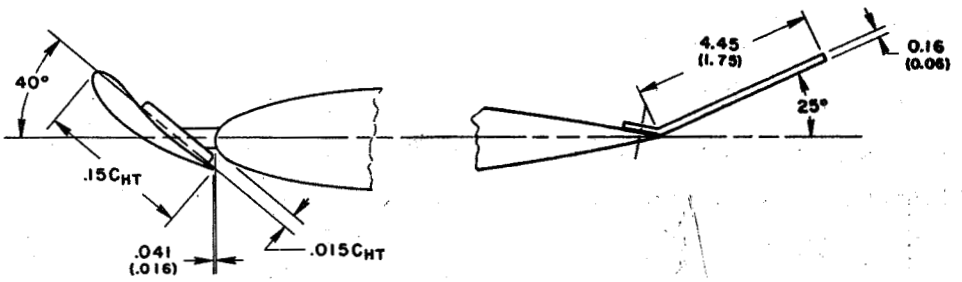

Detail of horizontal-tail elevator and leading-edge slat

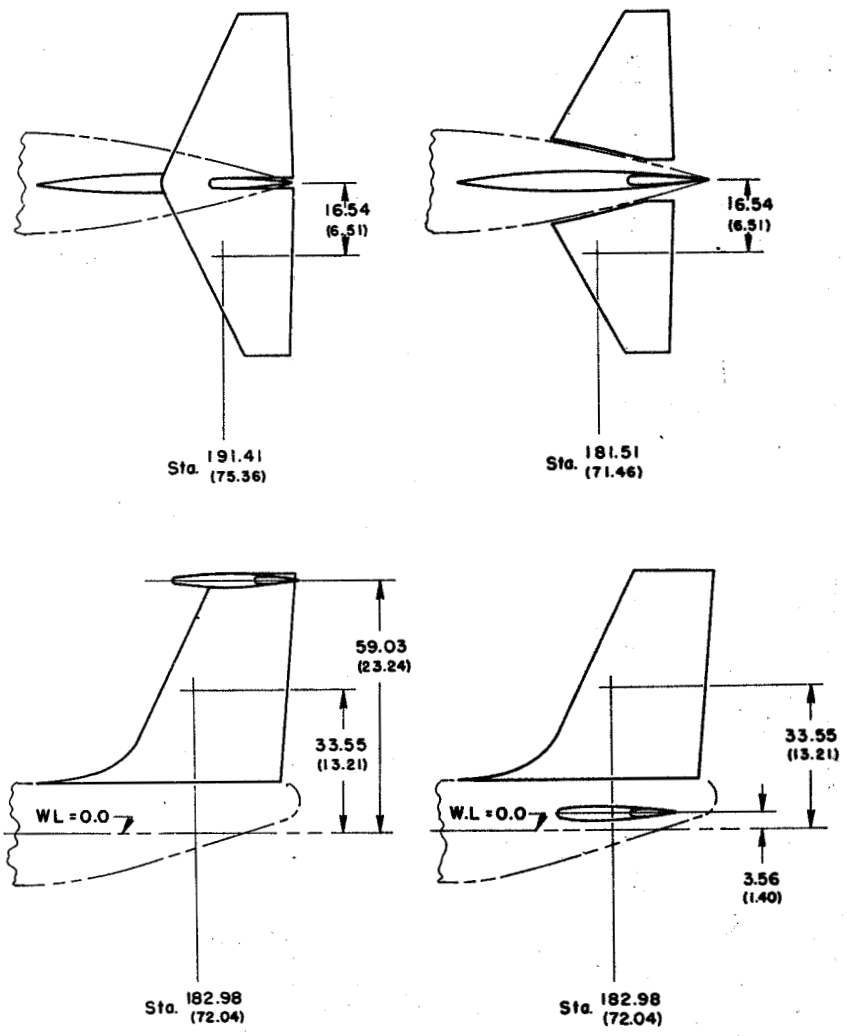

Figure 6.- Details of horizontal-tail elevator and leading-edge slat and locations of the quarter-chord mean geometric chord for vertical and horizontal tails. All dimensions are in centimeters; parenthetical values are in inches. WL indicates water line.

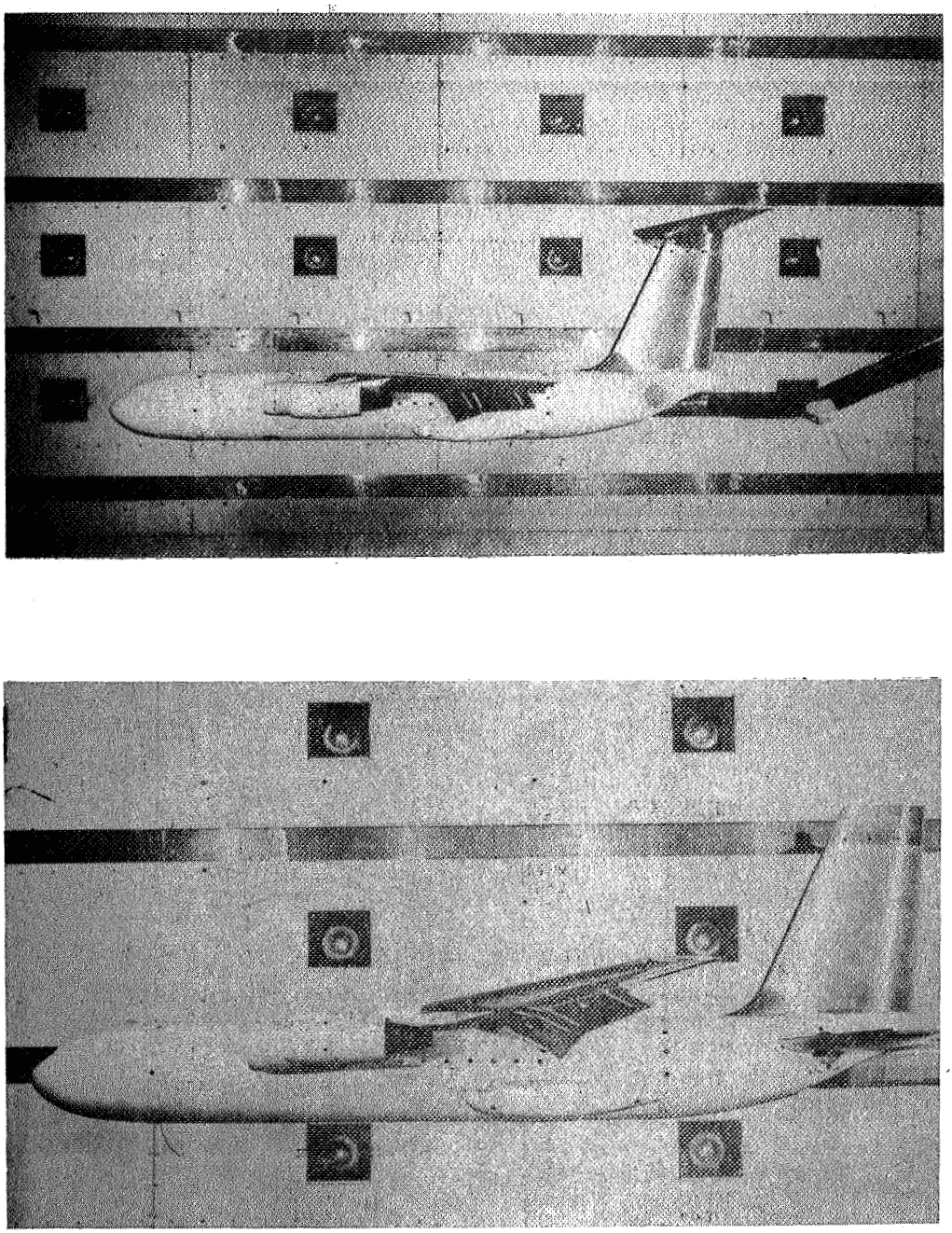

L-75-210

Figure 7.- Photographs of T-tail and low-tail installations.

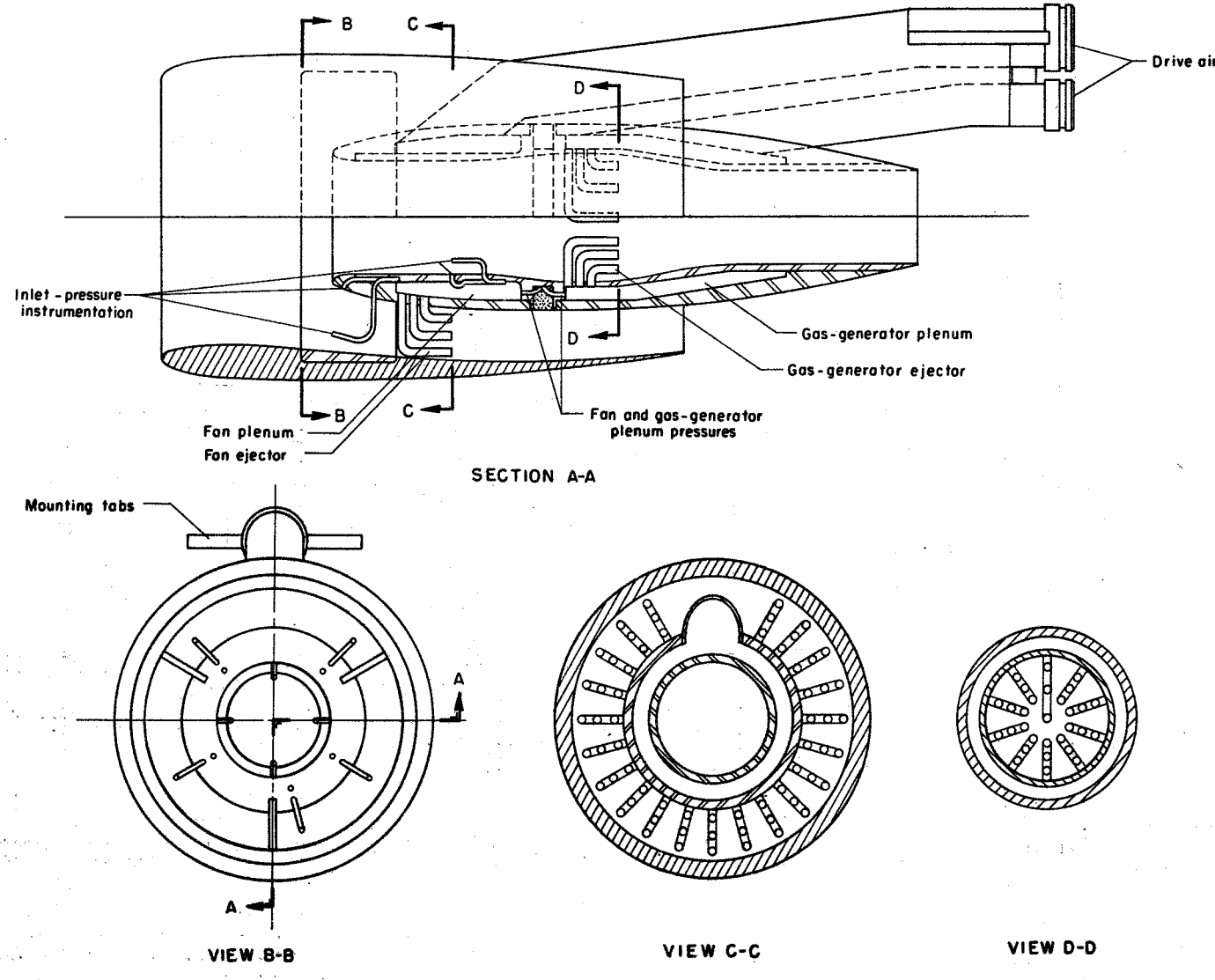

(a) Construction details.

Figure 8.- Schematic of dual air-ejector engine simulator. All dimensions are in centimeters; parenthetical values are in inches.

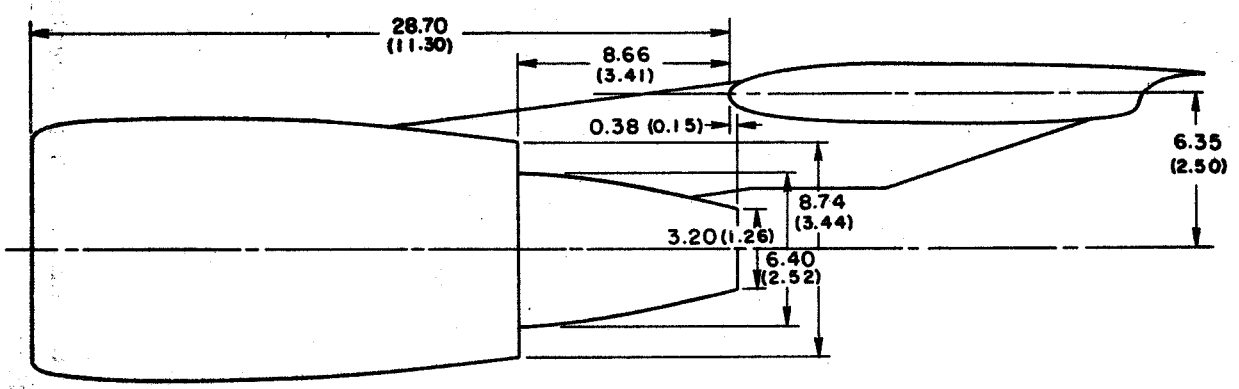

BPR 6.2 SIMULATOR

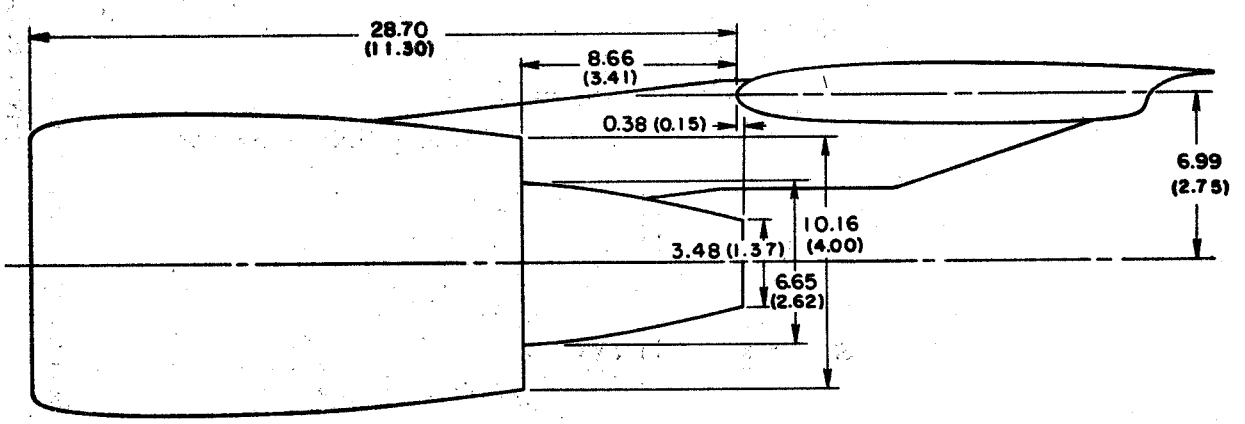

BPR 10.0 SIMULATOR

(b) Size and location details.

Figure 8.- Concluded.

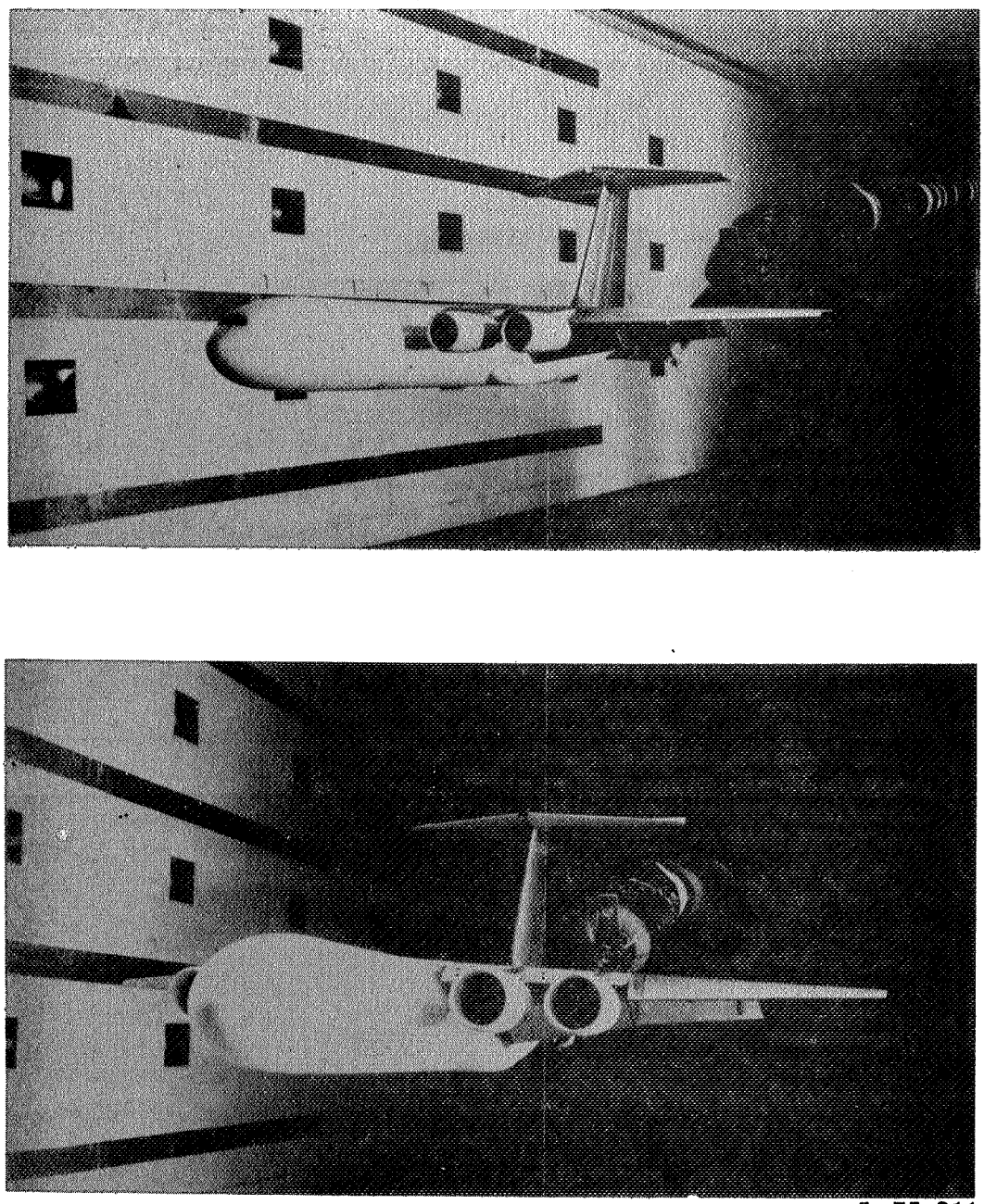

L-75-211

Figure 9.- Photographs showing BPR 6.2 and BPR 10.0 simulators installed on the model.

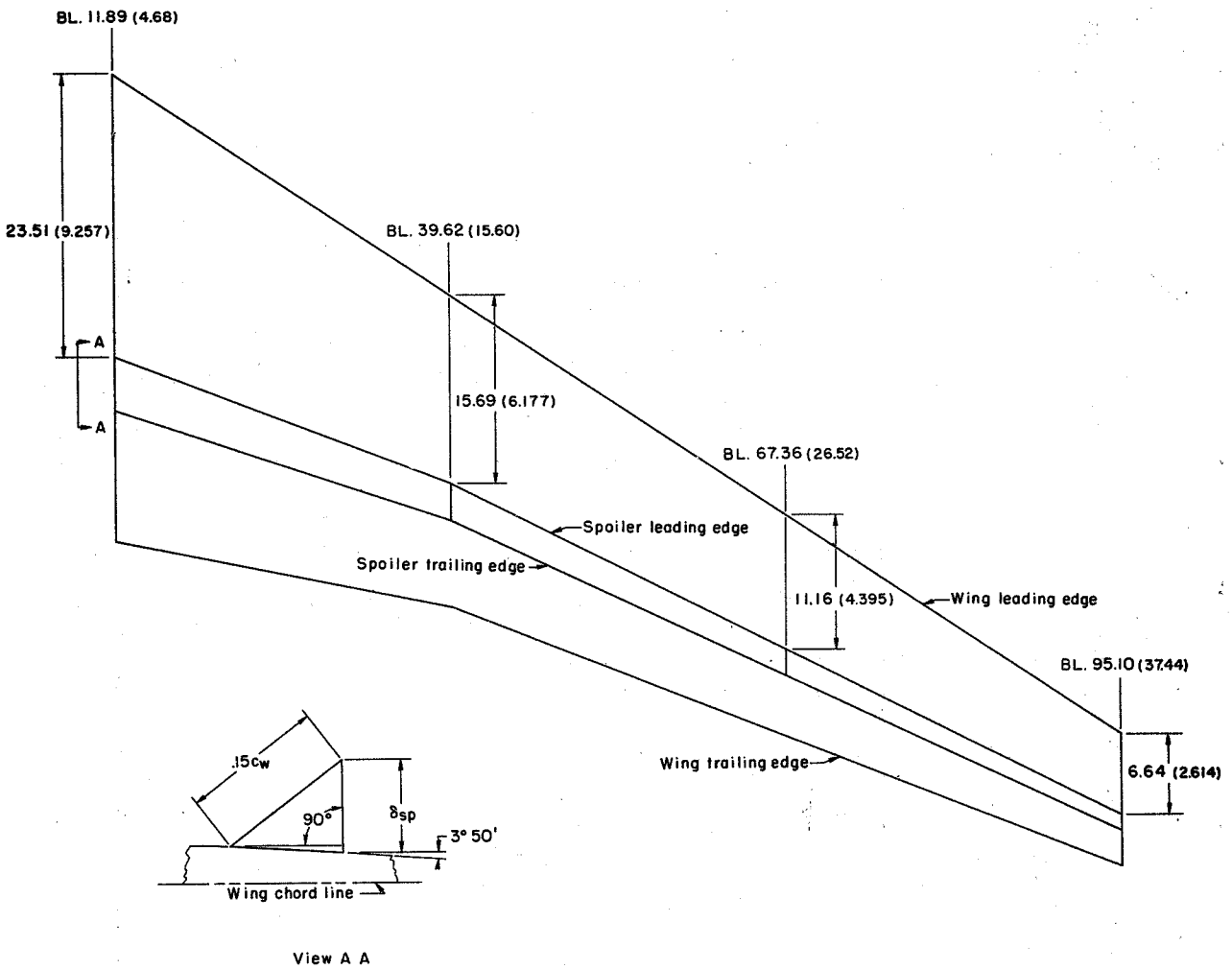

Figure 10.- Schematic of spoiler installation. All dimensions are in centimeters; parenthetical values are in inches. BL indicates butt line.

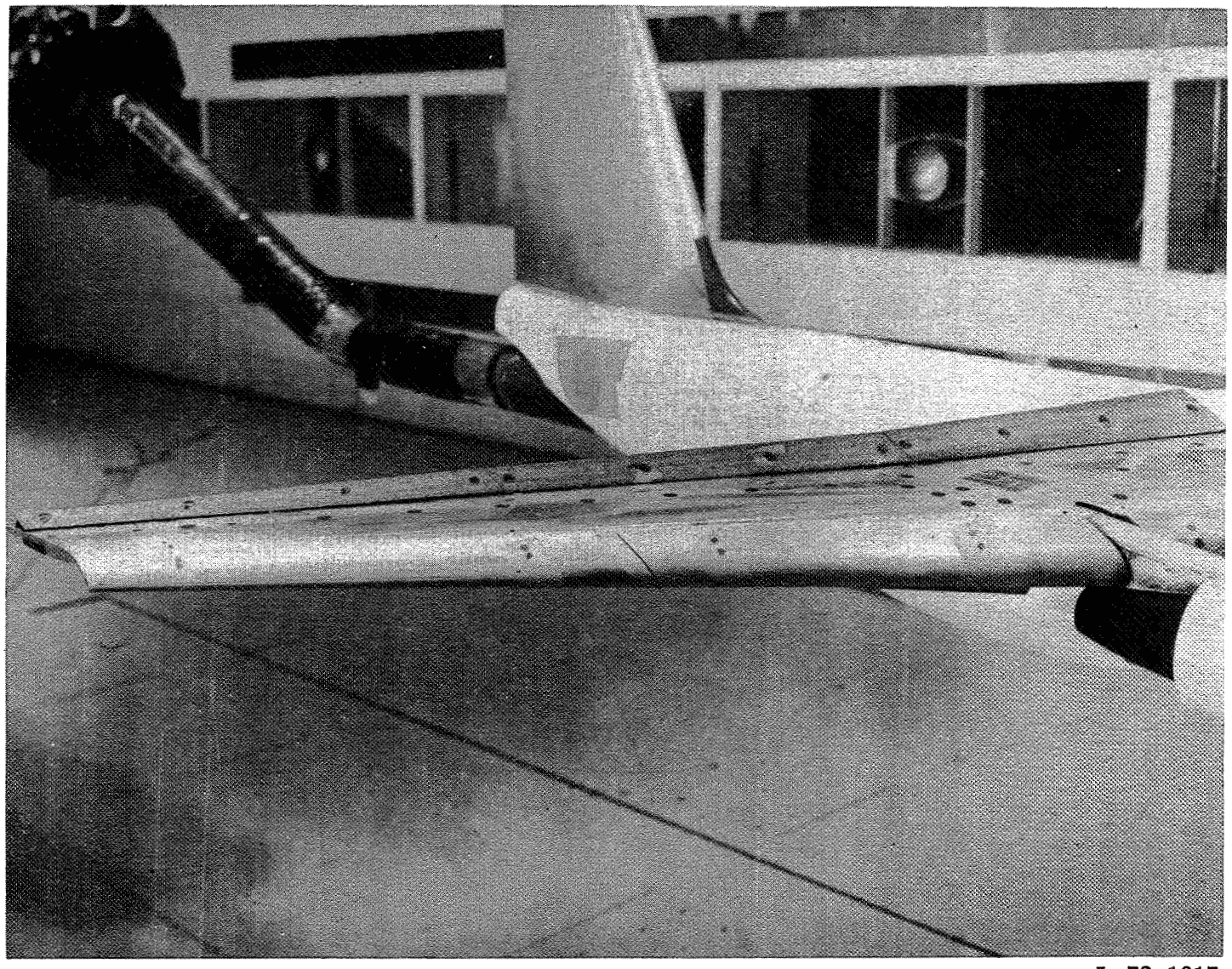

L-72-1317

Figure 11.- Photograph showing spoiler installed on wing of model.

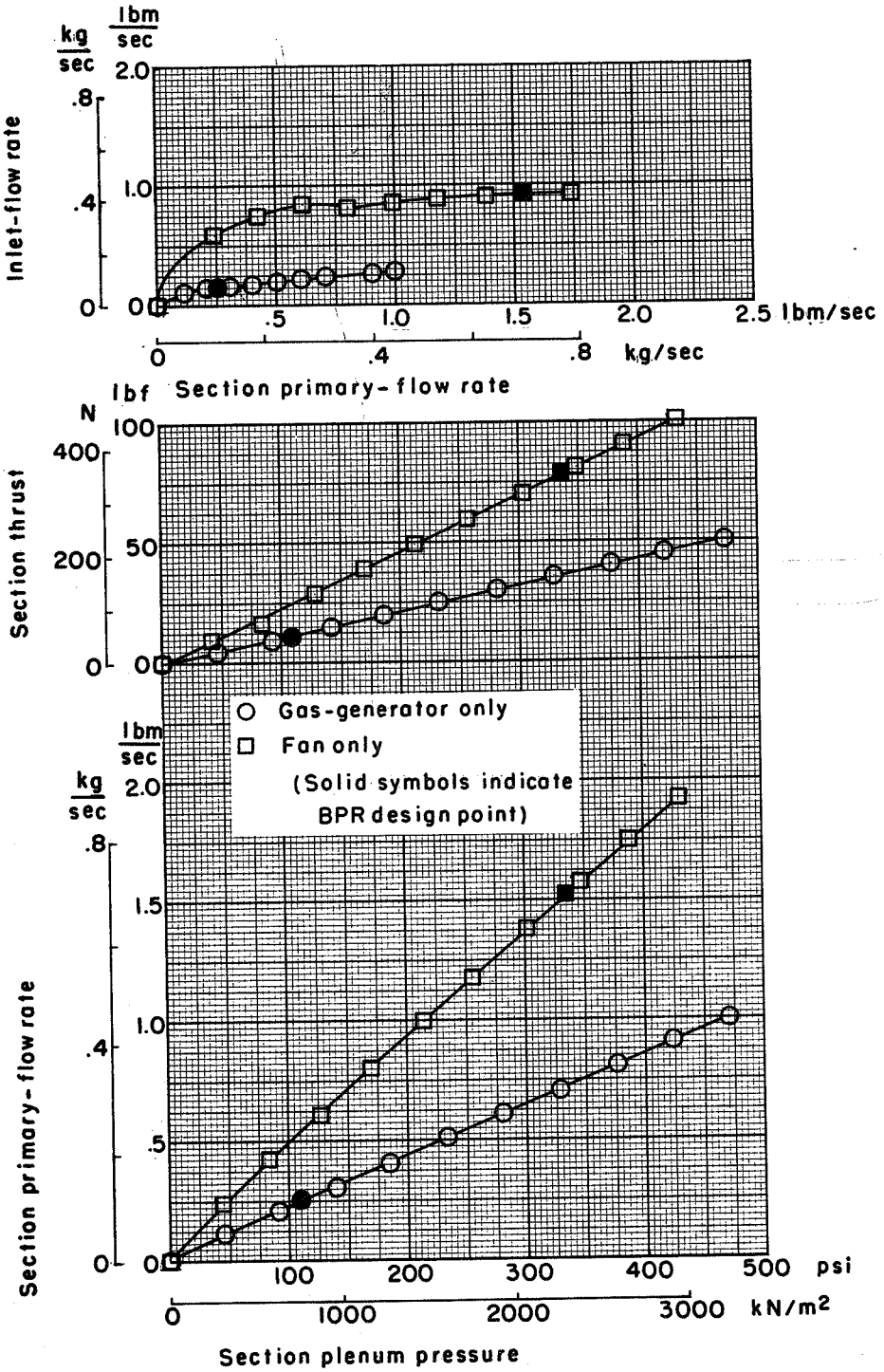

(a) BPR 6.2.

Figure 12.- Calibration curves for the engine simulators.

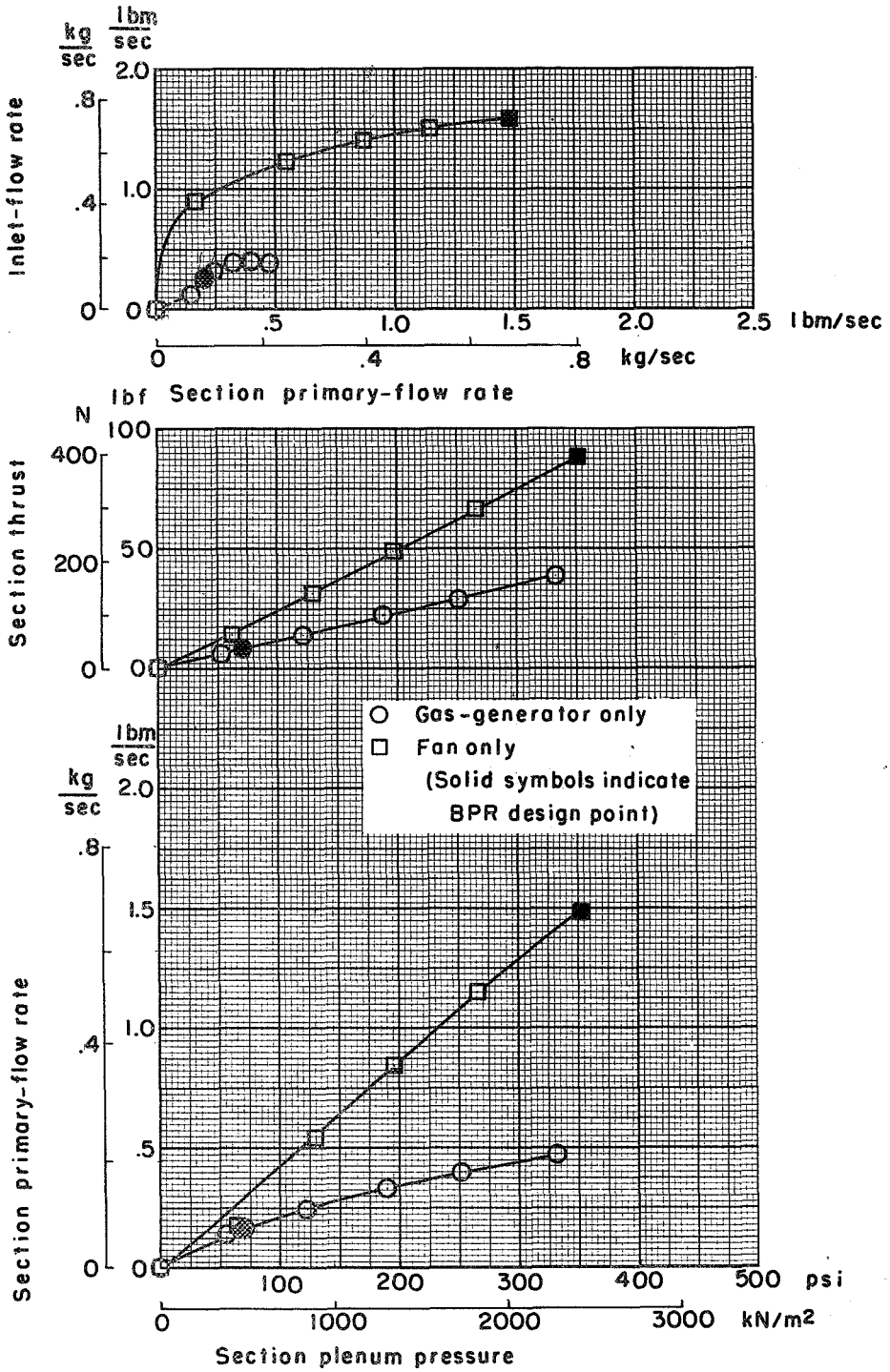

(b) BPR 10.0.

Figure 12.- Concluded.

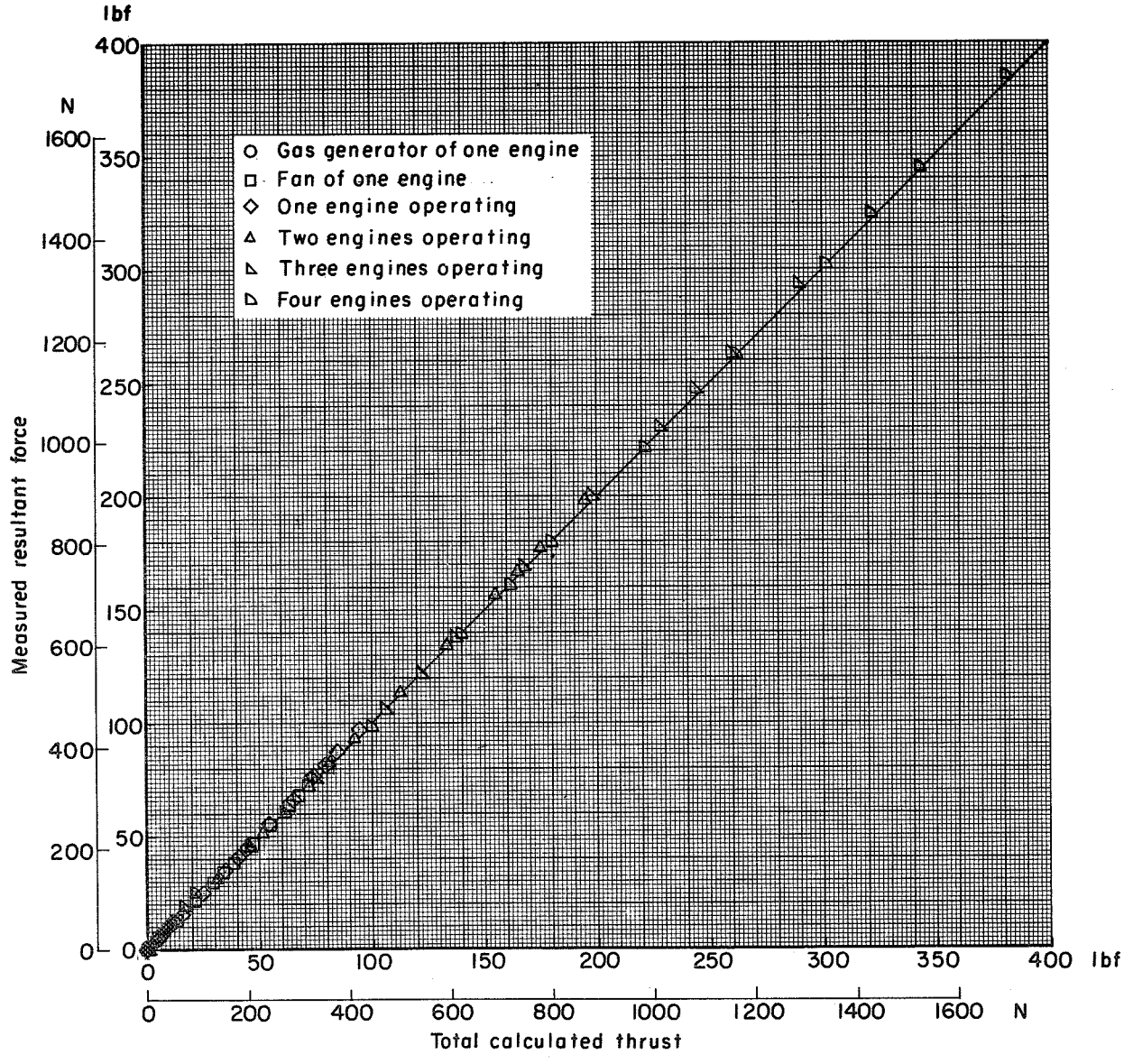

Figure 13.- Comparison of measured resultant force with total calculated thrust showing accuracy of thrust calibrations.

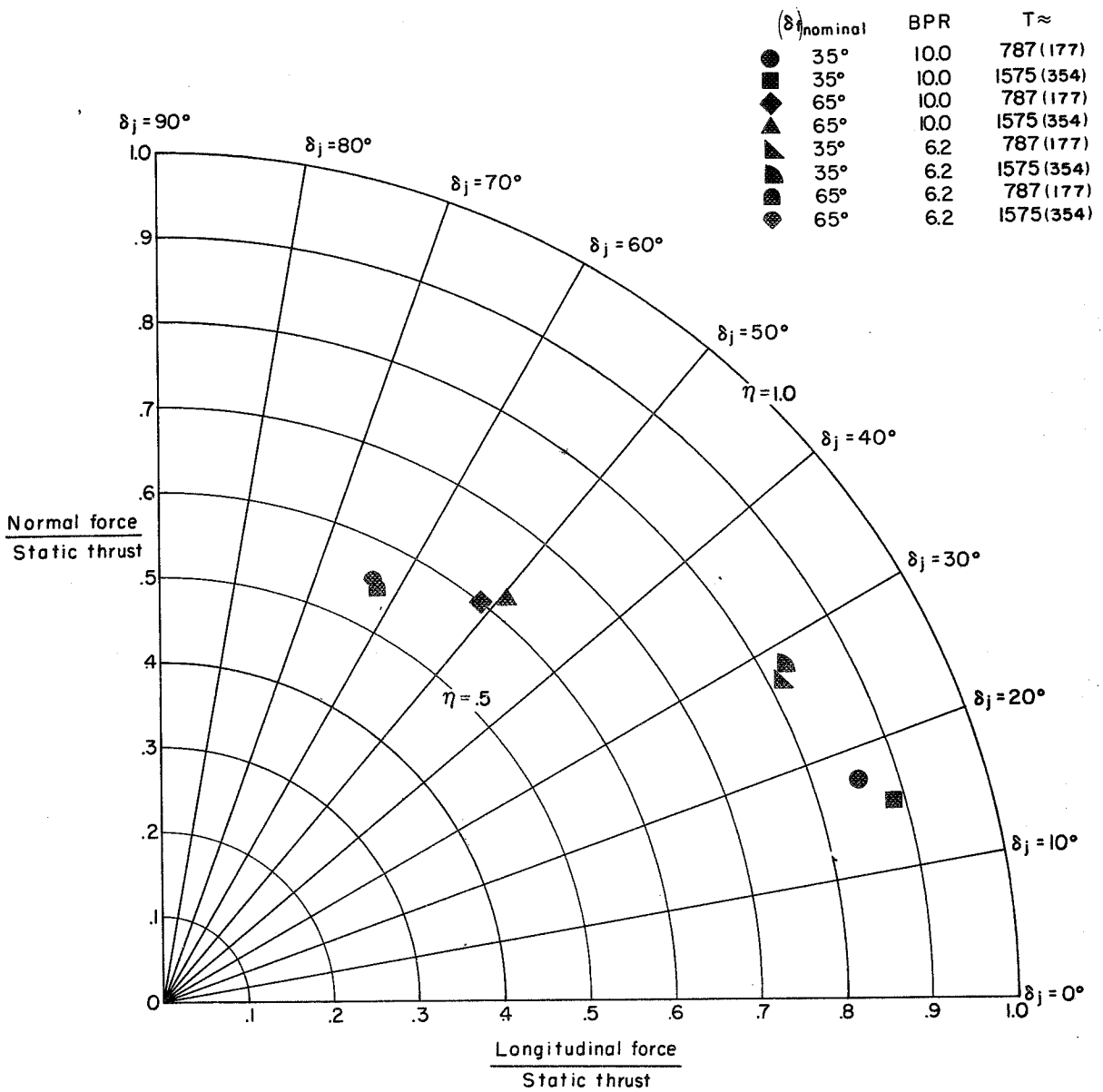

Figure 14.- Summary of static turning angles and thrust recovery factor.

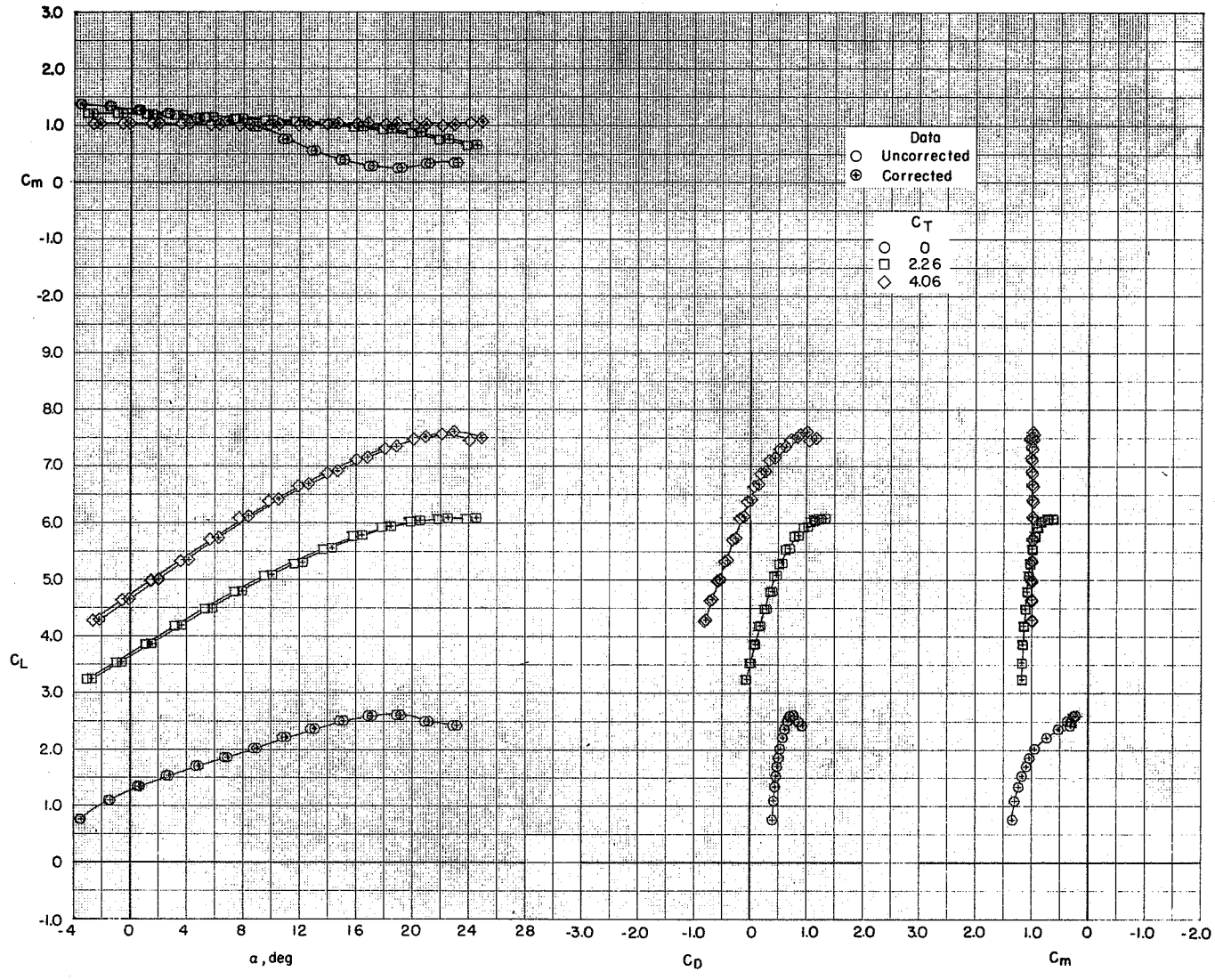

Figure 15.- Sample correction of V/STOL tunnel data to free air for landing configuration.

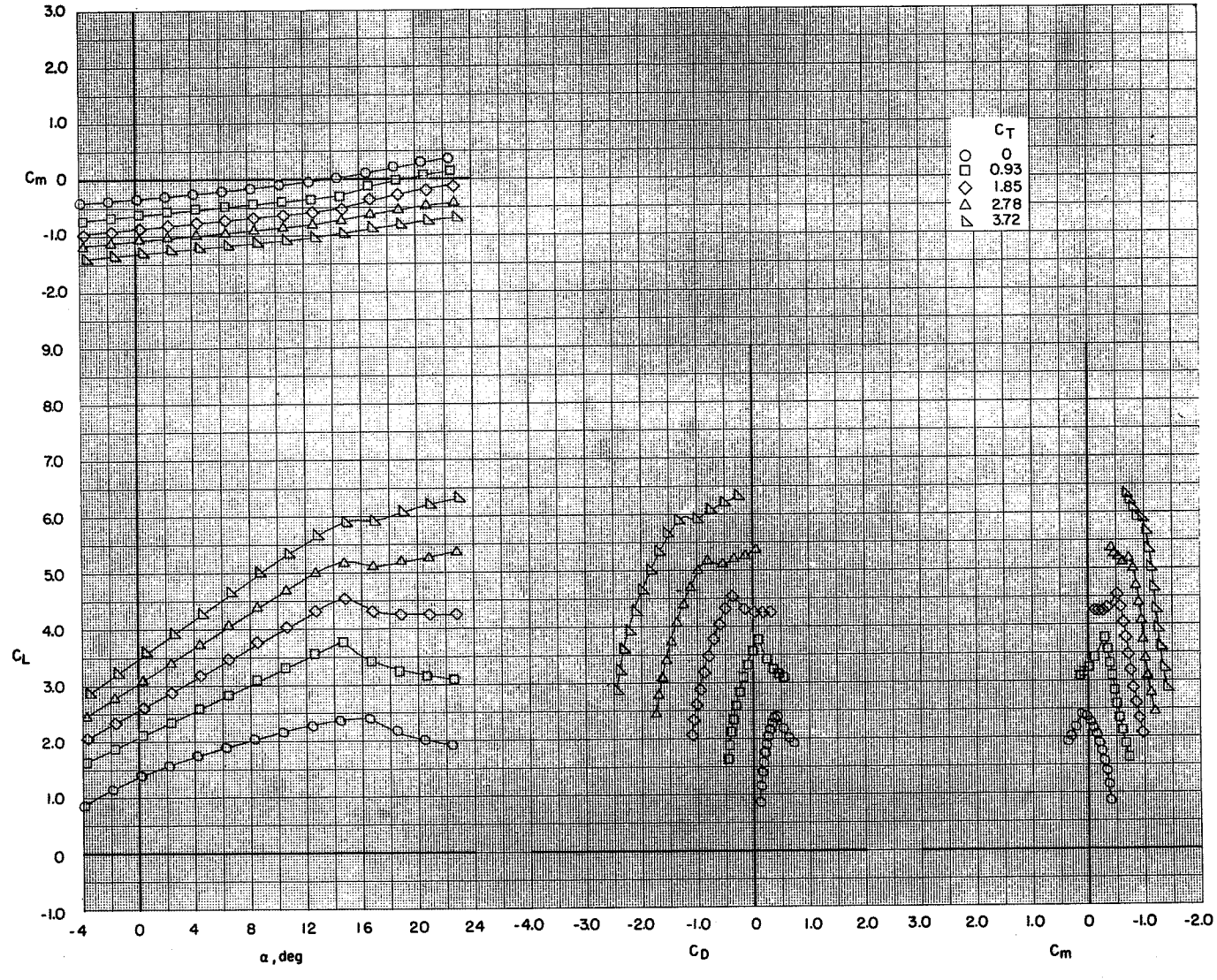

(a) $\delta_f = 0^o/35^o/35^o$.

Figure 16.- Effect of increasing thrust coefficient on the longitudinal aerodynamic characteristics of the model with various flap configurations. BPR 6.2; tail off; c_s = 15 percent; $\delta_s = 40^o$.

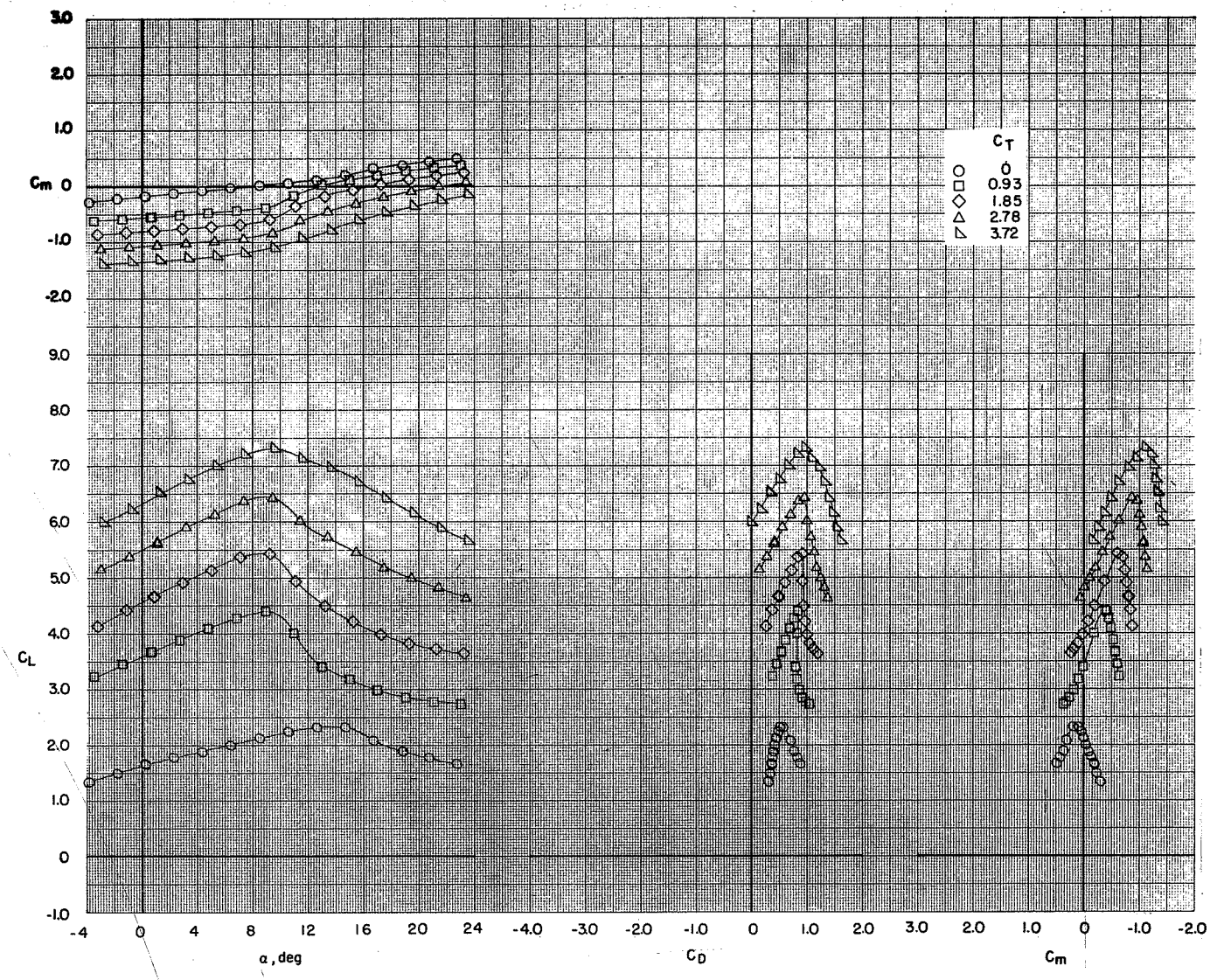

(b) $\delta_f = 0^o/65^o/65^o$.

Figure 16.- Concluded.

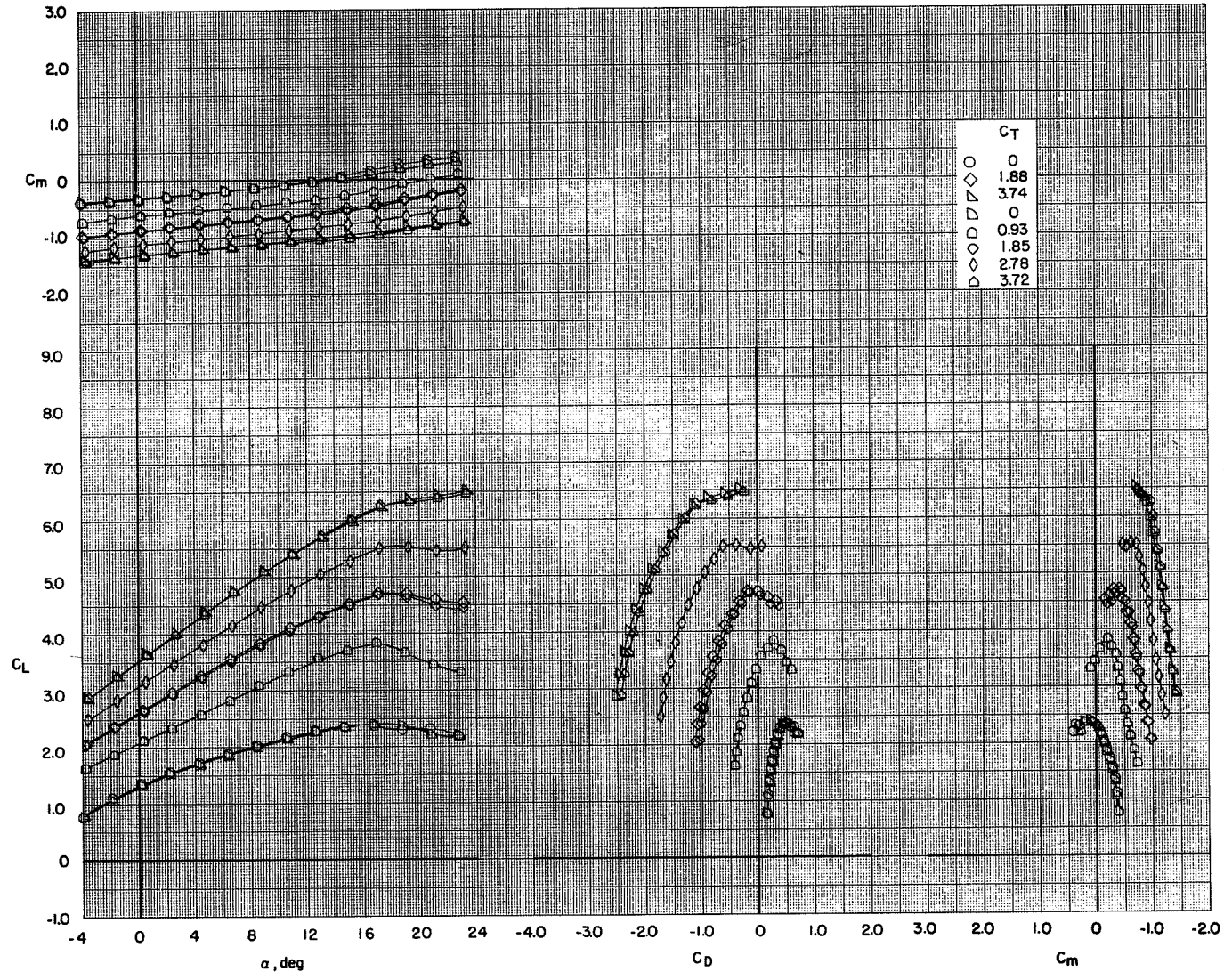

(a) $\delta_f = 0^o/35^o/35^o$.

Figure 17.- Effect of increasing thrust coefficient on the longitudinal aerodynamic characteristics of the model with various flap configurations. BPR 6.2; tail off; c_S = 15 percent; $\delta_S = 50^o$.

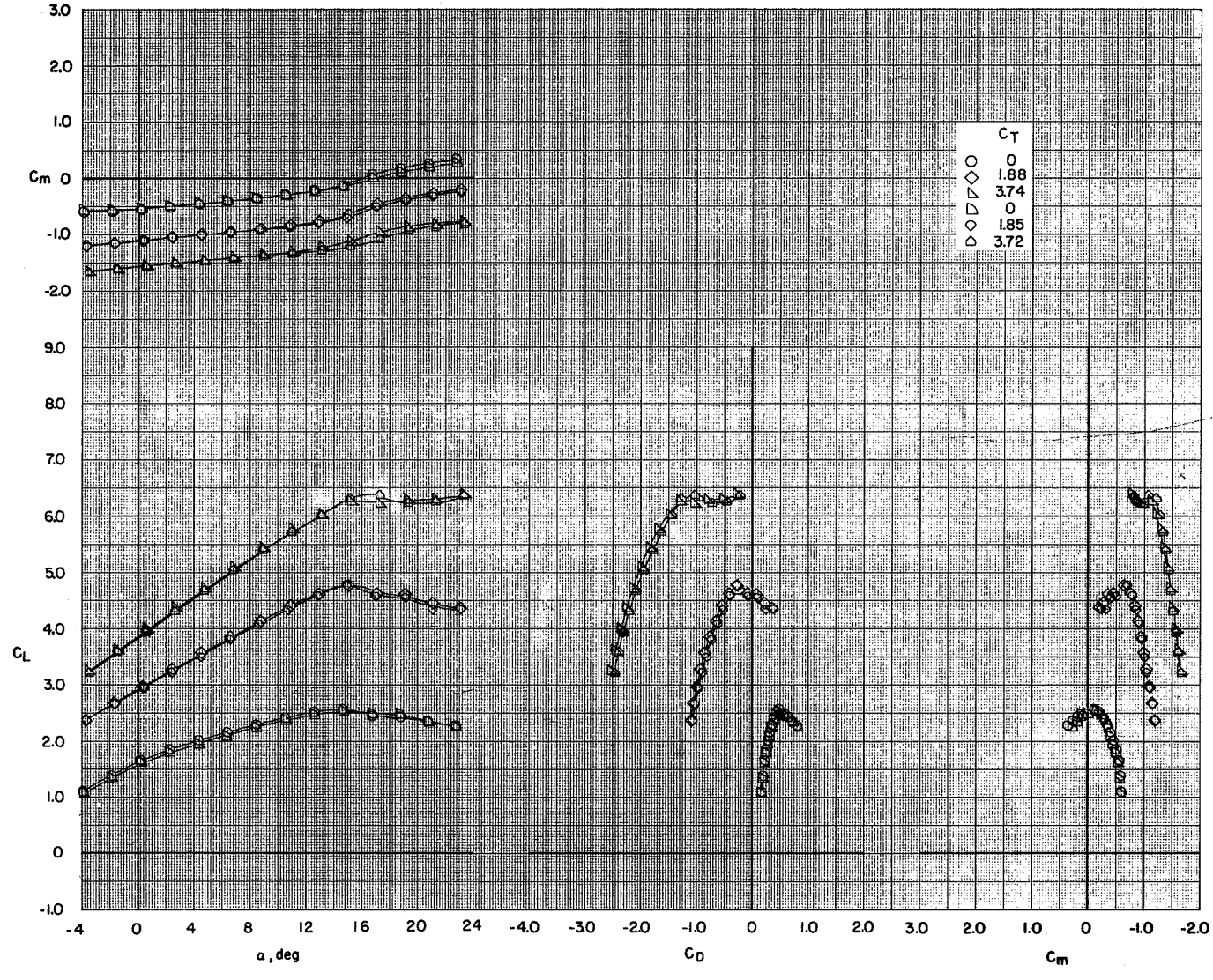

(b) $\delta_f = 35^o/35^o/35^o$.

Figure 17.- Continued.

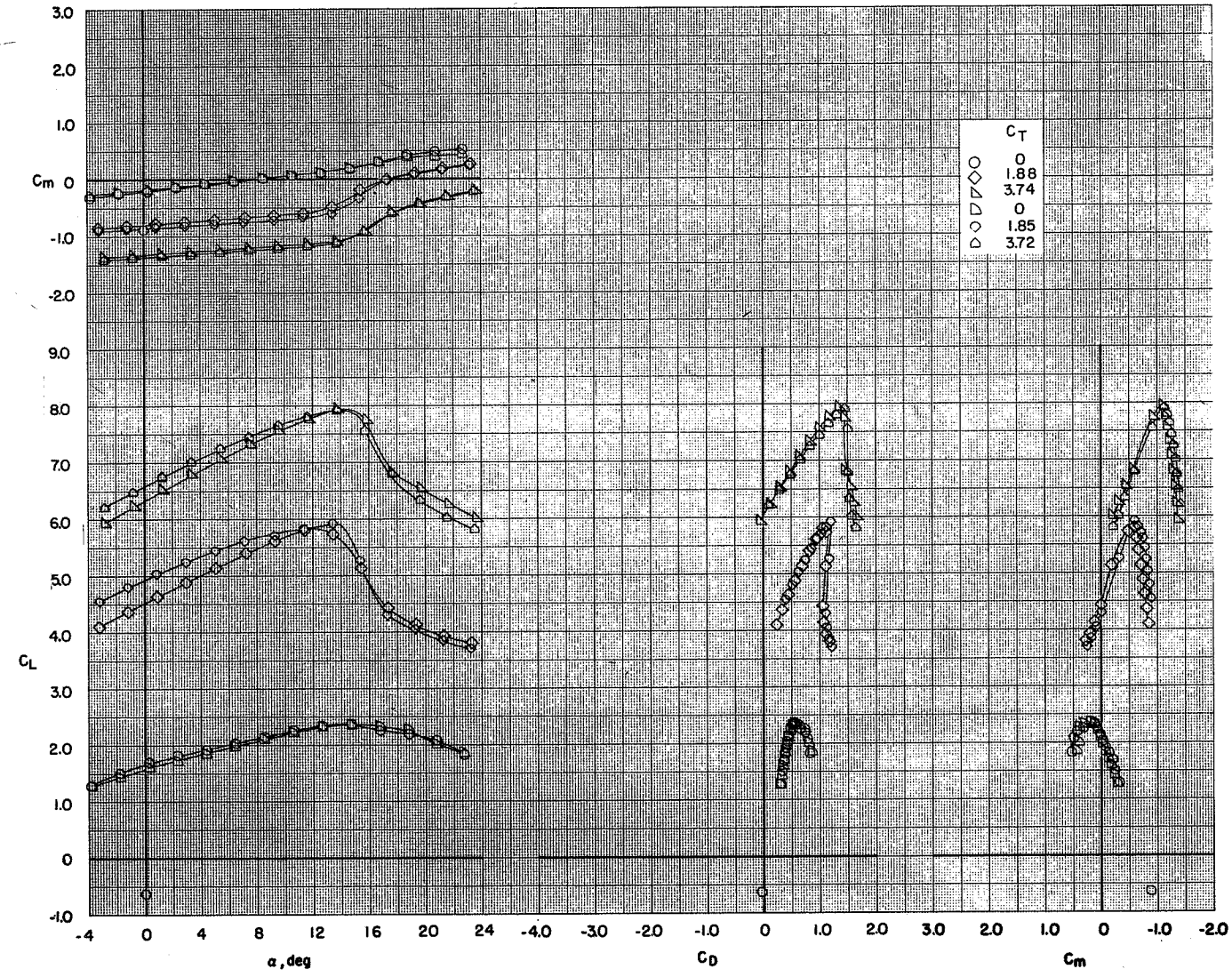

(c) $\delta_f = 0^o/65^o/65^o$.

Figure 17.- Continued.

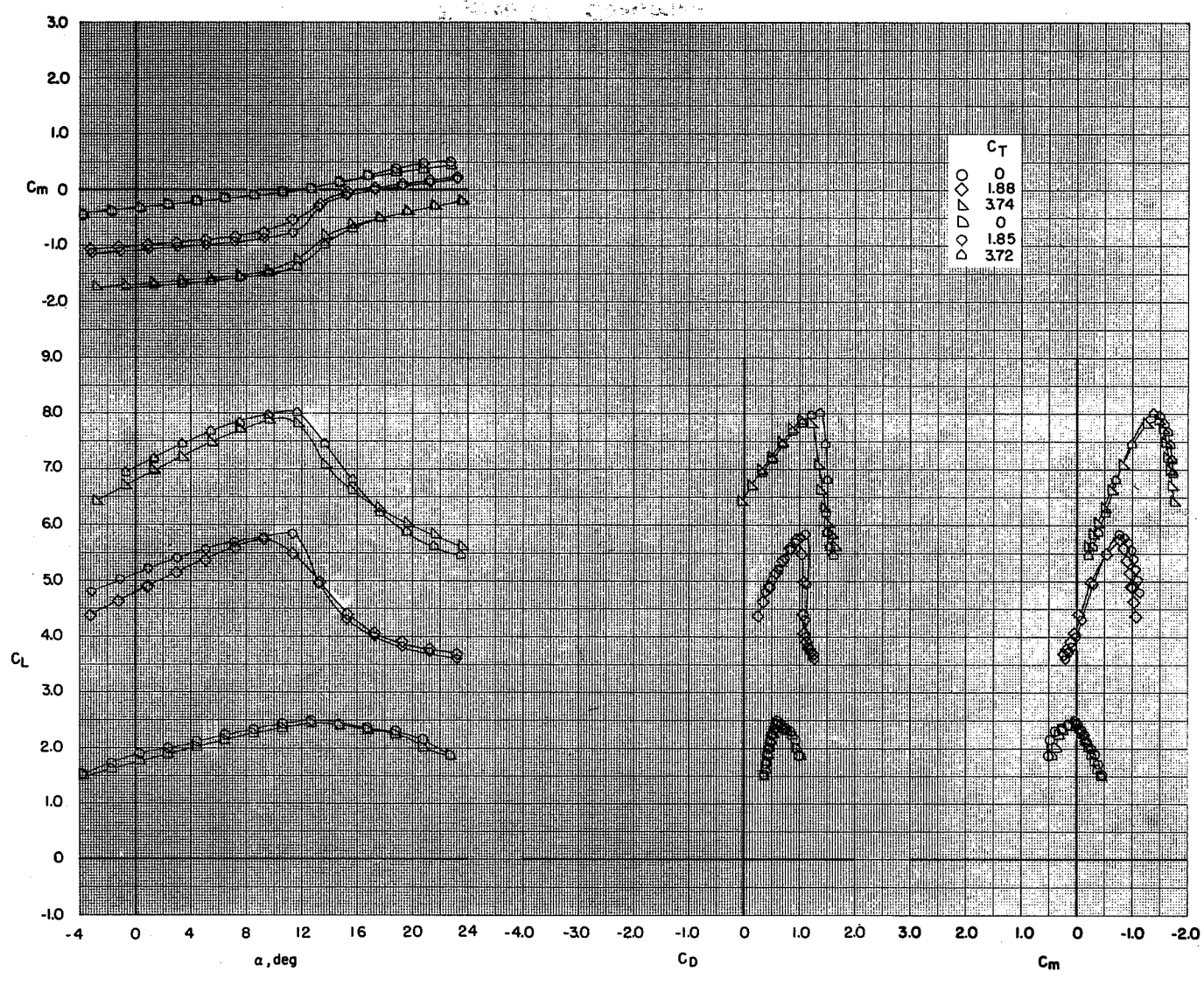

(d) $\delta_f = 65^o/65^o/65^o$.

Figure 17.- Concluded.

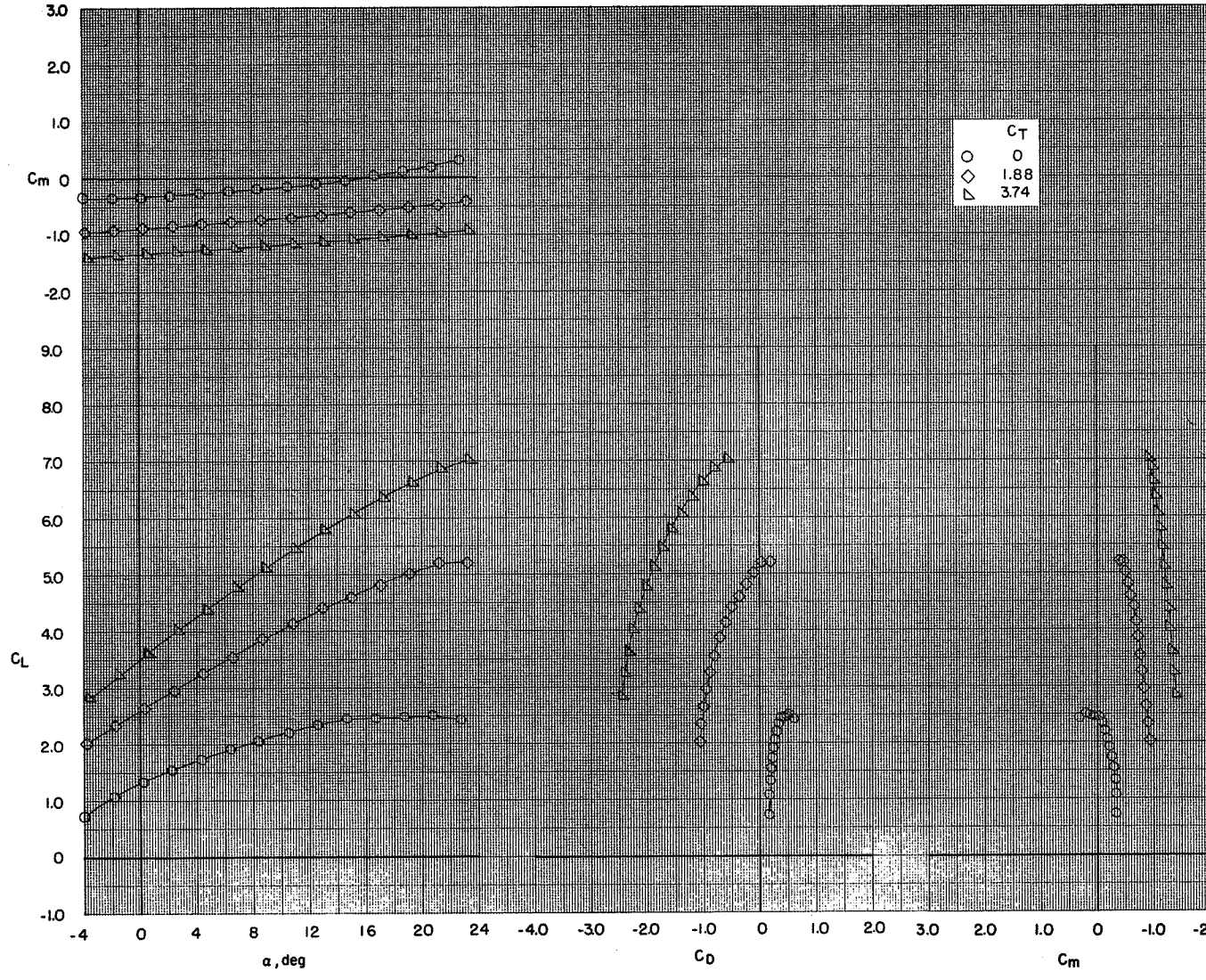

(a) $\delta_f = 0^o/35^o/35^o$.

Figure 18.- Effect of increasing thrust coefficient on the longitudinal aerodynamic characteristics of the model with various flap configurations. BPR 6.2; tail off; c_s = 20 percent; $\delta_s = 50^o$.

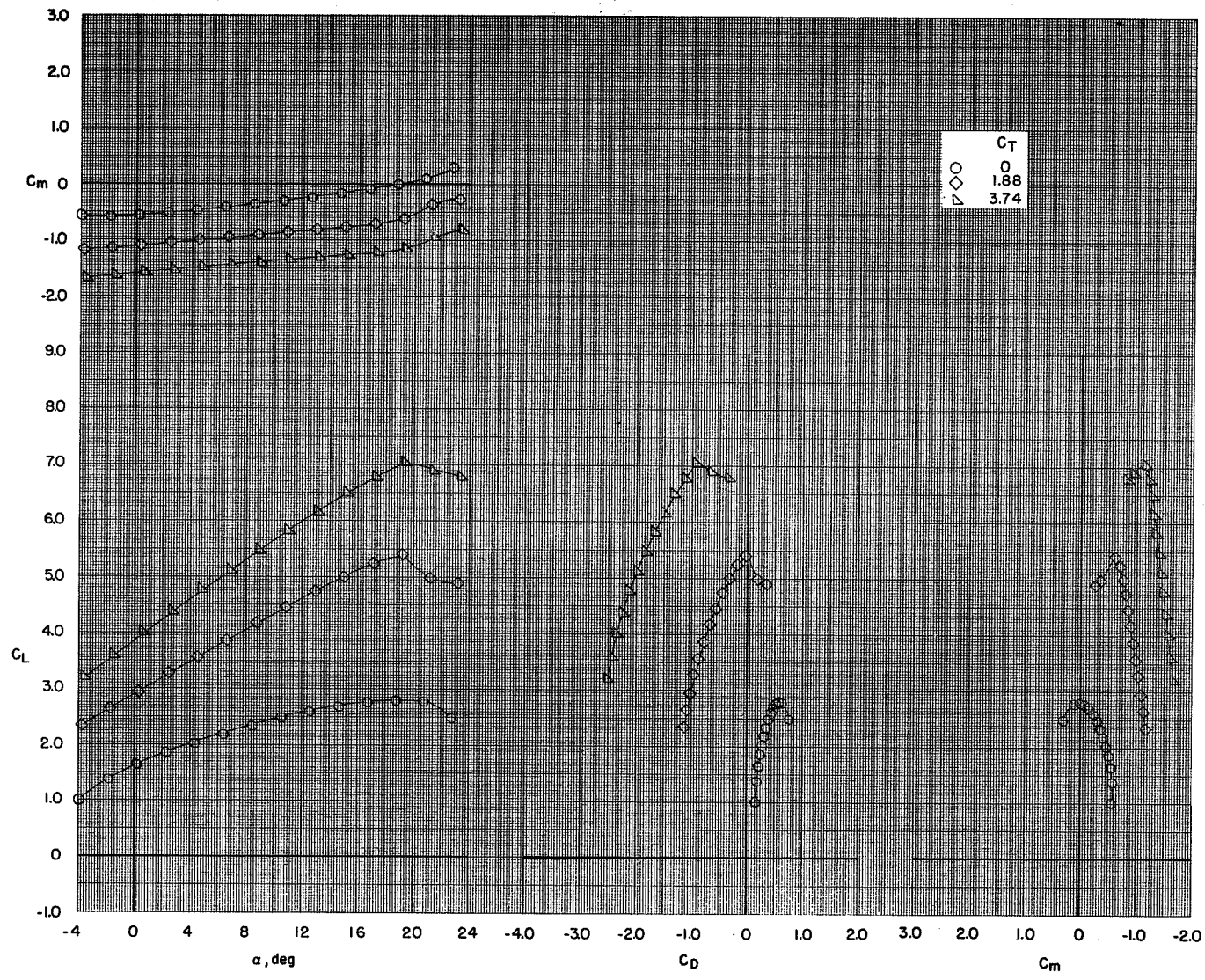

(b) $\delta_f = 35^o/35^o/35^o$.

Figure 18.- Continued.

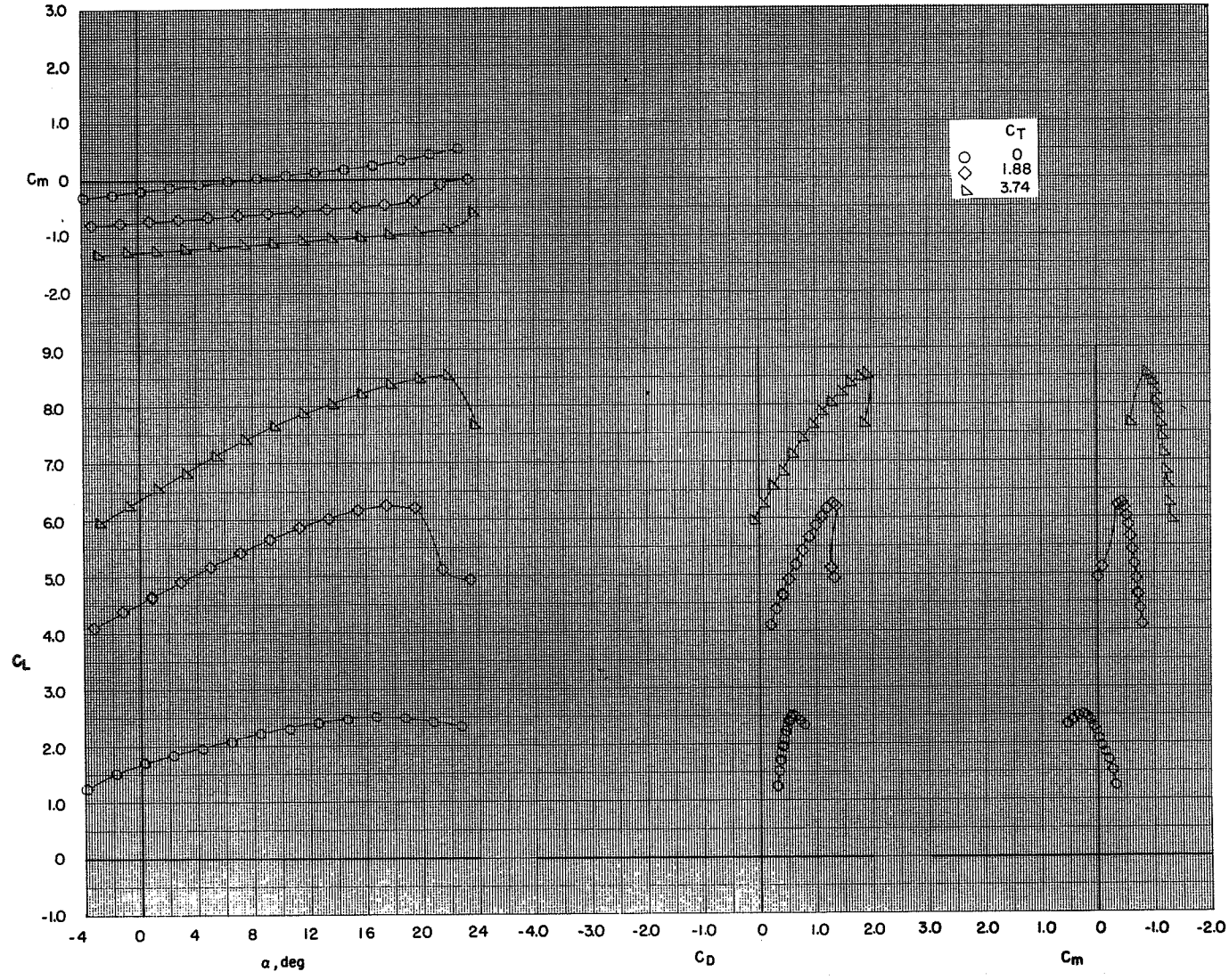

(c) $\delta_f = 0^o/65^o/65^o$.

Figure 18.- Continued.

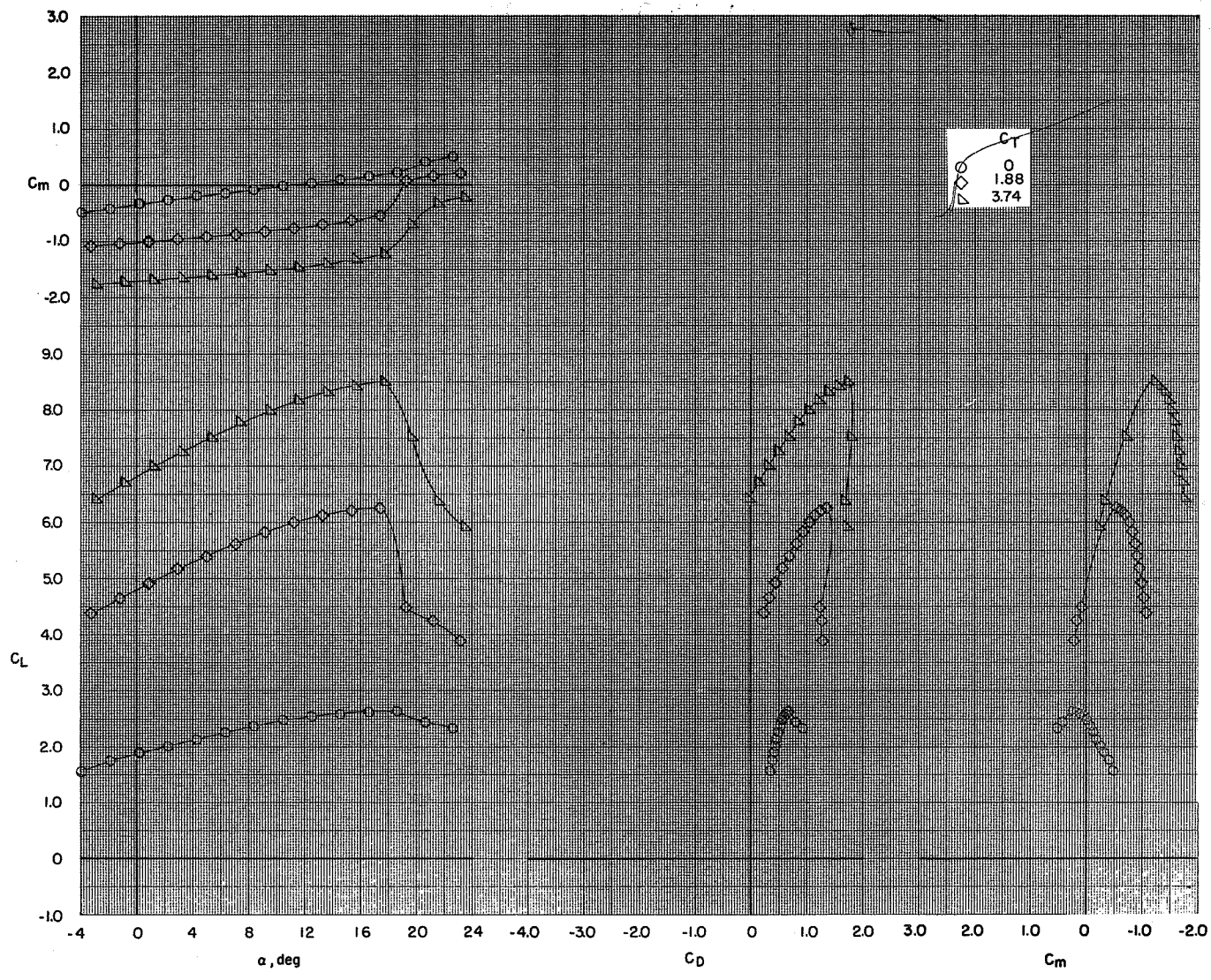

(d) $\delta_f = 65^o/65^o/65^o$.

Figure 18.- Concluded.

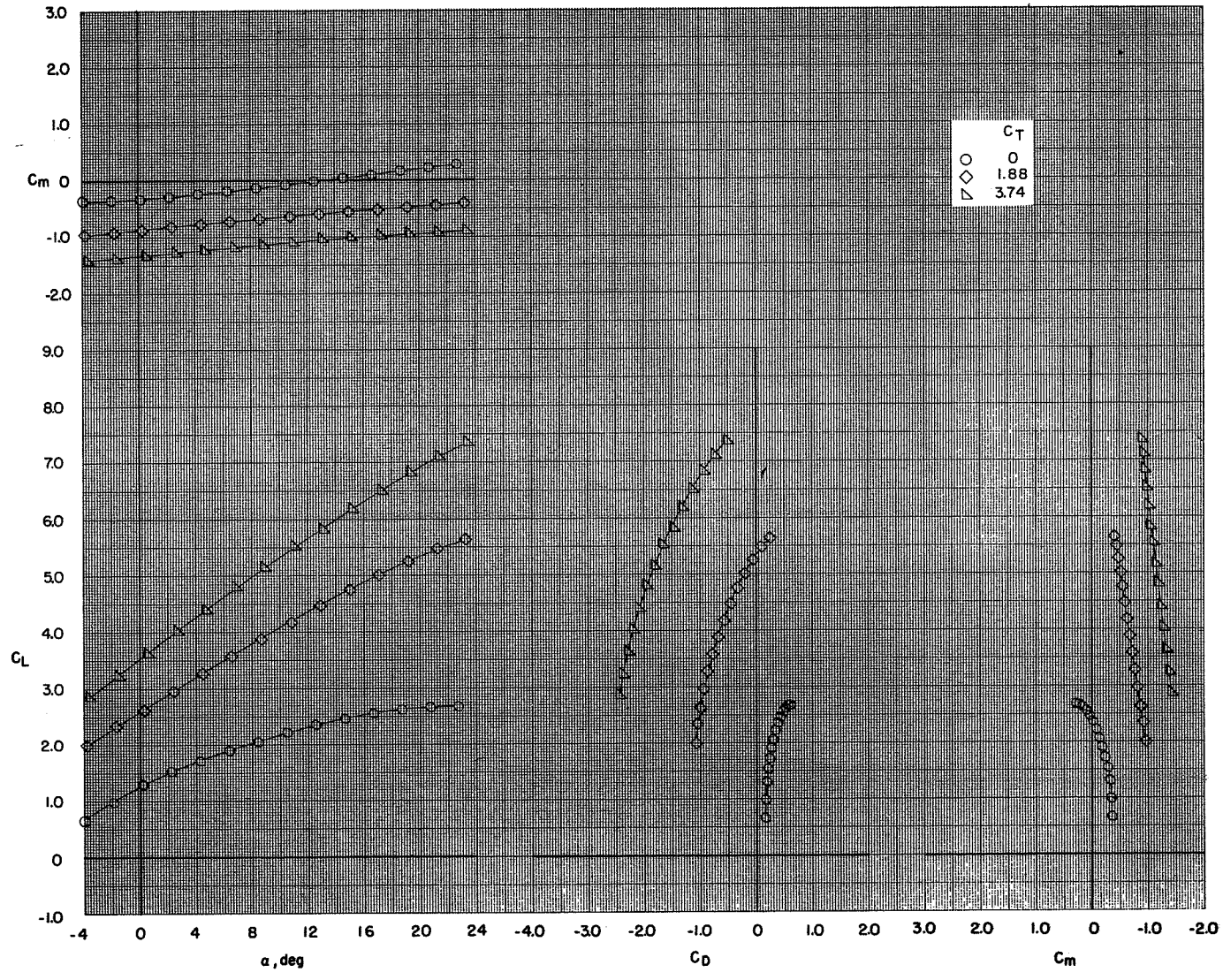

(a) $\delta_f = 0^o/35^o/35^o$.

Figure 19.- Effect of increasing thrust coefficient on the longitudinal aerodynamic characteristics of the model with various flap configurations. BPR 6.2; tail off; c_s = 25 percent; $\delta_s = 50^o$.

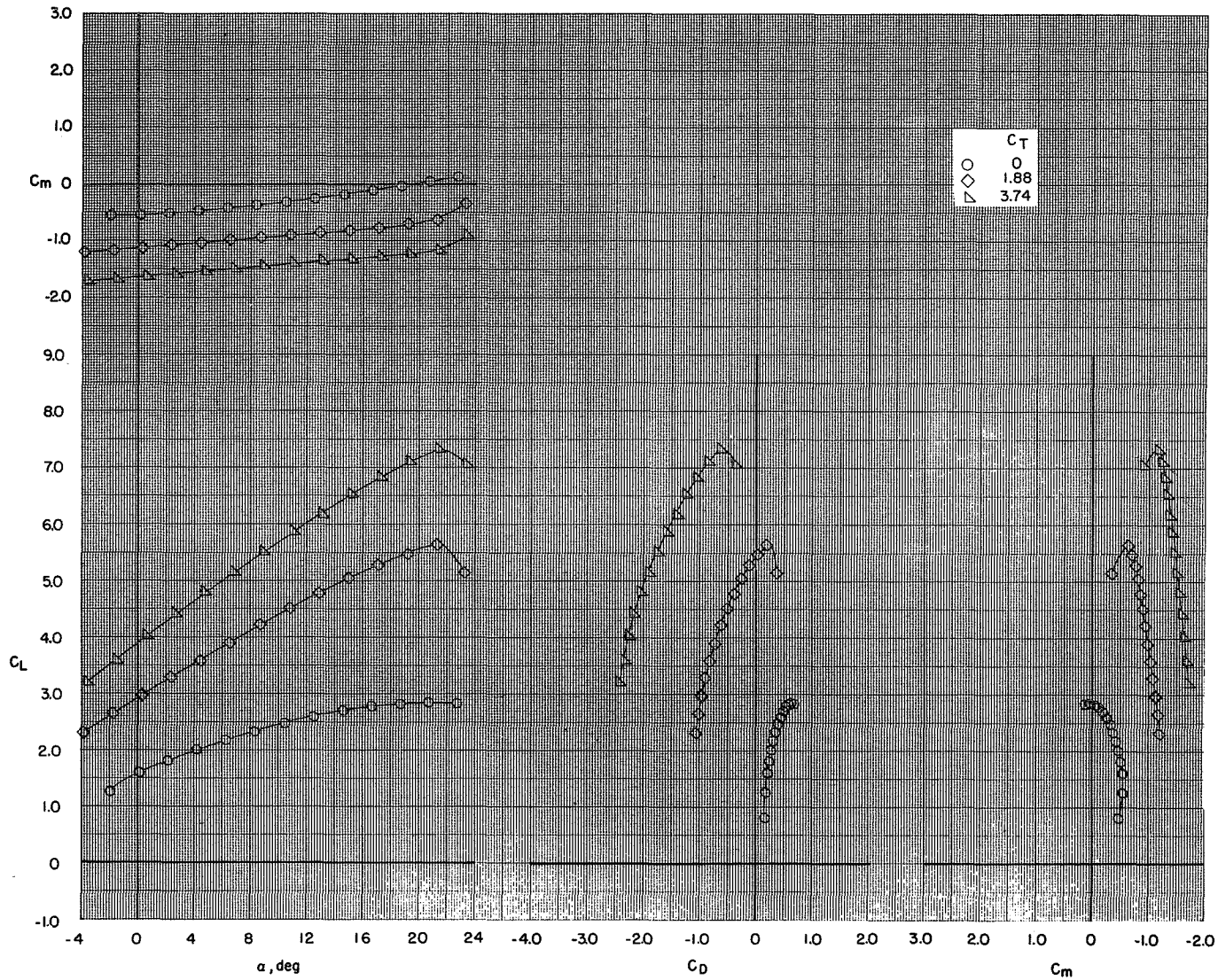

(b) $\delta_f = 35^o/35^o/35^o$.

Figure 19.- Continued.

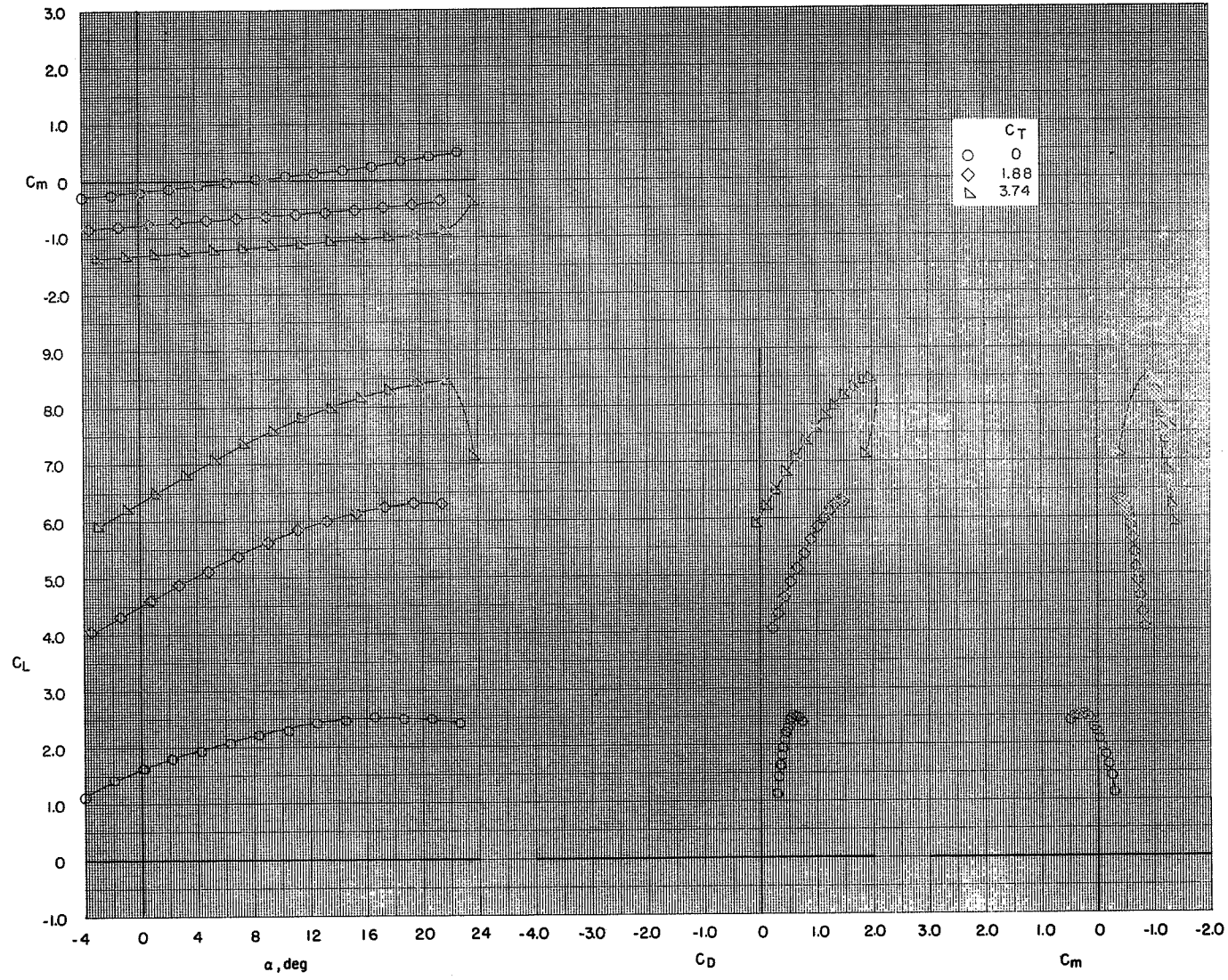

(c) $\delta_f = 0^o/65^o/65^o$.

Figure 19.- Continued.

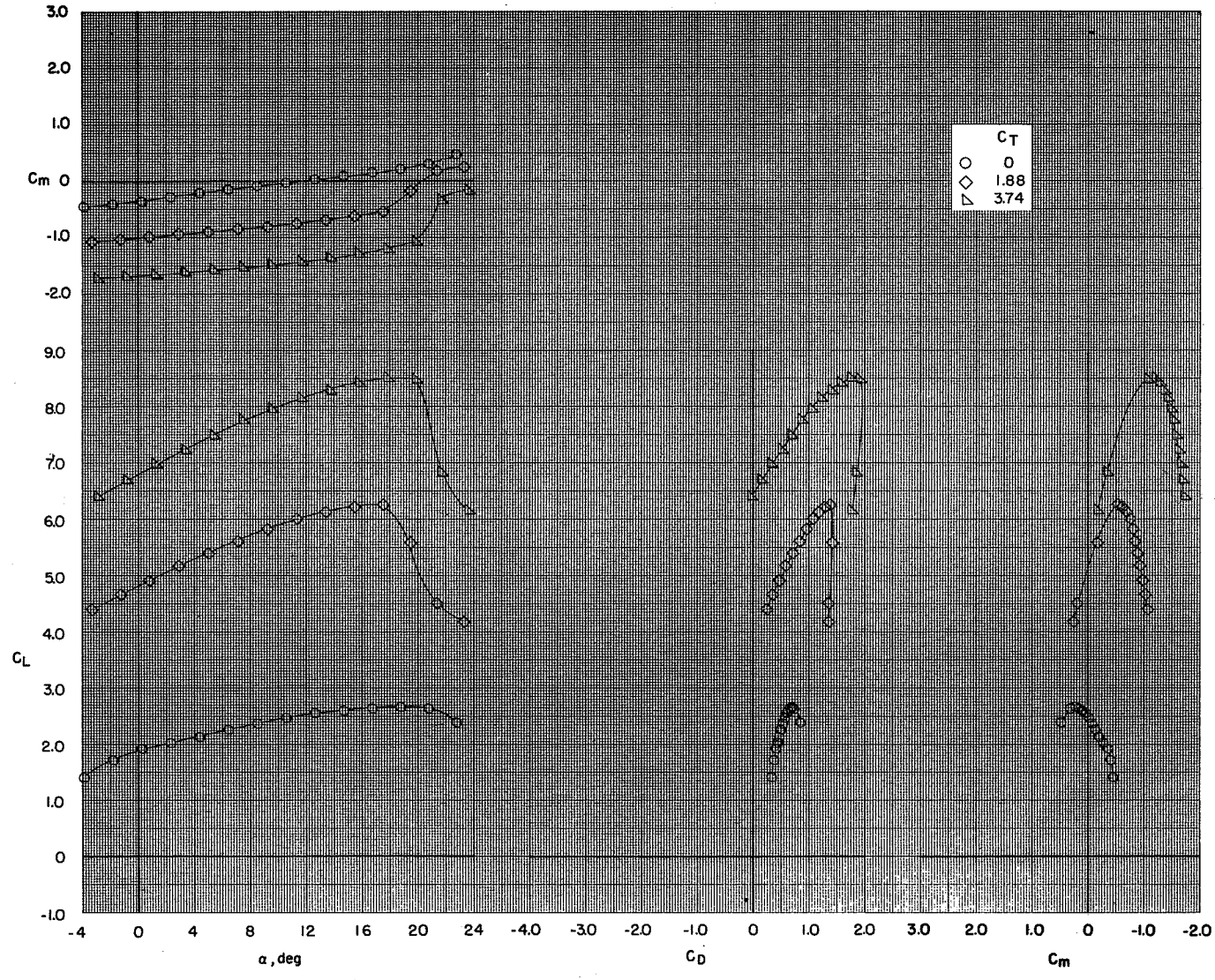

(d) $\delta_f = 65^o/65^o/65^o$.

Figure 19.- Concluded.

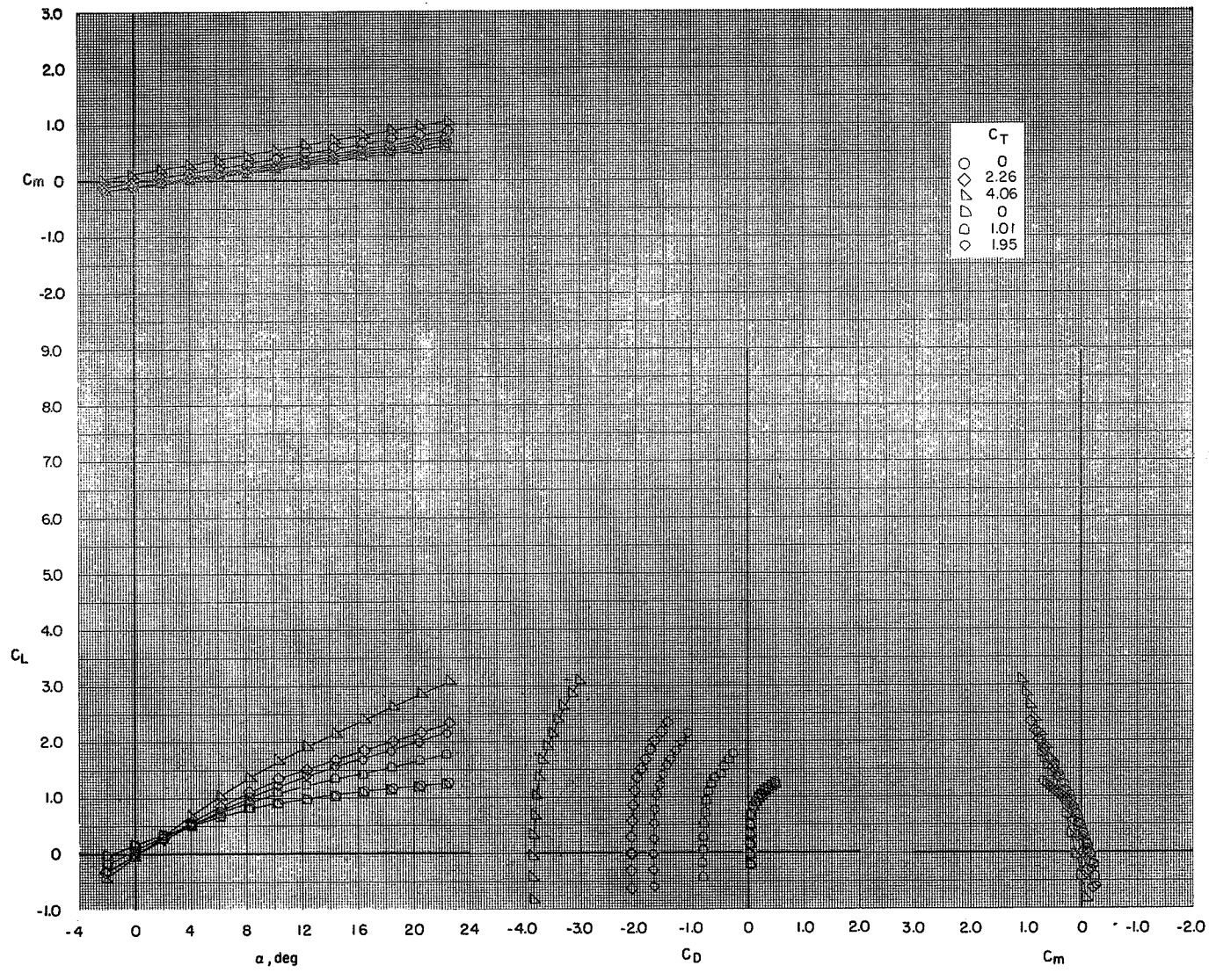

(a) $\delta_f = 0^o/0^o/0^o$.

Figure 20.- Effect of increasing thrust coefficient on the longitudinal aerodynamic characteristics of the model with various flap configurations. BPR 10.0; tail off; slat off.

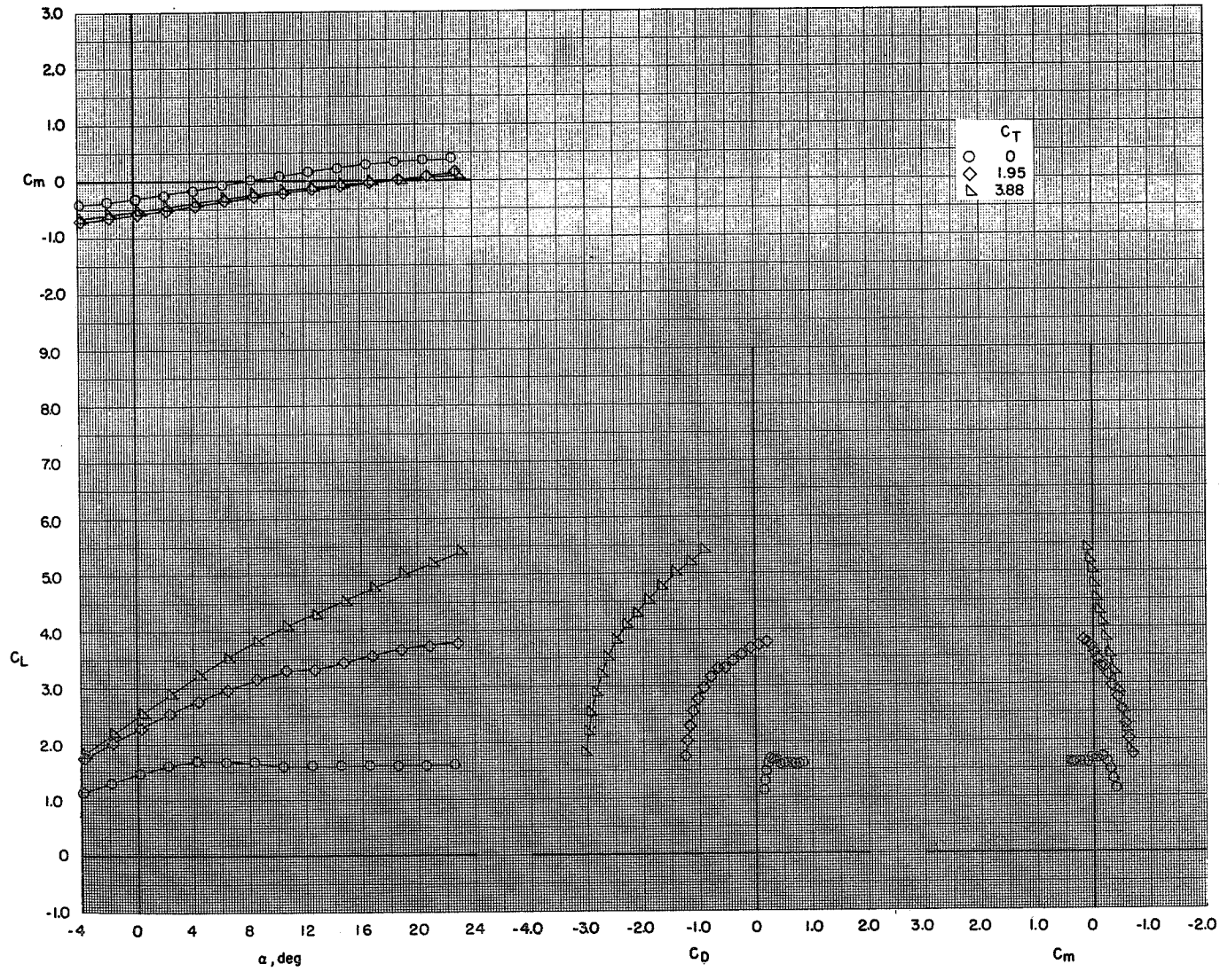

(b) $\delta_f = 0^o/35^o/35^o$.

Figure 20.- Continued.

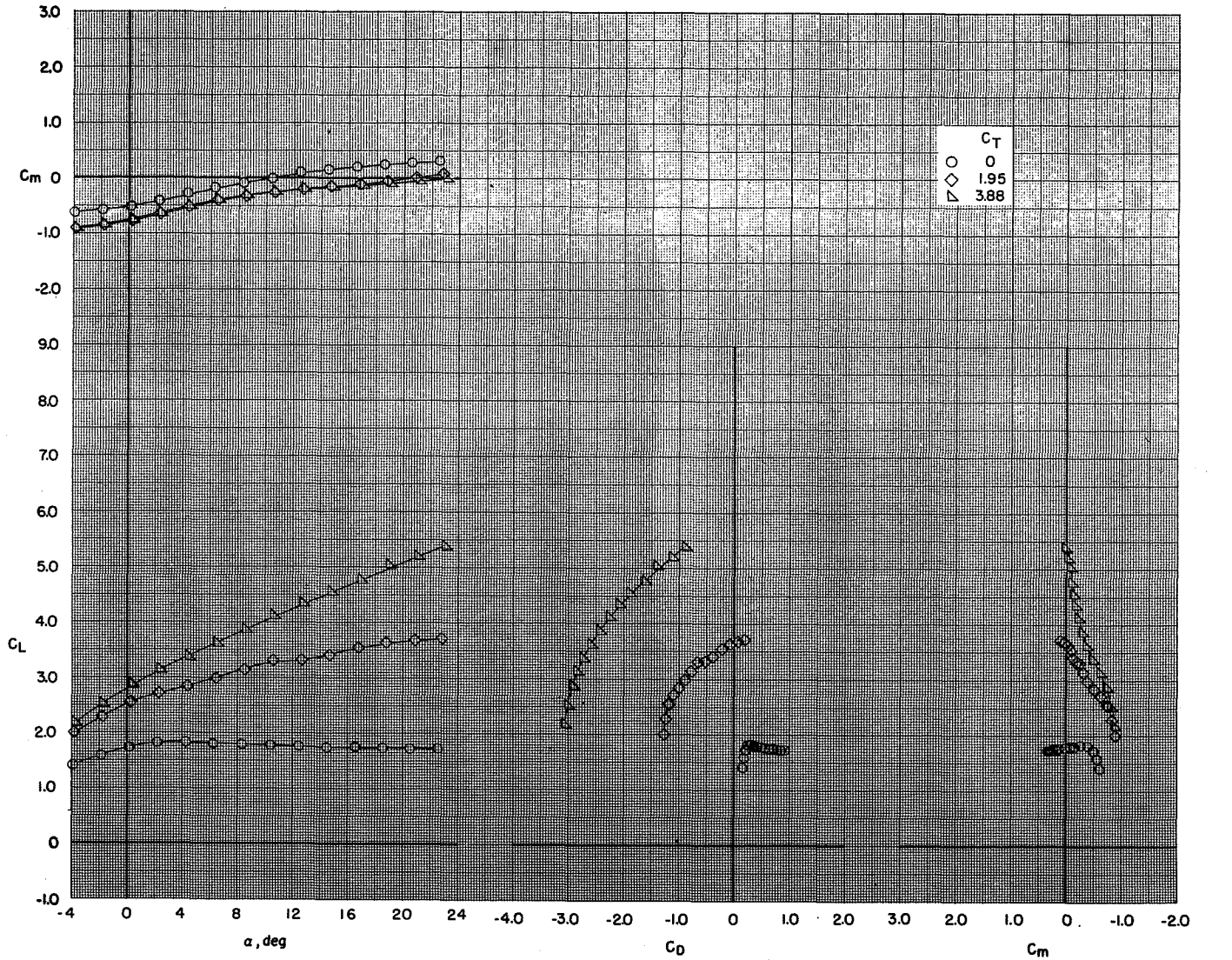

(c) $\delta_f = 35^o/35^o/35^o$.

Figure 20.- Continued.

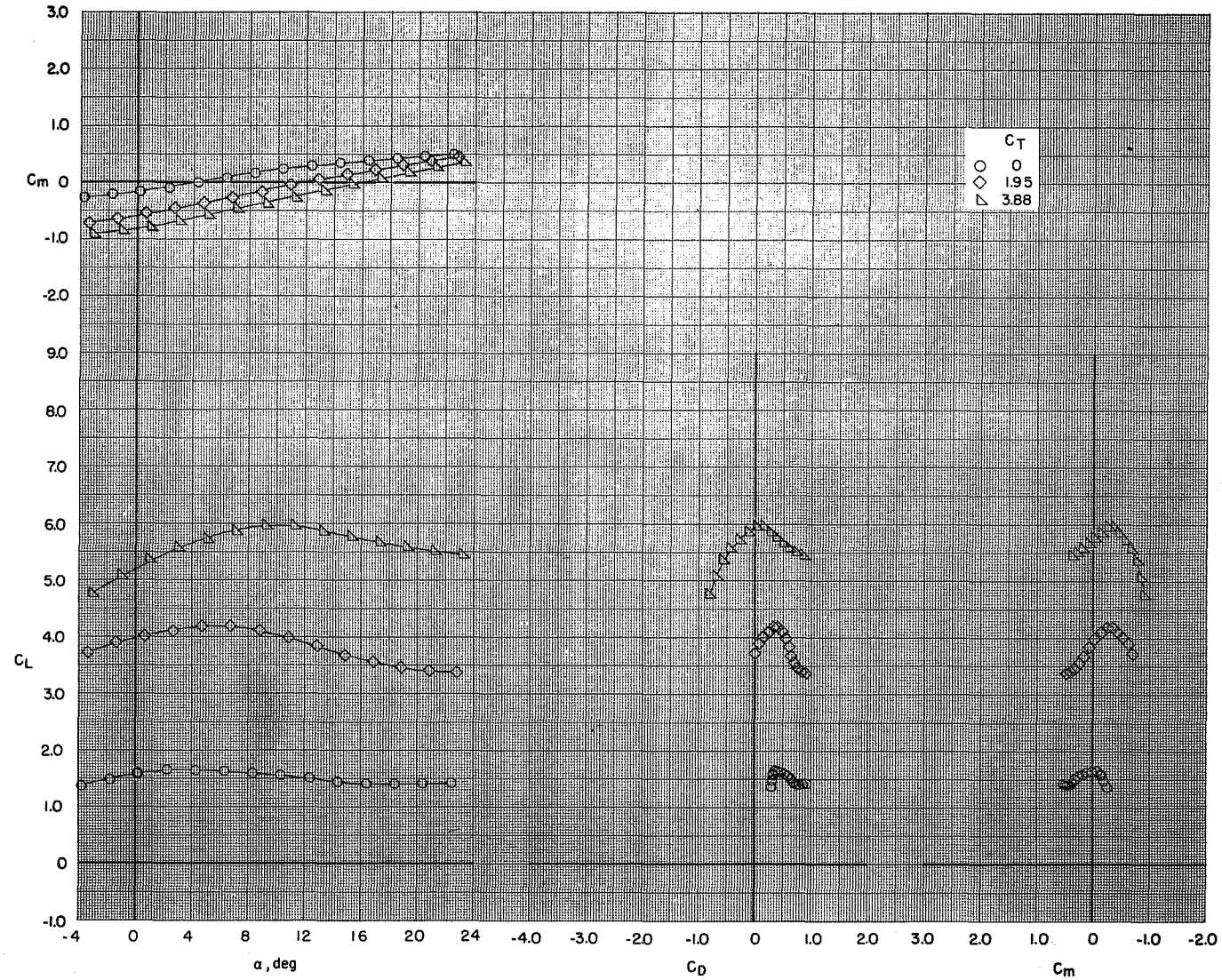

(d) $\delta_f = 0^o/65^o/65^o$.

Figure 20.- Continued.

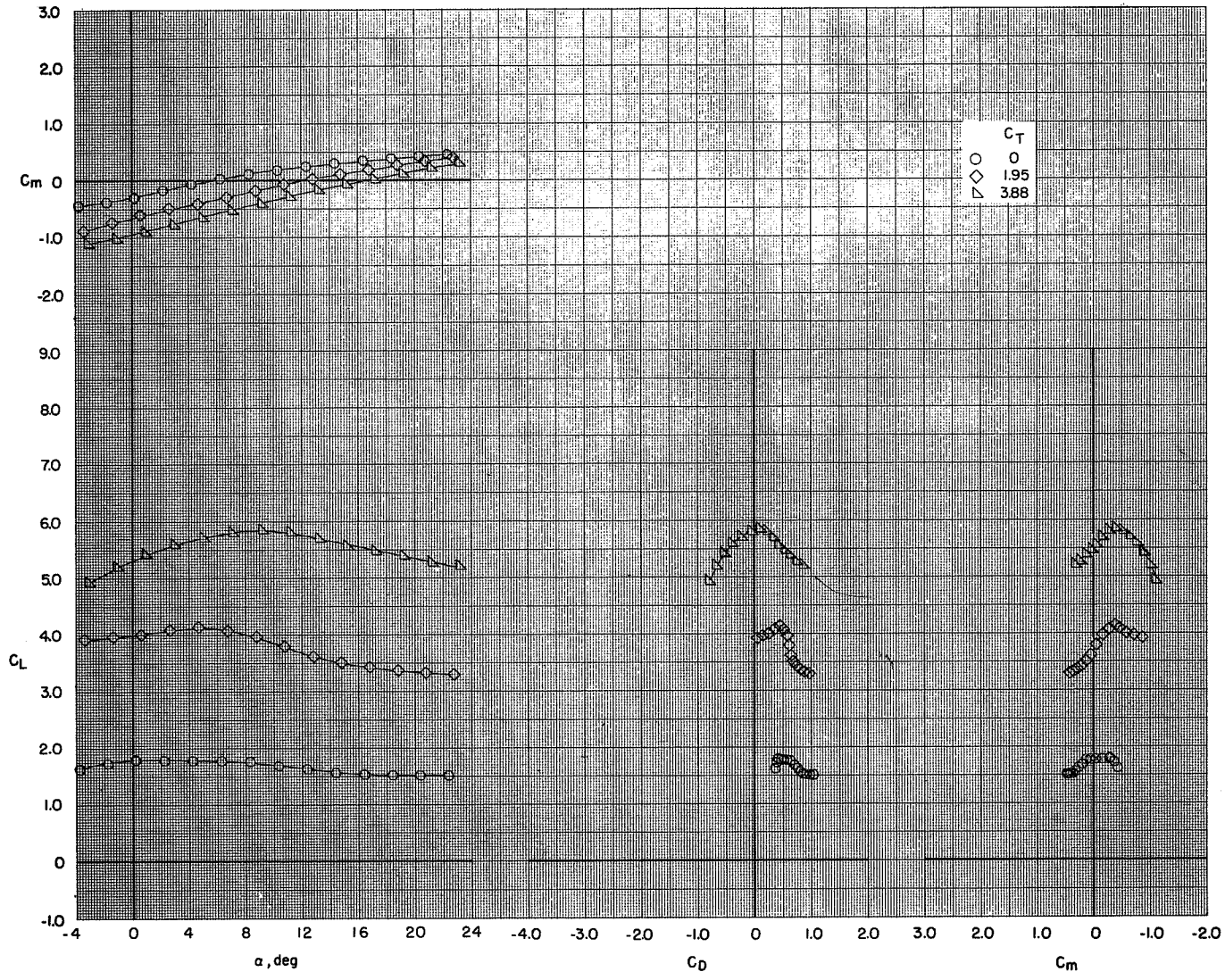

(e) $\delta_f = 65^o/65^o/65^o$.

Figure 20.- Concluded.

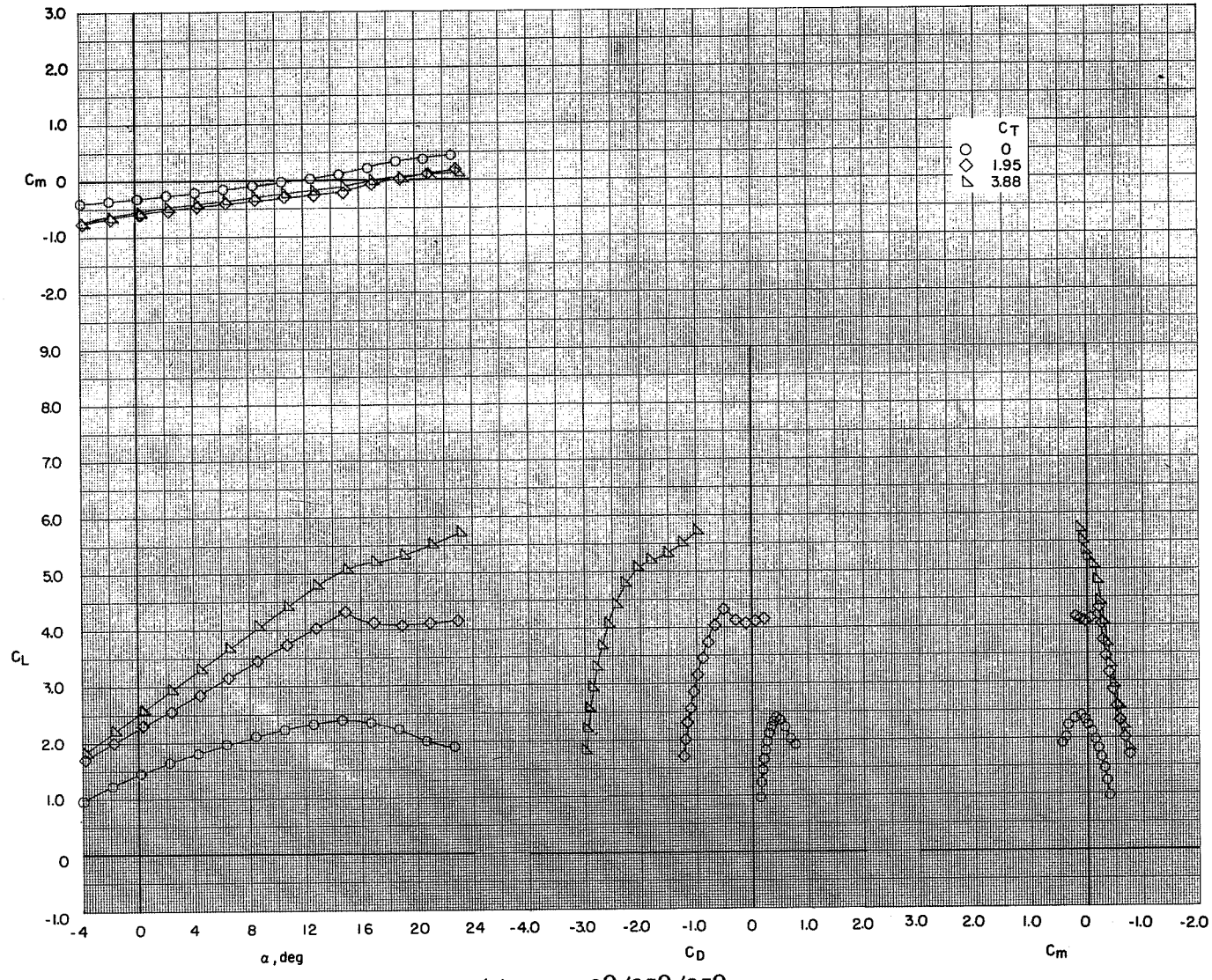

(a) $\delta_f = 0^o/35^o/35^o$.

Figure 21.- Effect of increasing thrust coefficient on the longitudinal aerodynamic characteristics of the model with various flap configurations. BPR 10.0; tail off; c_s = 15 percent; $\delta_s = 40^o$.

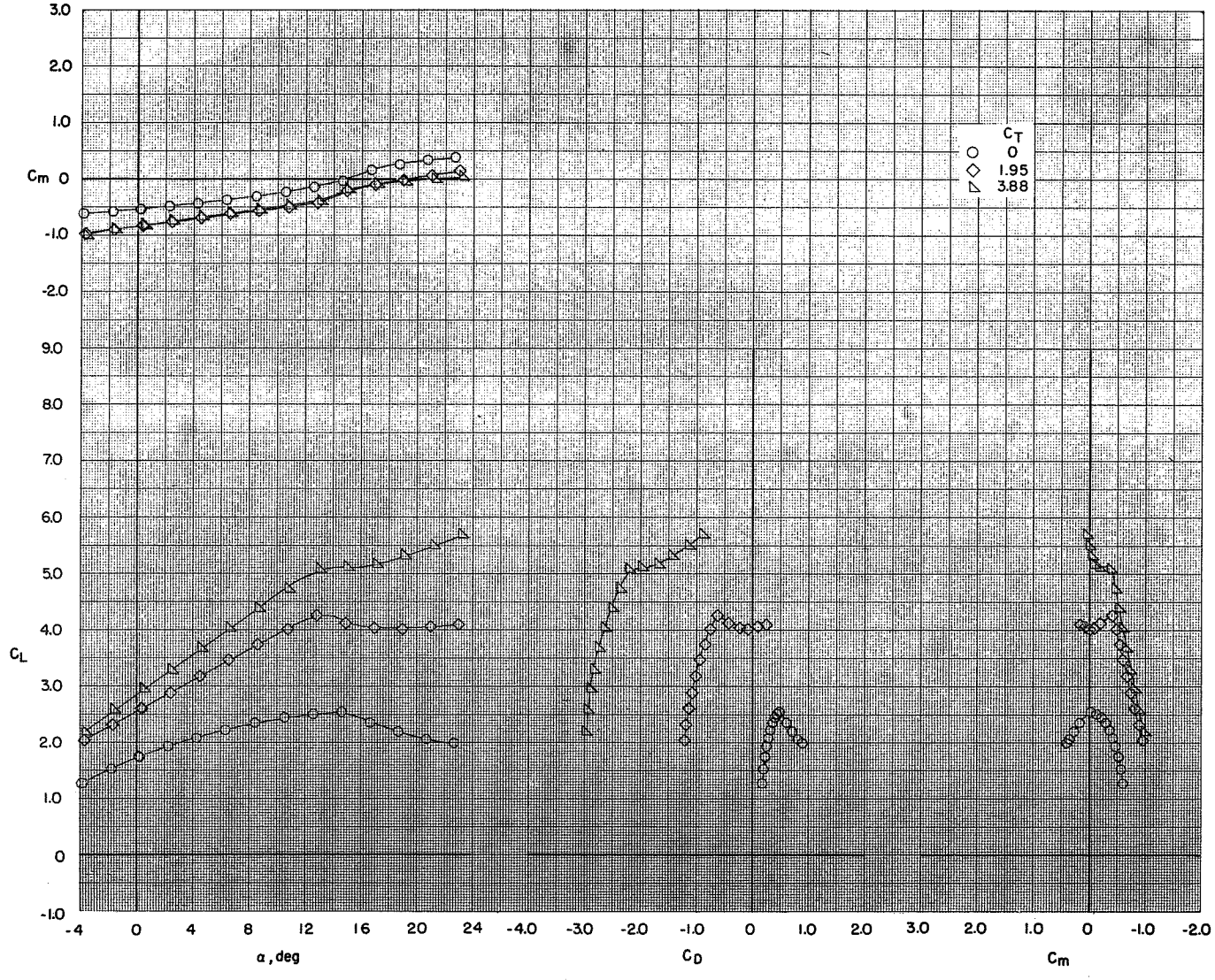

(b) $\delta_f = 35^o/35^o/35^o$.

Figure 21.- Continued.

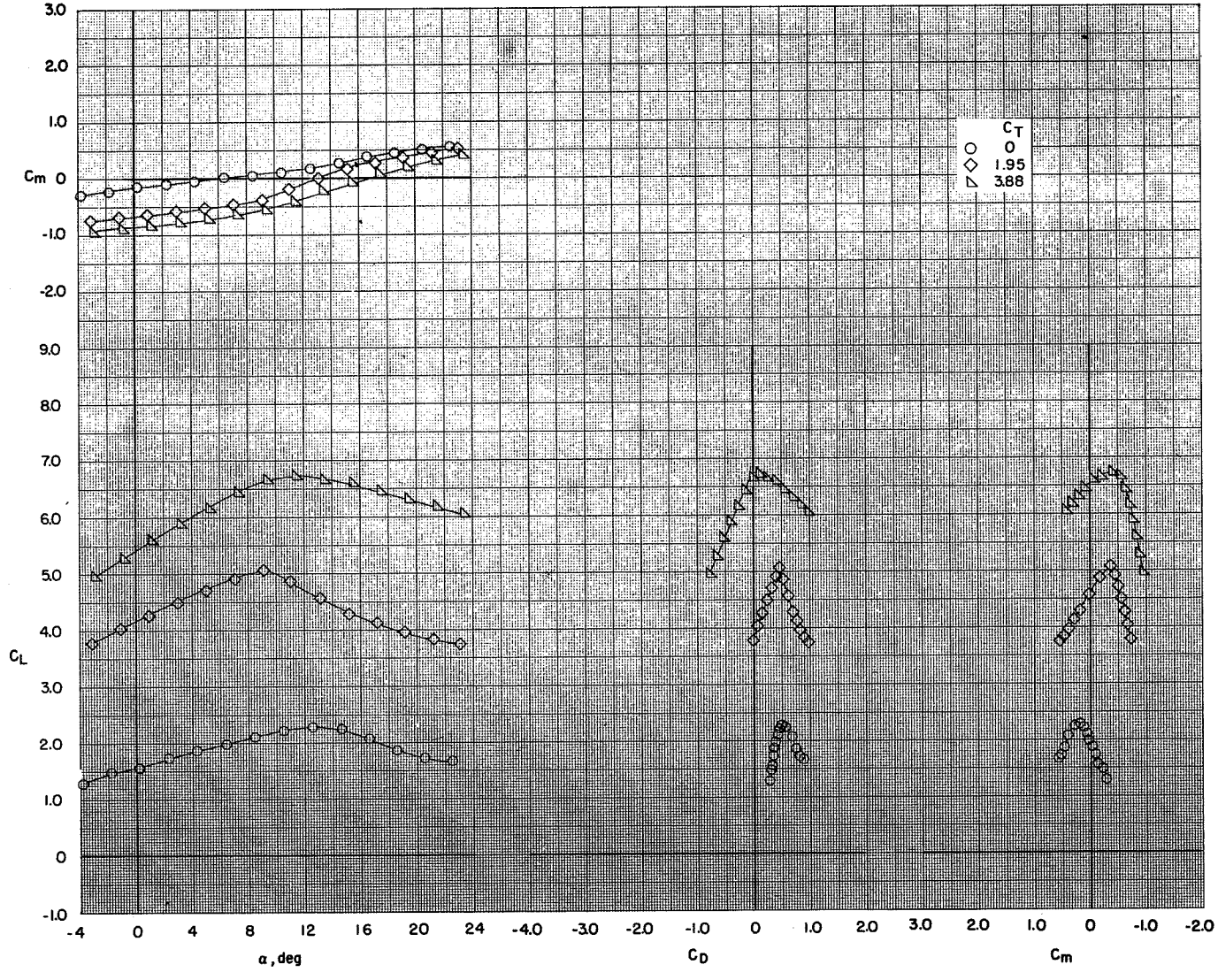

(c) $\delta_f = 0^o/65^o/65^o$.

Figure 21.- Continued.

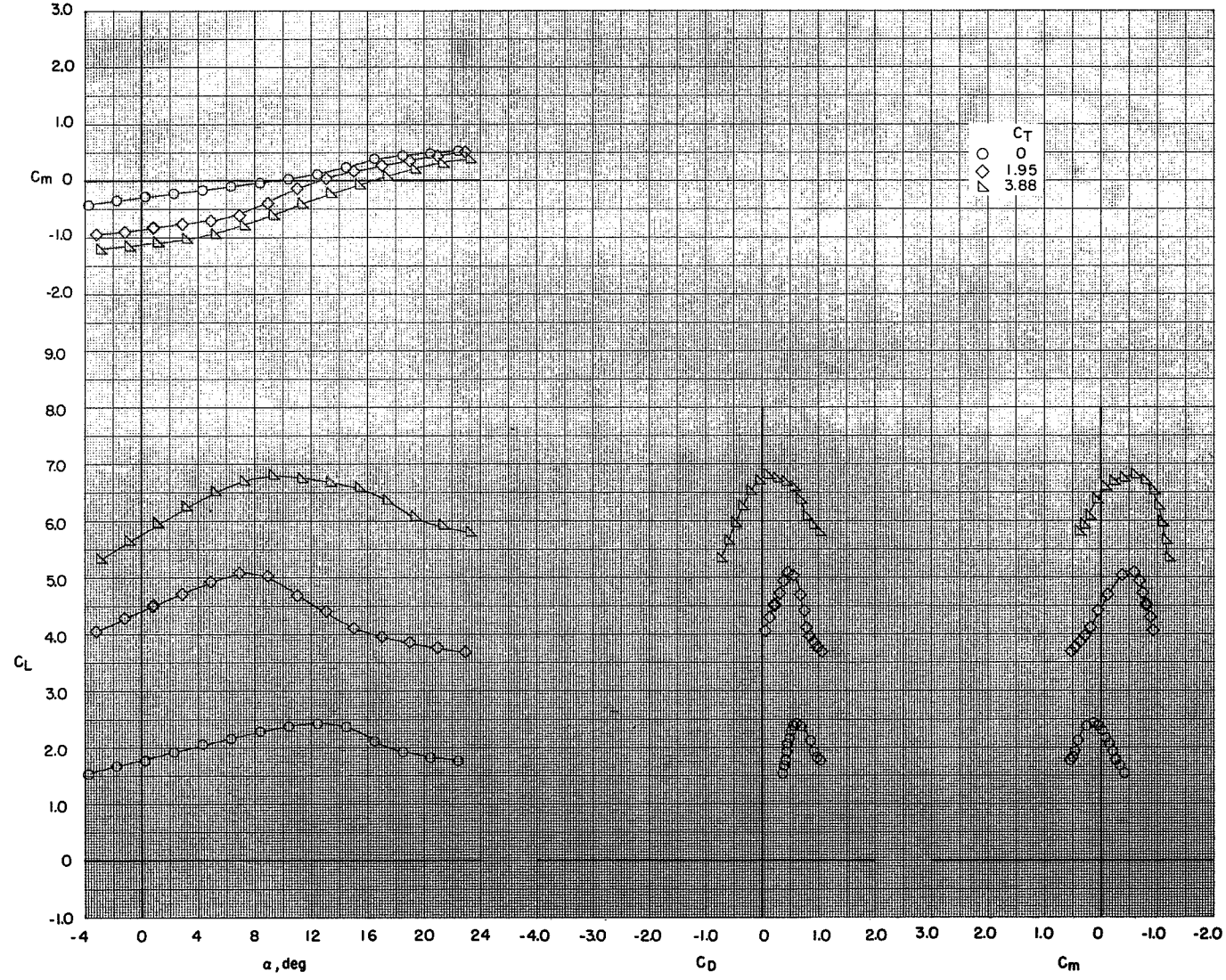

(d) $\delta_f = 65^o/65^o/65^o$.

Figure 21.- Concluded.

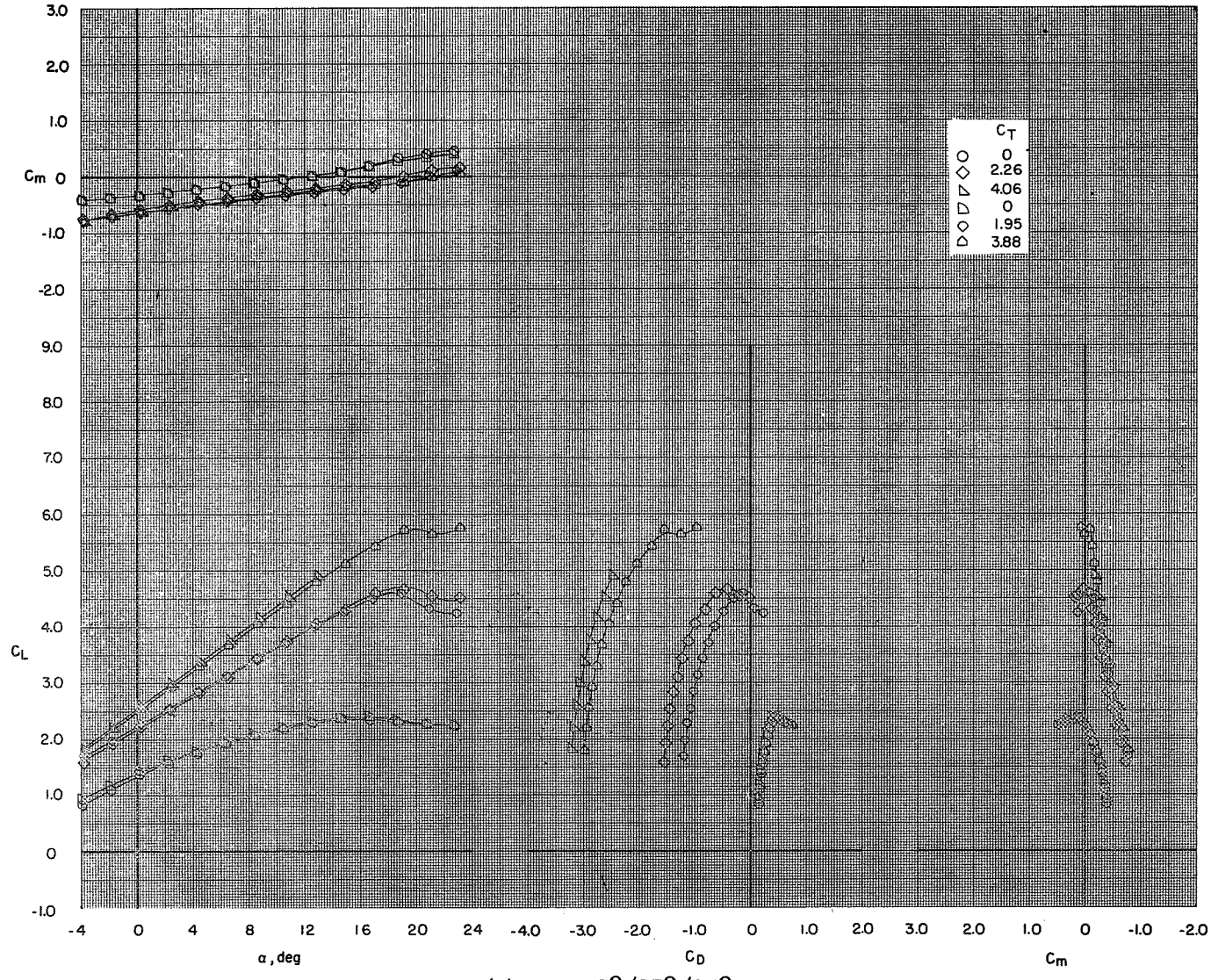

(a) $\delta_f = 0^o/35^o/35^o$.

Figure 22.- Effect of increasing thrust coefficient on the longitudinal aerodynamic characteristics of the model with various flap configurations. BPR 10.0; tail off; c_s = 15 percent; $\delta_s = 50^o$.

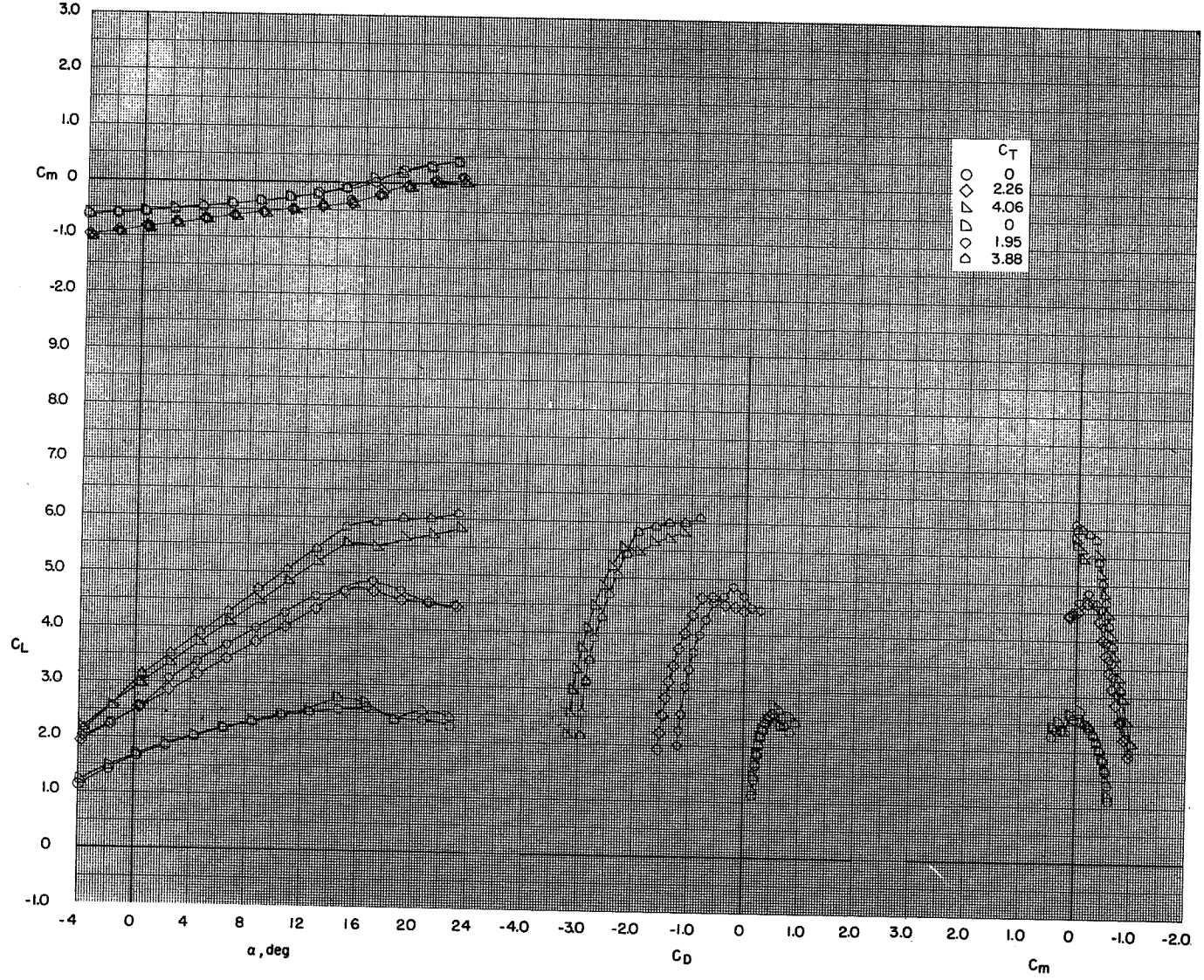

(b) $\delta_f = 35^o/35^o/35^o$.

Figure 22.- Continued.

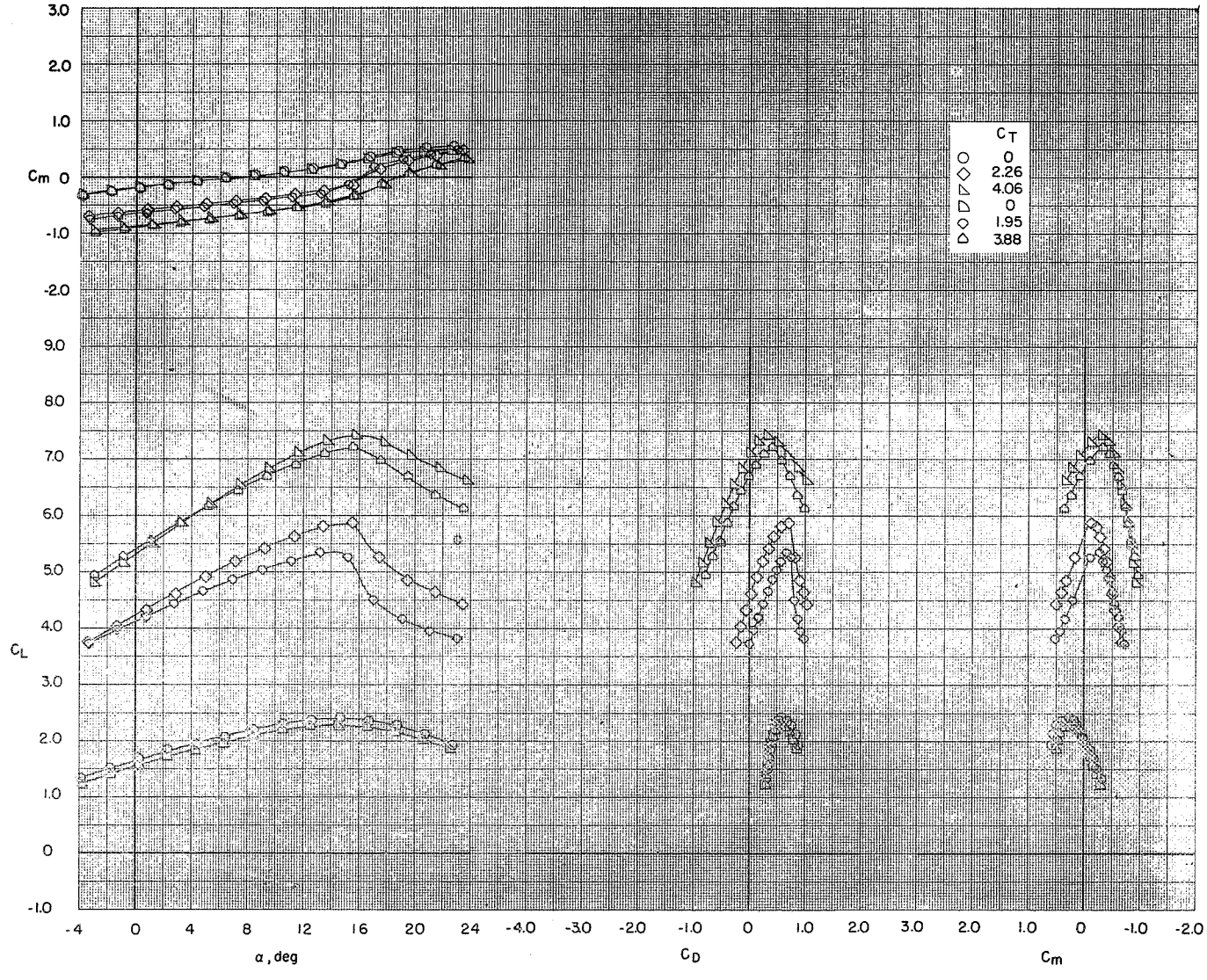

(c) $\delta_f = 0^o/65^o/65^o$.

Figure 22.- Continued.

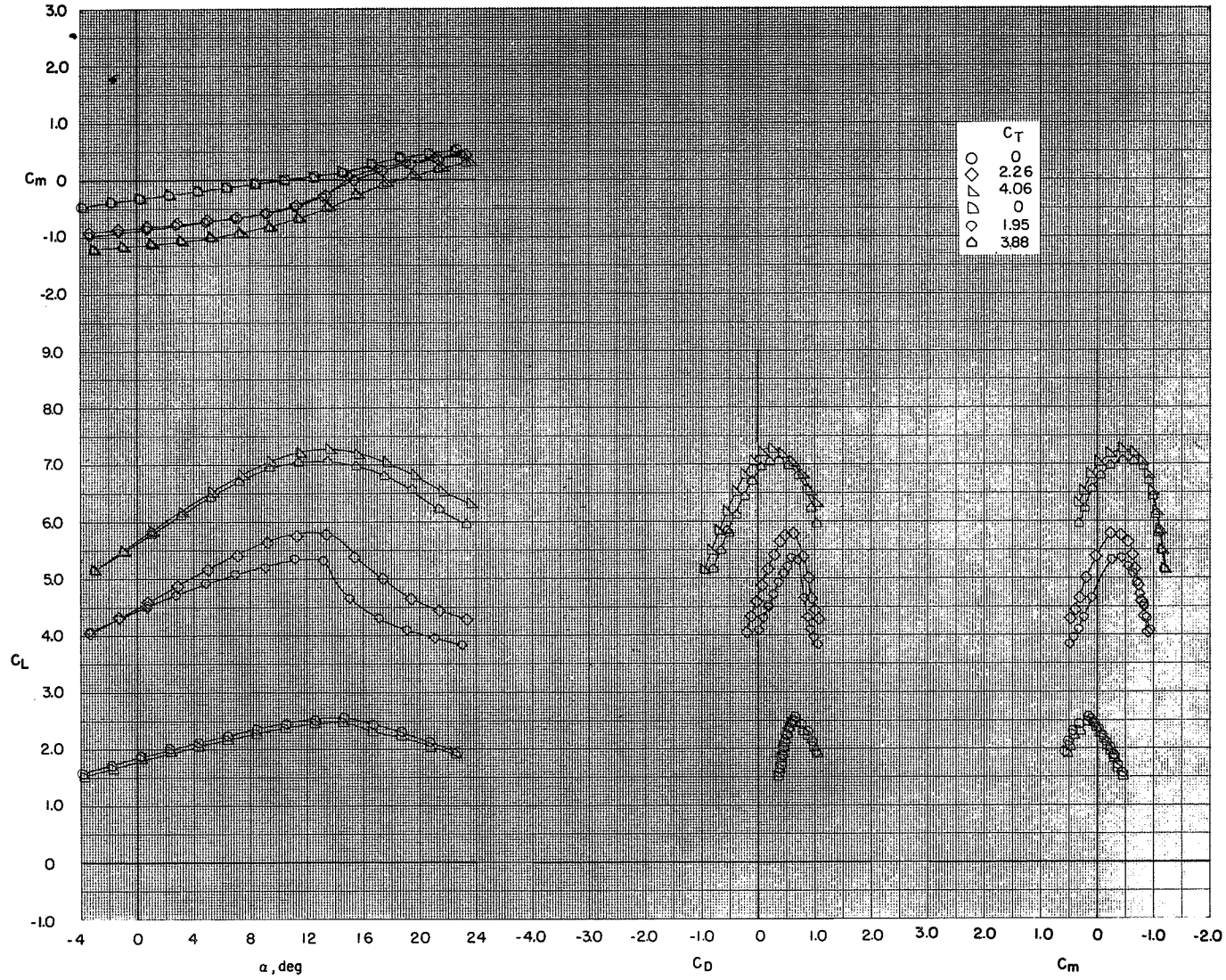

(d) $\delta_f = 65^o/65^o/65^o$.

Figure 22.- Concluded.

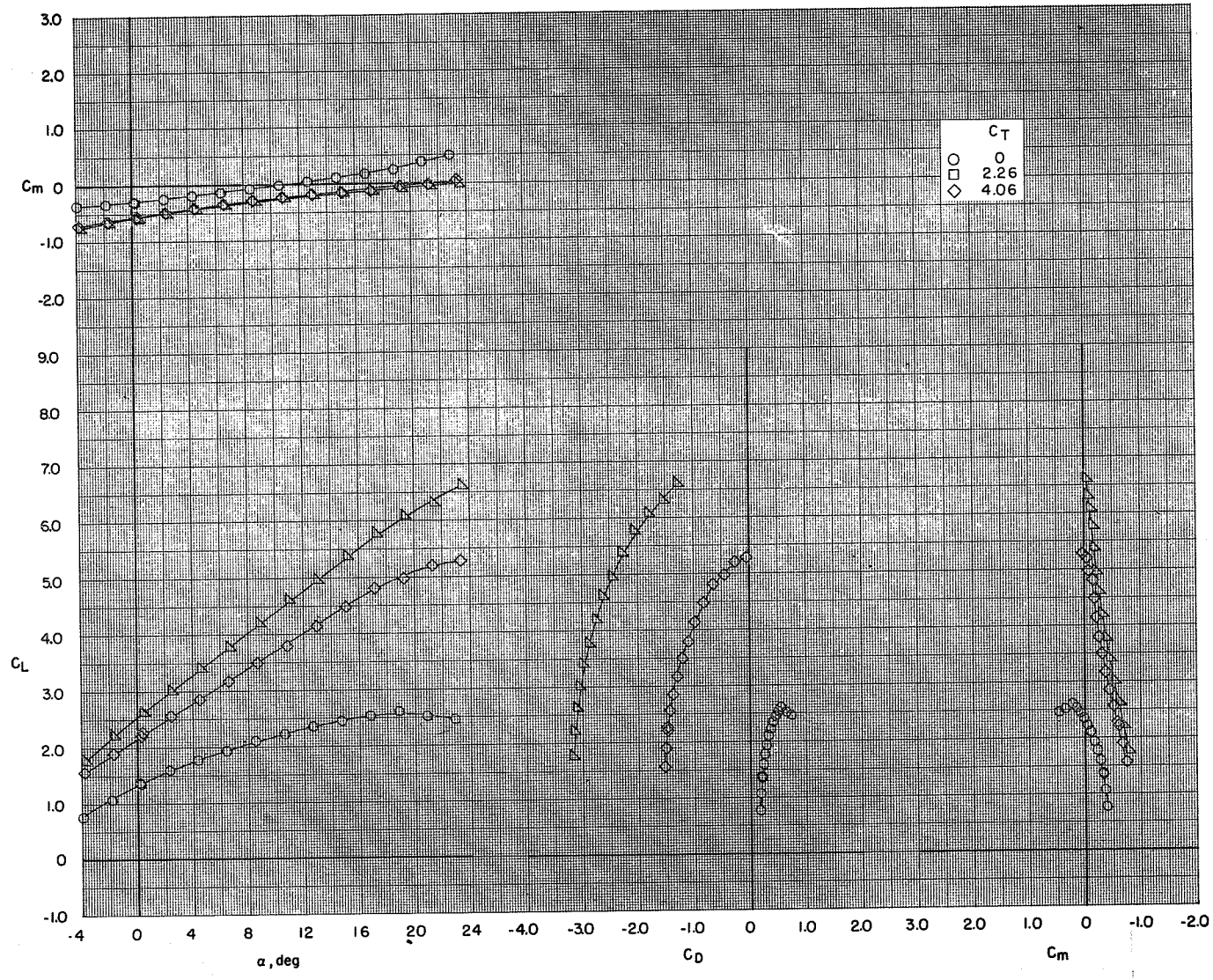

(a) $\delta_f = 0^o/35^o/35^o$.

Figure 23.- Effect of increasing thrust coefficient on the longitudinal aerodynamic characteristics of the model with various flap configurations. BPR 10.0; tail off; c_s = 20 percent; $\delta_s = 50^o$.

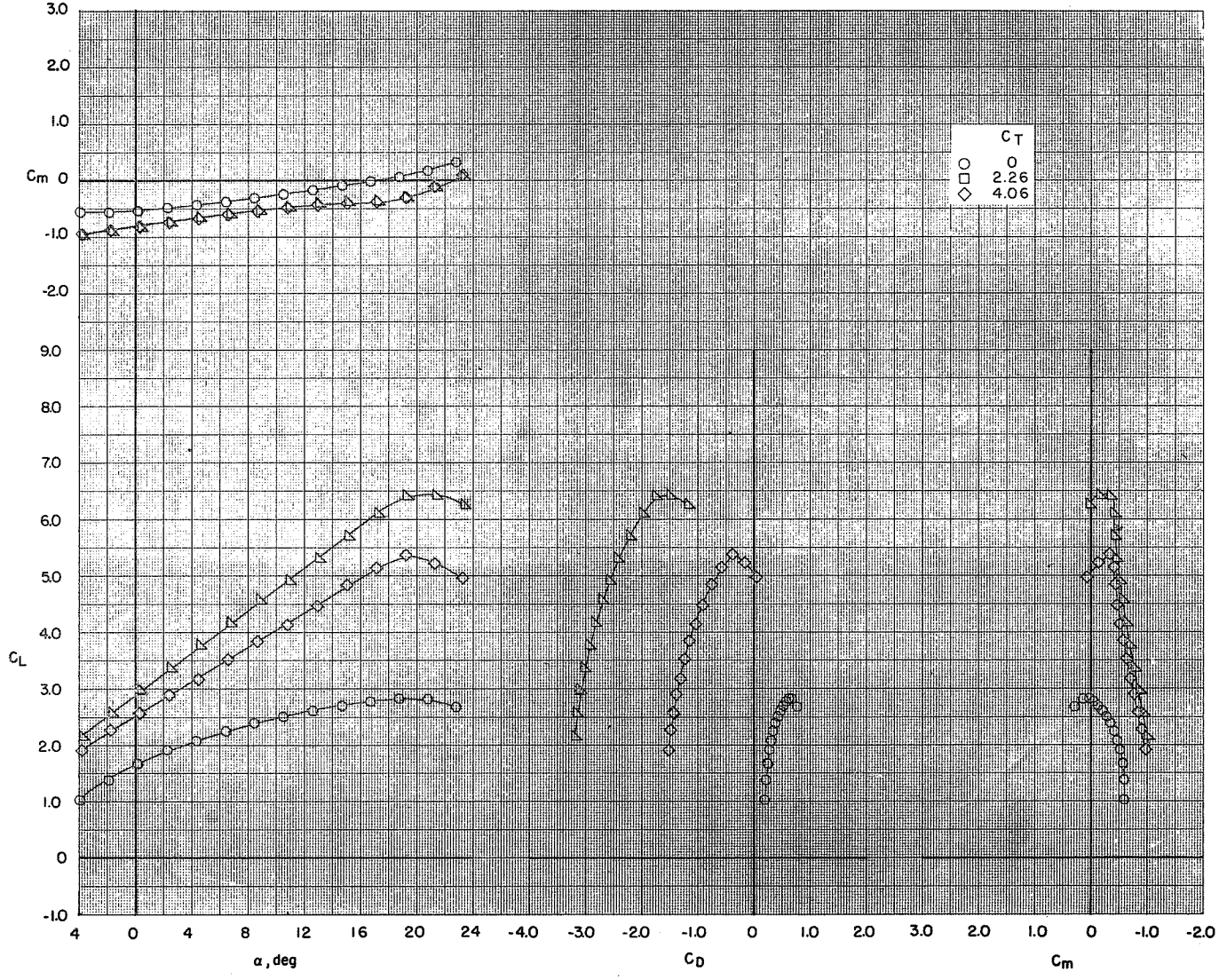

(b) $\delta_f = 35^o/35^o/35^o$.

Figure 23.- Continued.

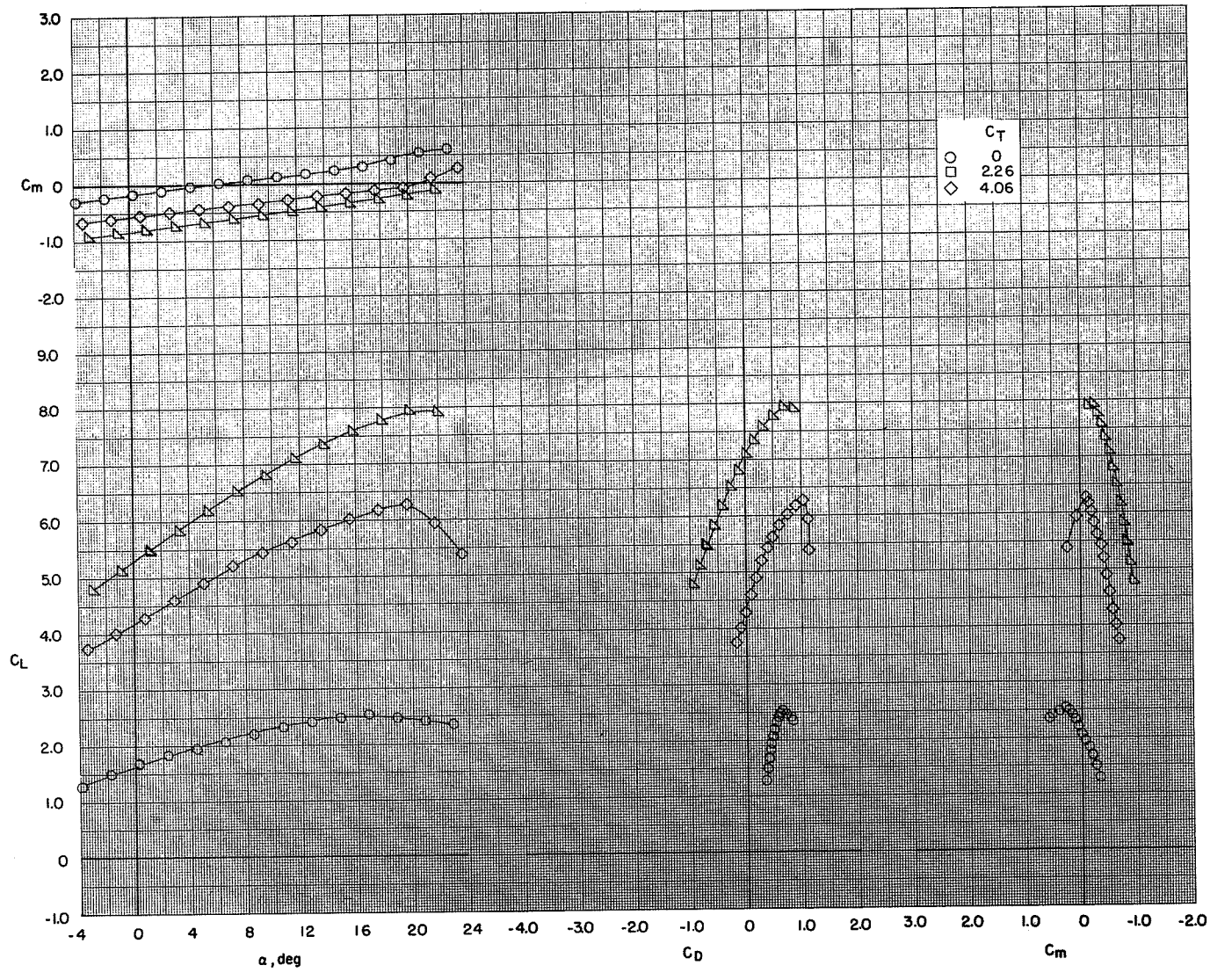

(c) $\delta_f = 0^o/65^o/65^o$.

Figure 23.- Continued.

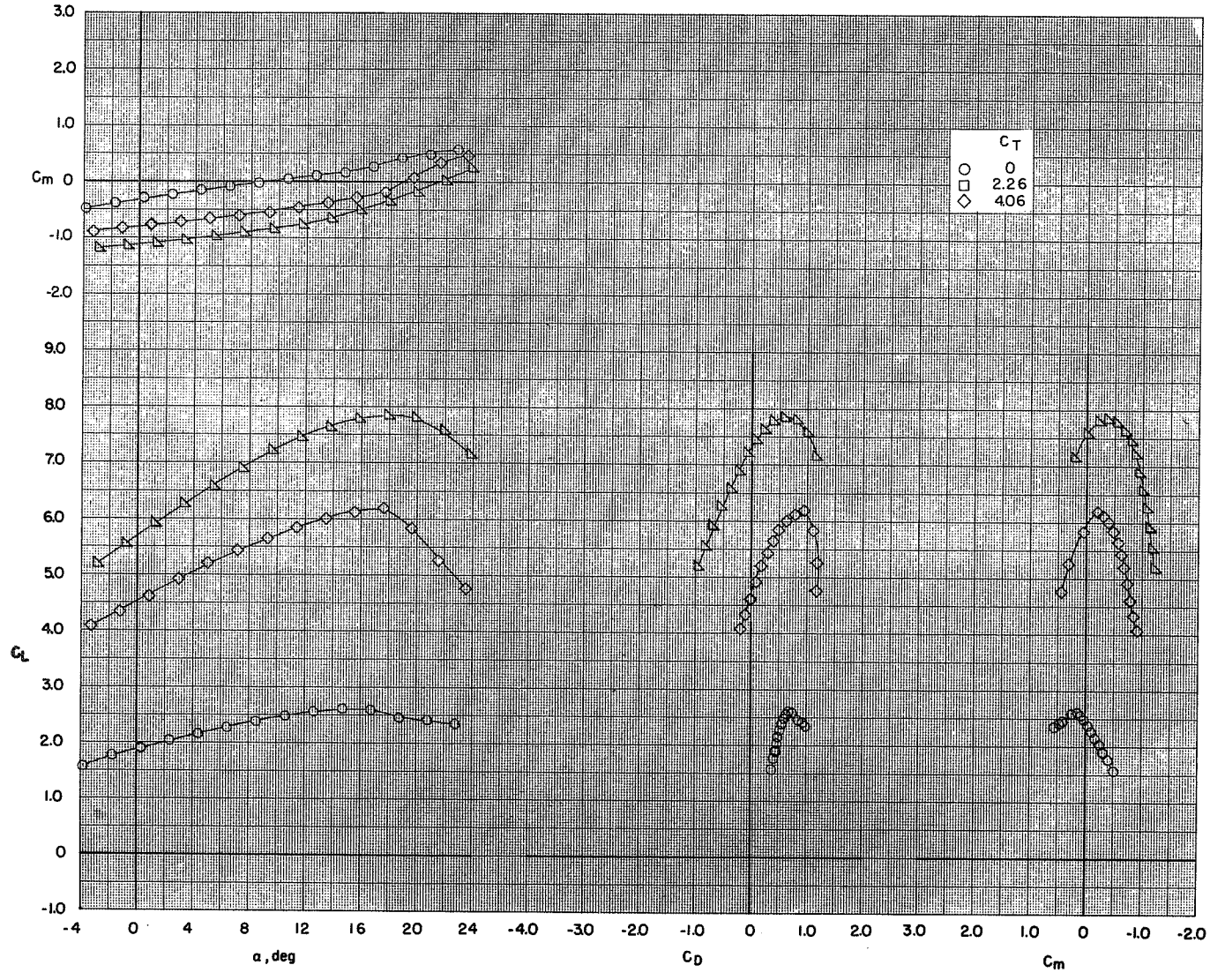

(d) $\delta_f = 65^o/65^o/65^o$.

Figure 23.- Concluded.

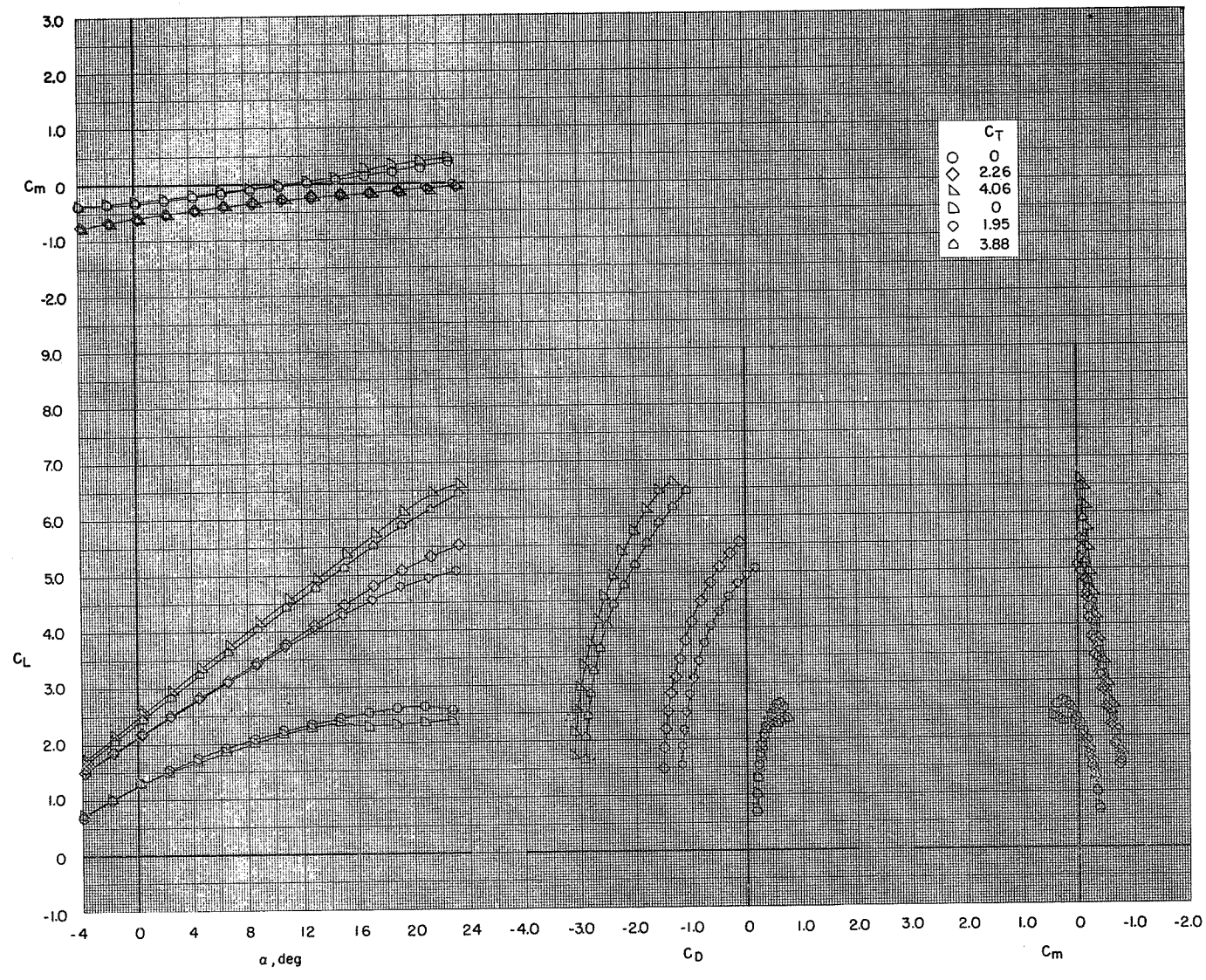

(a) $\delta_f = 0^o/35^o/35^o$.

Figure 24.- Effect of increasing thrust coefficient on the longitudinal aerodynamic characteristics of the model with various flap configurations. BPR 10.0; tail off; c_s = 25 percent; $\delta_s = 50^o$.

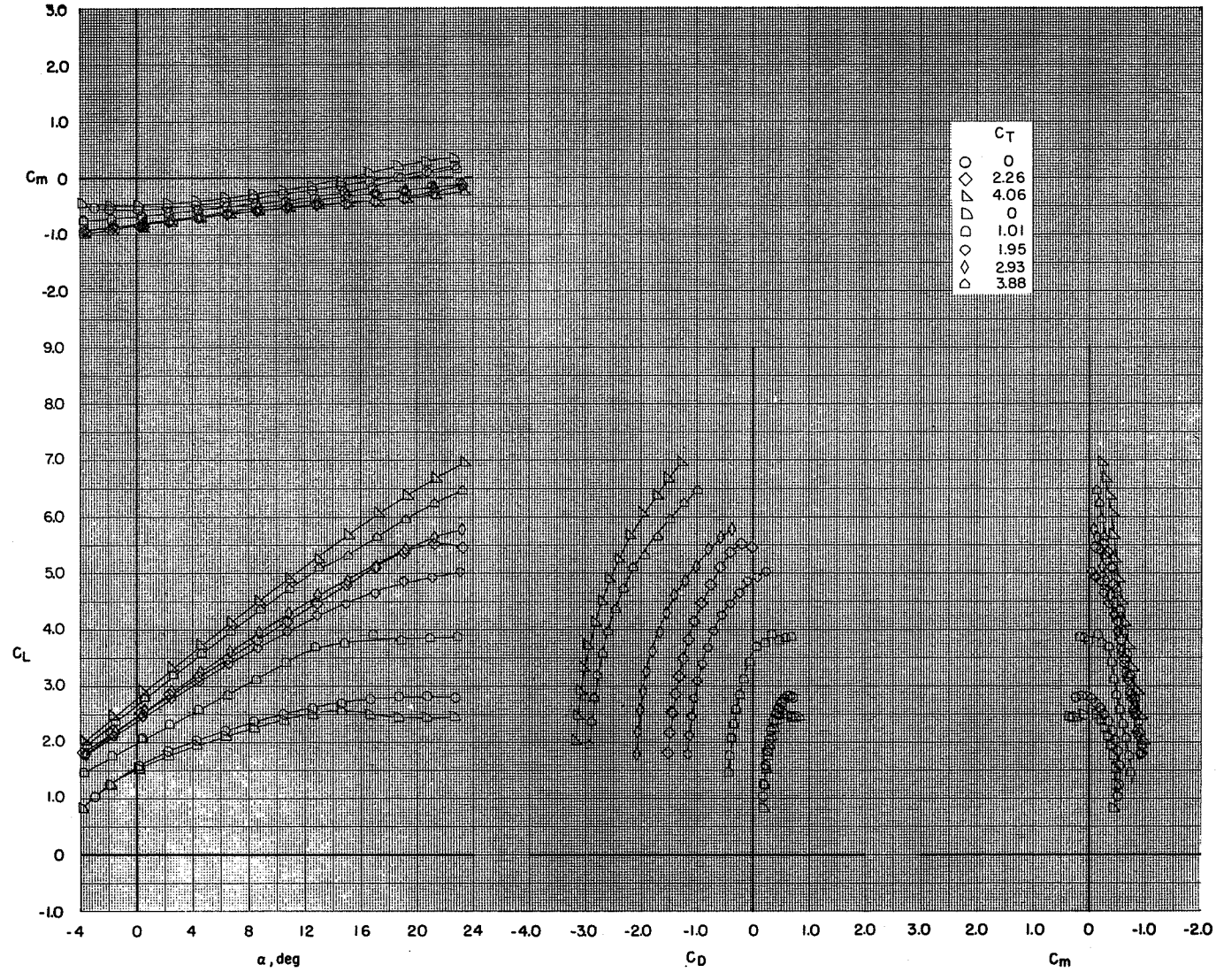

(b) $\delta_f = 35^o/35^o/35^o$.

Figure 24.- Continued.

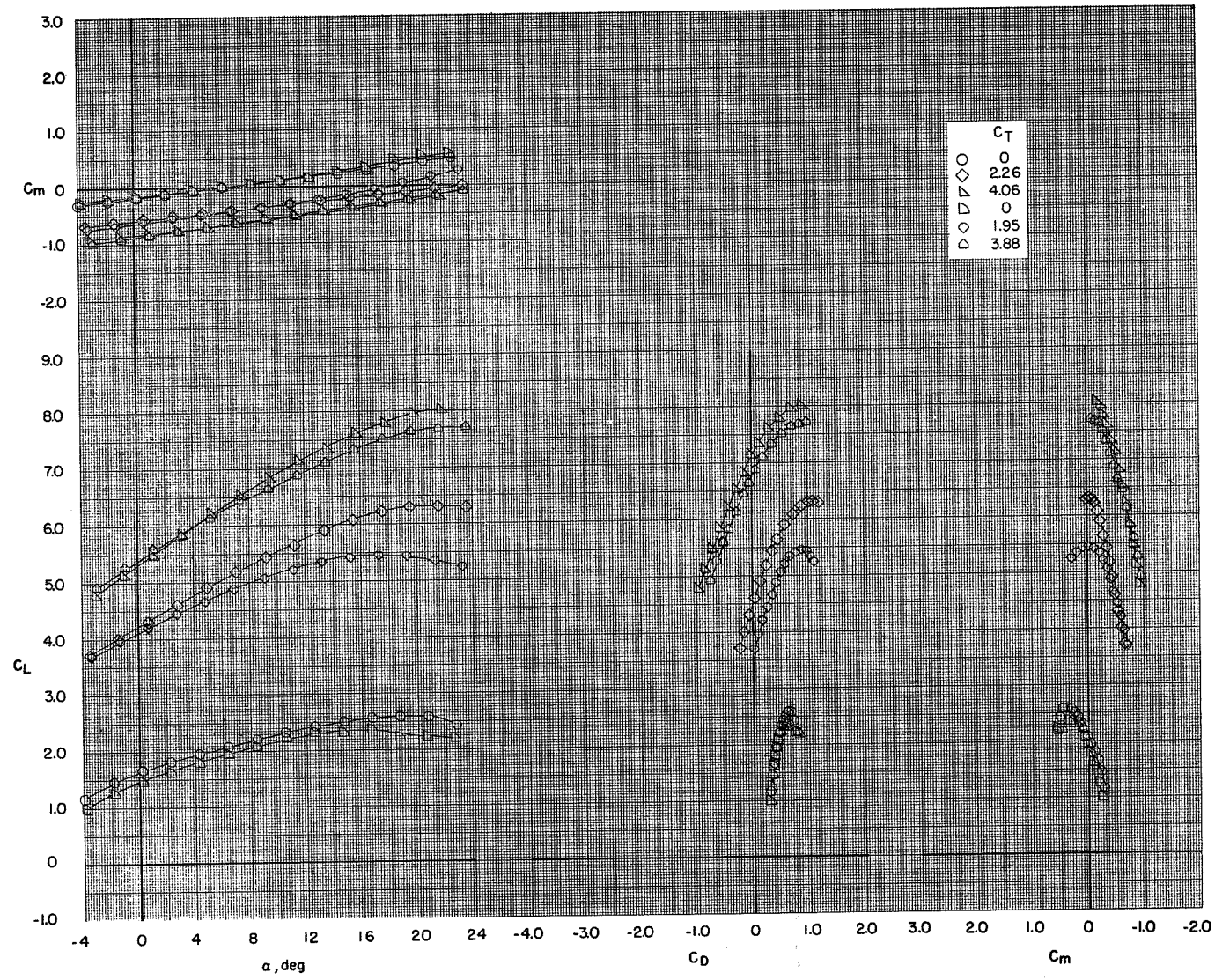

(c) $\delta_f = 0^o/65^o/65^o$.

Figure 24.- Continued.

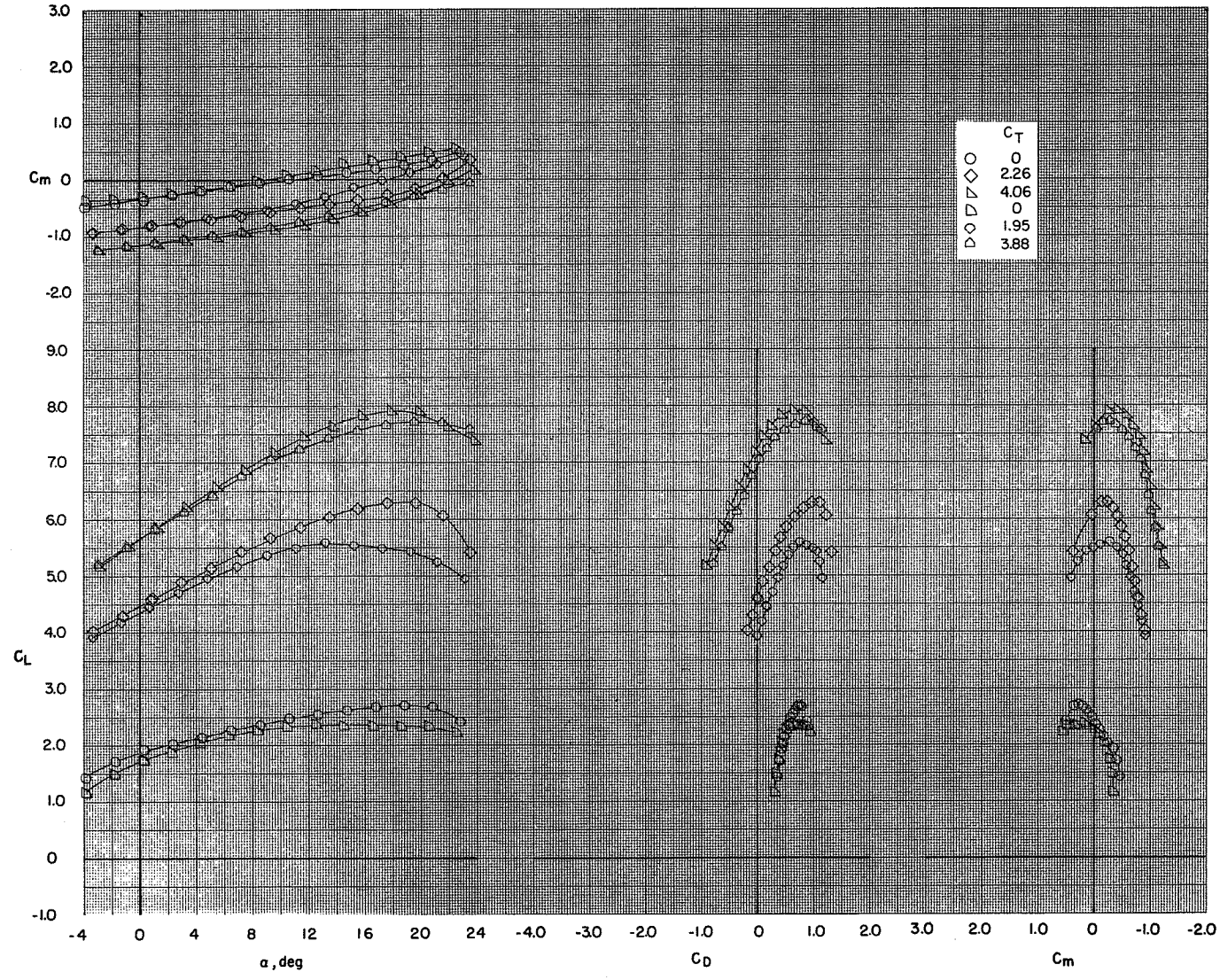

(d) $\delta_f = 65^o/65^o/65^o$.

Figure 24.- Concluded.

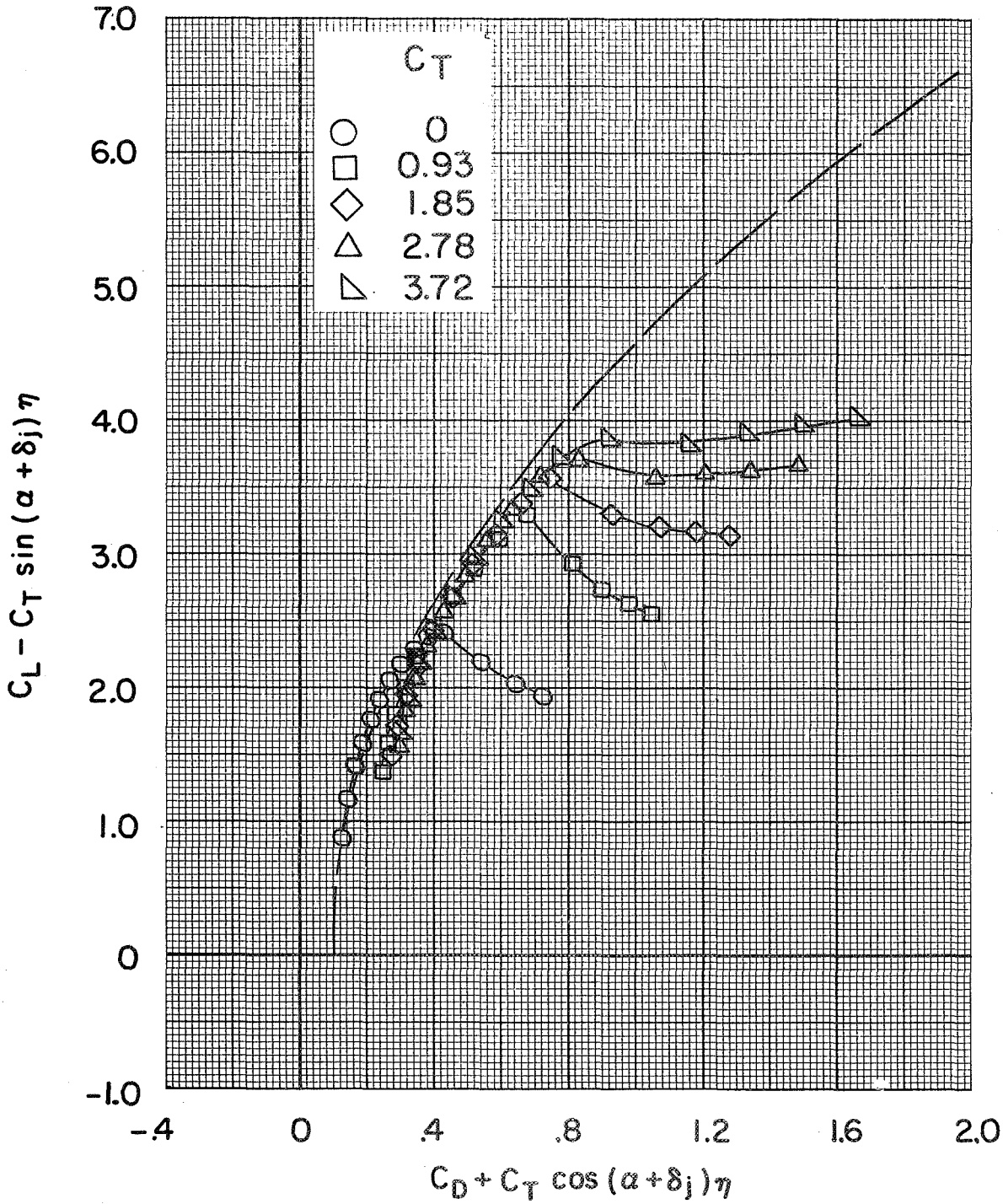

(a) $\delta_f = 0^o/35^o/35^o$.

Figure 25.- Effect of increasing thrust coefficient on the thrust-removed lift-drag polars. BPR 6.2; tail off; c_s = 15 percent; $\delta_s = 40^o$.

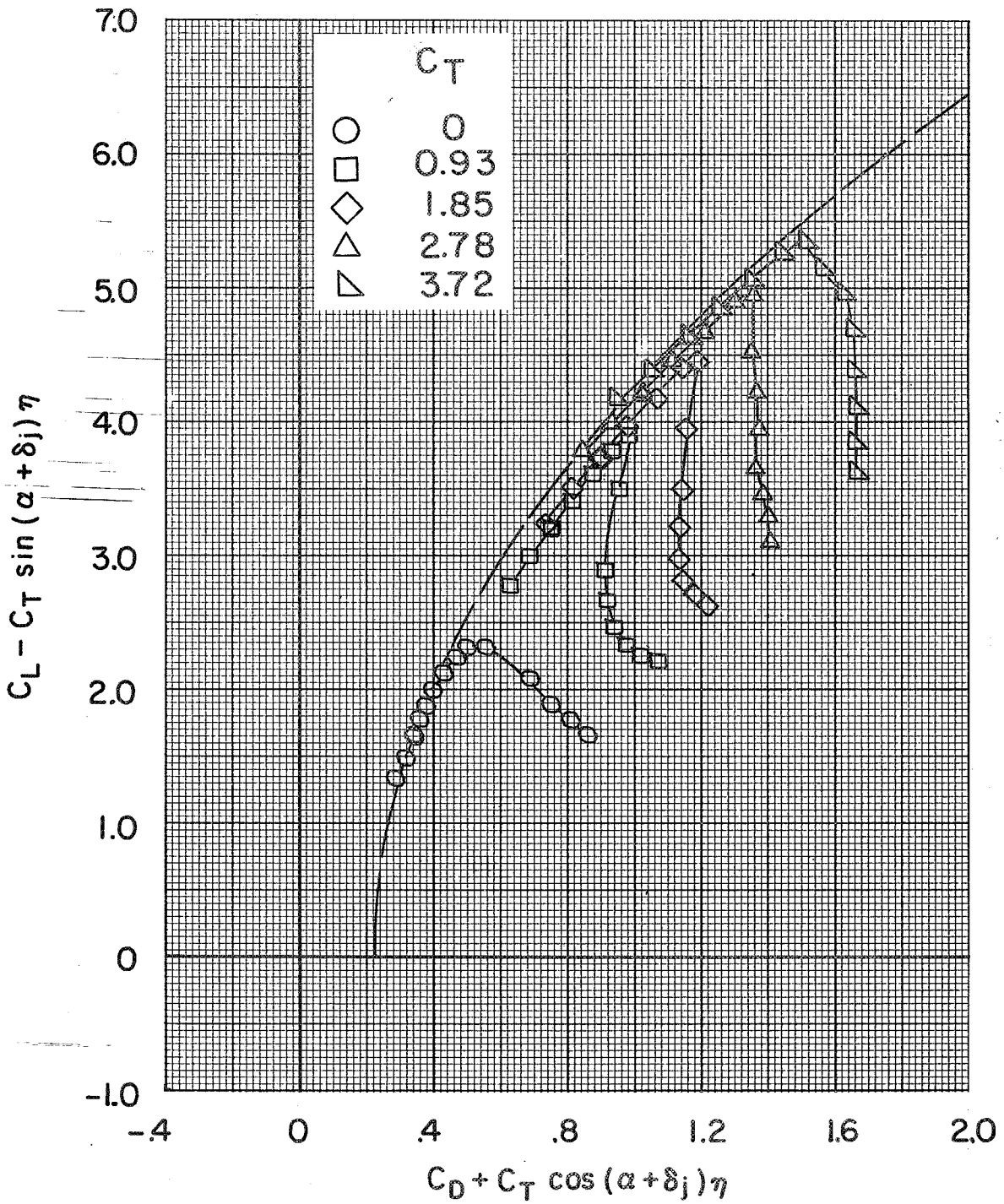

(b) $\delta_f = 0^o/65^o/65^o$.

Figure 25.- Concluded.

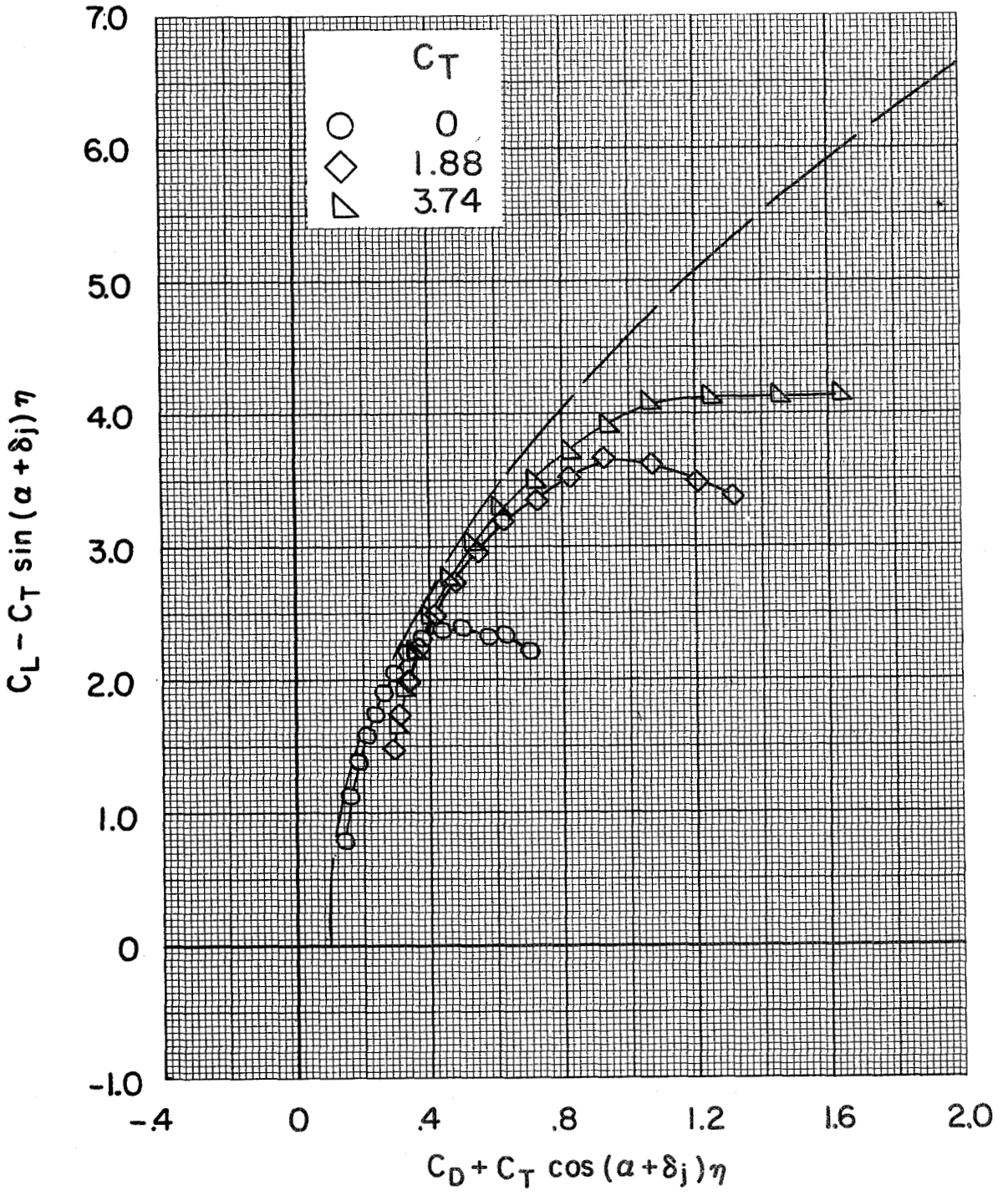

(a) $\delta_f = 0^o/35^o/35^o$.

Figure 26.- Effect of increasing thrust coefficient on the thrust-removed lift-drag polars. BPR 6.2; tail off; c_s = 15 percent; $\delta_s = 50^o$.

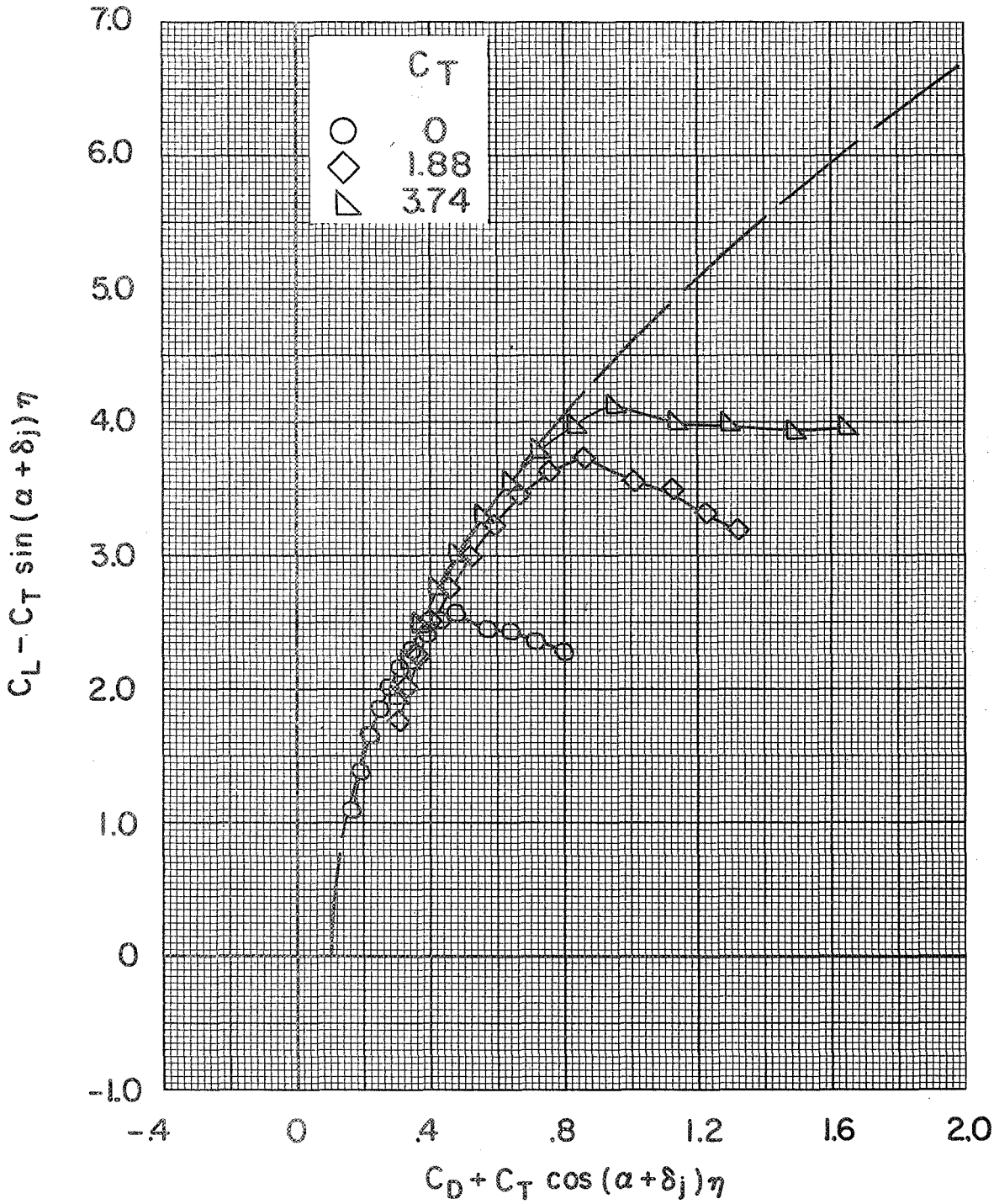

(b) $\delta_f = 35^o/35^o/35^o$.

Figure 26.- Continued.

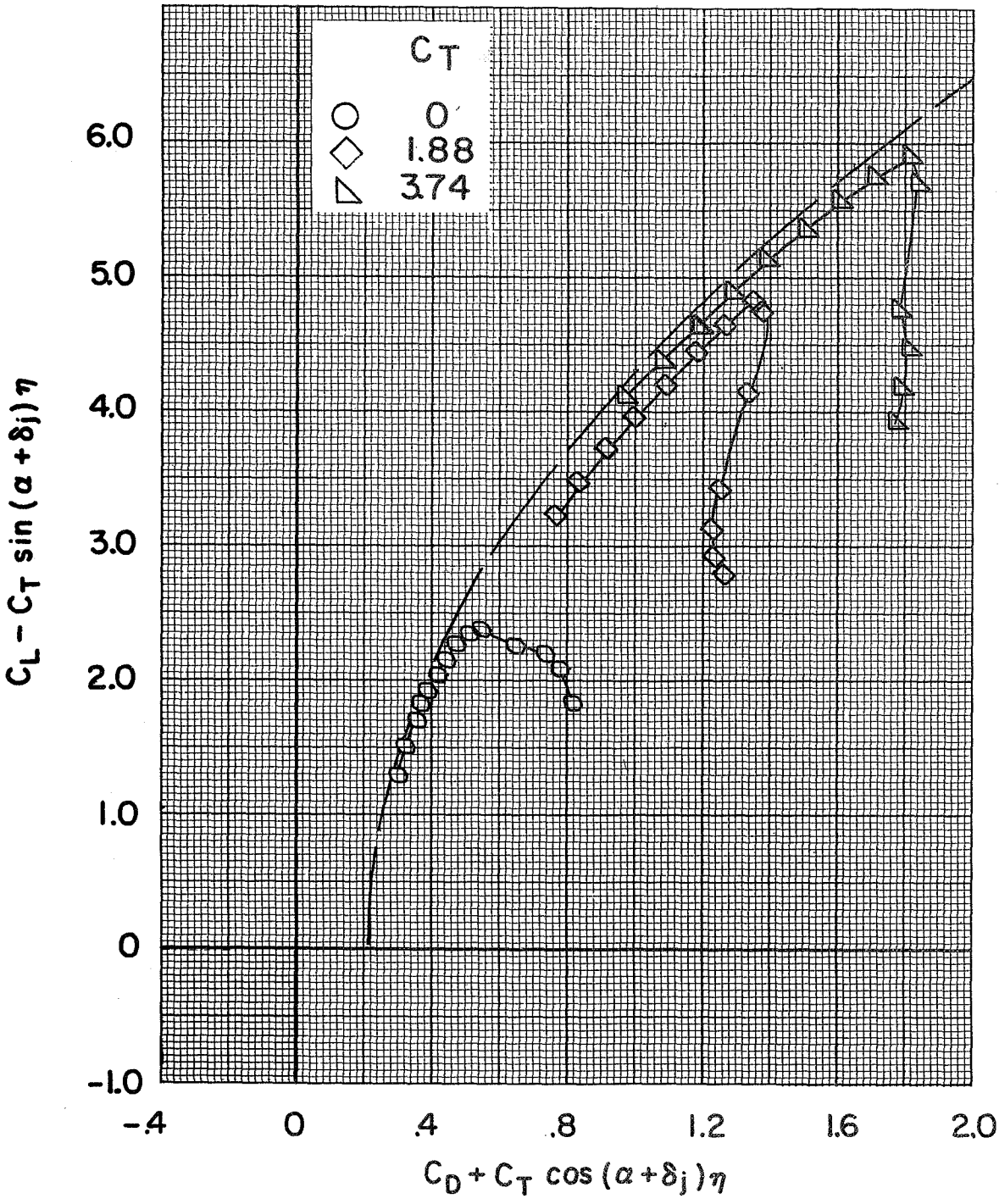

(c) $\delta_f = 0^o/65^o/65^o$.

Figure 26.- Continued.

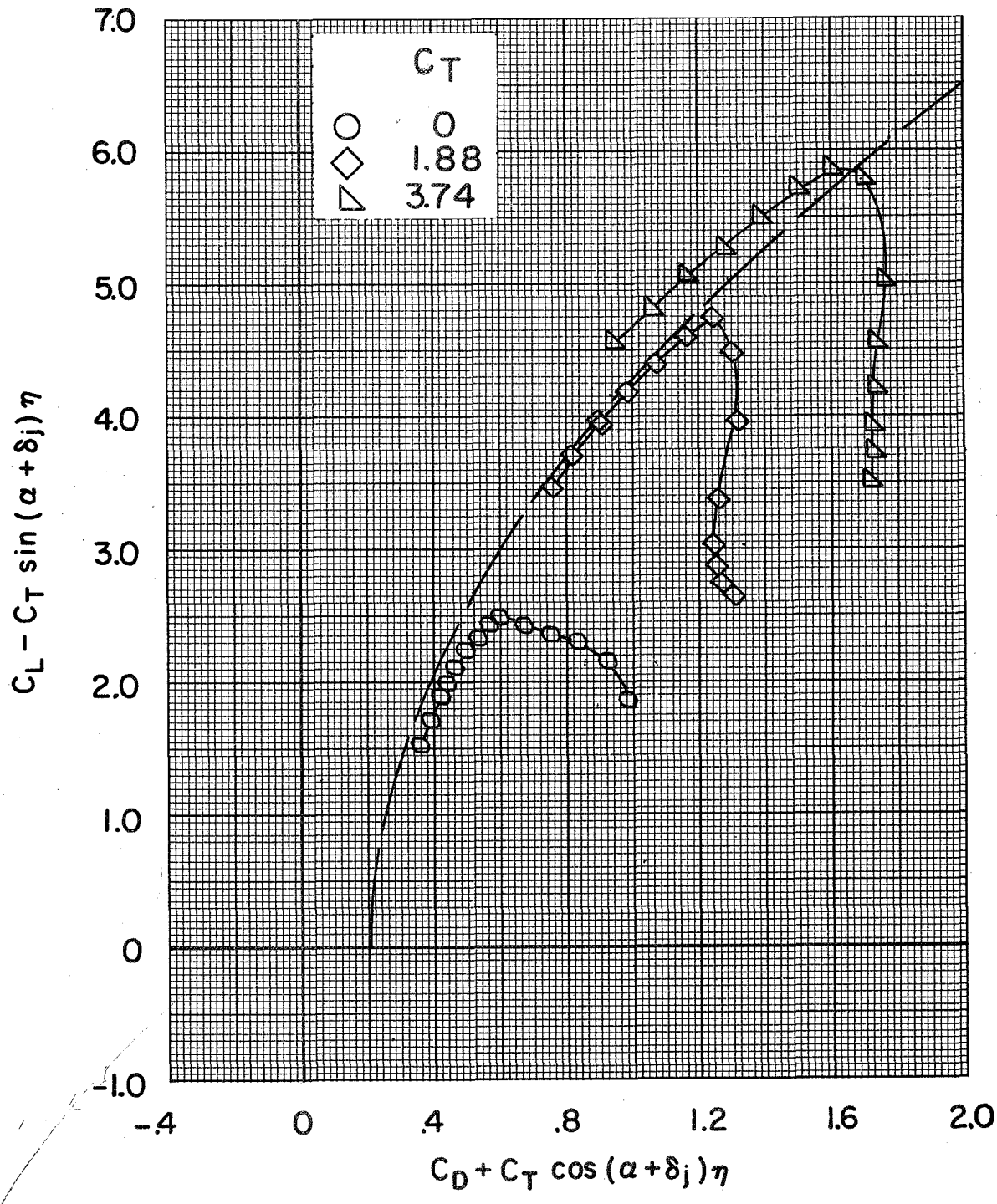

(d) $\delta_f = 65^o/65^o/65^o$.

Figure 26.- Concluded.

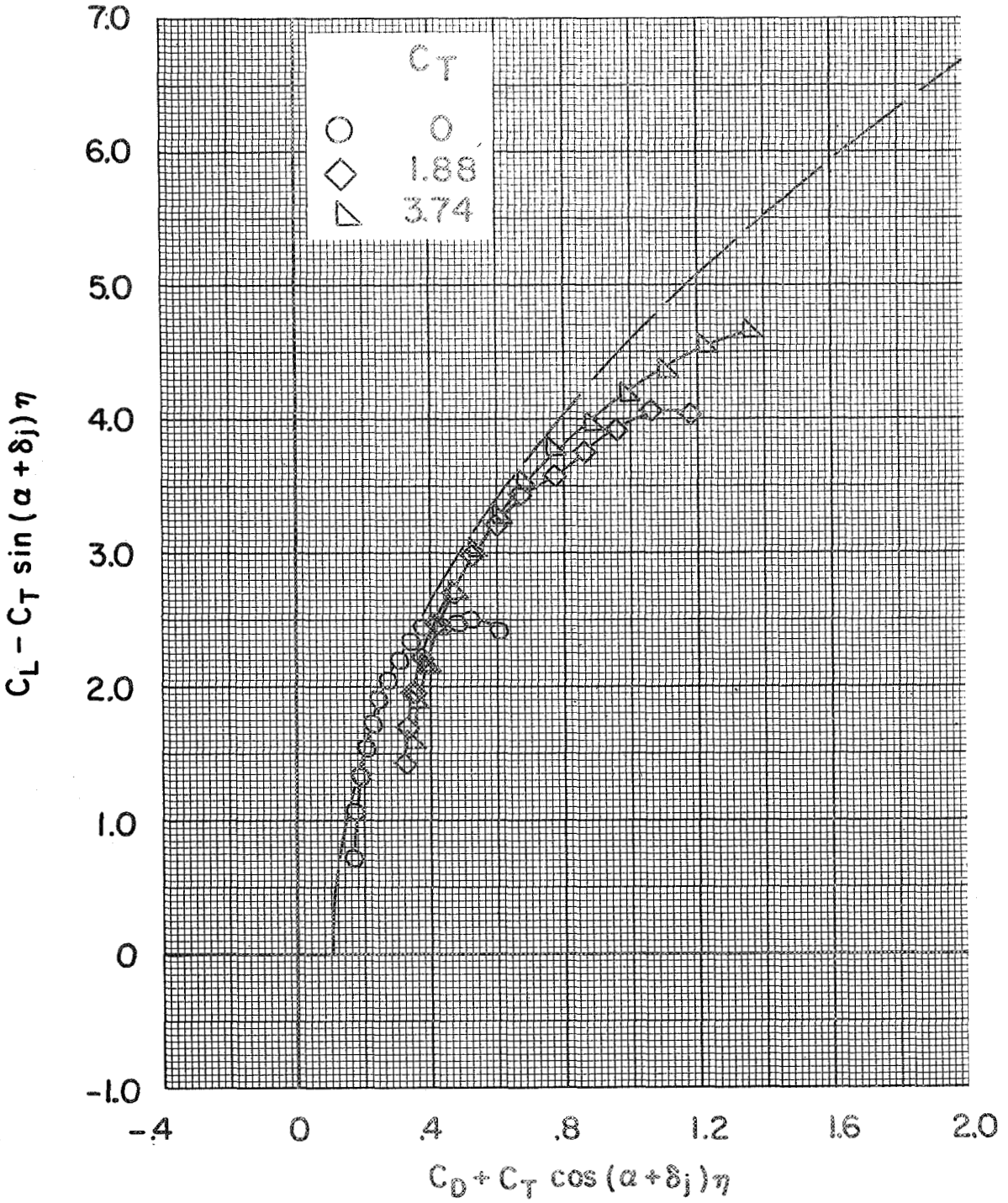

(a) $\delta_f = 0^o/35^o/35^o$.

Figure 27.- Effect of increasing thrust coefficient on the thrust-removed lift-drag polars. BPR 6.2; tail off; c_s = 20 percent; $\delta_s = 50^o$.

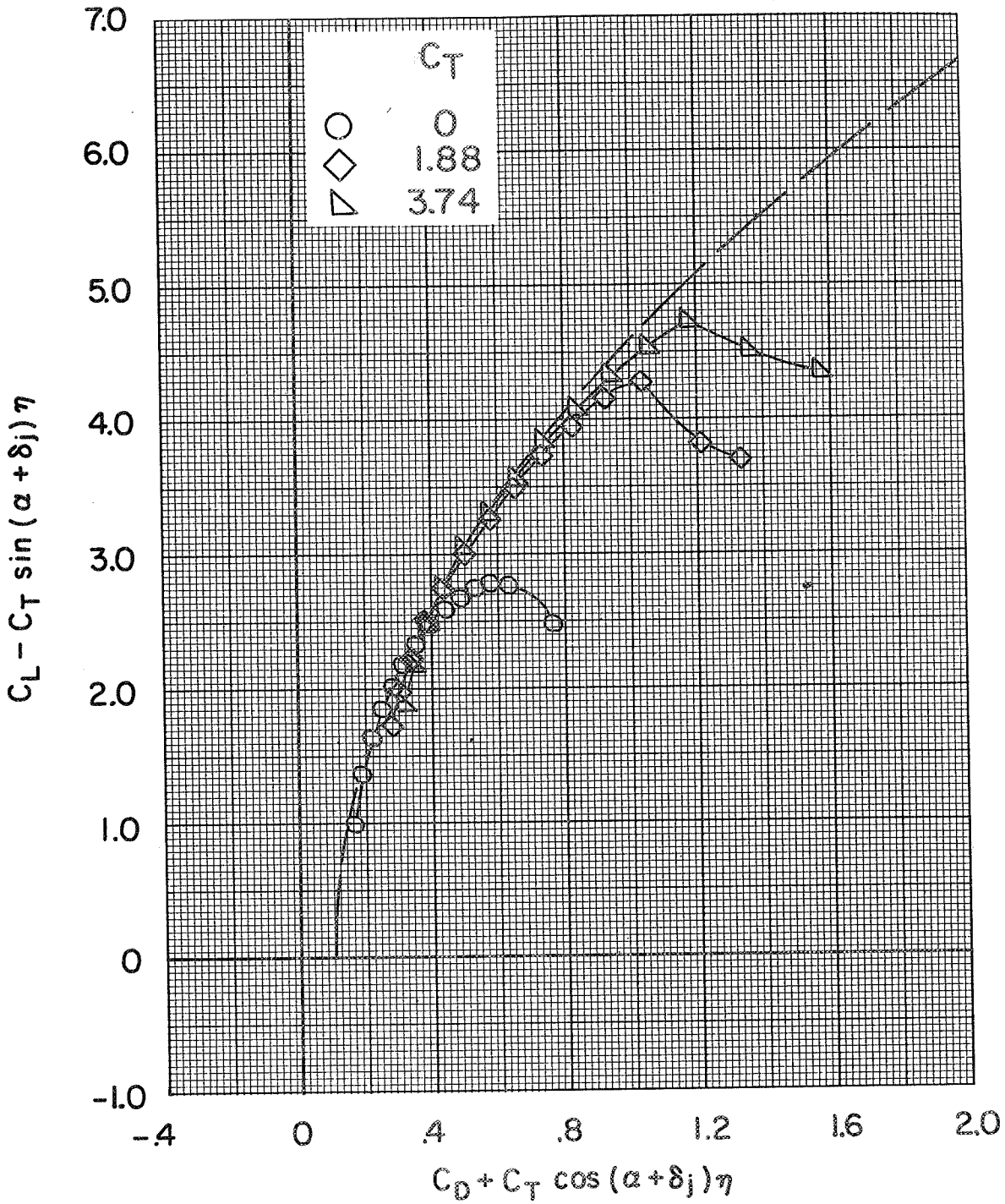

(b) $\delta_f = 35^o/35^o/35^o$.

Figure 27.- Continued.

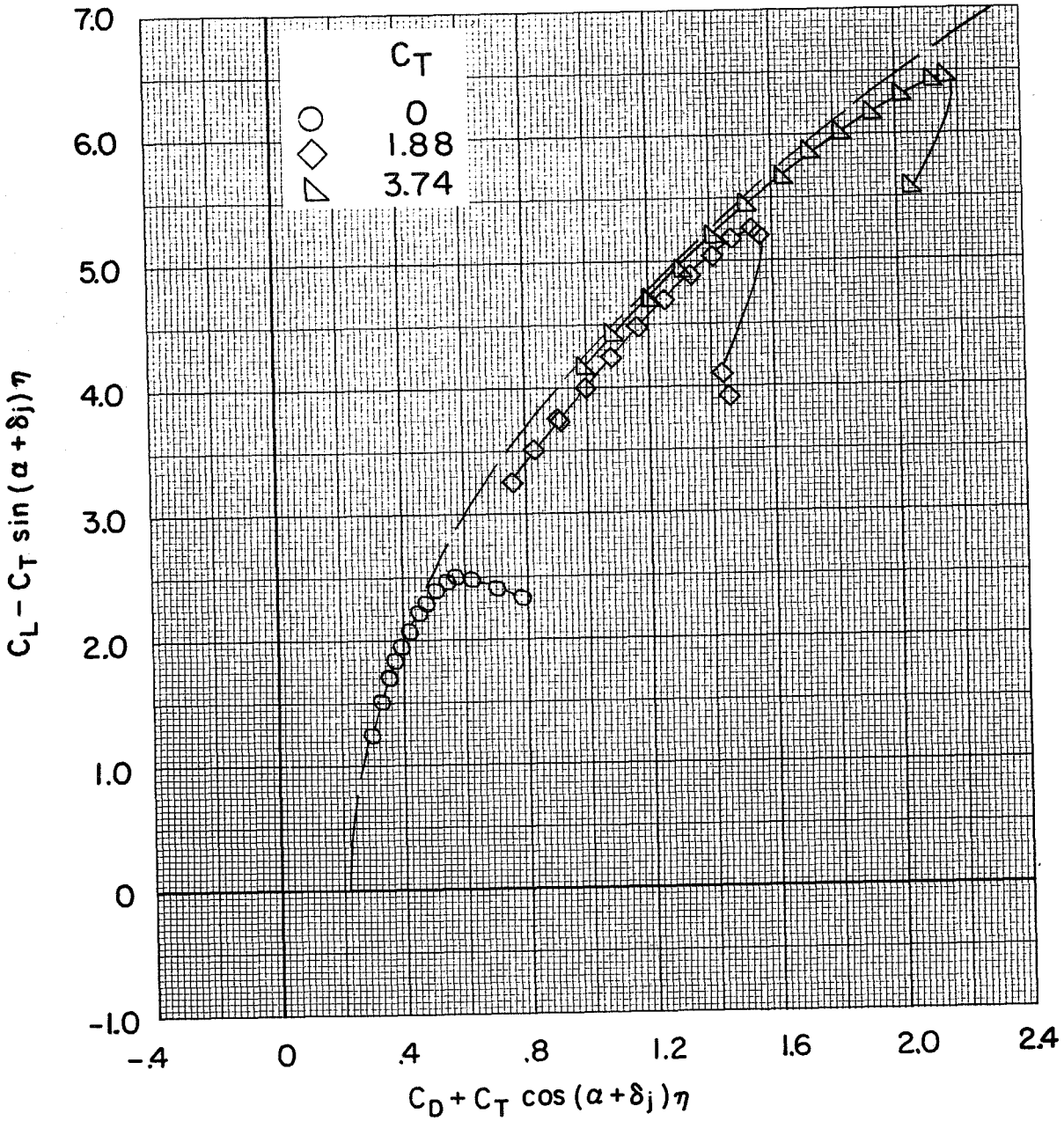

(c) $\delta_f = 0^o/65^o/65^o$.

Figure 27.- Continued.

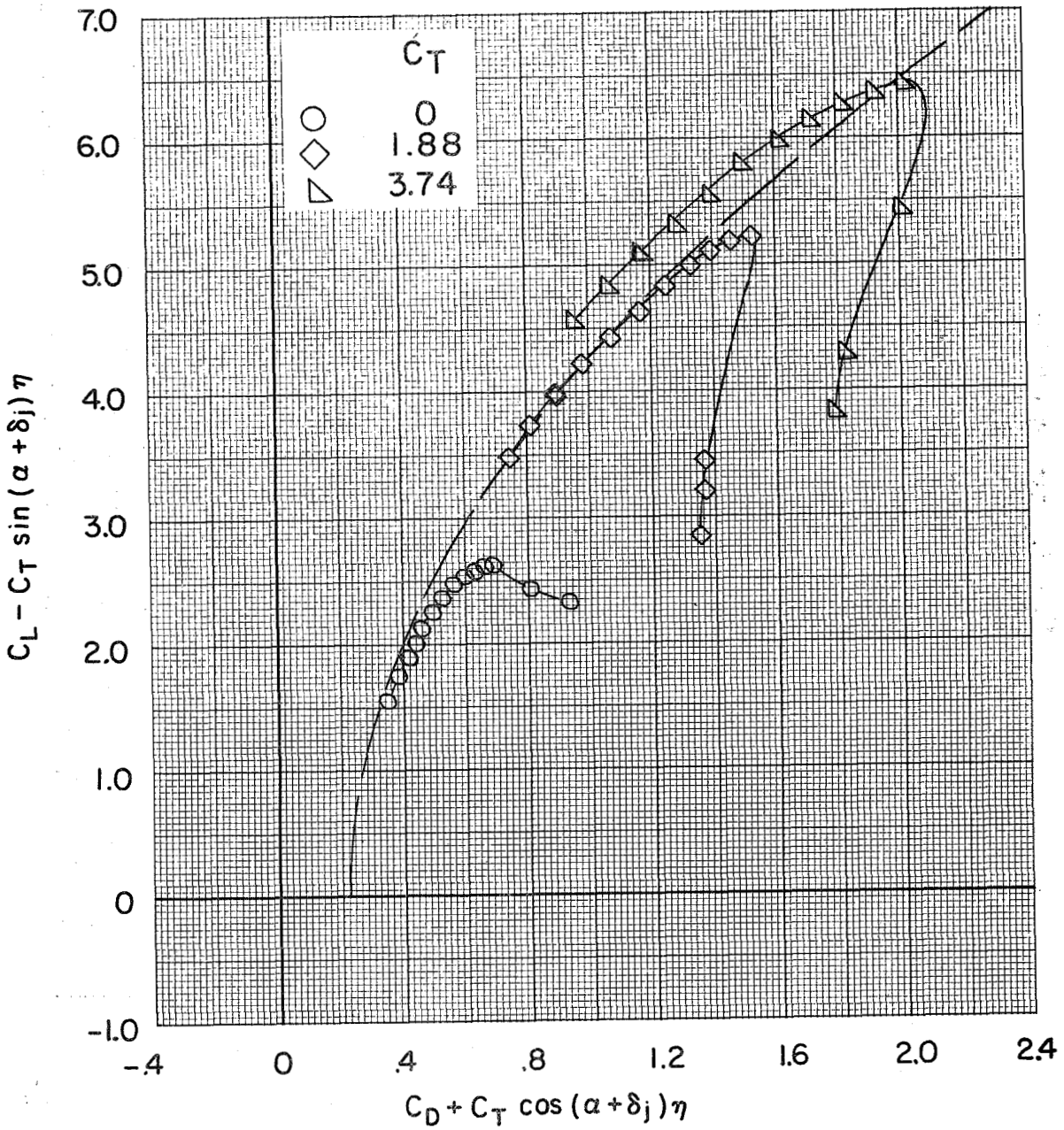

(d) $\delta_f = 65^o/65^o/65^o$.

Figure 27.- Concluded.

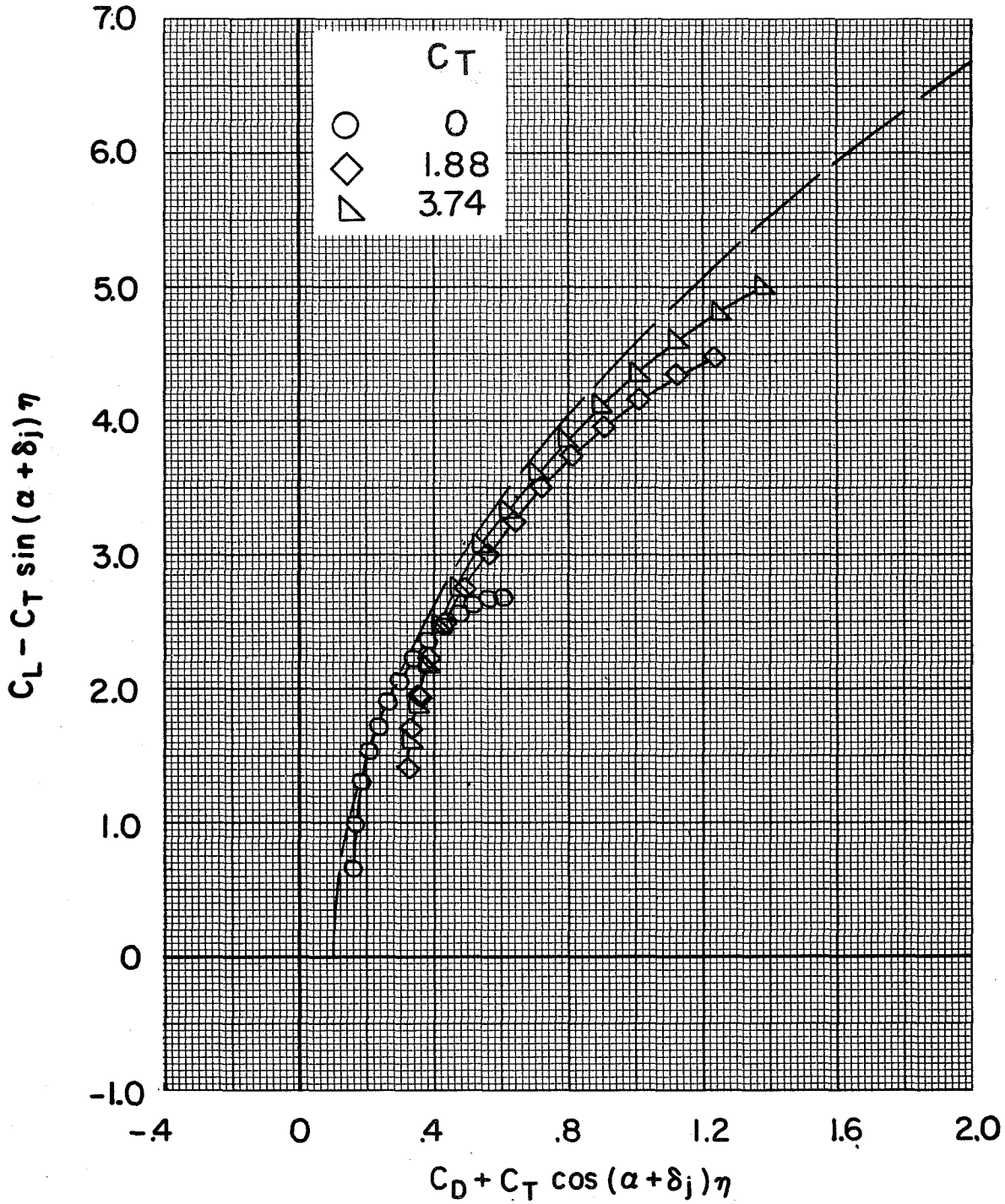

(a) $\delta_f = 0^o/35^o/35^o$.

Figure 28.- Effect of increasing thrust coefficient on the thrust-removed lift-drag polars. BPR 6.2; tail off; c_s = 25 percent; $\delta_s = 50^o$.

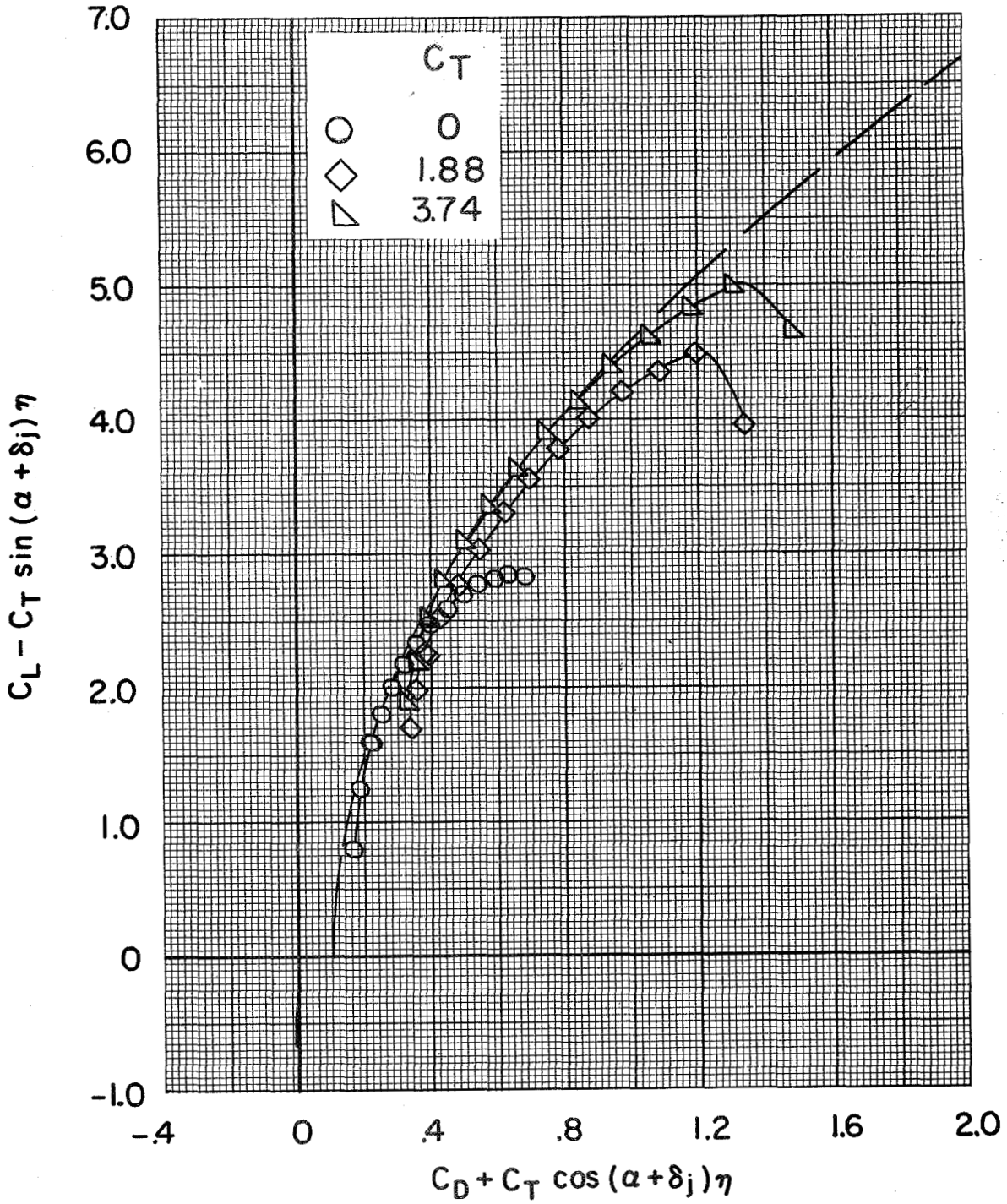

(b) $\delta_f = 35^o/35^o/35^o$.

Figure 28.- Continued.

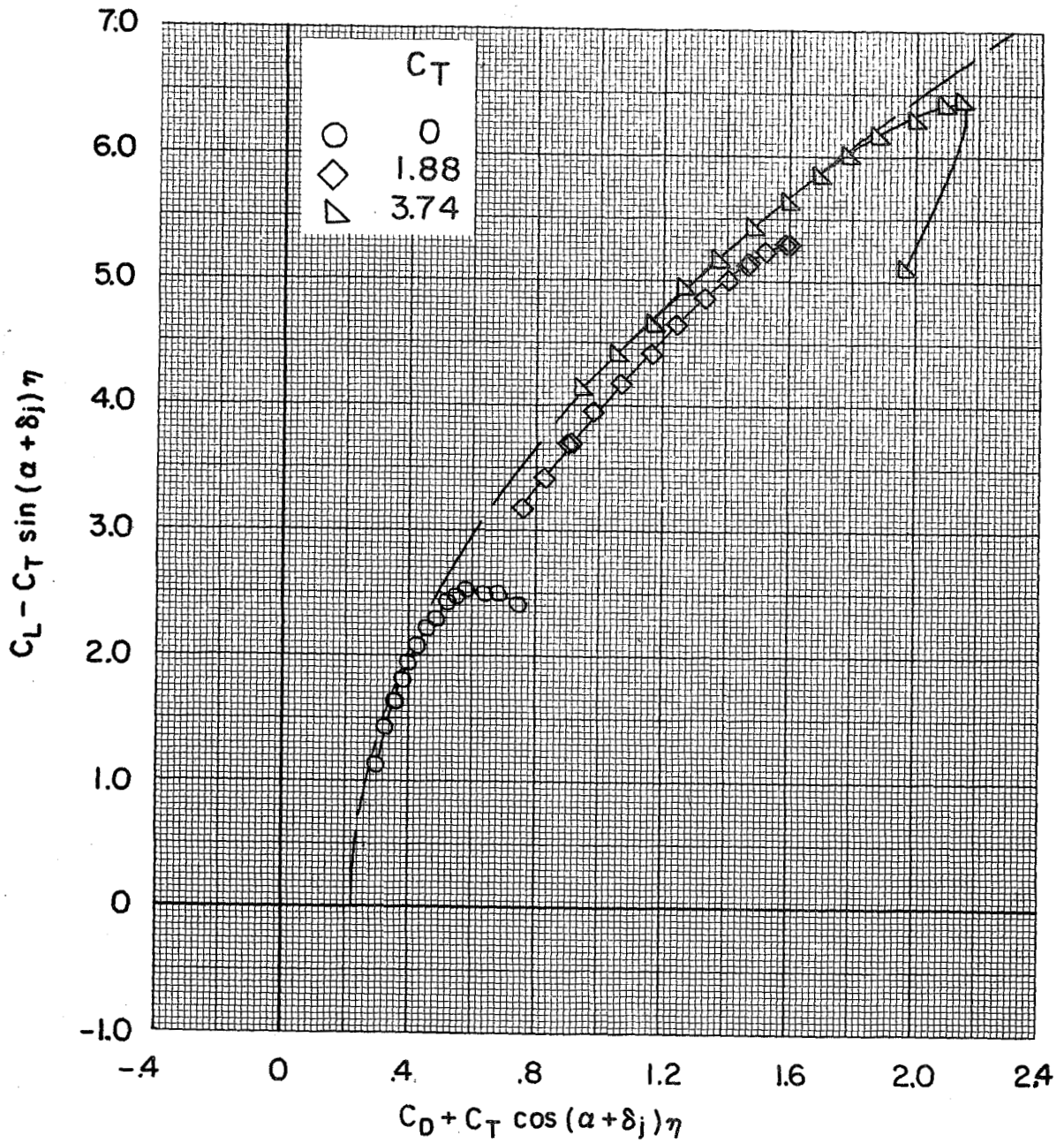

(c) $\delta_f = 0^o/65^o/65^o$.

Figure 28.- Continued.

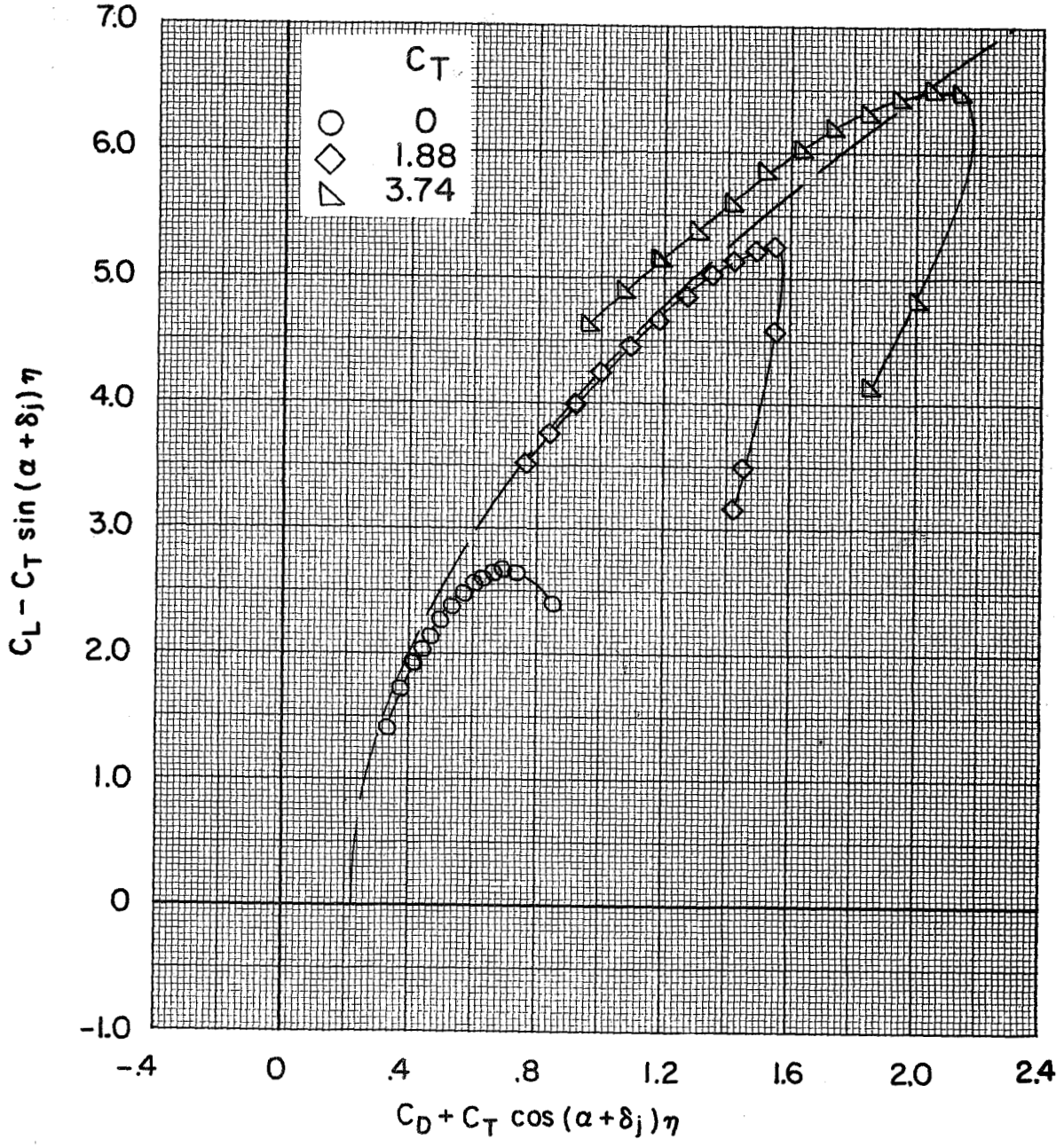

(d) $\delta_f = 65^o/65^o/65^o$.

Figure 28.- Concluded.

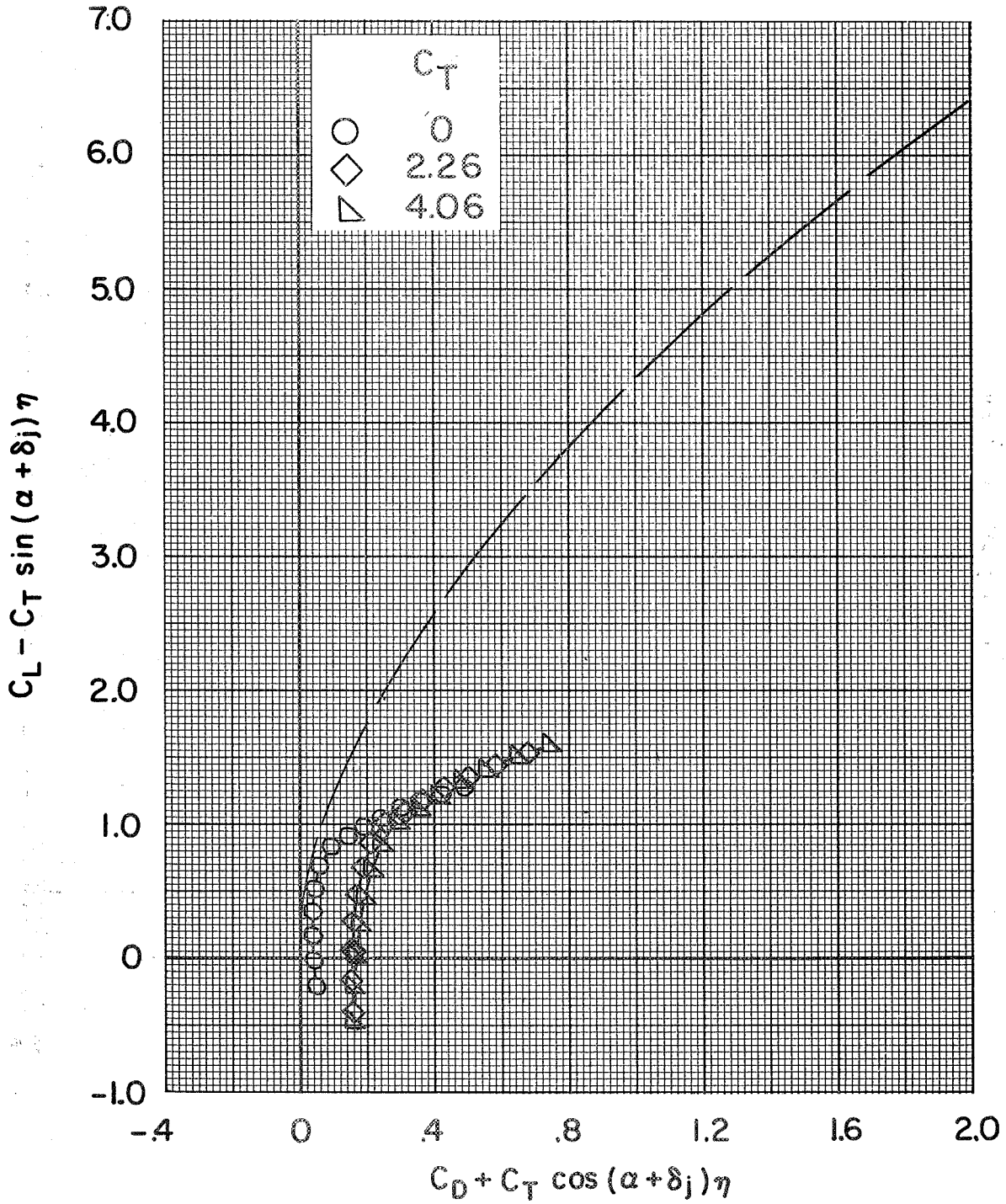

(a) $\delta_f = 0^o/0^o/0^o$.

Figure 29.- Effect of increasing thrust coefficient on the thrust-removed lift-drag polars. BPR 10.0; tail off; slat off.

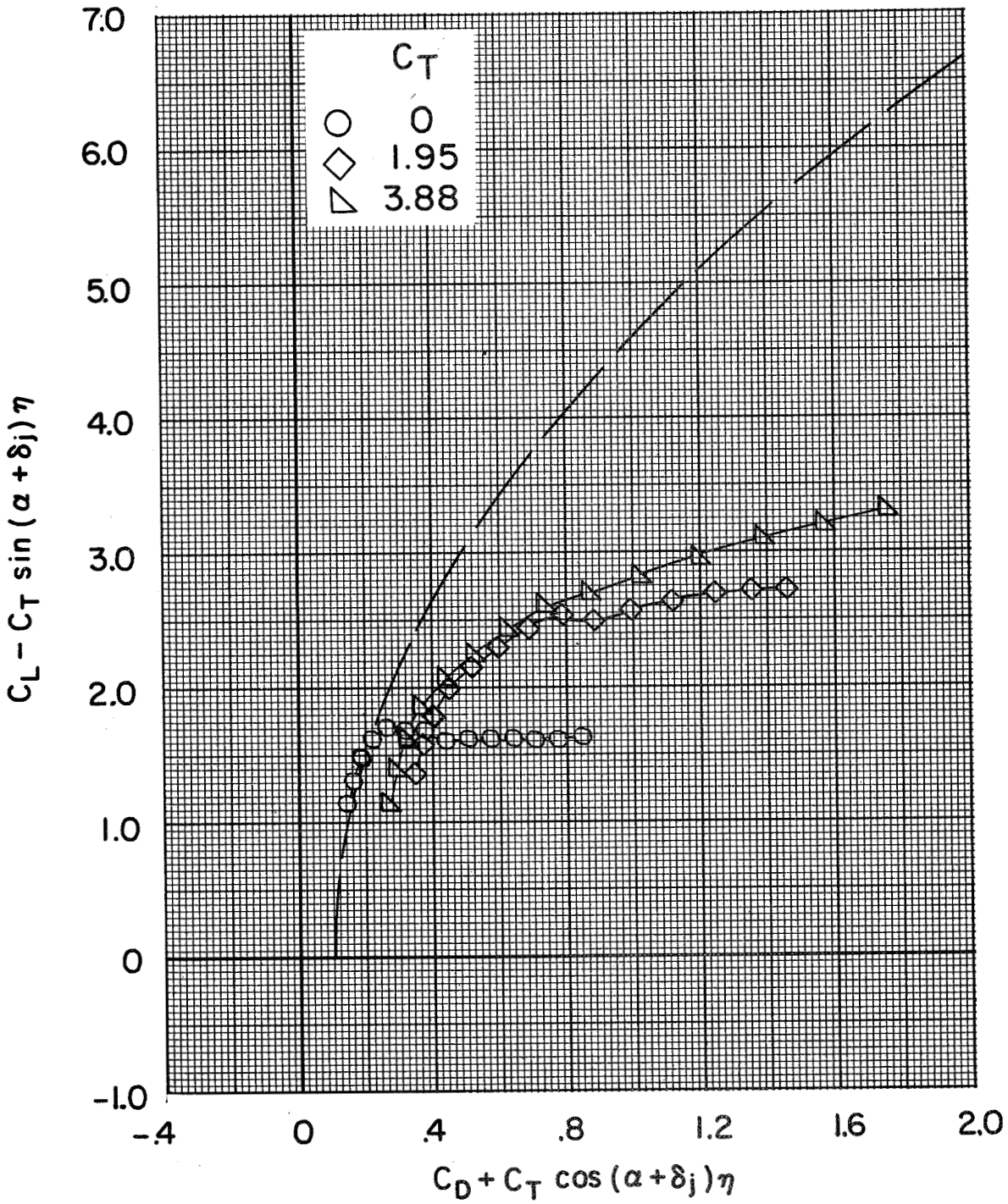

(b) $\delta_f = 0^o/35^o/35^o$.

Figure 29.- Continued.

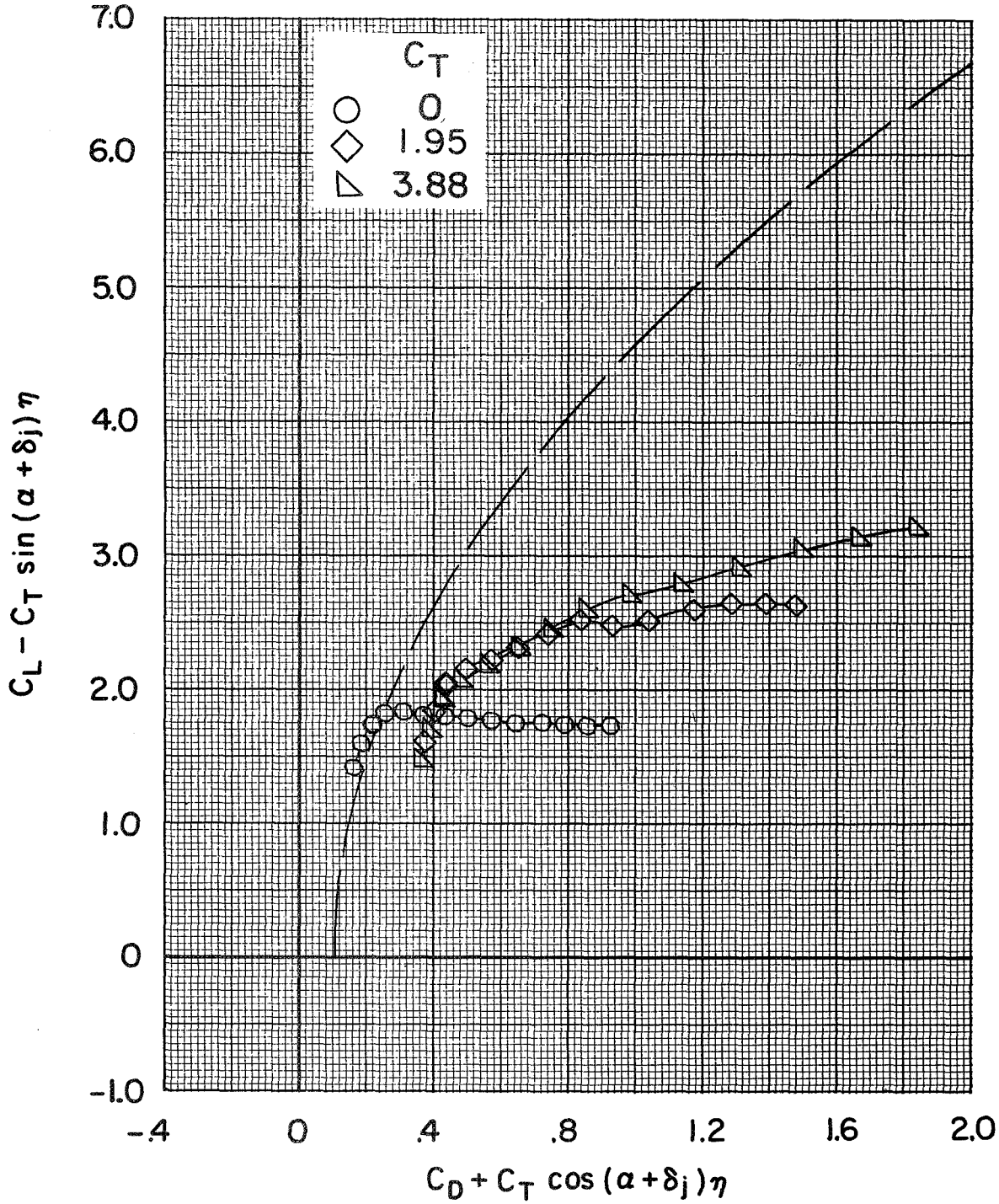

(c) $\delta_f = 35^o/35^o/35^o$.

Figure 29.- Continued.

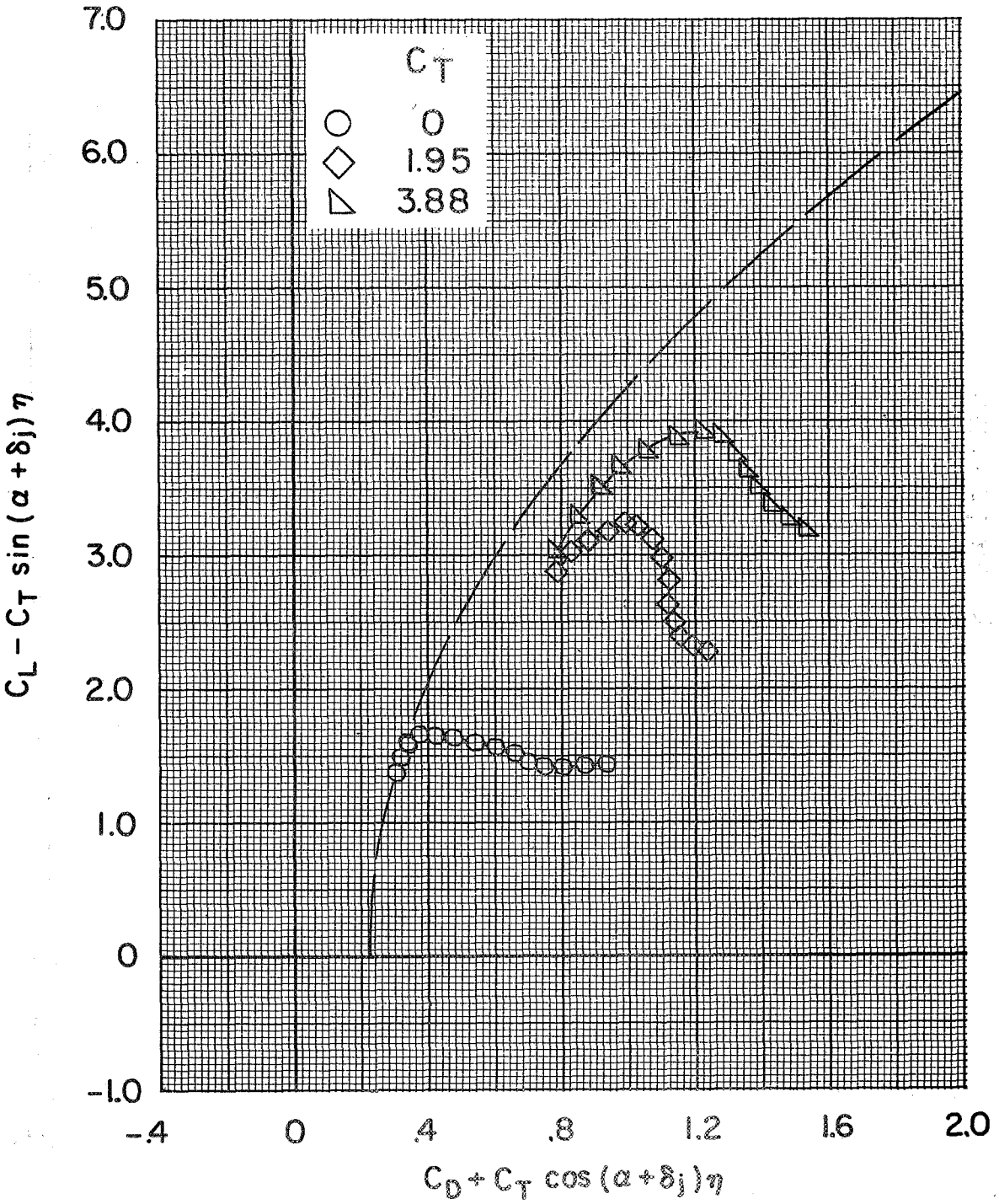

(d) $\delta_f = 0^o/65^o/65^o$.

Figure 29.- Continued.

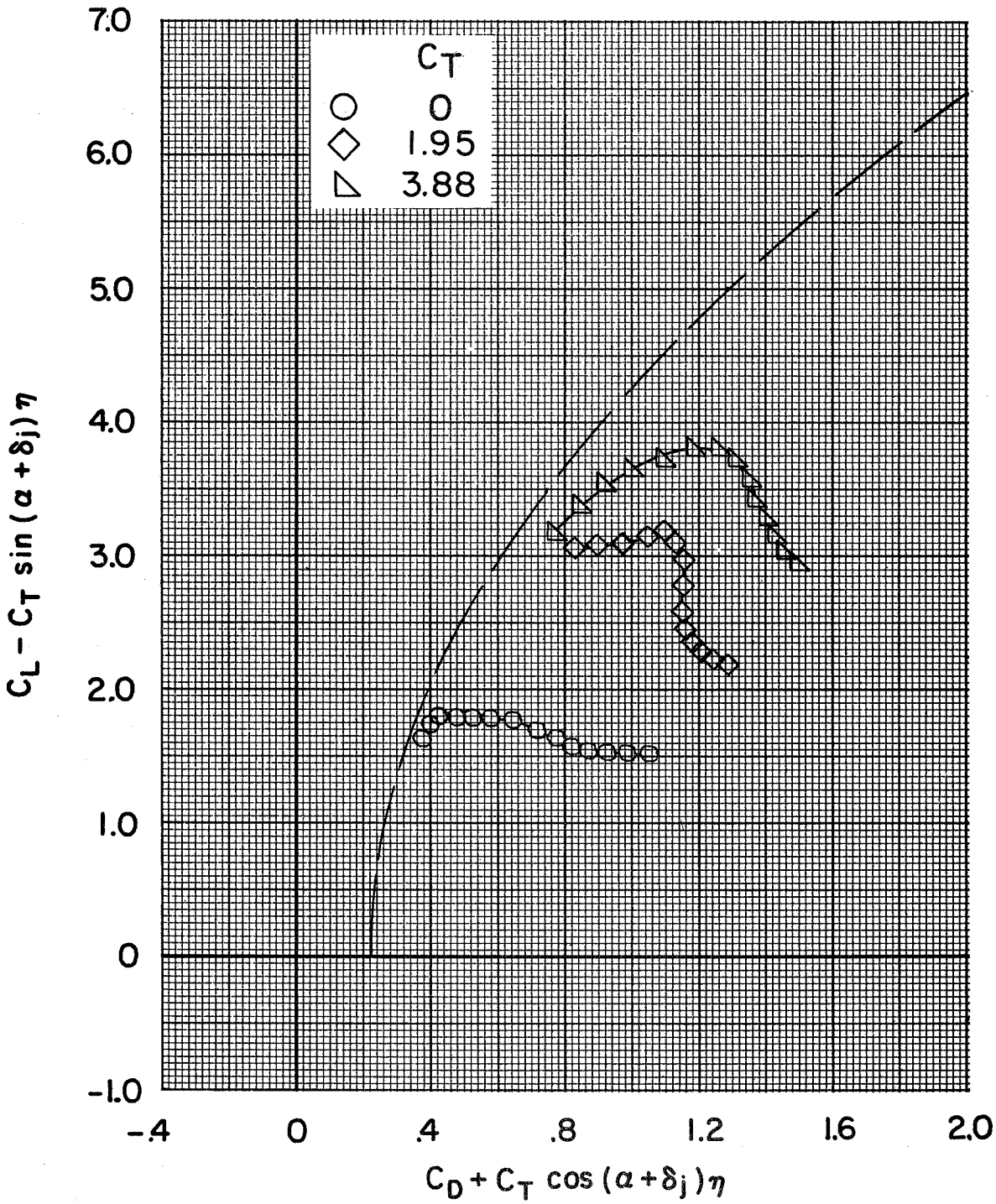

(e) $\delta_f = 65^o/65^o/65^o$.

Figure 29.- Concluded.

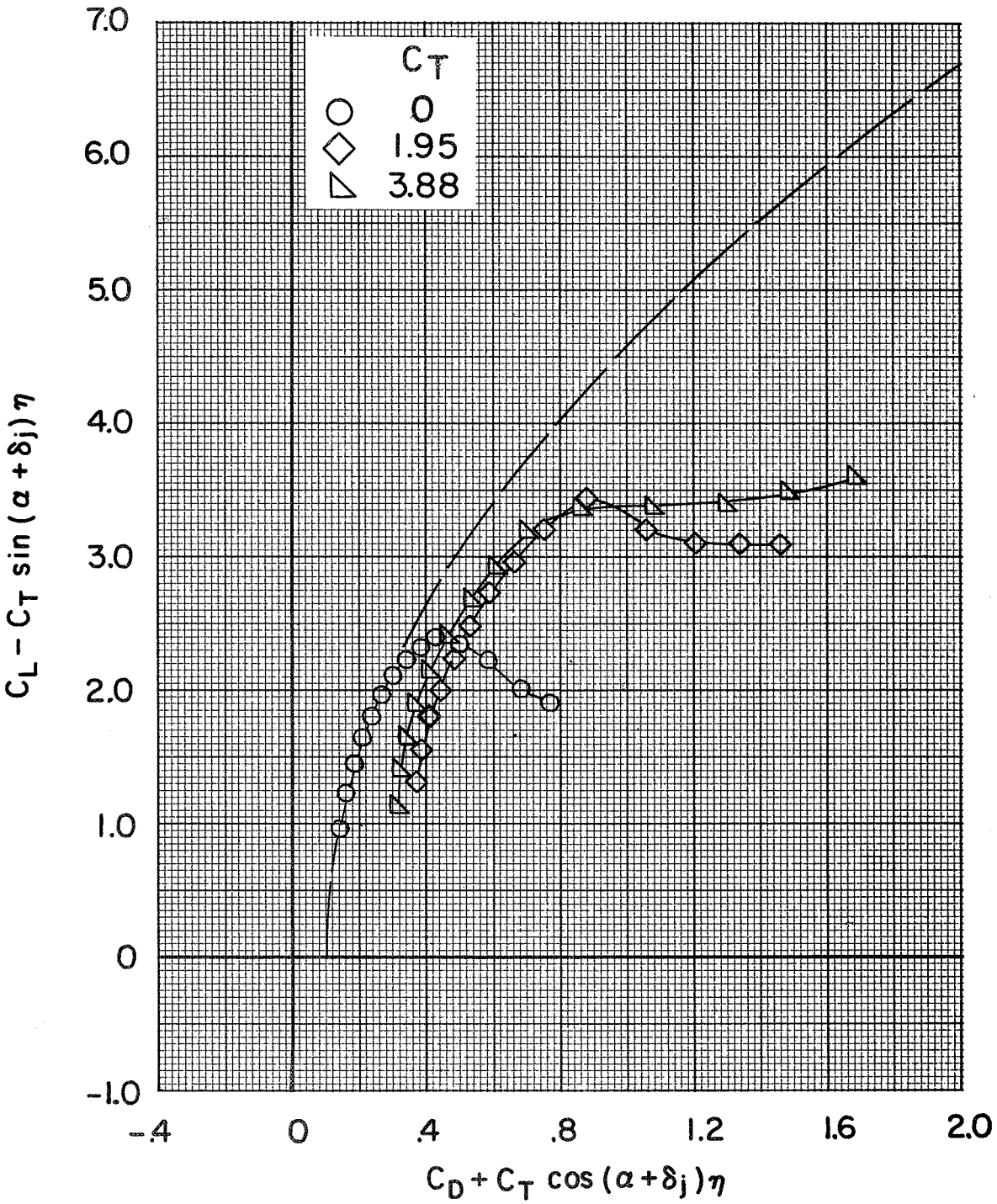

(a) $\delta_f = 0^o/35^o/35^o$.

Figure 30.- Effect of increasing thrust coefficient on the thrust-removed lift-drag polars. BPR 10.0; tail off; c_s = 15 percent; $\delta_s = 40^o$.

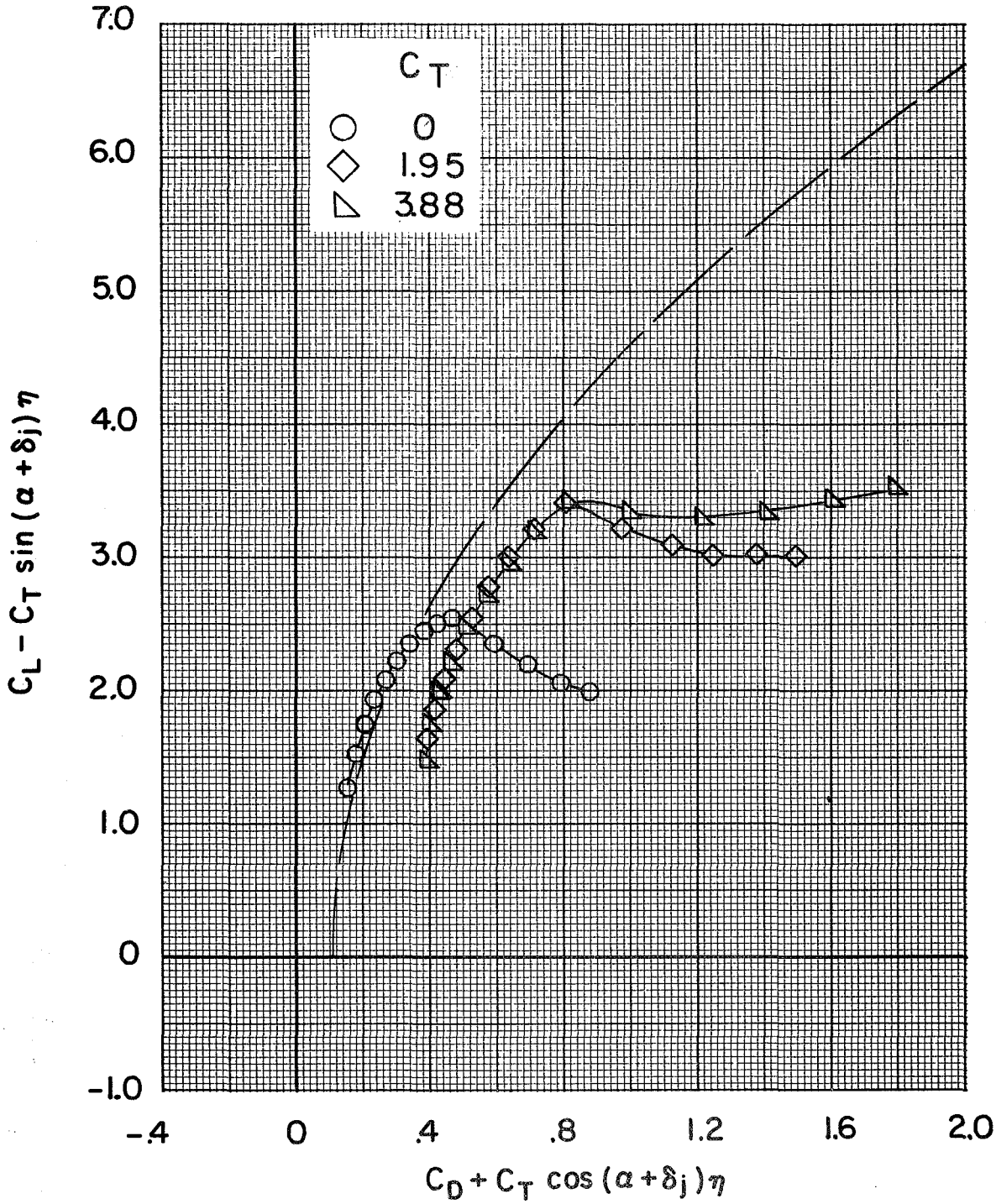

(b) $\delta_f = 35^o/35^o/35^o$.

Figure 30.- Continued.

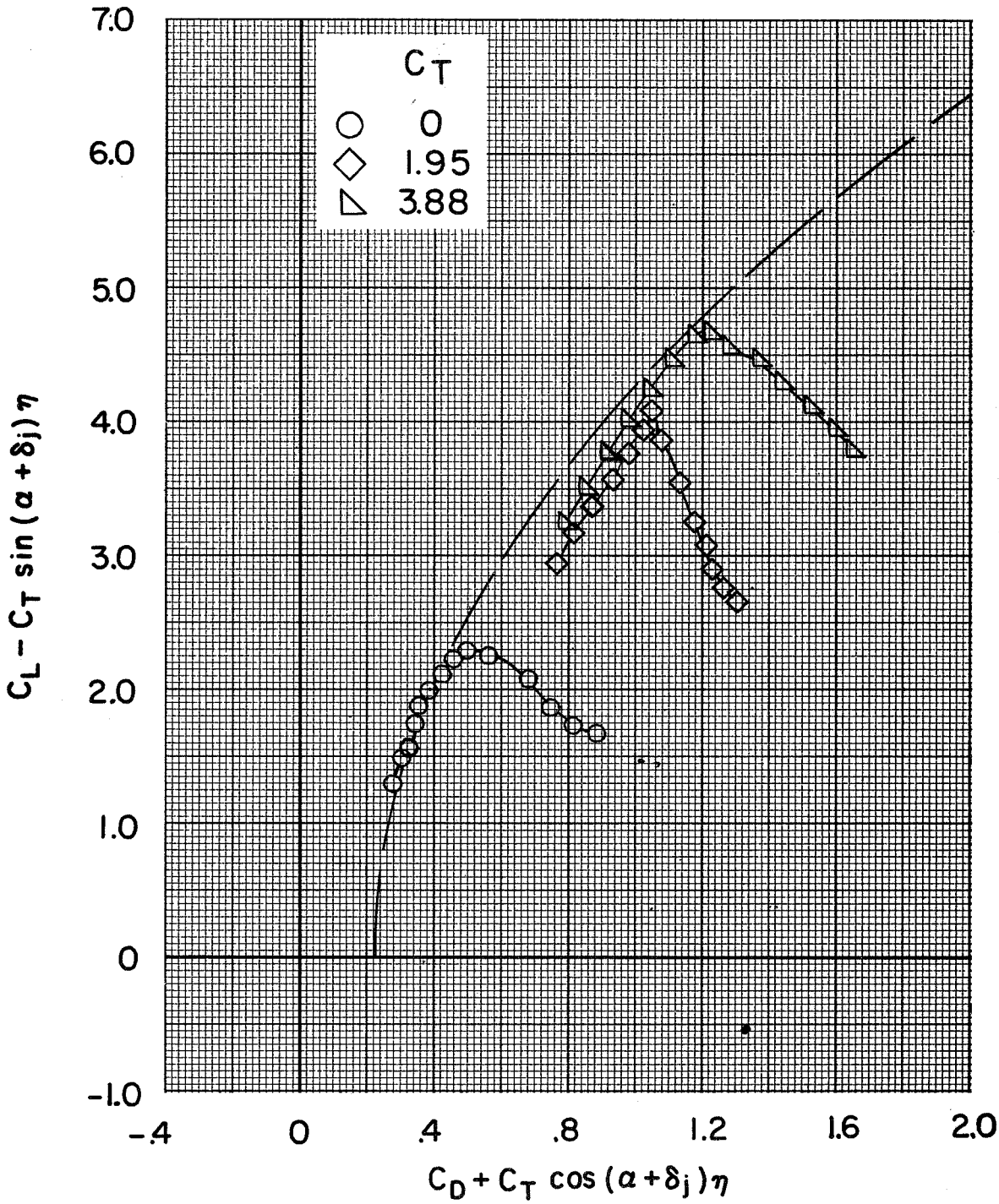

(c) $\delta_f = 0^o/65^o/65^o$.

Figure 30.- Continued.

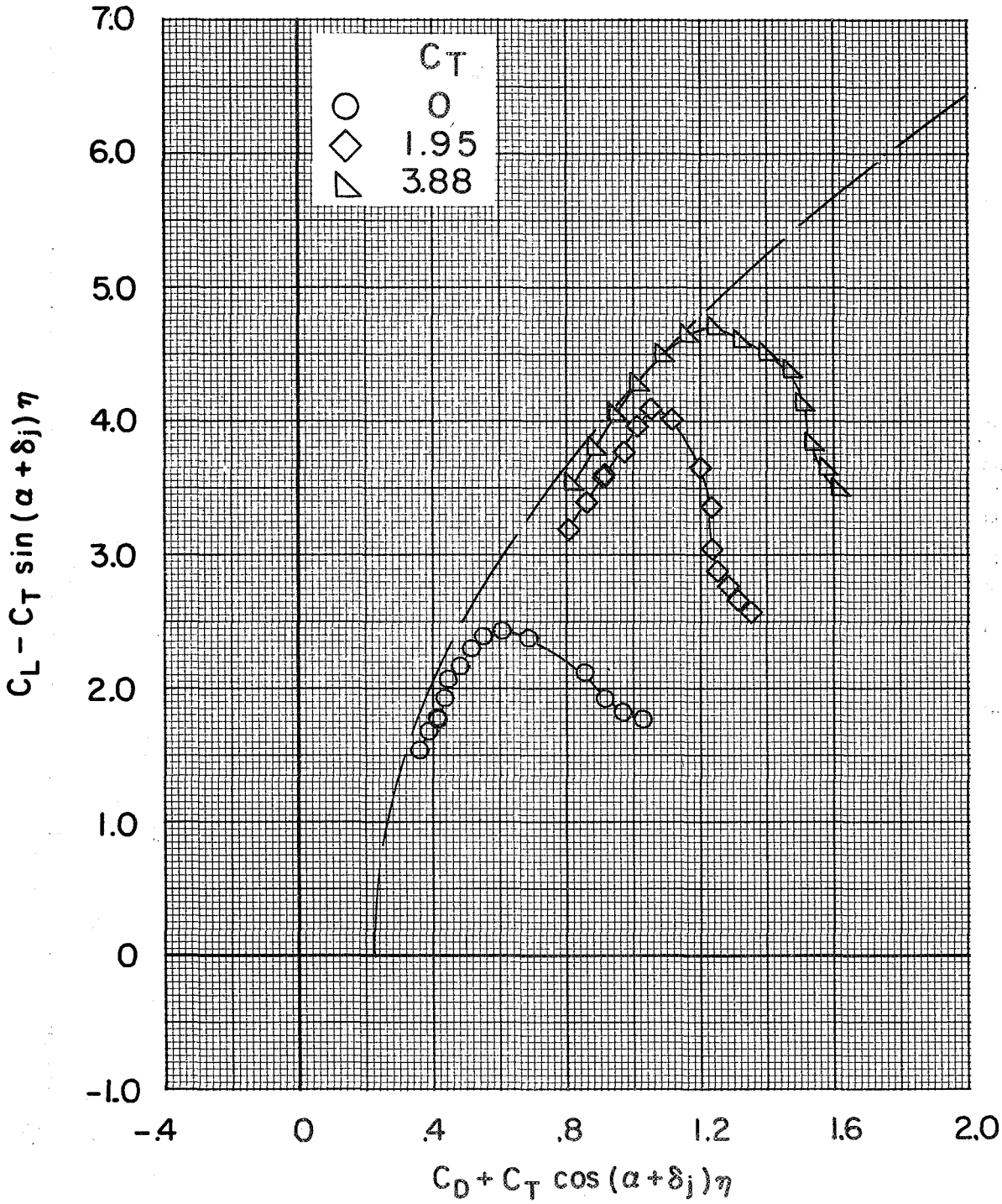

(d) $\delta_f = 65^o/65^o/65^o$.

Figure 30.- Concluded.

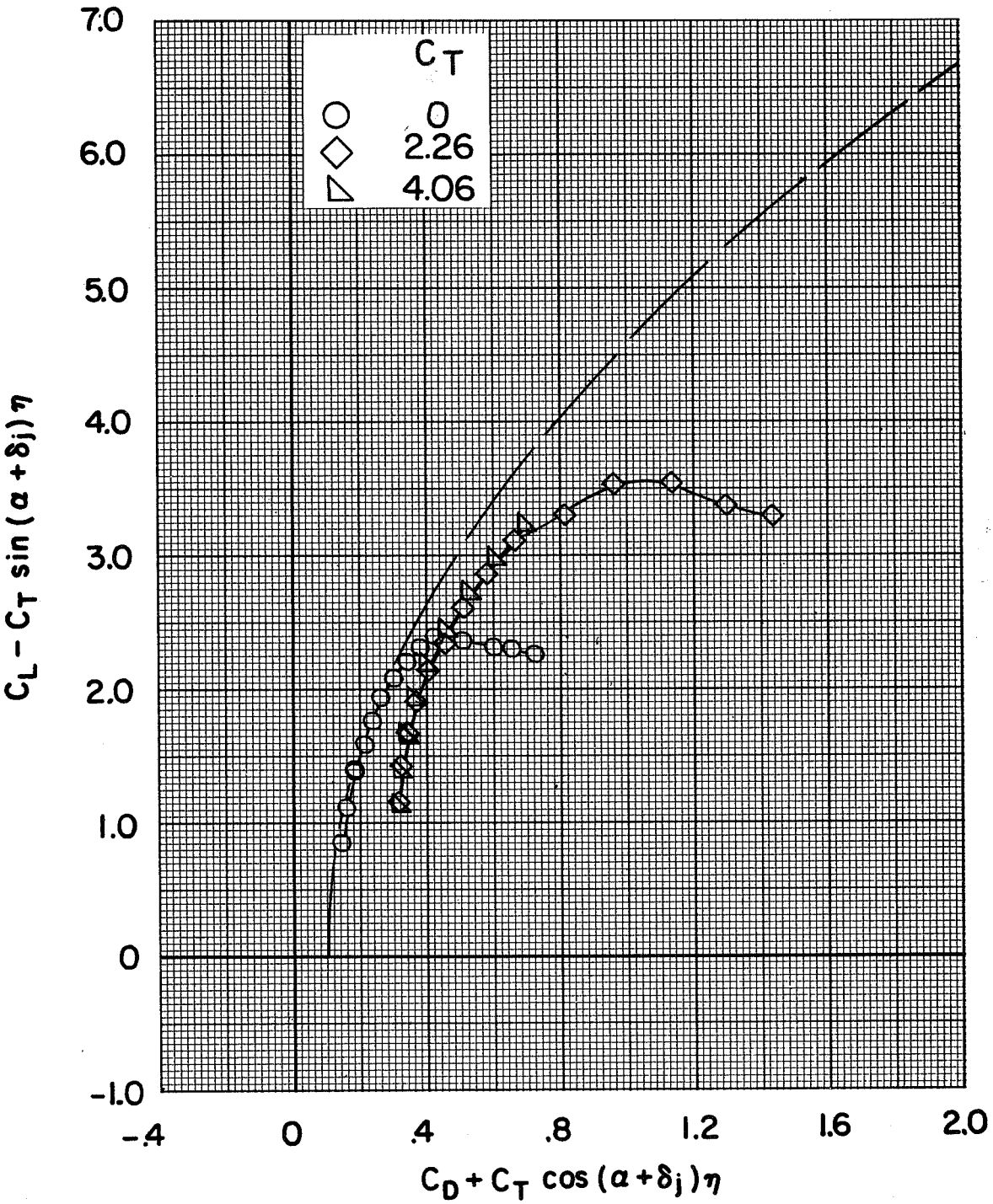

(a) $\delta_f = 0^o/35^o/35^o$.

Figure 31.- Effect of increasing thrust coefficient on the thrust-removed lift-drag polars. BPR 10.0; tail off; c_s = 15 percent; $\delta_s = 50^o$.

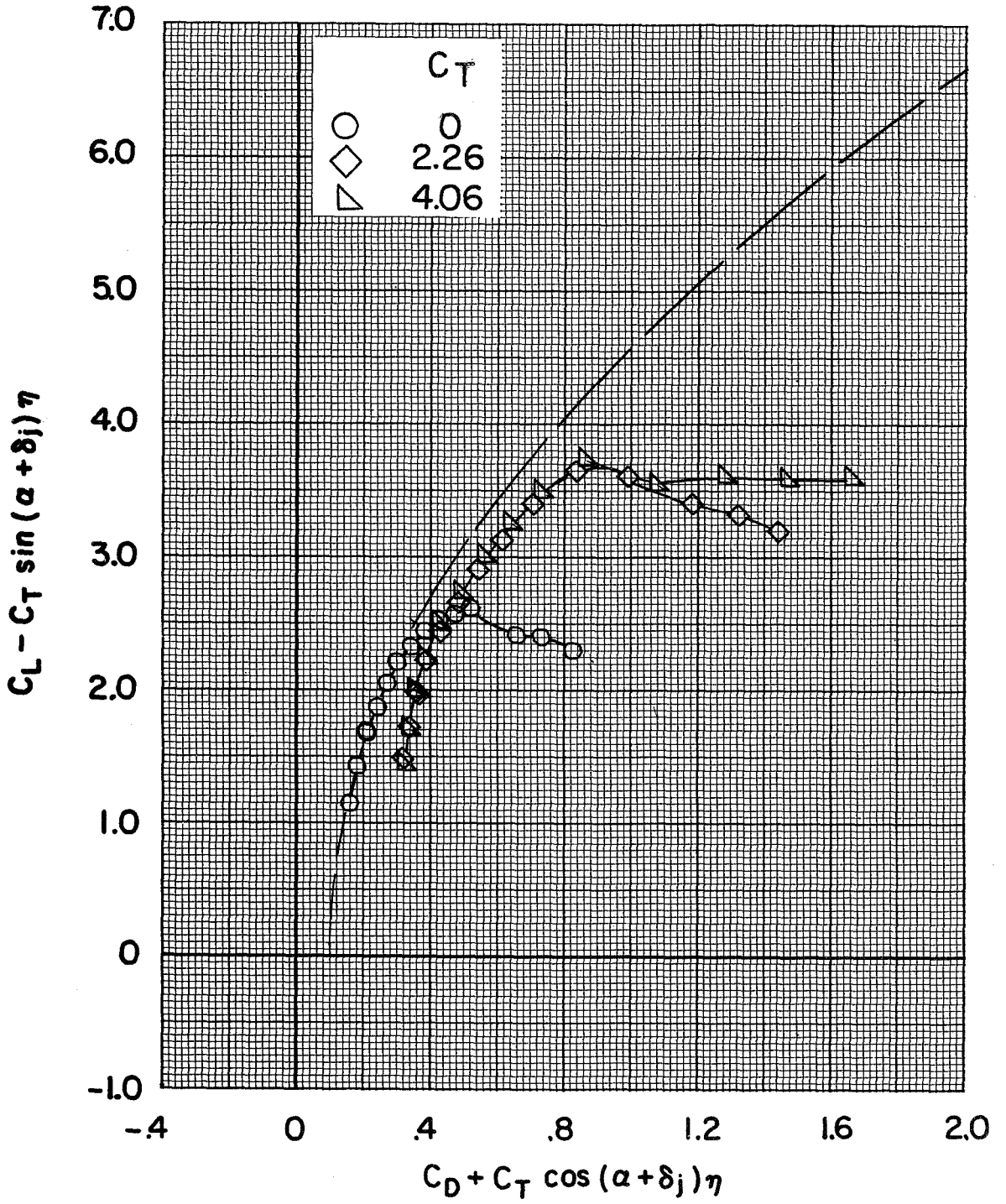

(b) $\delta_f = 35^o/35^o/35^o$.

Figure 31.- Continued.

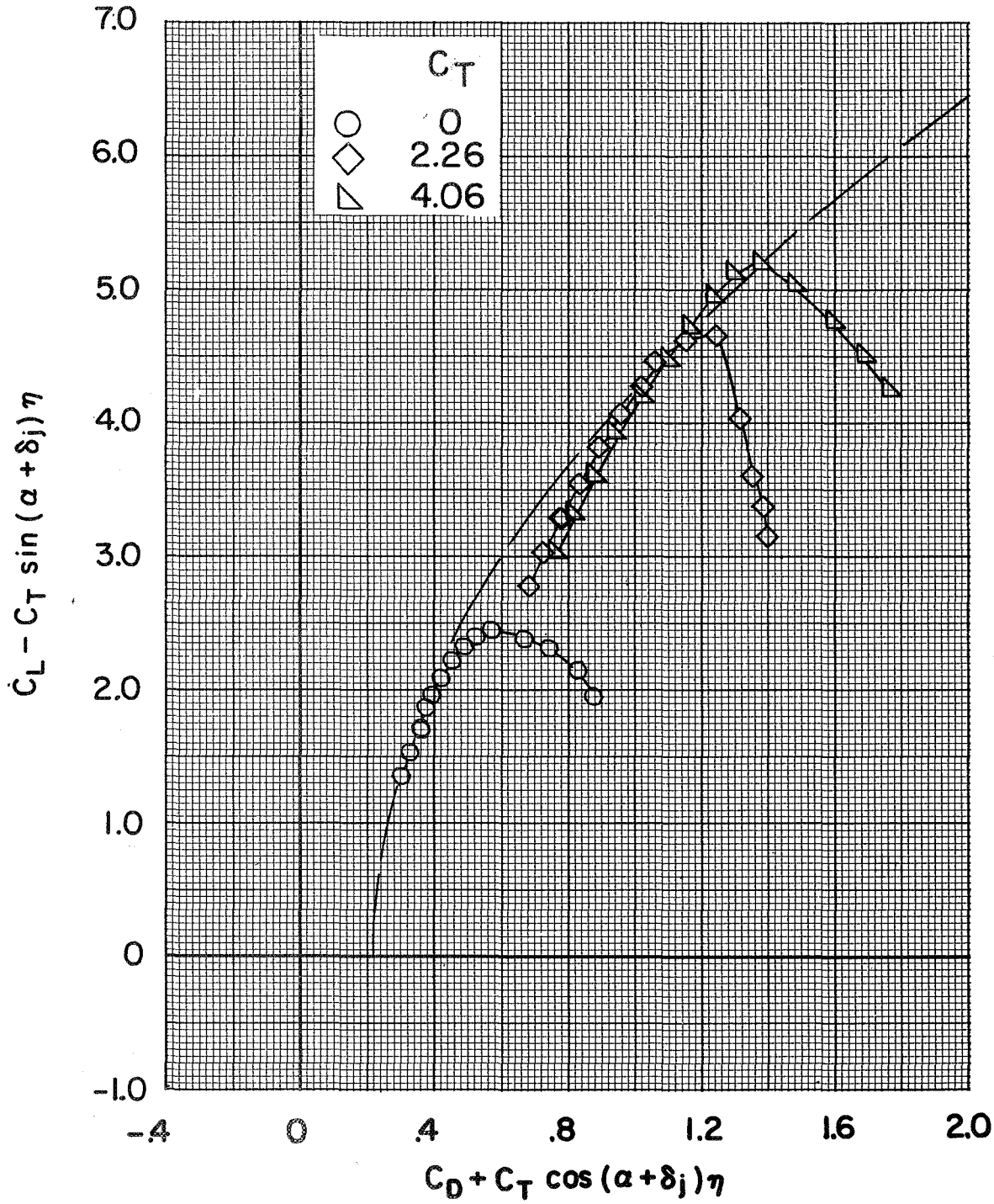

(c) $\delta_f = 0^o/65^o/65^o$.

Figure 31.- Continued.

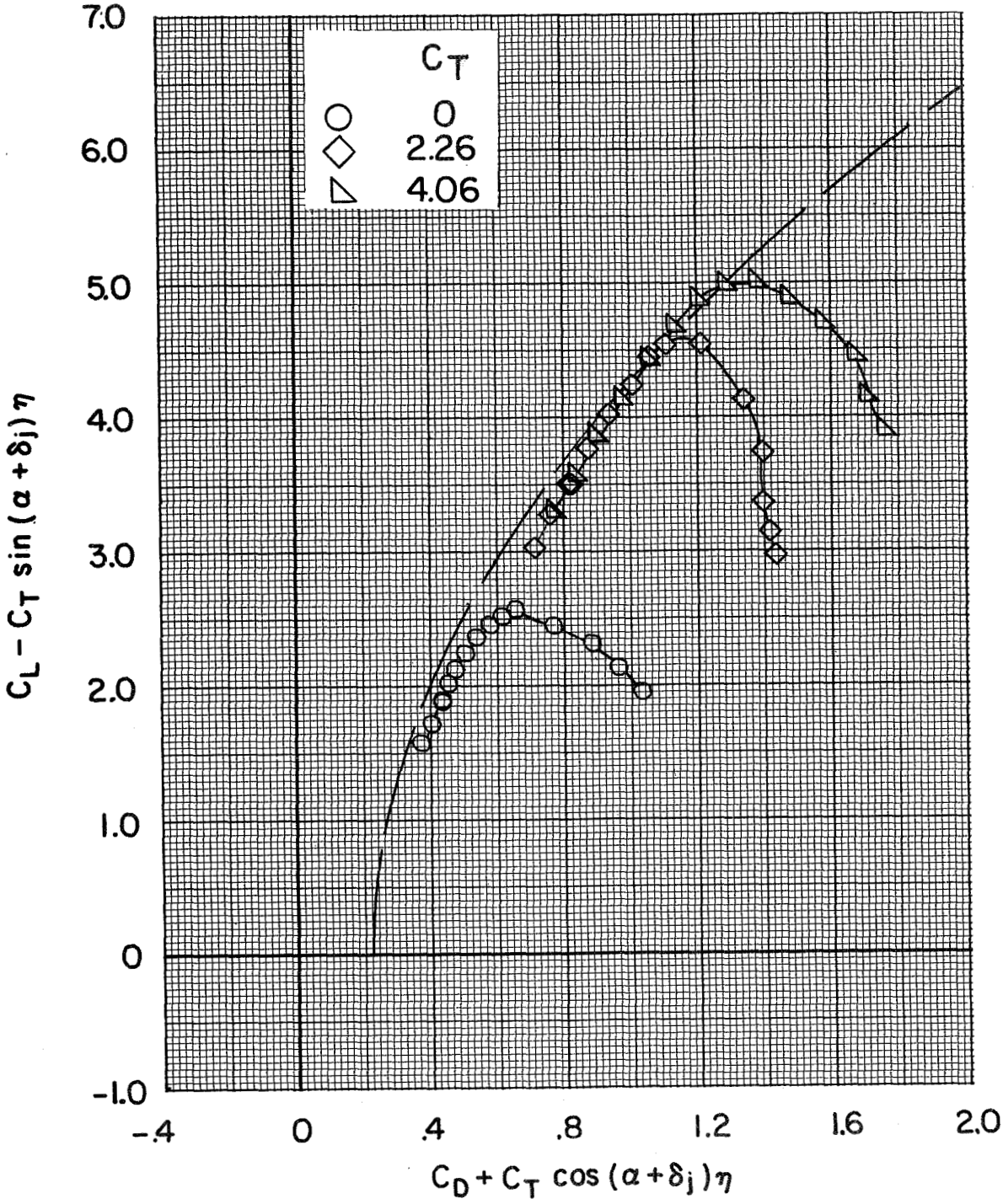

(d) $\delta_f = 65^o/65^o/65^o$.

Figure 31.- Concluded.

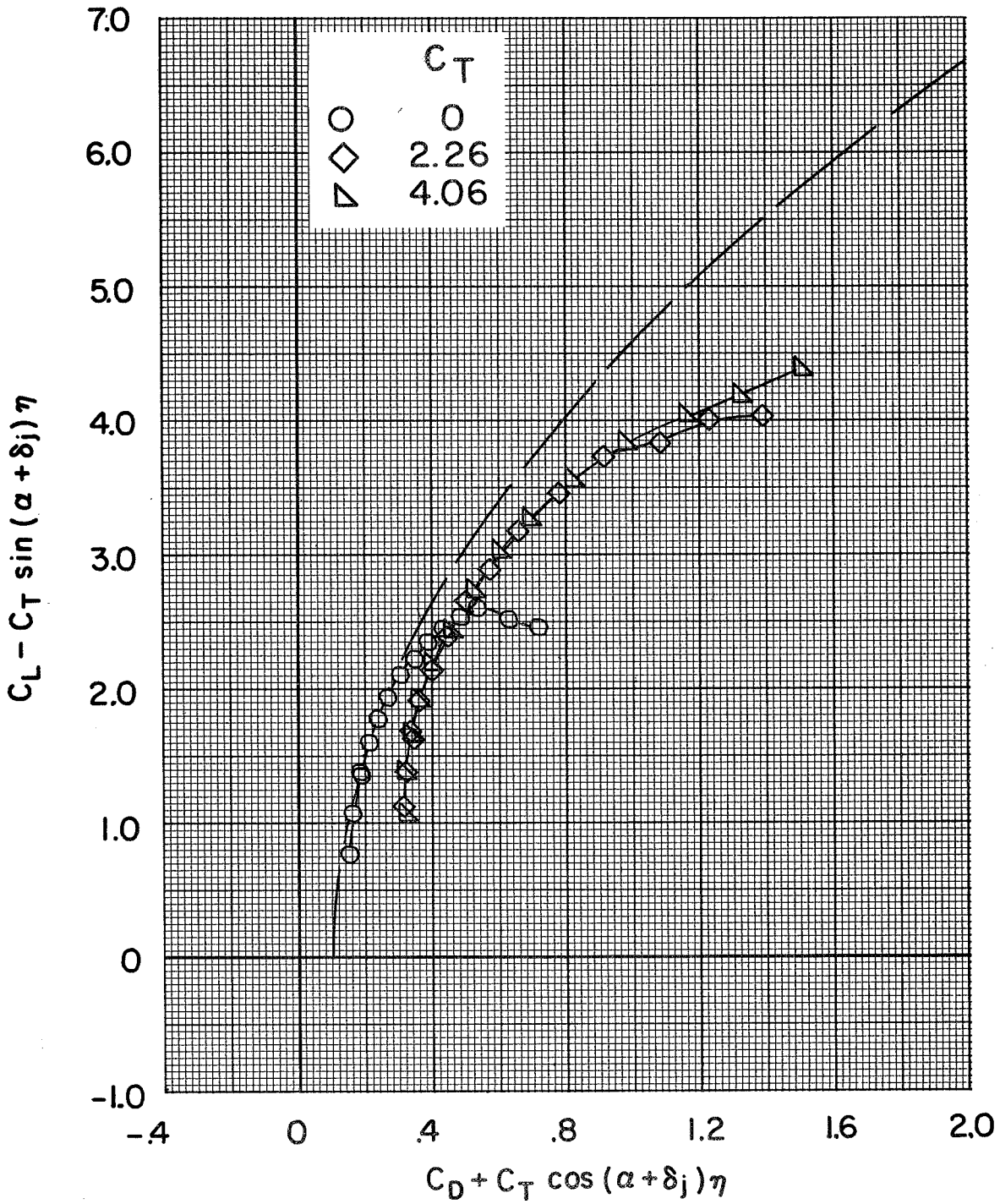

(a) $\delta_f = 0^o/35^o/35^o$.

Figure 32.- Effect of increasing thrust coefficient on the thrust-removed lift-drag polars. BPR 10.0; tail off; c_s = 20 percent; $\delta_s = 50^o$.

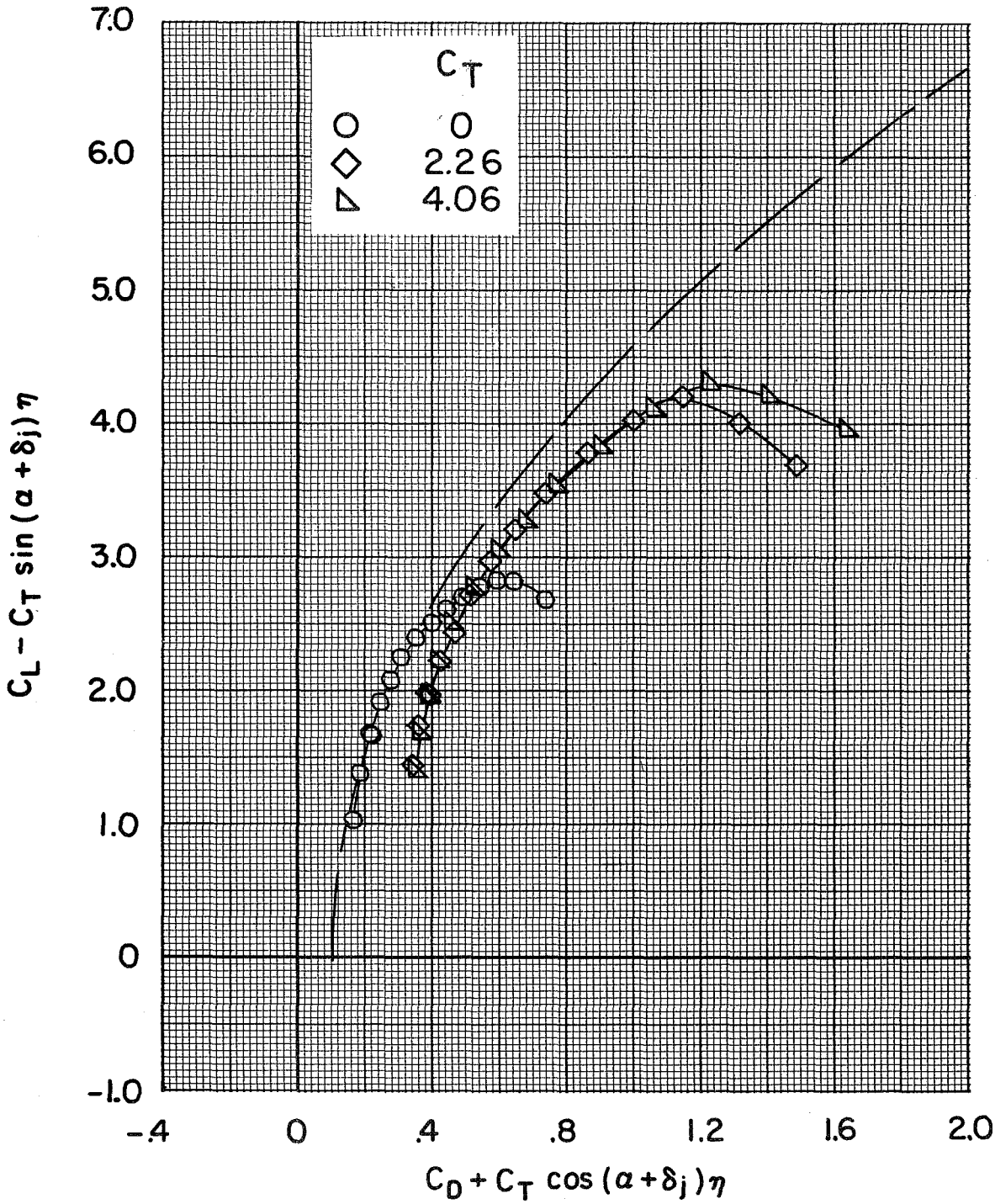

(b) $\delta_f = 35^o/35^o/35^o$.

Figure 32.- Continued.

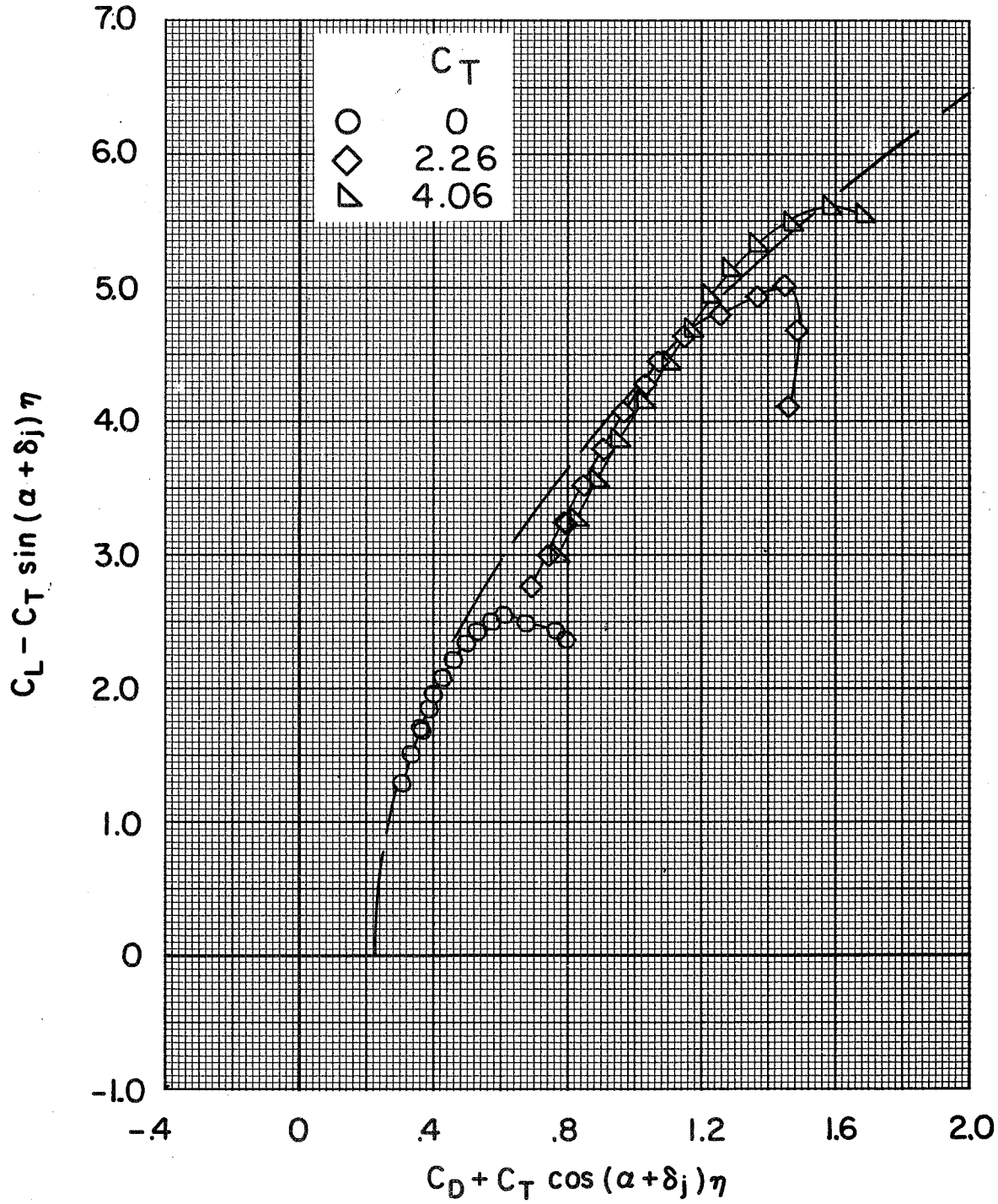

(c) $\delta_f = 0^o/65^o/65^o$.

Figure 32.- Continued.

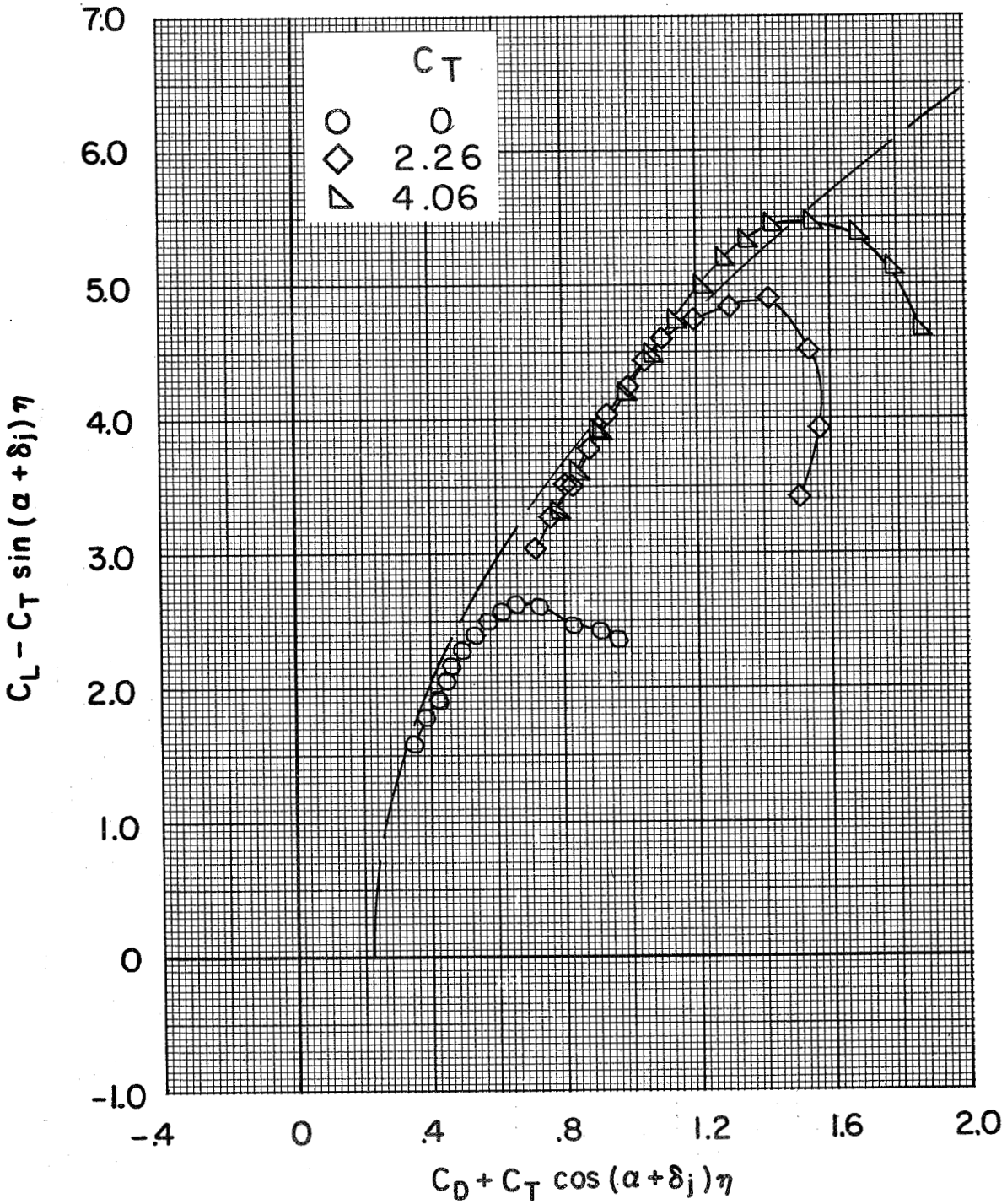

(d) $\delta_f = 65^o/65^o/65^o$.

Figure 32.- Concluded.

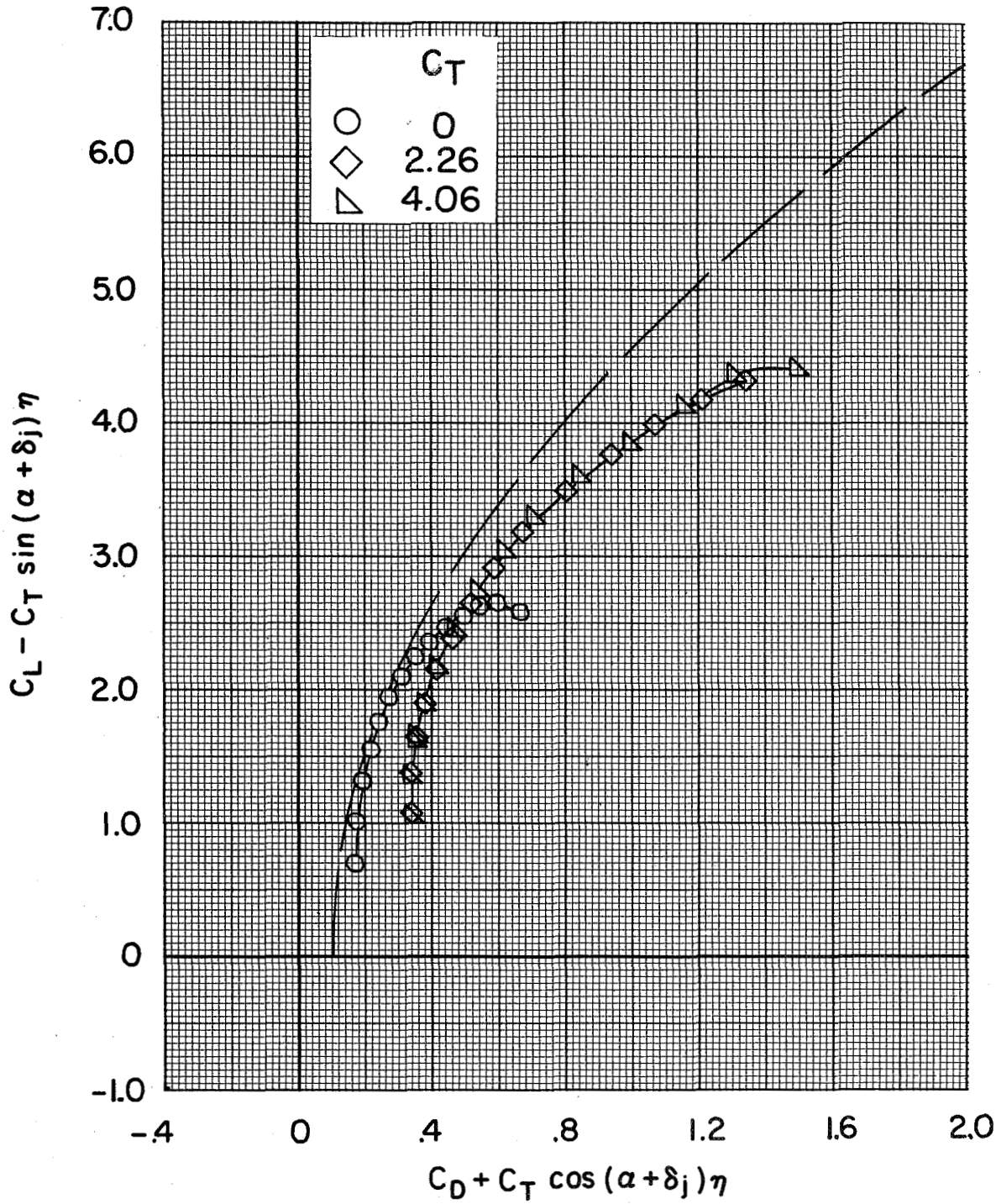

(a) $\delta_f = 0^o/35^o/35^o$.

Figure 33.- Effect of increasing thrust coefficient on the thrust-removed lift-drag polars. BPR 10.0; tail off; c_s = 25 percent; $\delta_s = 50^o$.

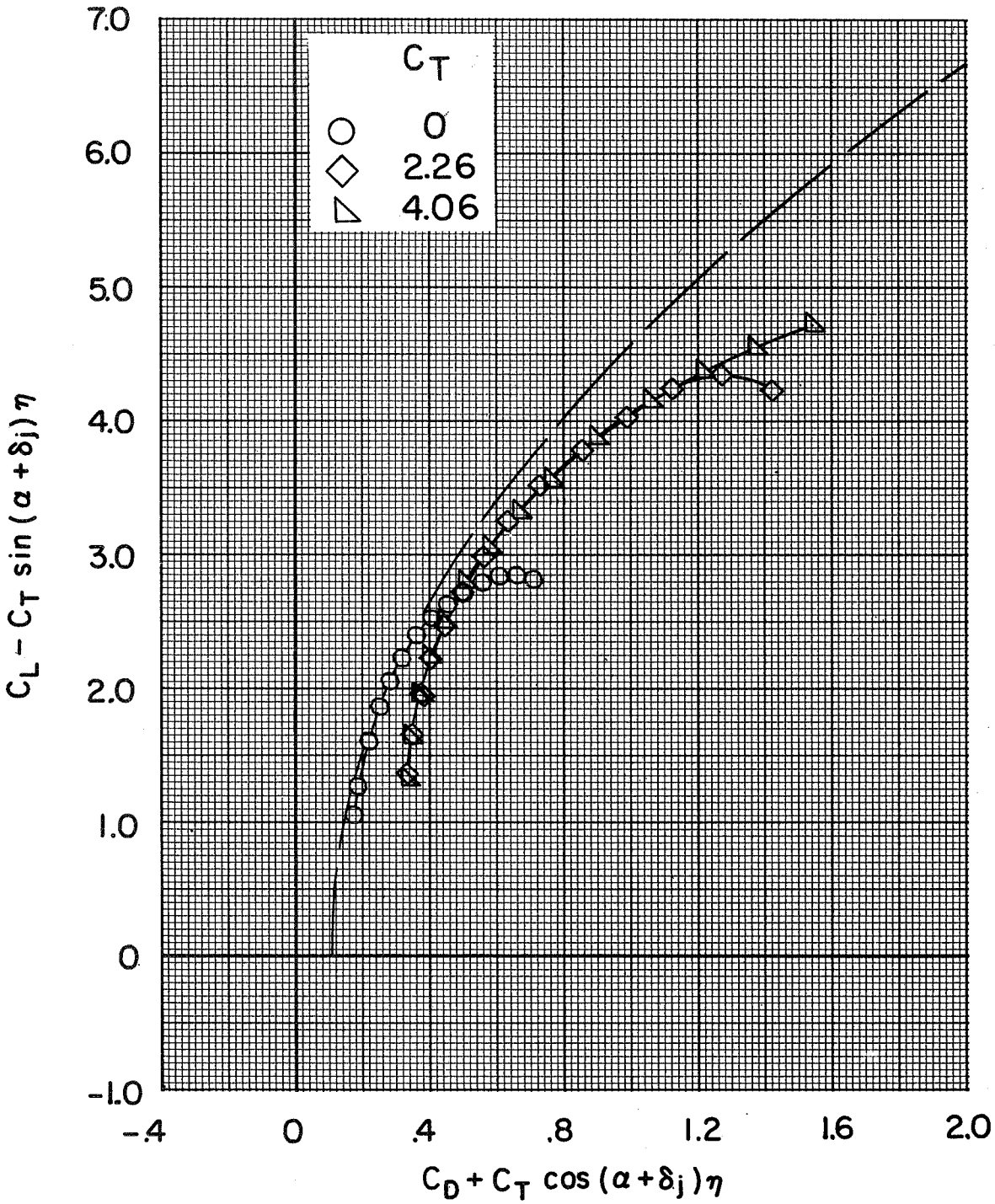

(b) $\delta_f = 35^o/35^o/35^o$.

Figure 33.- Continued.

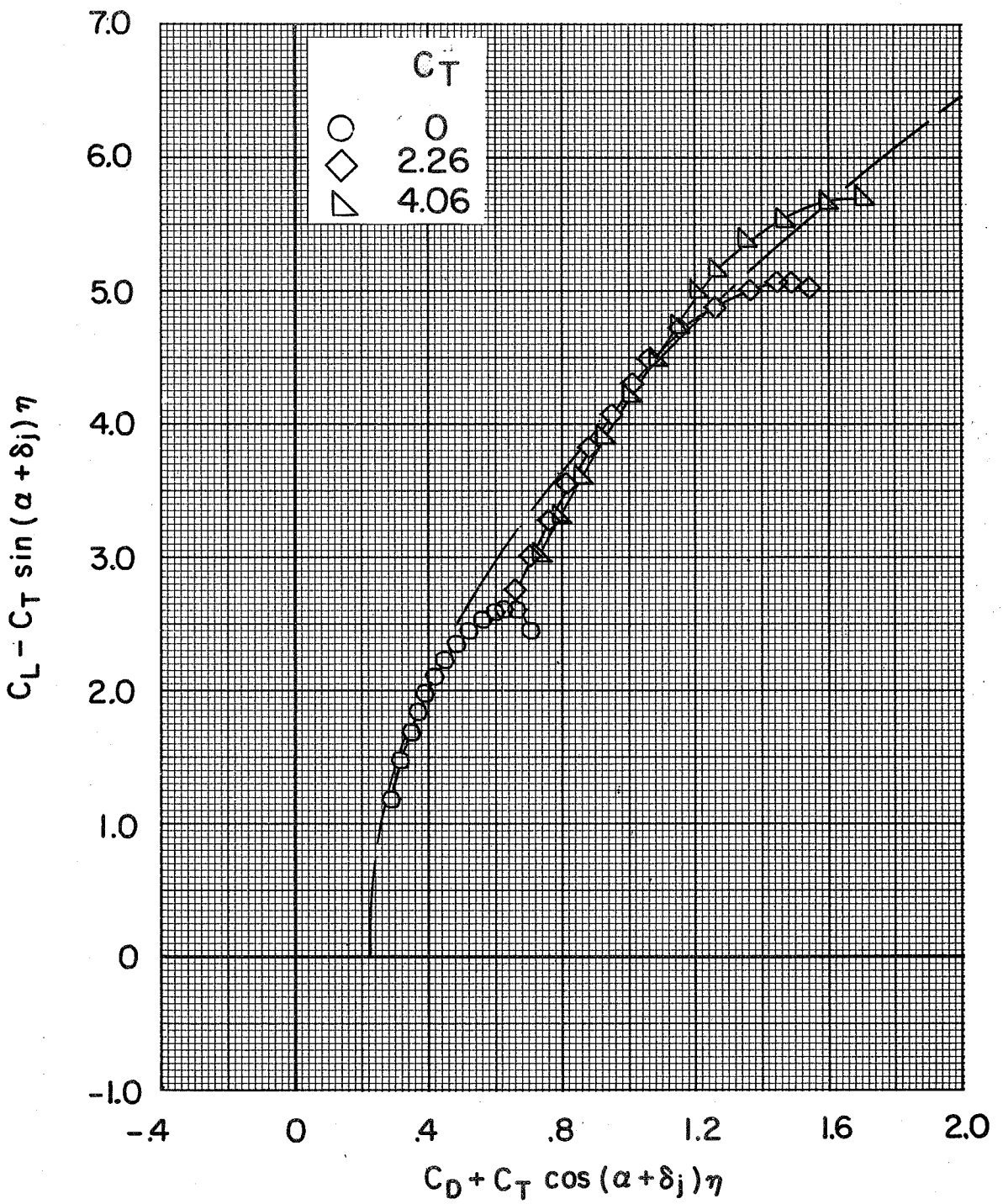

(c) $\delta_f = 0^o/65^o/65^o$.

Figure 33.- Continued.

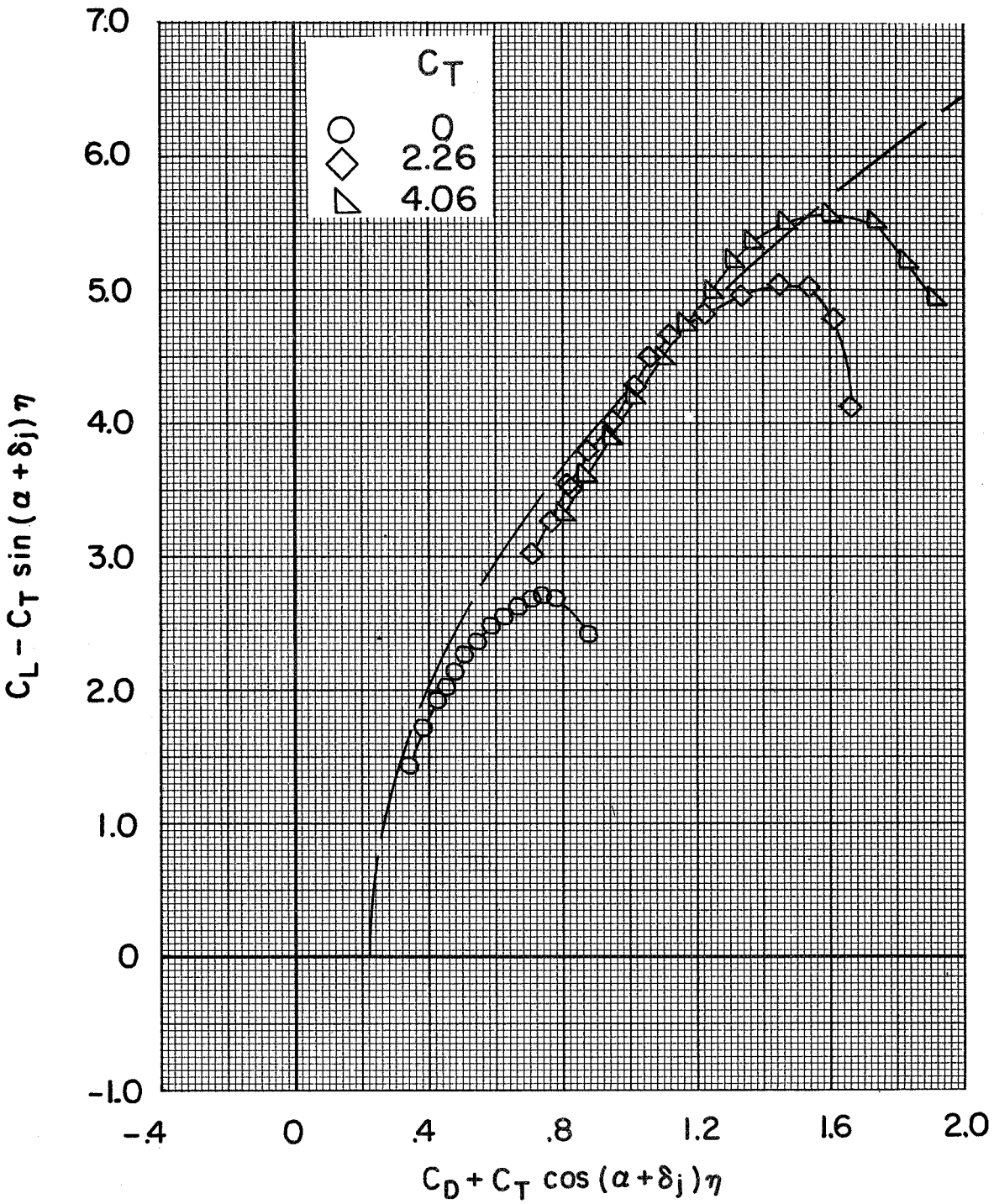

(d) $\delta_f = 65^o/65^o/65^o$.

Figure 33.- Concluded.

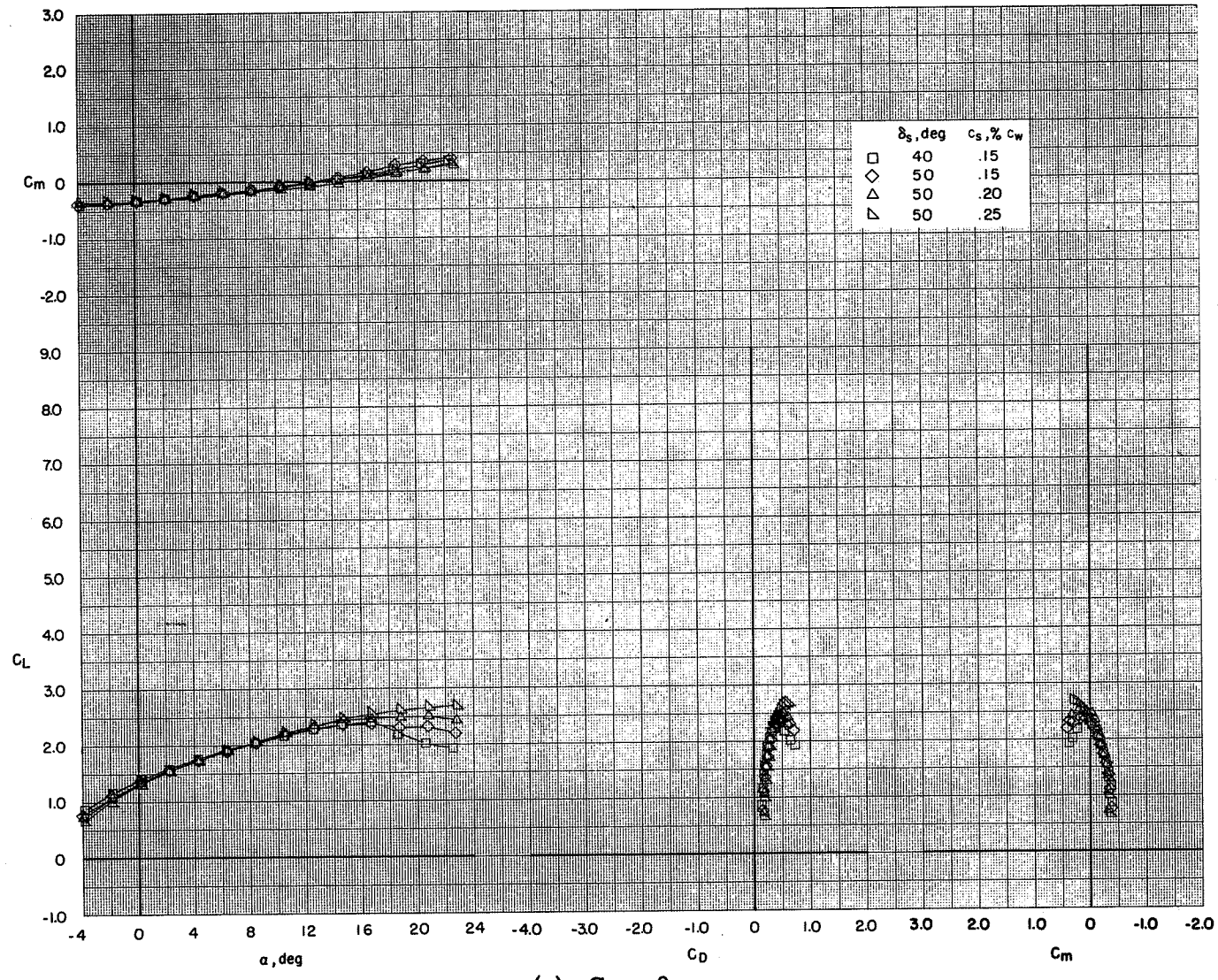

(a) $C_T = 0$.

Figure 34.- Effect of wing leading-edge slat configuration on the longitudinal aerodynamic characteristics of the model with flaps deflected. BPR 6.2; tail off; $\delta_f = 0^o/35^o/35^o$.

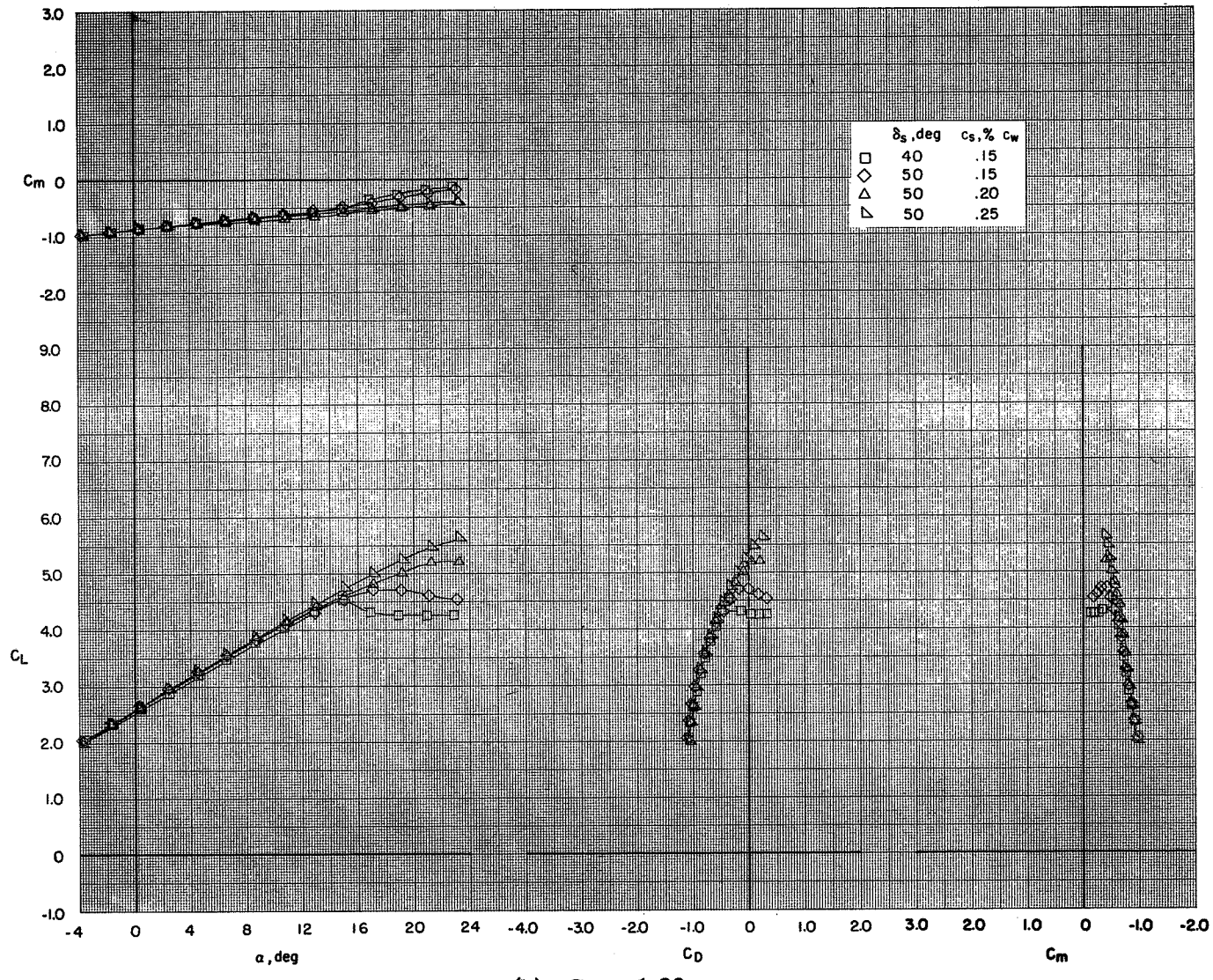

(b) $C_T = 1.88$.

Figure 34.- Continued.

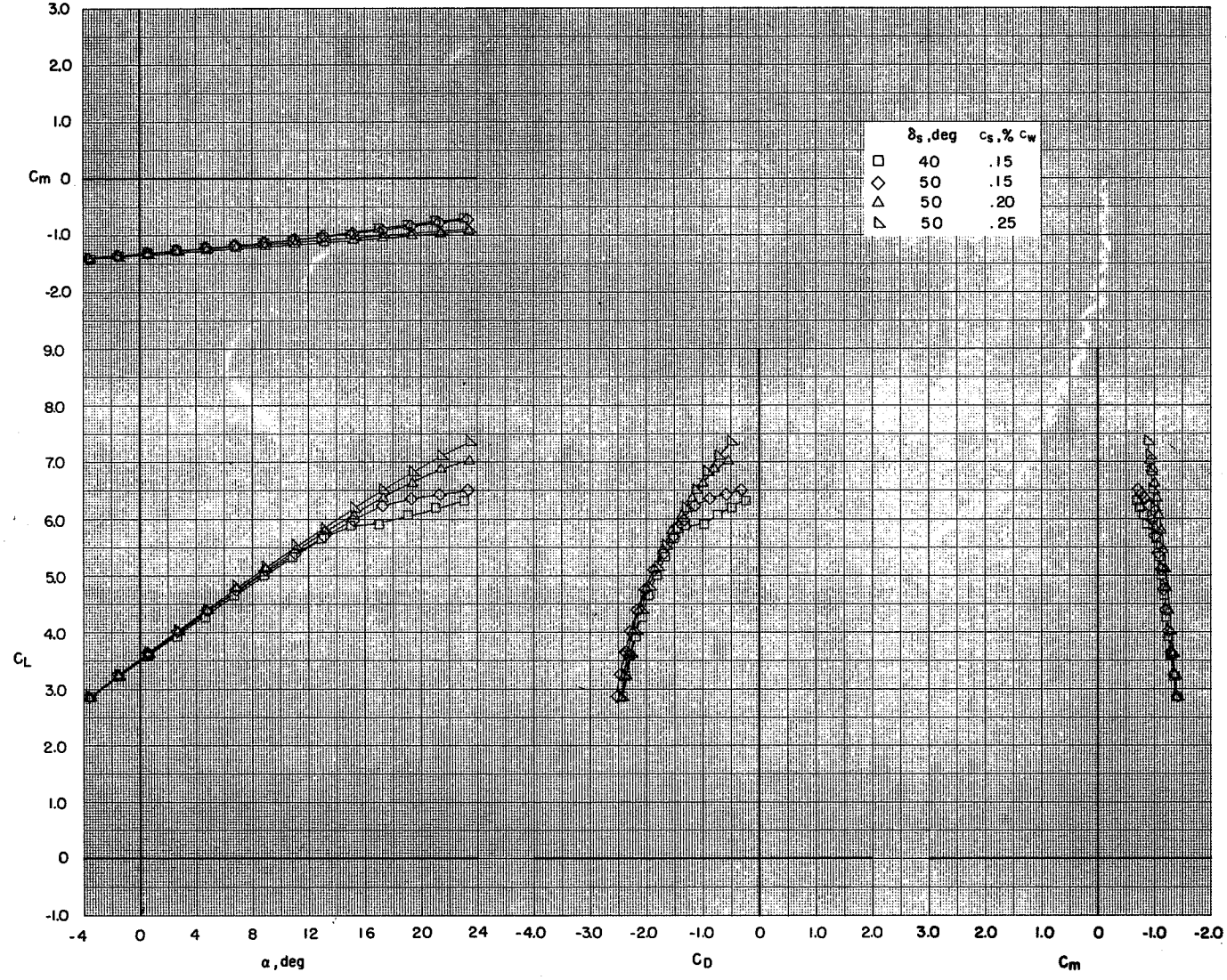

(c) $C_T = 3.74$.

Figure 34.- Concluded.

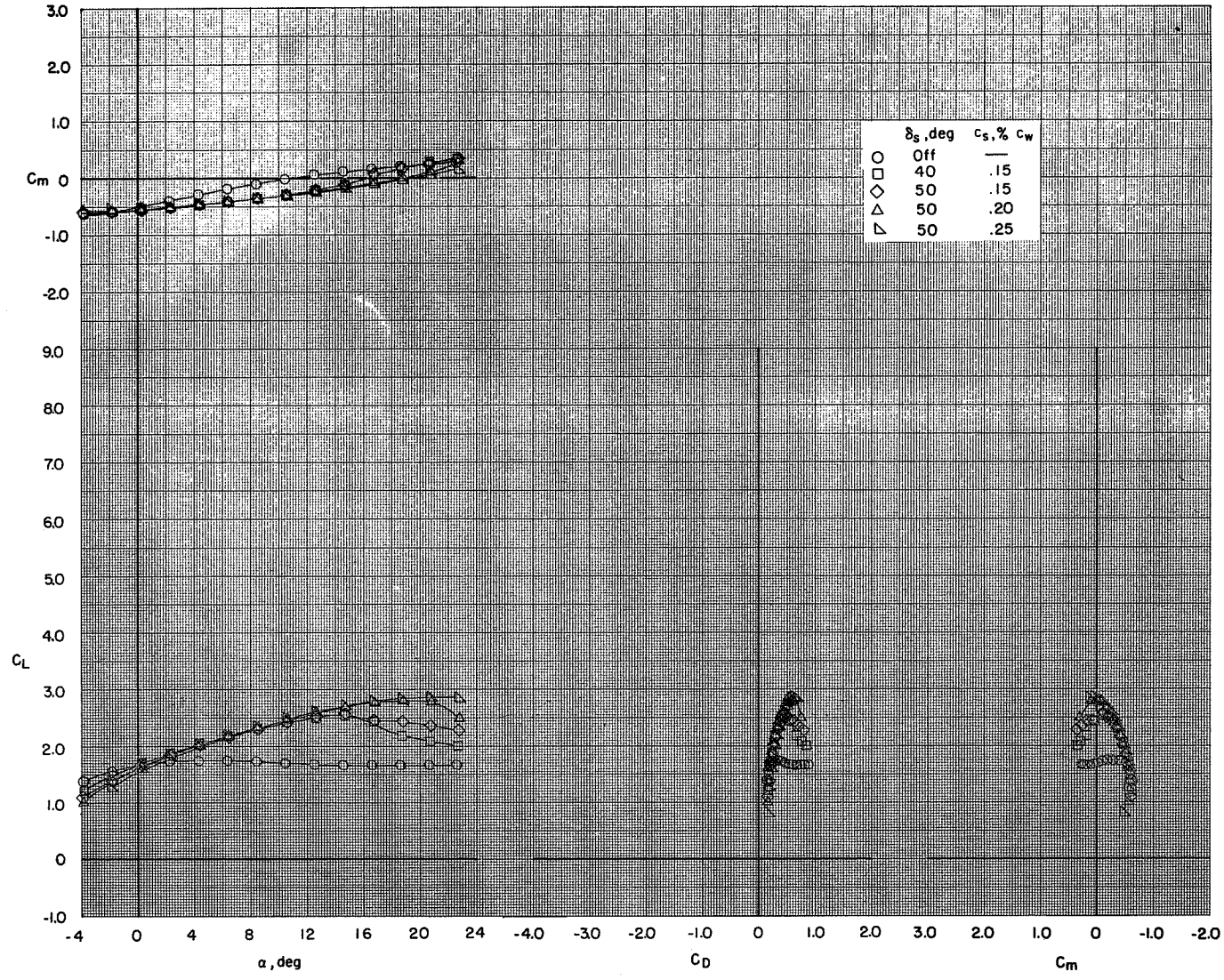

(a) $C_T = 0$.

Figure 35.- Effect of wing leading-edge slat configuration on the longitudinal aerodynamic characteristics of the model with flaps deflected. BPR 6.2; tail off; $\delta_f = 35^o/35^o/35^o$.

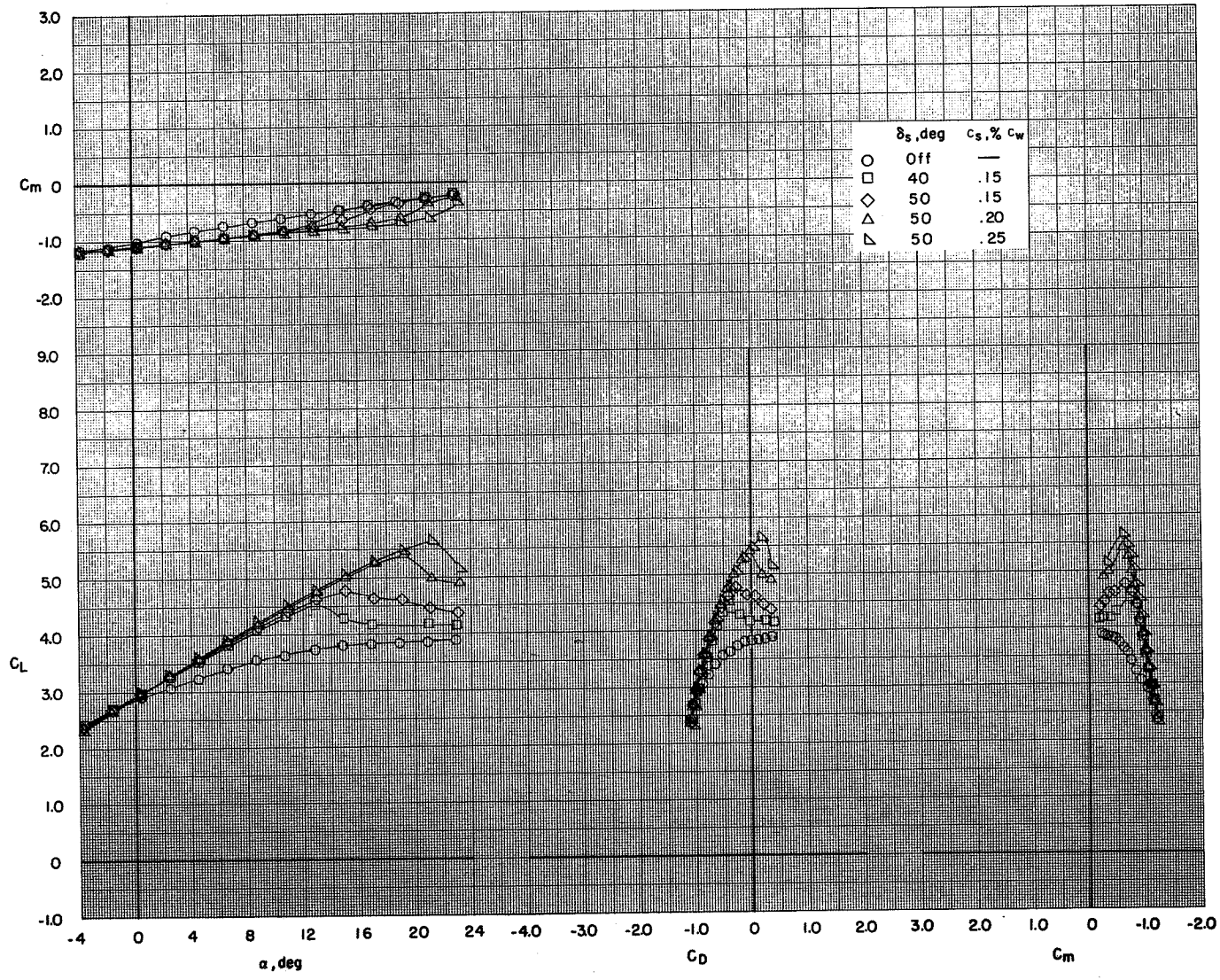

(b) $C_T = 1.88$.

Figure 35.- Continued.

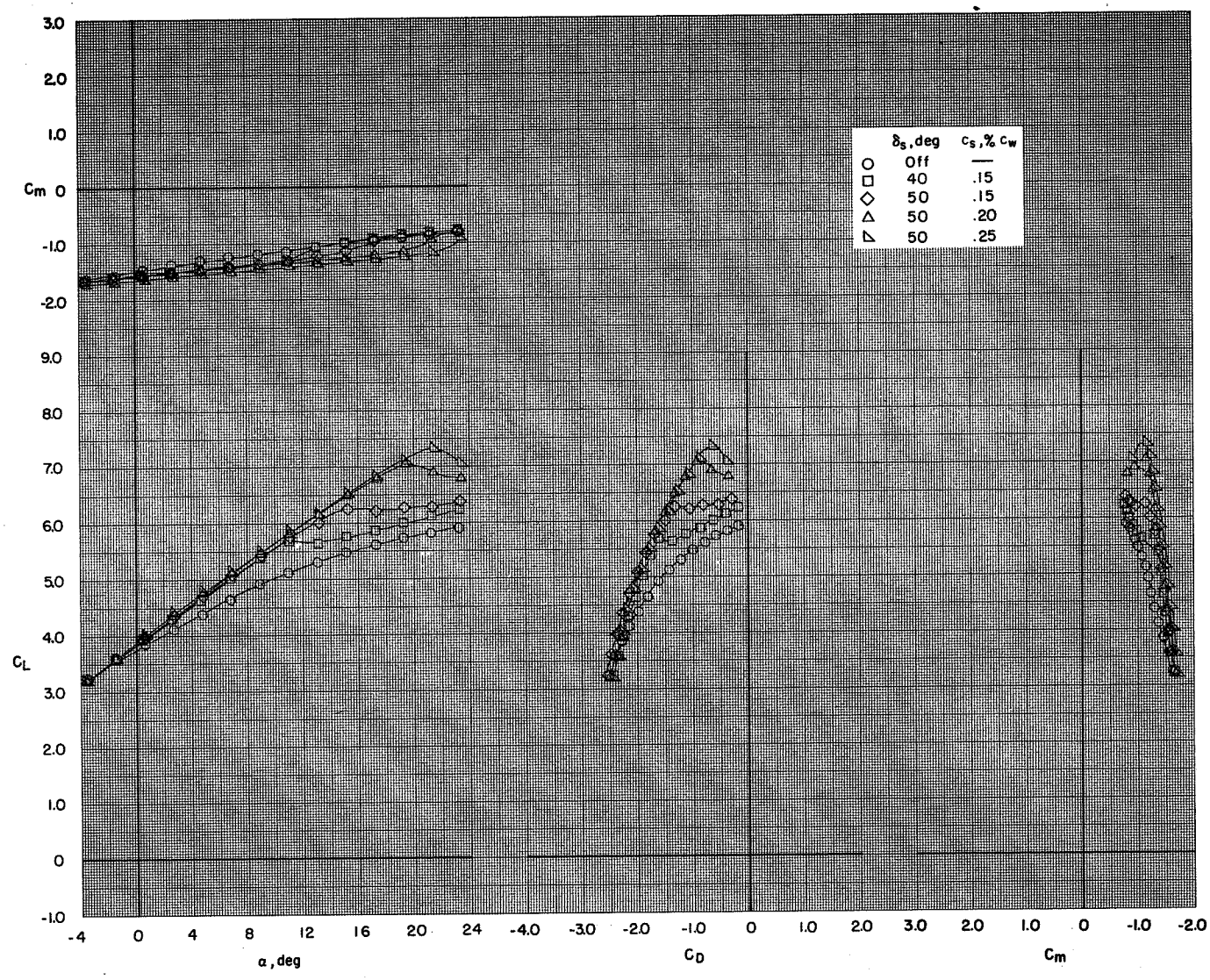

(c) $C_T = 3.74$.

Figure 35.- Concluded.

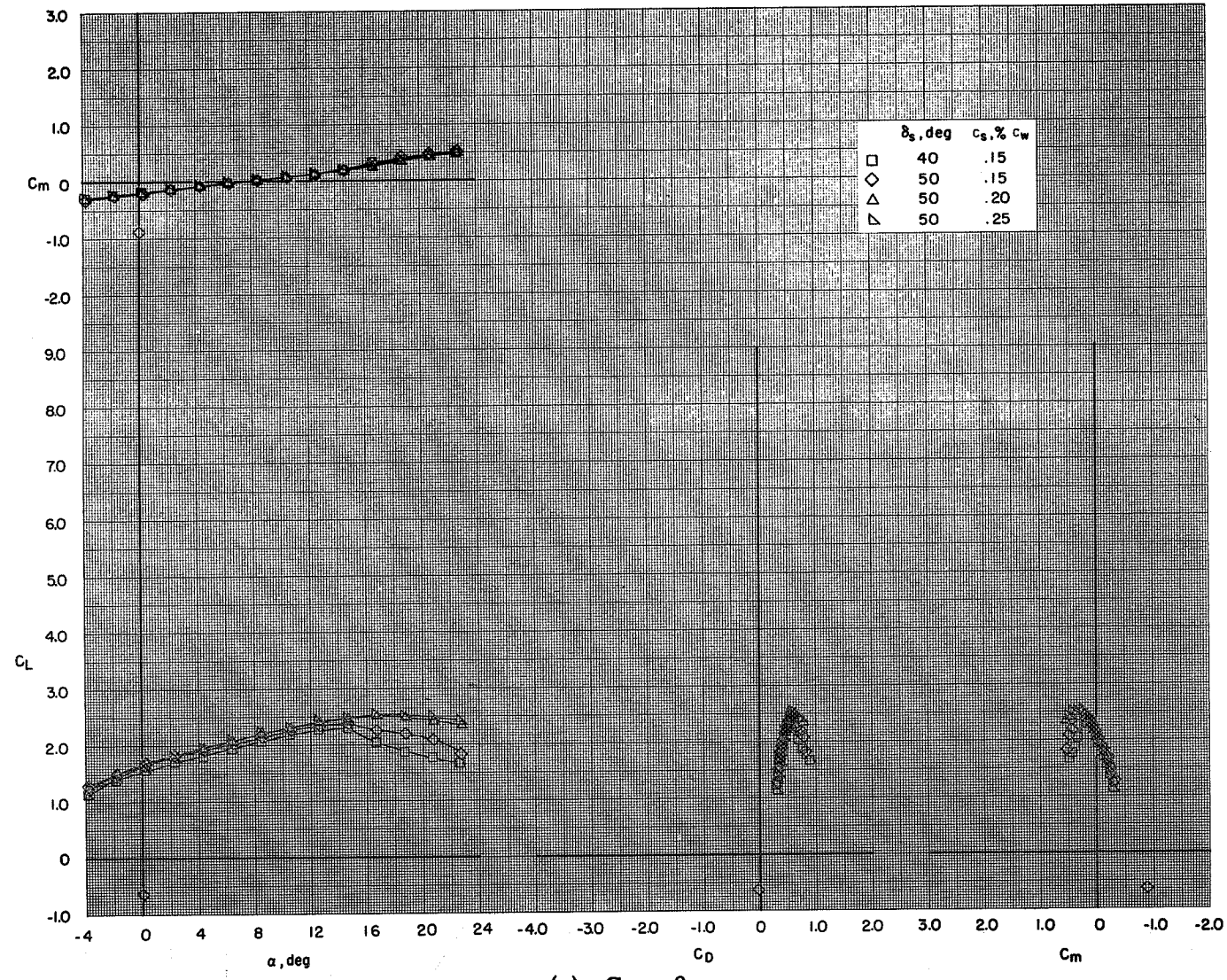

(a) $C_T = 0$.

Figure 36.- Effect of wing leading-edge slat configuration on the longitudinal aerodynamic characteristics of the model with flaps deflected. BPR 6.2; tail off; $\delta_f = 0^o/65^o/65^o$.

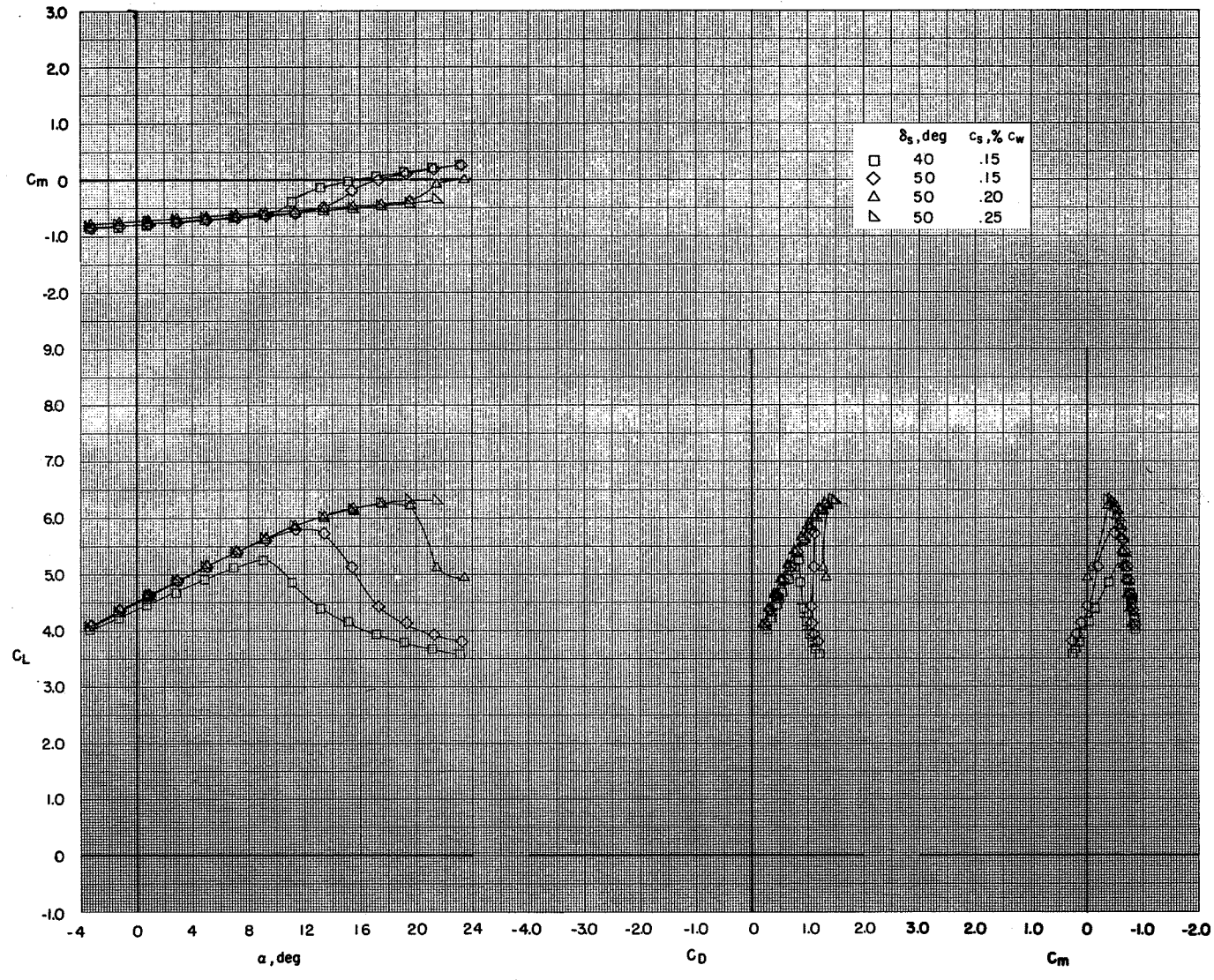

(b) $C_T = 1.88$.

Figure 36.- Continued.

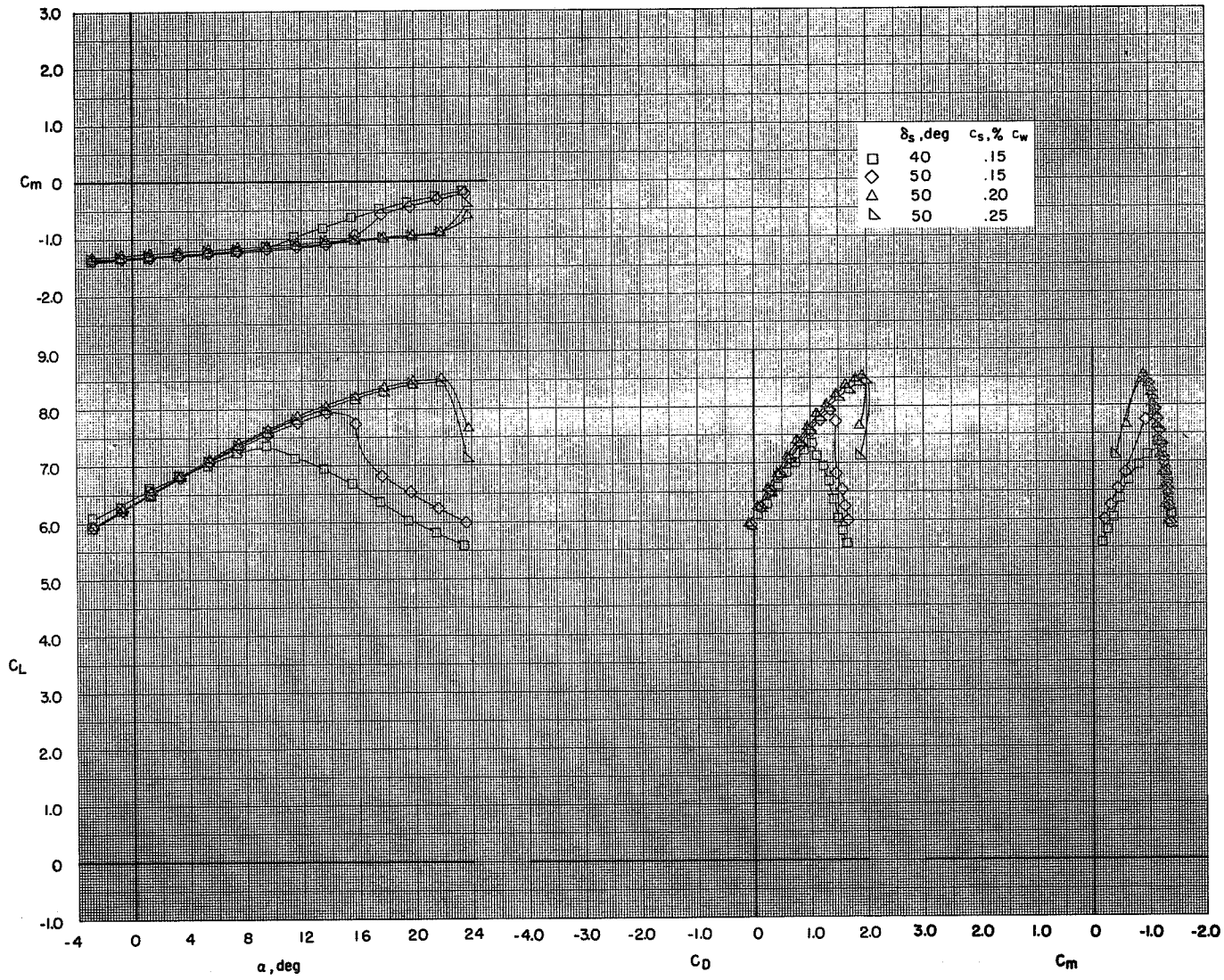

(c) $C_T = 3.74$.

Figure 36.- Concluded.

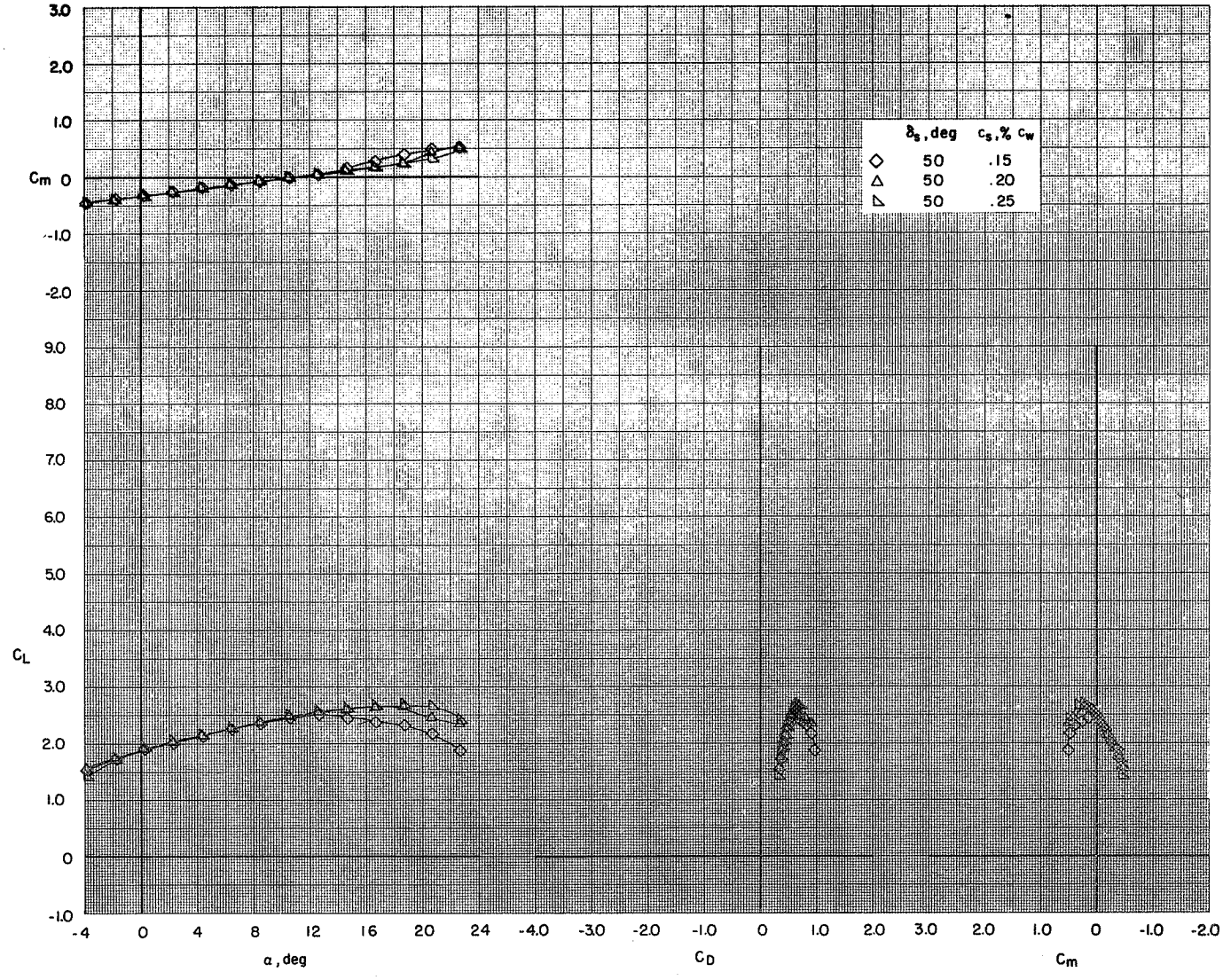

(a) $C_T = 0$.

Figure 37.- Effect of wing leading-edge slat configuration on the longitudinal aerodynamic characteristics of the model with flaps deflected. BPR 6.2; tail off; $\delta_f = 65^o/65^o/65^o$.

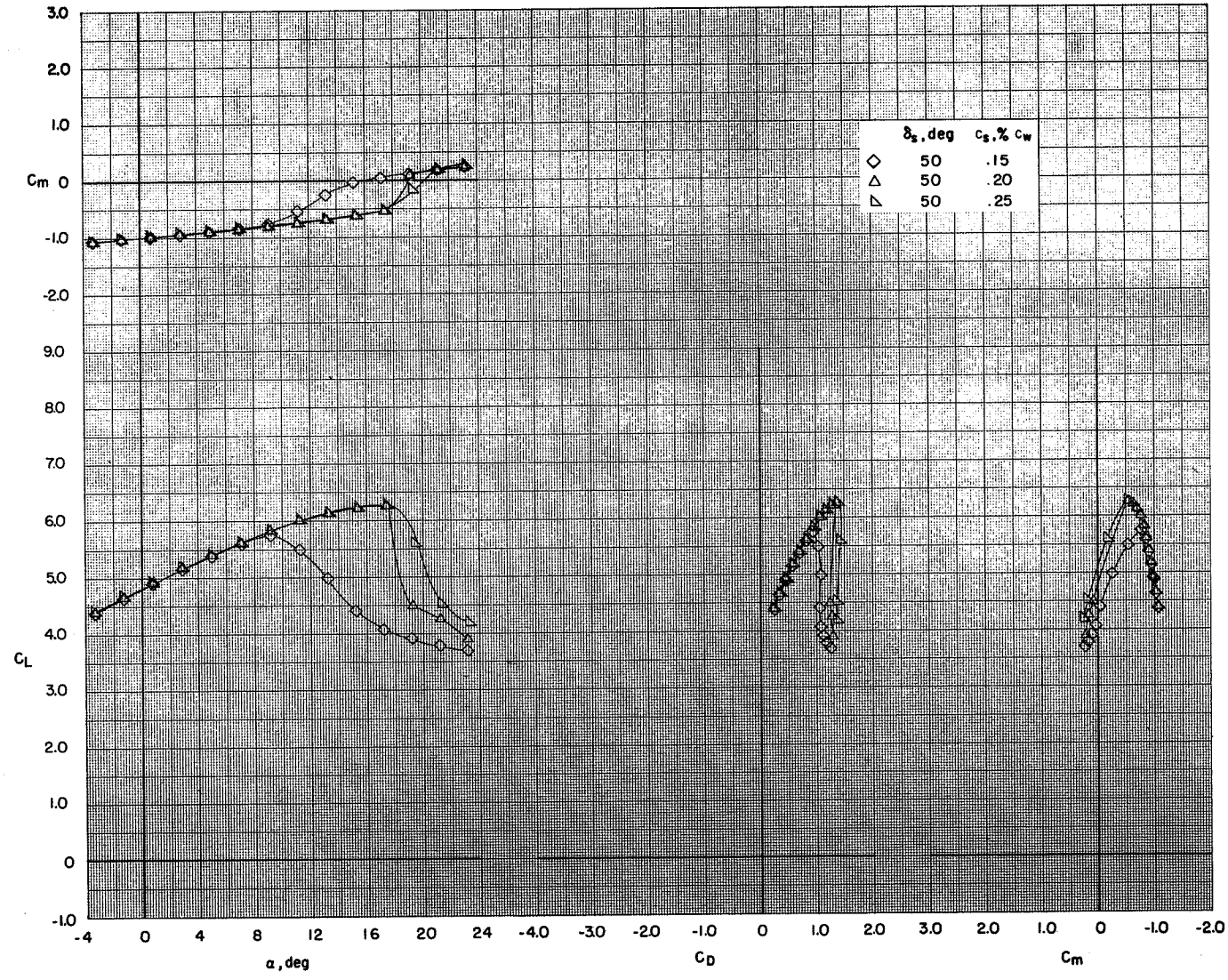

(b) $C_T = 1.88$.

Figure 37.- Continued.

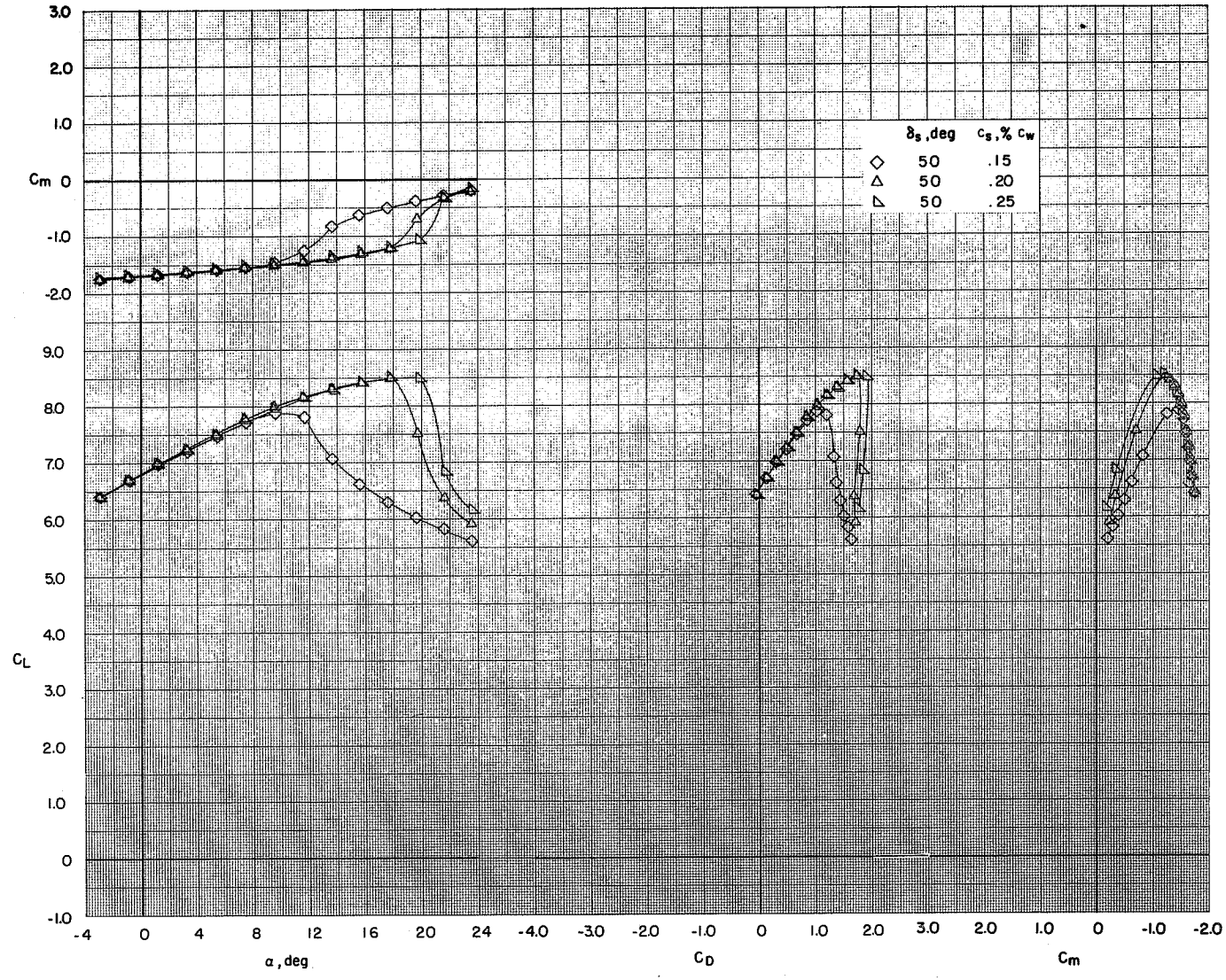

(c) $C_T = 3.74$.

Figure 37.- Concluded.

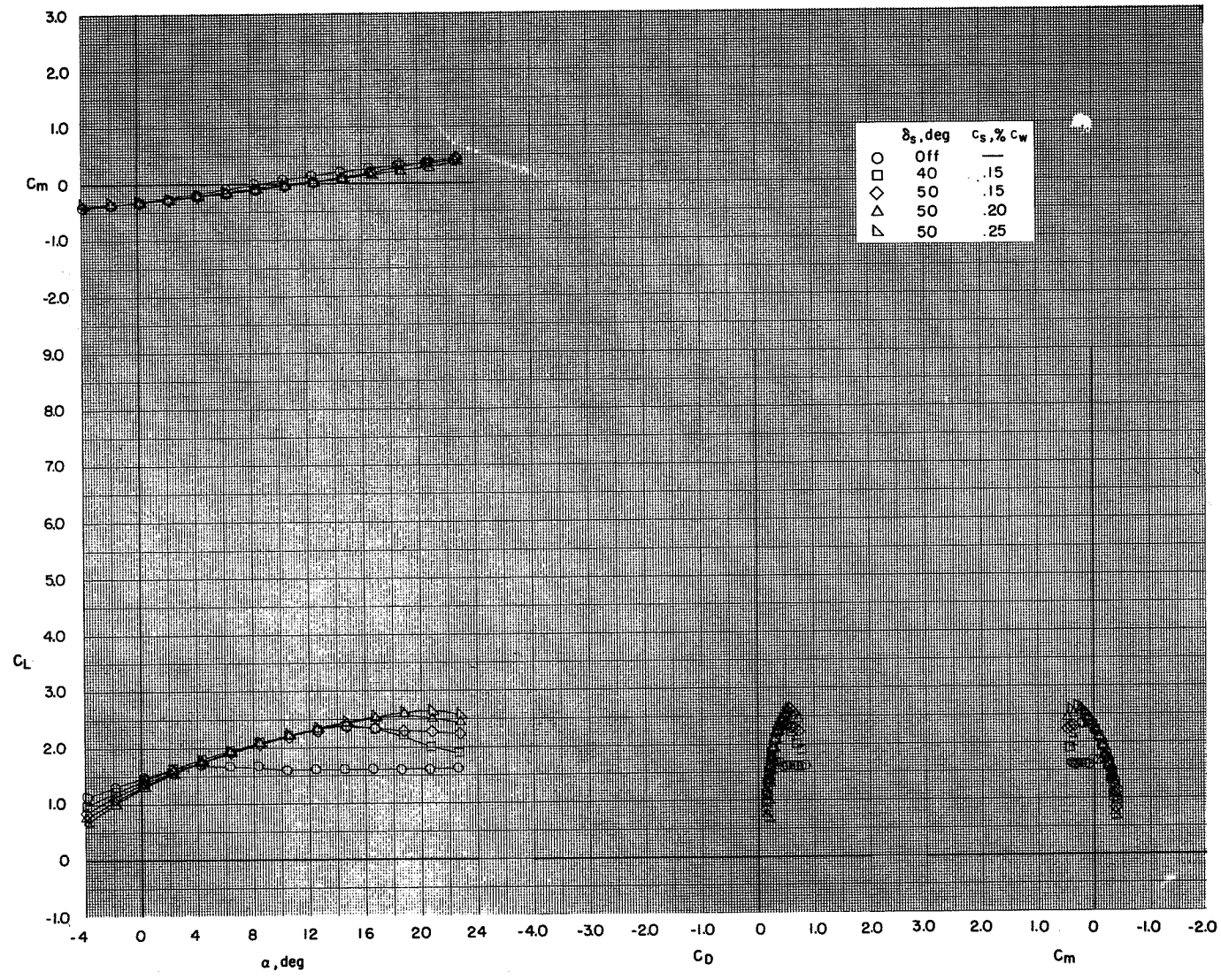

(a) $C_T = 0$.

Figure 38.- Effect of wing leading-edge slat configuration on the longitudinal aerodynamic characteristics of the model with flaps deflected. BPR 10.0; tail off; $\delta_f = 0^o/35^o/35^o$.

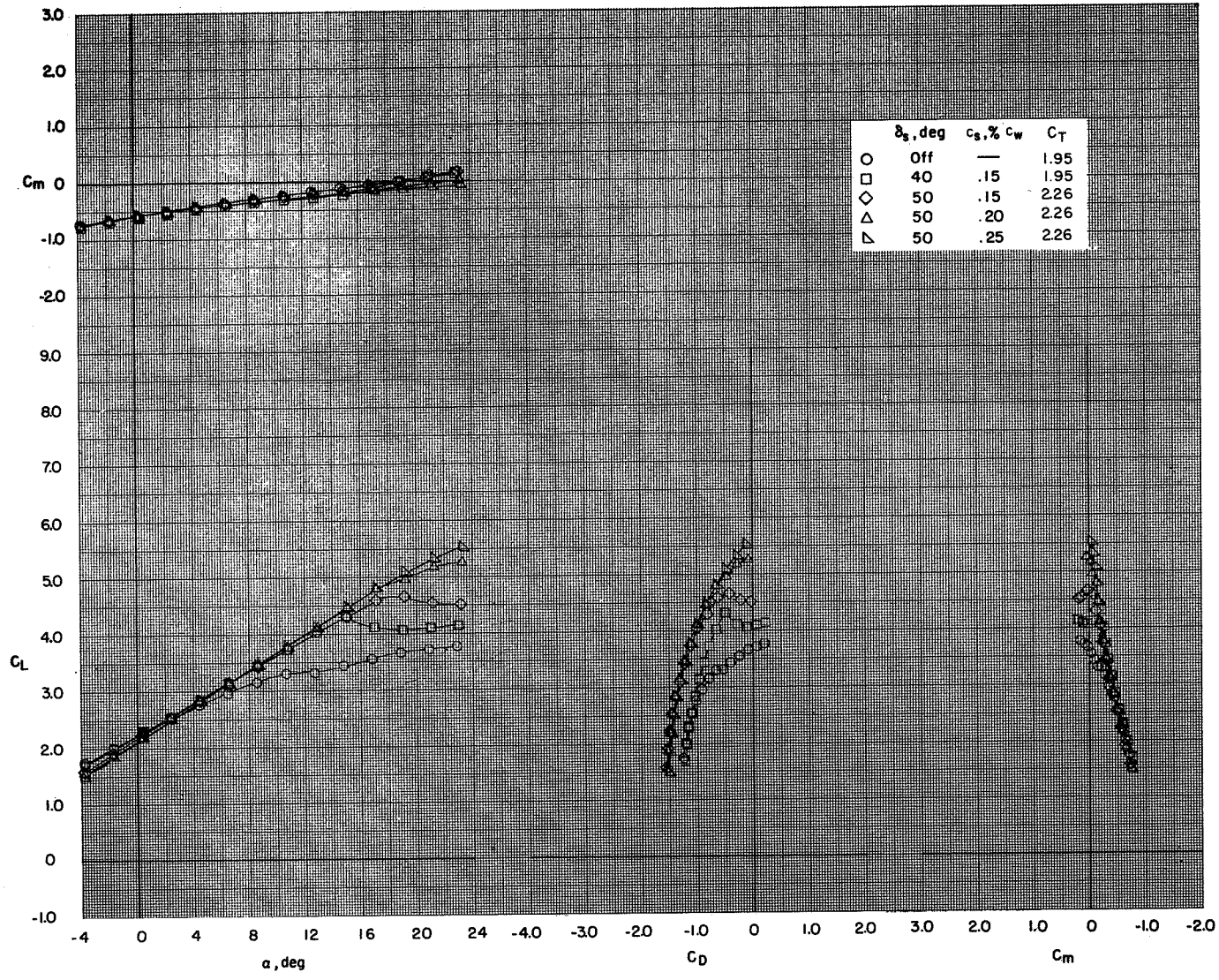

(b) $C_T \approx 2$.

Figure 38.- Continued.

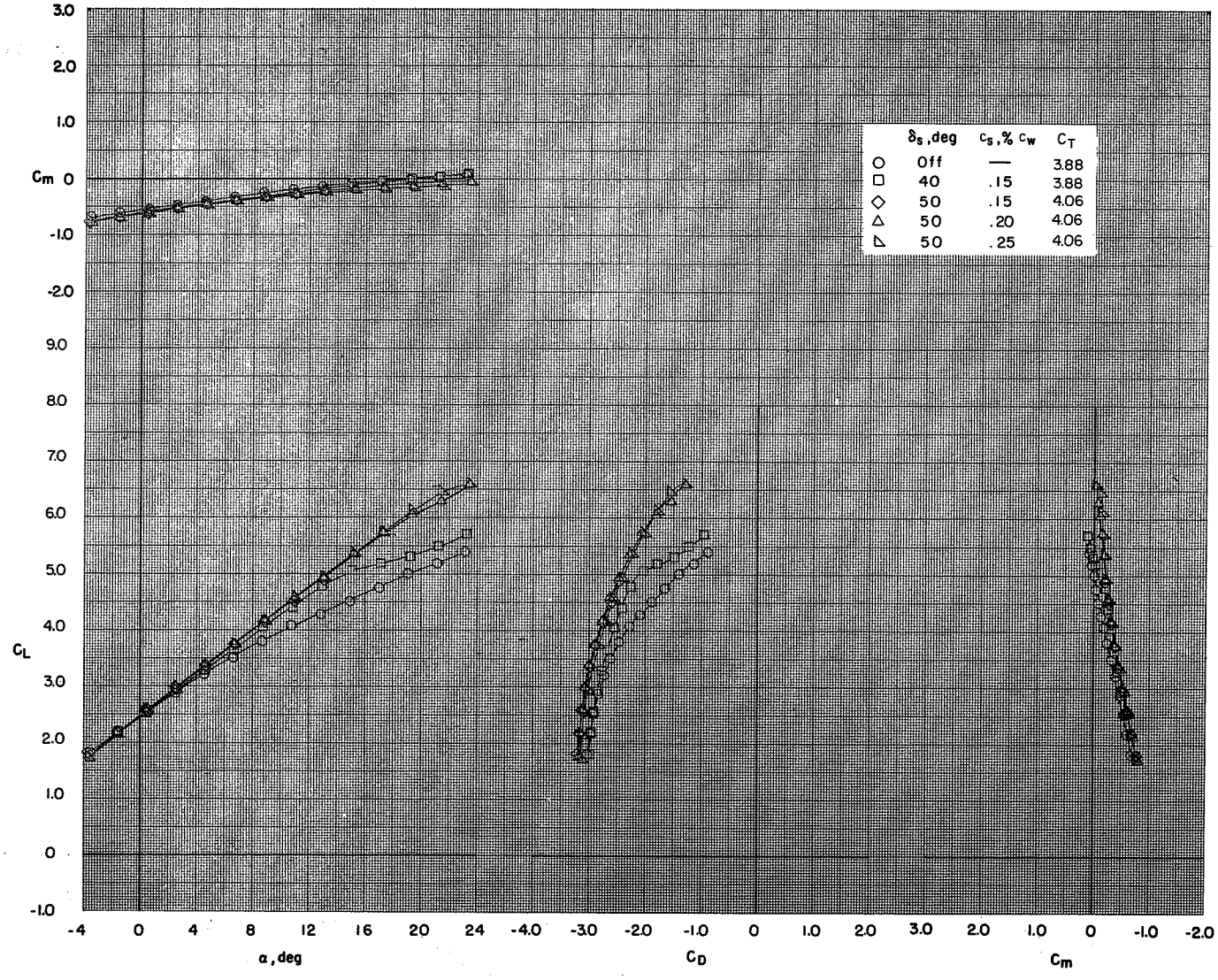

(c) $C_T \approx 4$.

Figure 38.- Concluded.

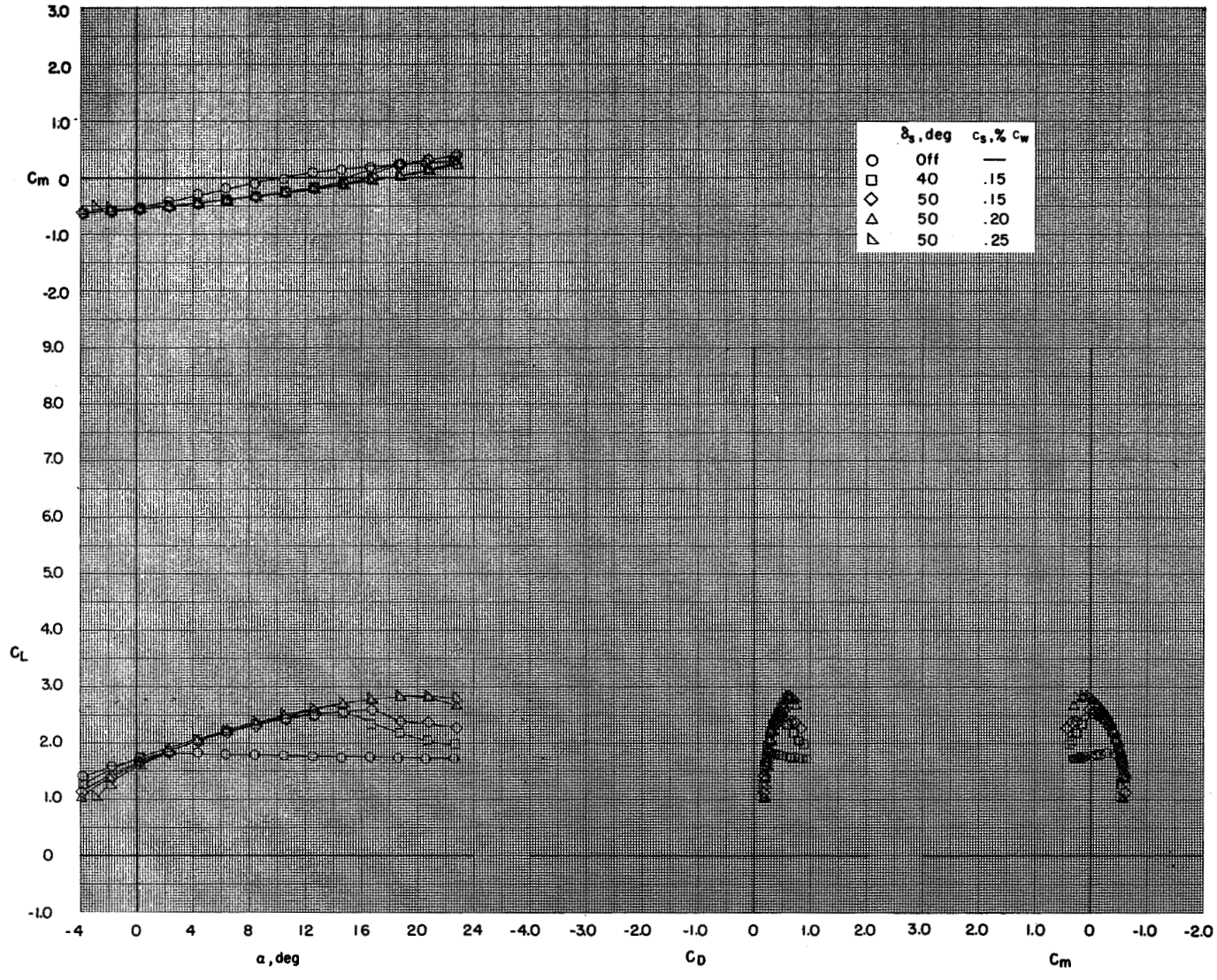

(a) $C_T = 0$.

Figure 39.- Effect of wing leading-edge slat configuration on the longitudinal aerodynamic characteristics of the model with flaps deflected. BPR 10.0; tail off; $\delta_f = 35^o/35^o/35^o$.

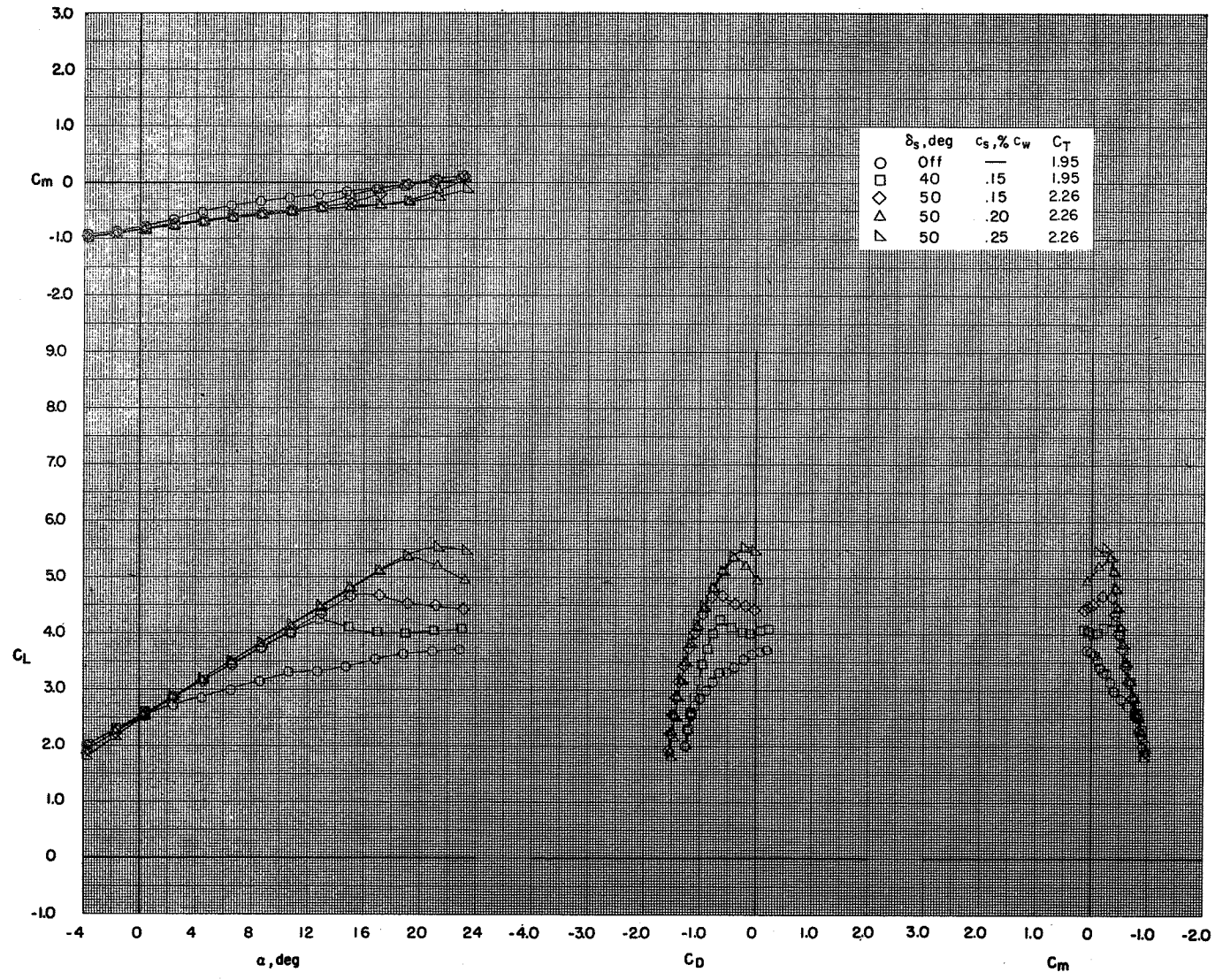

(b) $C_T \approx 2.$

Figure 39.- Continued.

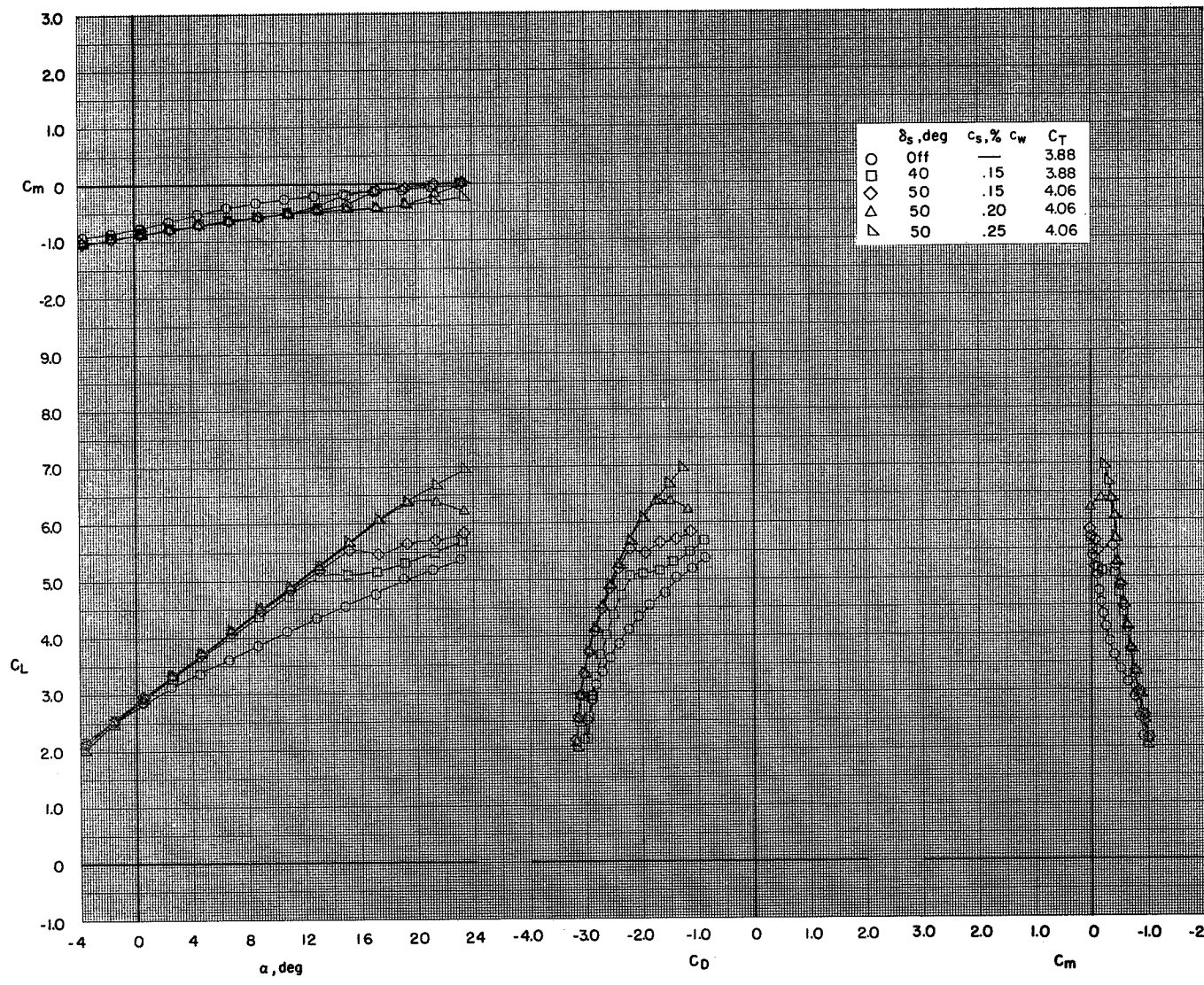

(c) $C_T \approx 4$.

Figure 39.- Concluded.

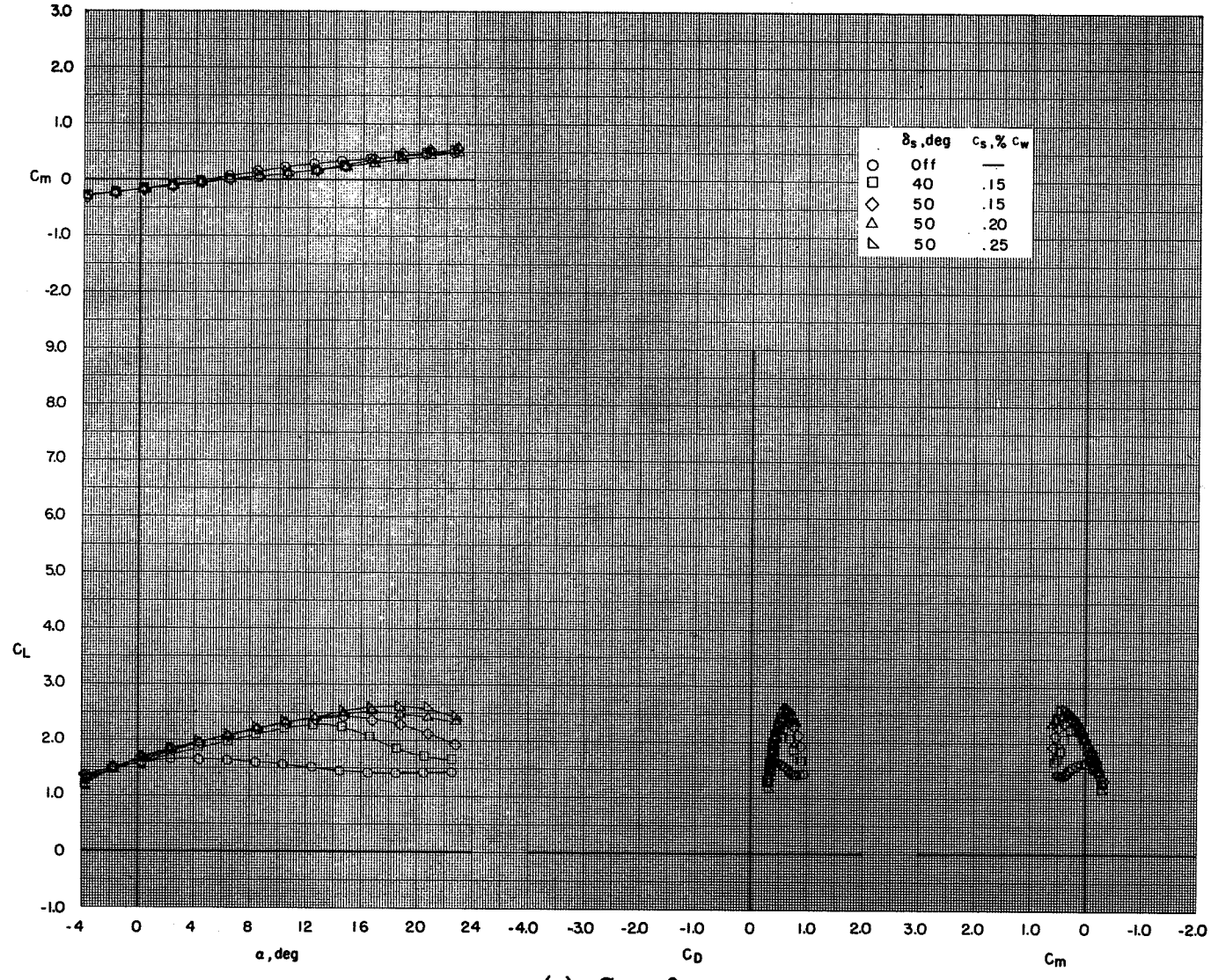

(a) $C_T = 0$.

Figure 40.- Effect of wing leading-edge slat configuration on the longitudinal aerodynamic characteristics of the model with flaps deflected. BPR 10.0; tail off; $\delta_f = 0^o/65^o/65^o$.

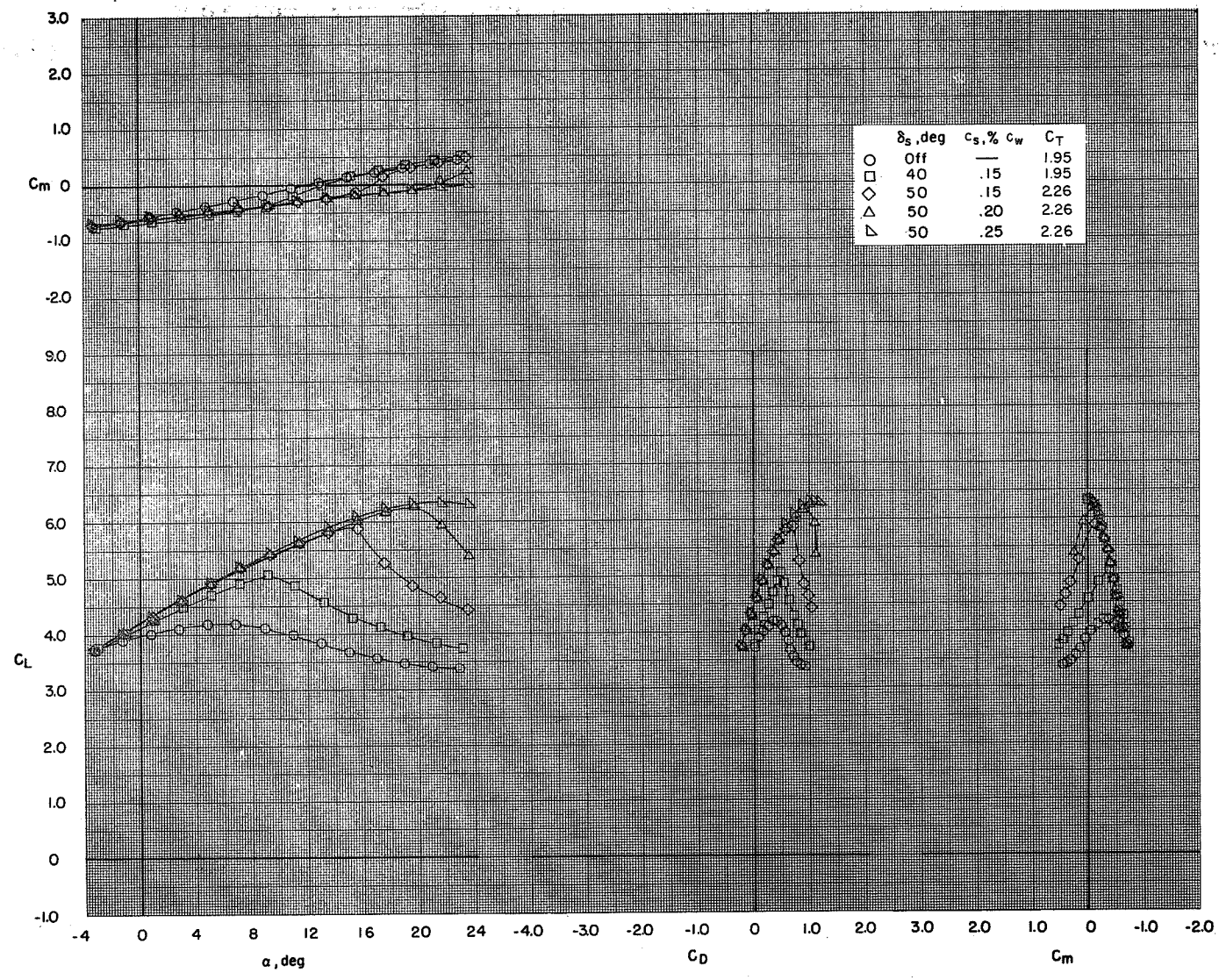

(b) $C_T \approx 2$.

Figure 40.- Continued.

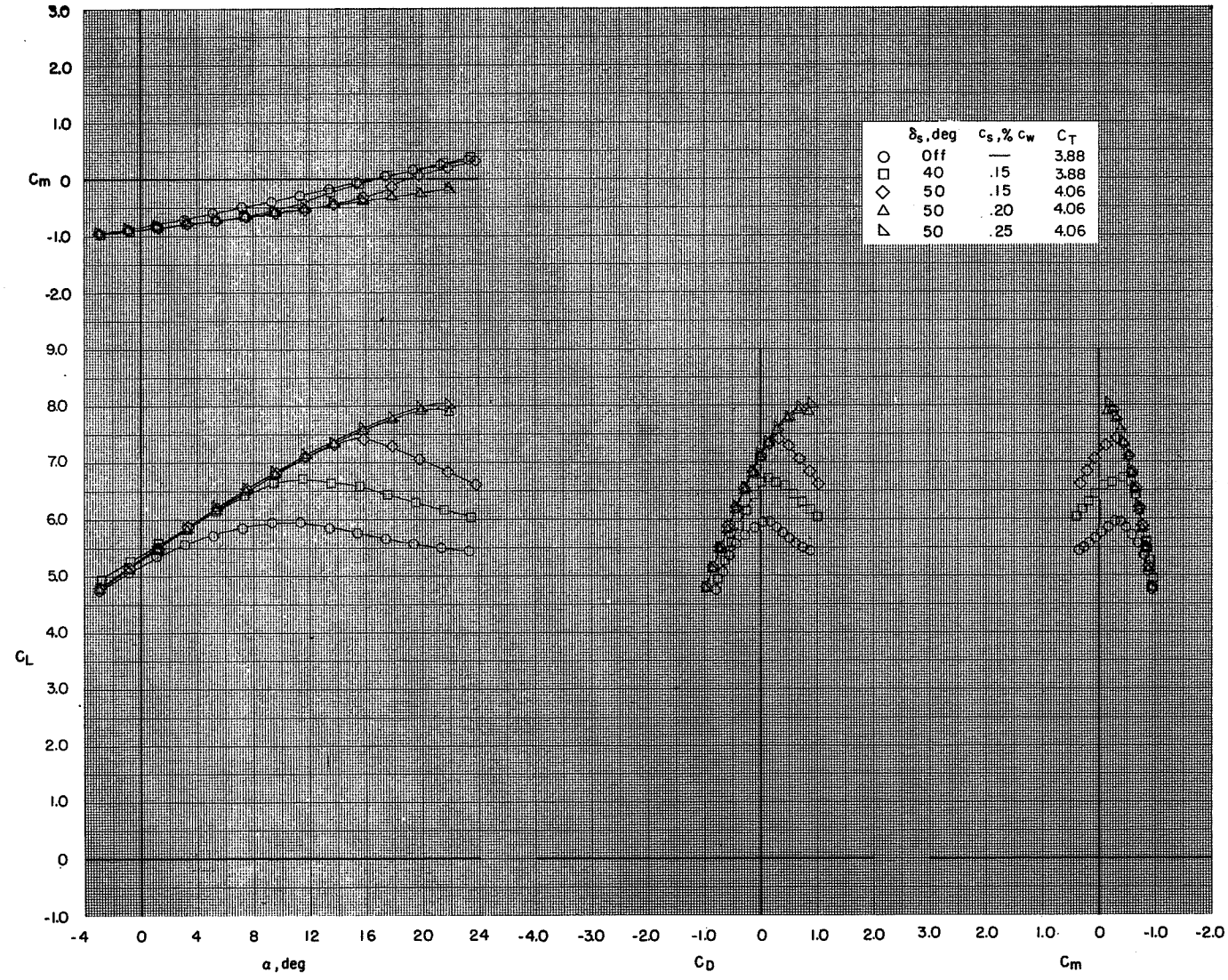

(c) $C_T \approx 4$.

Figure 40.- Concluded.

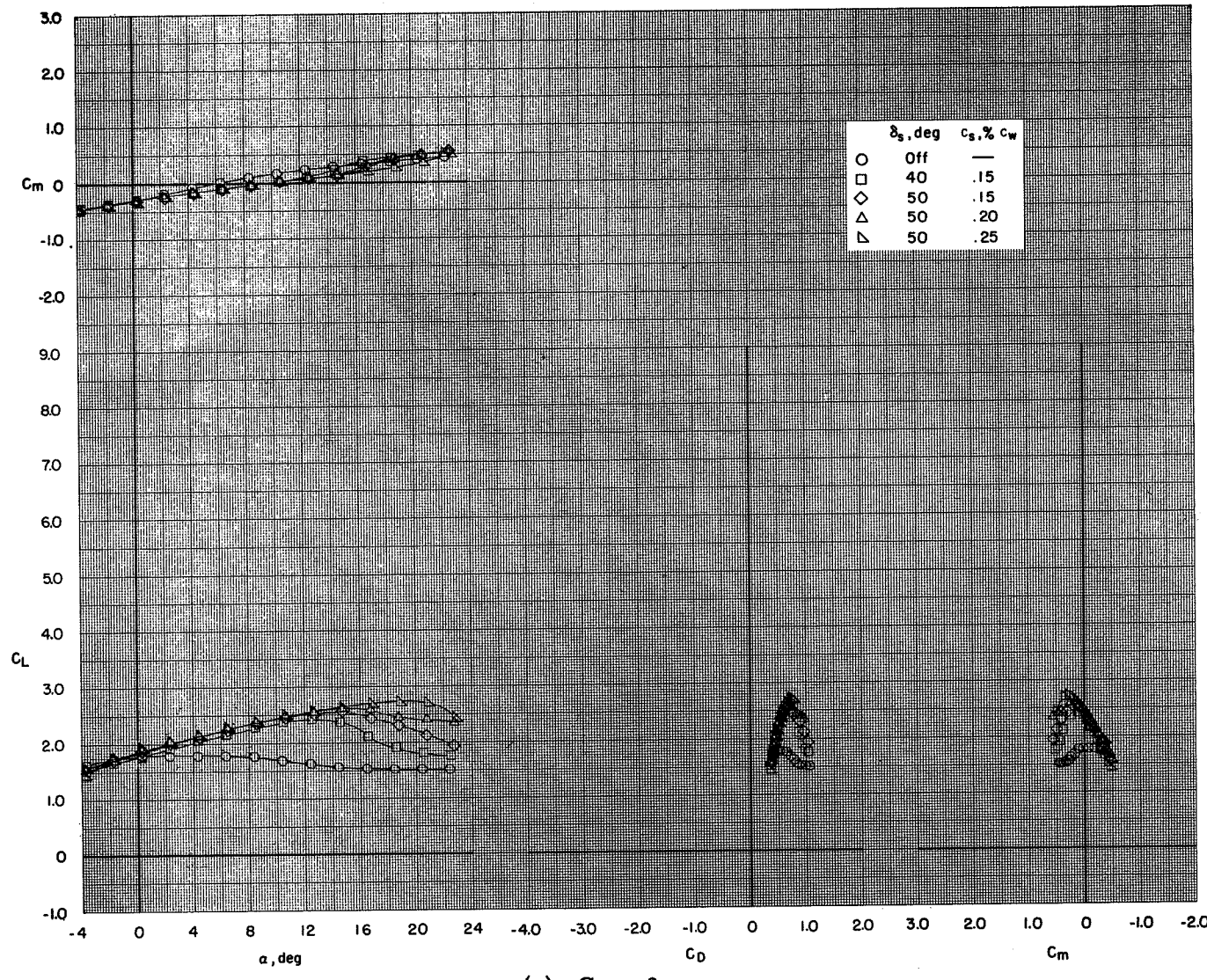

(a) $C_T = 0$.

Figure 41.- Effect of wing leading-edge slat configuration on the longitudinal aerodynamic characteristics of the model with flaps deflected. BPR 10.0; tail off; $\delta_f = 65^o/65^o/65^o$.

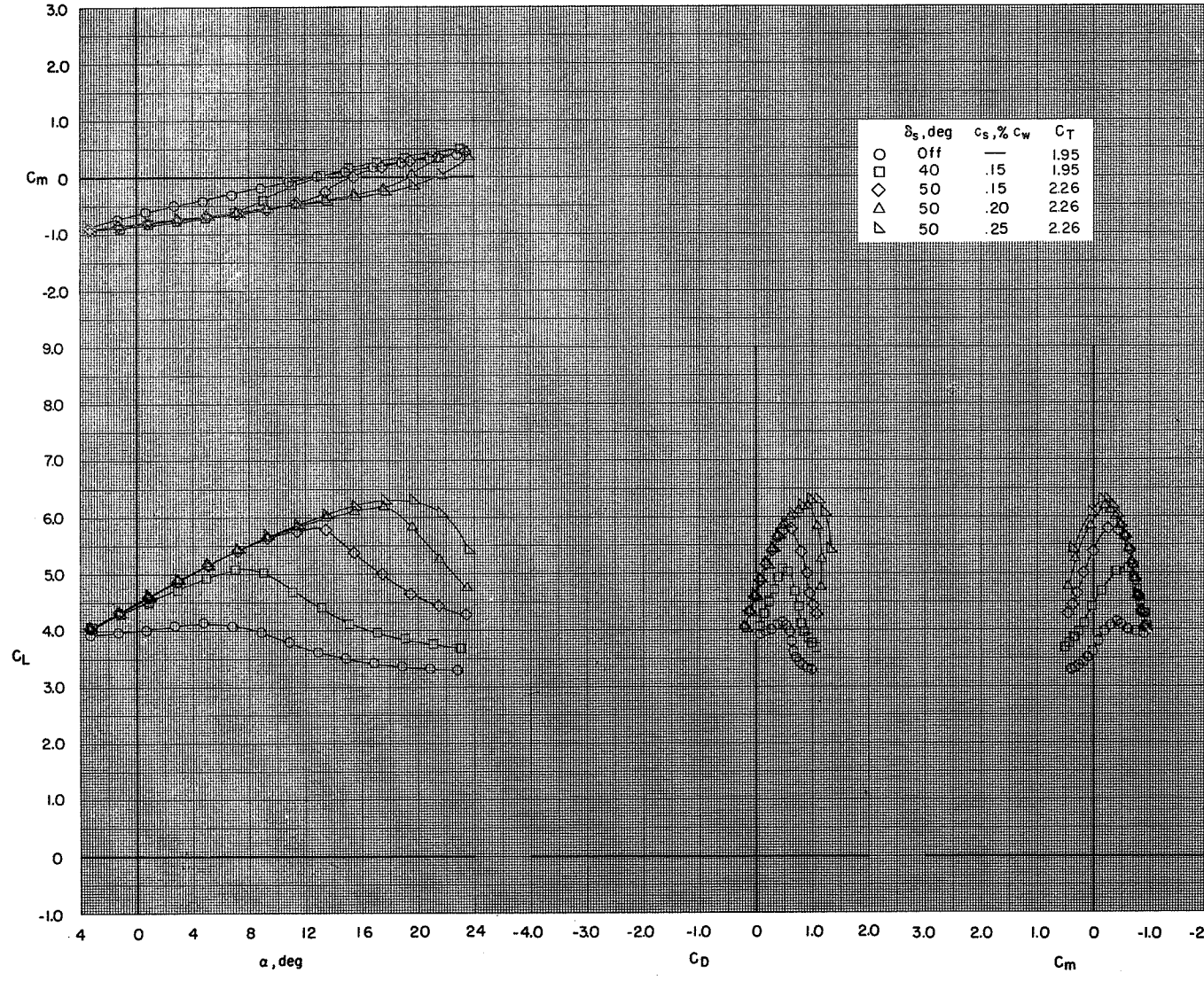

(b) $C_T \approx 2$.

Figure 41.- Continued.

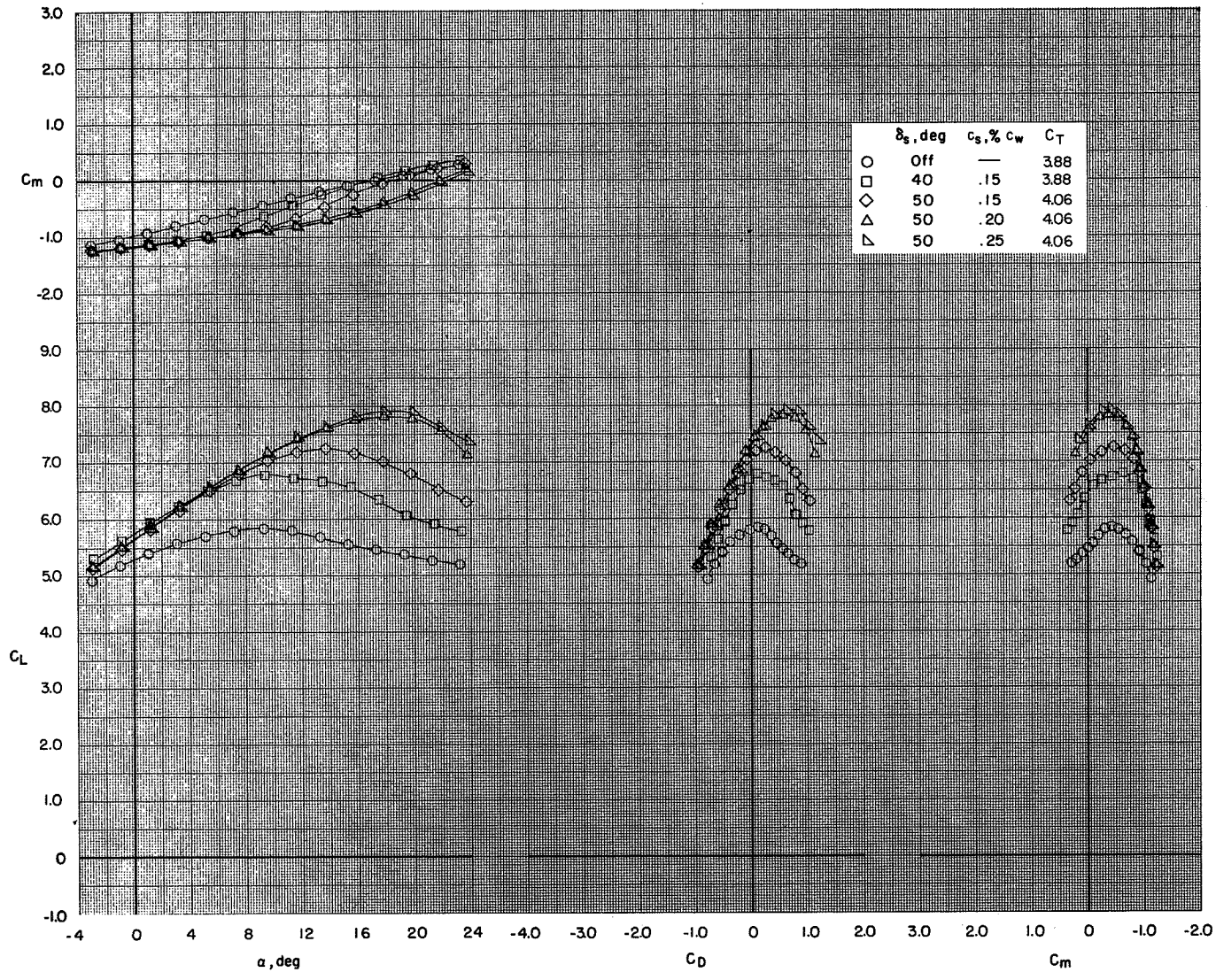

(c) $C_T \approx 4$.

Figure 41.- Concluded.

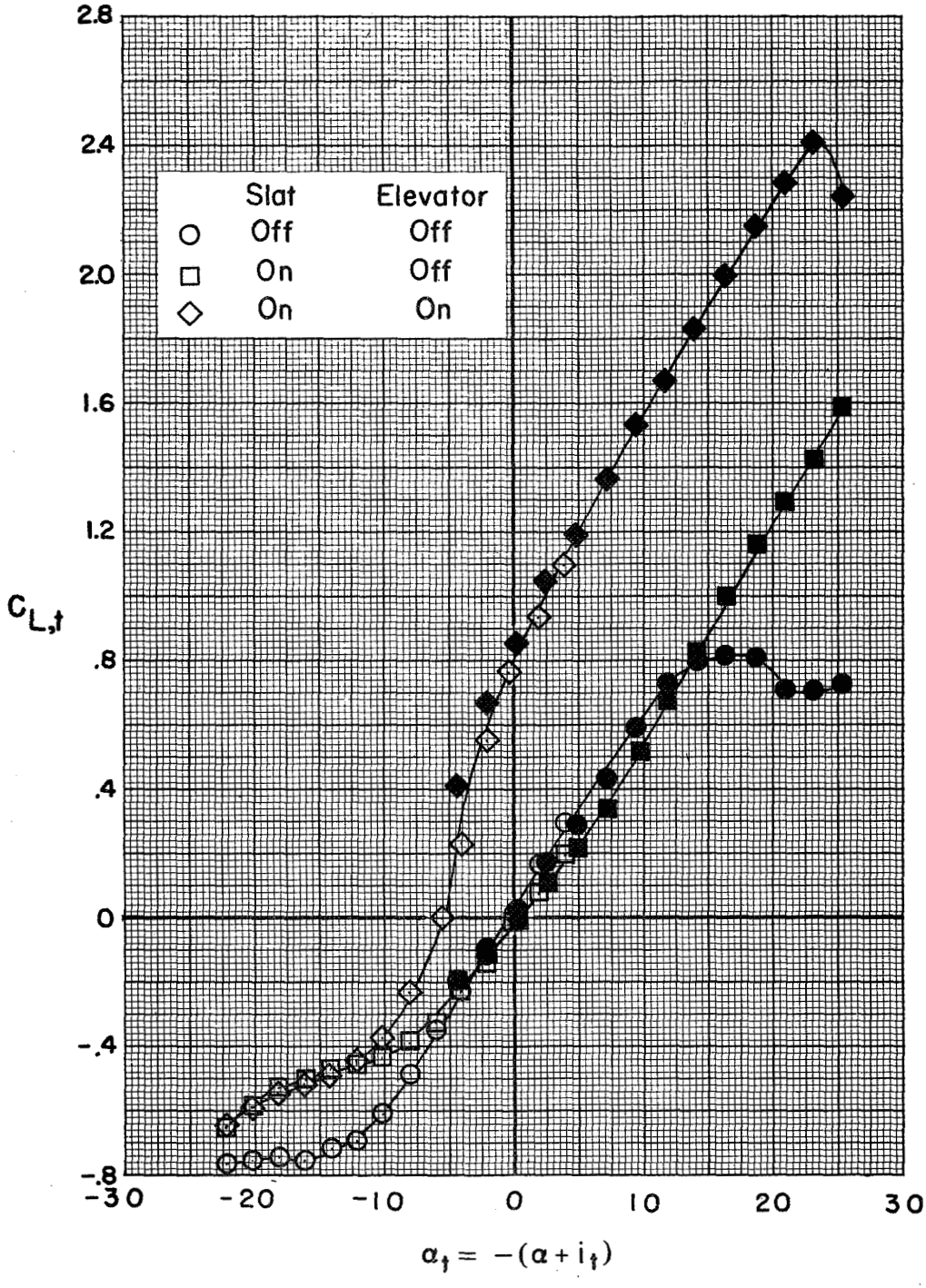

Figure 42.- Lift characteristics of horizontal tail.

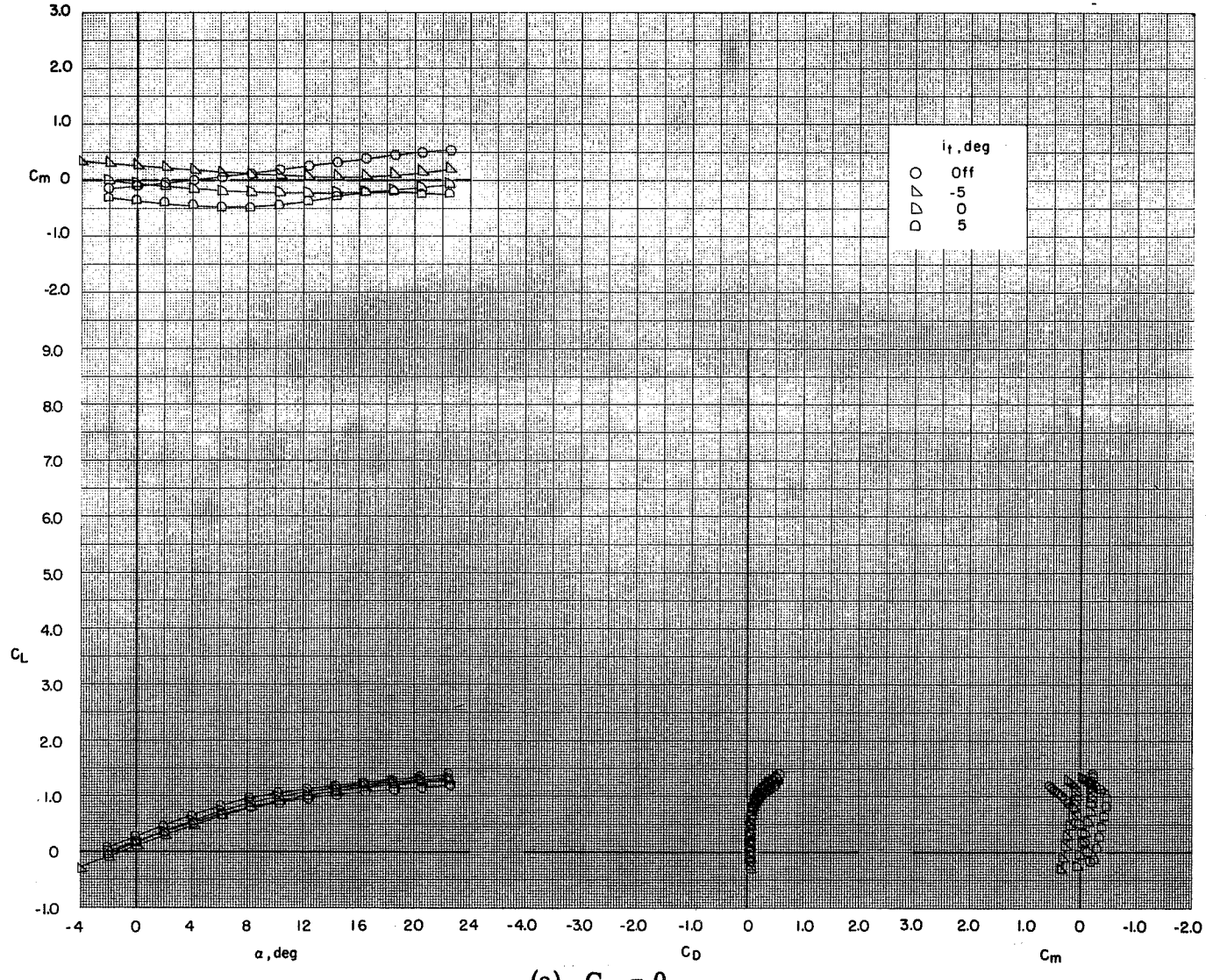

(a) $C_T = 0$.

Figure 43.- Effect of horizontal-tail incidence angle on the longitudinal aerodynamic characteristics of the model with flaps retracted and leading-edge slat off. BPR 6.2; T-tail; tail-slat off; elevators off; $\delta_f = 0^o/0^o/0^o$.

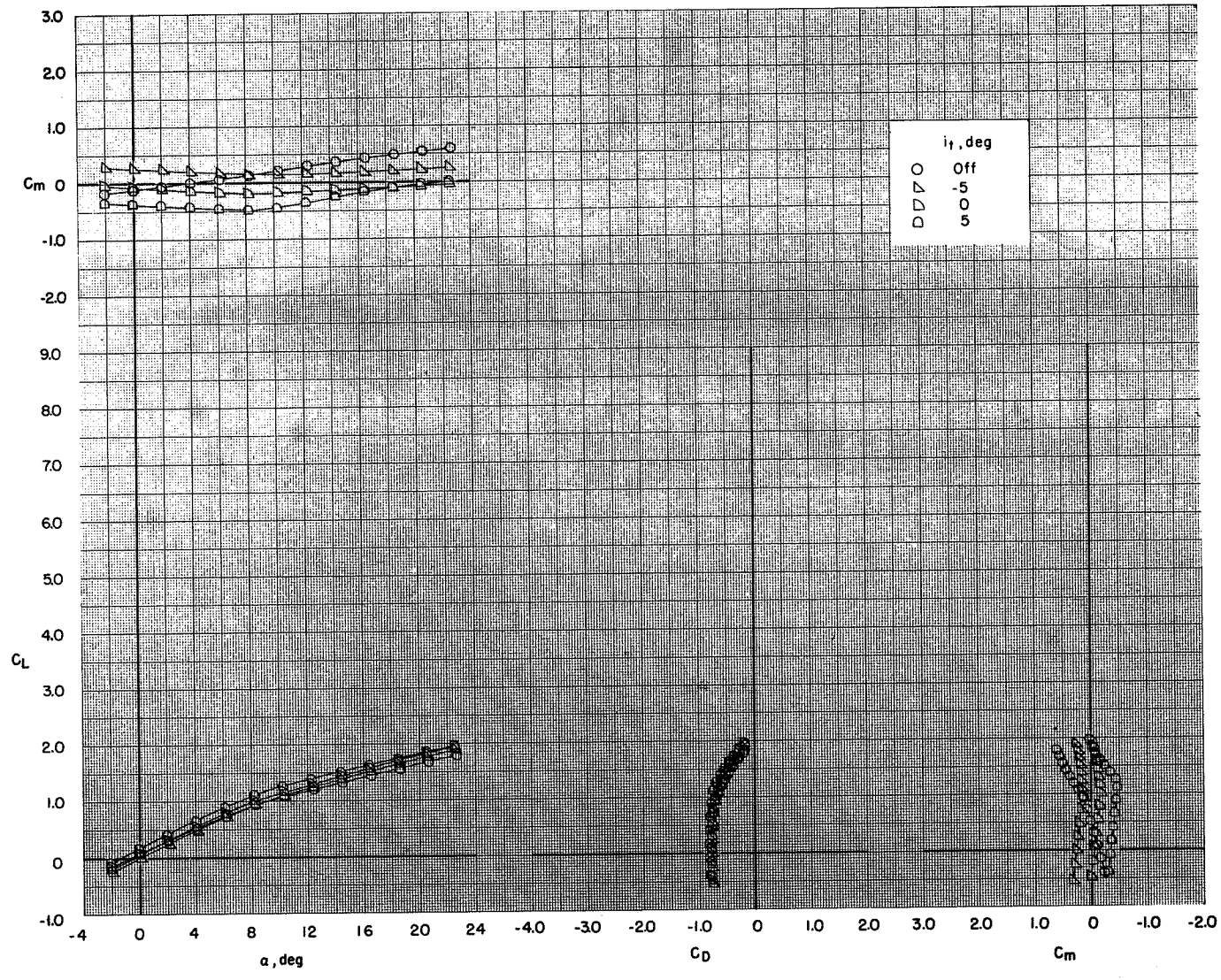

(b) $C_T = 0.94$.

Figure 43.- Continued.

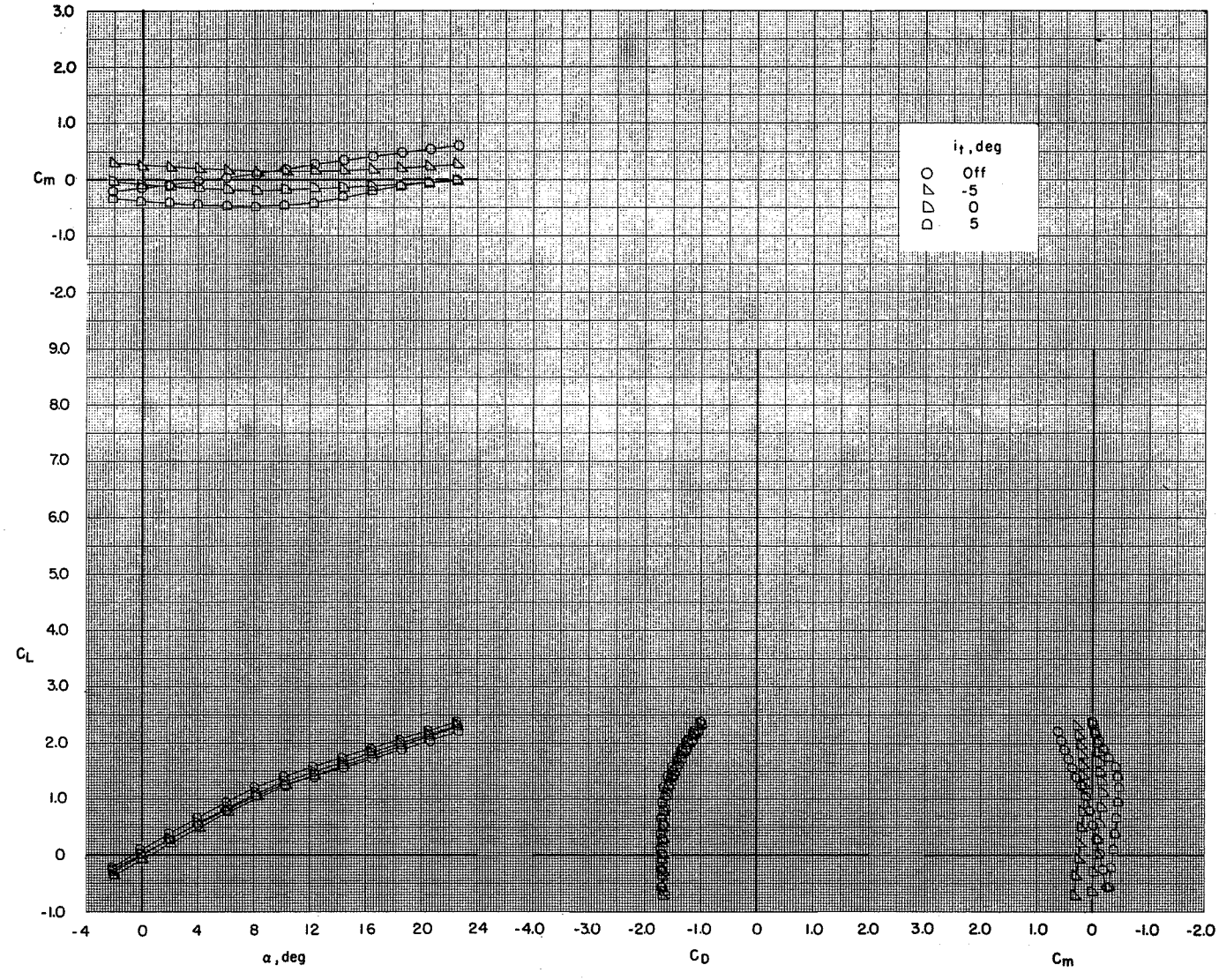

(c) $C_T = 1.85$.

Figure 43.- Continued.

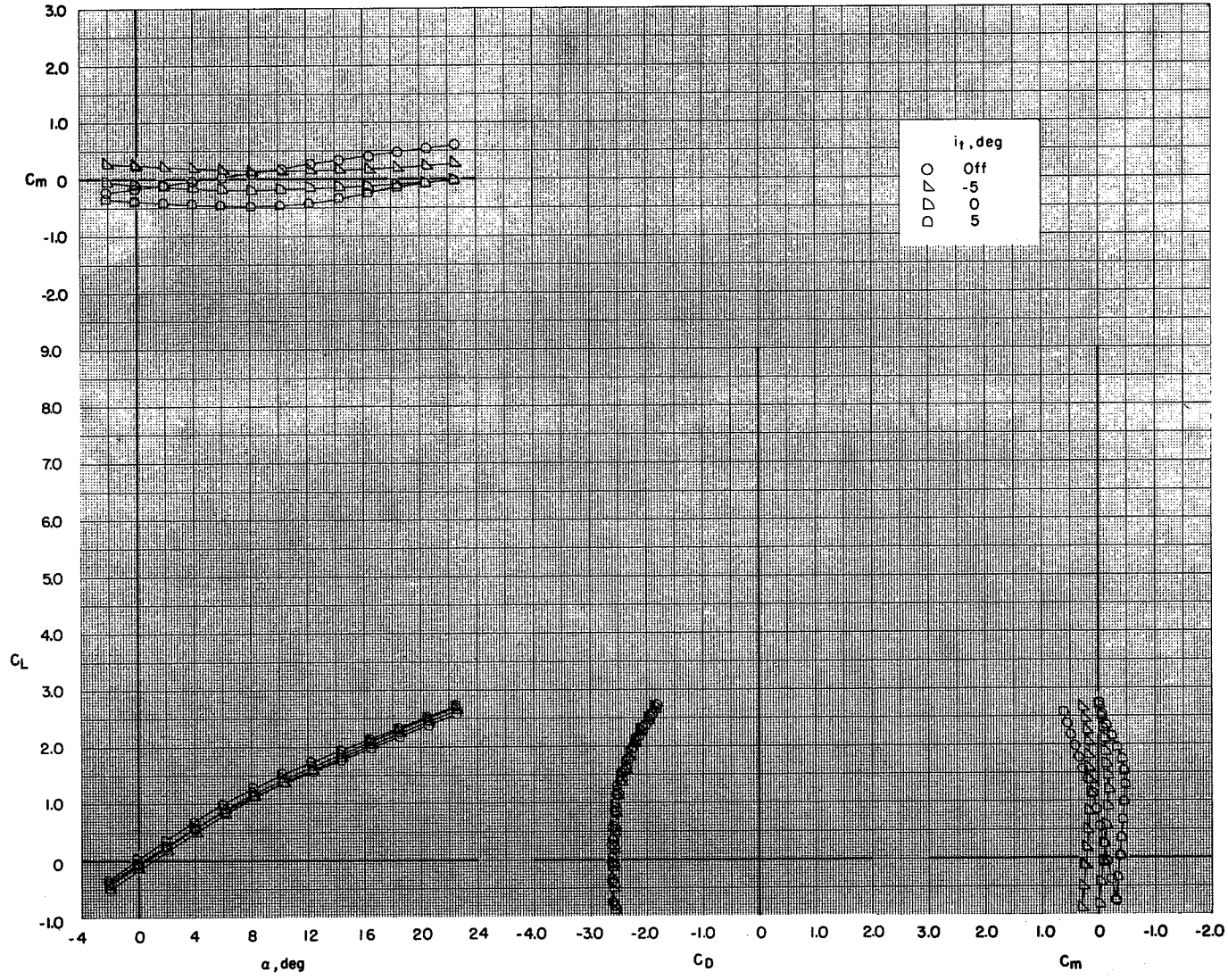

(d) $C_T = 2.77$.

Figure 43.- Continued.

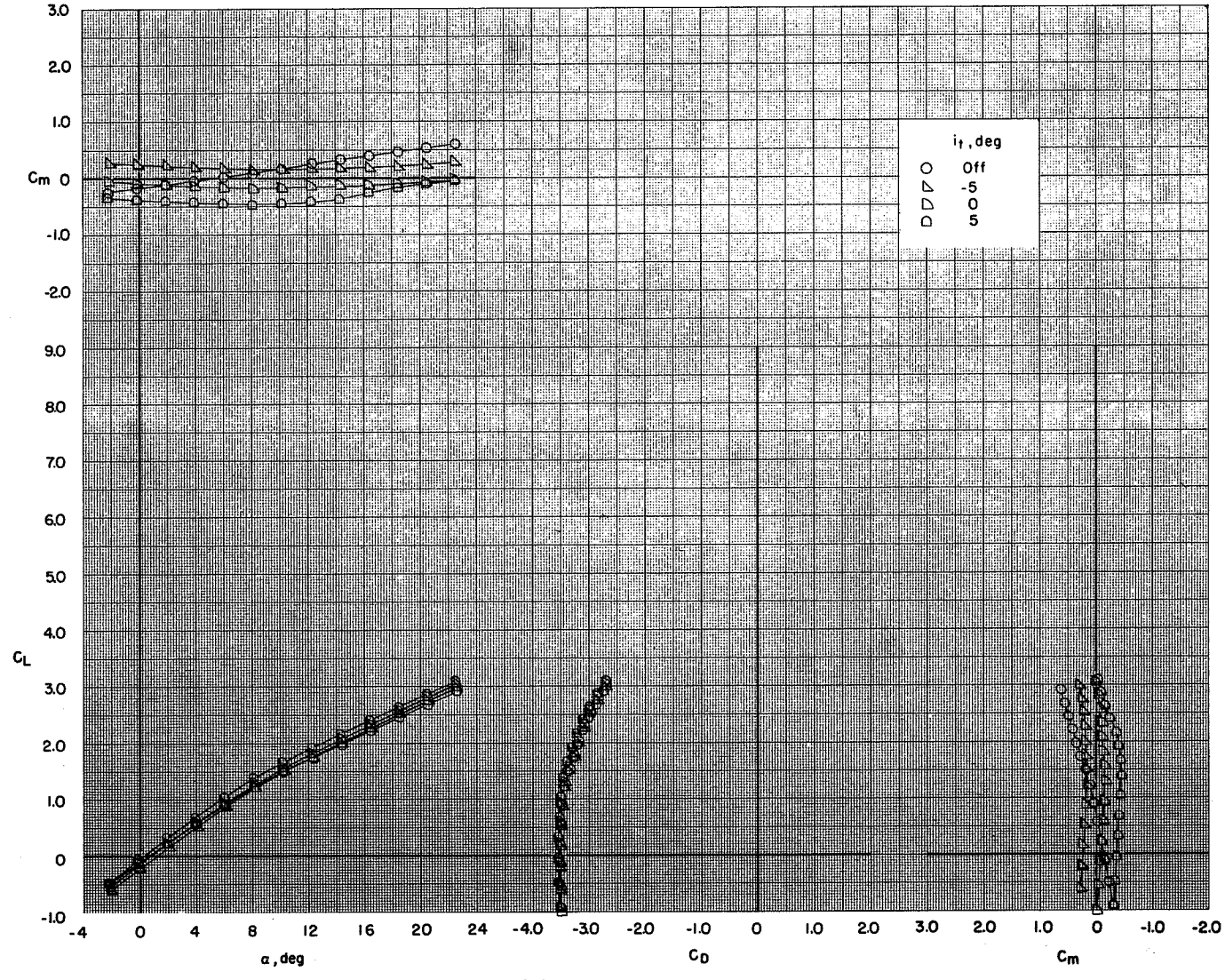

(e) $C_T = 3.70$.

Figure 43.- Concluded.

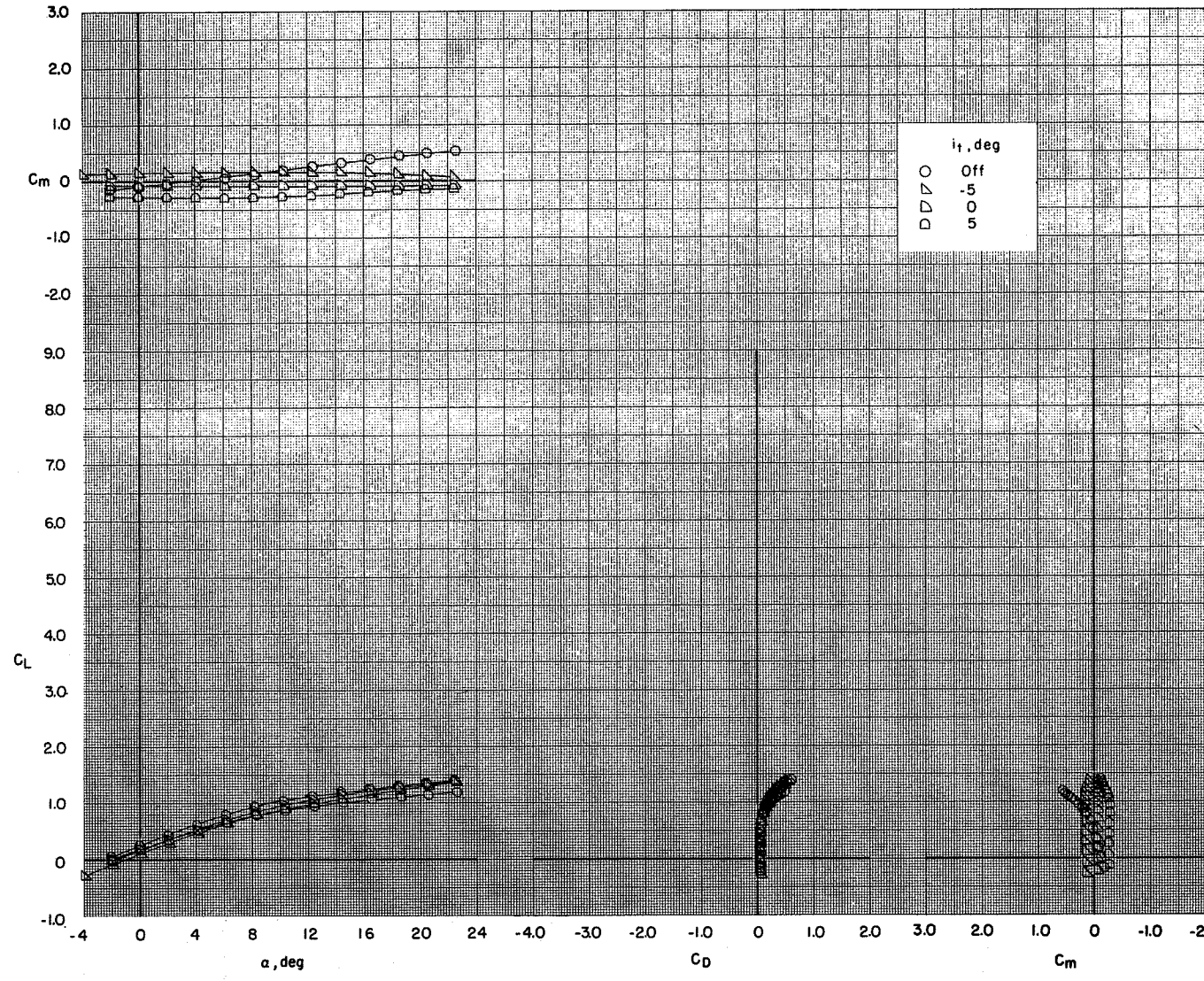

(a) $C_T = 0$.

Figure 44.- Effect of horizontal-tail incidence angle on the longitudinal aerodynamic characteristics of the model with flaps retracted and leading-edge slat off. BPR 6.2; low tail; tail-slat off; elevators off; $\delta_f = 0^o/0^o/0^o$.

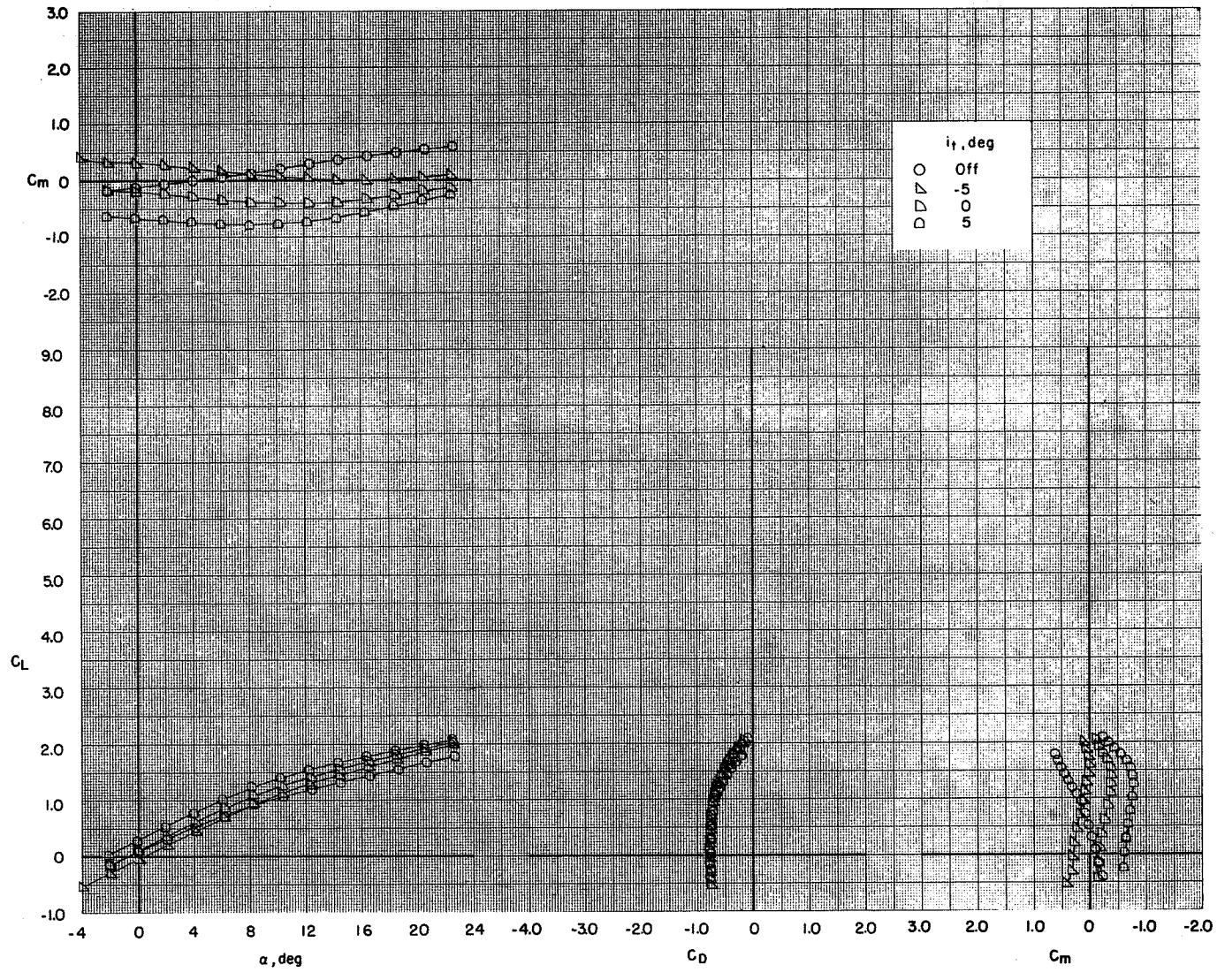

(b) $C_T = 0.94$.

Figure 44.- Continued.

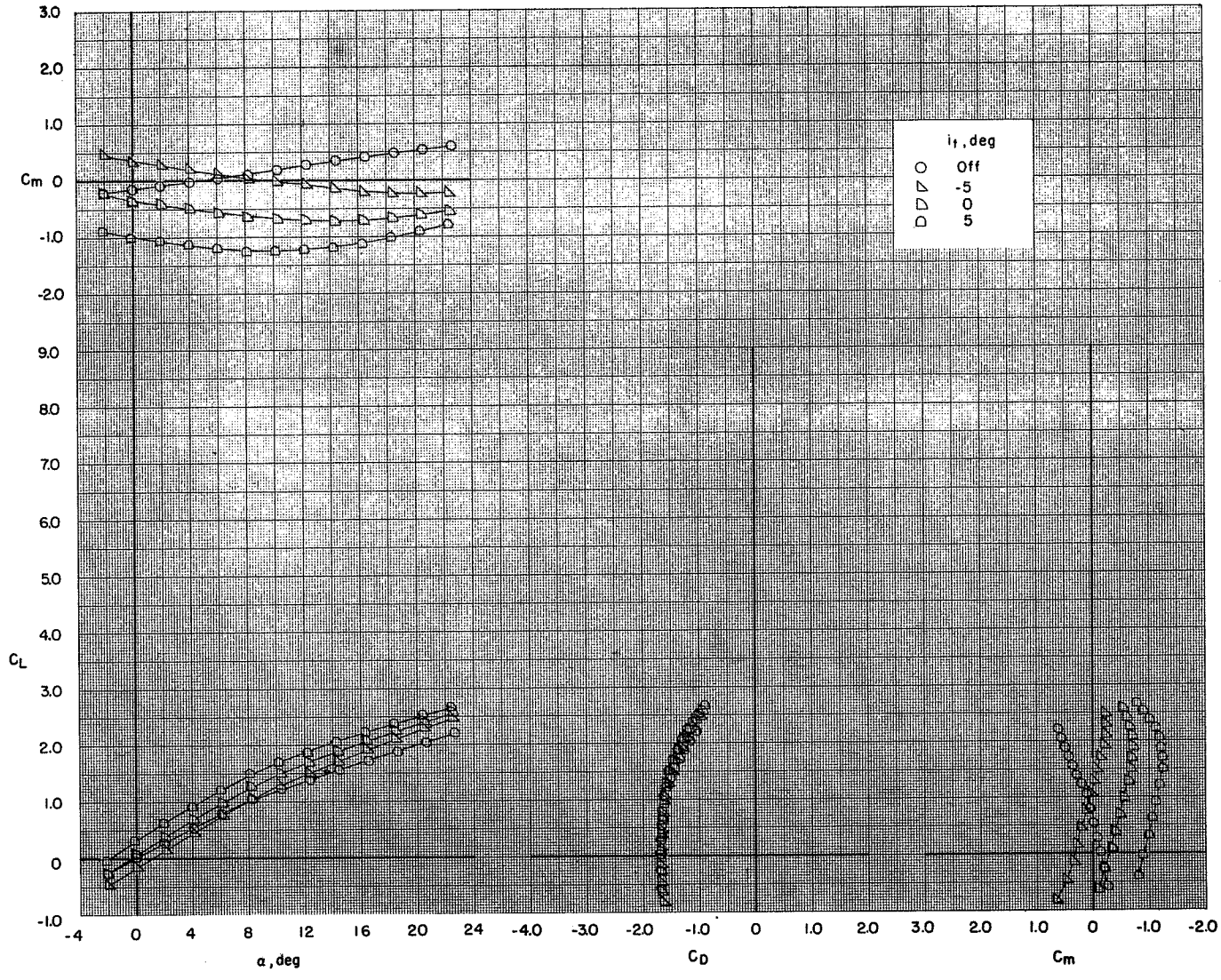

(c) $C_T = 1.85$.

Figure 44.- Continued.

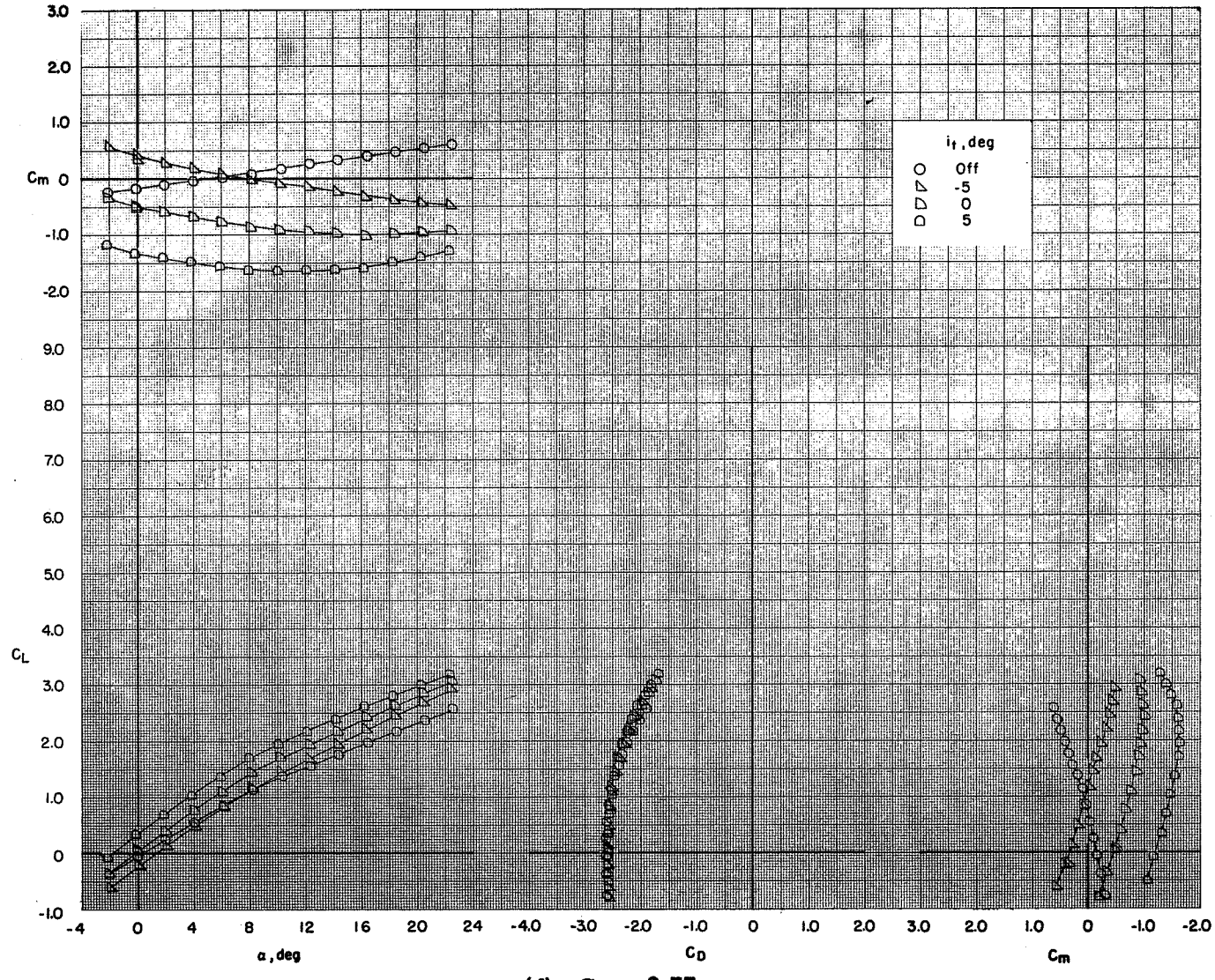

(d) $C_T = 2.77$.

Figure 44.- Continued.

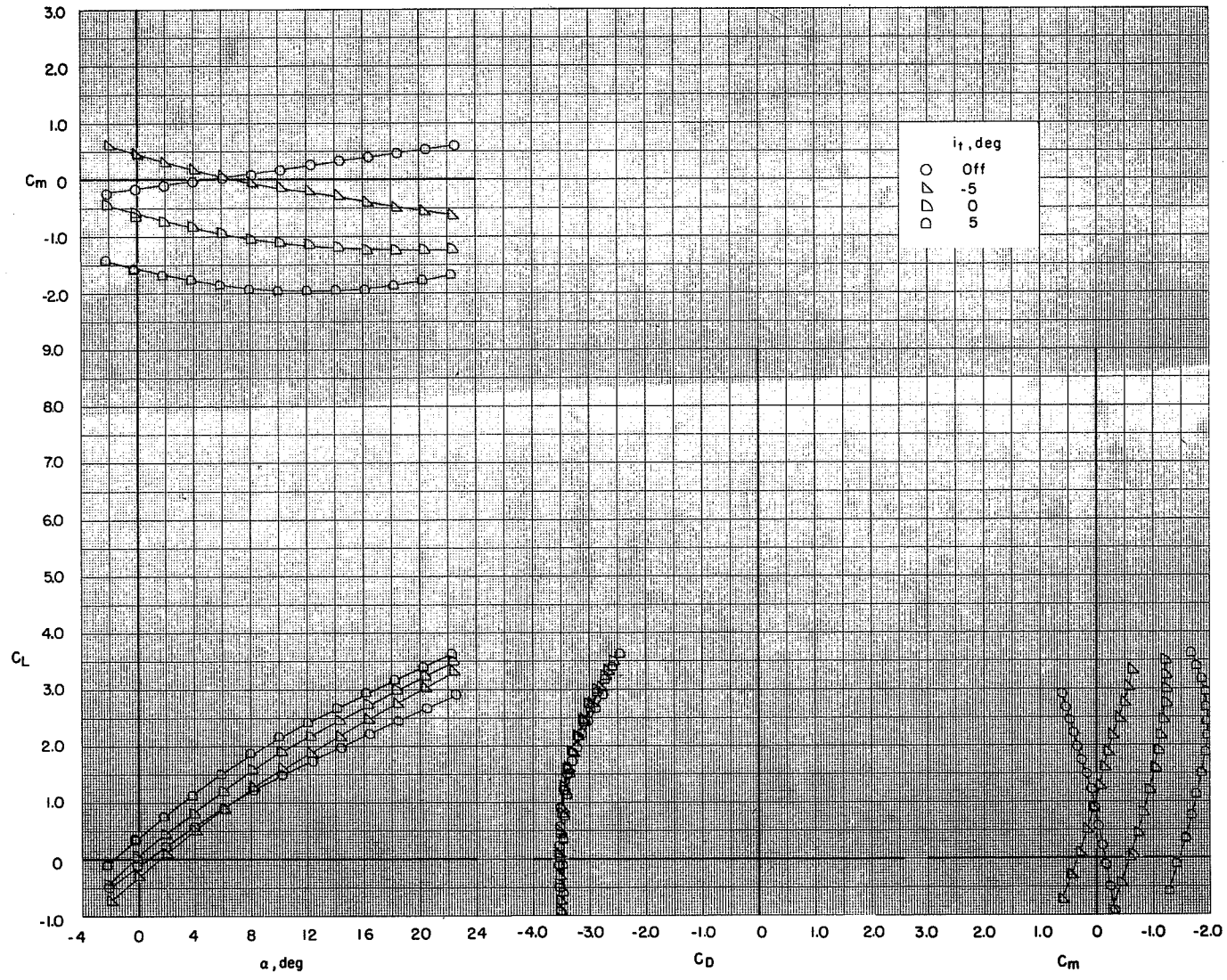

(e) $C_T = 3.70$.

Figure 44.- Concluded.

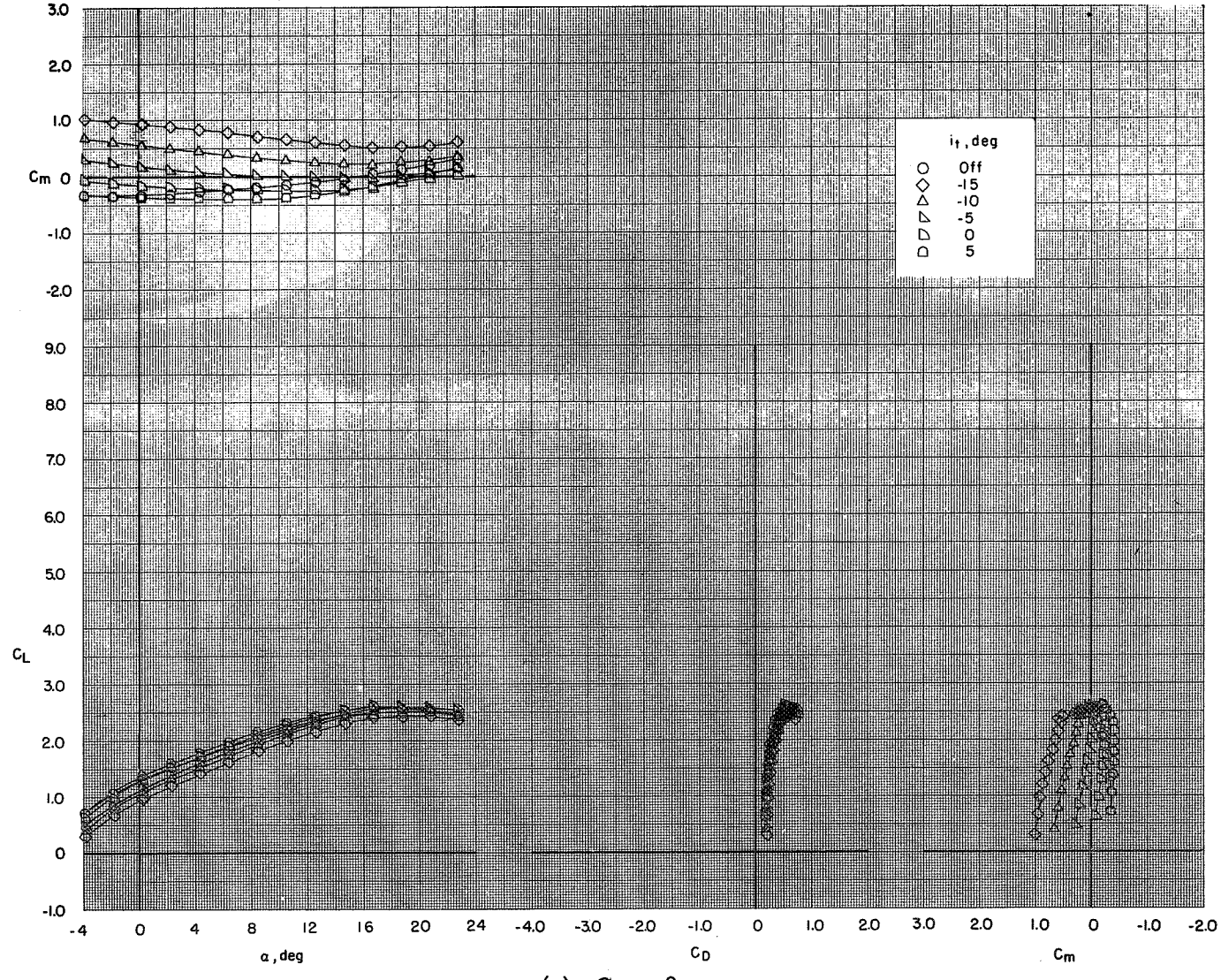

(a) $C_T = 0$.

Figure 45.- Effect of horizontal-tail incidence angle on the longitudinal aerodynamic characteristics of the model with flaps deflected and leading-edge slat on. BPR 6.2; T-tail; elevators off; $\delta_f = 0^o/35^o/35^o$; $c_s = 20$ percent; $\delta_s = 50^o$.

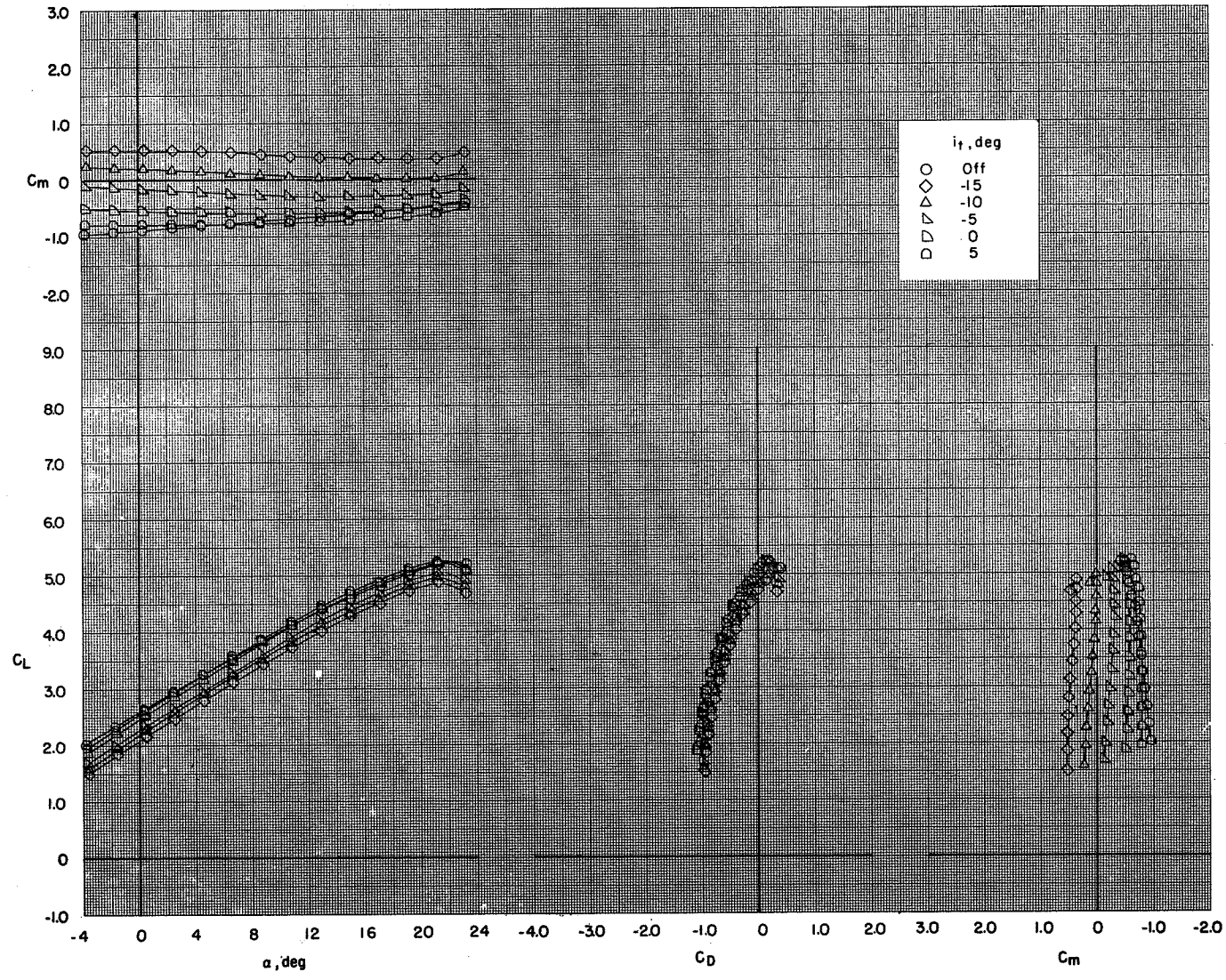

(b) $C_T = 1.88$.

Figure 45.- Continued.

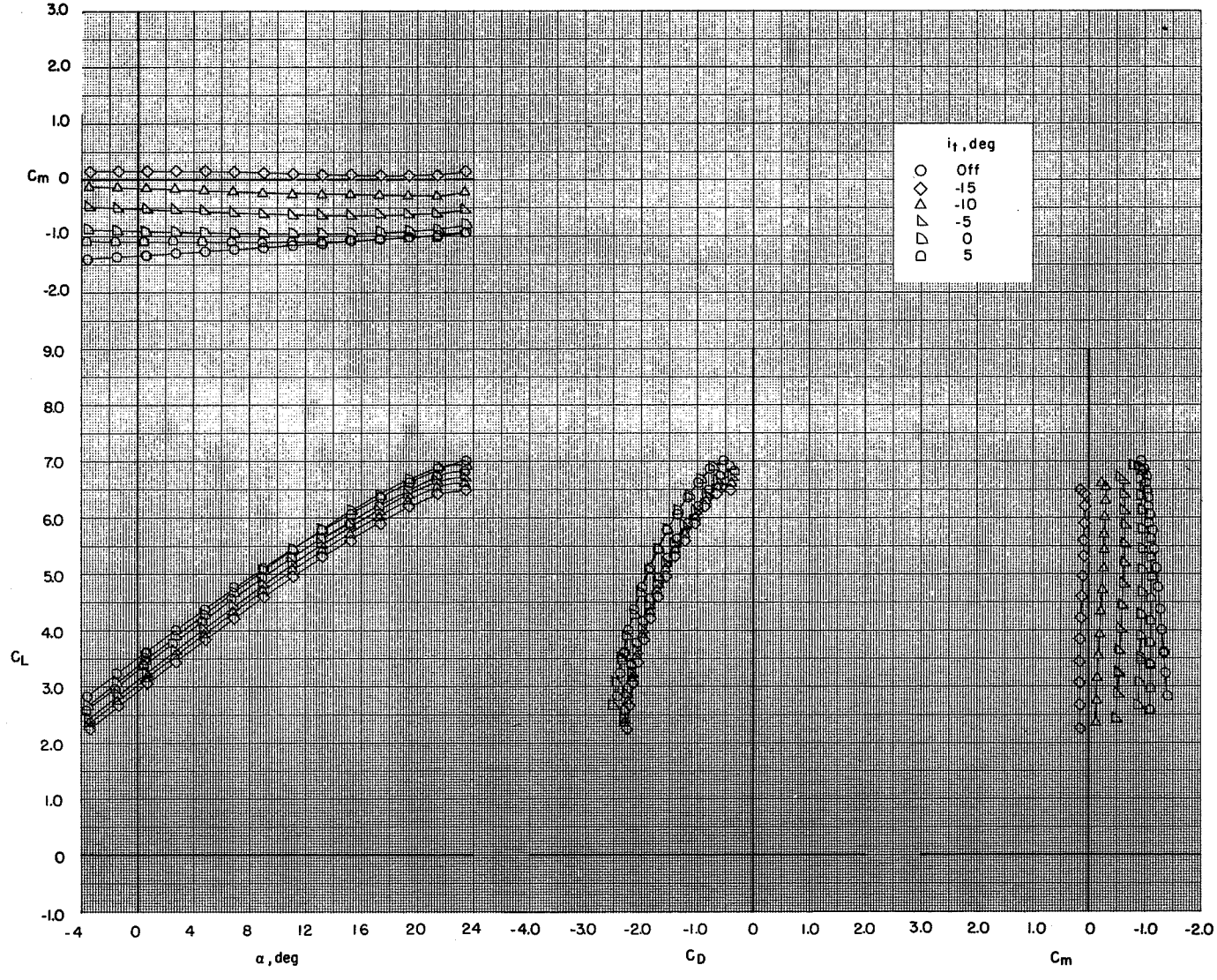

(c) $C_T = 3.74$.

Figure 45.- Concluded.

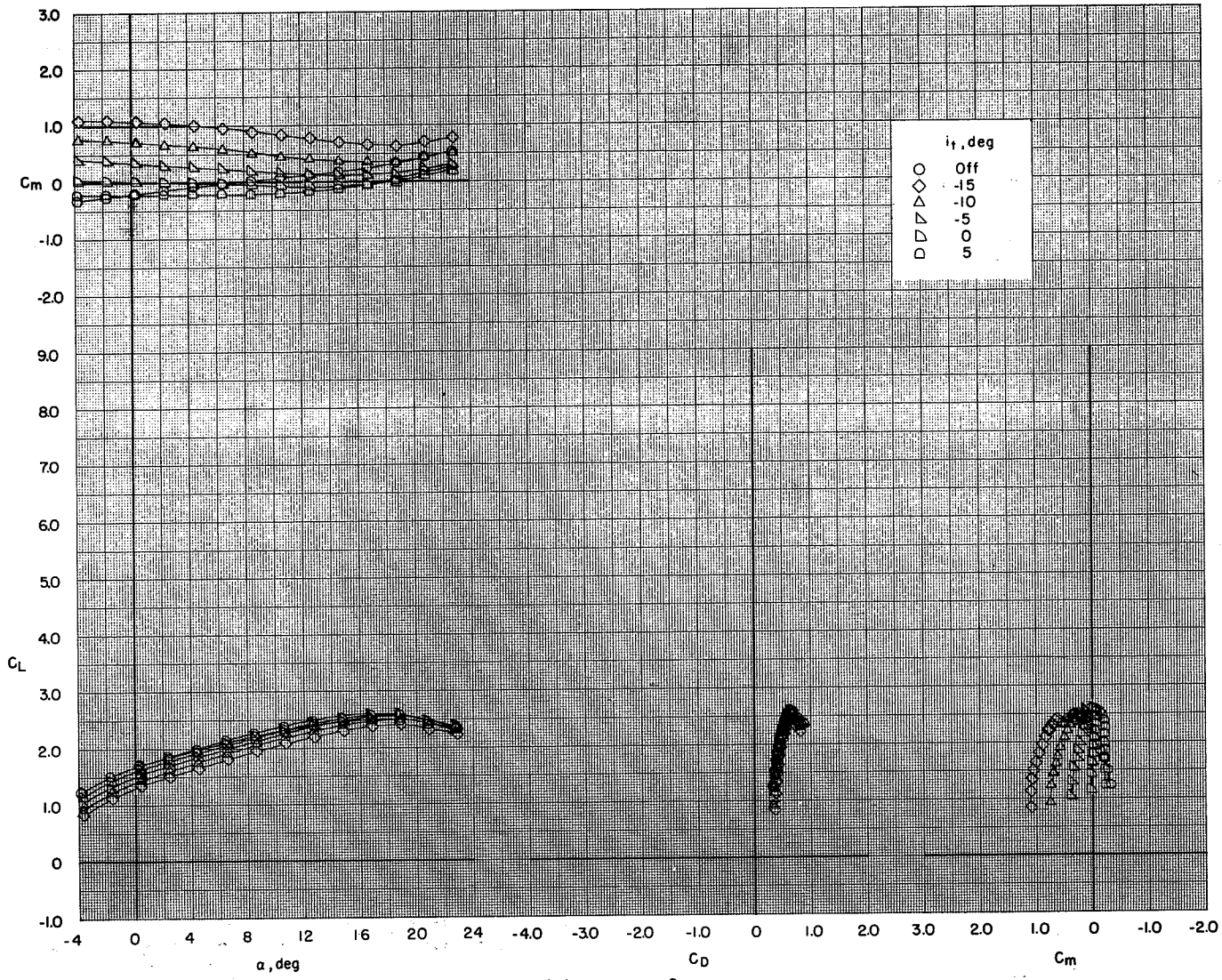

(a) $C_T = 0$.

Figure 46.- Effect of horizontal-tail incidence angle on the longitudinal aerodynamic characteristics of the model with flaps deflected and leading-edge slat on. BPR 6.2; T-tail; elevators off; $\delta_f = 0^o/65^o/65^o$; $c_s = 20$ percent; $\delta_s = 50^o$.

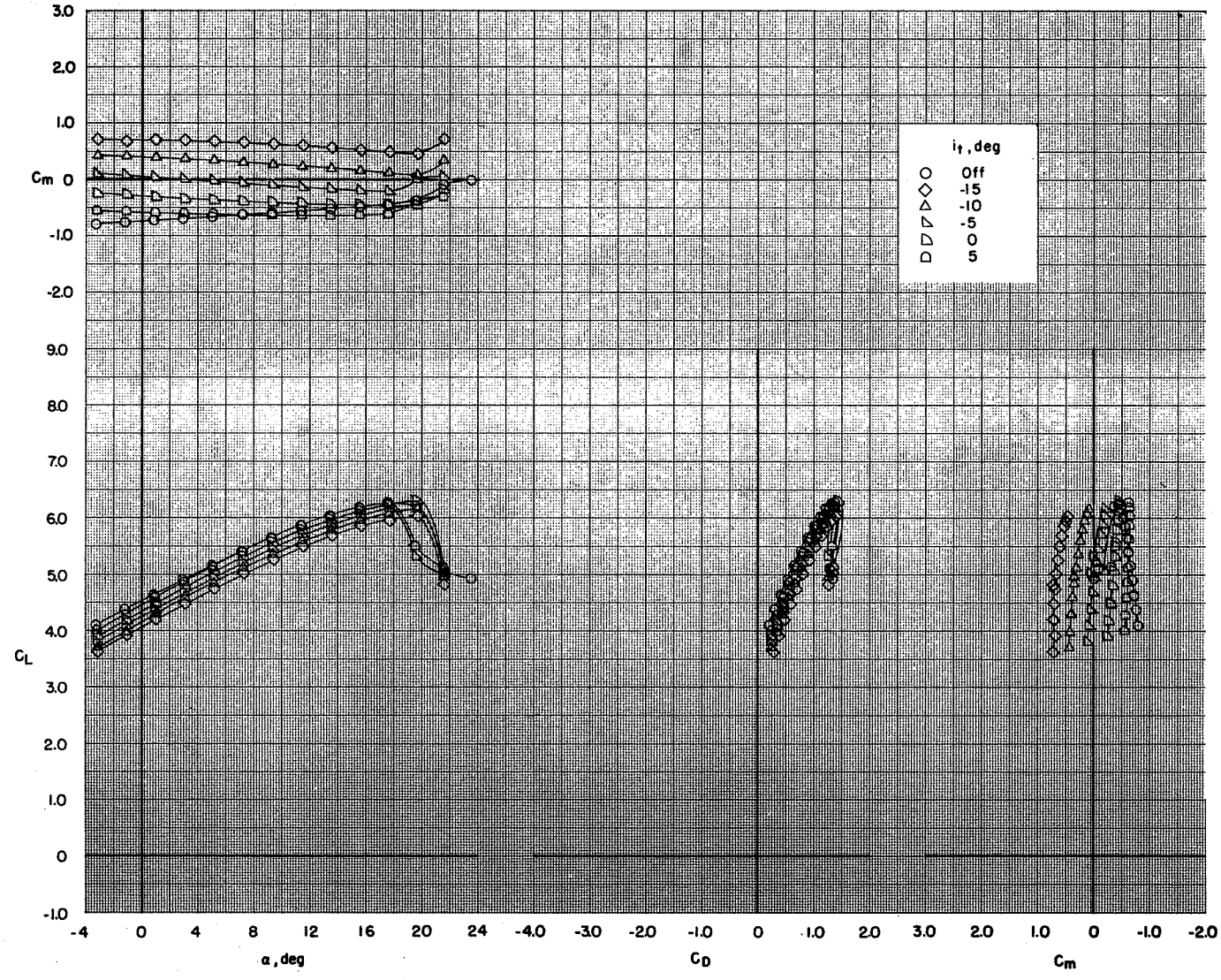

(b) $C_T = 1.88$.

Figure 46.- Continued.

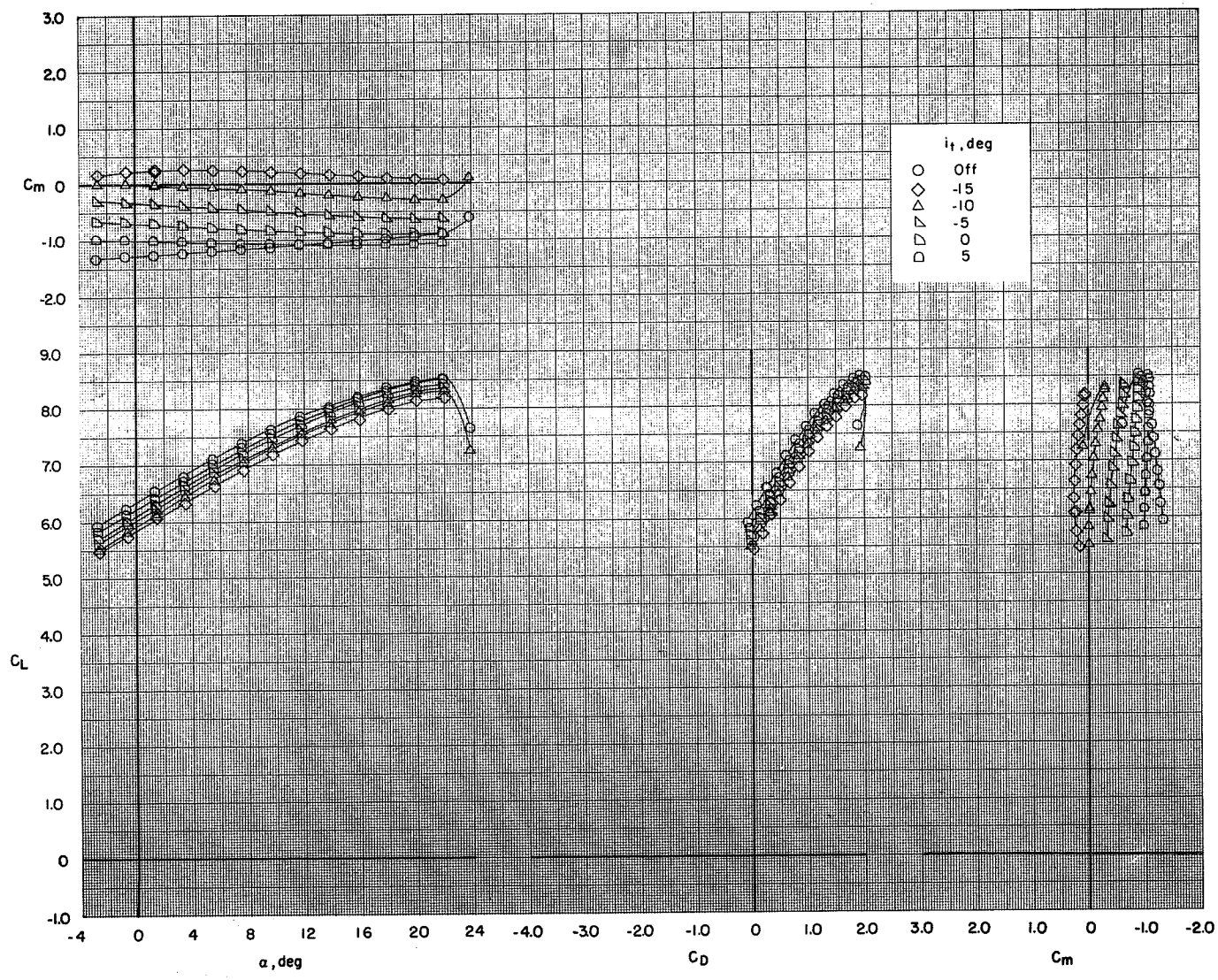

(c) $C_T = 3.74$.

Figure 46.- Concluded.

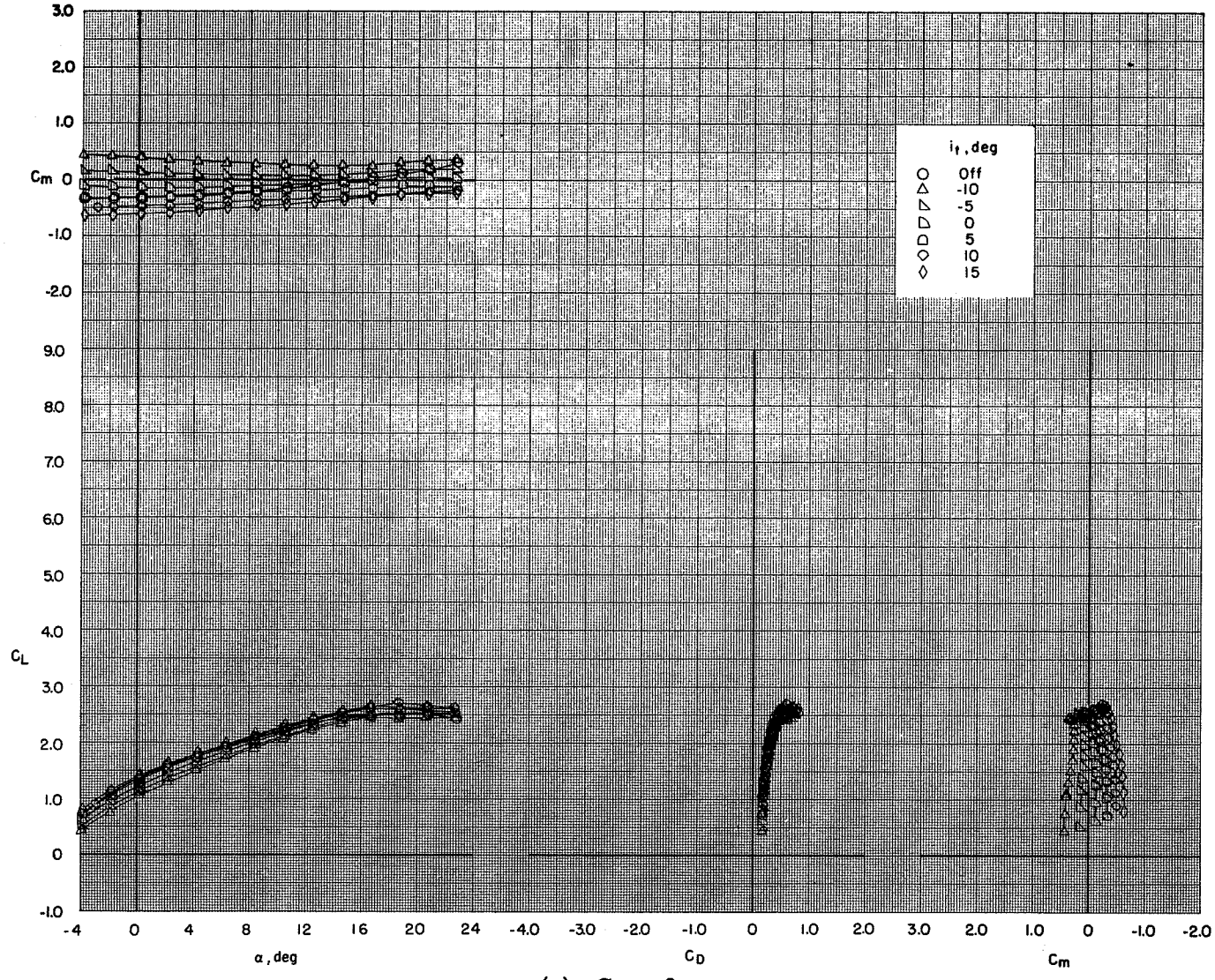

(a) $C_T = 0$.

Figure 47.- Effect of horizontal-tail incidence angle on the longitudinal aerodynamic characteristics of the model with flaps deflected and leading-edge slat on. BPR 6.2; low tail; elevators off; $\delta_f = 0^o/35^o/35^o$; $c_s = 20$ percent; $\delta_s = 50^o$.

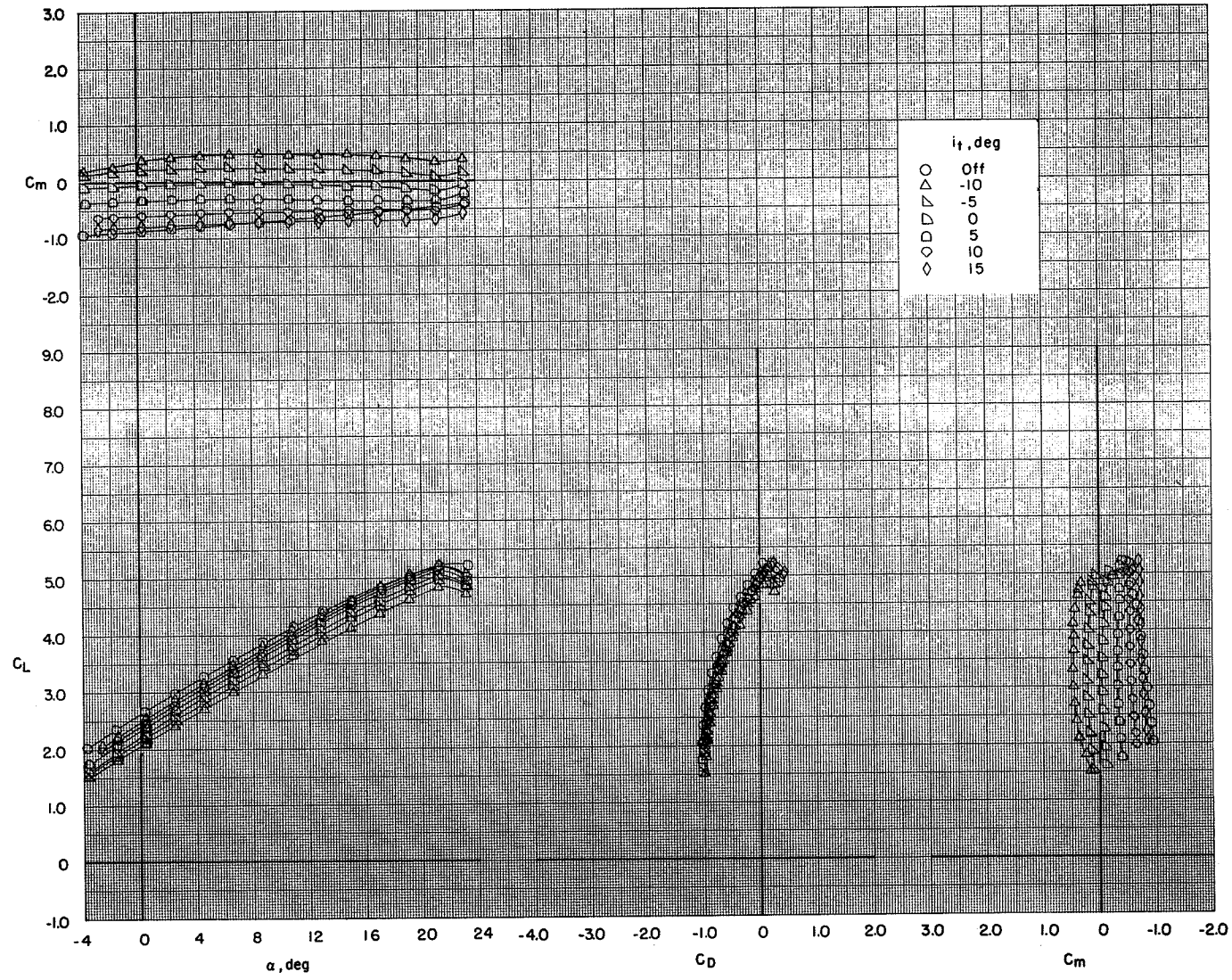

(b) $C_T = 1.88$.

Figure 47.- Continued.

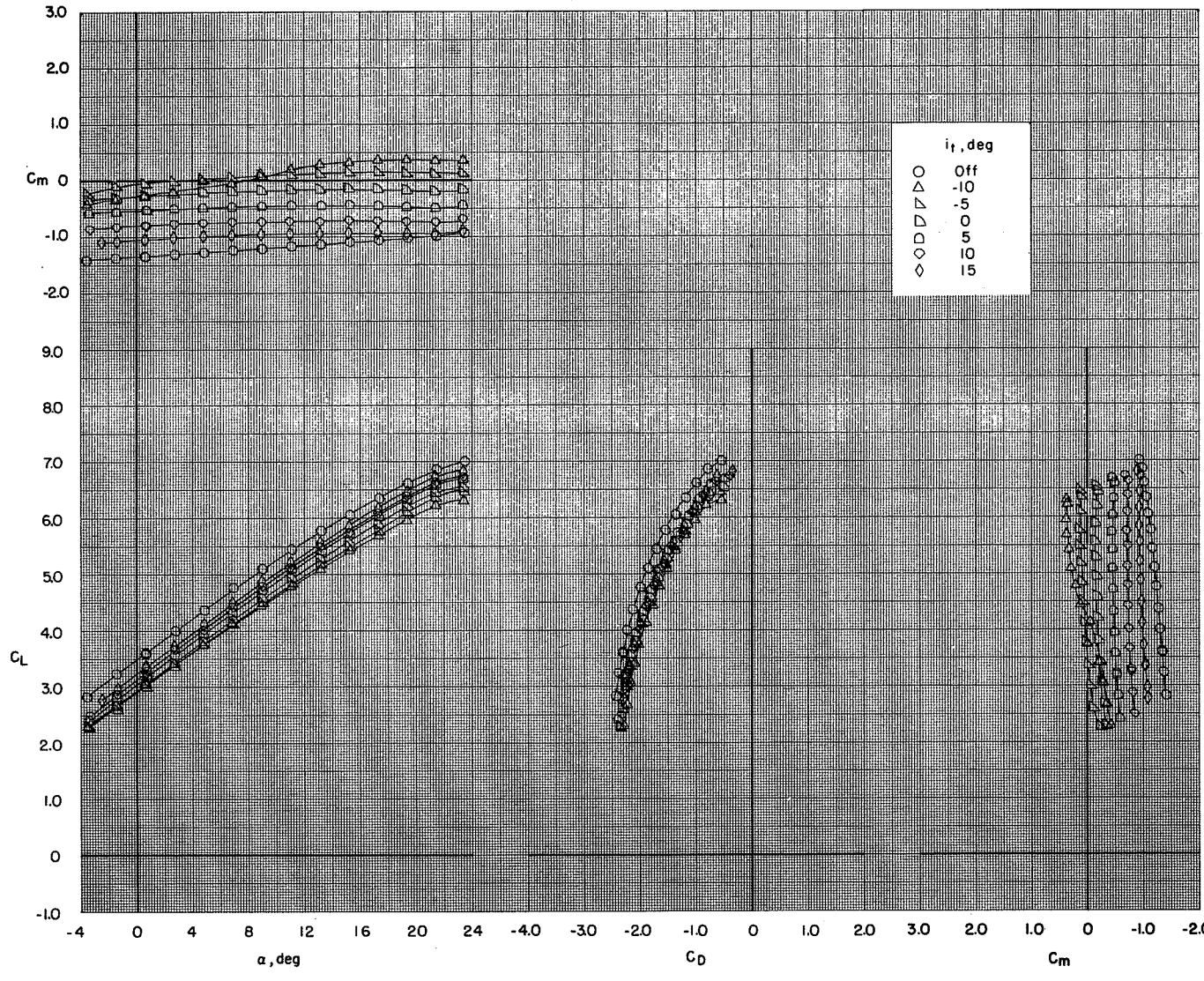

(c) $C_T = 3.74$.

Figure 47.- Concluded.

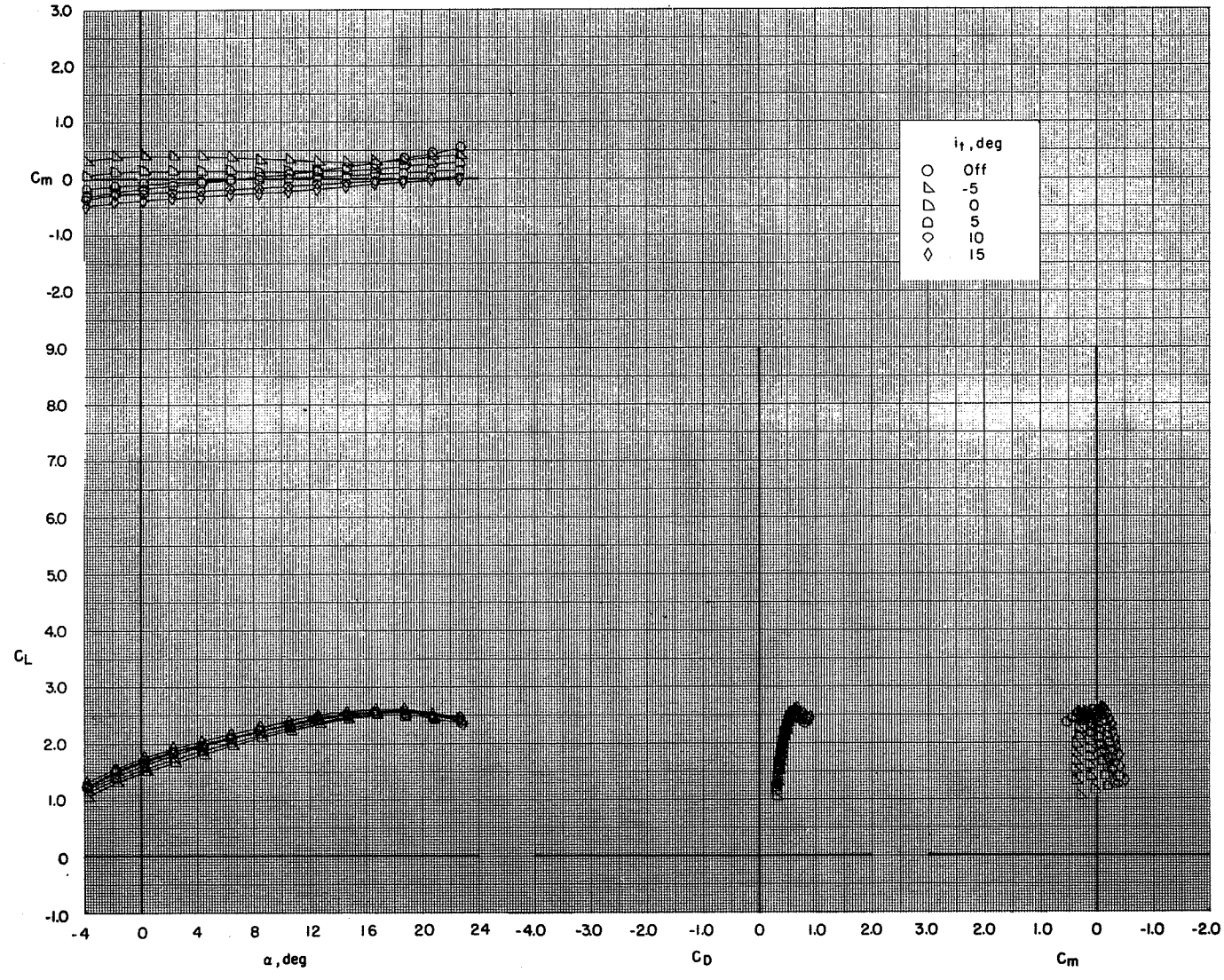

(a) $C_T = 0$.

Figure 48.- Effect of horizontal-tail incidence angle on the longitudinal aerodynamic characteristics of the model with flaps deflected and leading-edge slat on. BPR 6.2; low tail; elevators off; $\delta_f = 0^o/65^o/65^o$; $c_s = 20$ percent; $\delta_s = 50^o$.

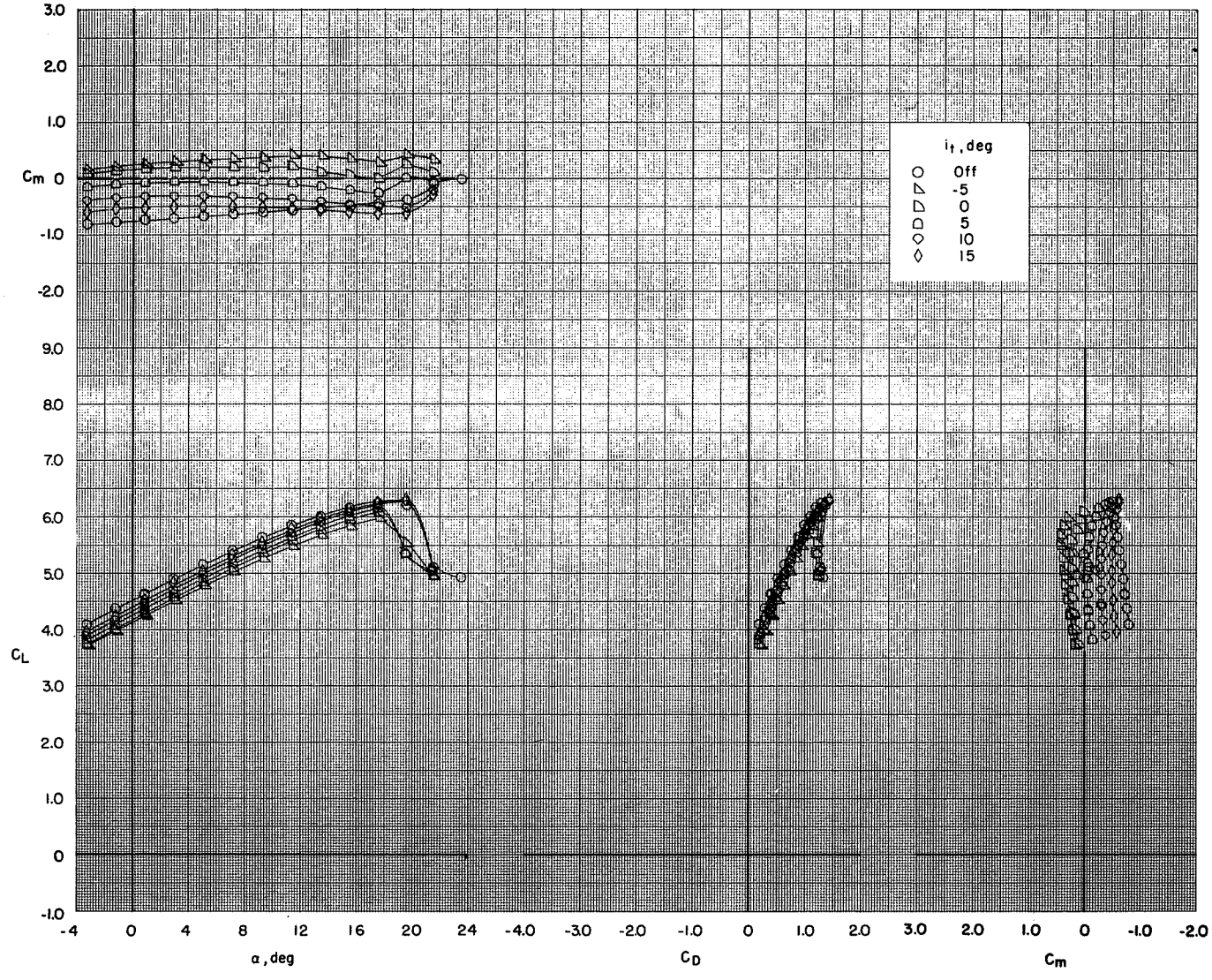

(b) $C_T = 1.88$.

Figure 48.- Continued.

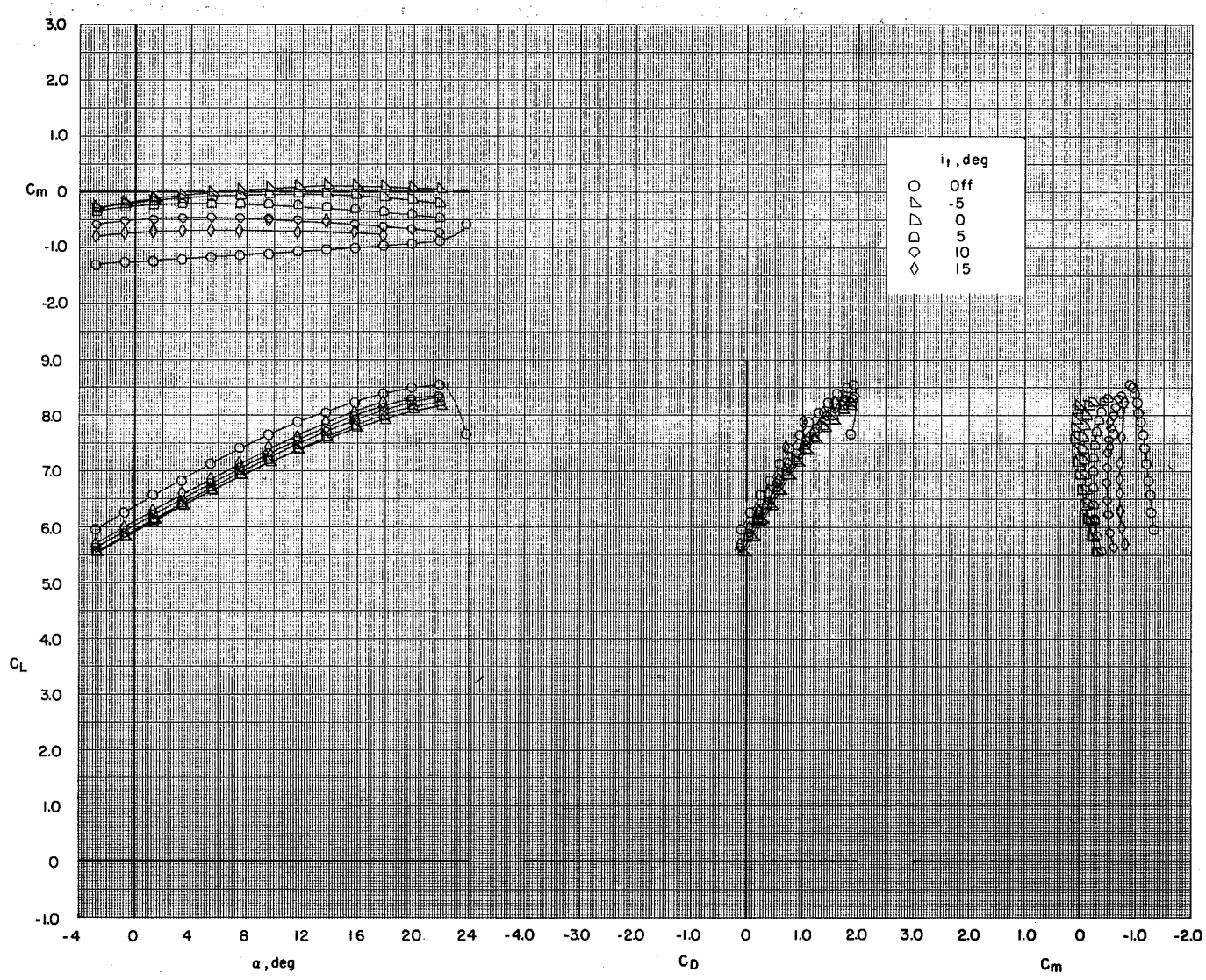

(c) $C_T = 3.74$.

Figure 48.- Concluded.

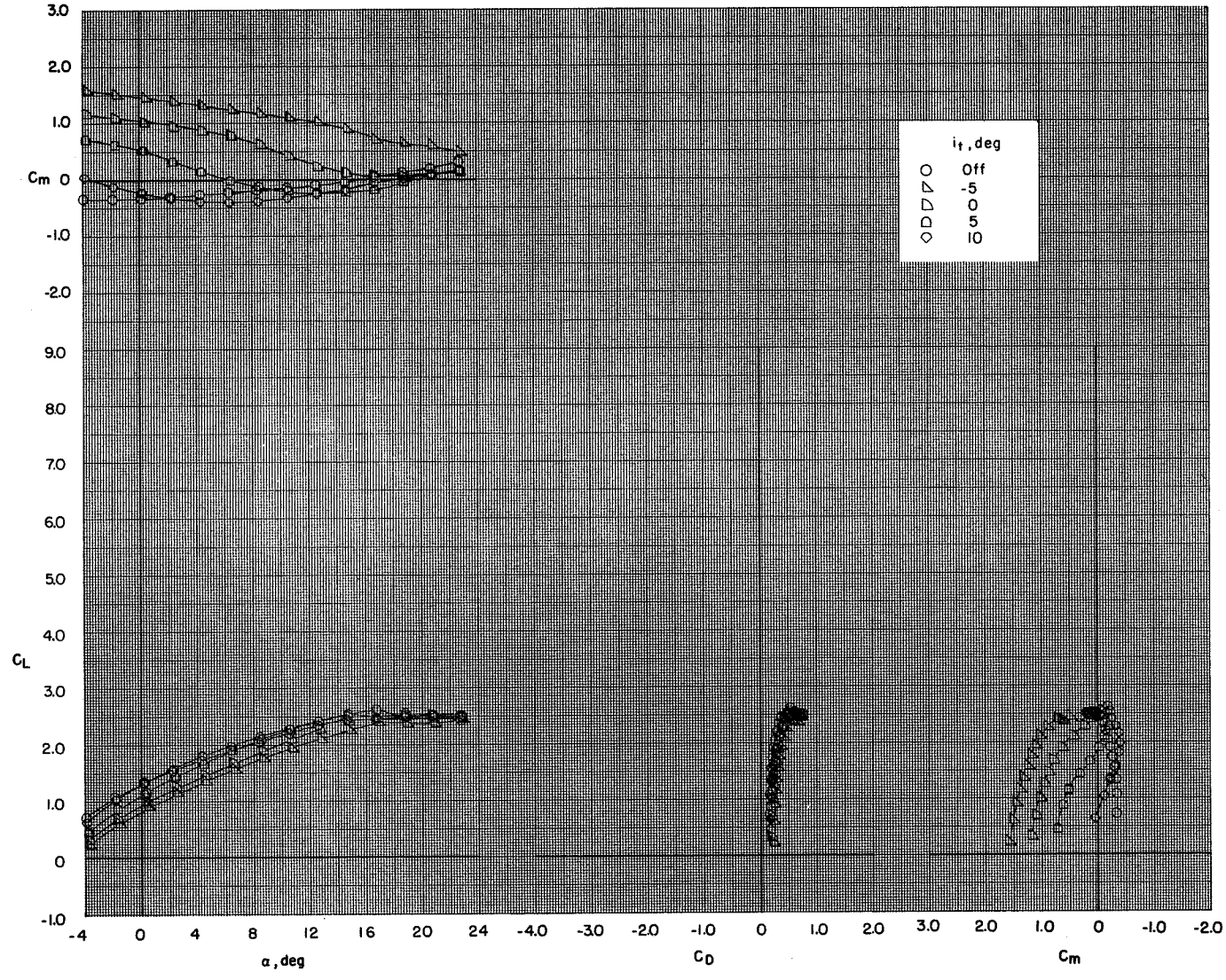

(a) $C_T = 0$.

Figure 49.- Effect of horizontal-tail incidence angle on the longitudinal aerodynamic characteristics of the model with flaps deflected and leading-edge slat on. BPR 6.2; T-tail; $\delta_f = 0^o/35^o/35^o$; $c_s = 20$ percent; $\delta_s = 50^o$; elevators on.

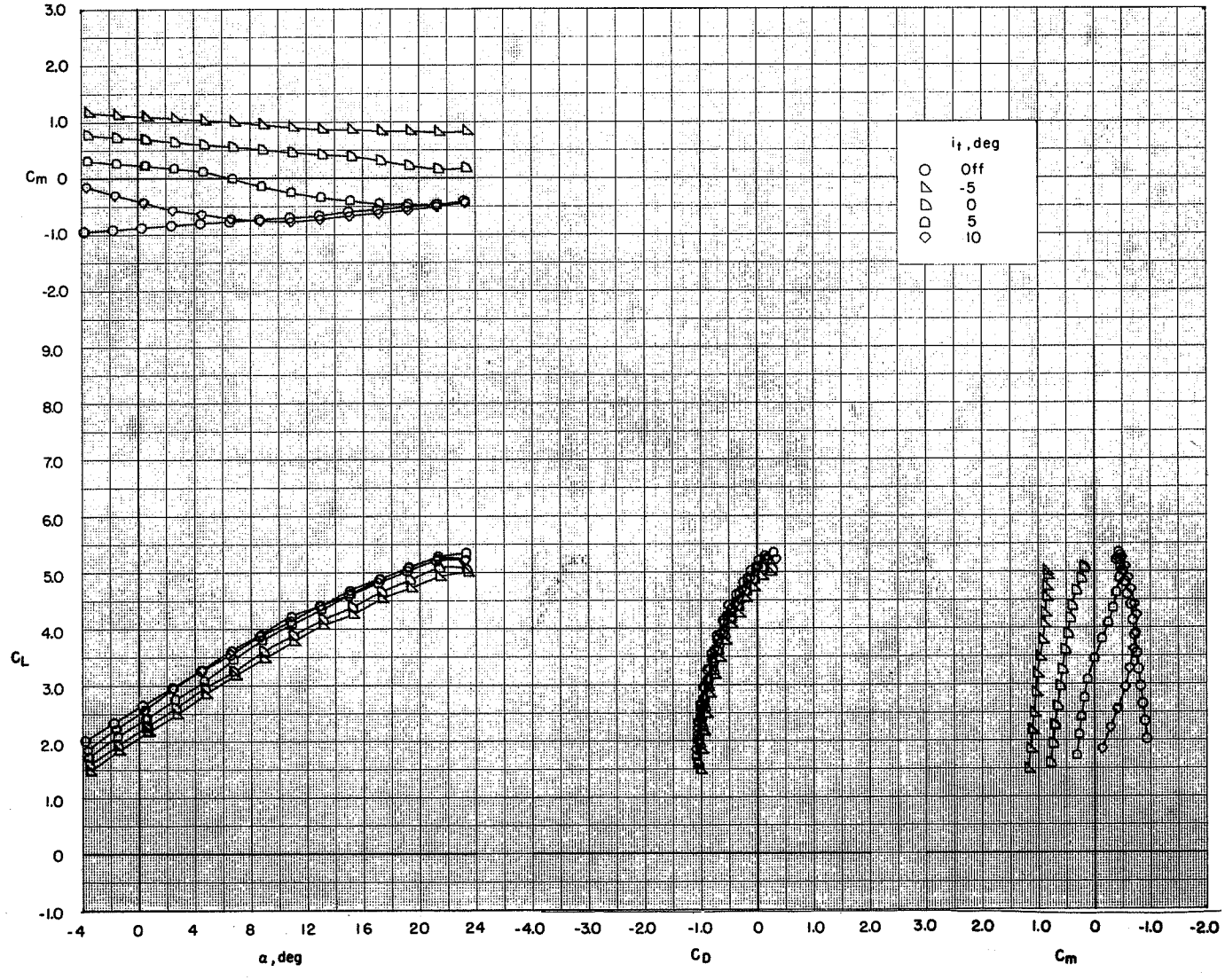

(b) $C_T = 1.88$.

Figure 49.- Continued.

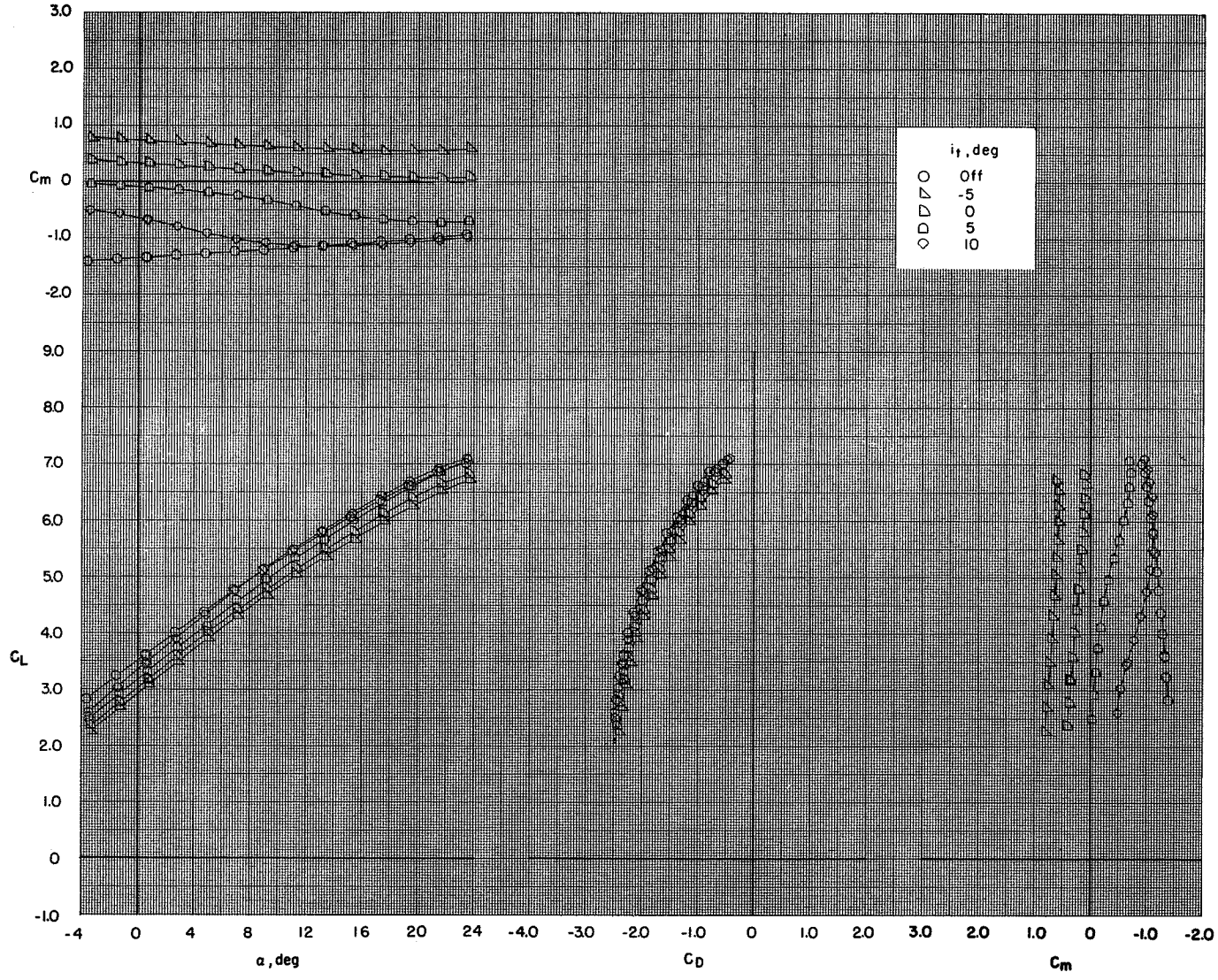

(c) $C_T = 3.74$.

Figure 49.- Concluded.

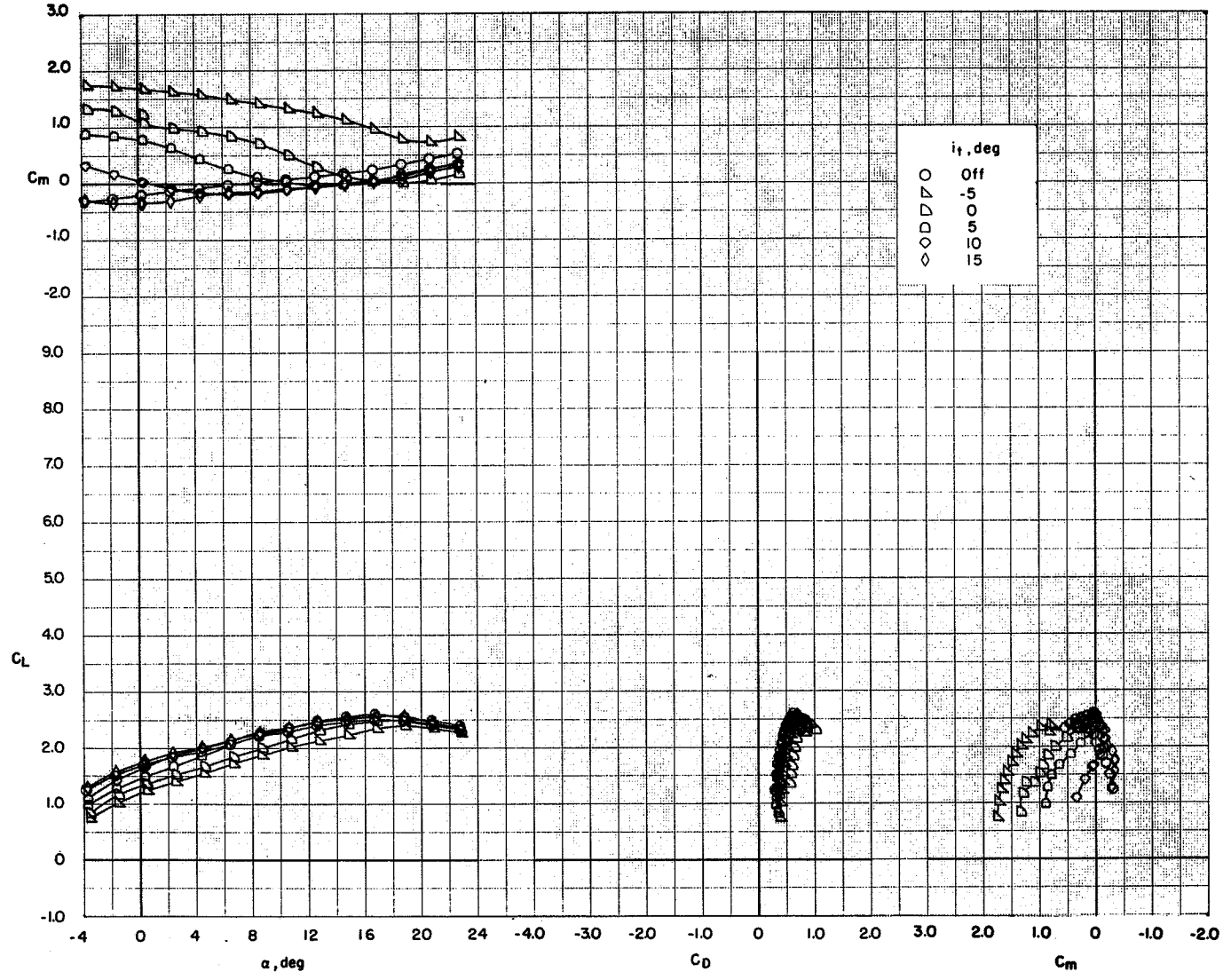

(a) $C_T = 0$.

Figure 50.- Effect of horizontal-tail incidence angle on the longitudinal aerodynamic characteristics of the model with flaps deflected and leading-edge slat on. BPR 6.2; T-tail; $\delta_f = 0^o/65^o/65^o$; $c_s = 20$ percent; $\delta_s = 50^o$; elevators on.

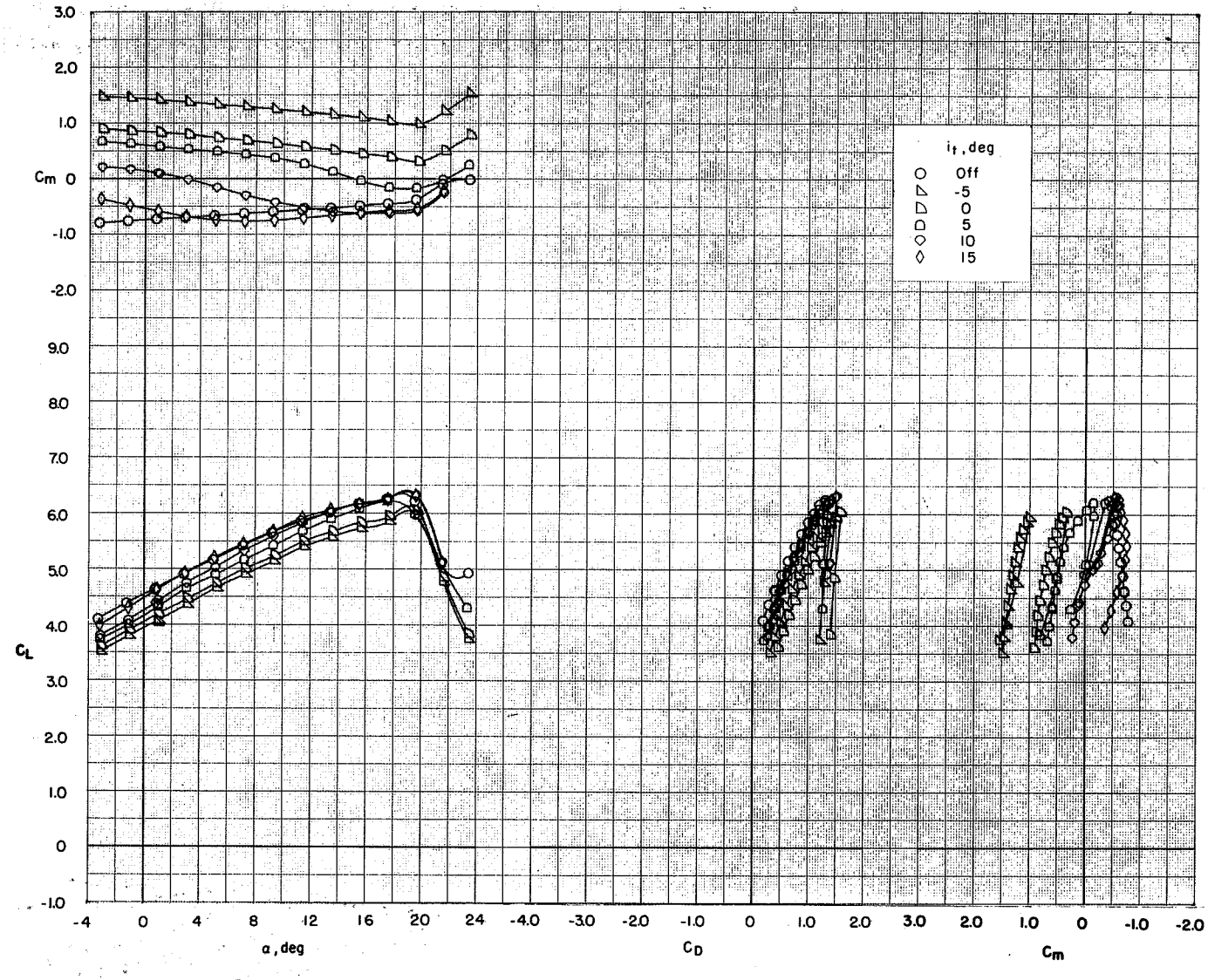

(b) $C_T = 1.88$.

Figure 50.- Continued.

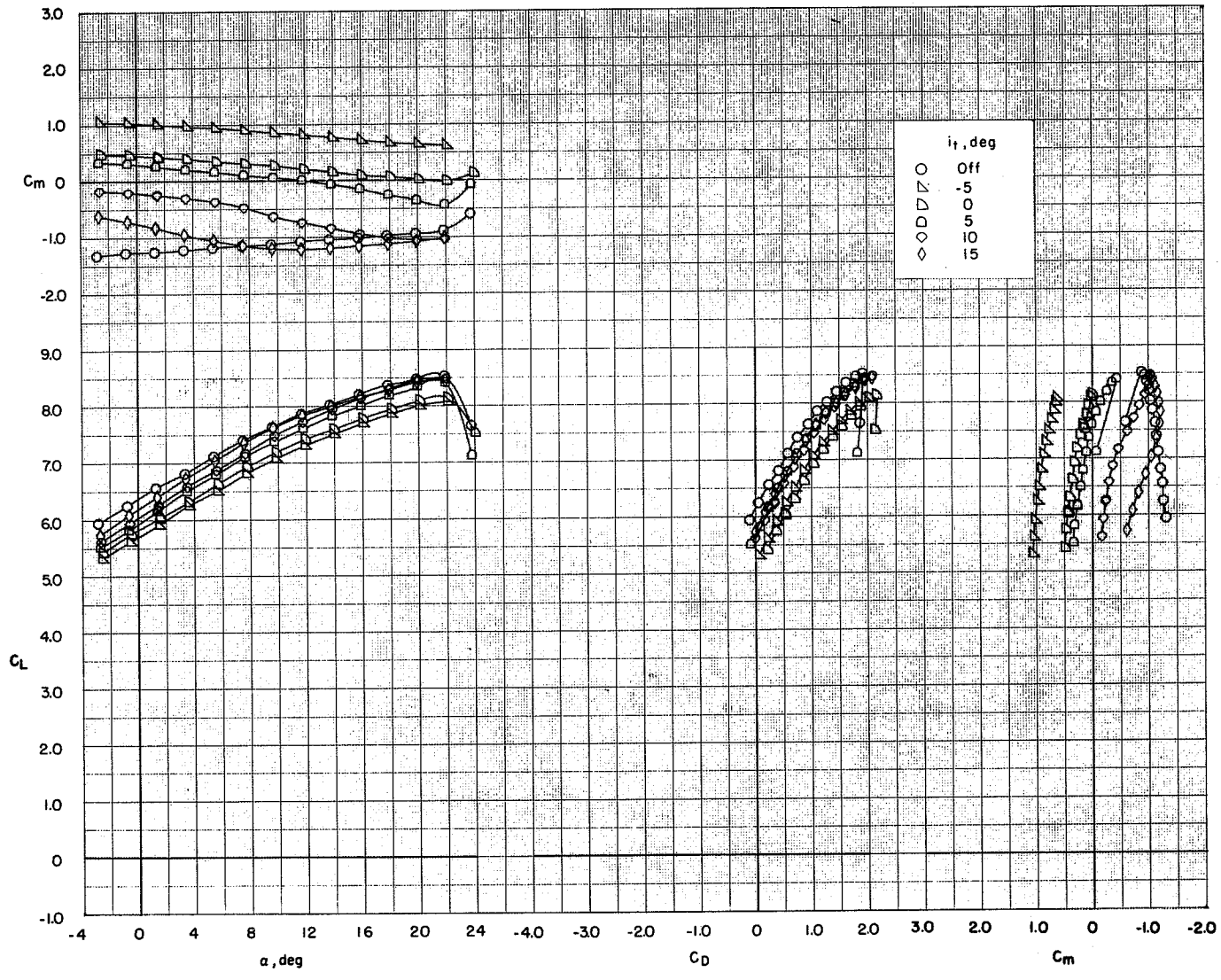

(c) $C_T = 3.74$.

Figure 50.- Concluded.

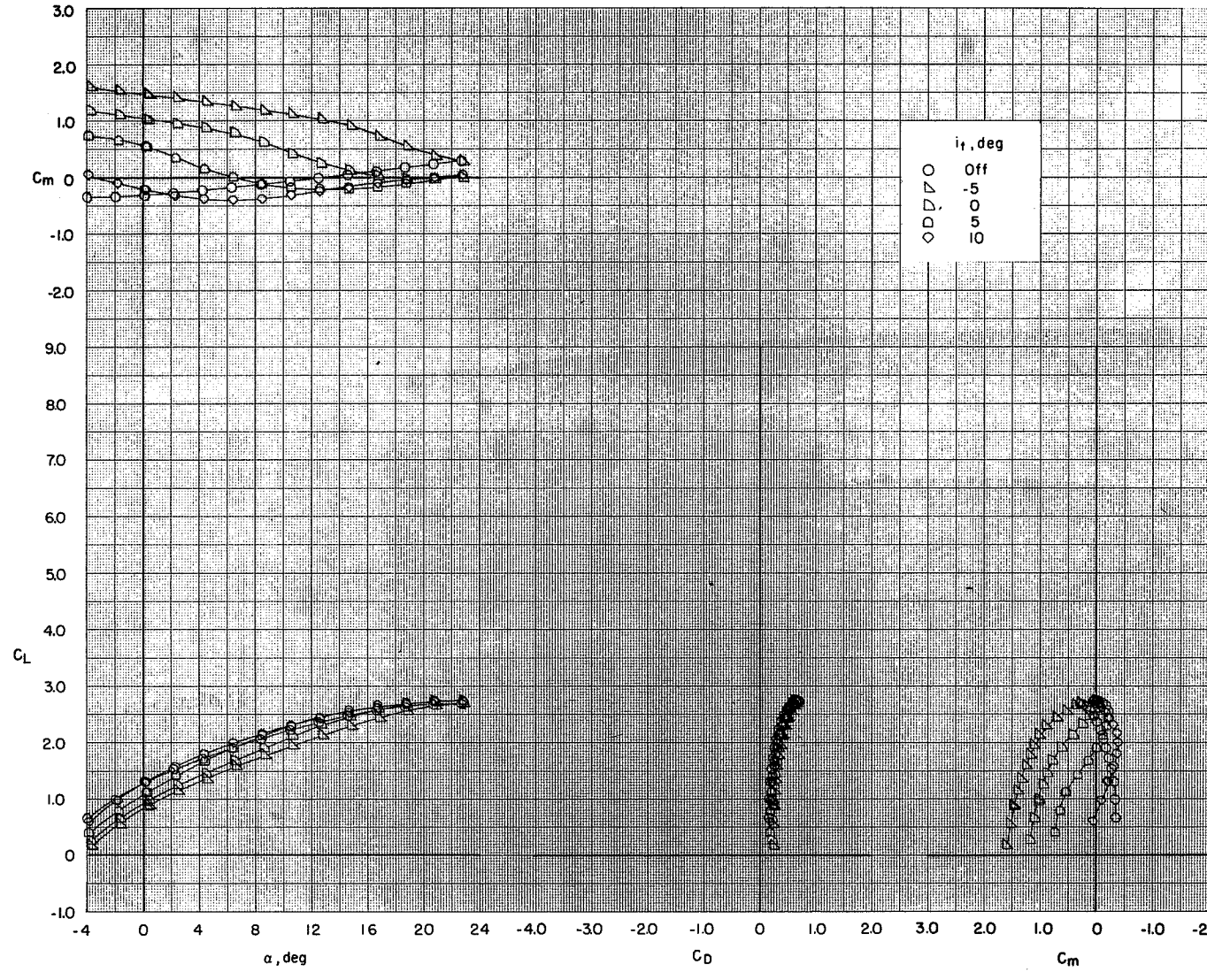

(a) $C_T = 0$.

Figure 51.- Effect of horizontal-tail incidence angle on the longitudinal aerodynamic characteristics of the model with flaps deflected and leading-edge slat on. BPR 6.2; T-tail; $\delta_f = 0^o/35^o/35^o$; $c_s = 25$ percent; $\delta_s = 50^o$; elevators on.

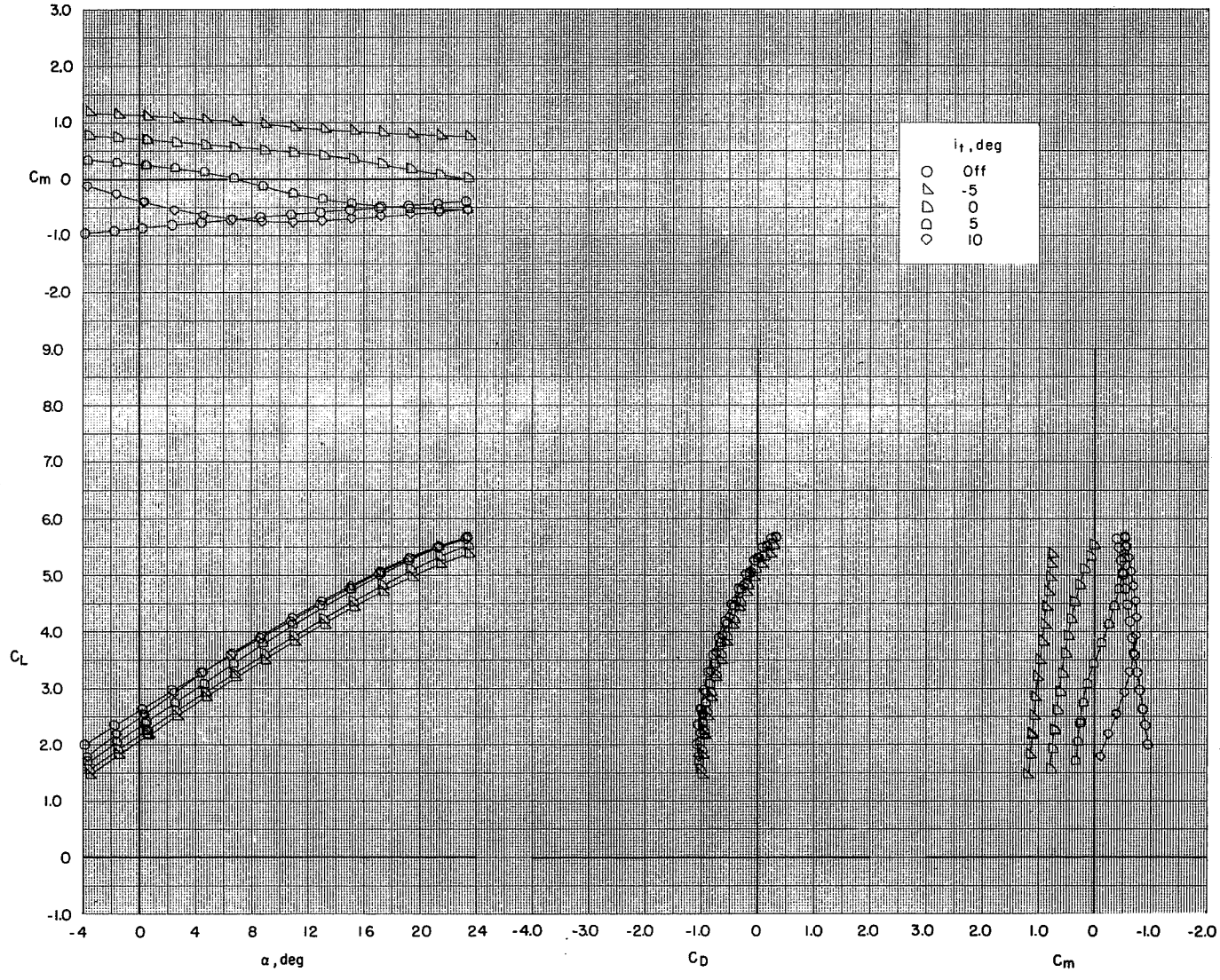

(b) $C_T = 1.88$.

Figure 51.- Continued.

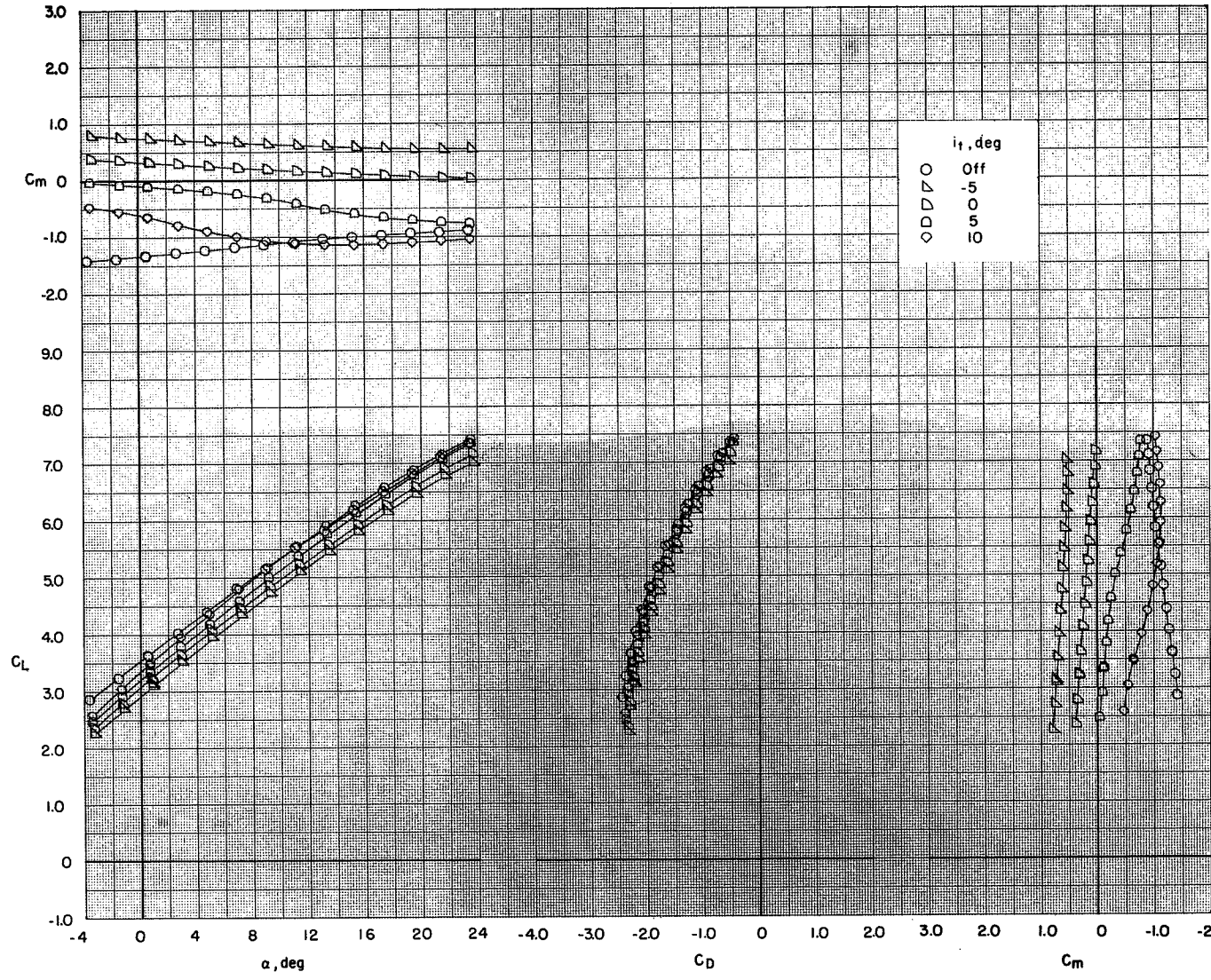

(c) $C_T = 3.74$.

Figure 51.- Concluded.

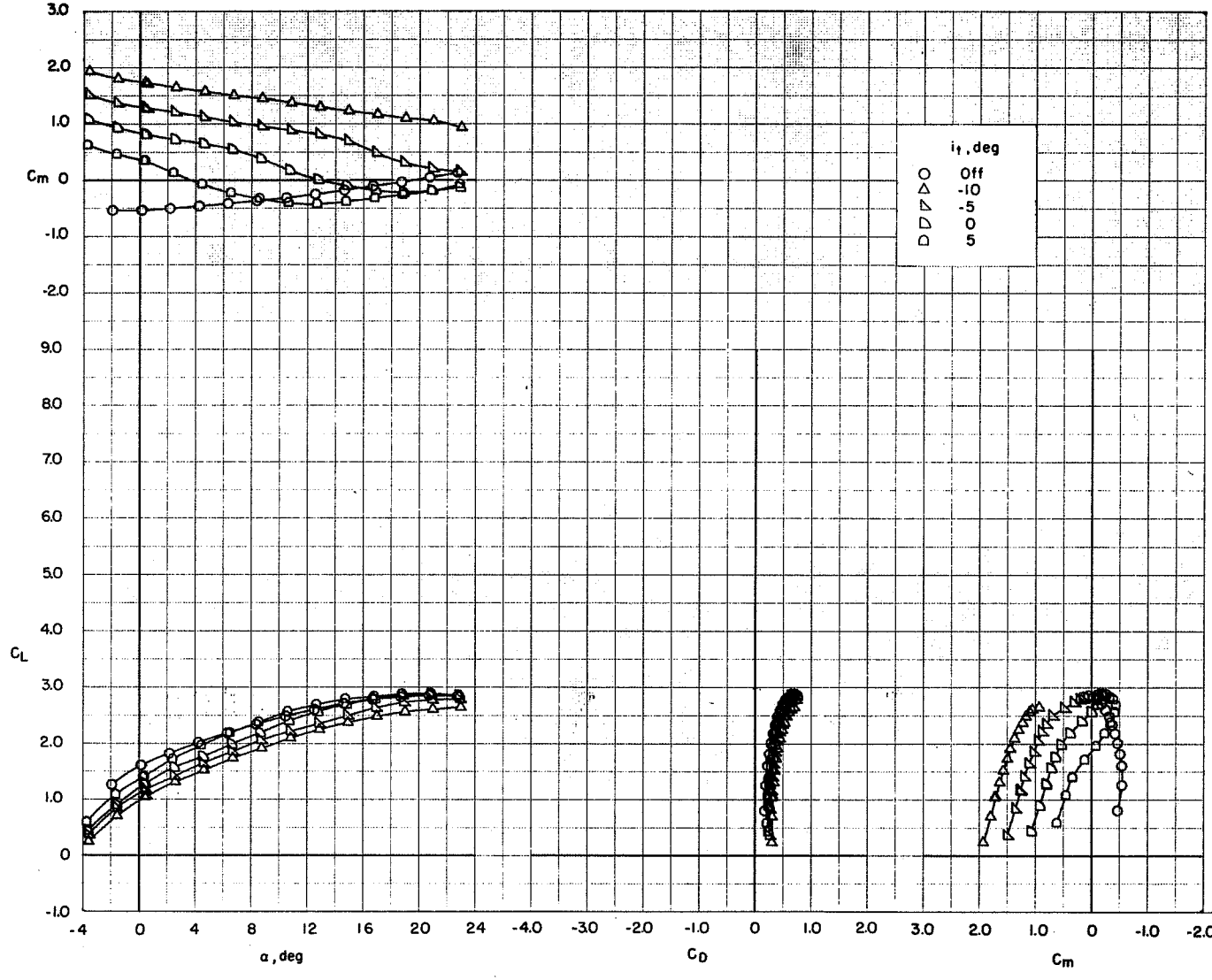

(a) $C_T = 0$.

Figure 52.- Effect of horizontal-tail incidence angle on the longitudinal aerodynamic characteristics of the model with flaps deflected and leading-edge slat on. BPR 6.2; T-tail; $\delta_f = 35^o/35^o/35^o$; $c_s = 25$ percent; $\delta_s = 50^o$; elevators on.

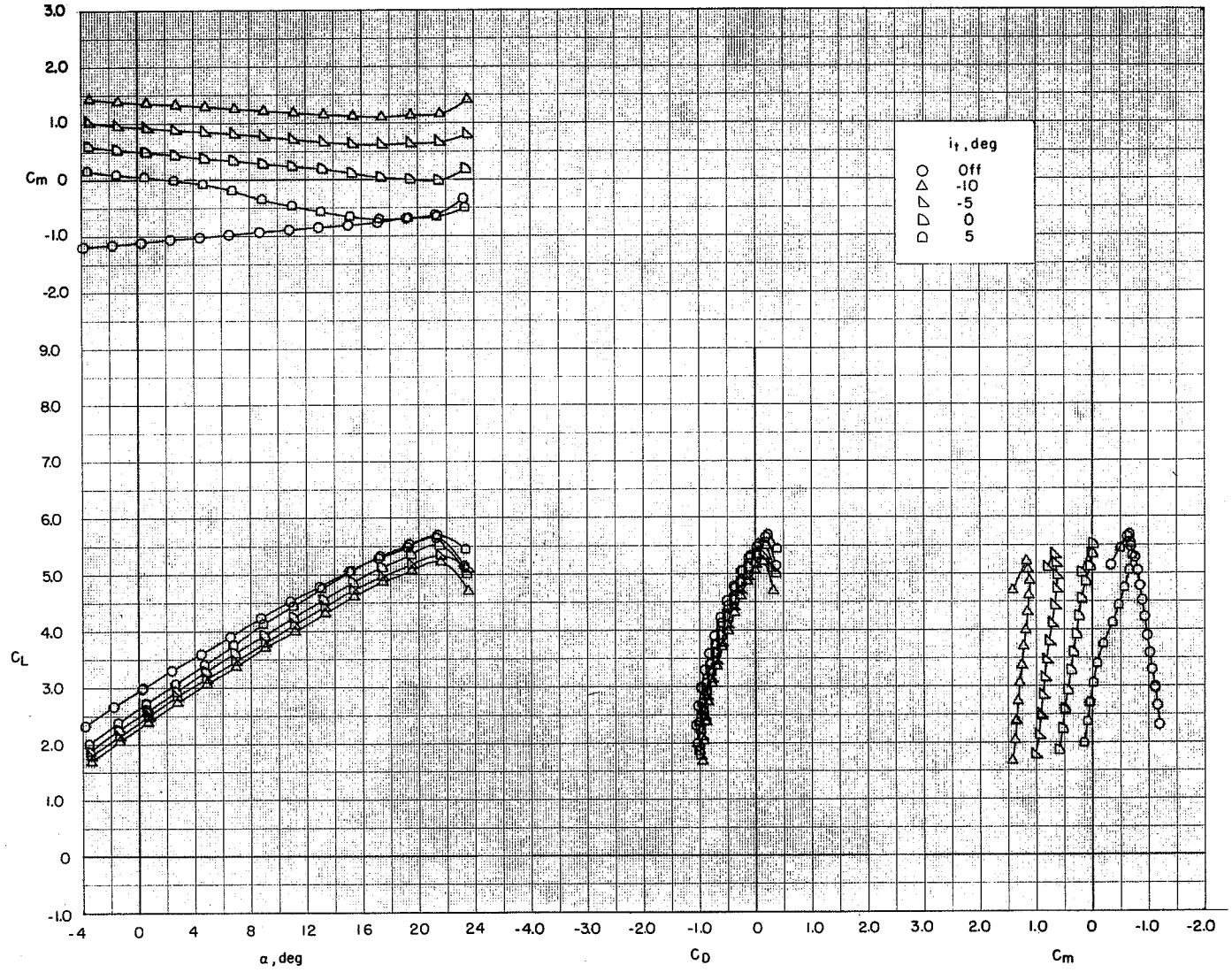

(b) $C_T = 1.88$.

Figure 52.- Continued.

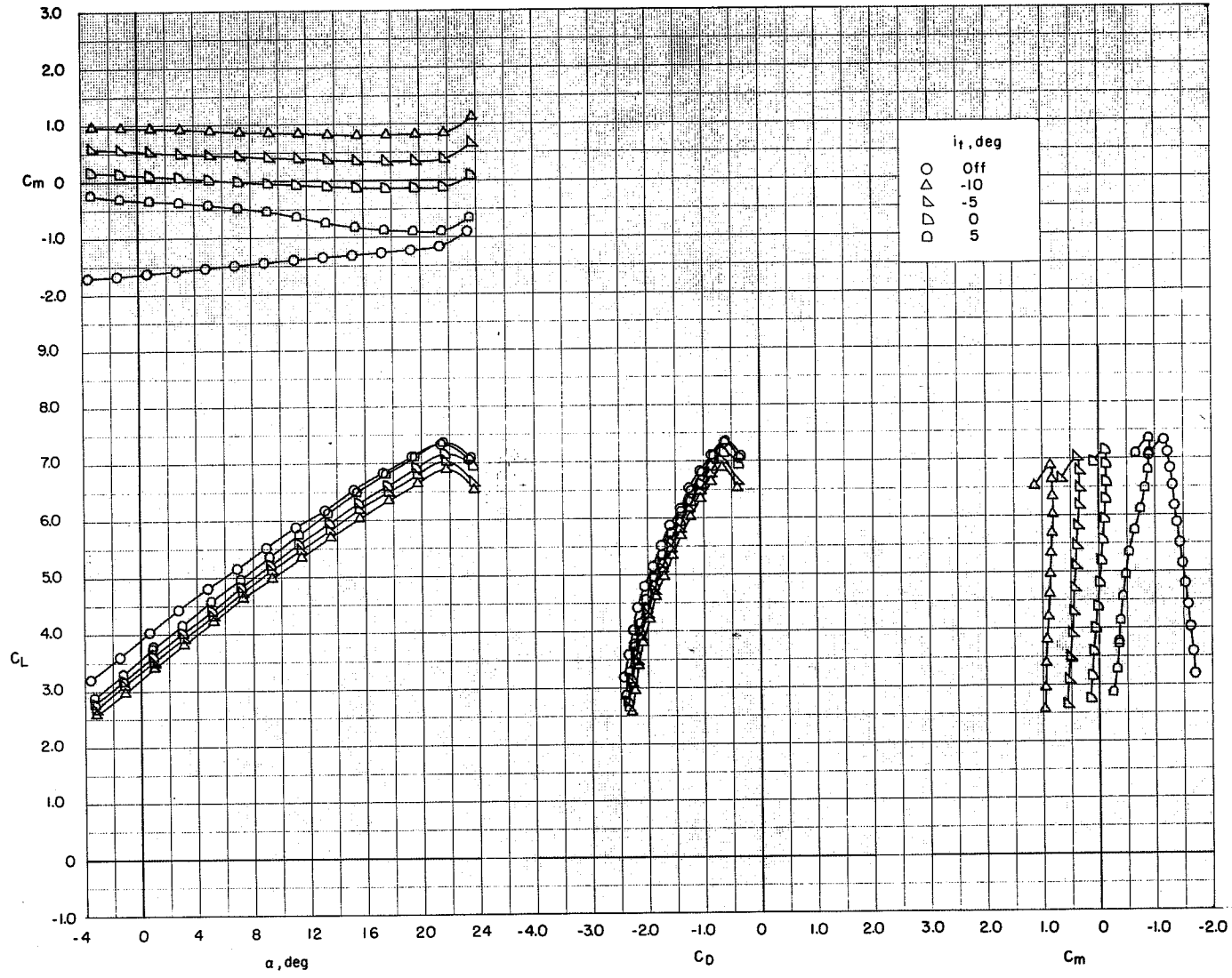

(c) $C_T = 3.74$.

Figure 53.- Concluded.

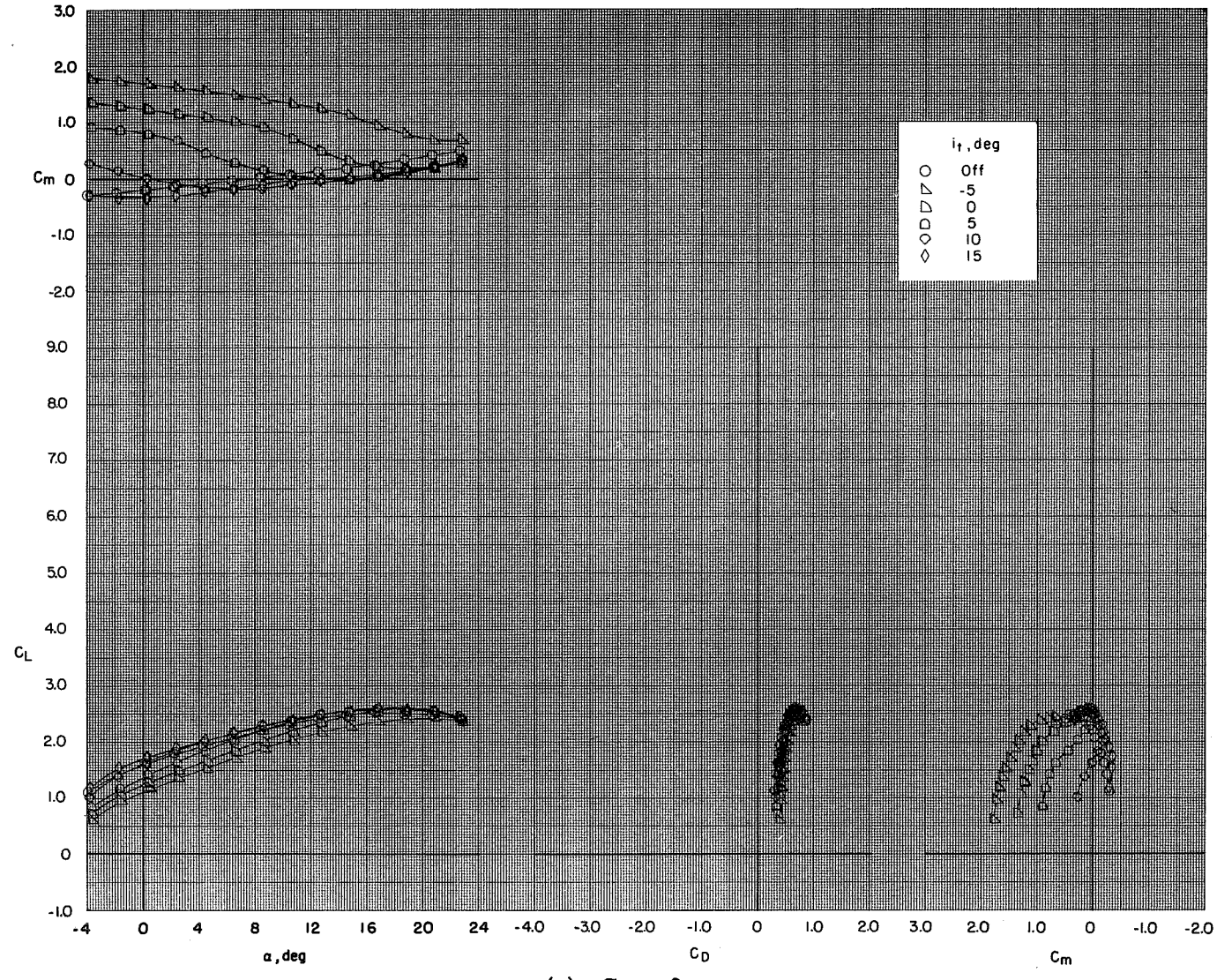

(a) $C_T = 0$.

Figure 53.- Effect of horizontal-tail incidence angle on the longitudinal aerodynamic characteristics of the model with flaps deflected and leading-edge slat on. BPR 6.2; T-tail; $\delta_f = 0^o/65^o/65^o$; c_S = 25 percent; $\delta_S = 50^o$; elevators on.

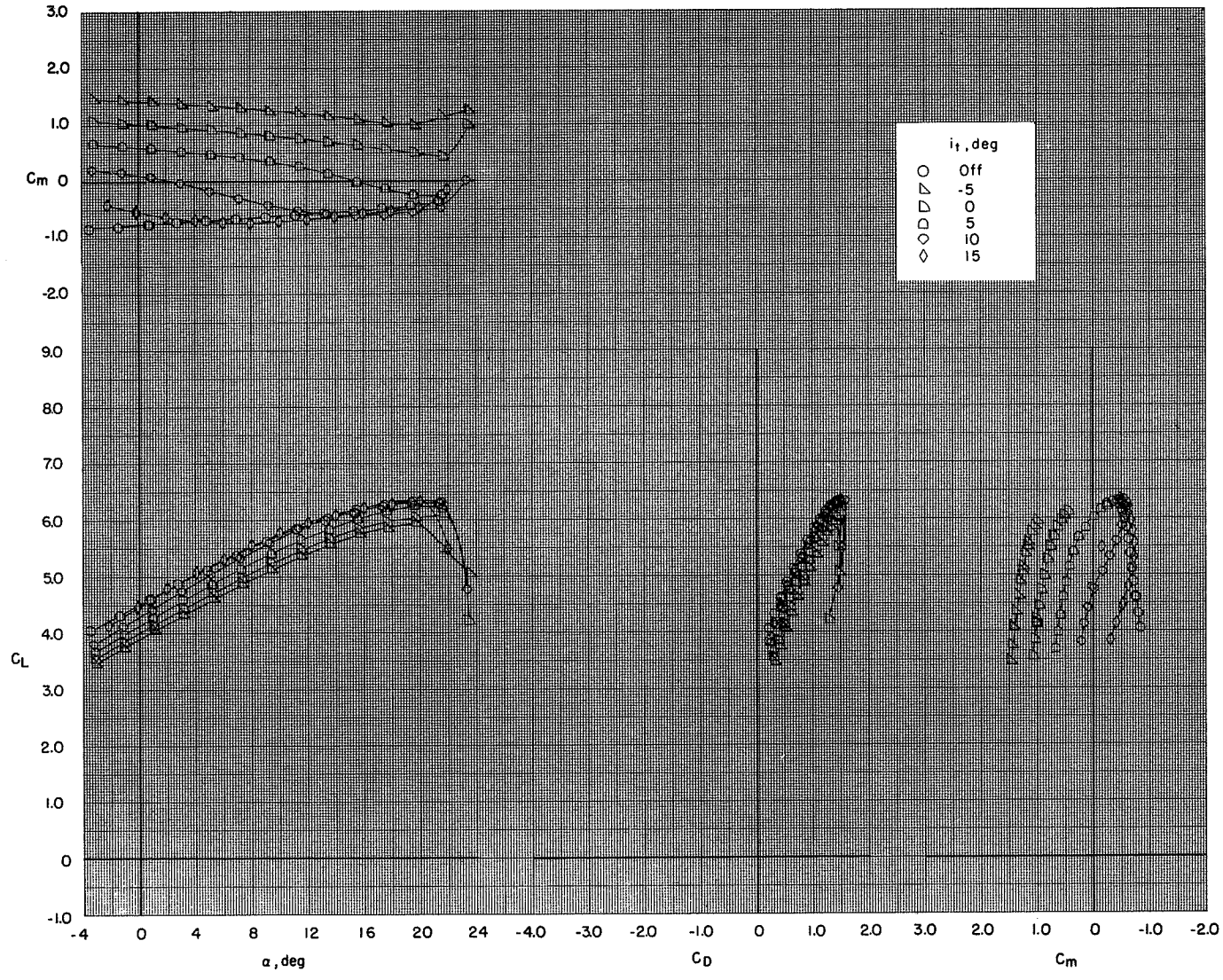

(b) $C_T = 1.88$.

Figure 53.- Continued.

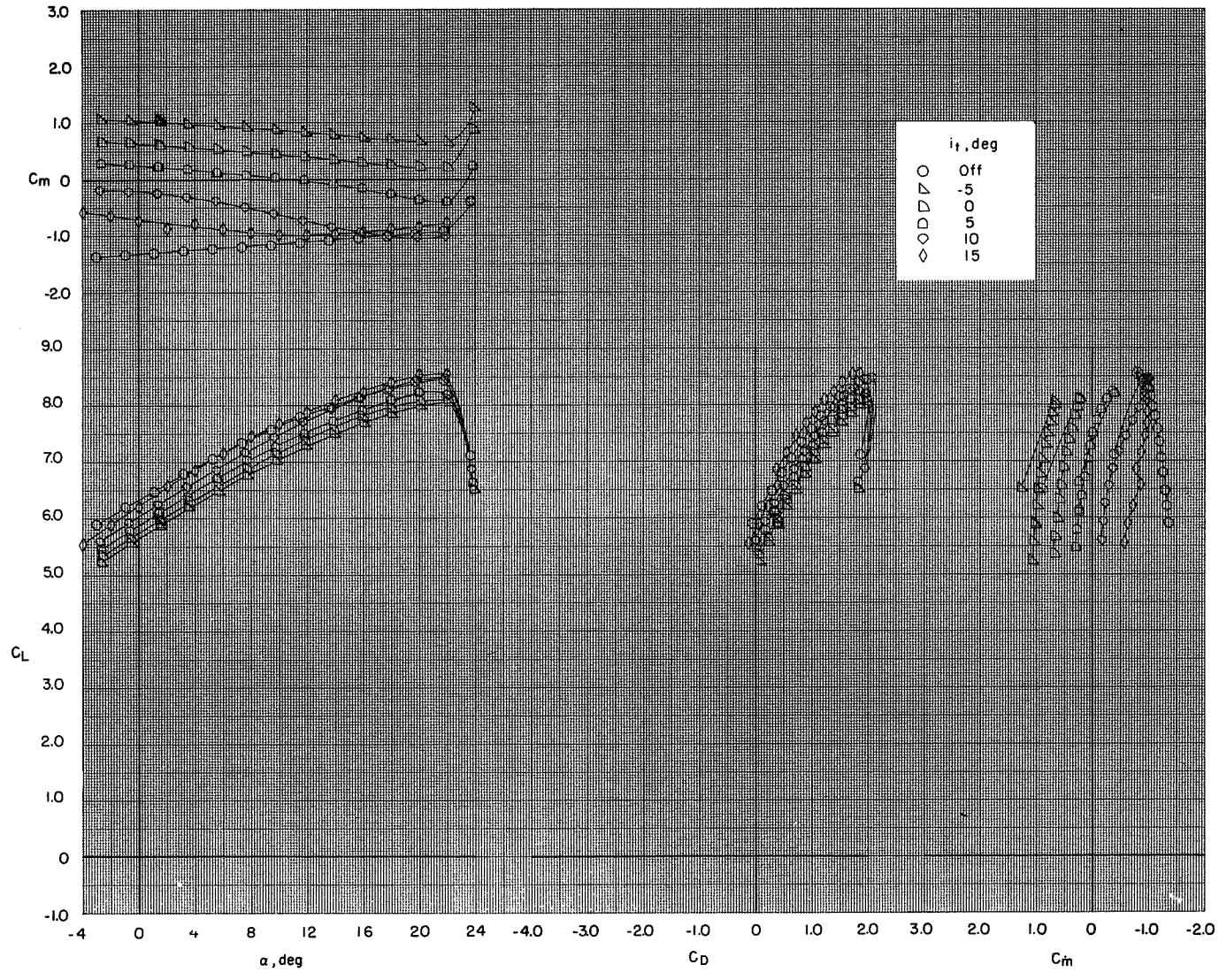

(c) $C_T = 3.74$.

Figure 53.- Concluded.

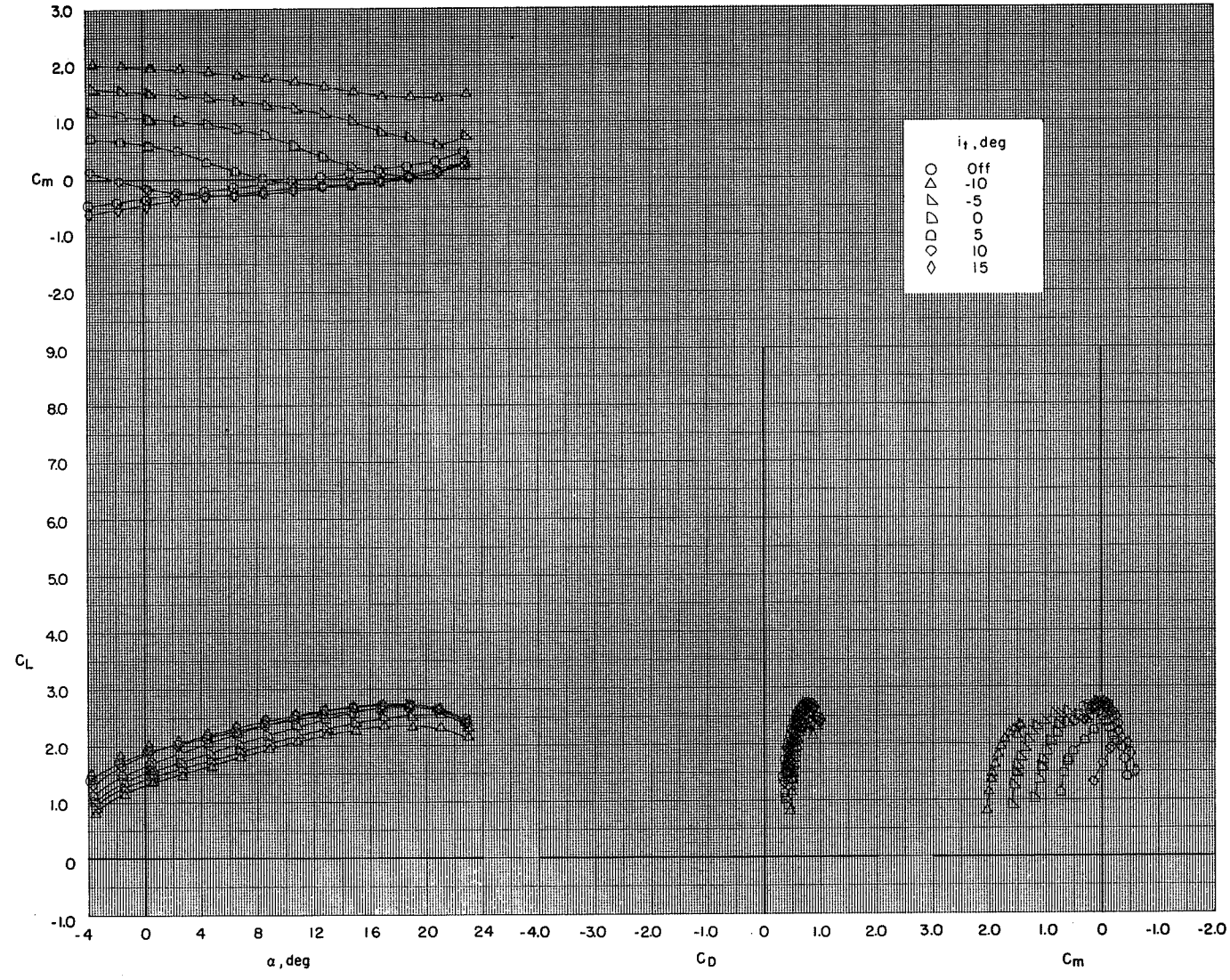

(a) $C_T = 0$.

Figure 54.- Effect of horizontal-tail incidence angle on the longitudinal aerodynamic characteristics of the model with flaps deflected and leading-edge slat on. BPR 6.2; T-tail; $\delta_f = 65^o/65^o/65^o$; $c_s = 25$ percent; $\delta_s = 50^o$; elevators on.

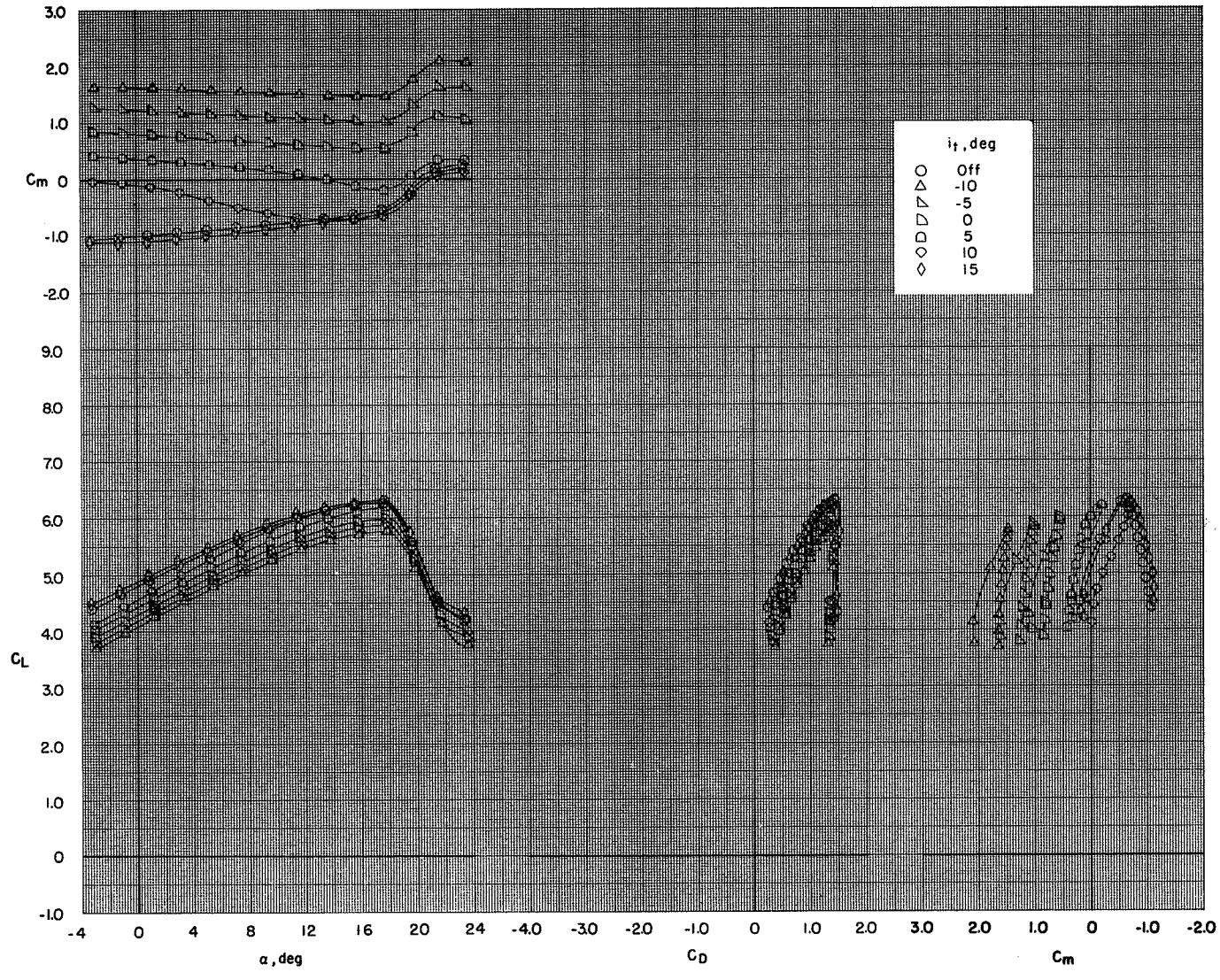

(b) $C_T = 1.88$.

Figure 54.- Continued.

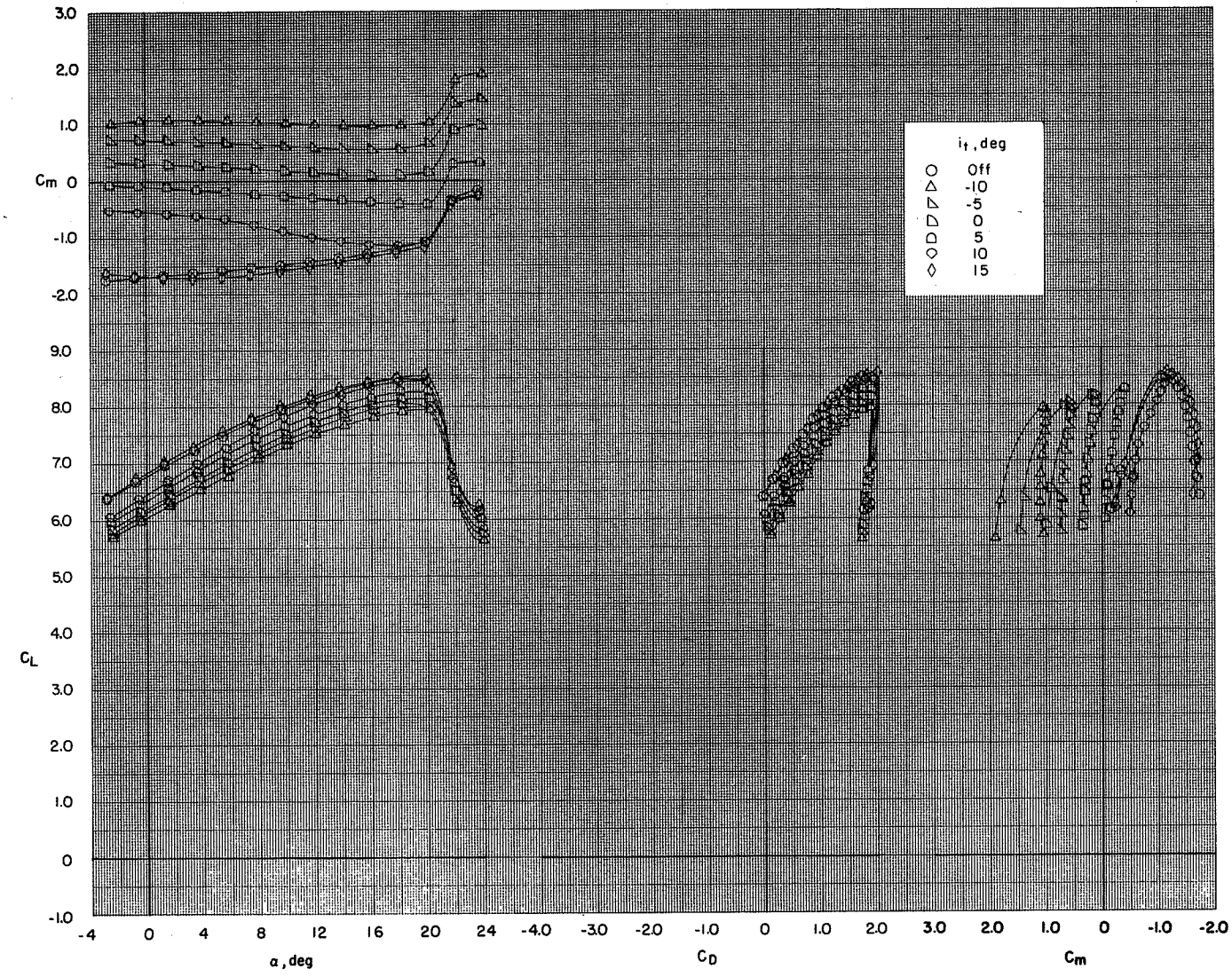

(c) $C_T = 3.74$.

Figure 54.- Concluded.

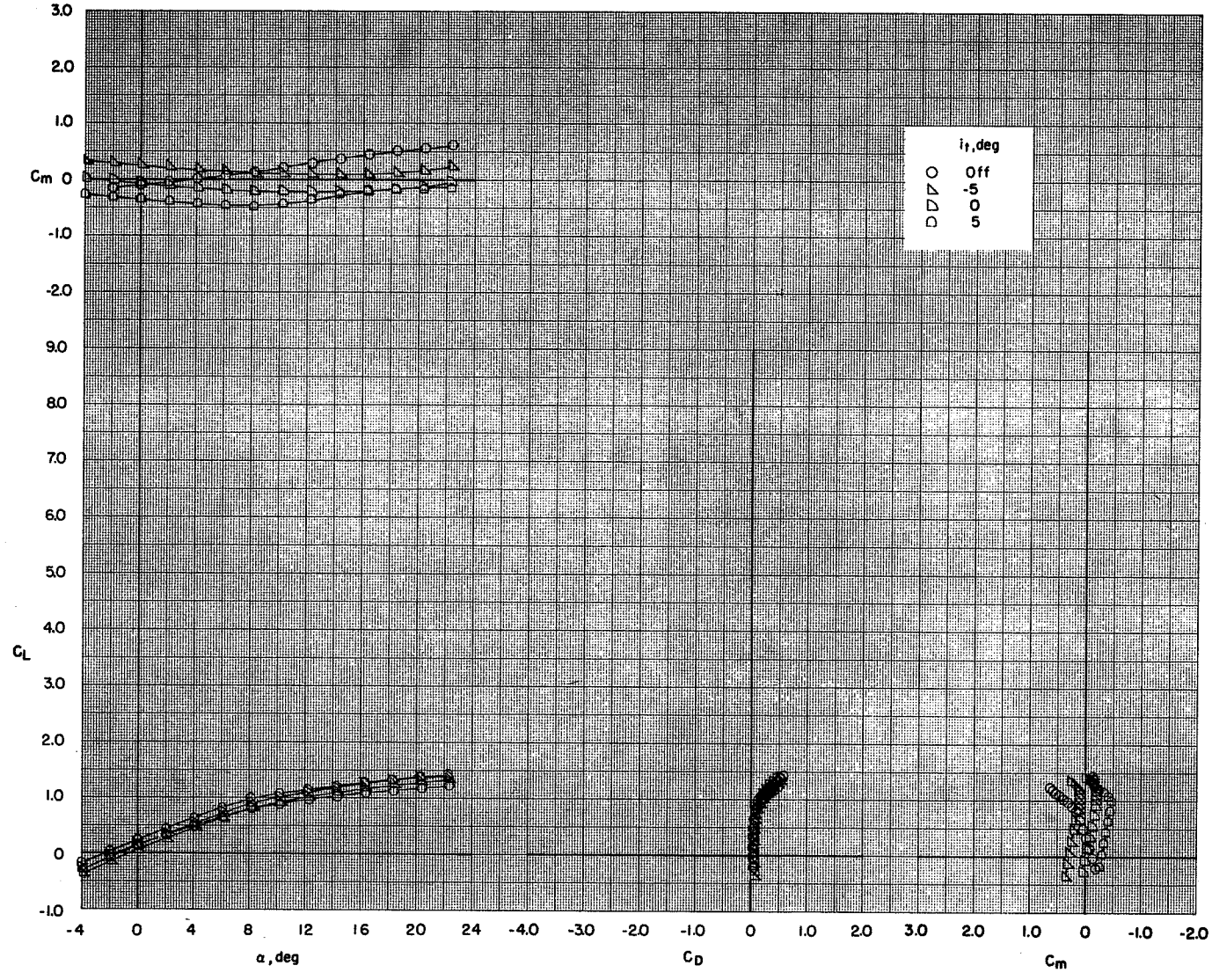

(a) $C_T = 0$.

Figure 55.- Effect of horizontal-tail incidence angle on the longitudinal aerodynamic characteristics of the model with flaps retracted and leading-edge slat off. BPR 10.0; T-tail; $\delta_f = 0^o/0^o/0^o$; elevators on.

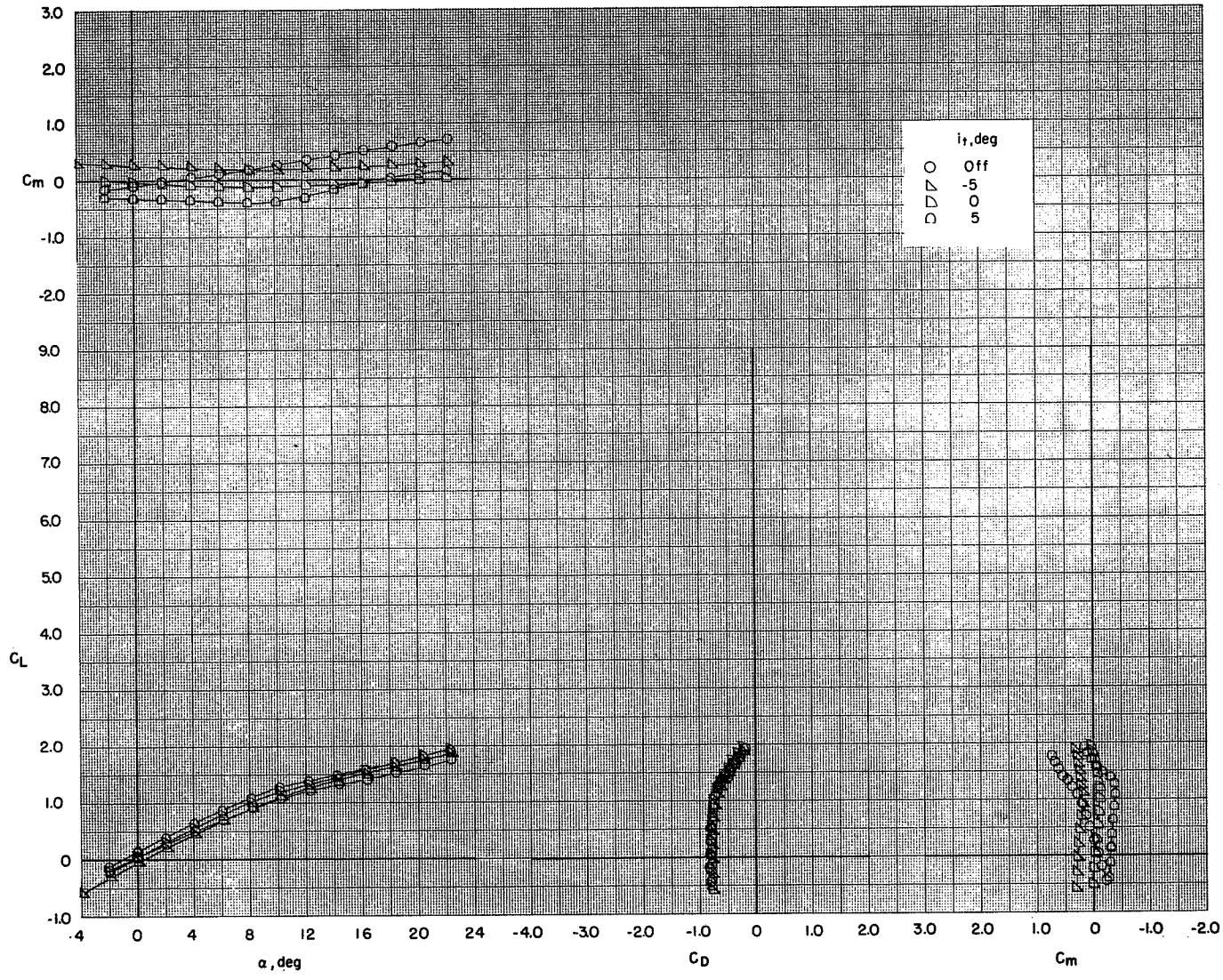

(b) $C_T = 1.01$.

Figure 55.- Continued.

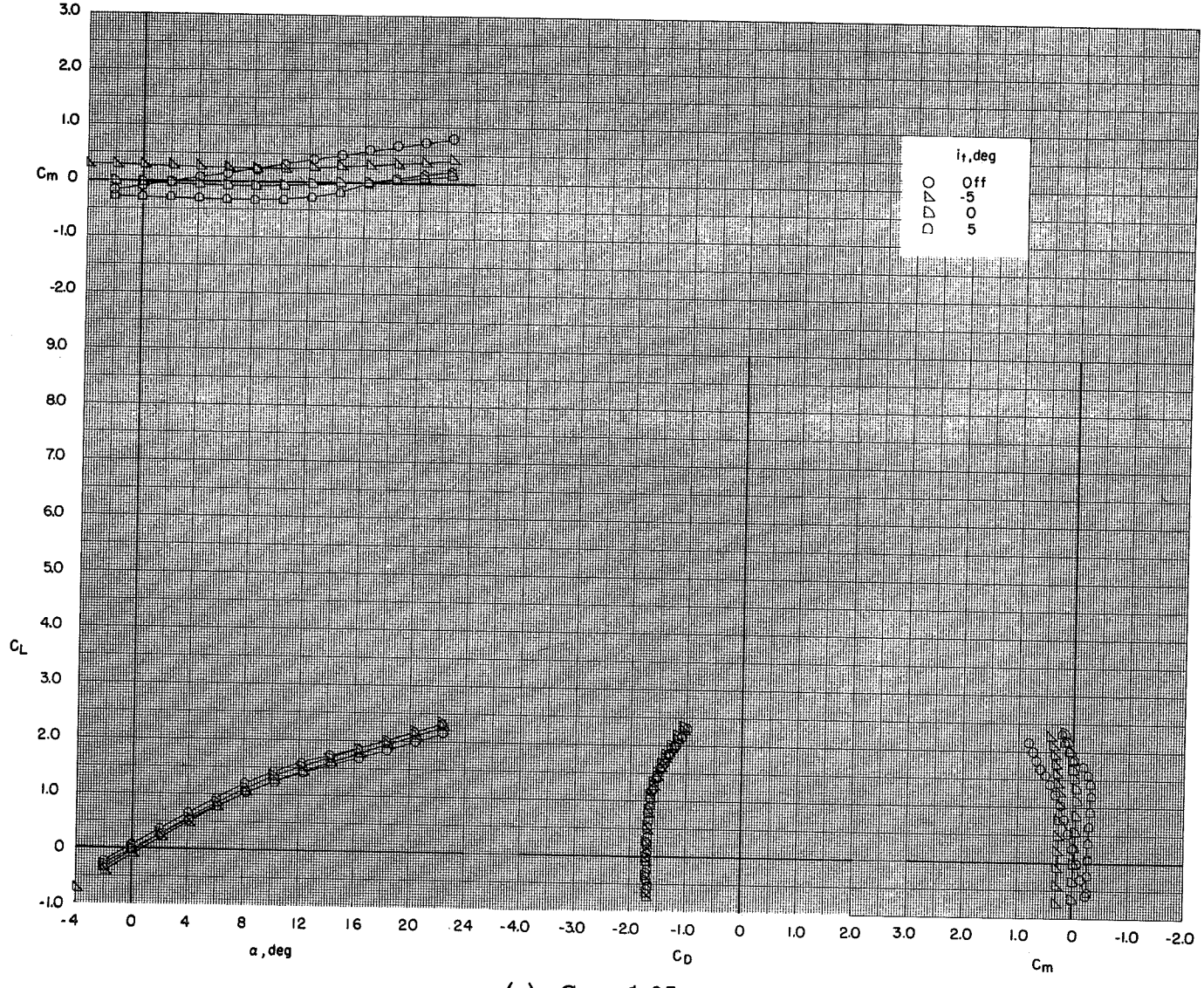

(c) $C_T = 1.95$.

Figure 55.- Concluded.

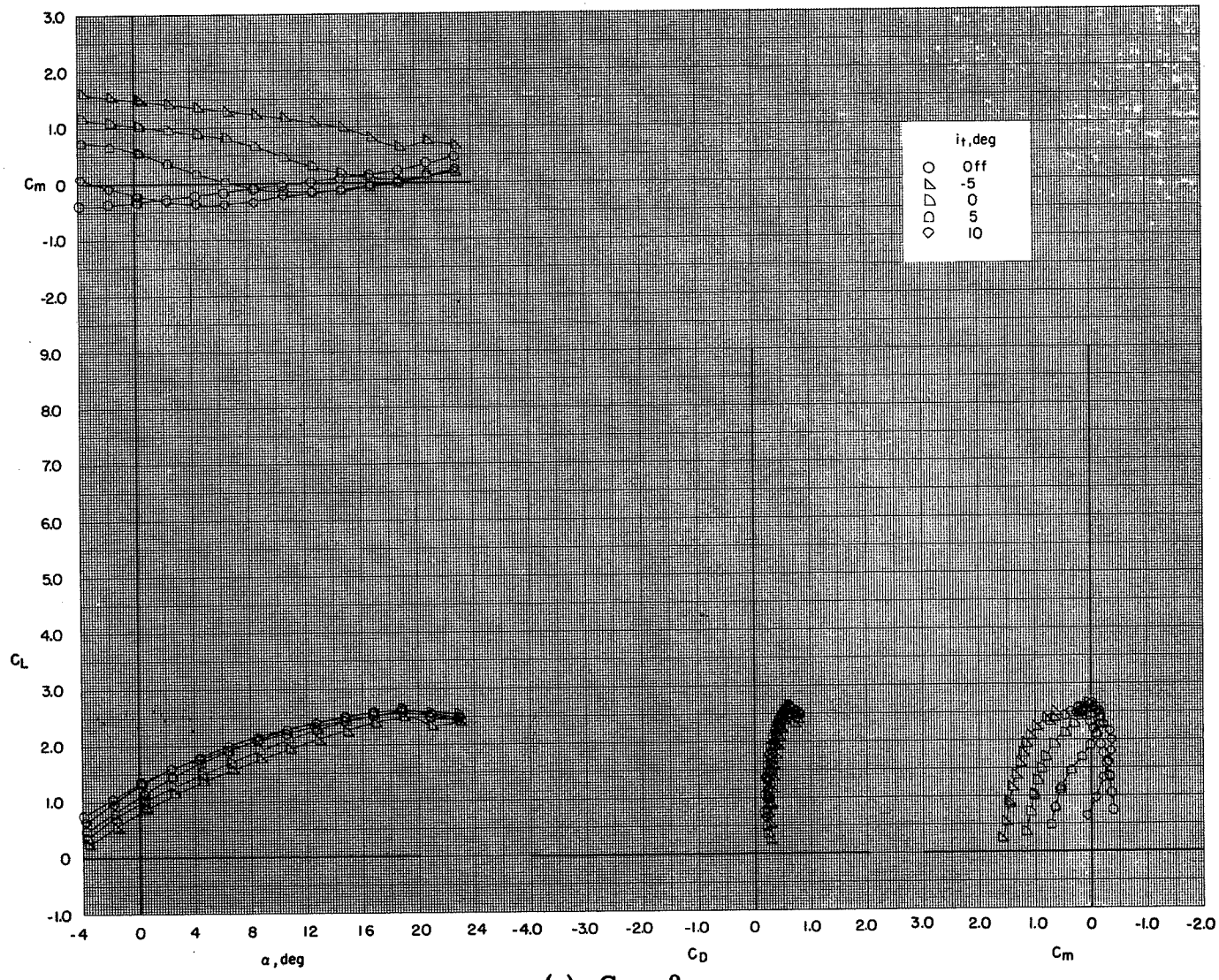

(a) $C_T = 0$.

Figure 56.- Effect of horizontal-tail incidence angle on the longitudinal aerodynamic characteristics of the model with flaps deflected and leading-edge slat on. BPR 10.0; T-tail; $\delta_f = 0^o/35^o/35^o$; $c_s = 20$ percent; $\delta_s = 50^o$; elevators on.

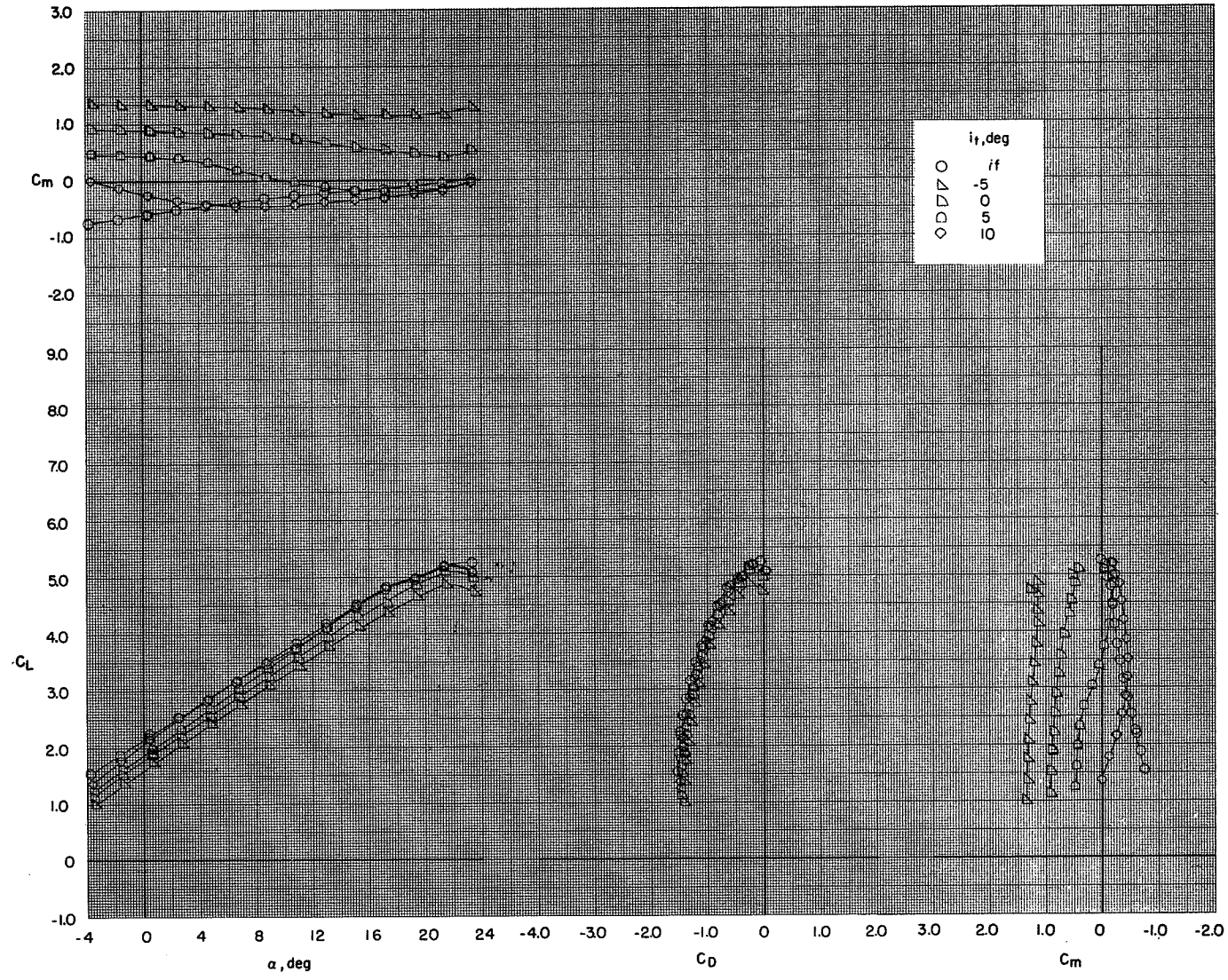

(b) $C_T = 2.26$.

Figure 56.- Continued.

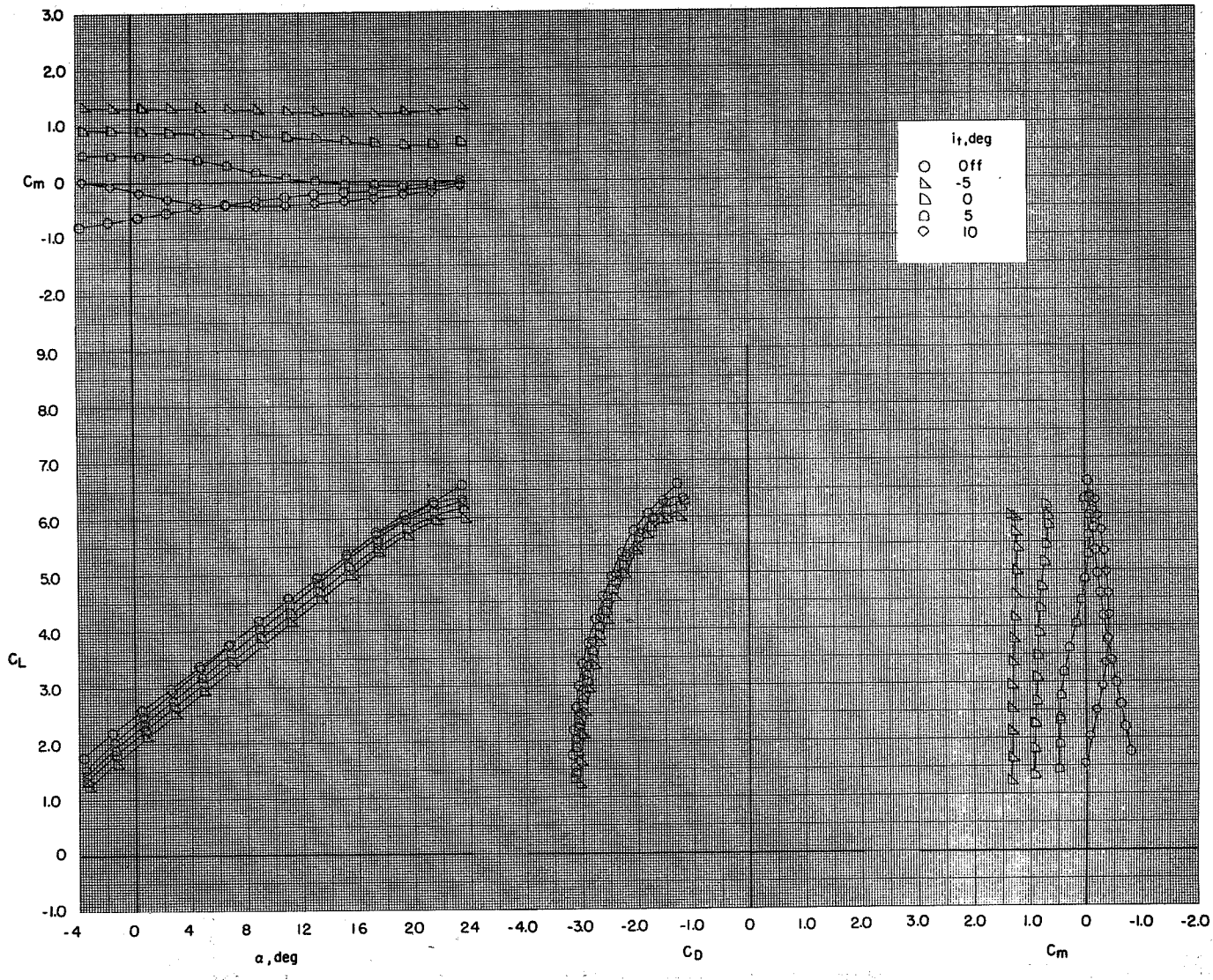

(c) $C_T = 4.06$.

Figure 56.- Concluded.

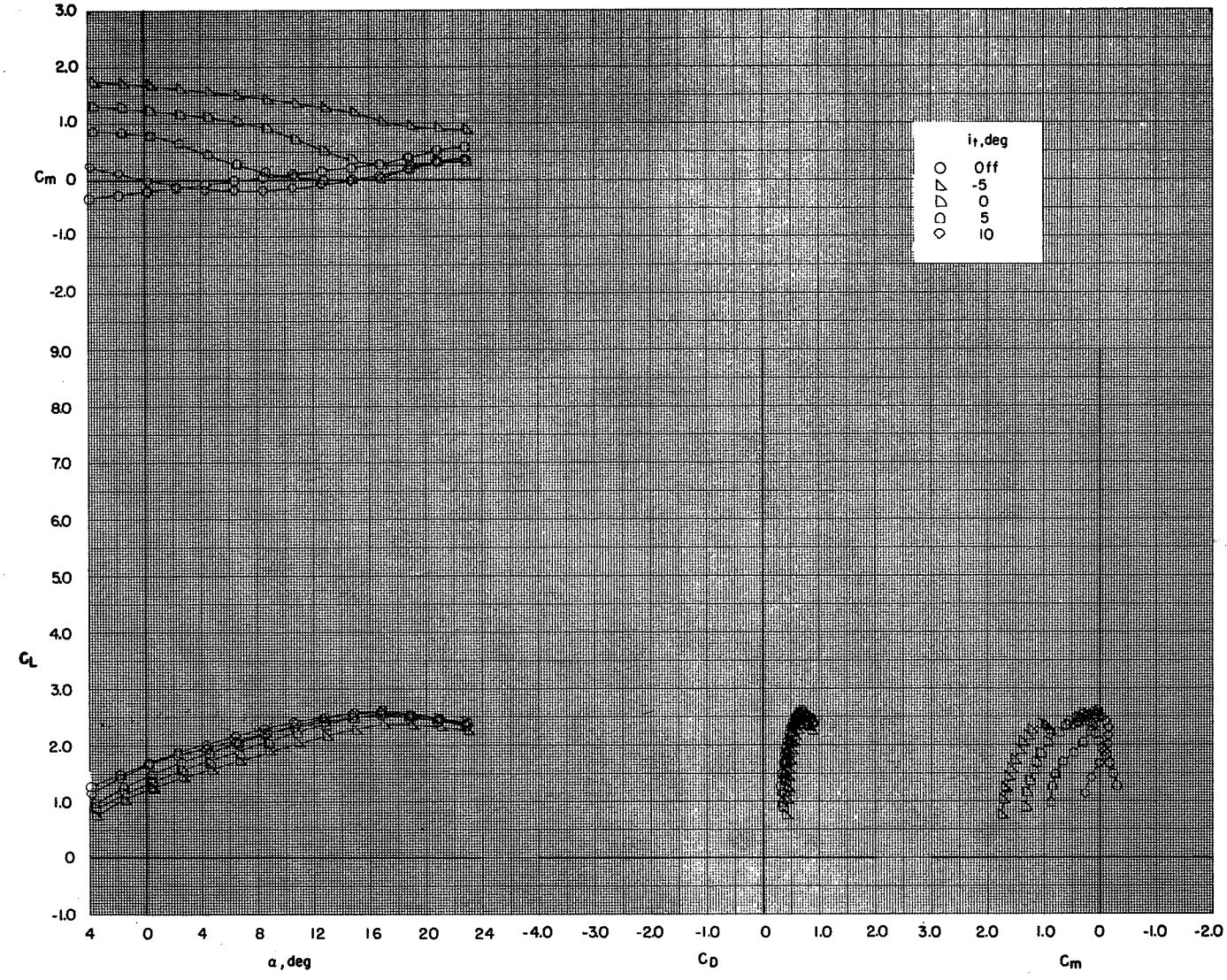

(a) $C_T = 0$.

Figure 57.- Effect of horizontal-tail incidence angle on the longitudinal aerodynamic characteristics of the model with flaps deflected and leading-edge slat on. BPR 10.0; T-tail; $\delta_f = 0^o/65^o/65^o$; $c_s = 20$ percent; $\delta_s = 50^o$; elevators on.

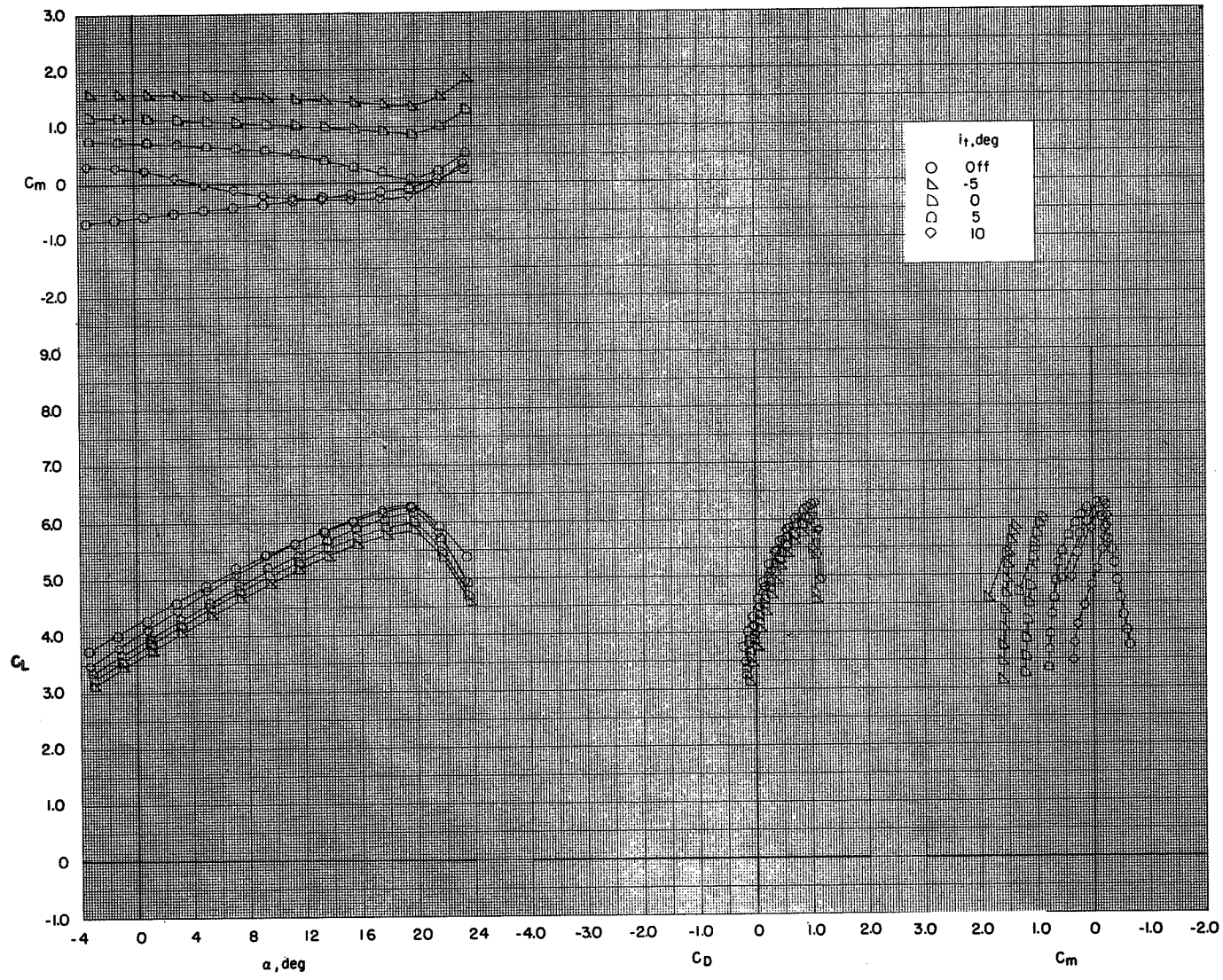

(b) $C_T = 2.26$.

Figure 57.- Continued.

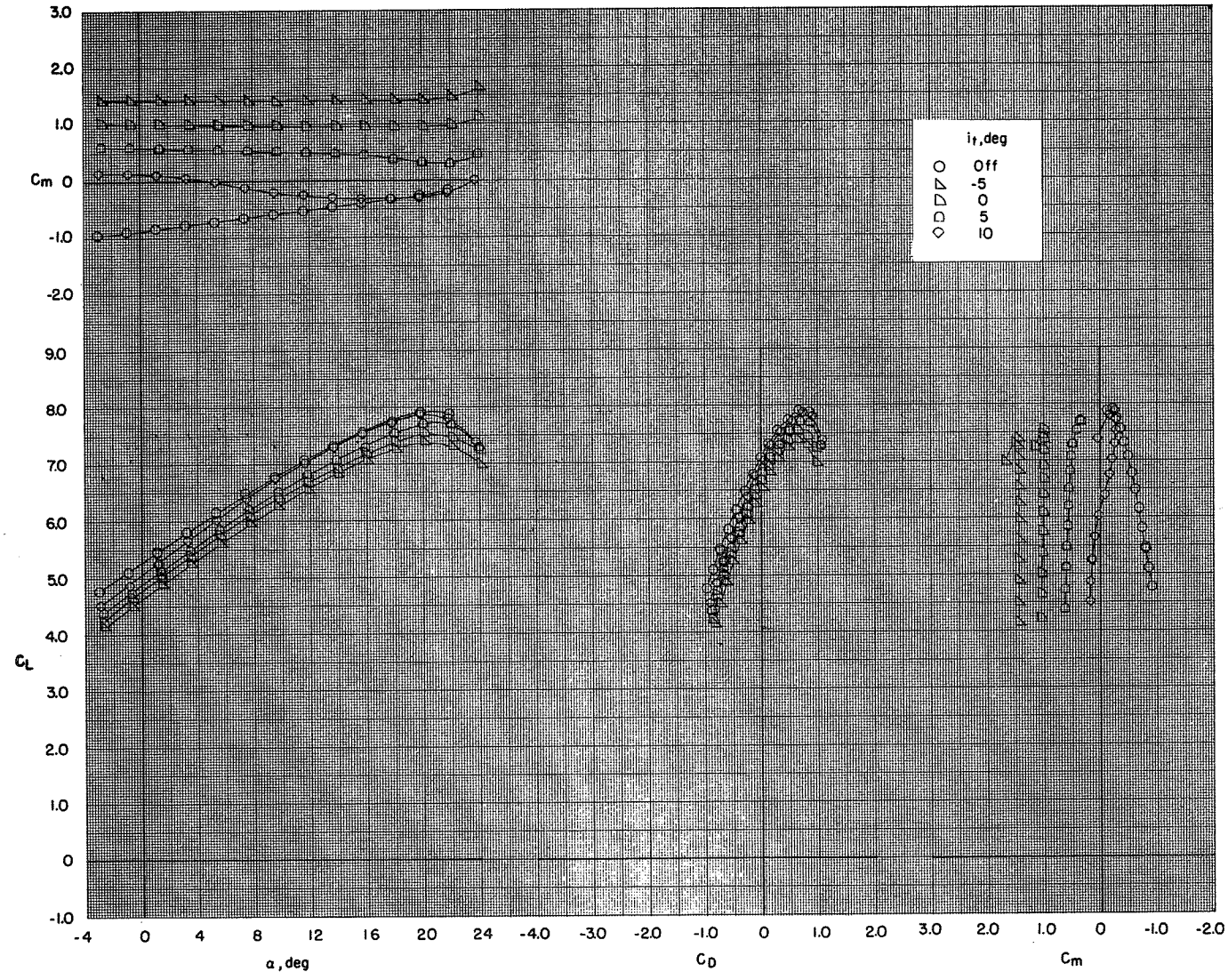

(c) $C_T = 4.06$.

Figure 57.- Concluded.

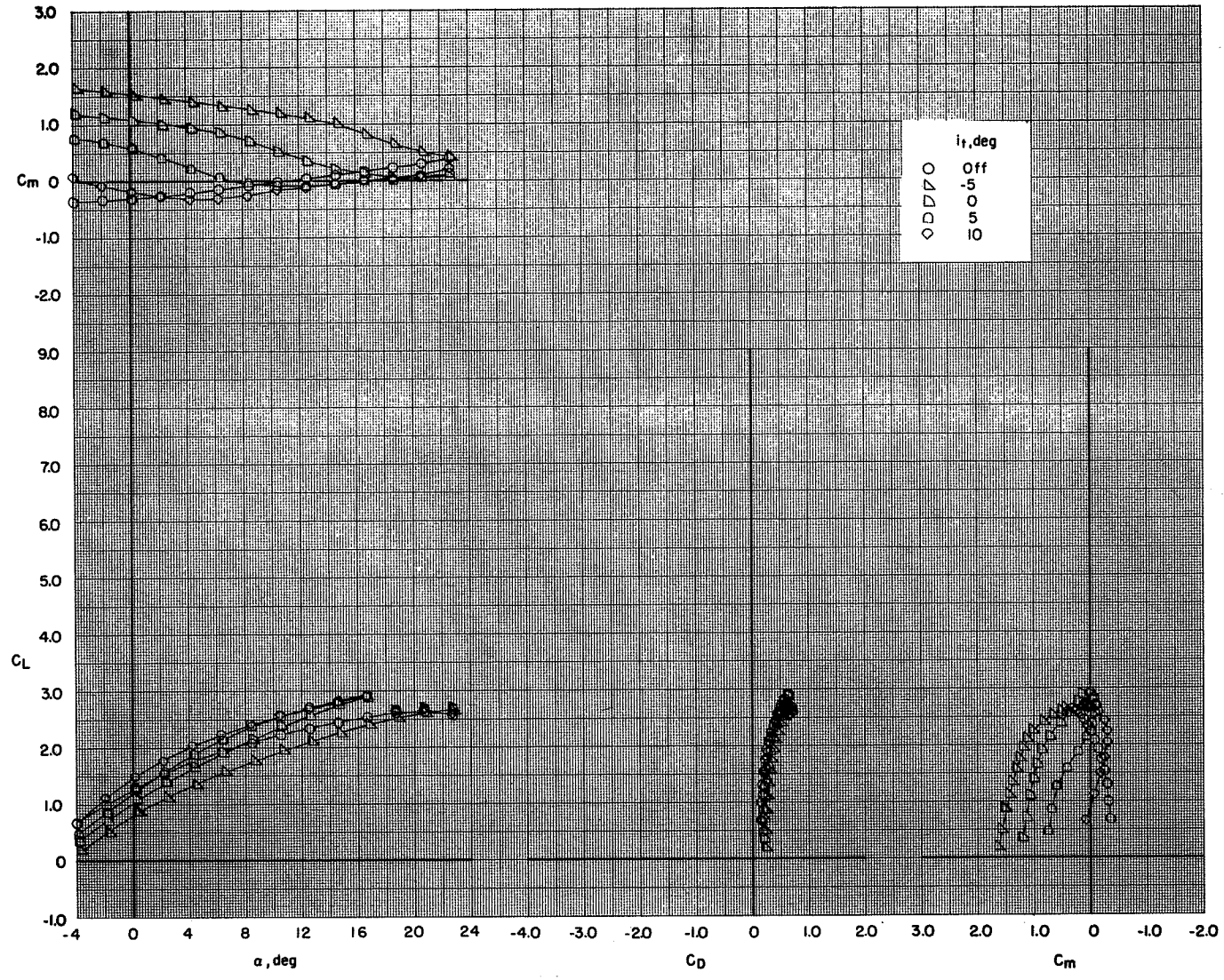

(a) $C_T = 0$.

Figure 58.- Effect of horizontal-tail incidence angle on the longitudinal aerodynamic characteristics of the model with flaps deflected and leading-edge slat on. BPR 10.0; T-tail; $\delta_f = 0^o/35^o/35^o$; c_s = 25 percent; $\delta_s = 50^o$; elevators on.

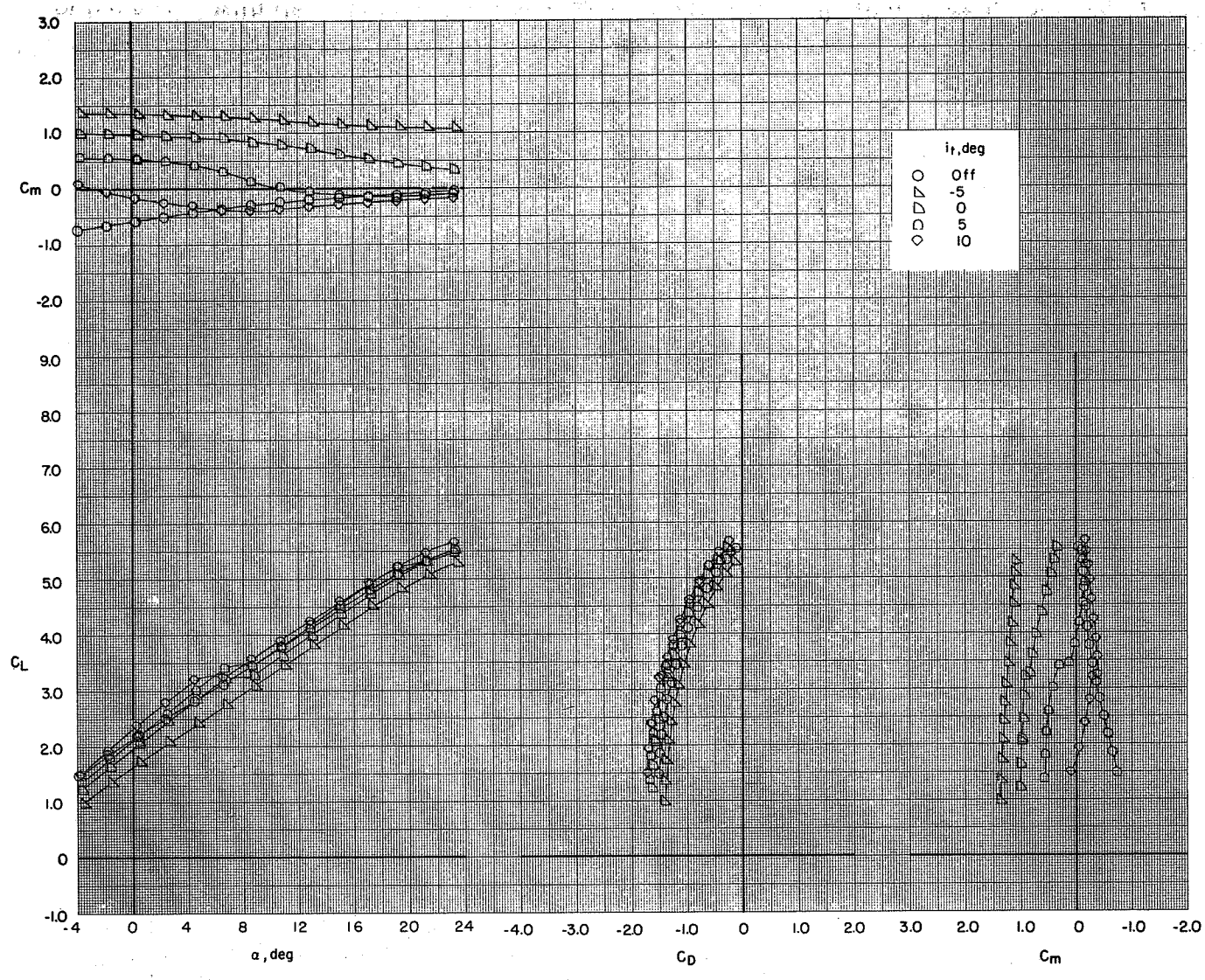

(b) $C_T = 2.26$.

Figure 58.- Continued.

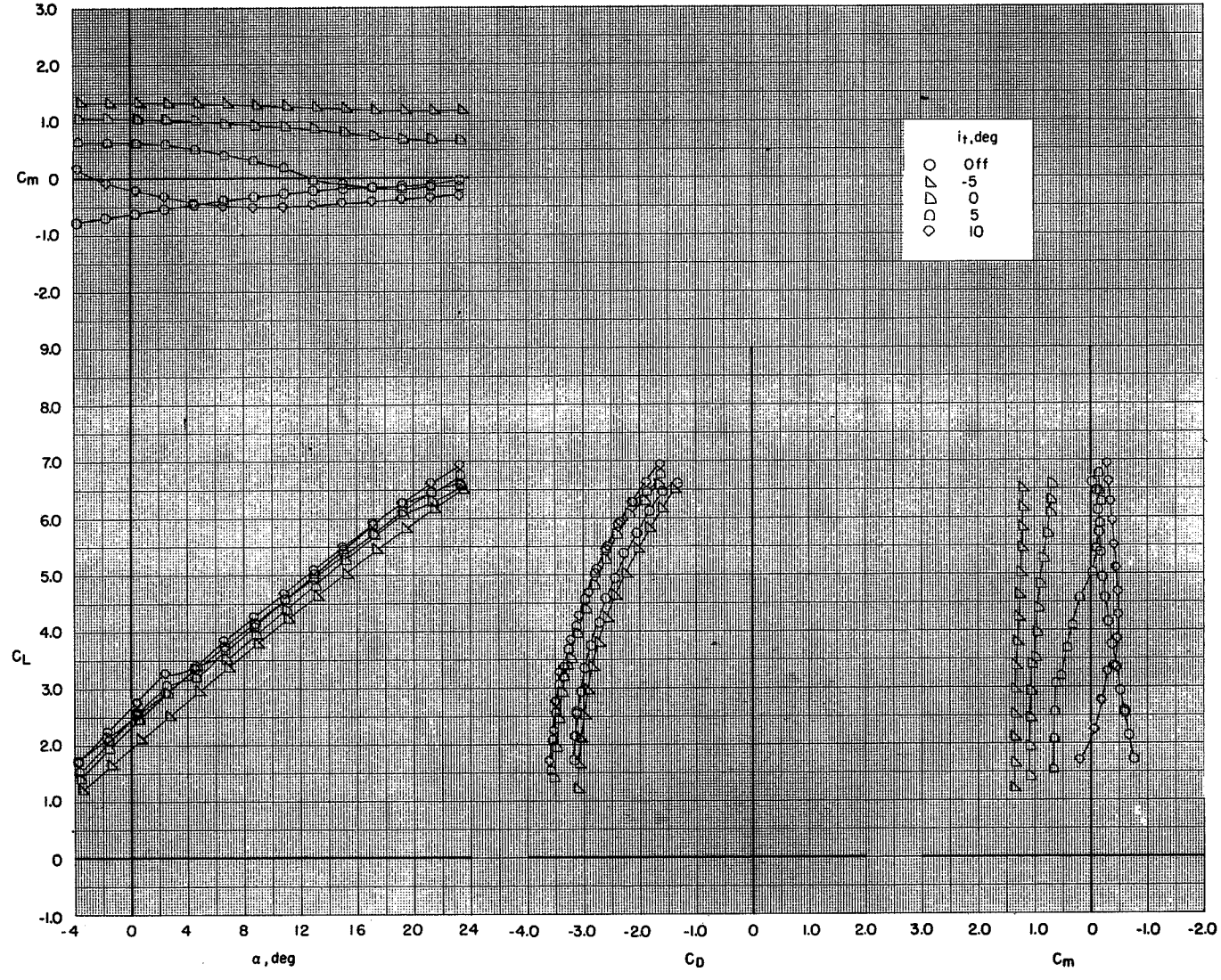

(c) $C_T = 4.06$.

Figure 58.- Concluded.

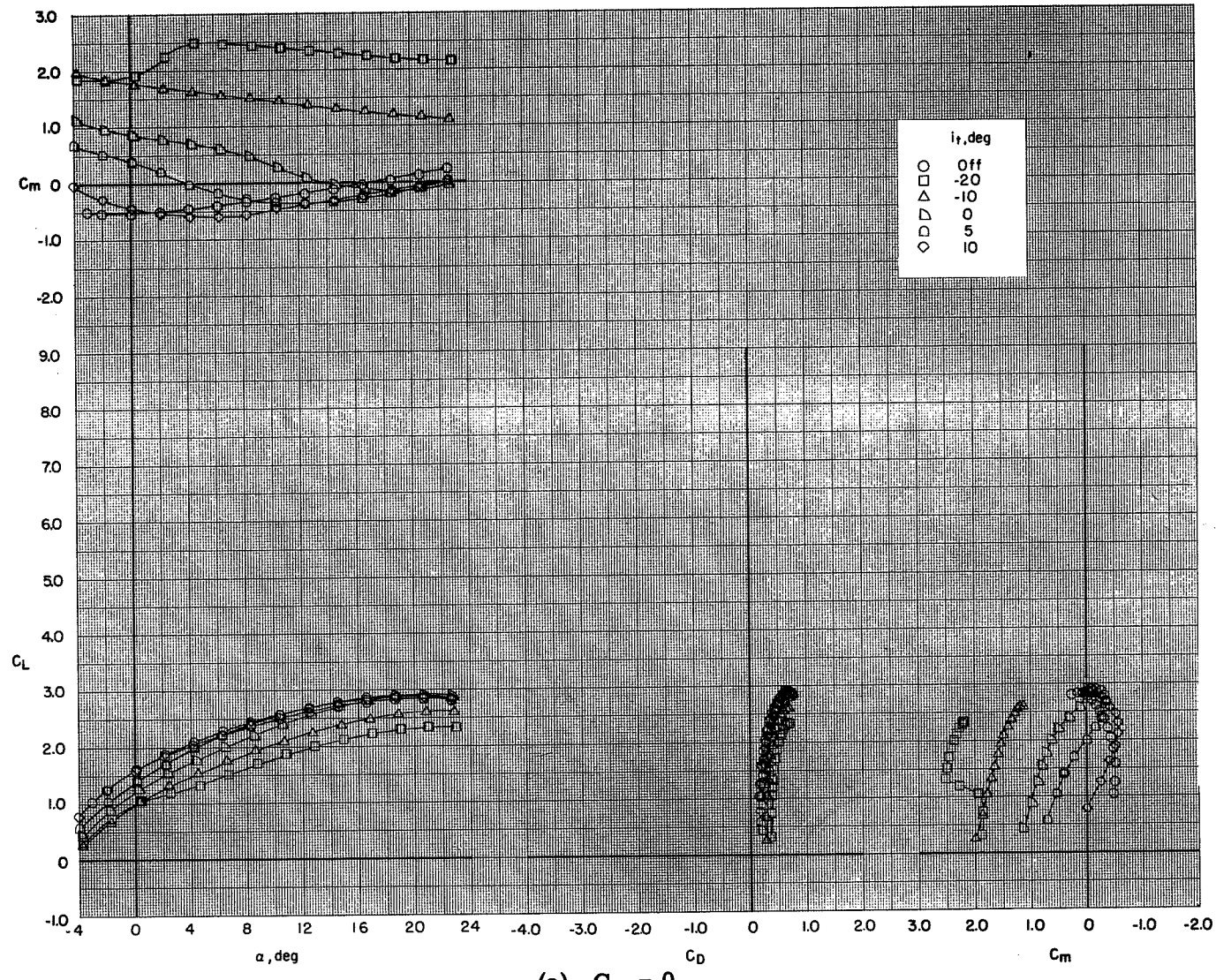

(a) $C_T = 0$.

Figure 59.- Effect of horizontal-tail incidence angle on the longitudinal aerodynamic characteristics of the model with flaps deflected and leading-edge slat on. BPR 10.0; T-tail; $\delta_f = 35^o/35^o/35^o$; $c_s = 25$ percent; $\delta_s = 50^o$; elevators on.

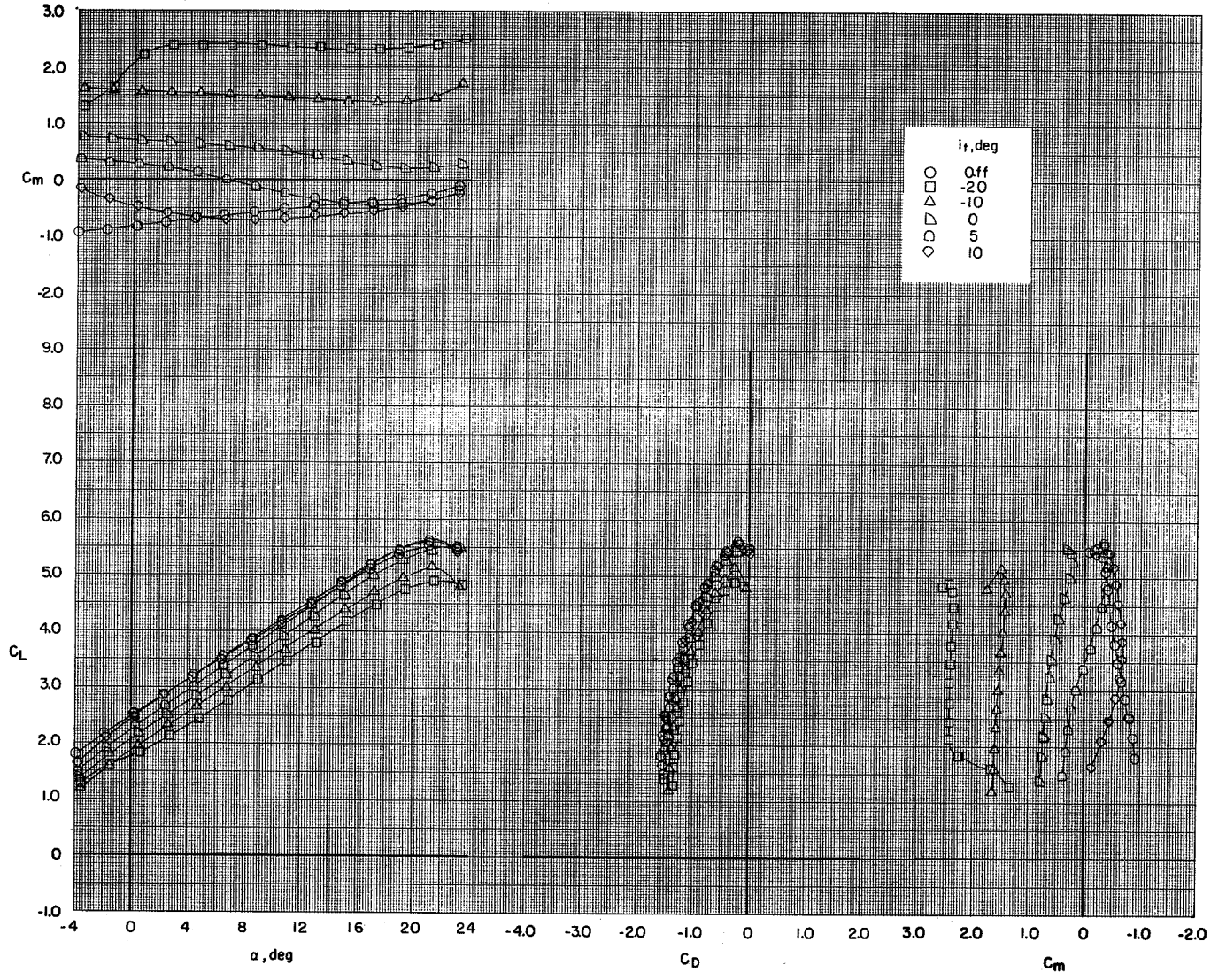

(b) $C_T = 2.26$.

Figure 59.- Continued.

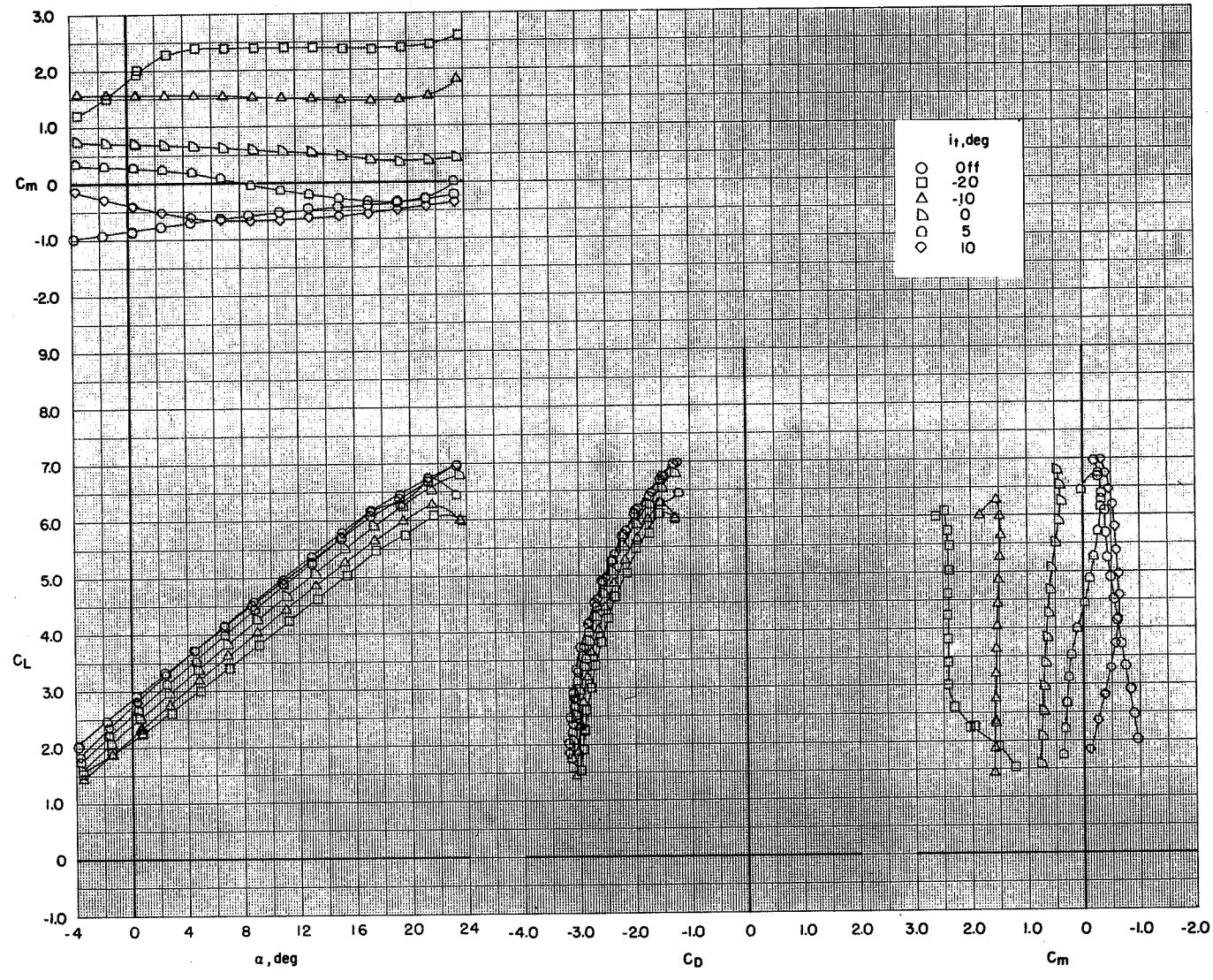

(c) $C_T = 4.06$.

Figure 59.- Concluded.

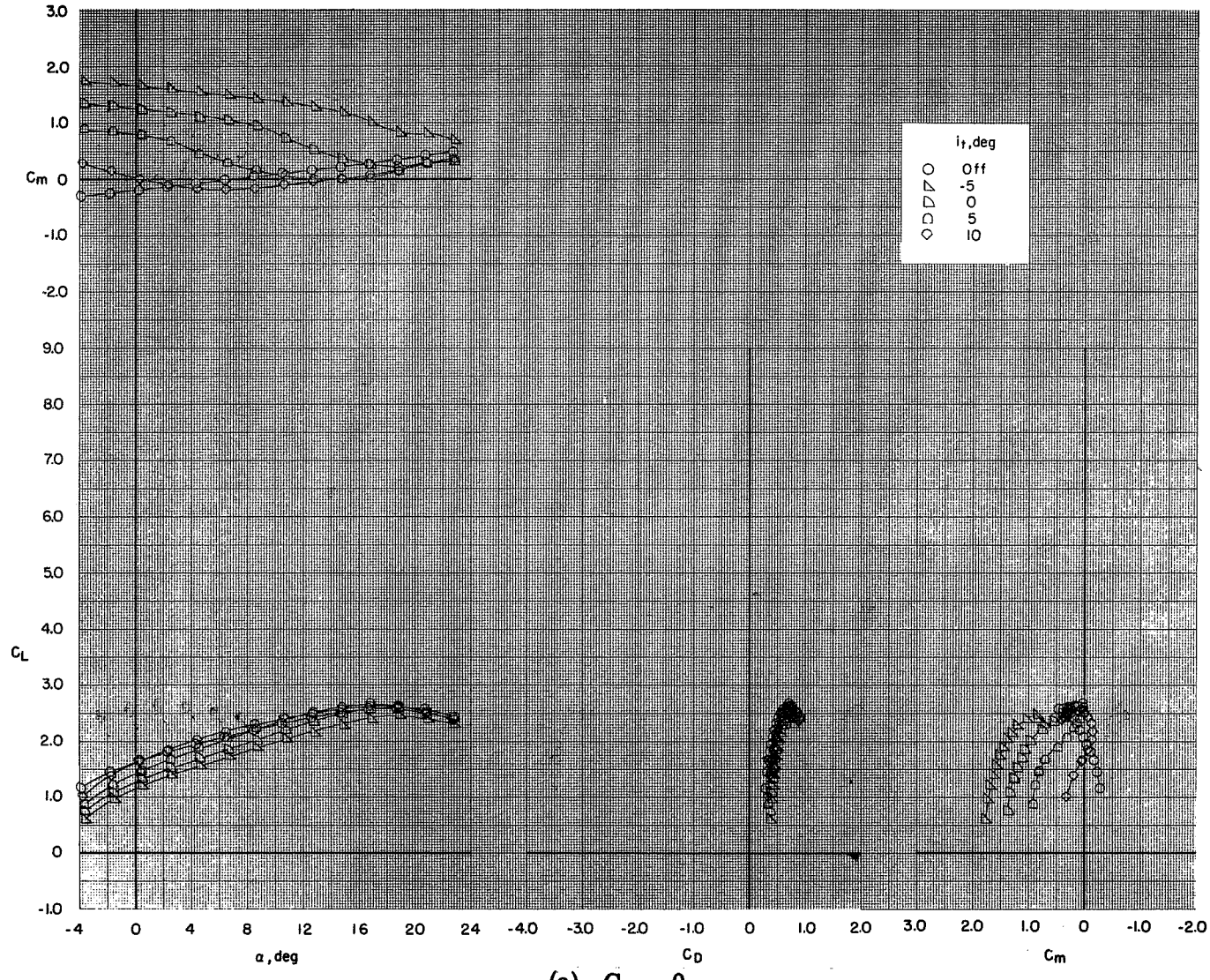

(a) $C_T = 0$.

Figure 60.- Effect of horizontal-tail incidence angle on the longitudinal aerodynamic characteristics of the model with flaps deflected and leading-edge slat on. BPR 10.0; T-tail; $\delta_f = 0^o/65^o/65^o$; $c_s = 25$ percent; $\delta_s = 50^o$; elevators on.

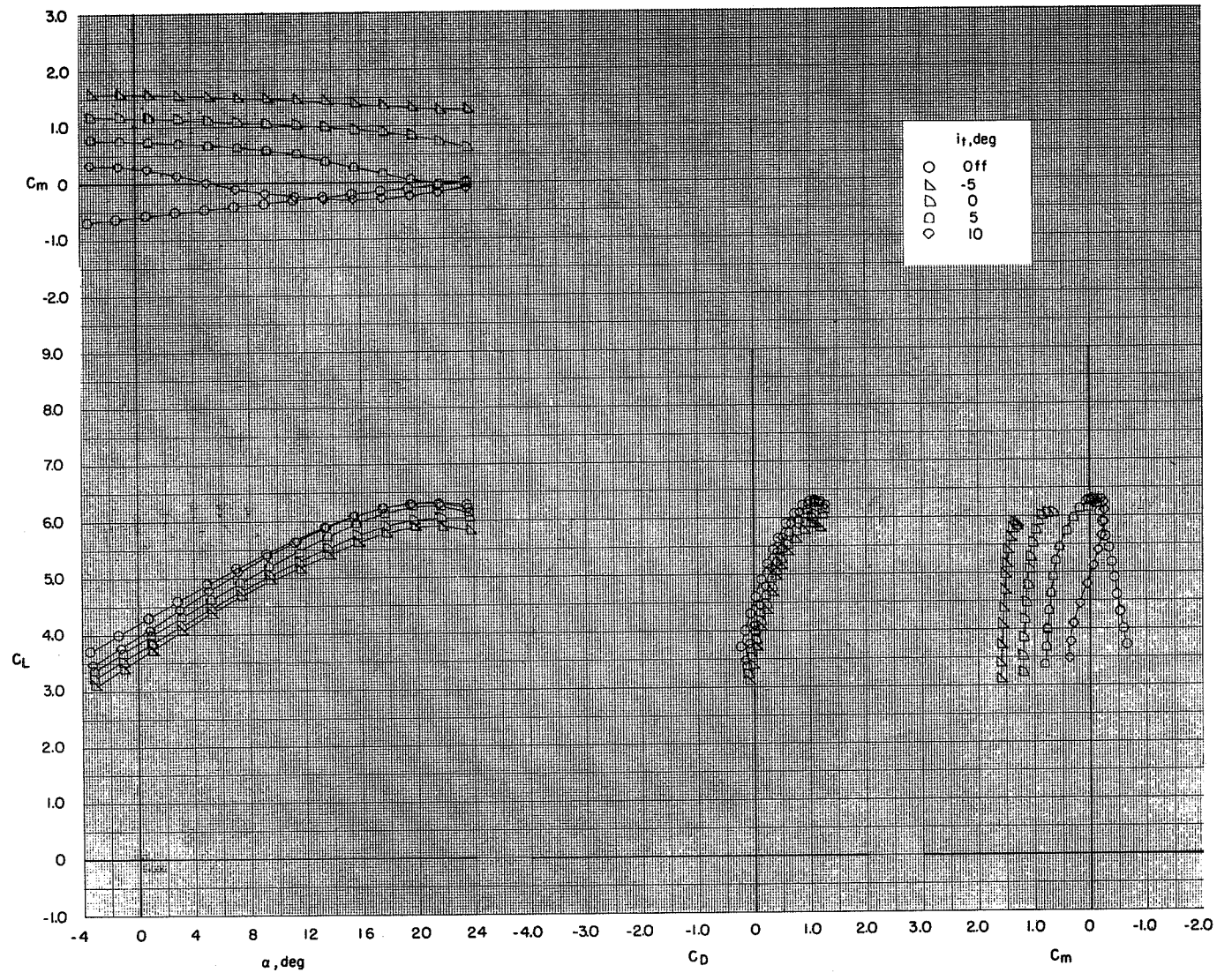

(b) $C_T = 2.26$.

Figure 60.- Continued.

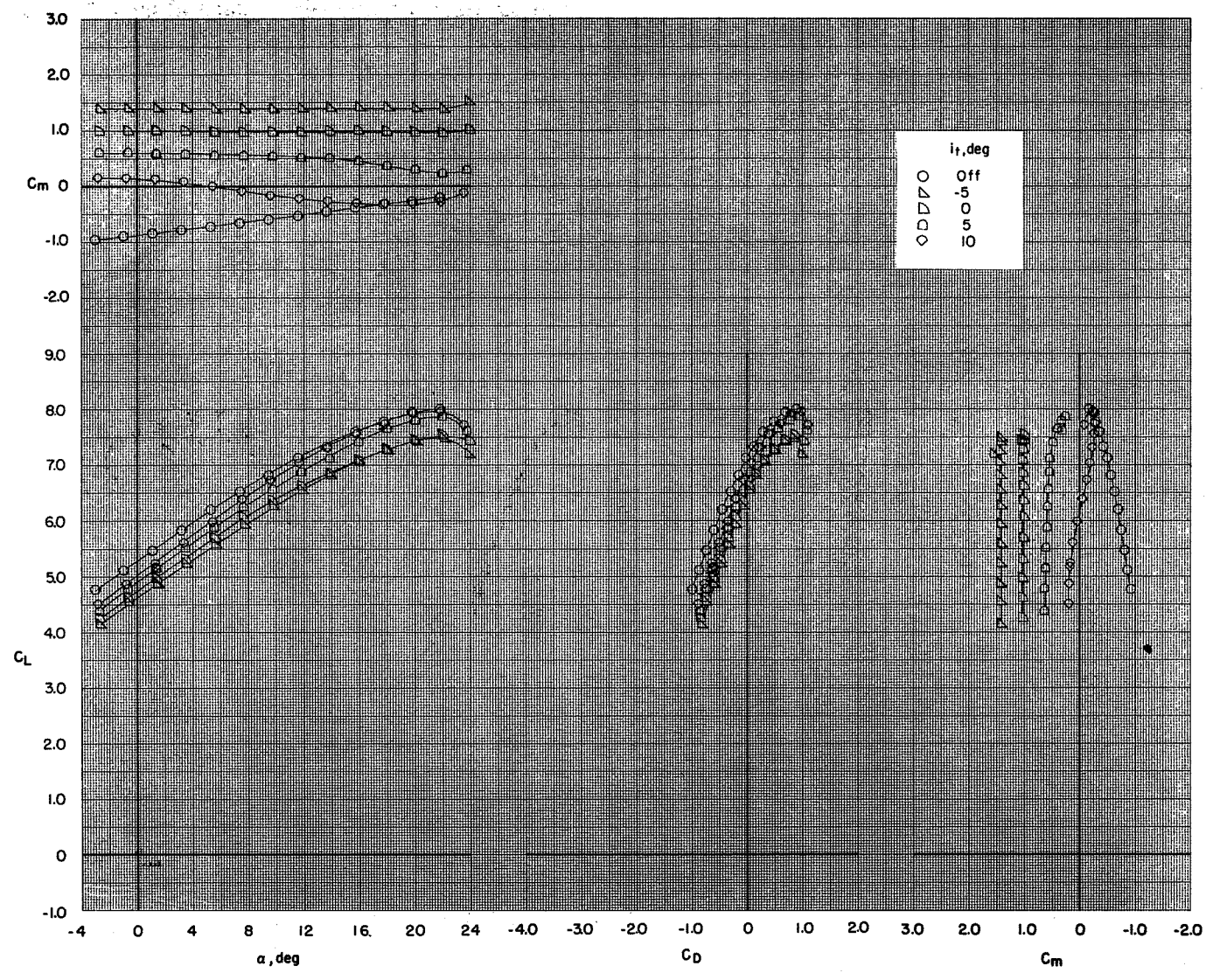

(c) $C_T = 4.06$.

Figure 60.- Concluded.

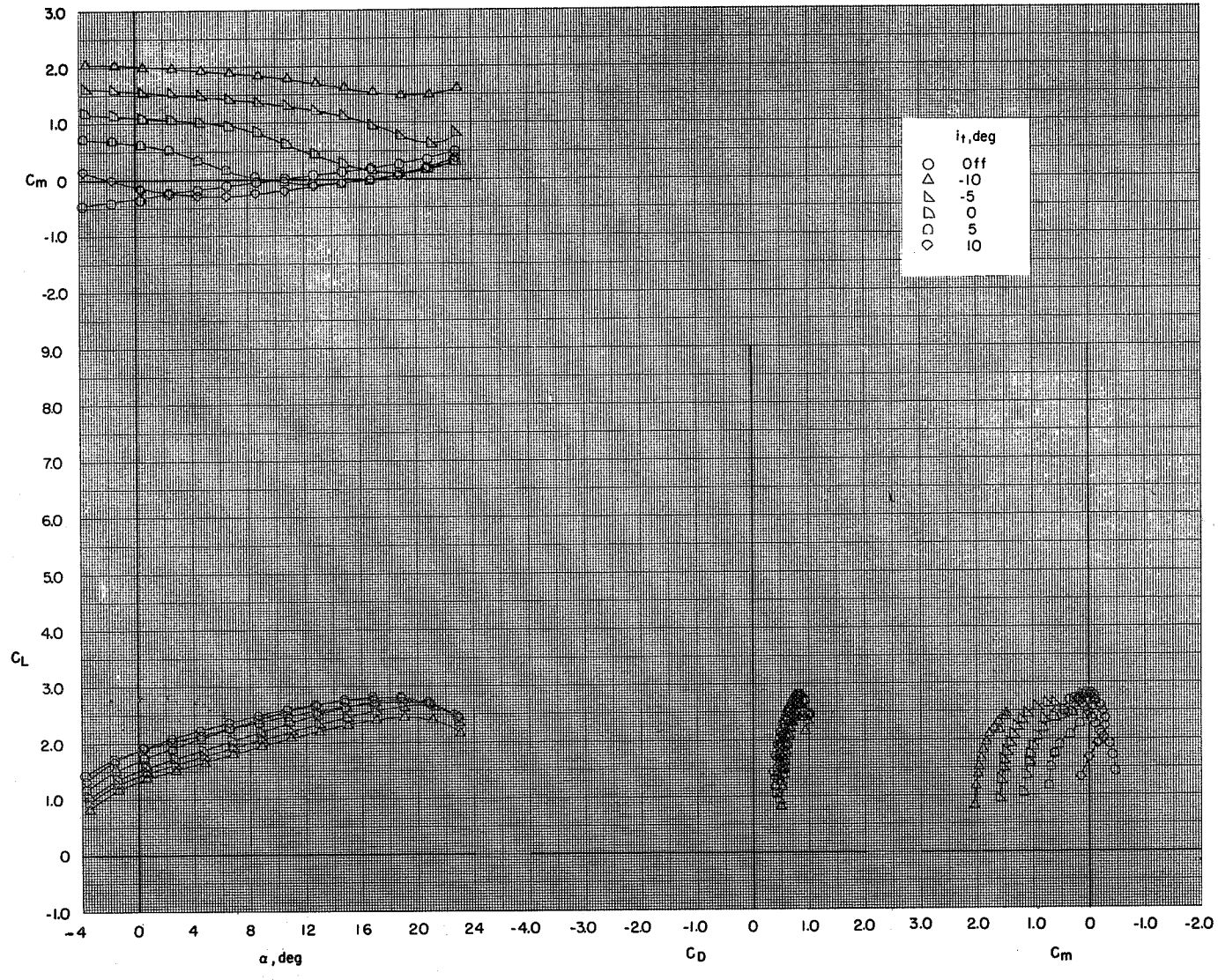

(a) $C_T = 0$.

Figure 61.- Effect of horizontal-tail incidence angle on the longitudinal aerodynamic characteristics of the model with flaps deflected and leading-edge slat on. BPR 10.0; T-tail; $\delta_f = 65^o/65^o/65^o$; c_s = 25 percent; $\delta_s = 50^o$; elevators on.

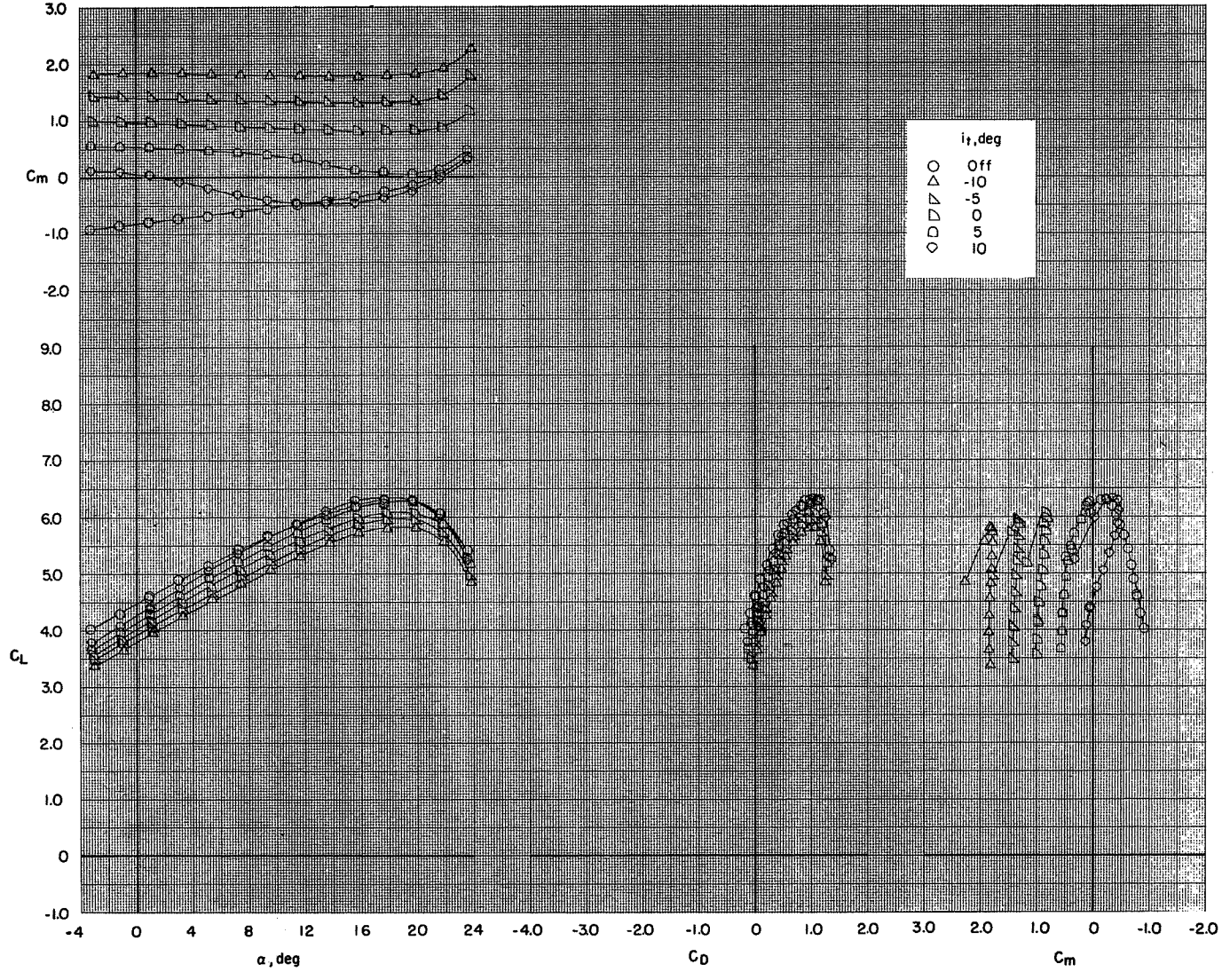

(b) $C_T = 2.26$.

Figure 61.- Continued.

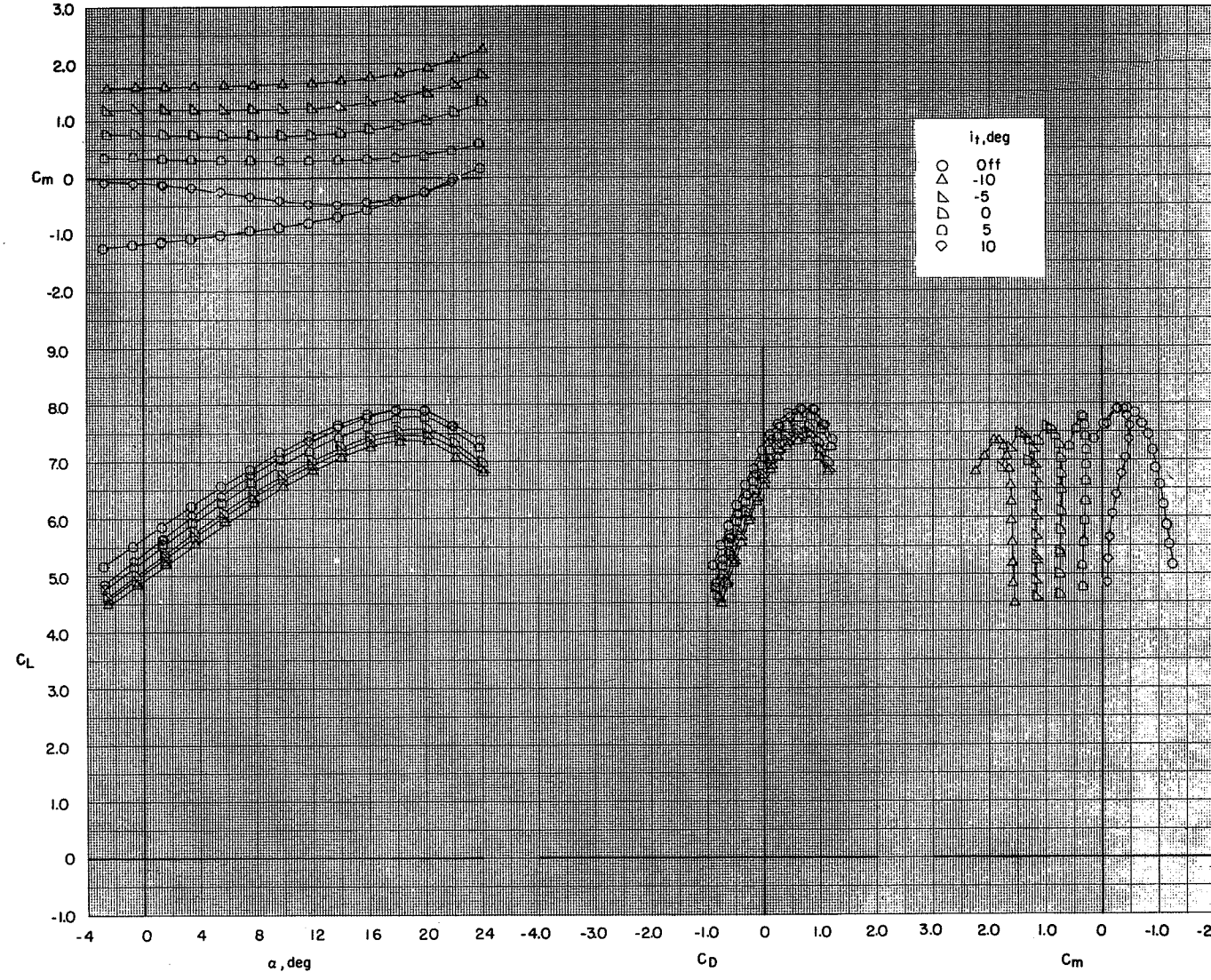

(c) $C_T = 4.06$.

Figure 61.- Concluded.

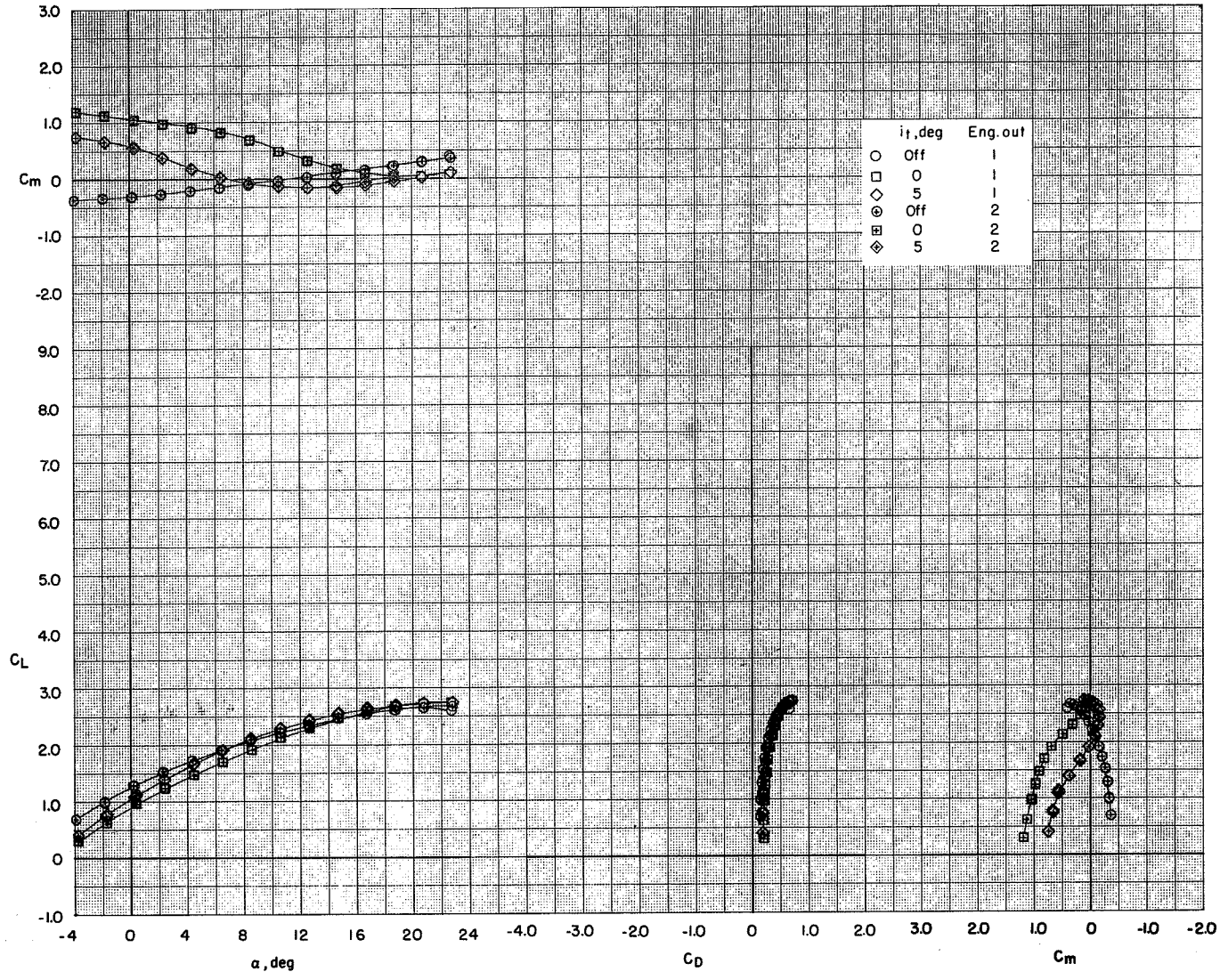

(a) $C_T = 0.$

Figure 62.- Comparison of outboard engine (engine 1) and inboard engine (engine 2) out effects on the aerodynamic characteristics of the model with flaps deflected and leading-edge slat on. BPR 10.0; T-tail; $\delta_f = 0^o/35^o/35^o$; $c_s = 25$ percent; $\delta_s = 50^o$.

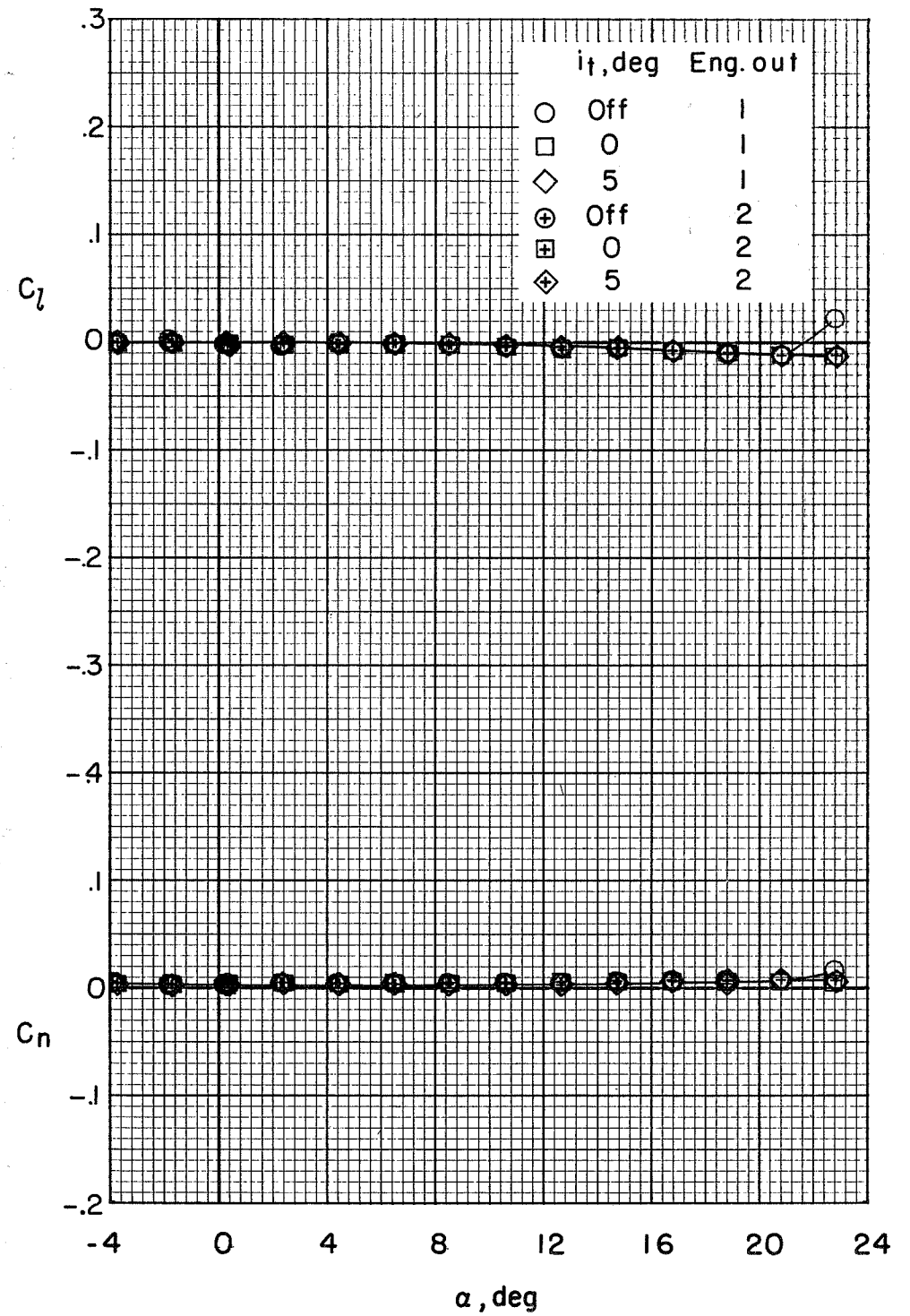

(a) Concluded.

Figure 62.- Continued.

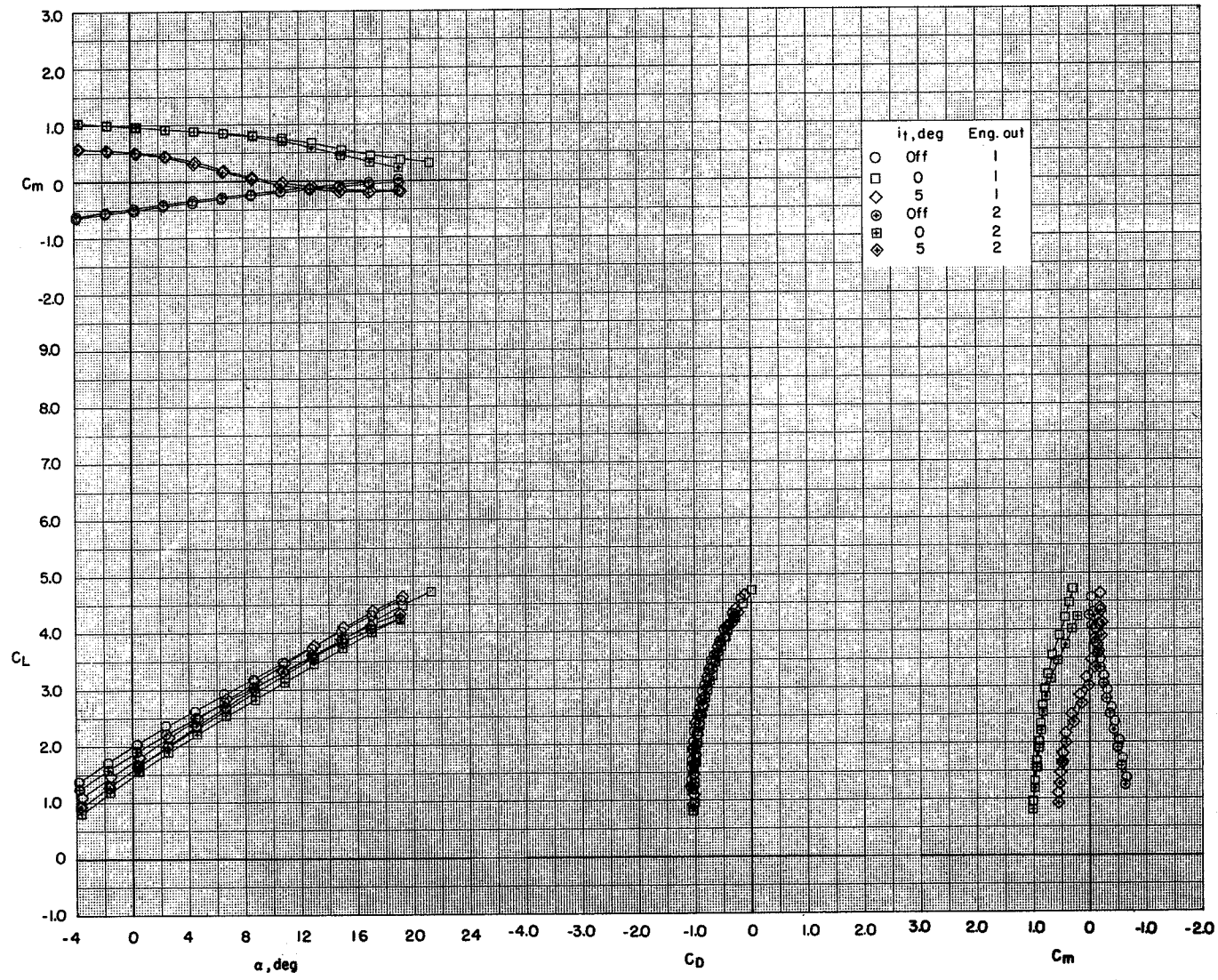

(b) $C_T = 1.69$.

Figure 62.- Continued.

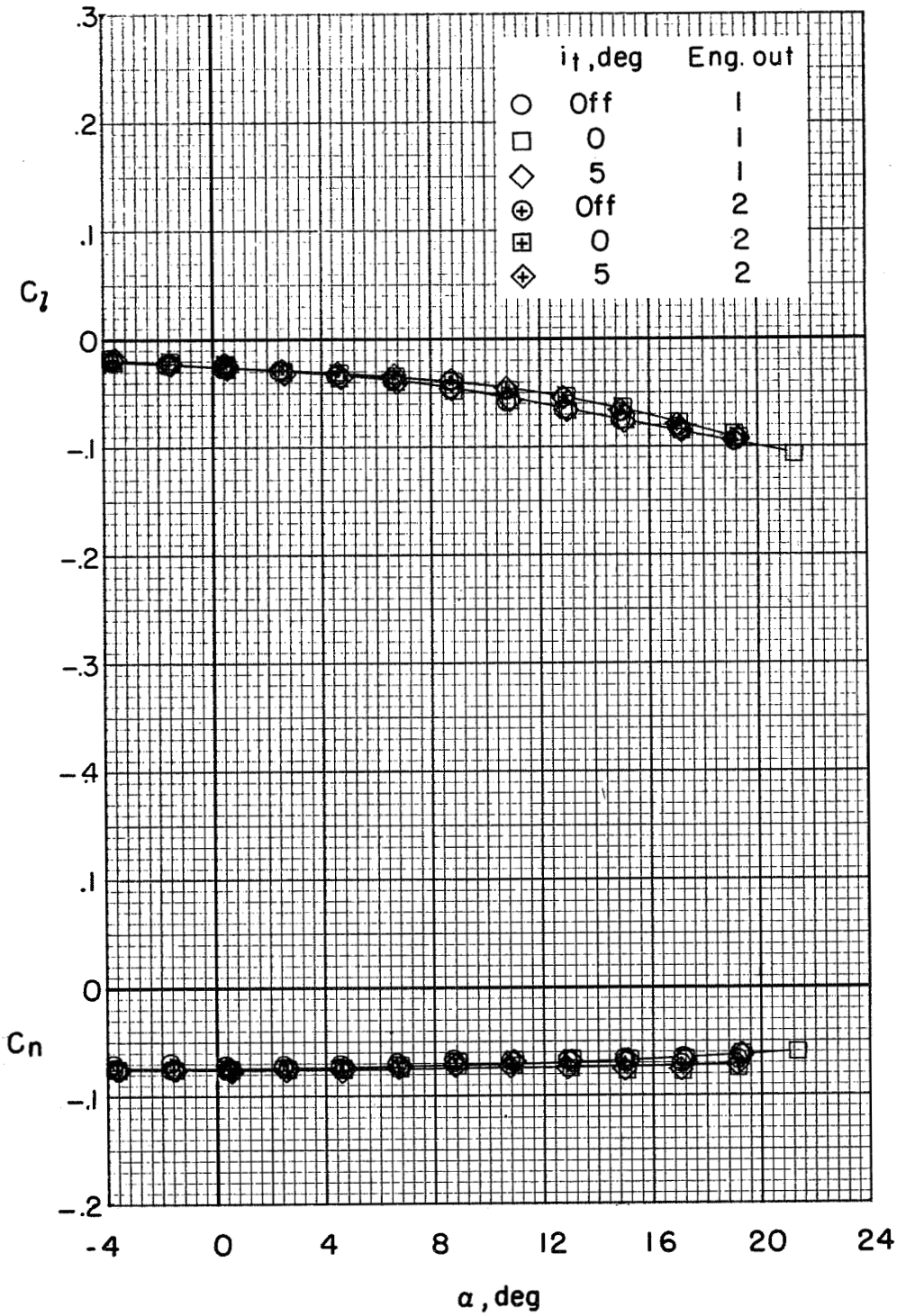

(b) Concluded.

Figure 62.- Continued.

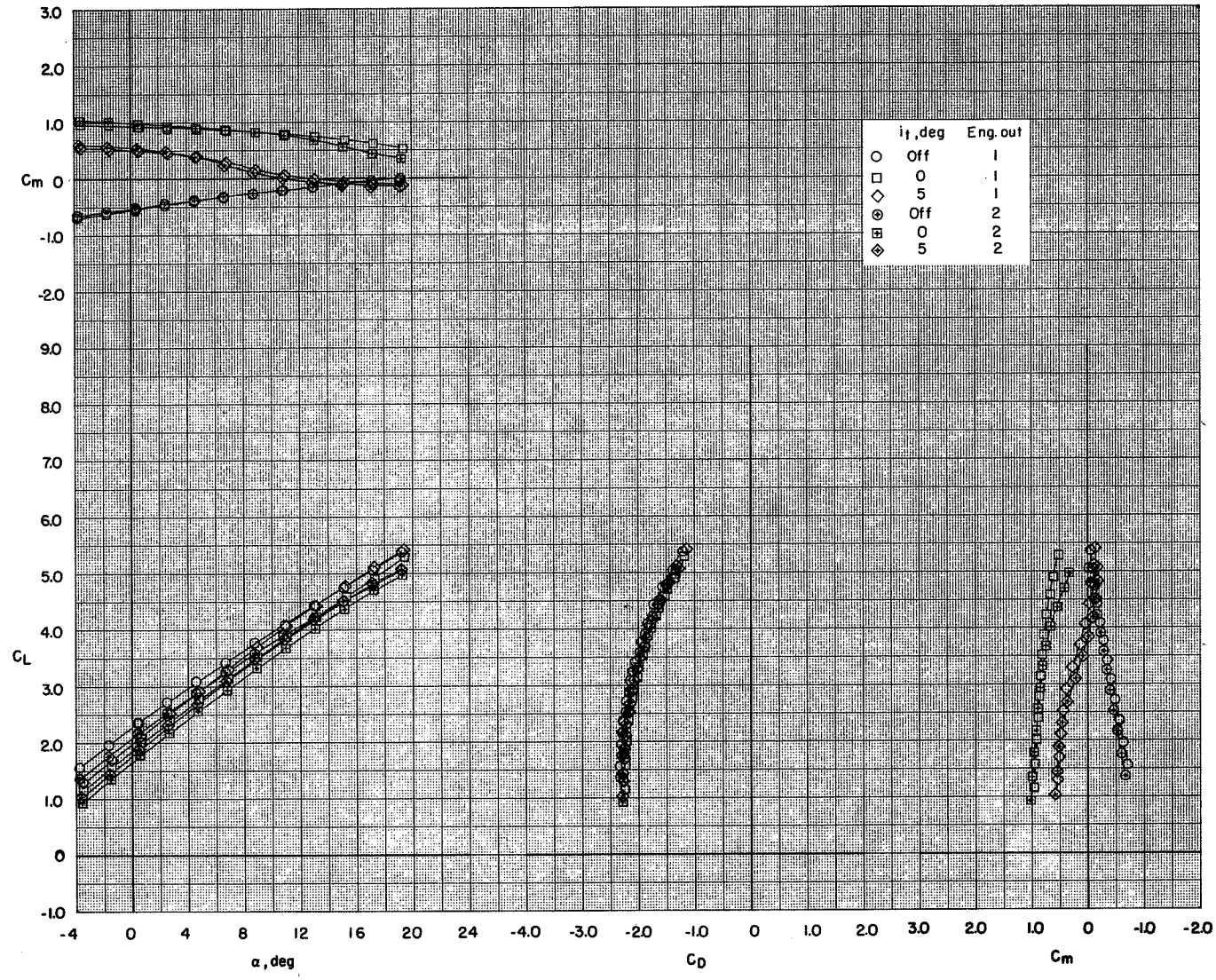

(c) $C_T = 3.04$.

Figure 62.- Continued.

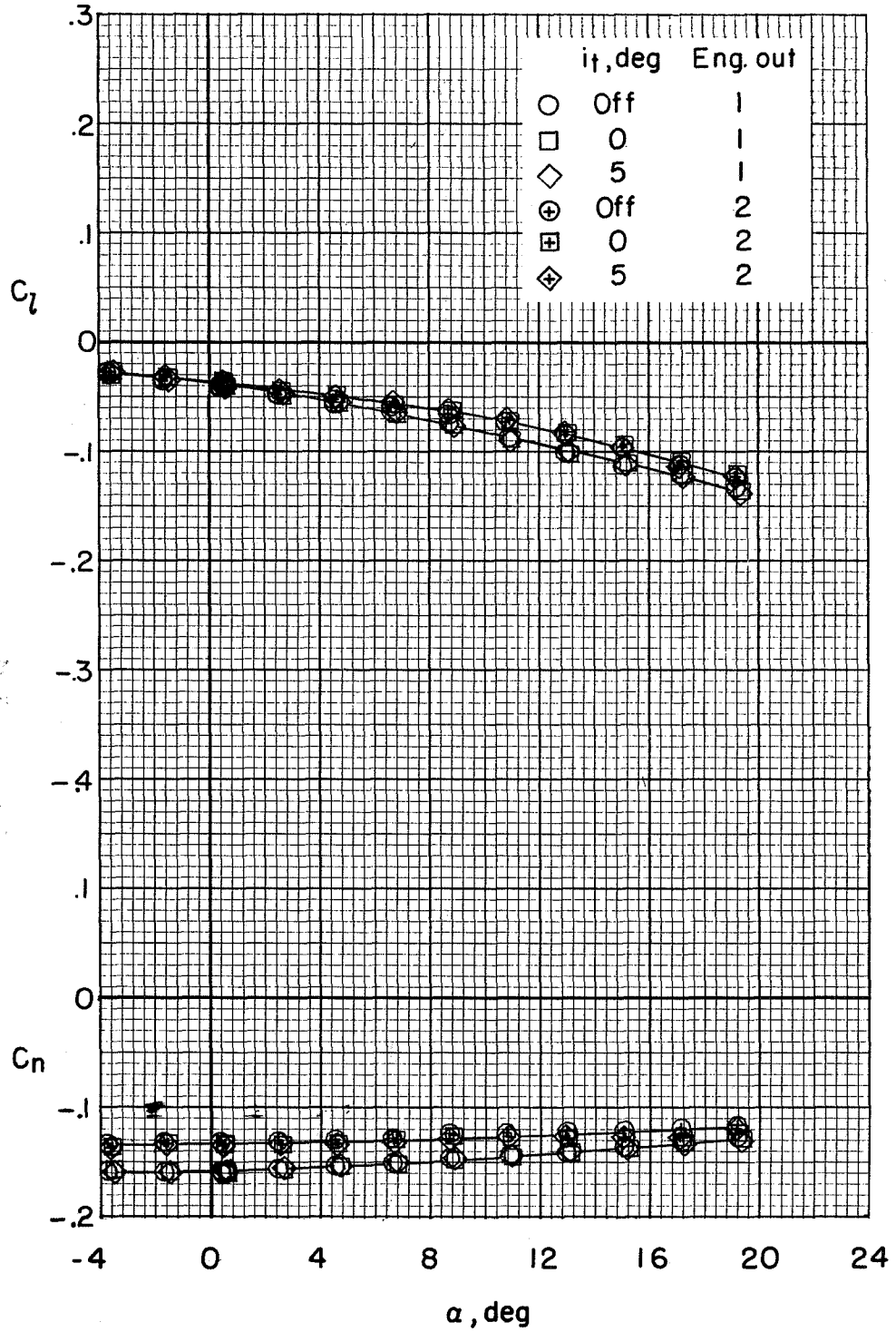

(c) Concluded.

Figure 62.- Concluded.

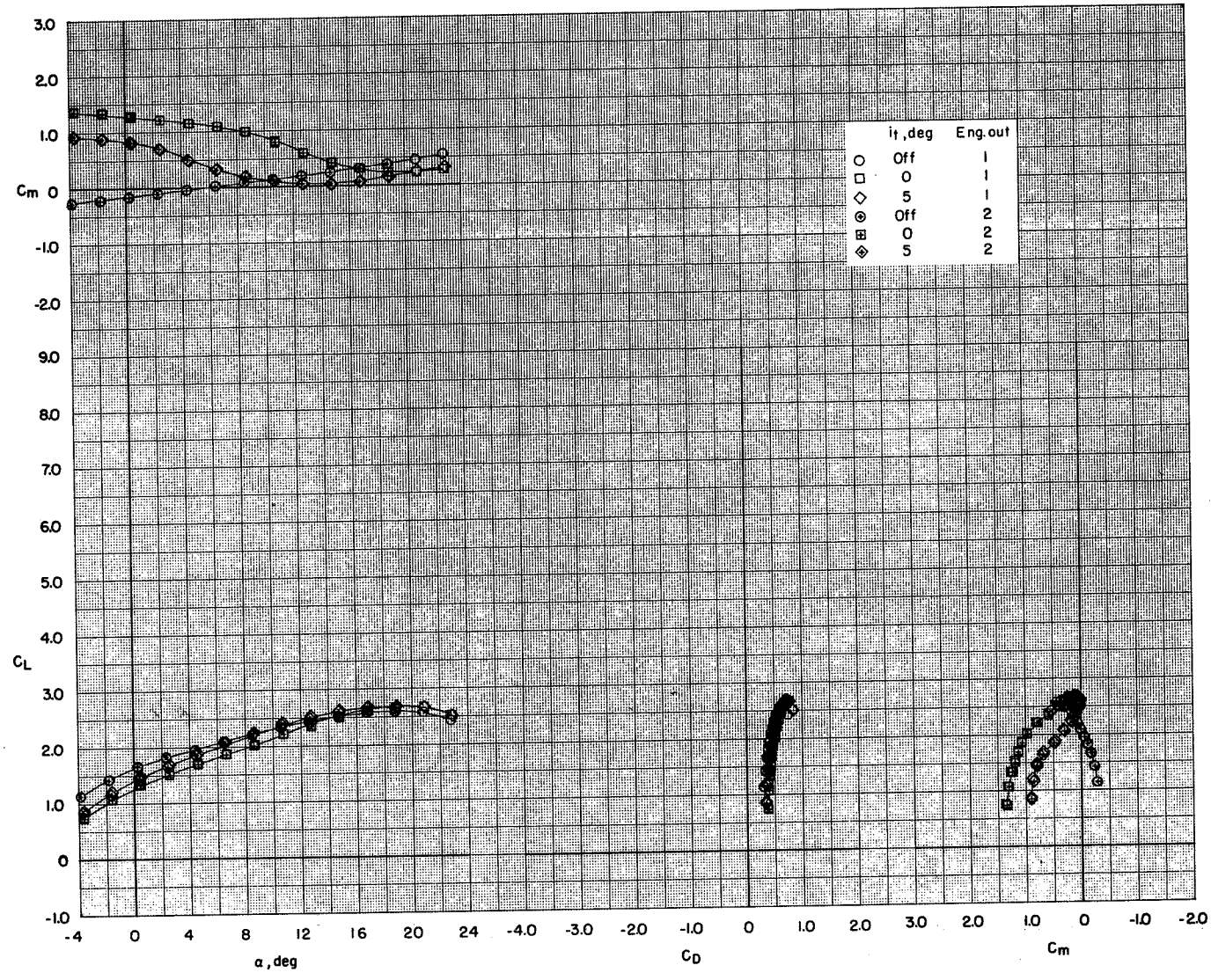

(a) $C_T = 0$.

Figure 63.- Comparison of outboard engine (engine 1) and inboard engine (engine 2) out effects on the aerodynamic characteristics of the model with flaps deflected and leading-edge slat on. BPR 10.0; T-tail; $\delta_f = 0^o/65^o/65^o$; $c_s = 25$ percent; $\delta_s = 50^o$.

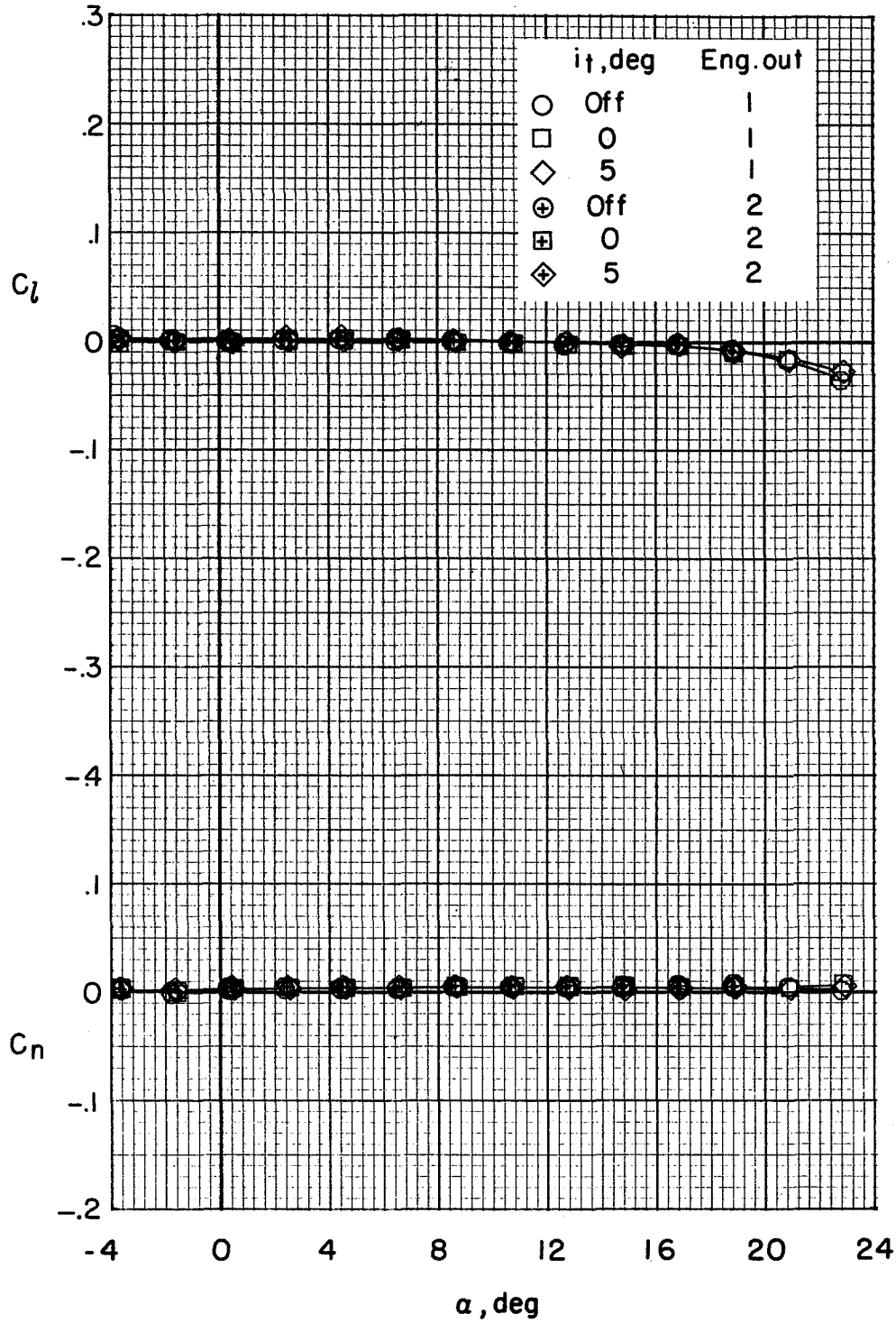

(a) Concluded.

Figure 63.- Continued.

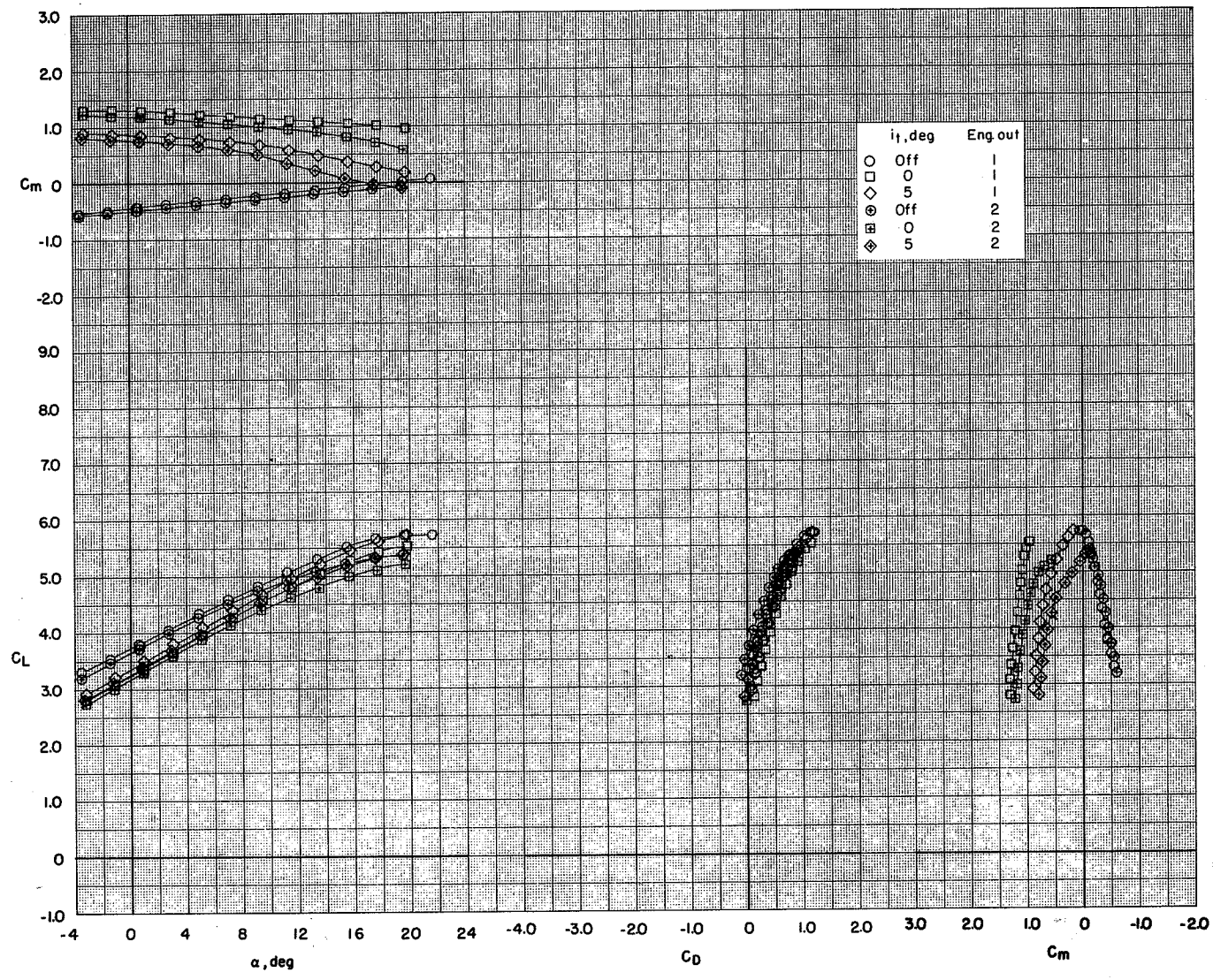

(b) $C_T = 1.69$.

Figure 63.- Continued.

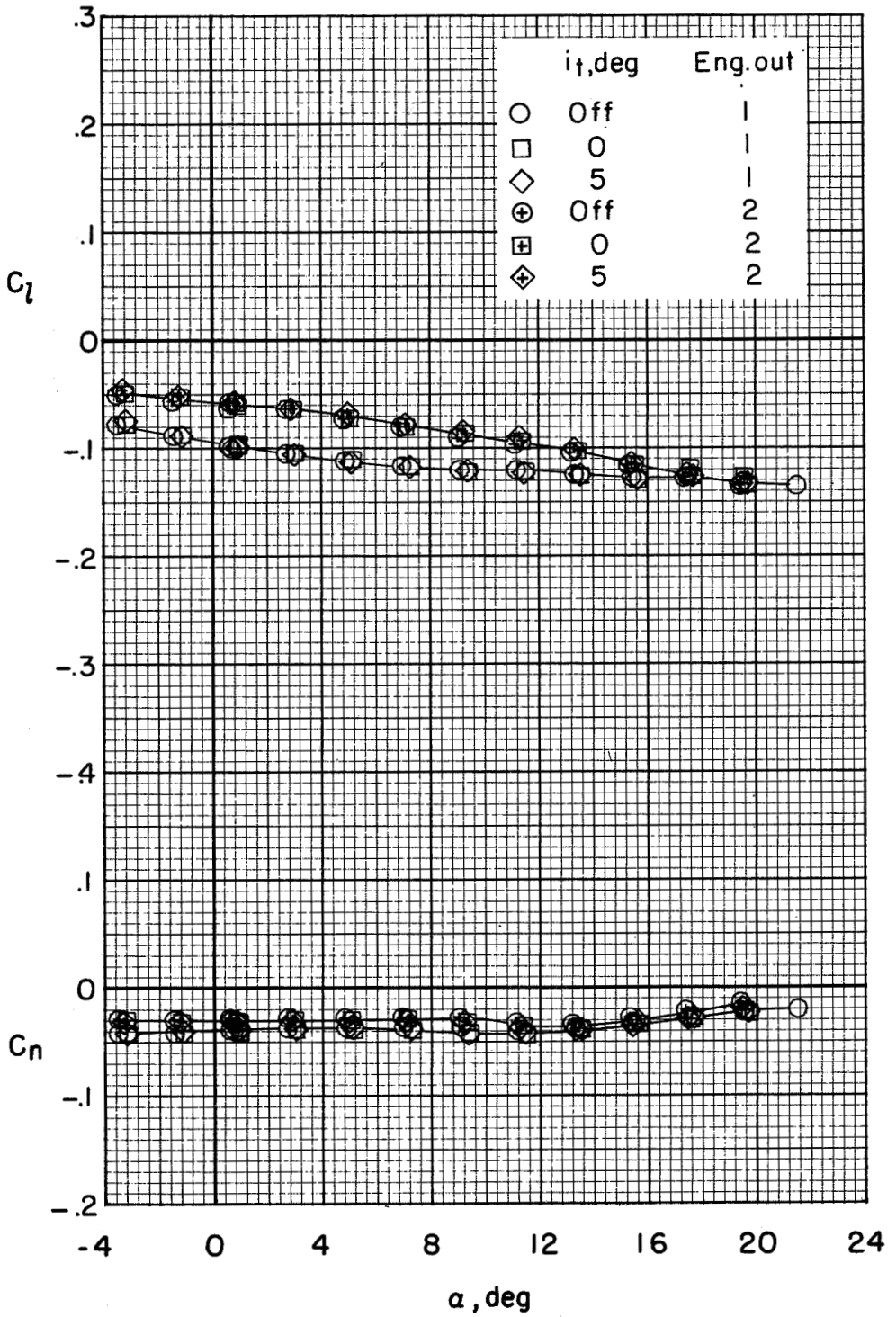

(b) Concluded.

Figure 63.- Continued.

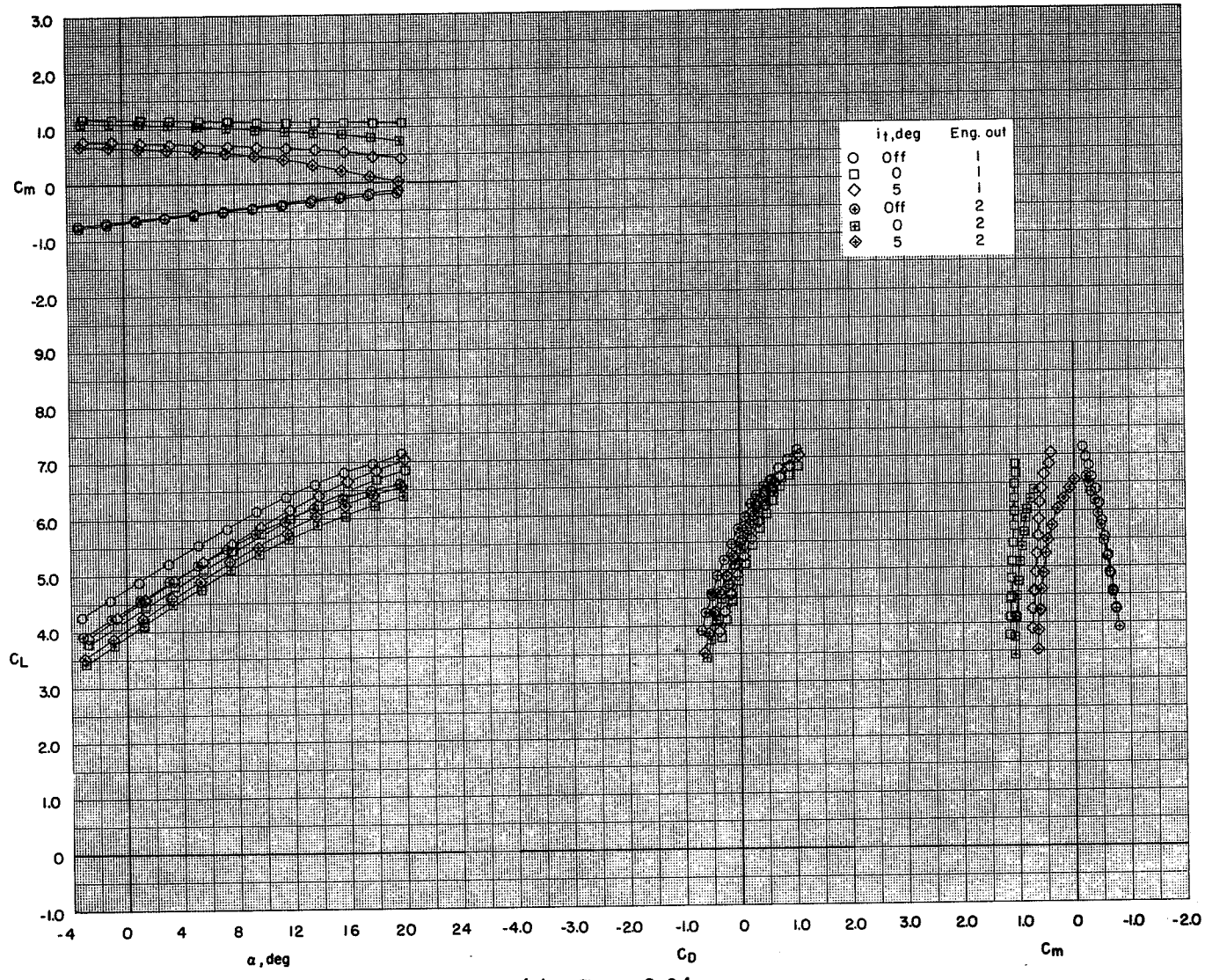

(c) $C_T = 3.04$.

Figure 63.- Continued.

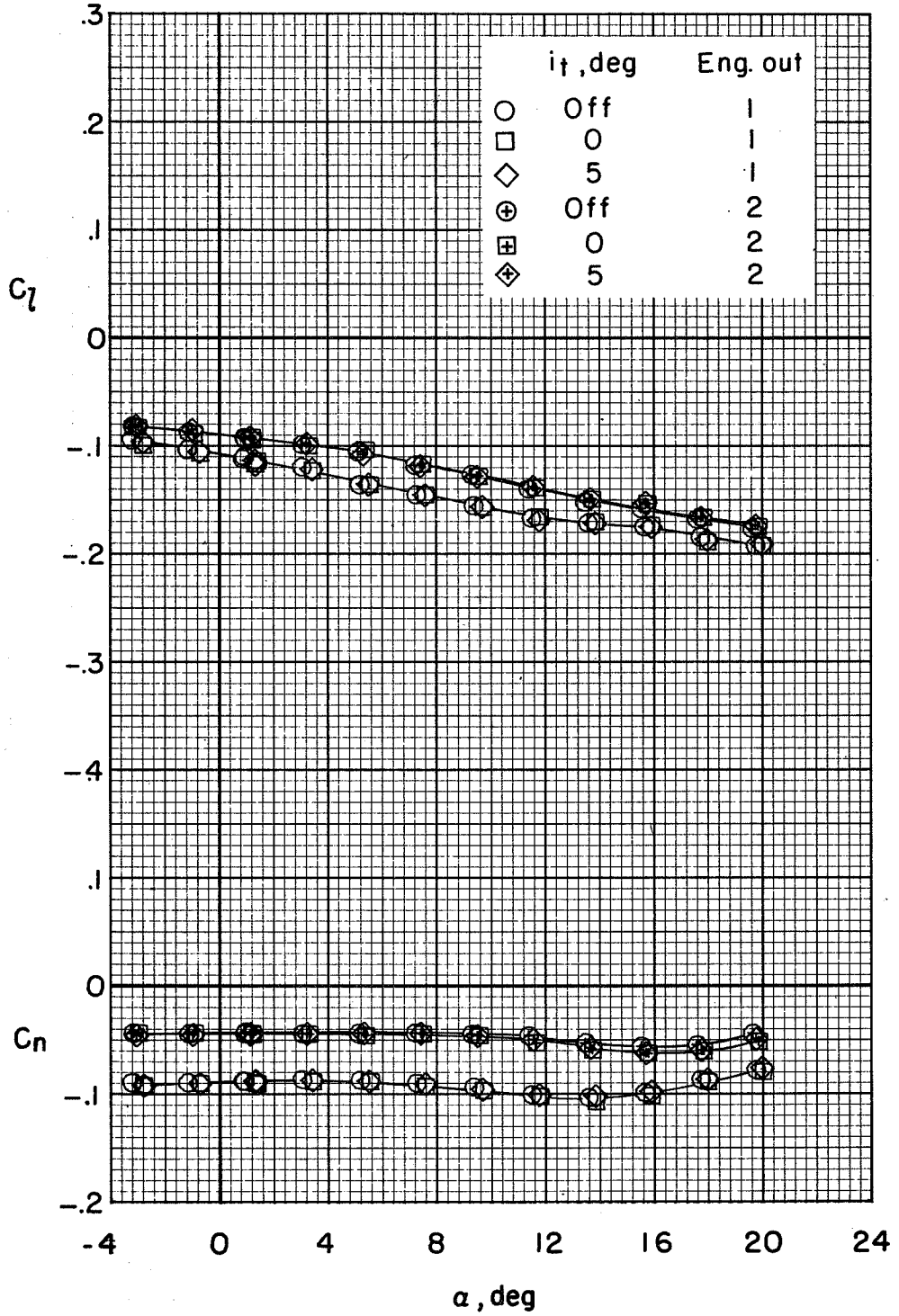

(c) Concluded.

Figure 63.- Concluded.

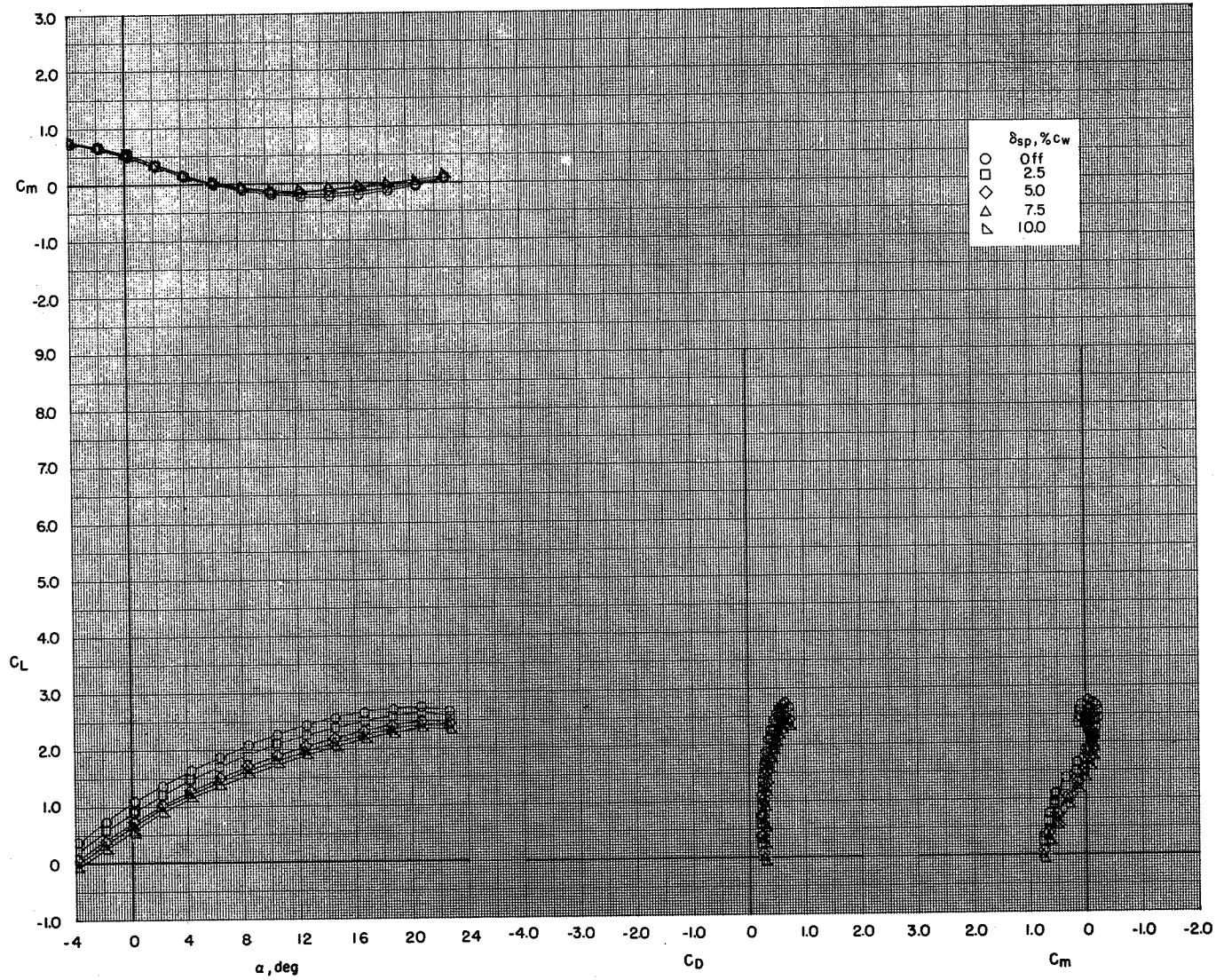

(a) $C_T = 0$.

Figure 64.- Effect of spoiler projection on the aerodynamic characteristics of the model with flaps deflected and leading-edge slat on. BPR 6.2; T-tail at 5^o; $\delta_f = 0^o/35^o/35^o$; $c_s = 25$ percent; $\delta_s = 50^o$; left outboard engine out.

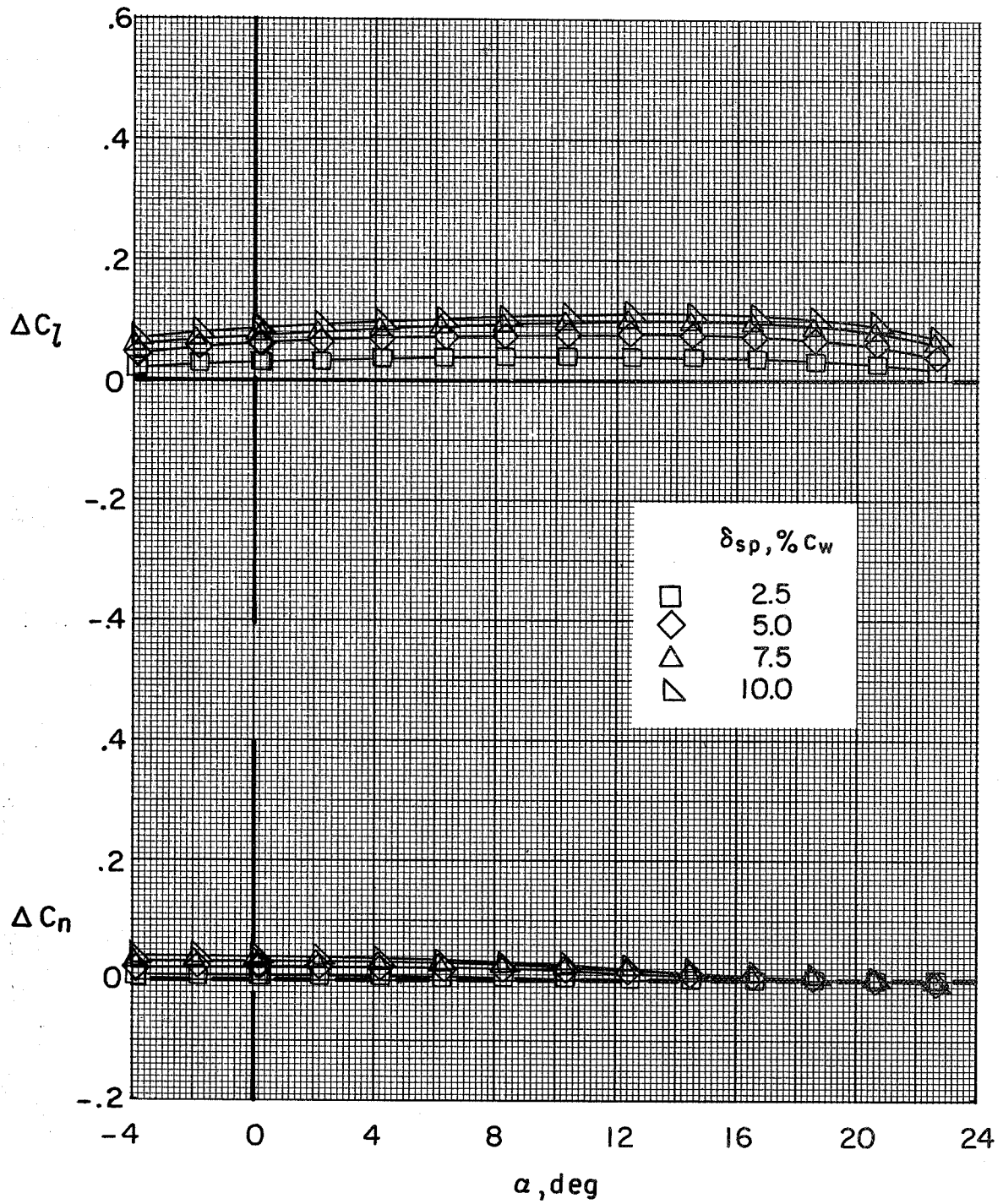

(a) Concluded.

Figure 64.- Continued.

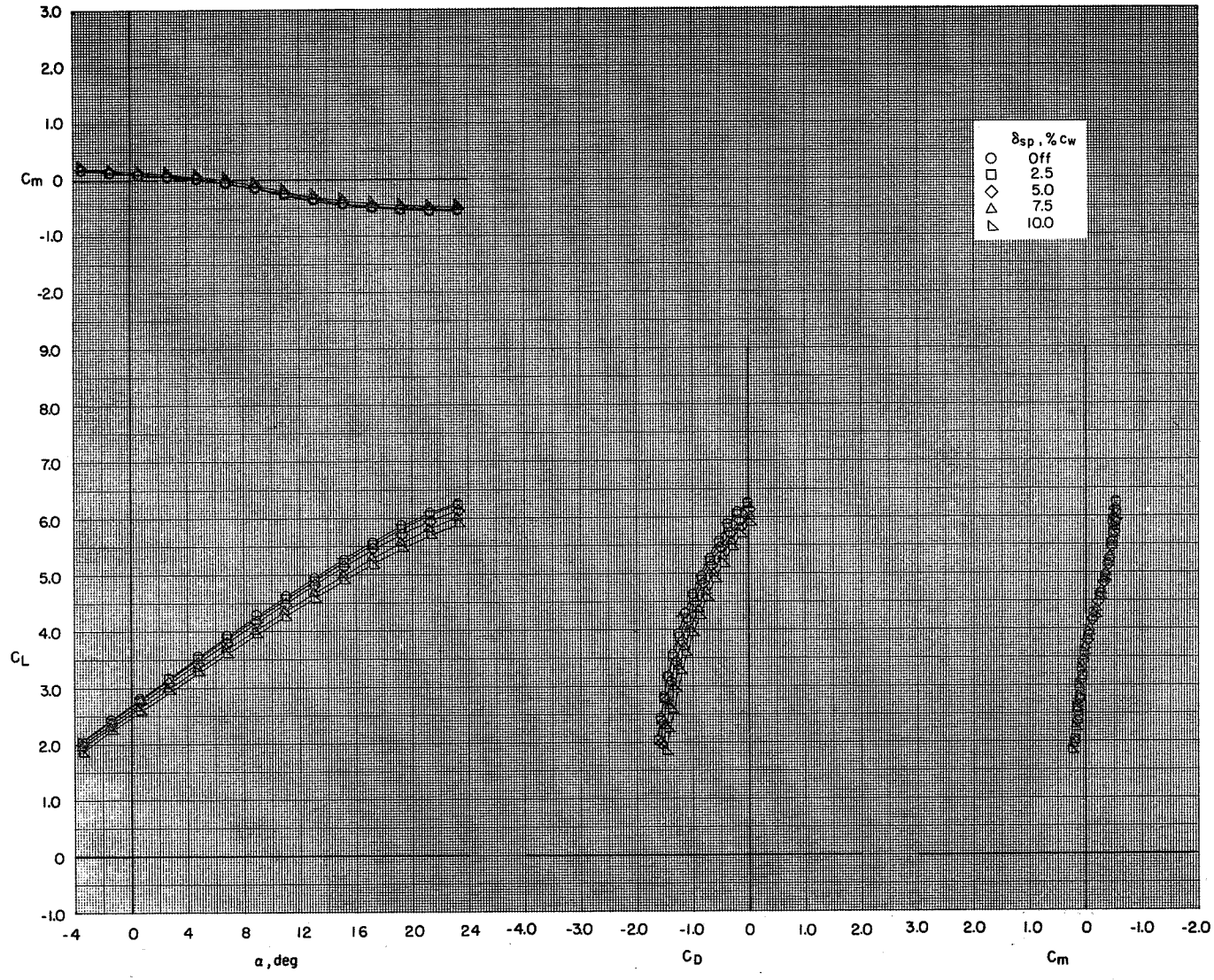

(c) $C_T = 2.72$.

Figure 64.- Continued.

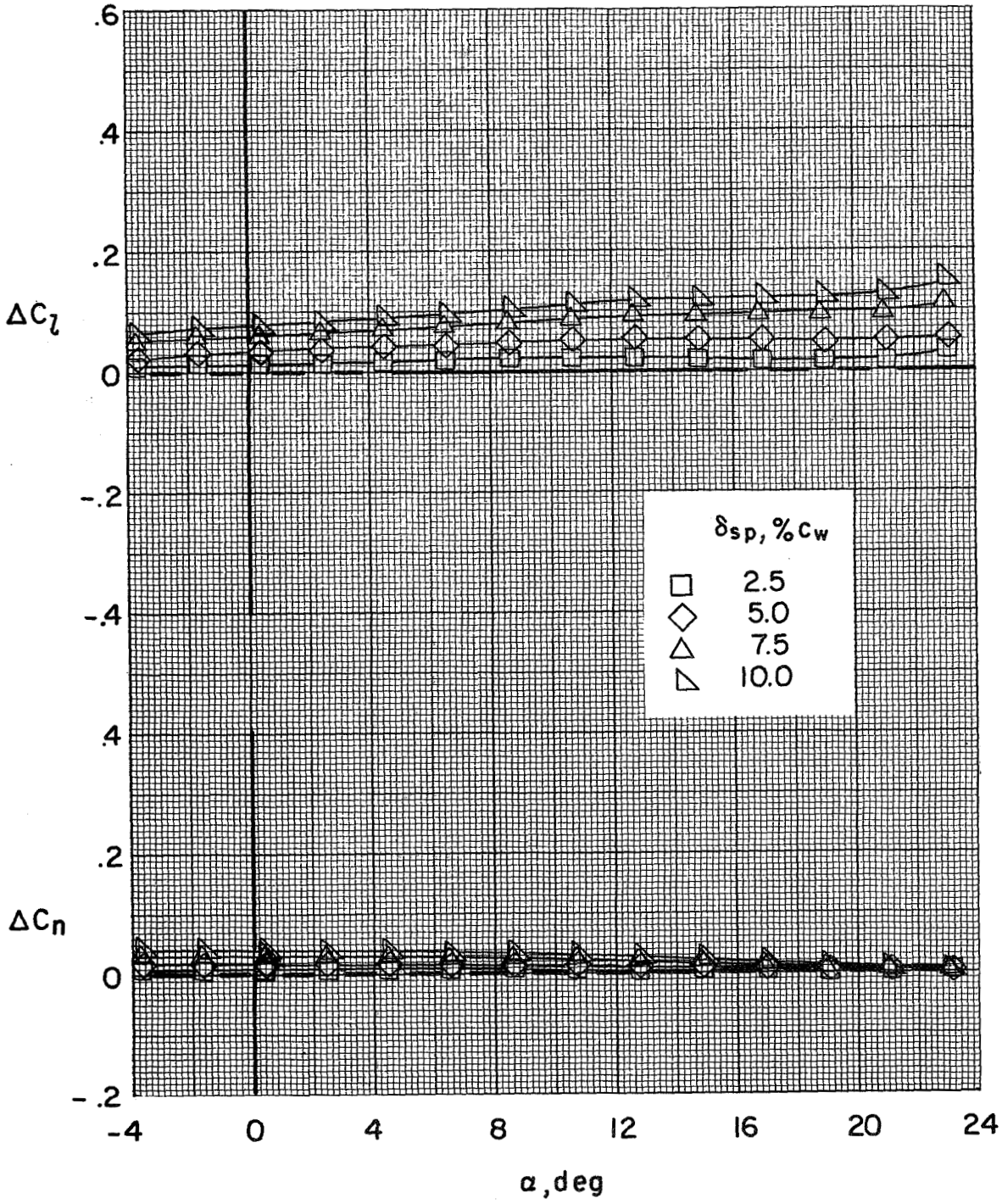

(b) Concluded.

Figure 64.- Continued.

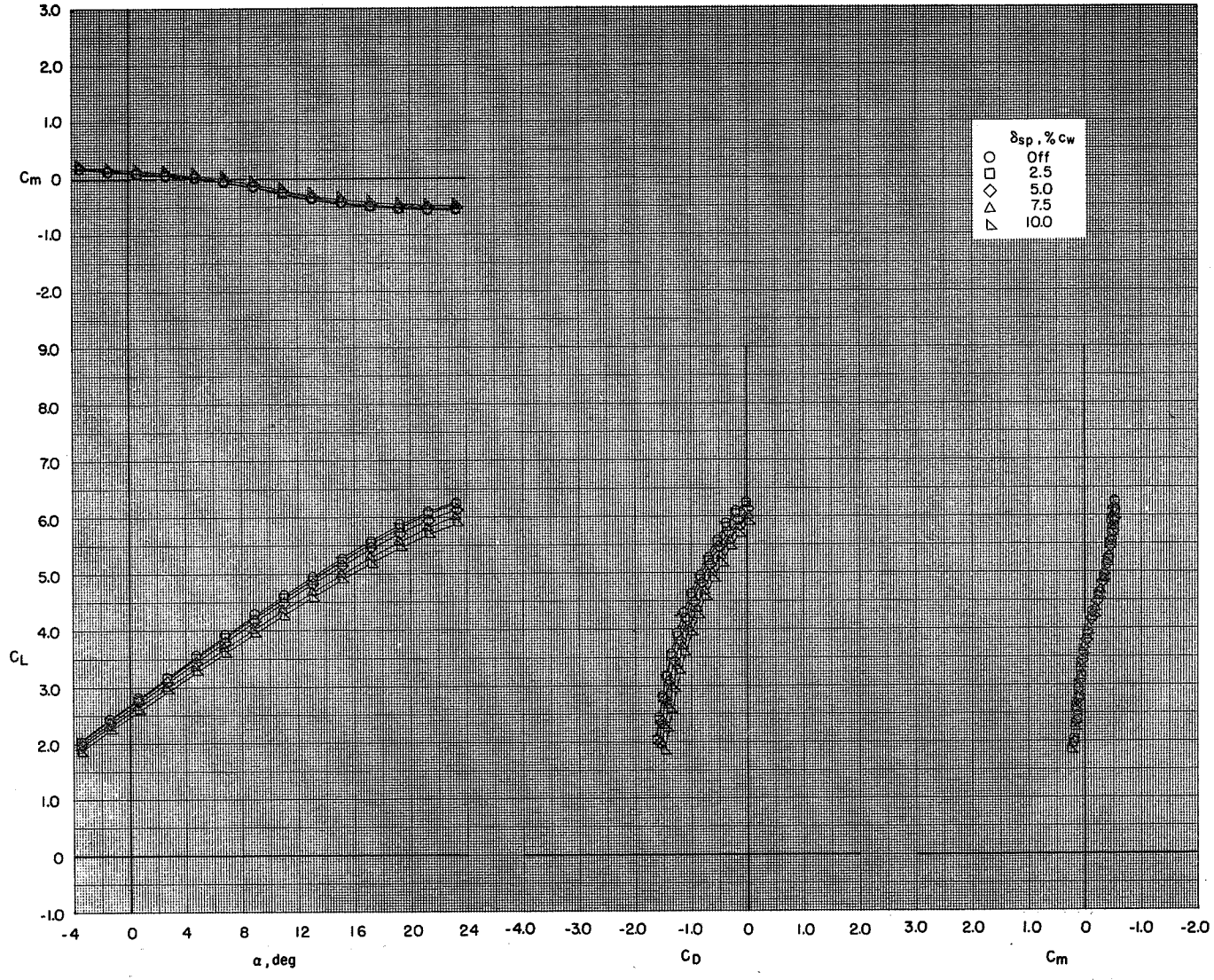

(c) $C_T = 2.72$.

Figure 64.- Continued.

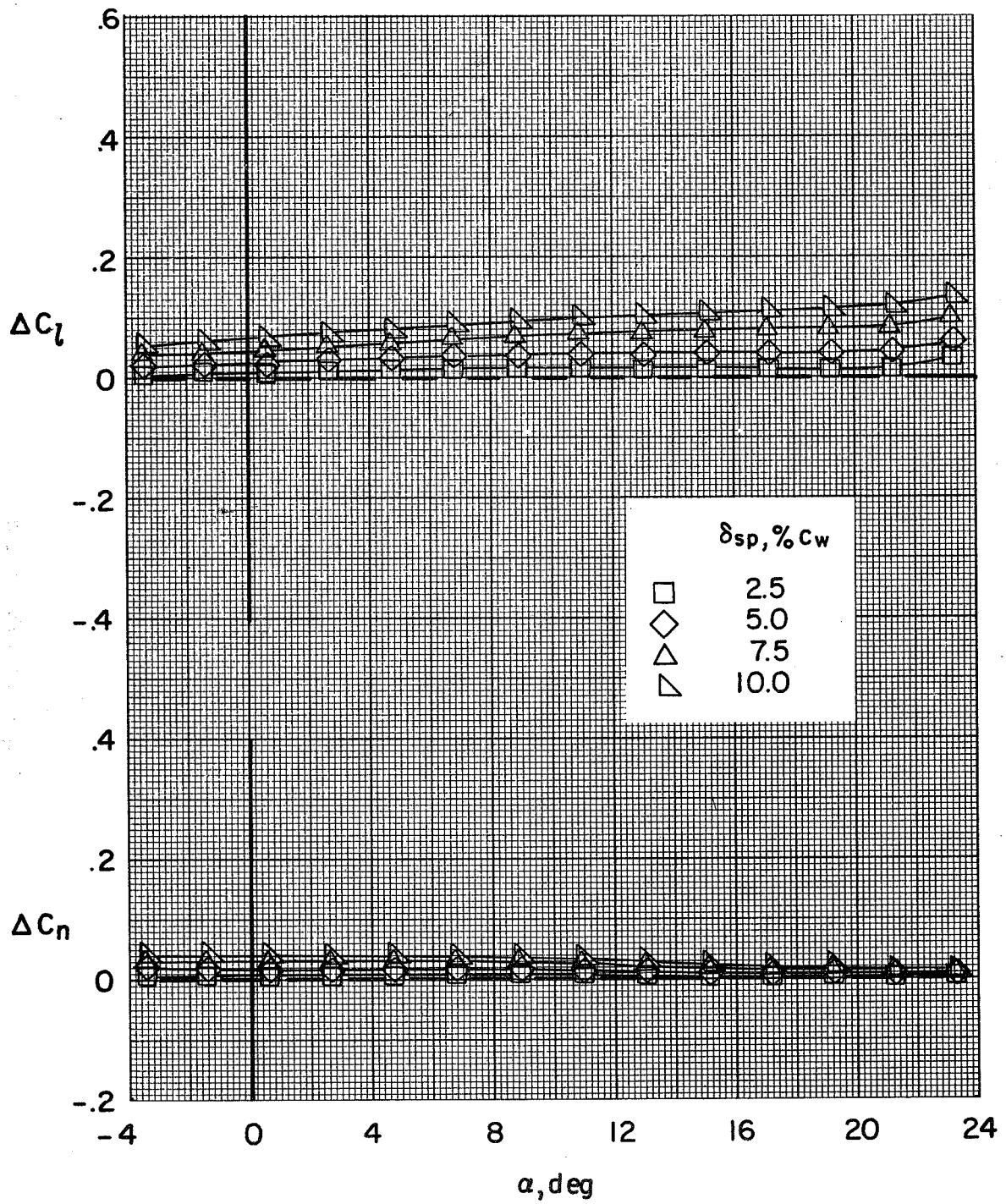

(c) Concluded.

Figure 64.- Concluded.

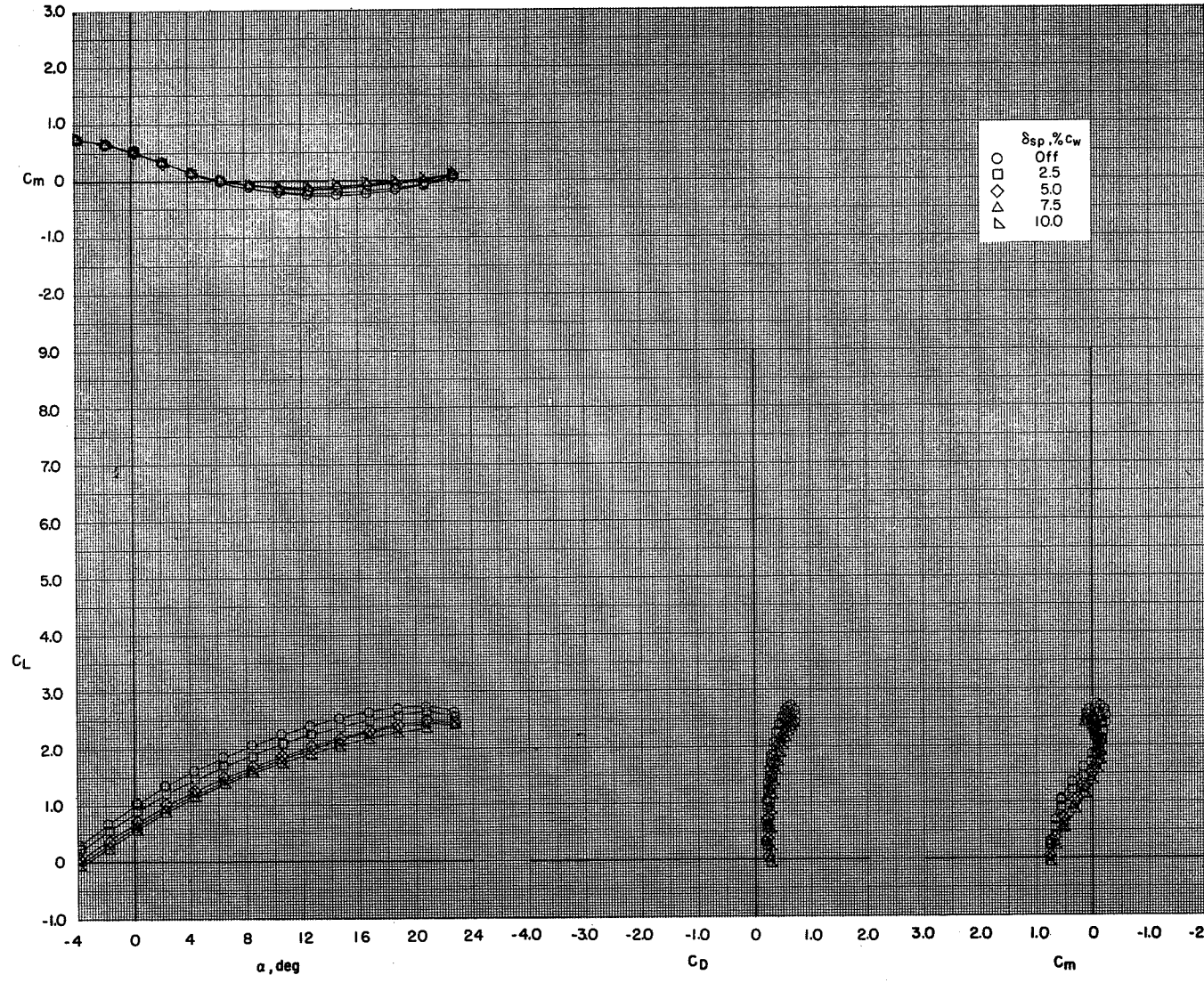

(a) $C_T = 0$.

Figure 65.- Effect of spoiler projection on the aerodynamic characteristics of the model with flaps deflected and leading-edge slat on. BPR 6.2; T-tail at 5^o; $\delta_f = 0^o/35^o/35^o$; $c_s = 25$ percent; $\delta_s = 50^o$; left inboard engine out.

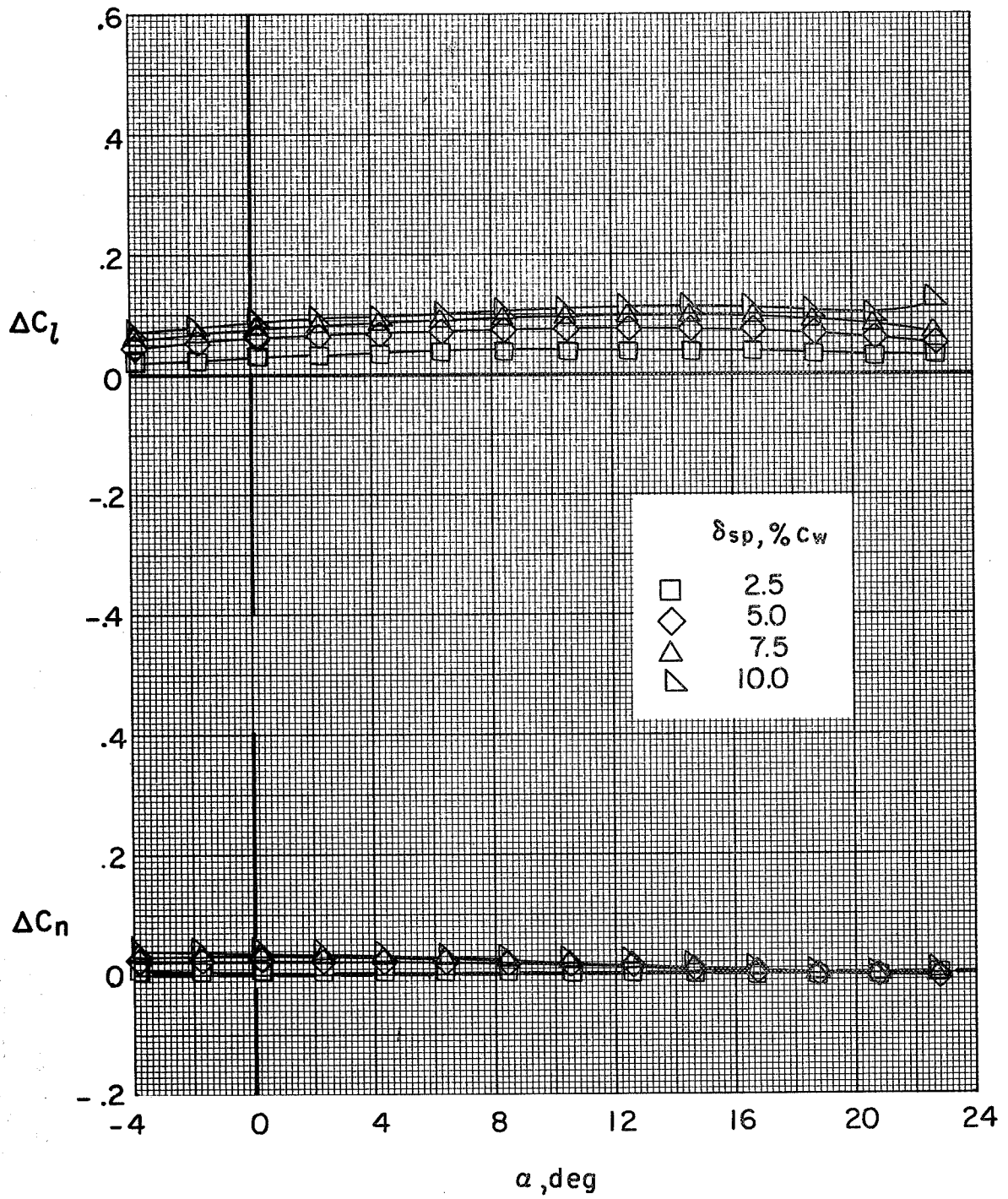

(a) Concluded.

Figure 65.- Continued.

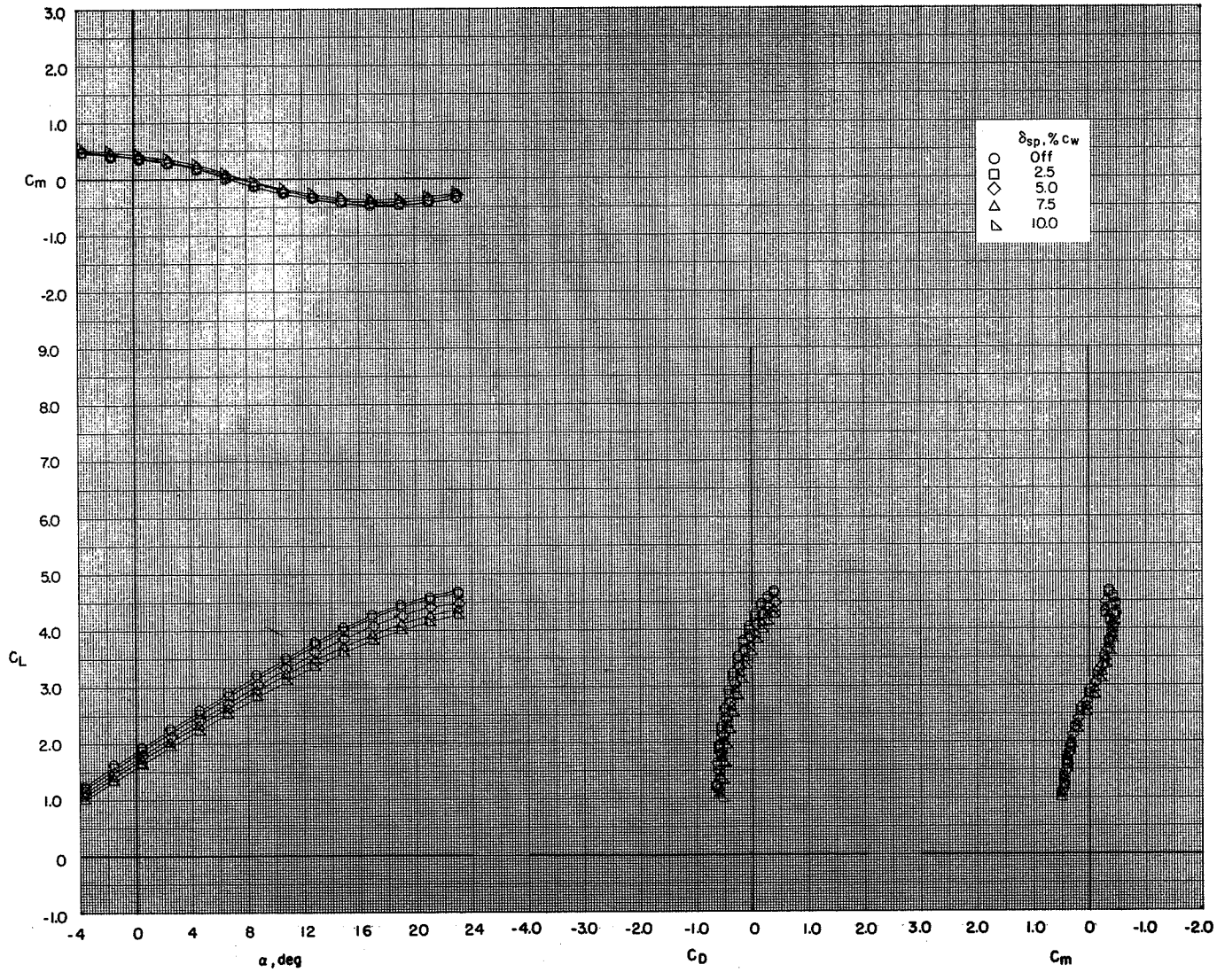

(b) $C_T = 1.36$.

Figure 65.- Continued.

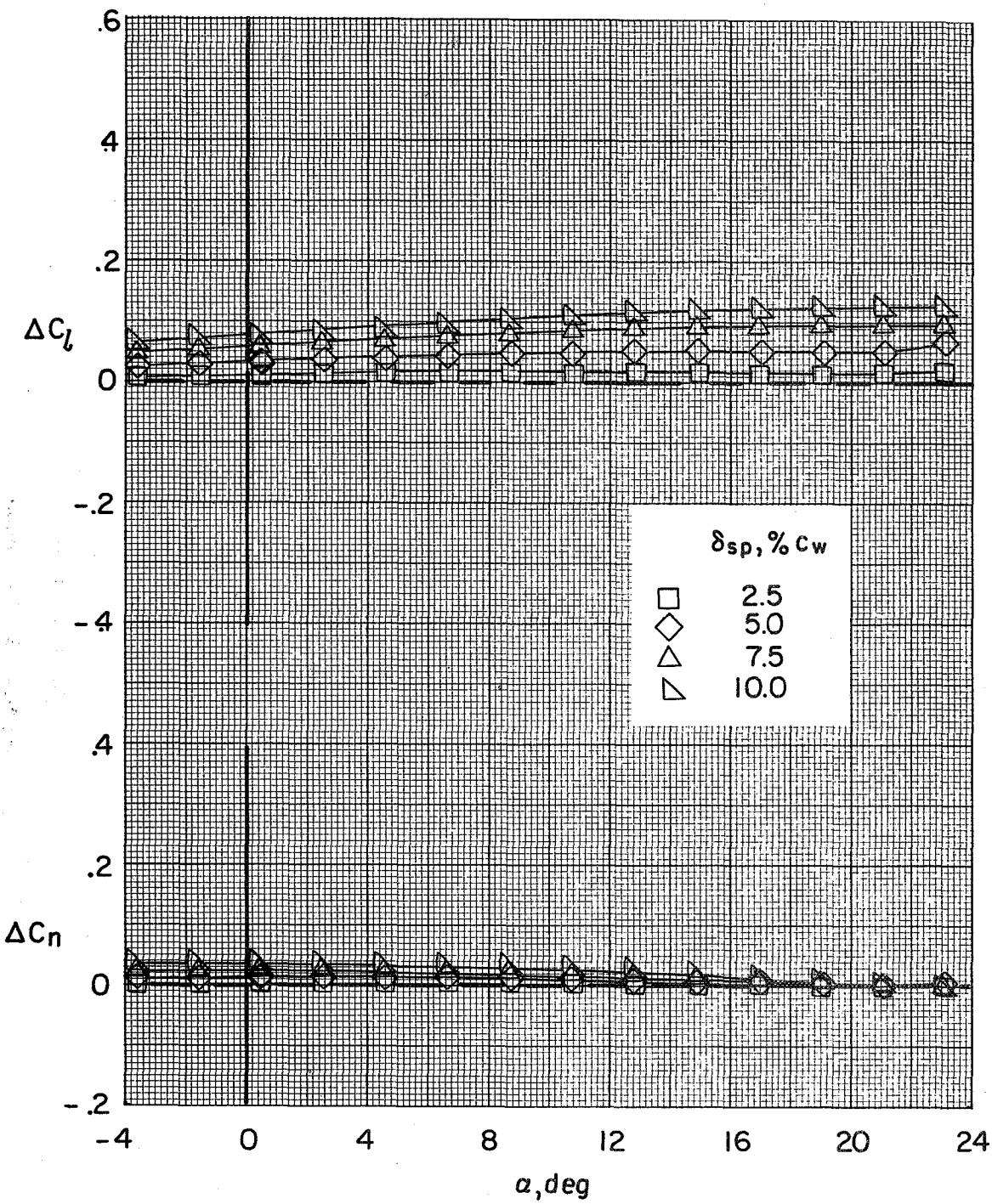

(b) Concluded.

Figure 65.- Continued.

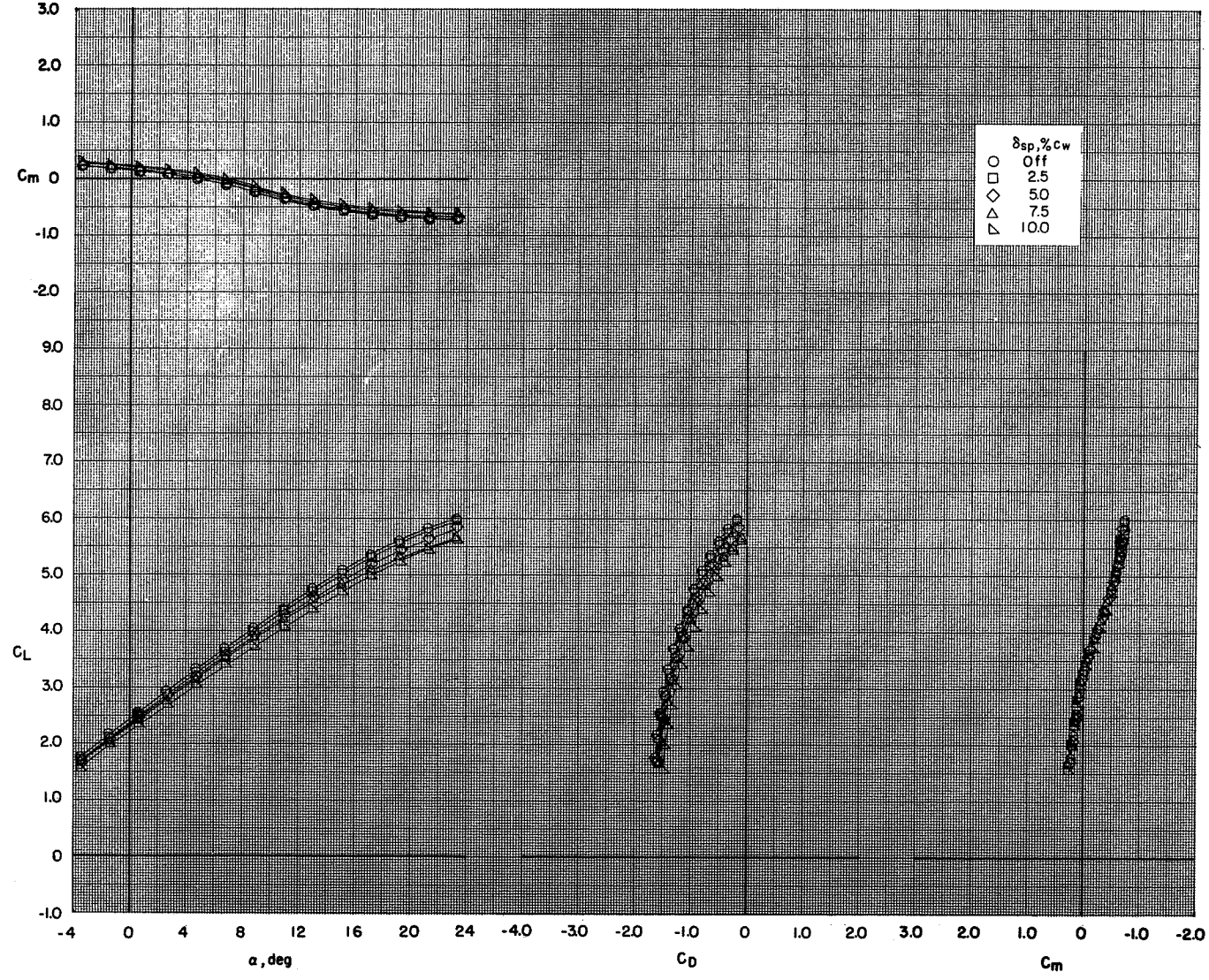

(c) $C_T = 2.72$.

Figure 65.- Continued.

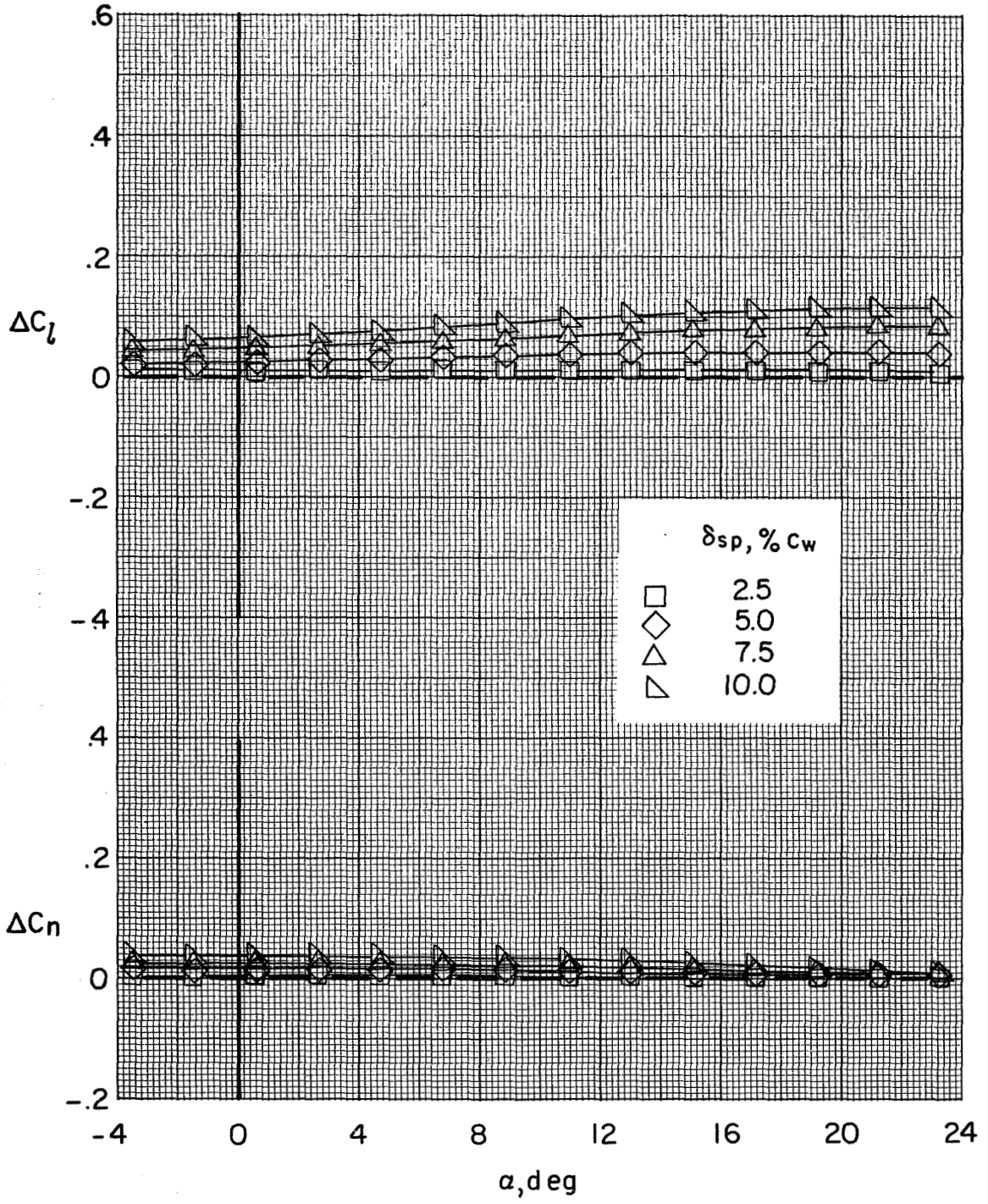

(c) Concluded.

Figure 65.- Concluded.

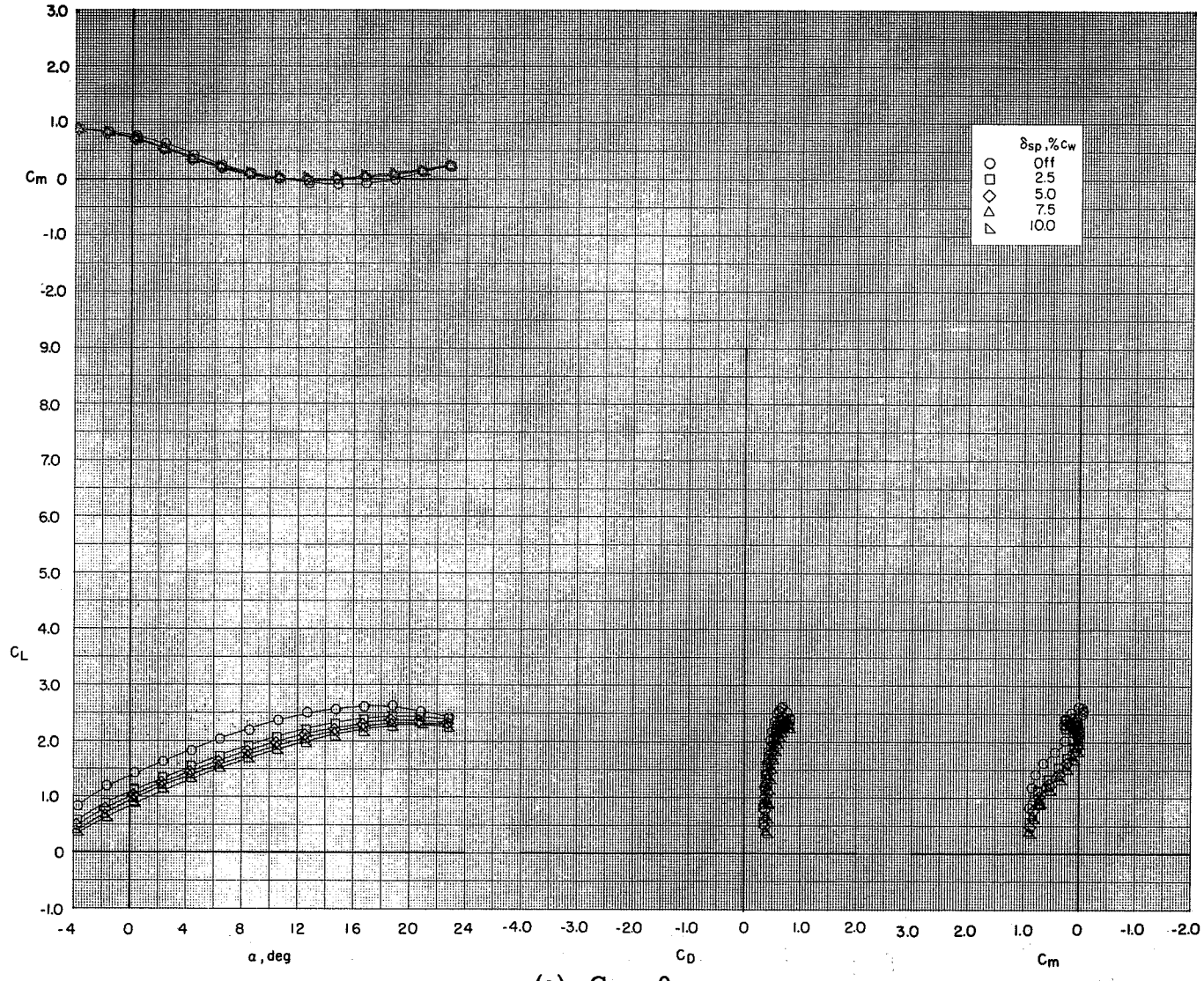

(a) $C_T = 0$.

Figure 66.- Effect of spoiler projection on the aerodynamic characteristics of the model with flaps deflected and leading-edge slat on. BPR 6.2; T-tail at 5^o; $\delta_f = 0^o/65^o/65^o$; $c_s = 25$ percent; $\delta_s = 50^o$; left outboard engine out.

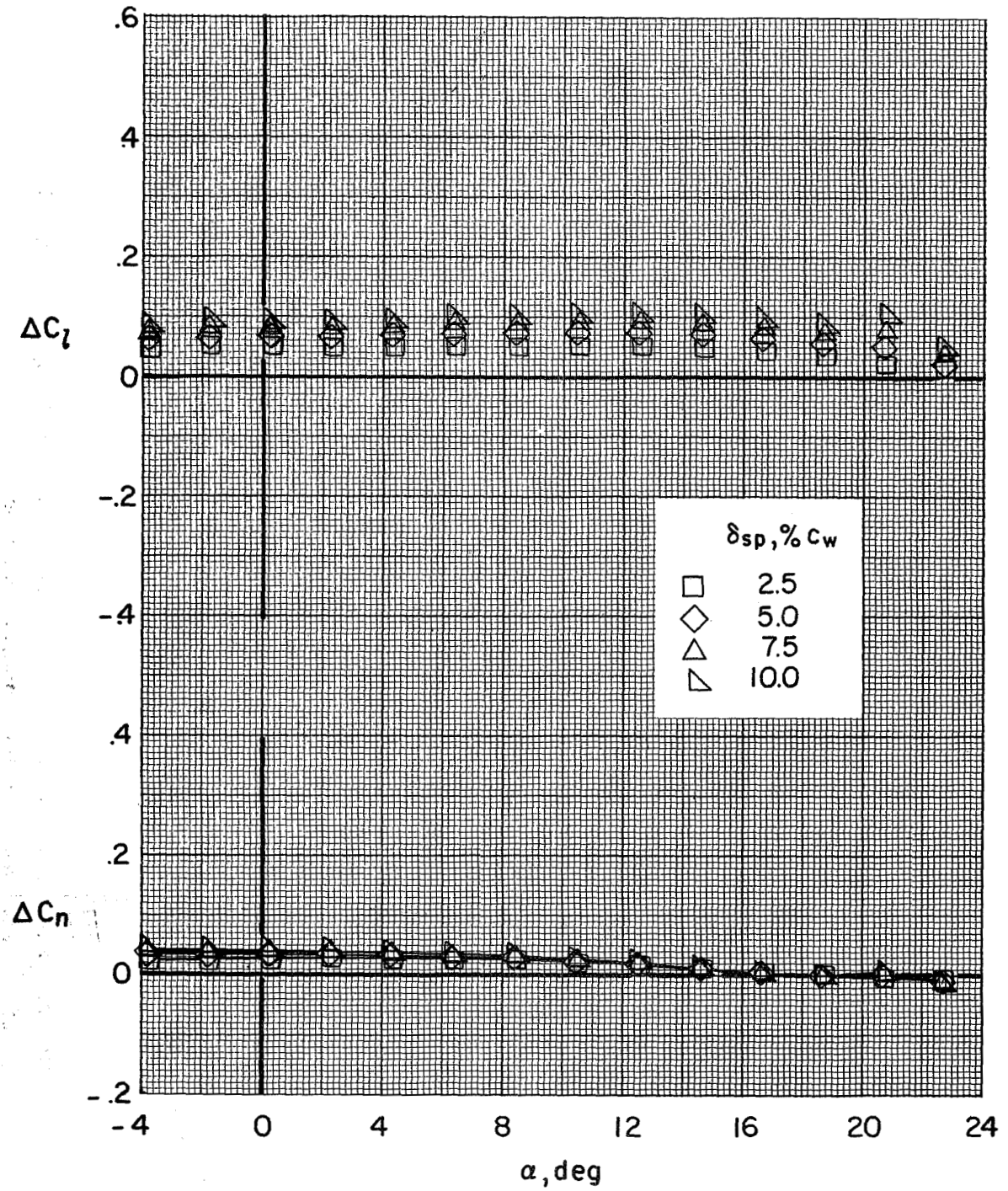

(a) Concluded.

Figure 66.- Continued.

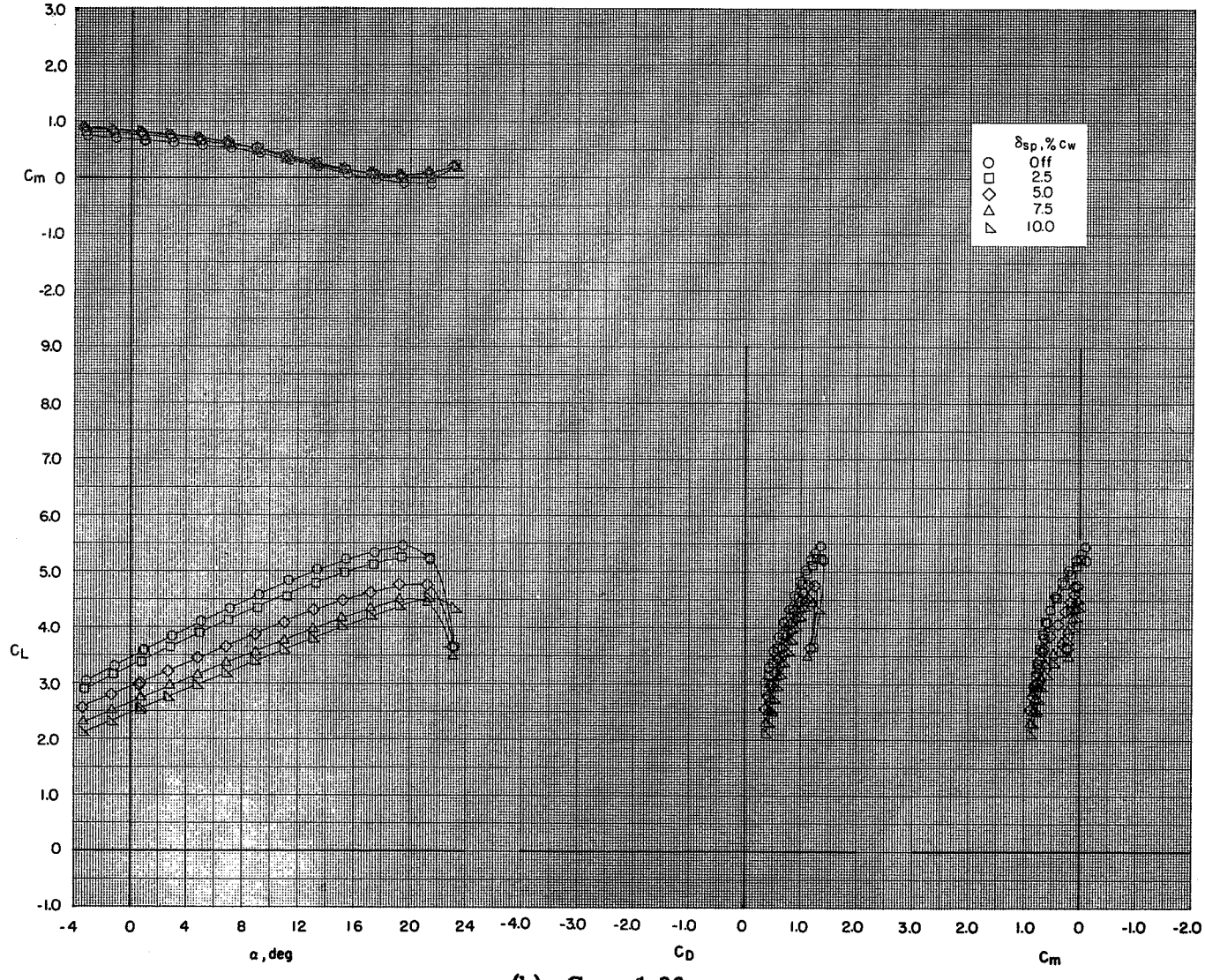

(b) $C_T = 1.36$.

Figure 66.- Continued.

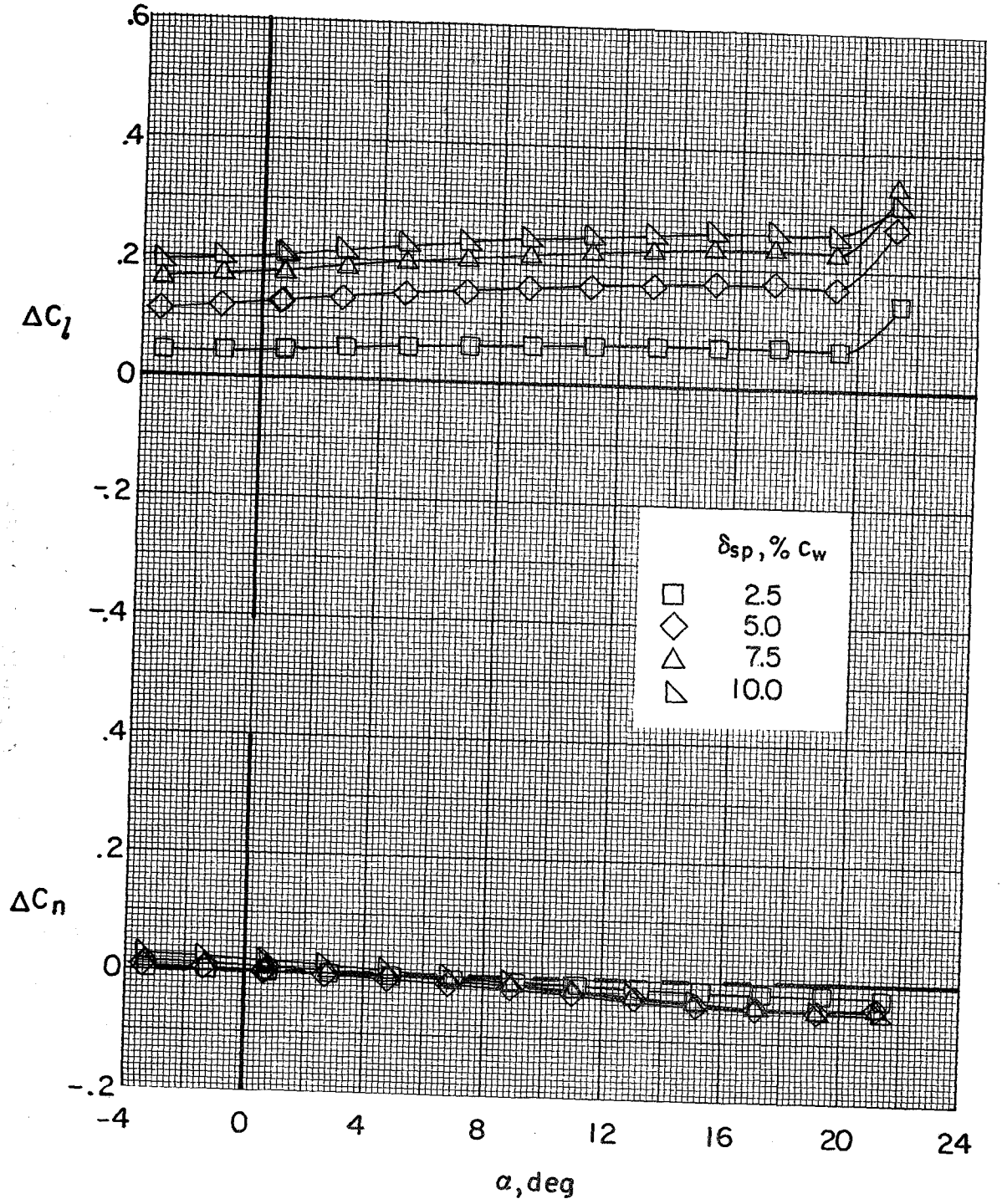

(b) Concluded.

Figure 66.- Continued.

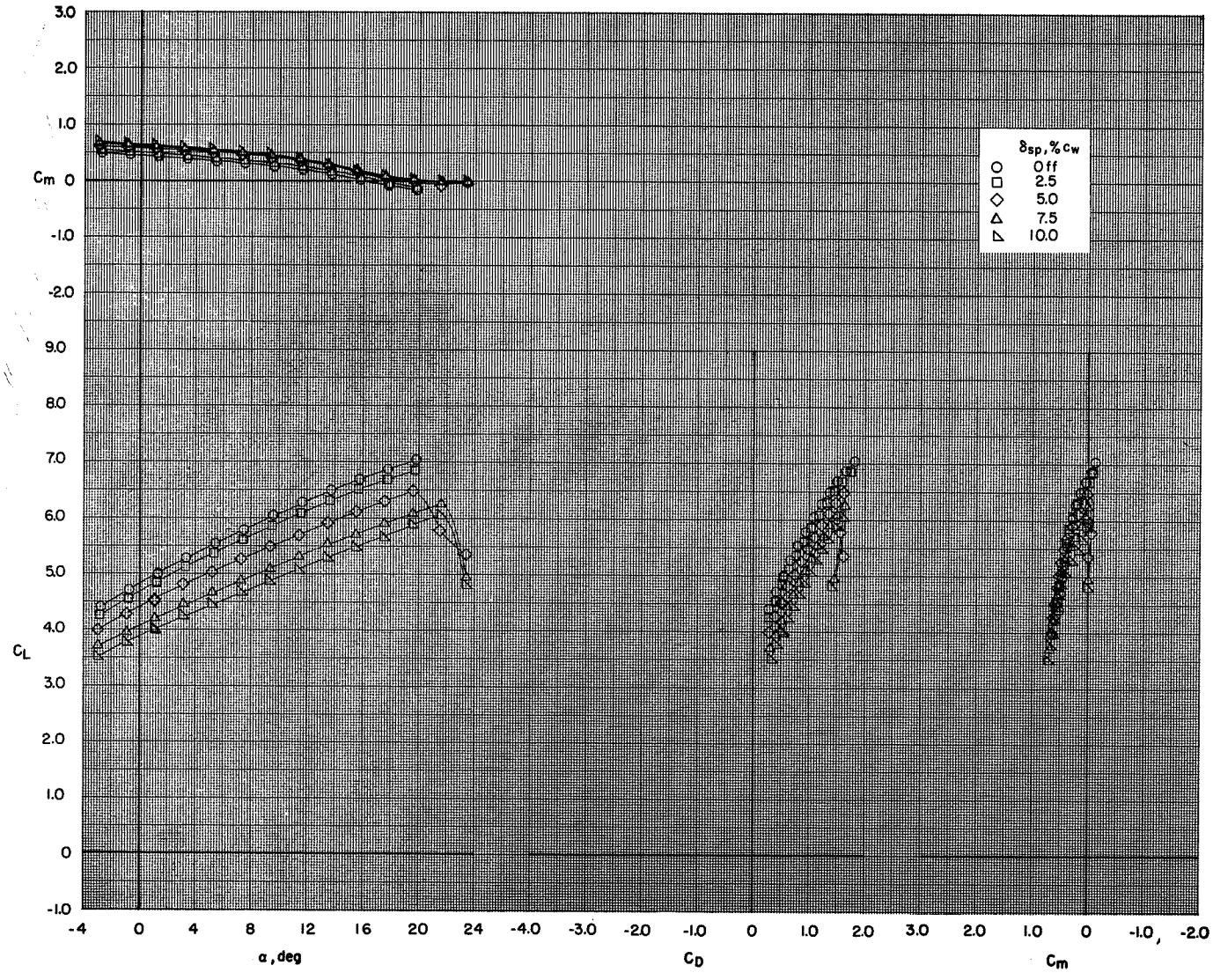

(c) $C_T = 2.72$.

Figure 66.- Continued.

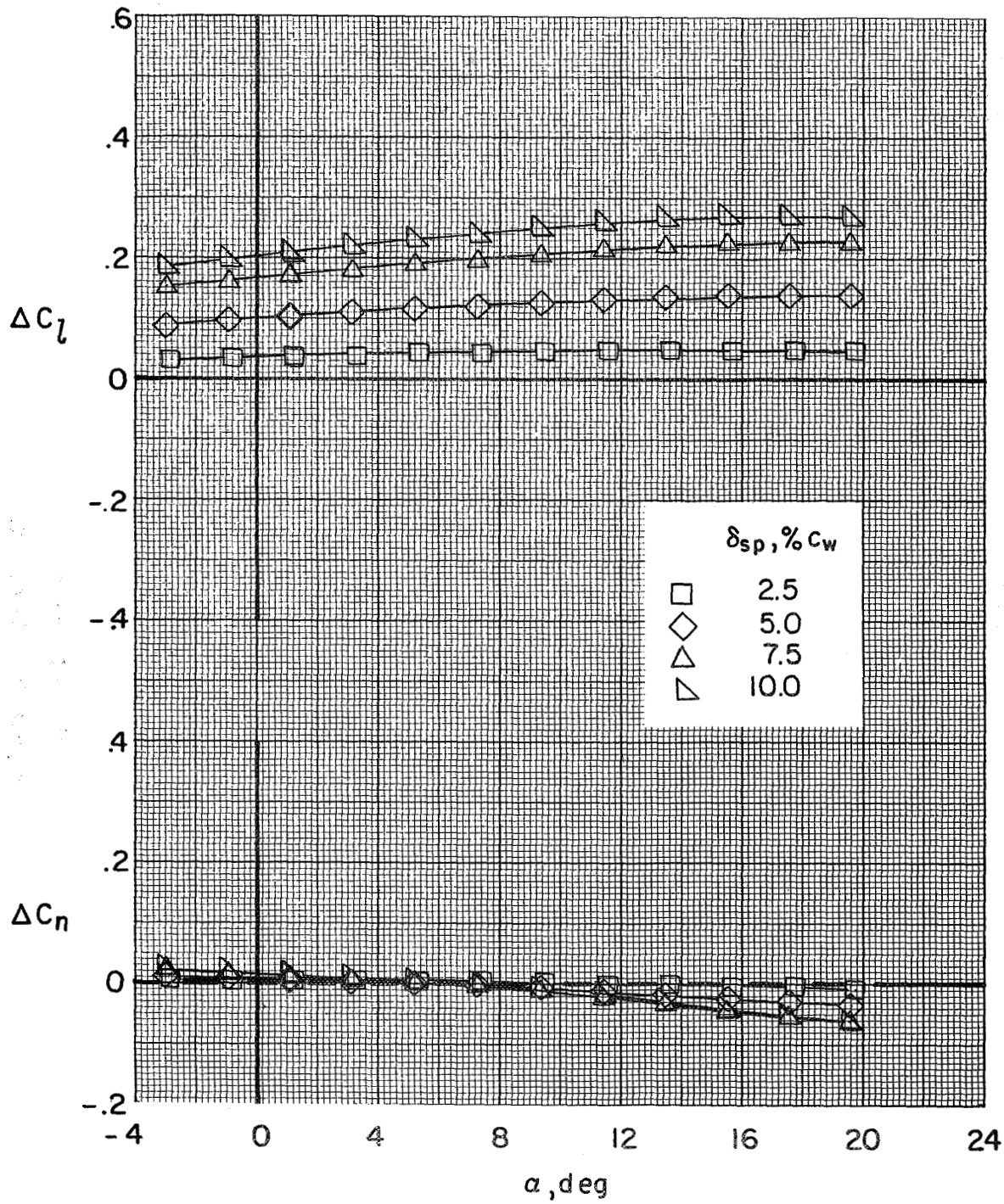

(c) Concluded.

Figure 66.- Concluded.

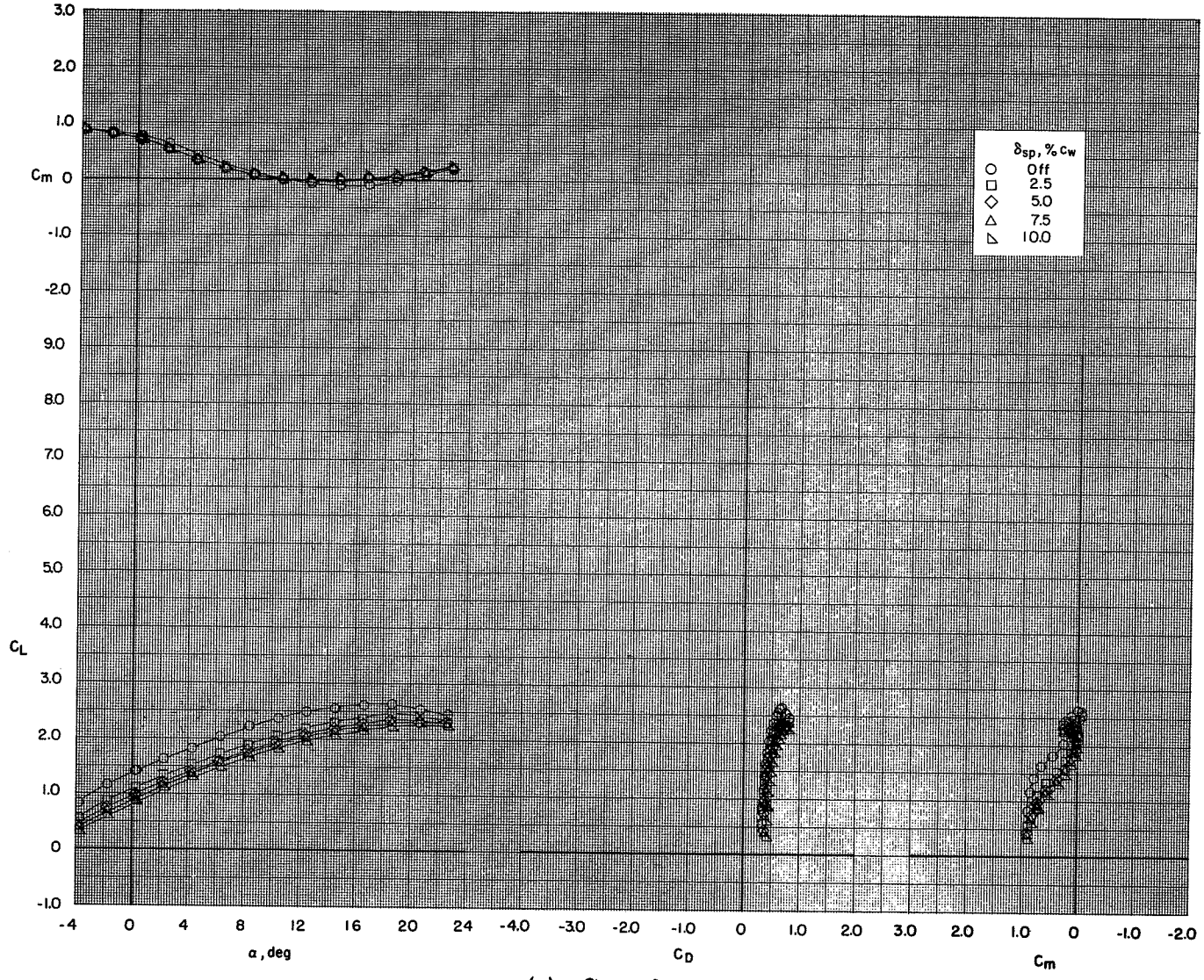

(a) $C_T = 0$.

Figure 67.- Effect of spoiler projection on the aerodynamic characteristics of the model with flaps deflected and leading-edge slat on. BPR 6.2; T-tail at 5^o; $\delta_f = 0^o/65^o/65^o$; c_S = 25 percent; $\delta_S = 50^o$; left inboard engine out.

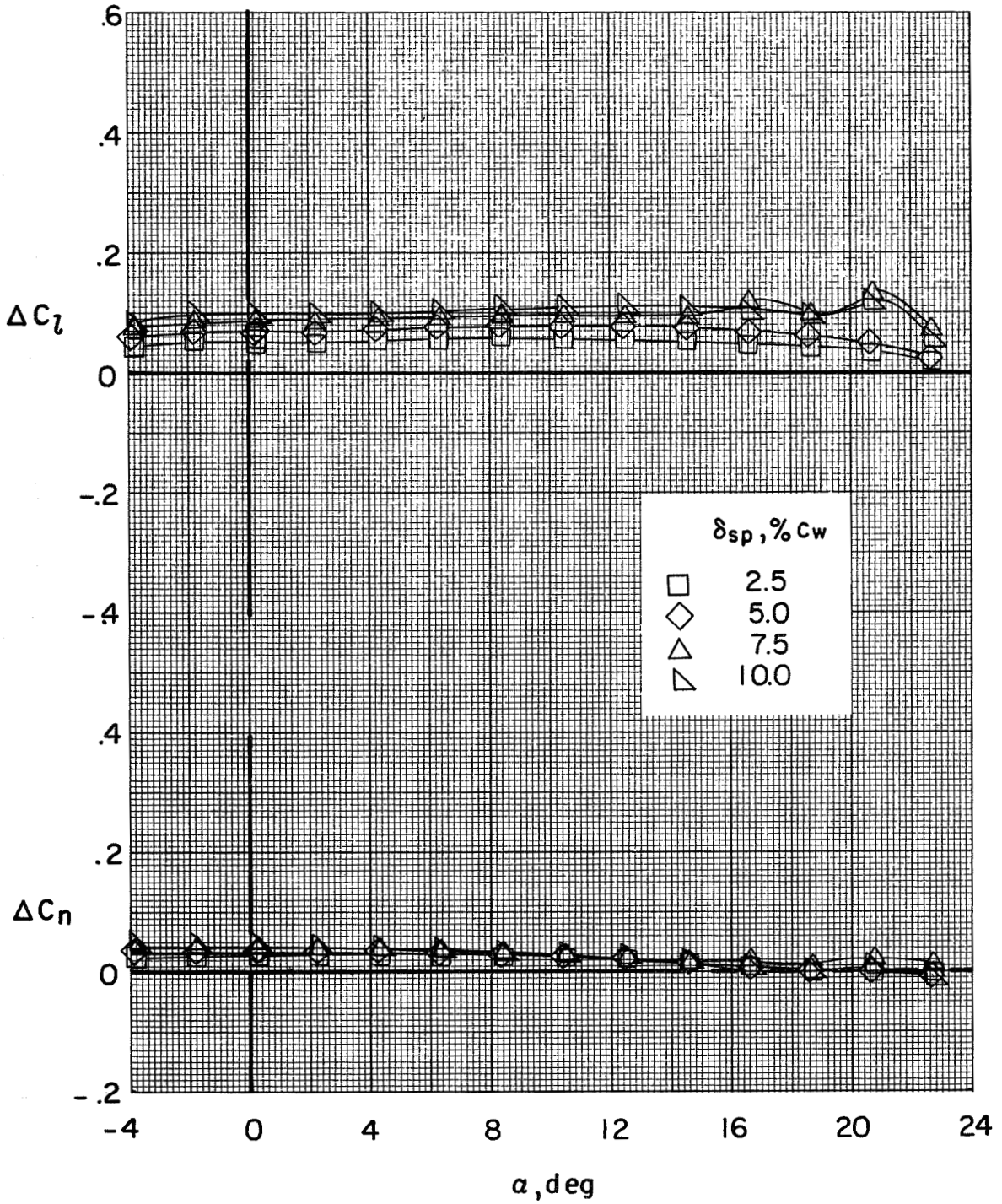

(a) Concluded.

Figure 67.- Continued.

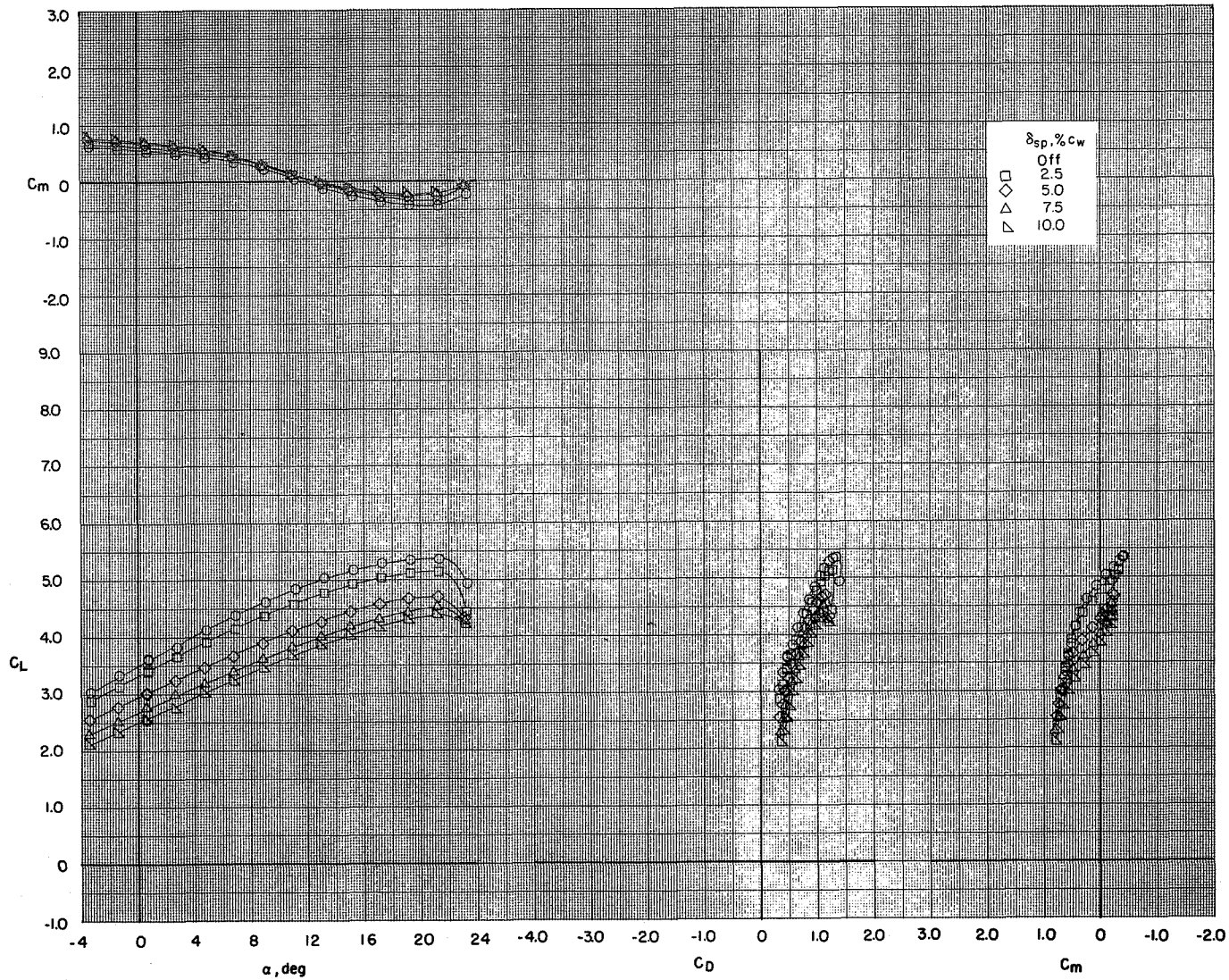

(b) $C_T = 1.36$.

Figure 67.- Continued.

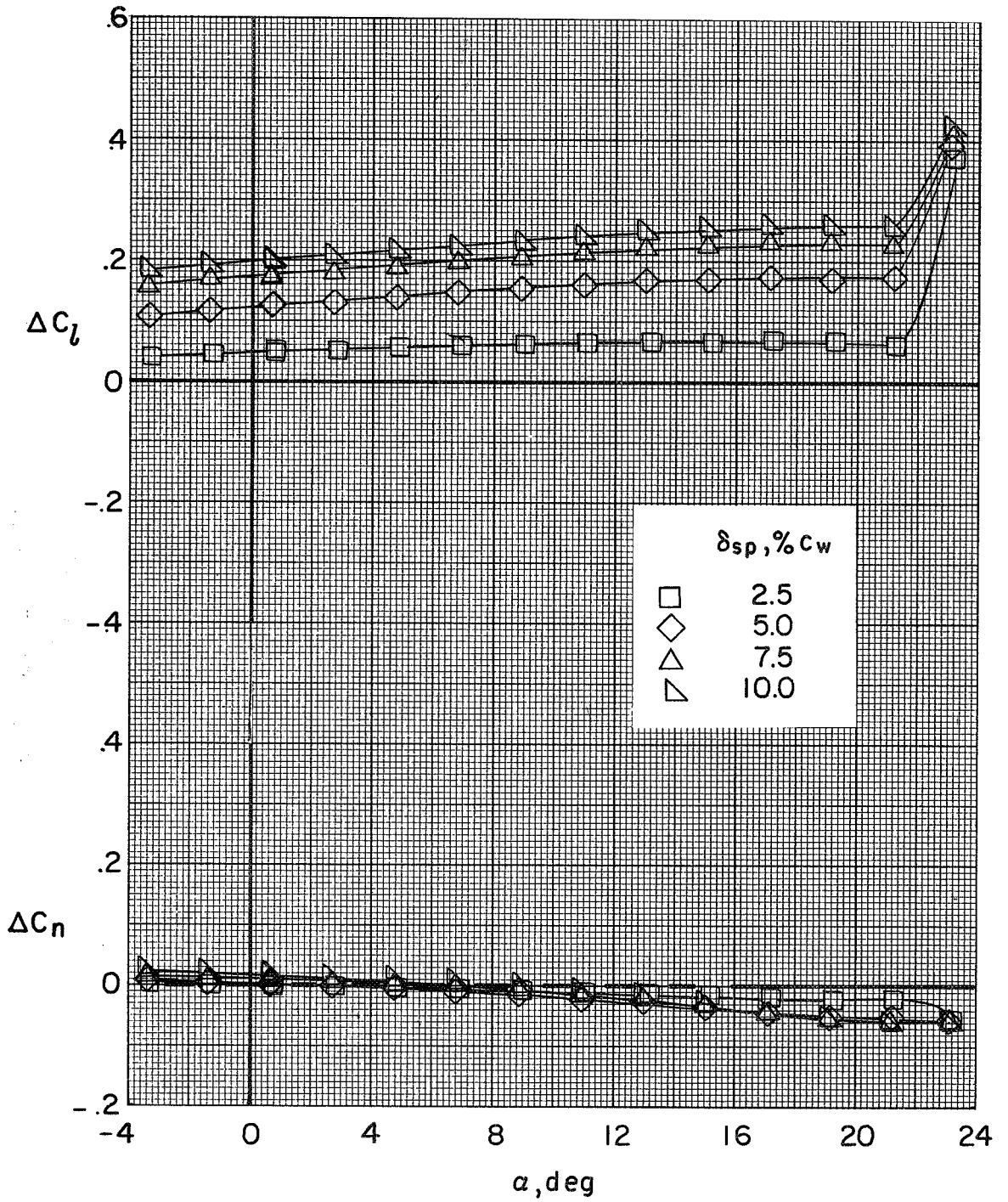

(b) Concluded.

Figure 67.- Continued.

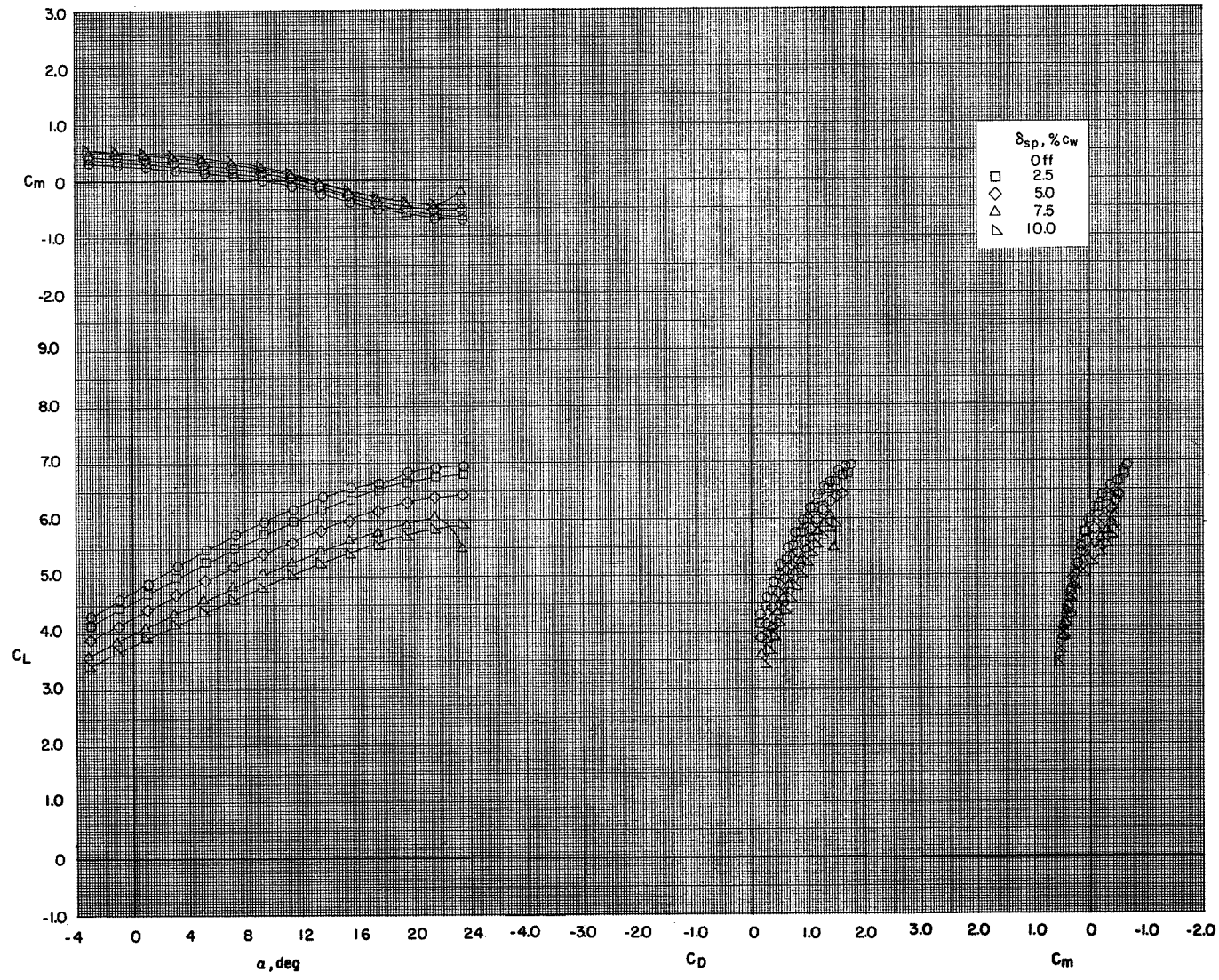

(c) $C_T = 2.72$.

Figure 67.- Continued.

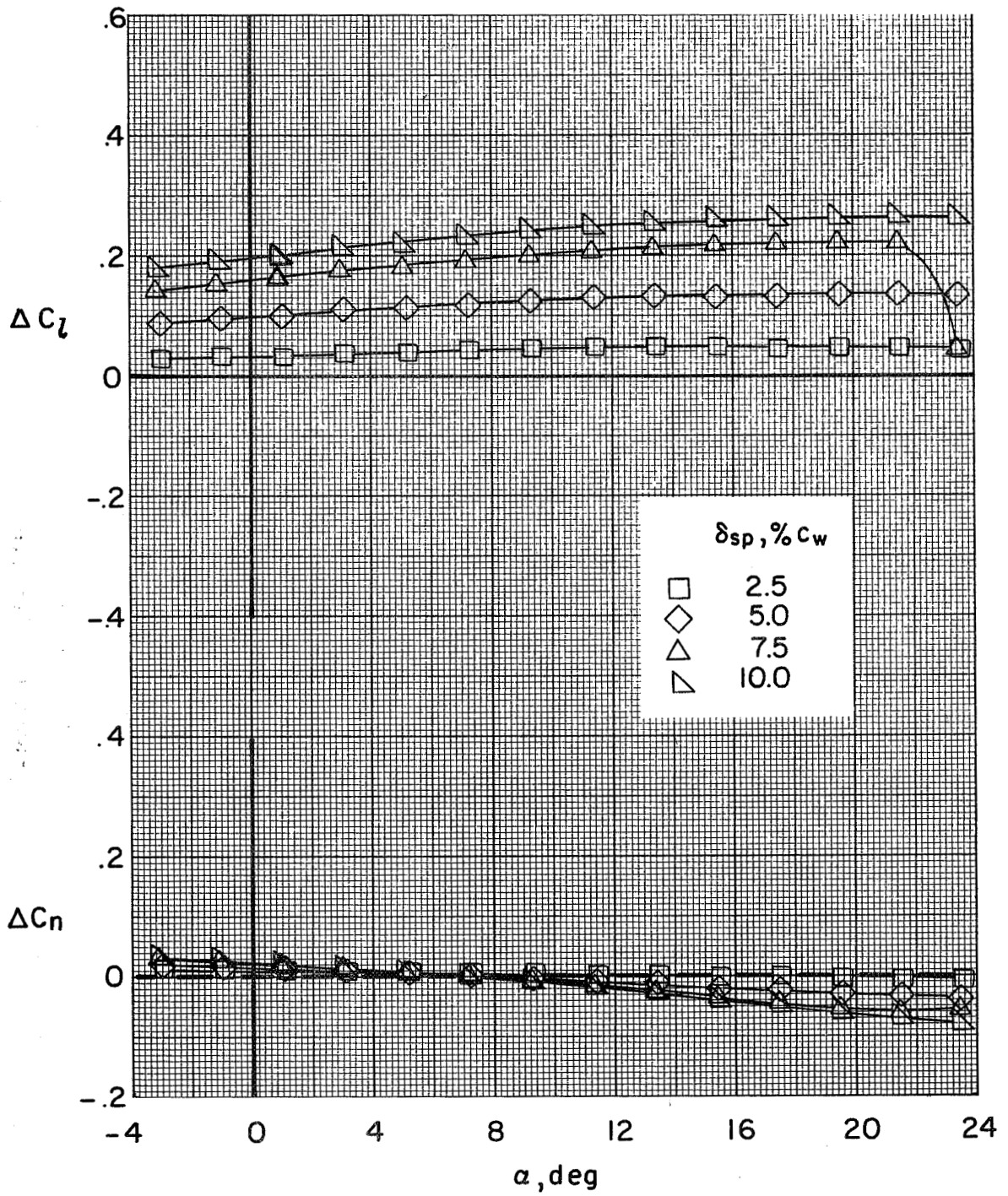

(c) Concluded.

Figure 67.- Concluded.

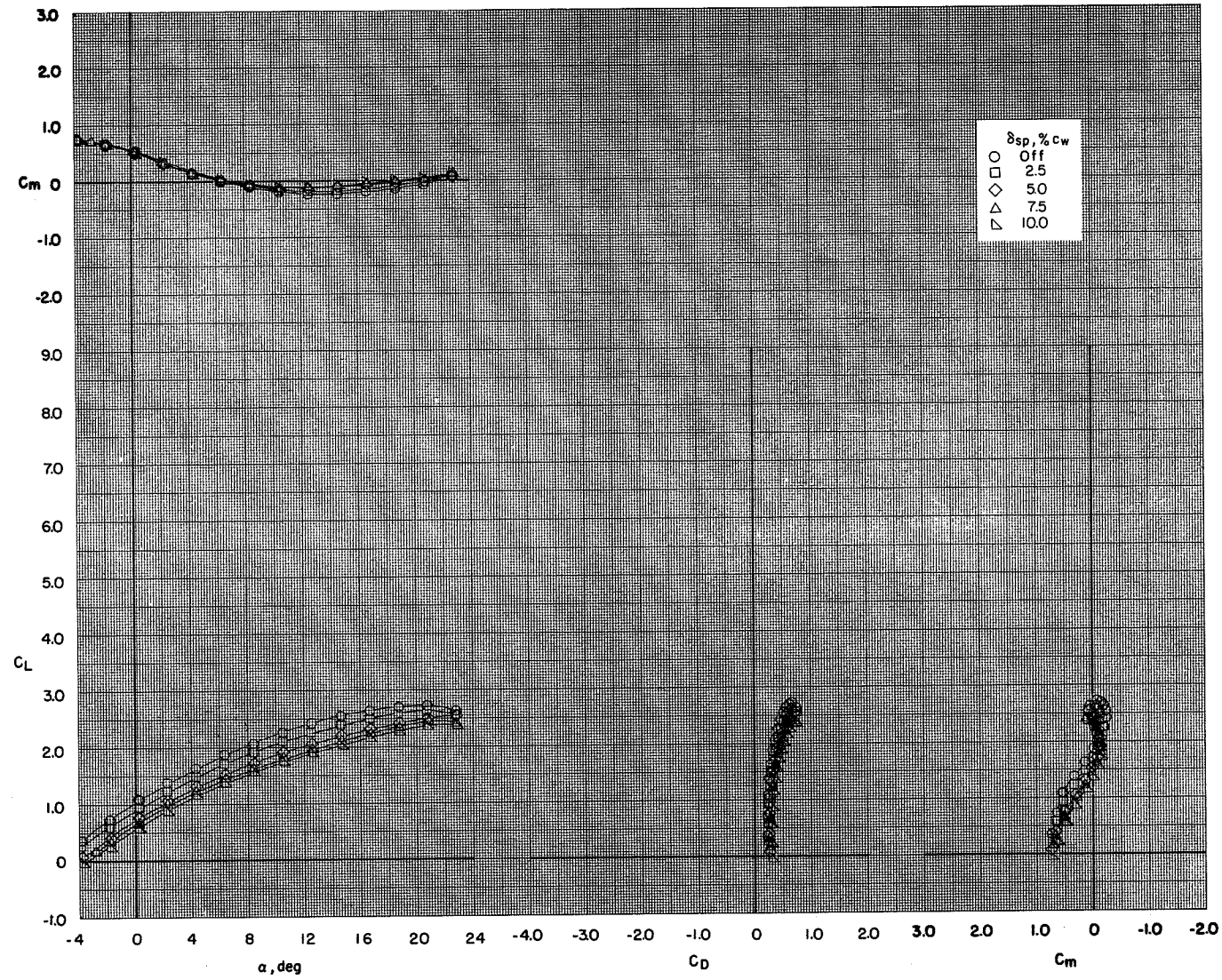

(a) $C_T = 0$.

Figure 68.- Effect of spoiler projection on the aerodynamic characteristics of the model with flaps deflected and leading-edge slat on. BPR 10.0; T-tail at 5^o; $\delta_f = 0^o/35^o/35^o$; $c_s = 25$ percent; $\delta_s = 50^o$; symmetrical power.

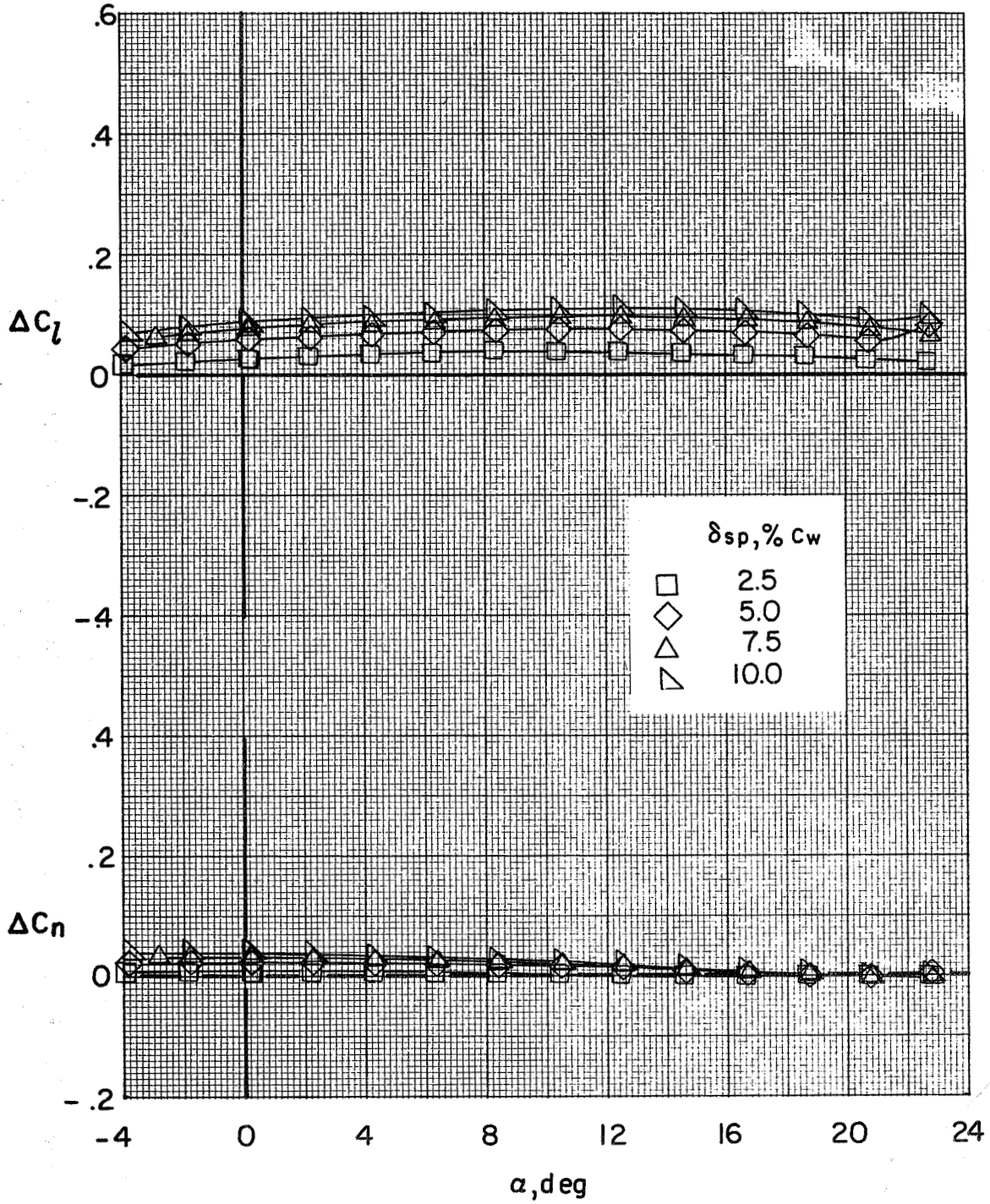

(a) Concluded.

Figure 68.- Continued.

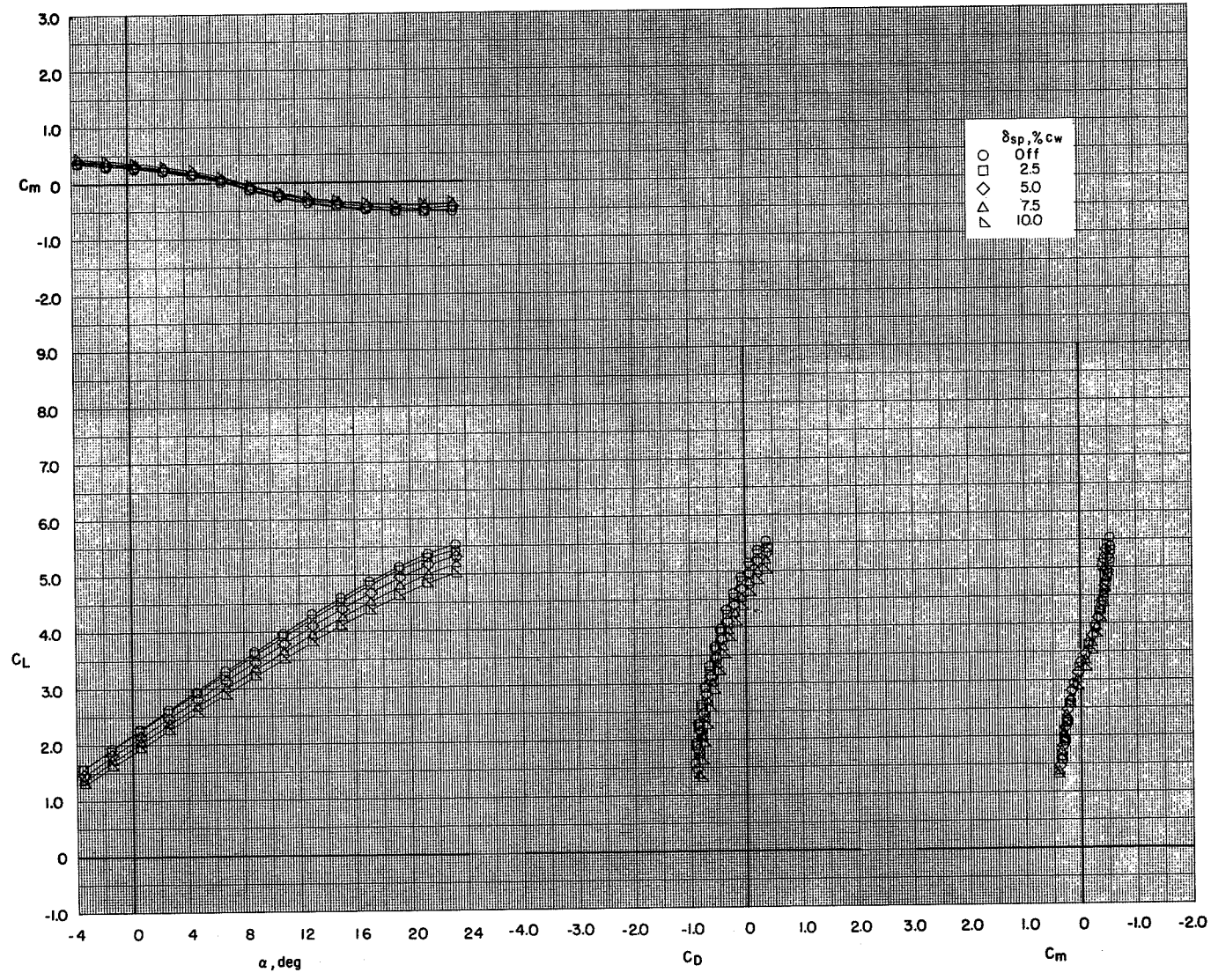

(b) $C_T = 2.26$.

Figure 68.- Continued.

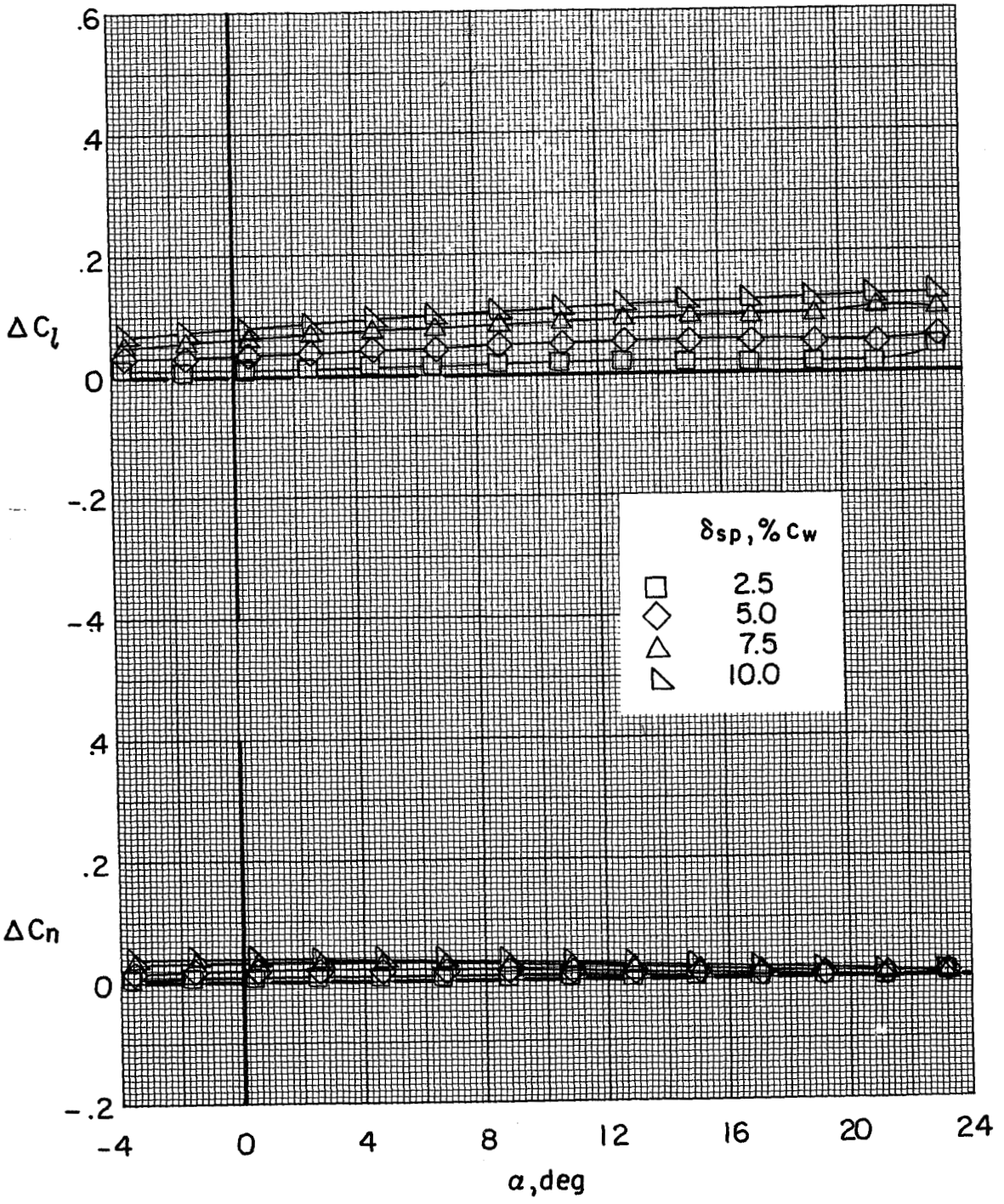

(b) Concluded.

Figure 68.- Continued.

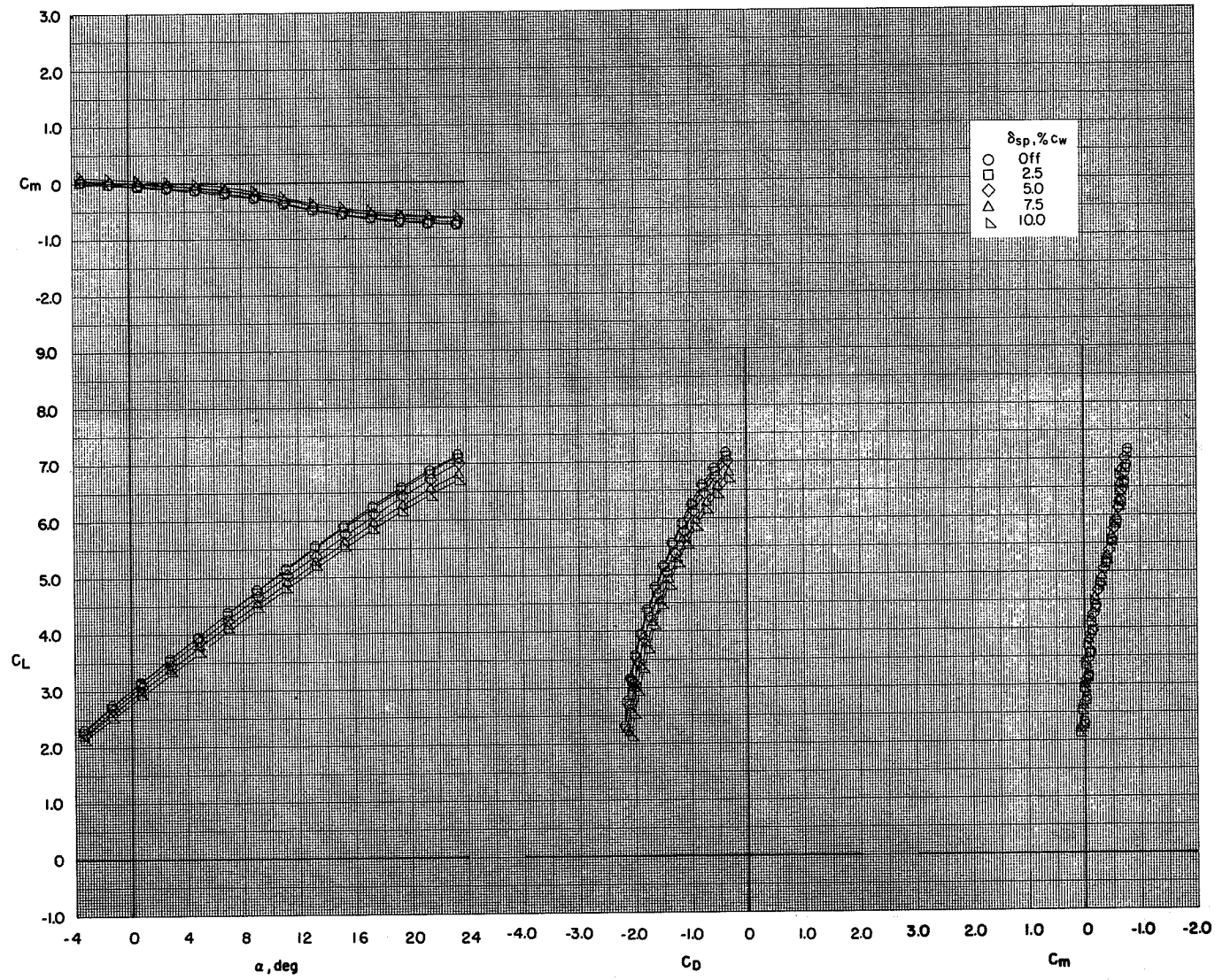

(c) $C_T = 4.06$.

Figure 68.- Continued.

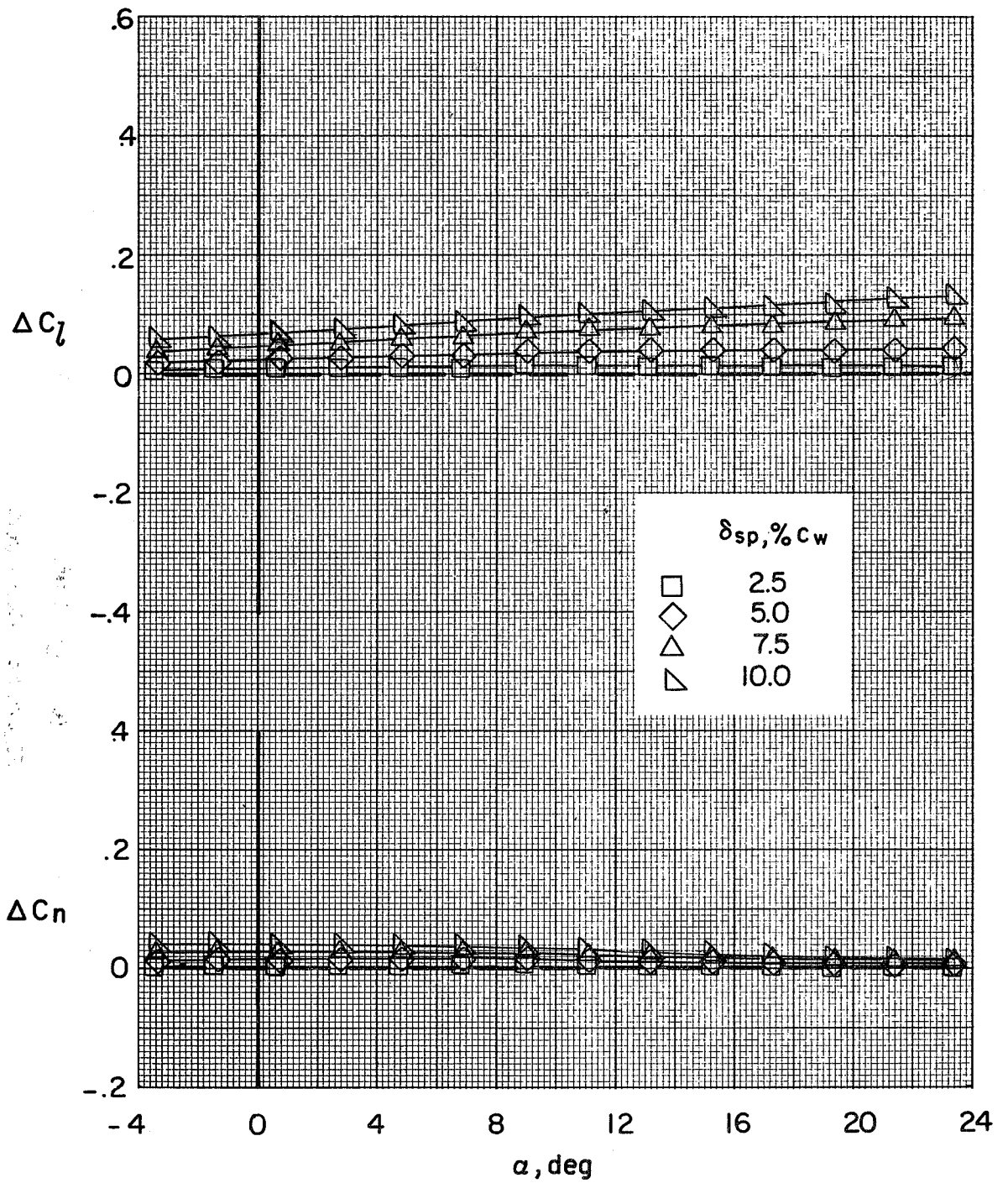

(c) Concluded.

Figure 68.- Concluded.

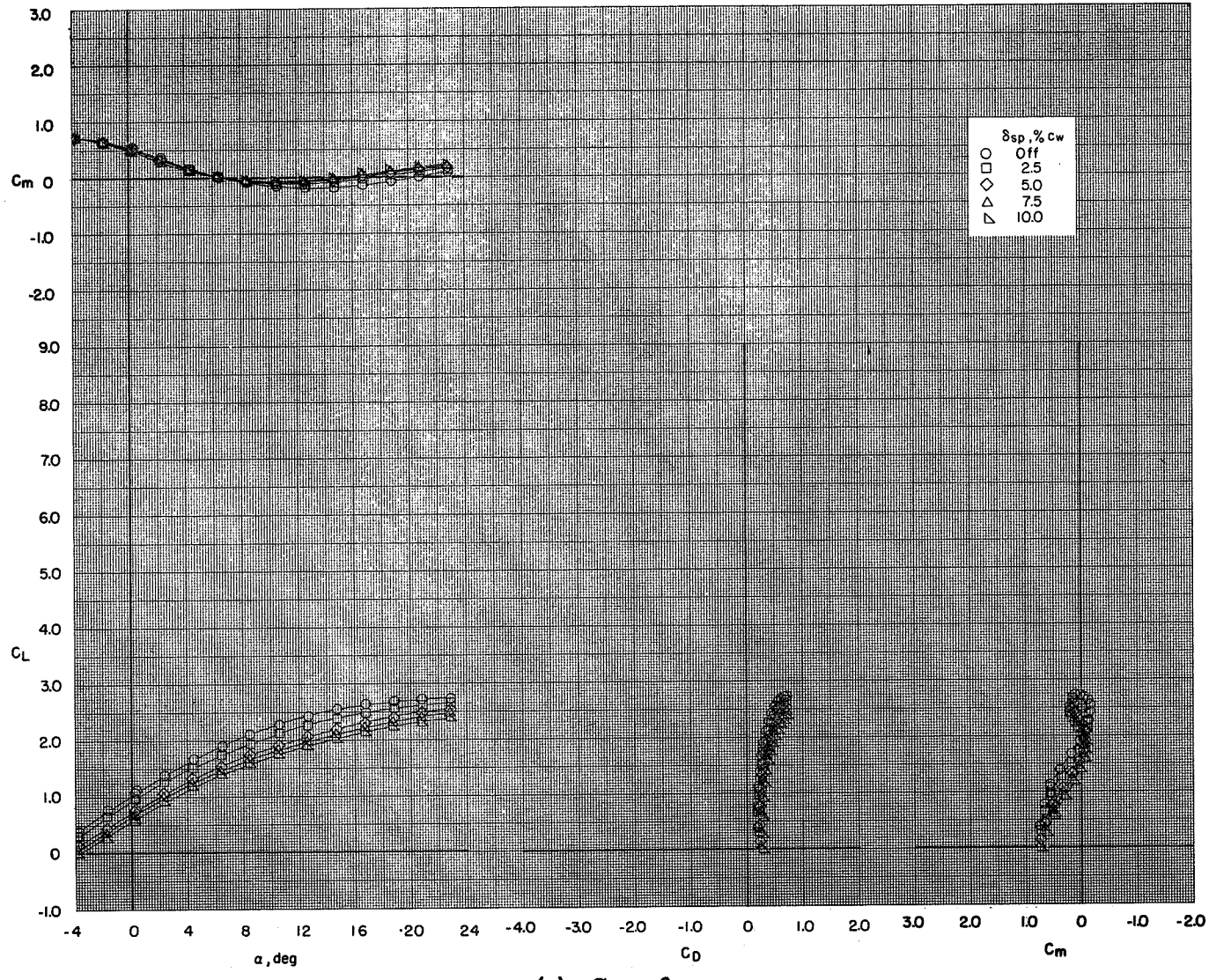

(a) $C_T = 0.$

Figure 69.- Effect of spoiler projection on the aerodynamic characteristics of the model with flaps deflected and leading-edge slat on. BPR 10.0; T-tail at 5^o; $\delta_f = 0^o/35^o/35^o$; $c_s = 25$ percent; $\delta_s = 50^o$; left outboard engine out.

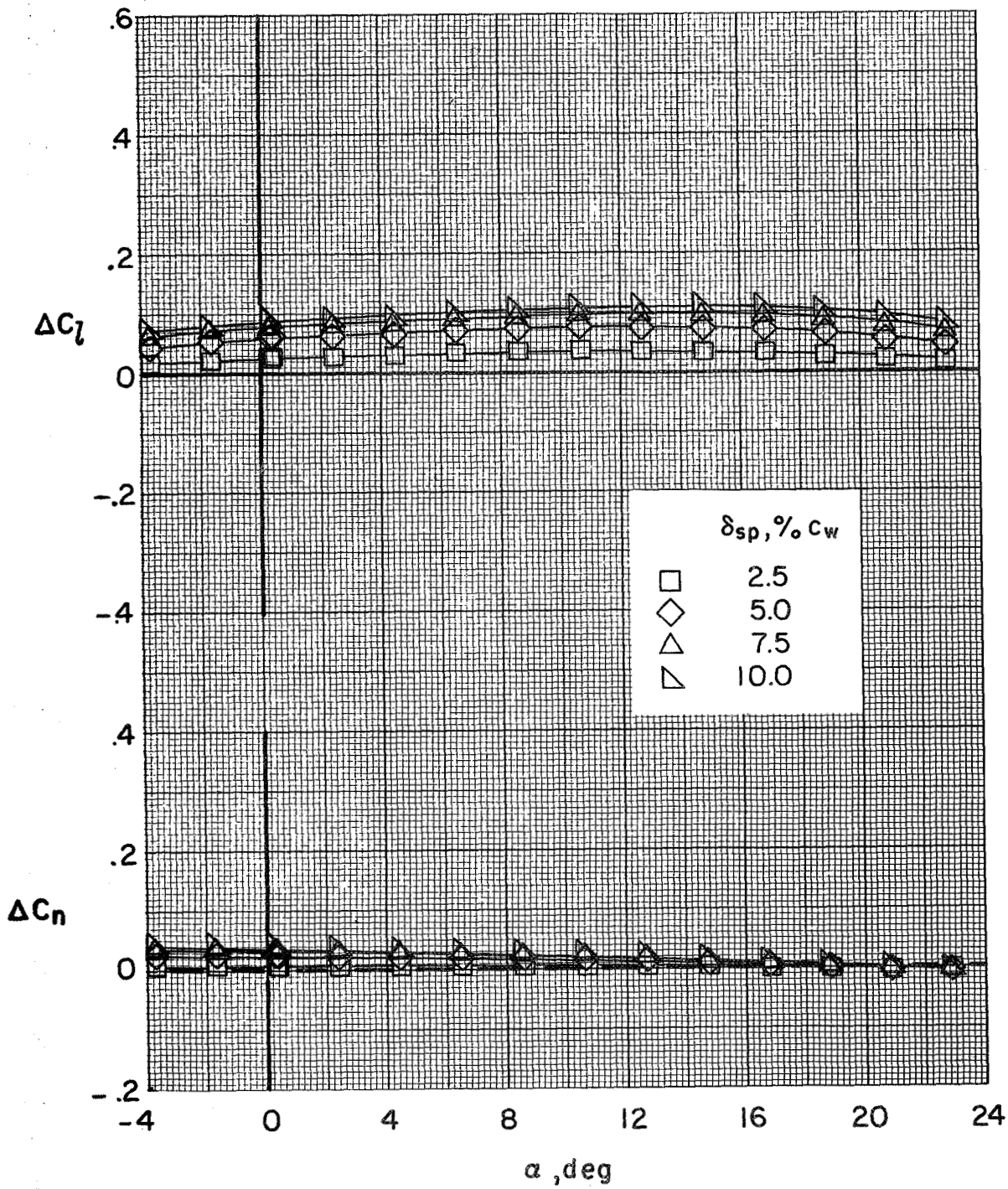

(a) Concluded.

Figure 69.- Continued.

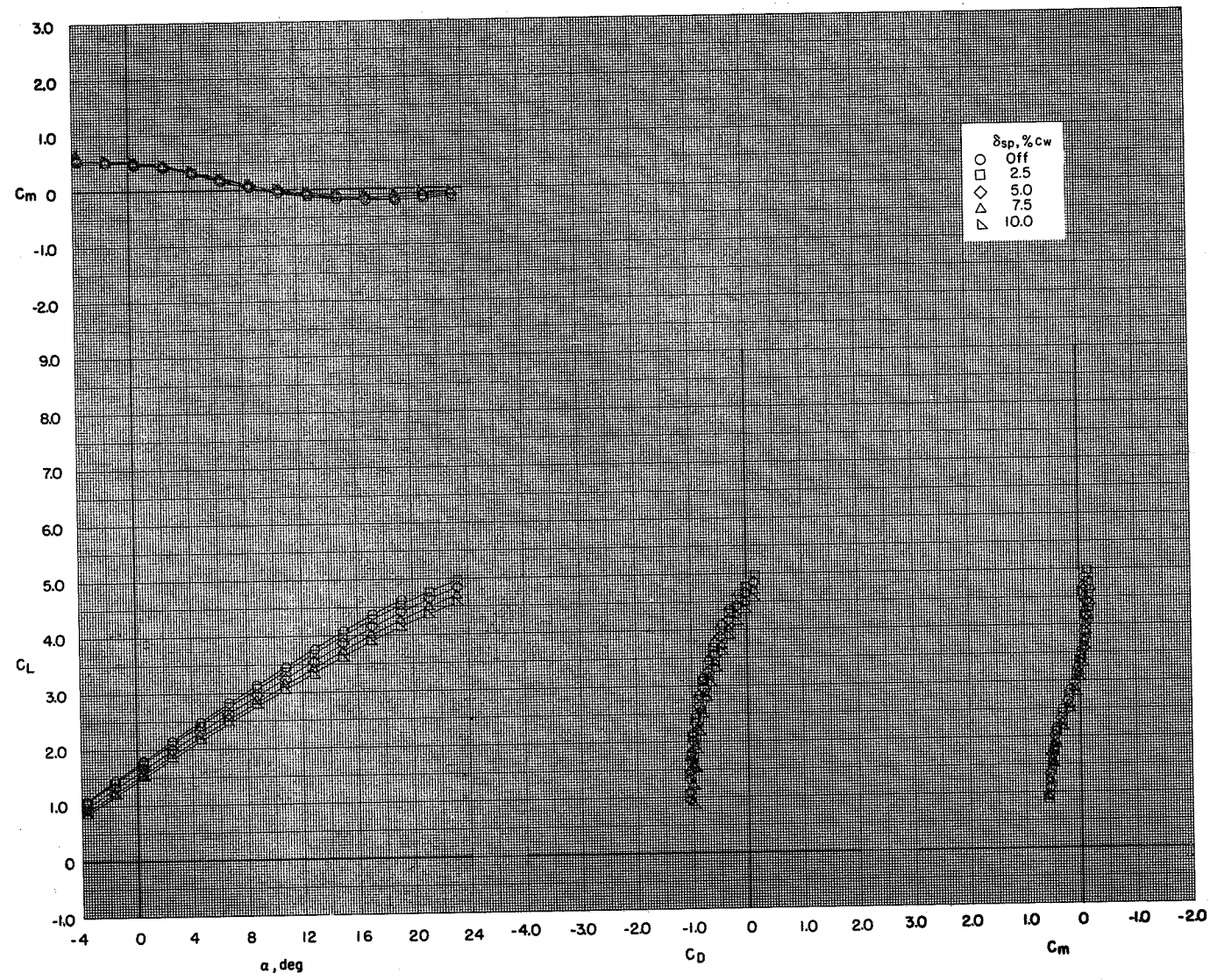

(b) $C_T = 1.69$.

Figure 69.- Continued.

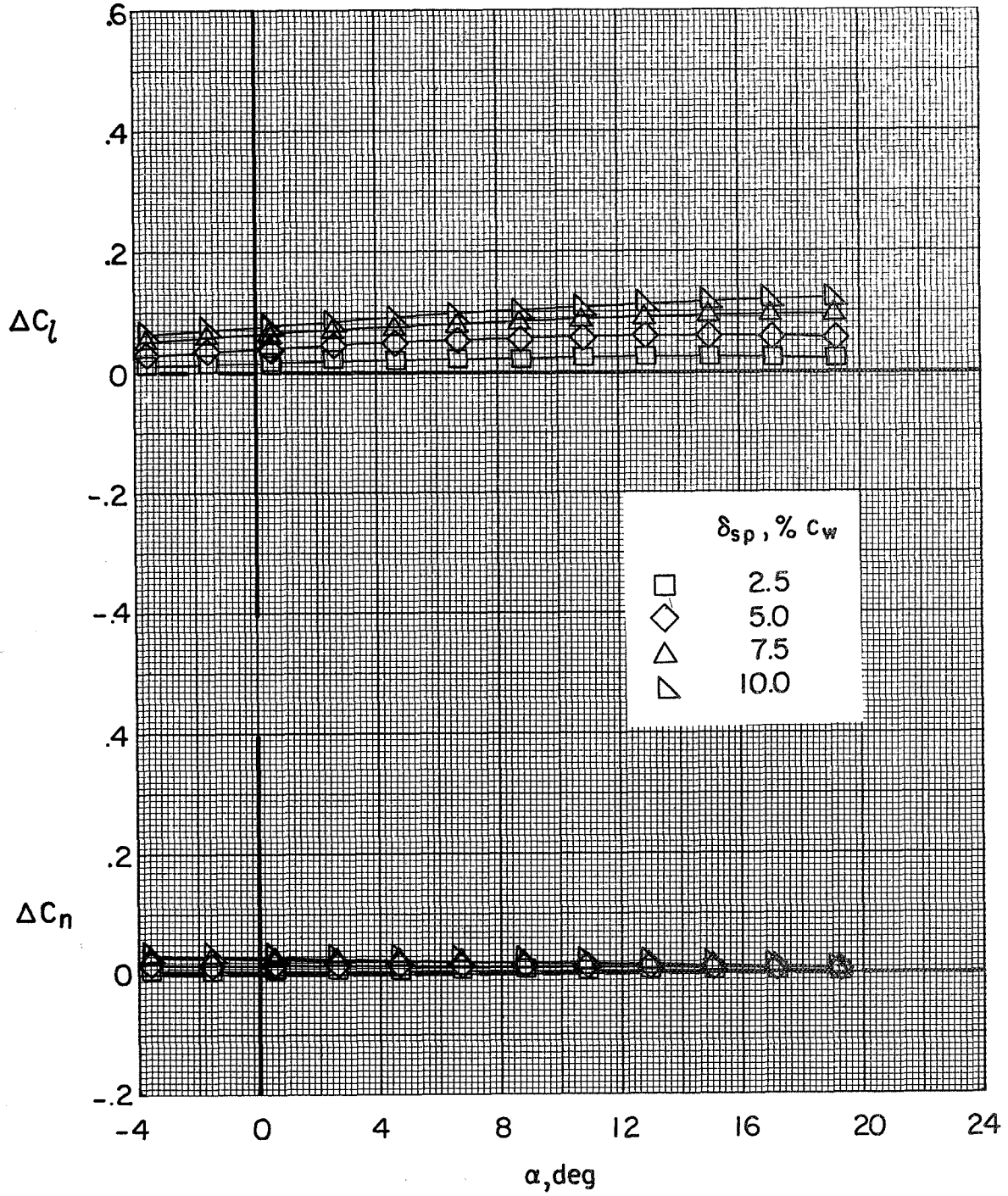

(b) Concluded.

Figure 69.- Continued.

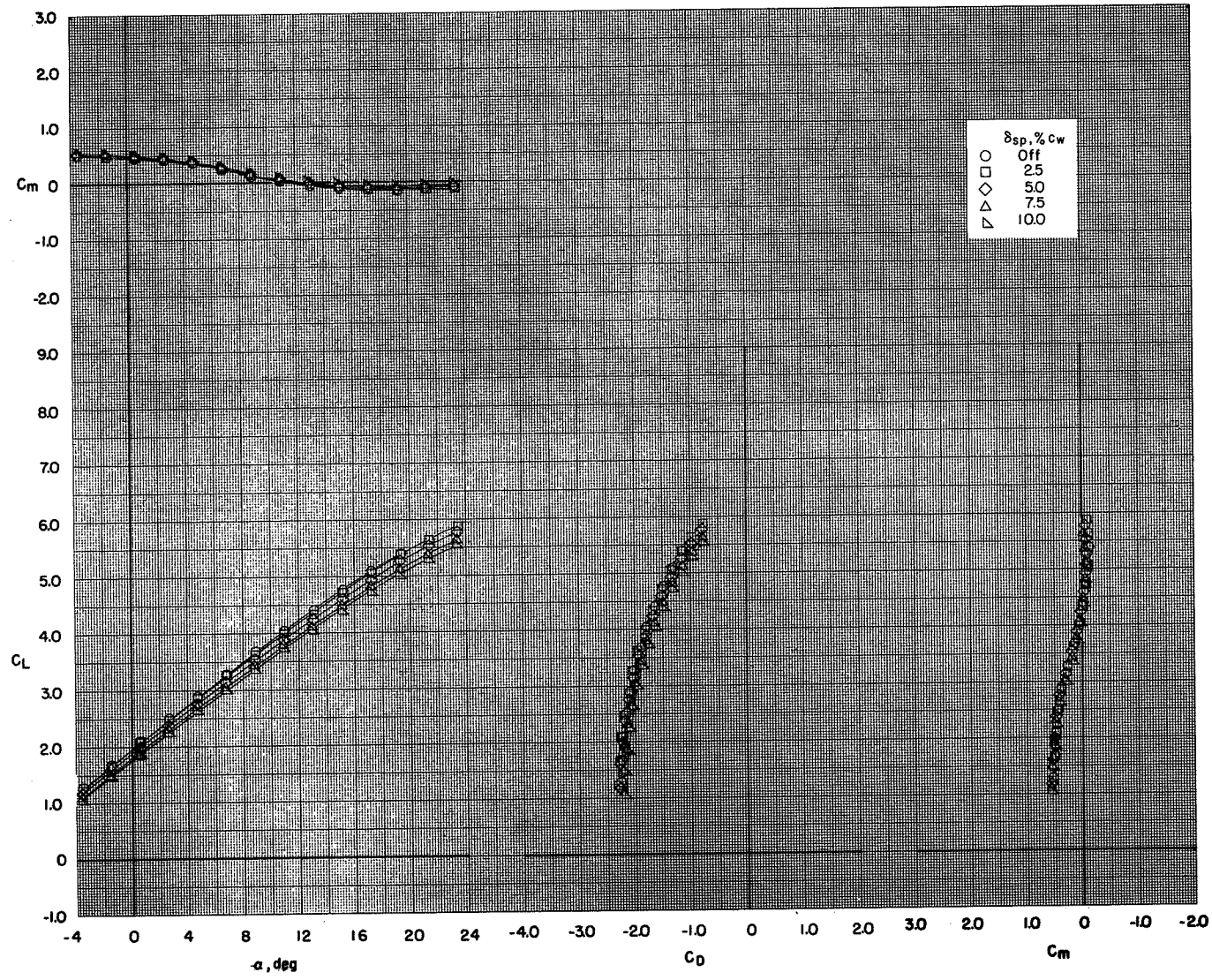

(c) $C_T = 3.04$.

Figure 69.- Continued.

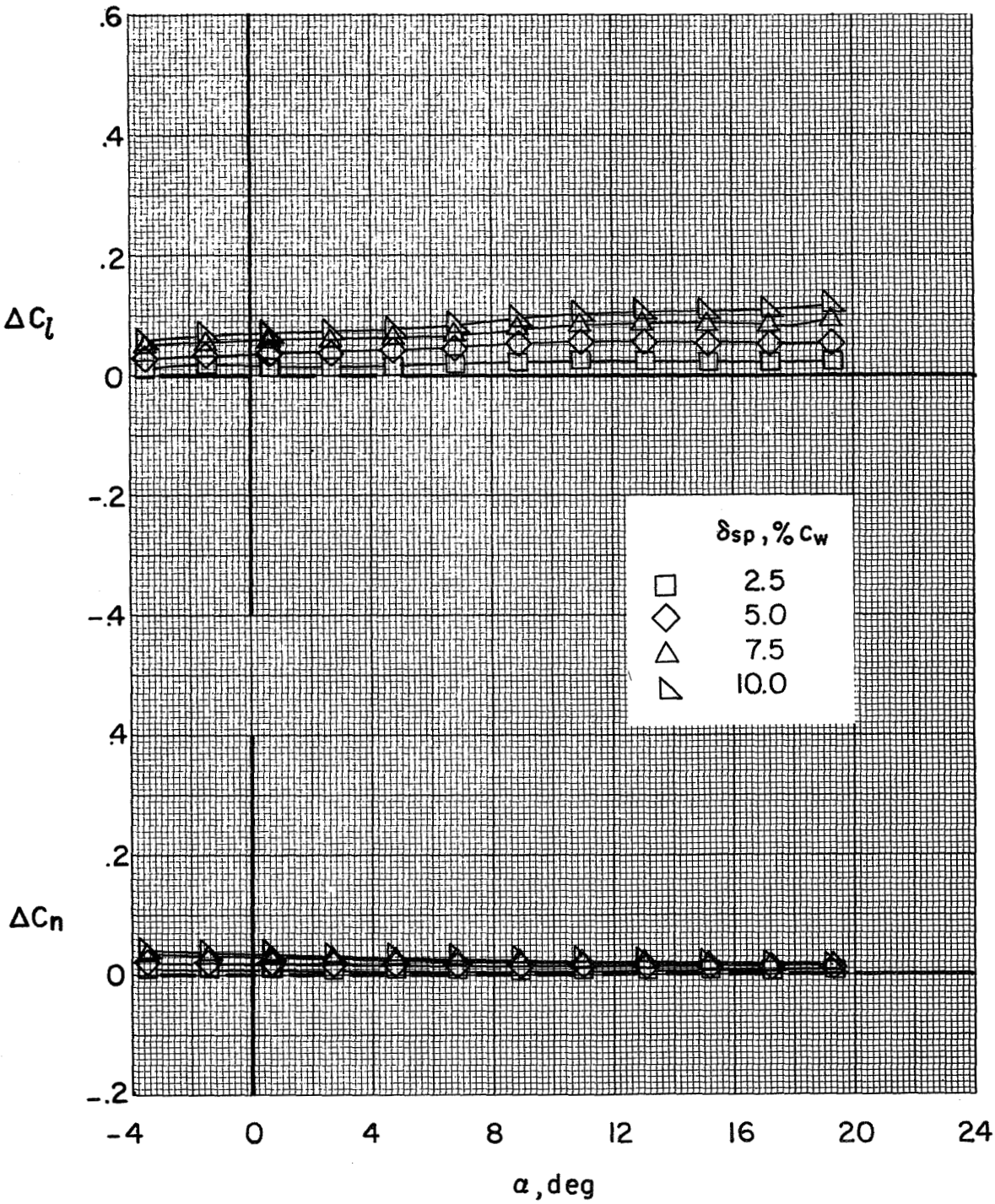

(c) Concluded.

Figure 69.- Concluded.

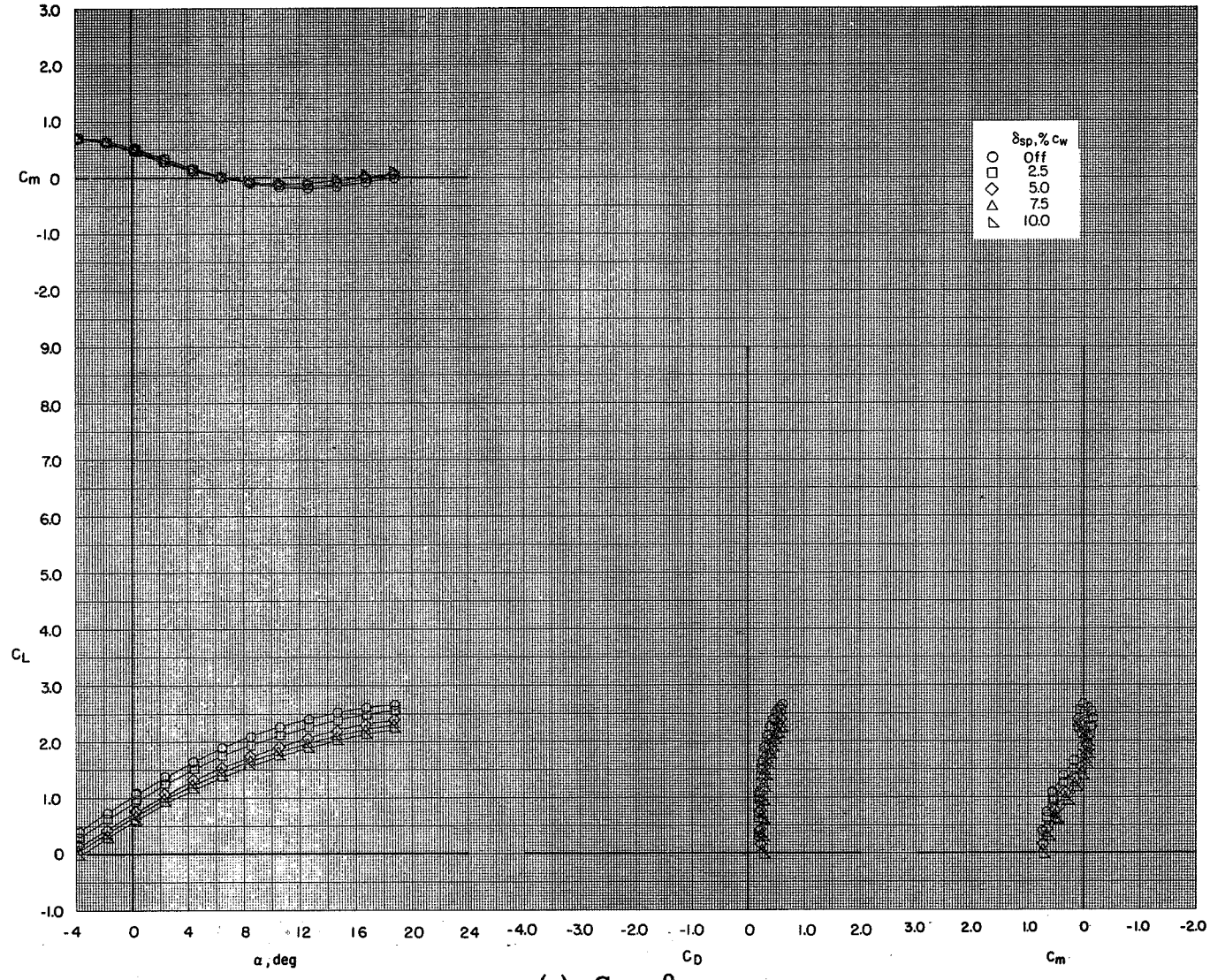

(a) $C_T = 0$.

Figure 70.- Effect of spoiler projection on the aerodynamic characteristics of the model with flaps deflected and leading-edge slat on. BPR 10.0; T-tail at 5^o; $\delta_f = 0^o/35^o/35^o$; c_s = 25 percent; $\delta_s = 50^o$; left inboard engine out.

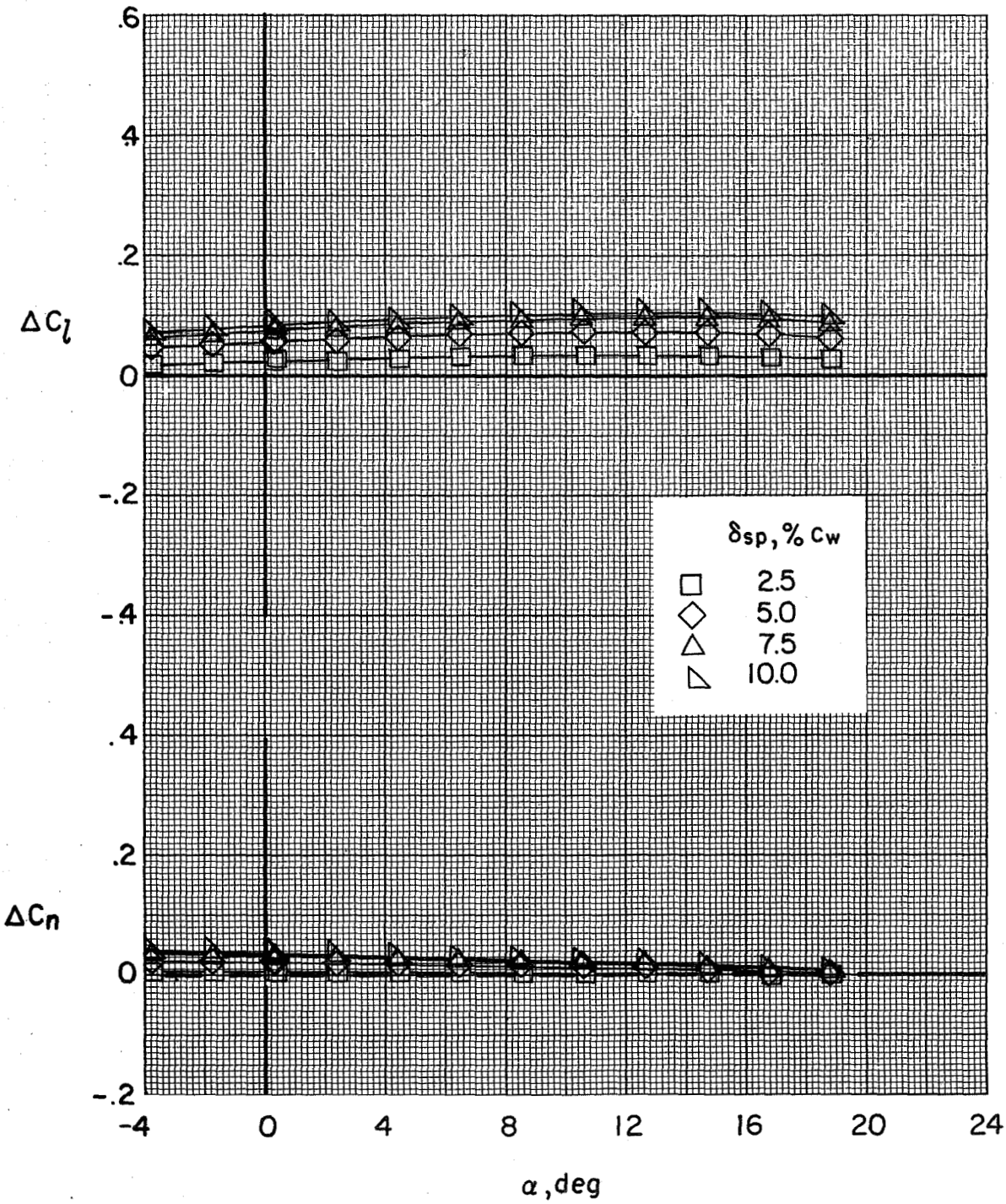

(a) Concluded.

Figure 70.- Continued.

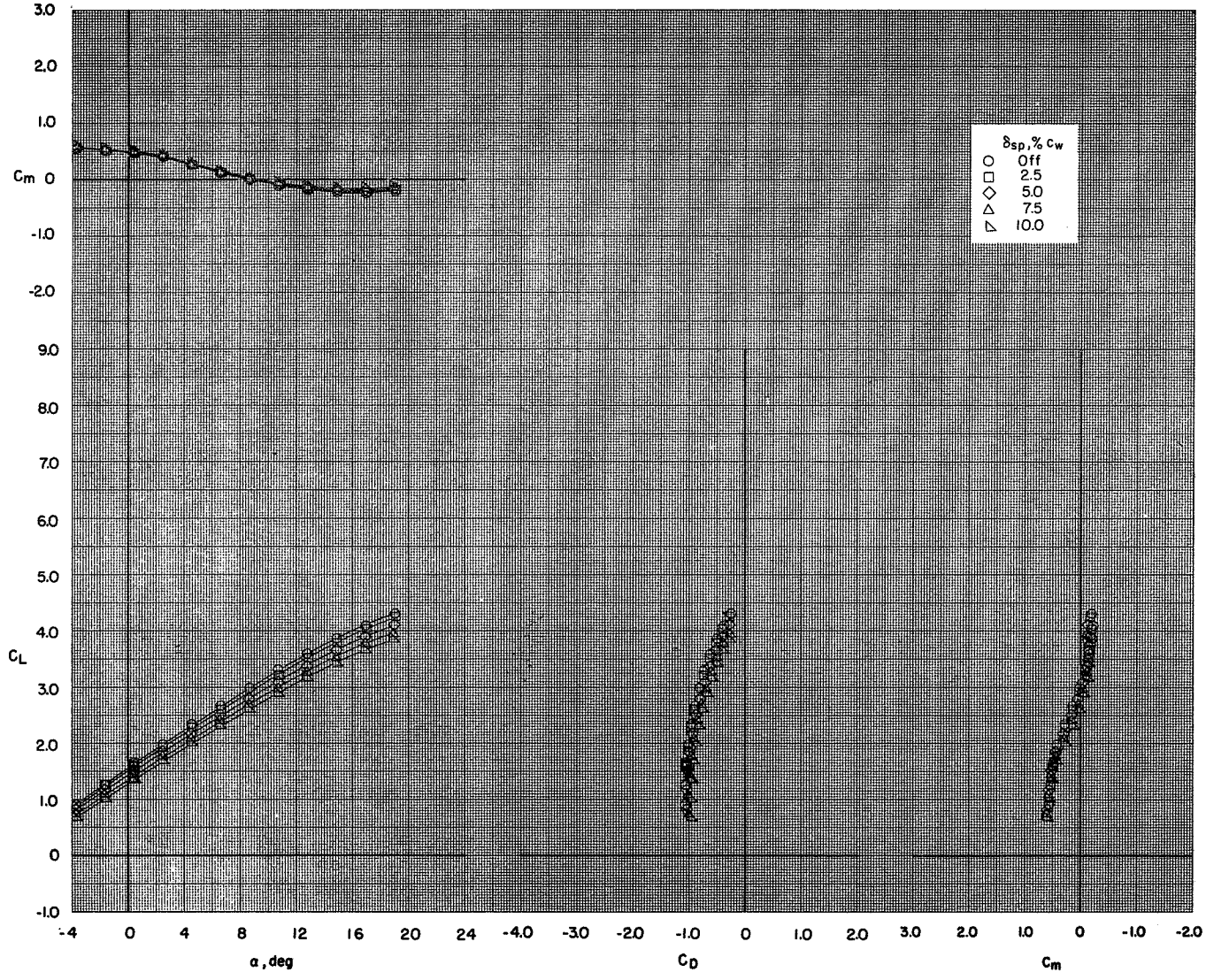

(b) $C_T = 1.69$.

Figure 70.- Continued.

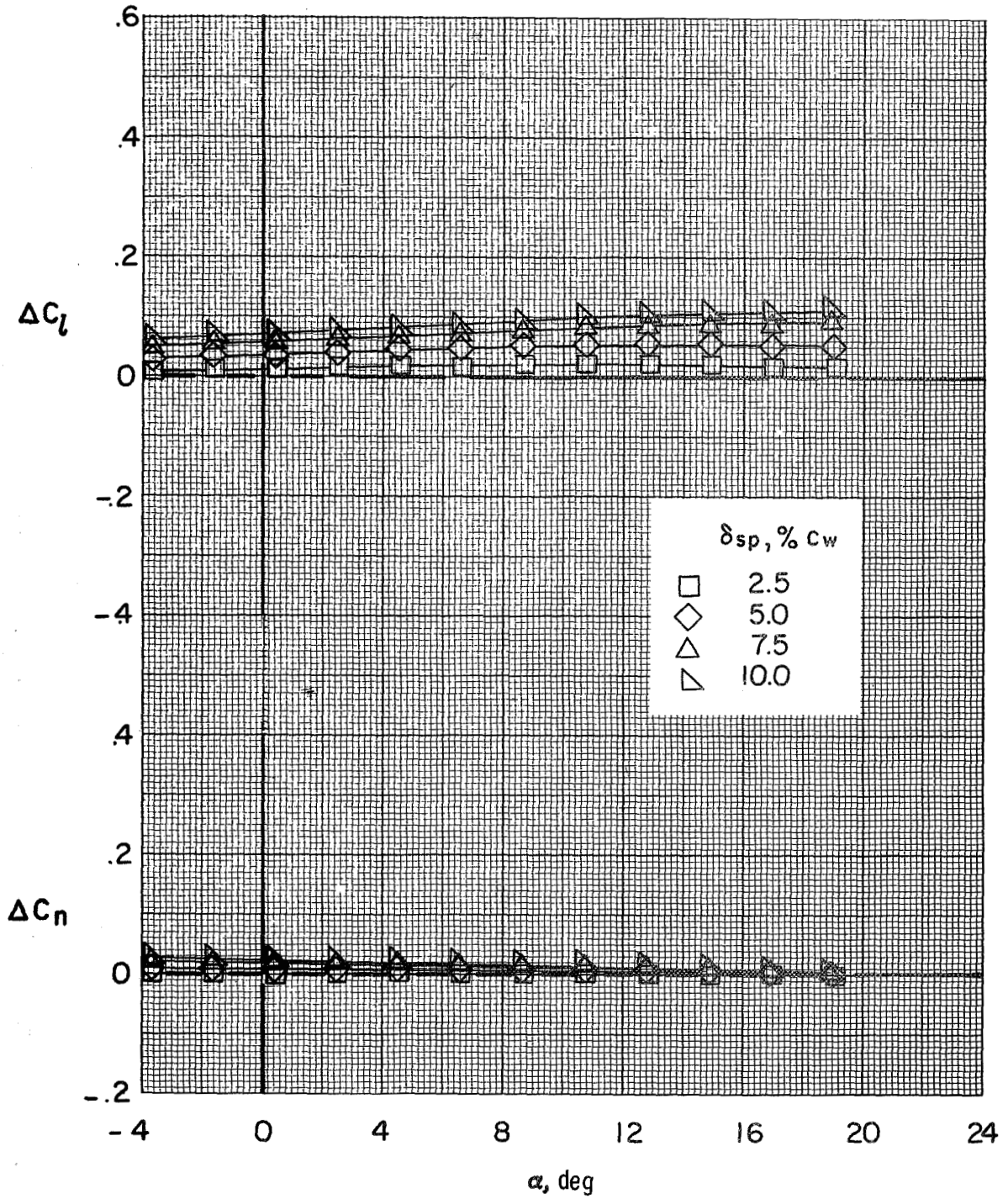

(b) Concluded.

Figure 70.- Continued.

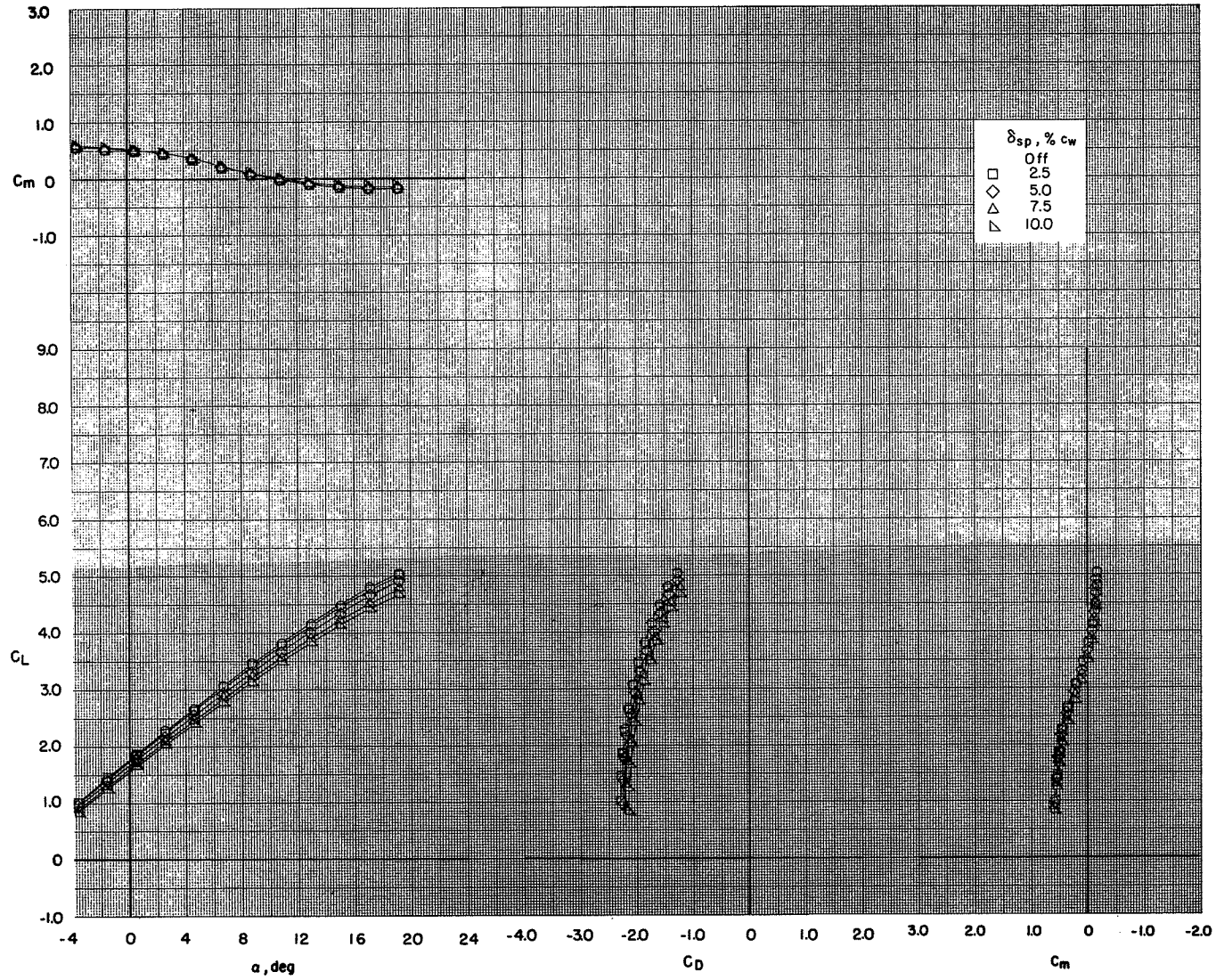

(c) $C_T = 3.04$.

Figure 70.- Continued.

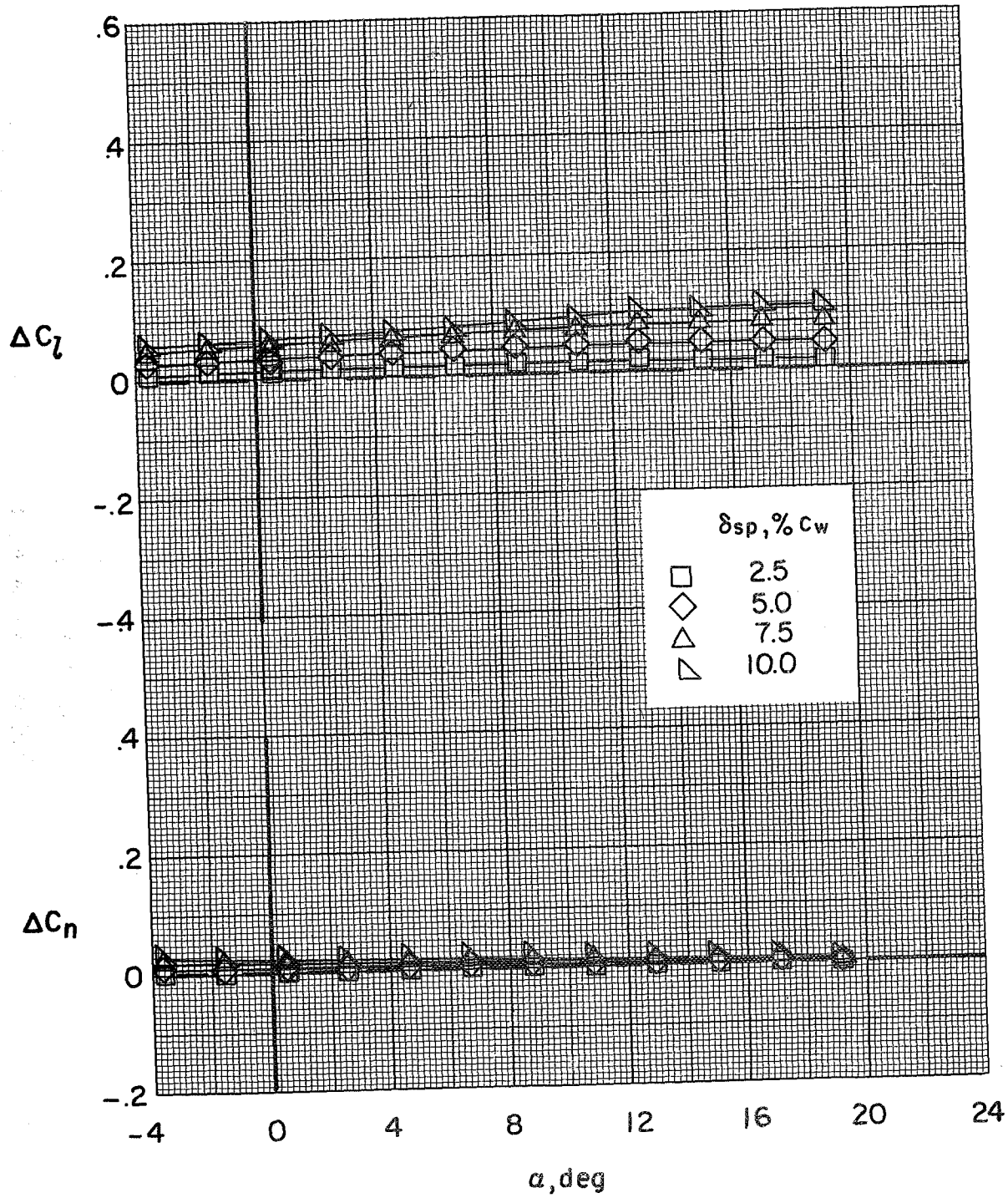

(c) Concluded.

Figure 70.- Concluded.

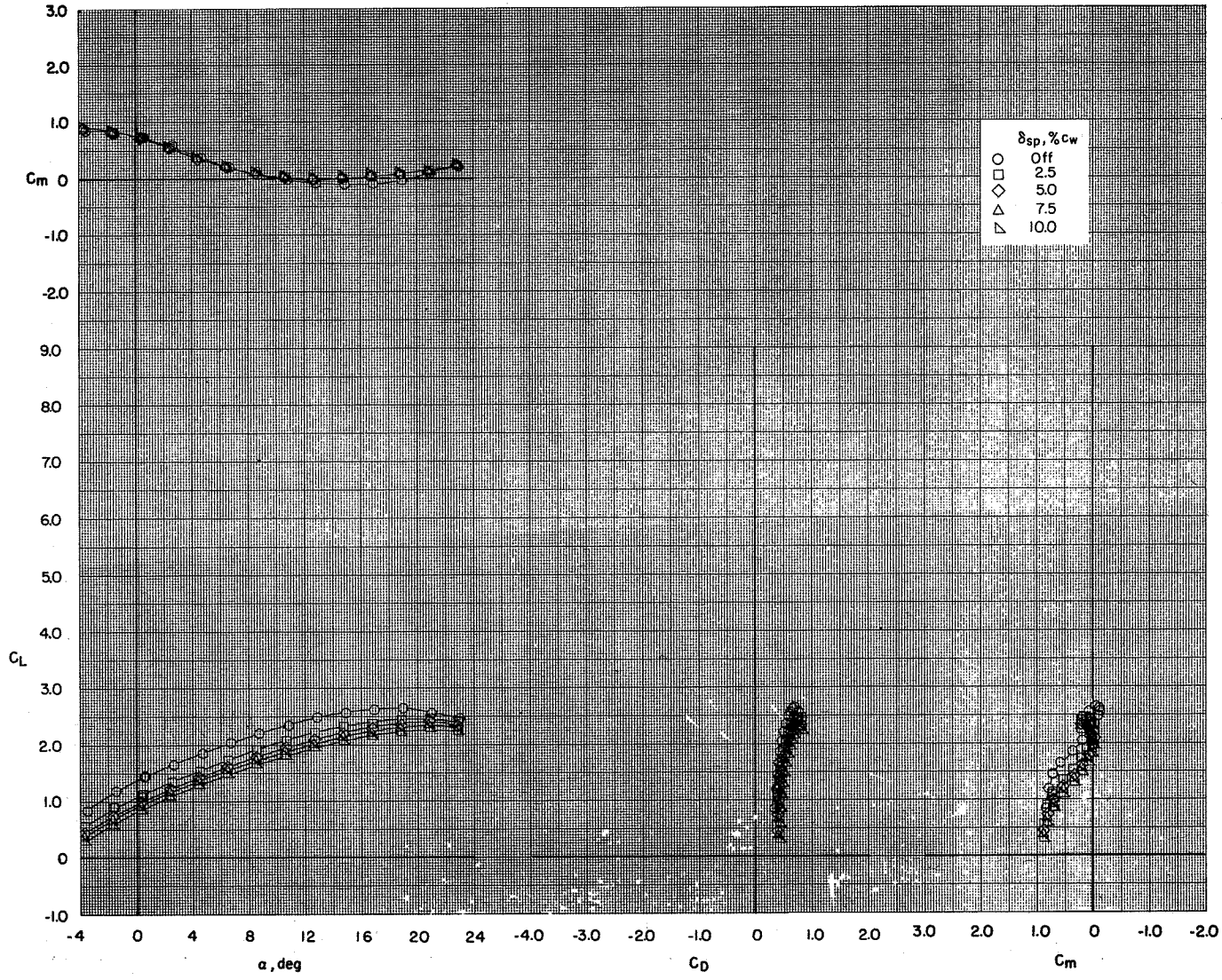

(a) $C_T = 0$.

Figure 71.- Effect of spoiler projection on the aerodynamic characteristics of the model with flaps deflected and leading-edge slat on. BPR 10.0; T-tail at 5^o; $\delta_f = 0^o/65^o/65^o$; $c_s = 25$ percent; $\delta_s = 50^o$; symmetrical power.

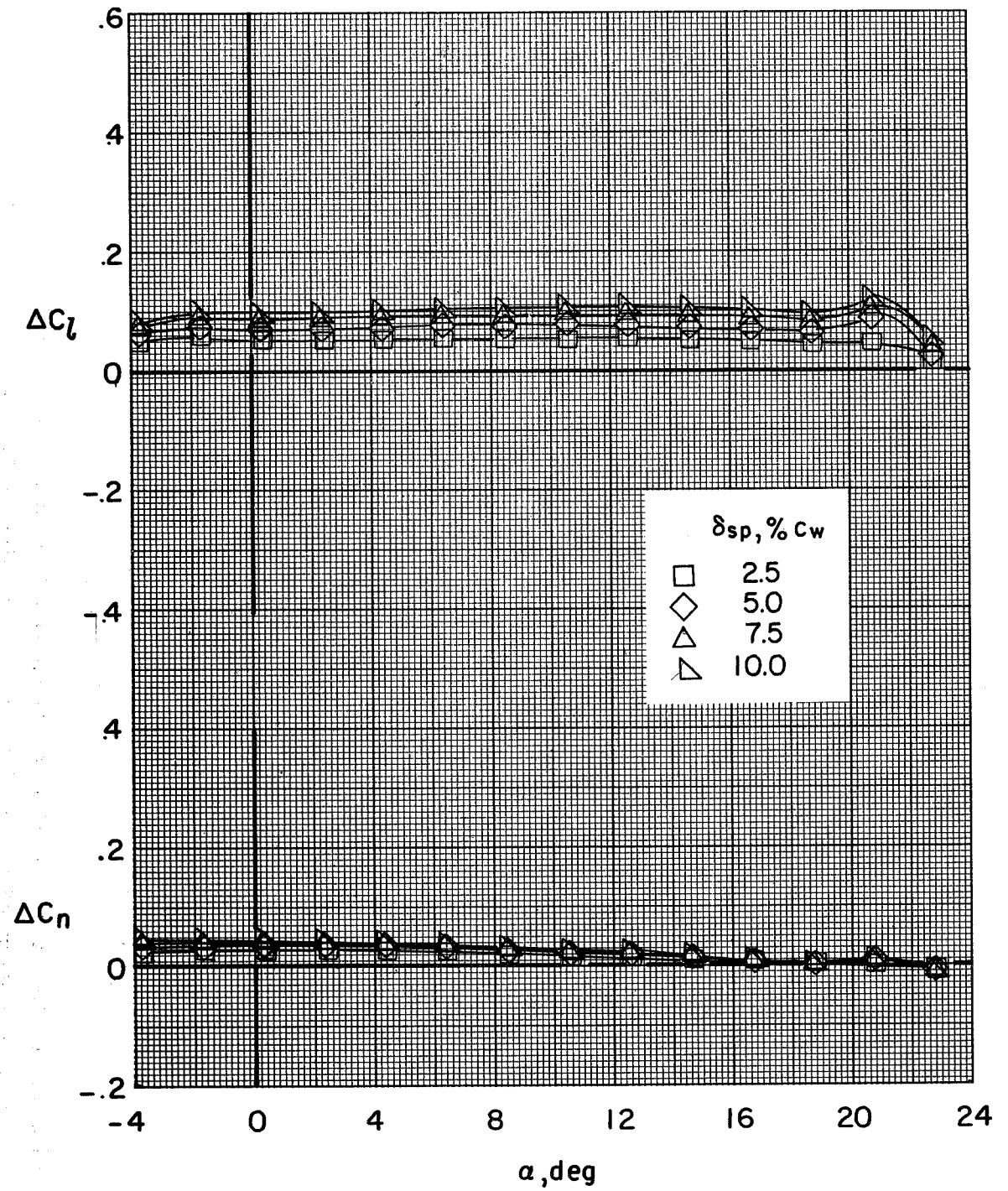

(a) Concluded.

Figure 71.- Continued.

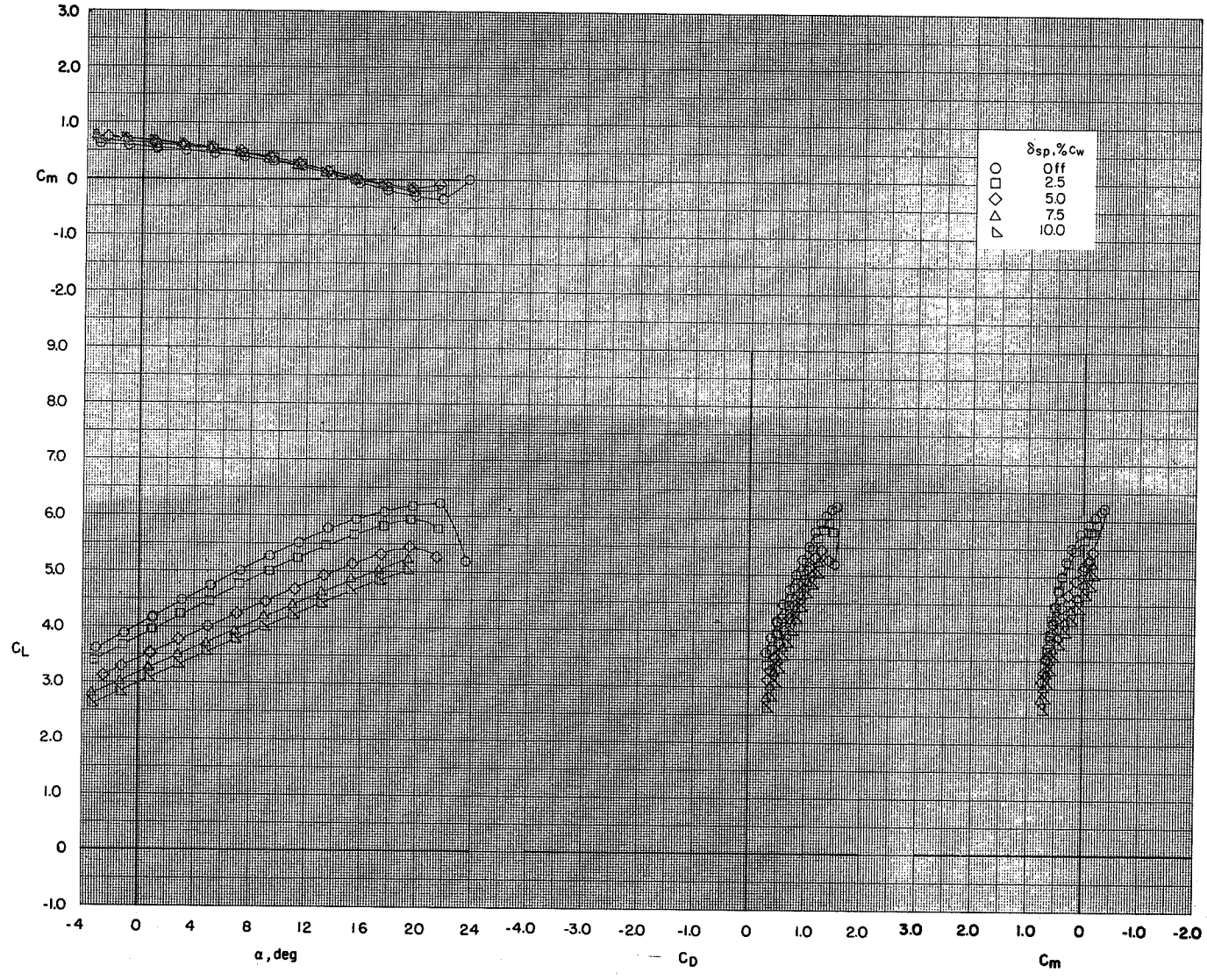

(b) $C_T = 2.26$.

Figure 71.- Continued.

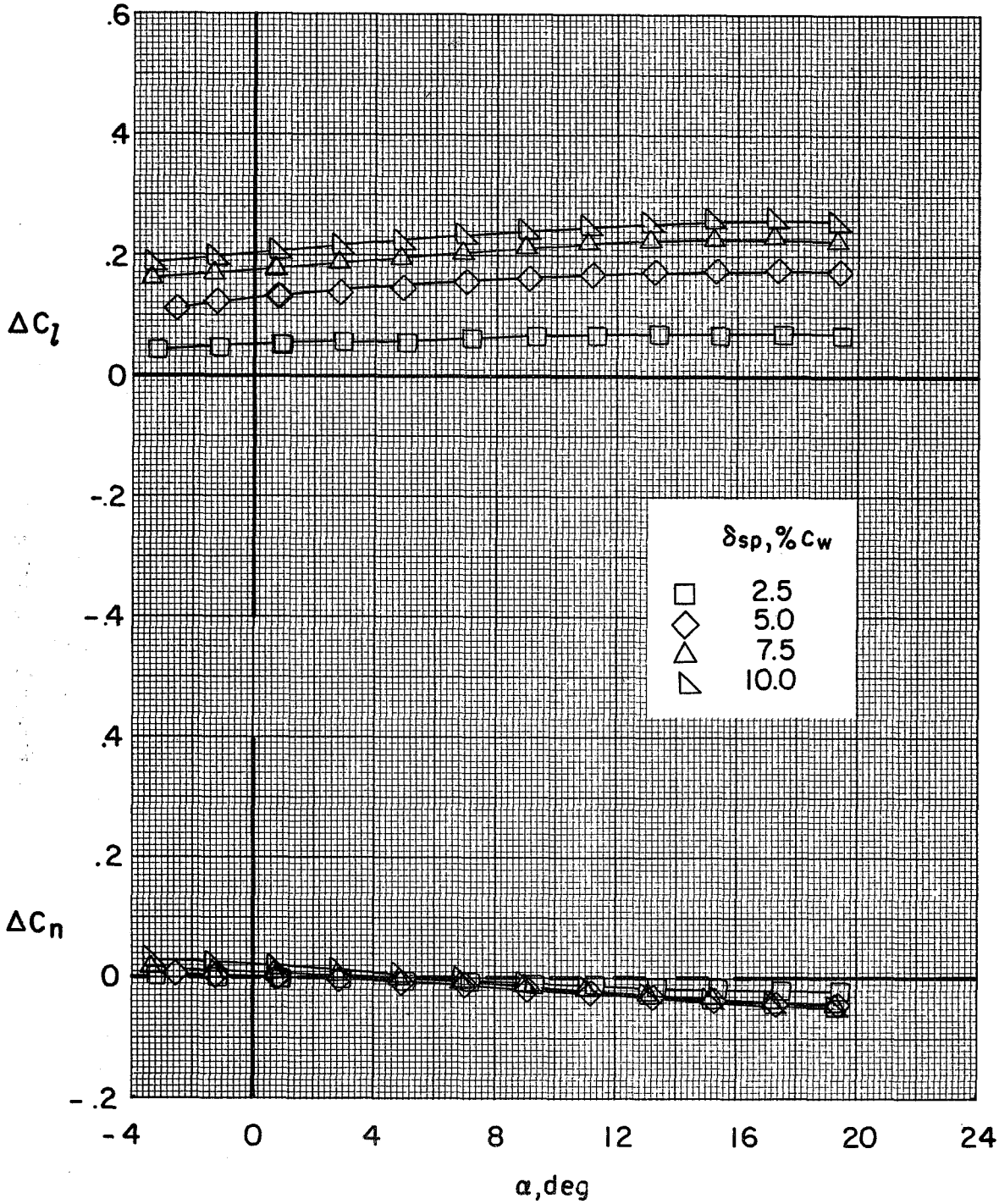

(b) Concluded.

Figure 71.- Continued.

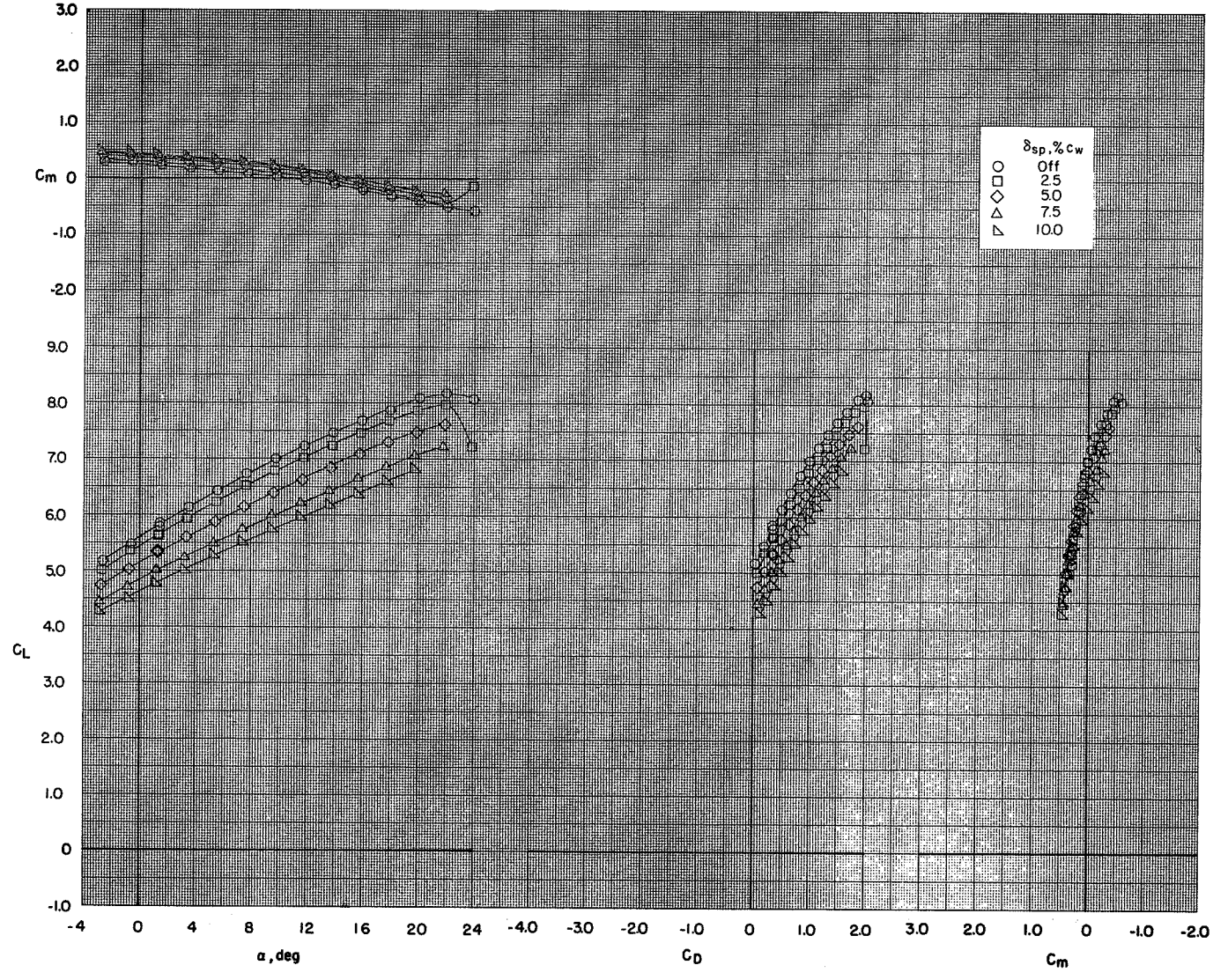

(c) $C_T = 4.06$.

Figure 71.- Continued.

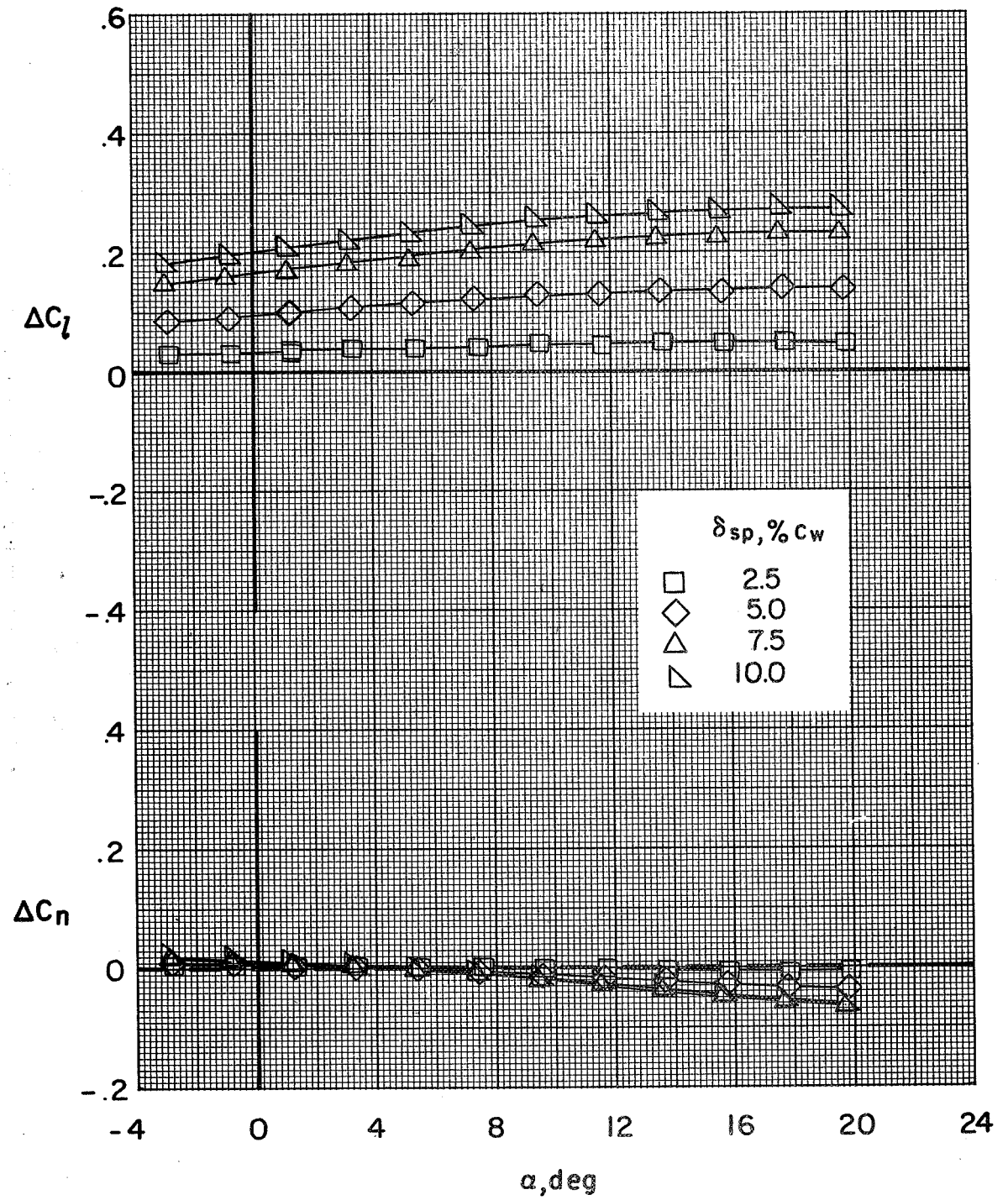

(c) Concluded.

Figure 71.- Concluded.

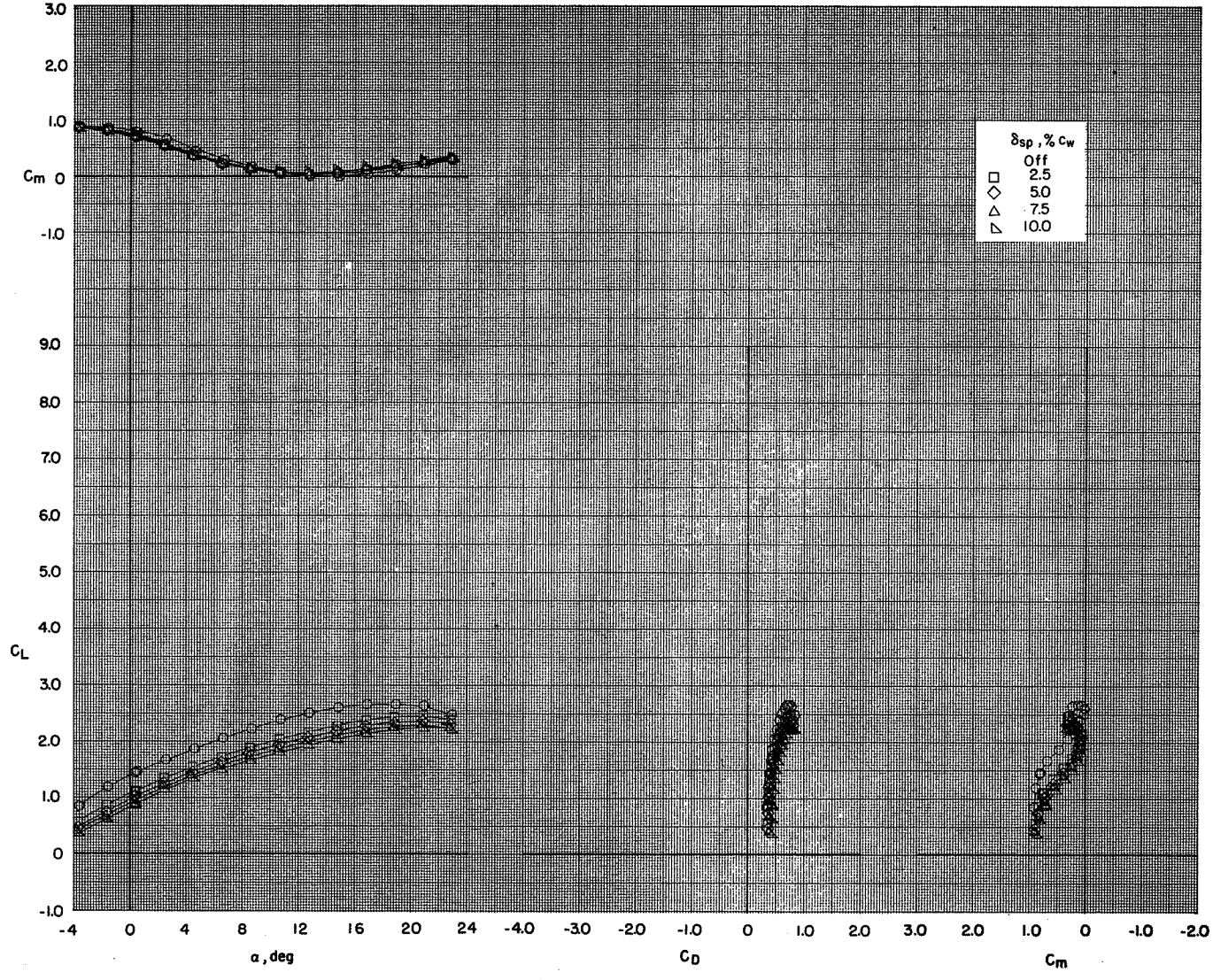

(a) $C_T = 0$.

Figure 72.- Effect of spoiler projection on the aerodynamic characteristics of the model with flaps deflected and leading-edge slat on. BPR 10.0; T-tail at 5^o; $\delta_f = 0^o/65^o/65^o$; c_s = 25 percent; $\delta_s = 50^o$; left outboard engine out.

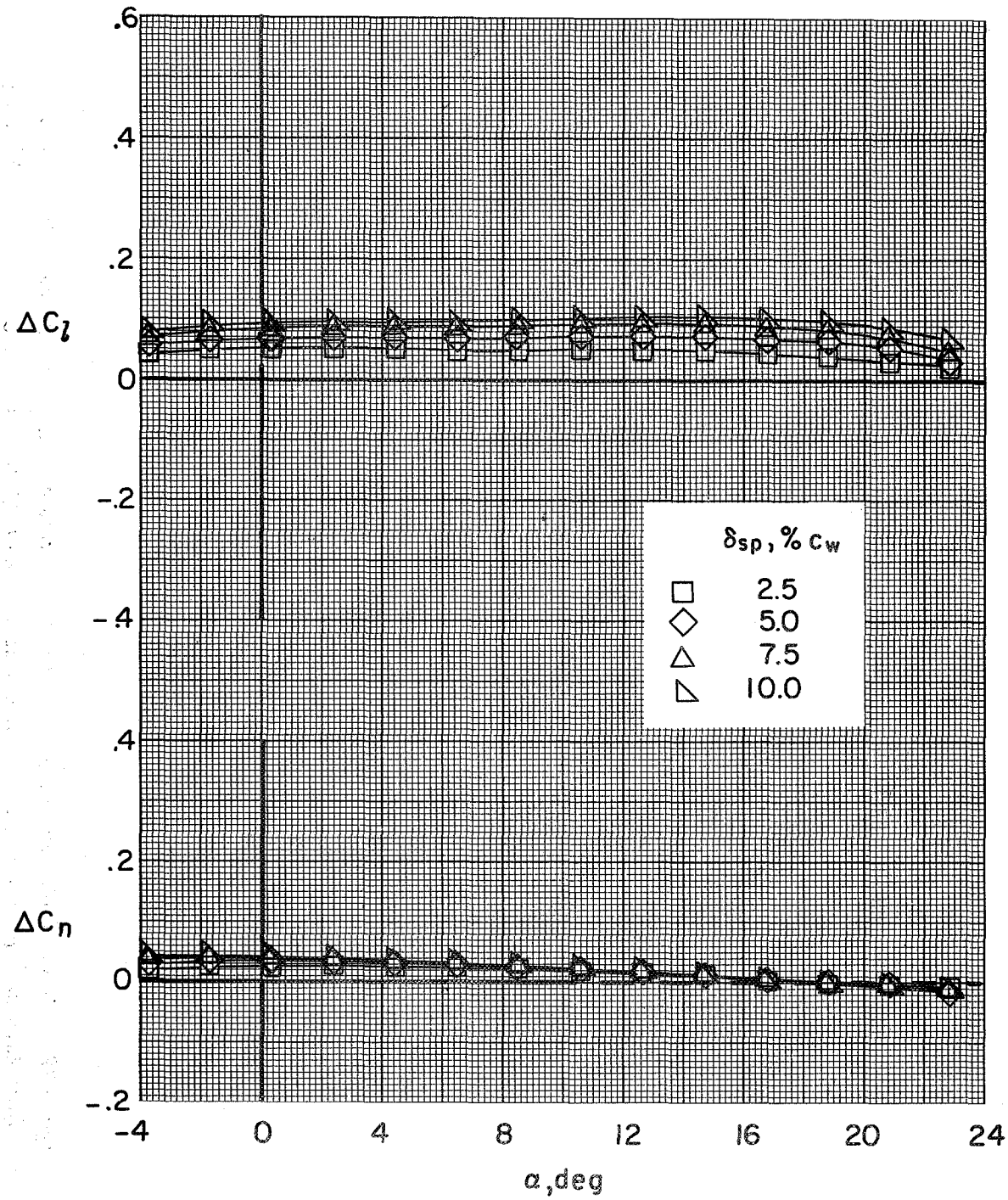

(a) Concluded.

Figure 72.- Continued.

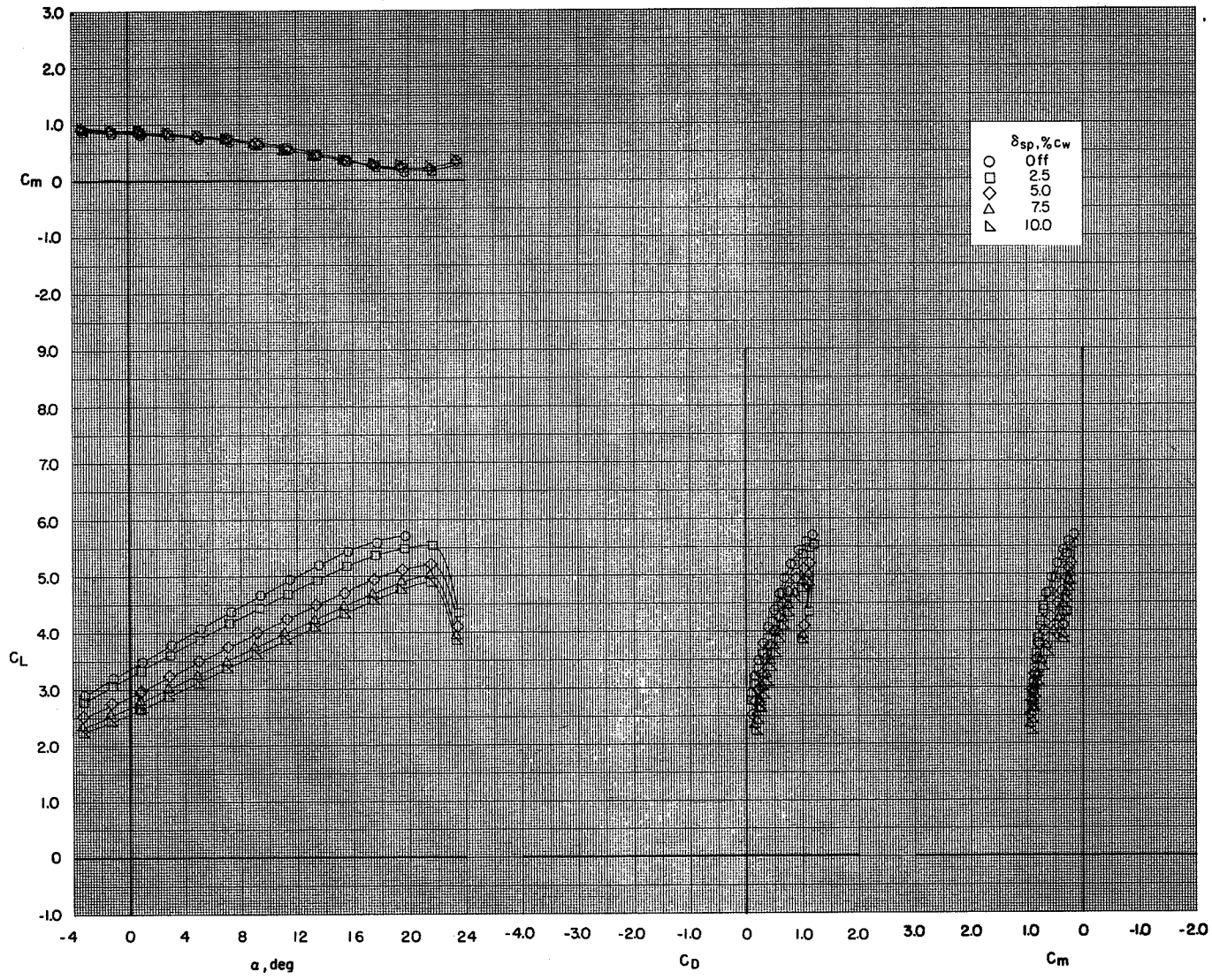

(b) $C_T = 1.69$.

Figure 72.- Continued.

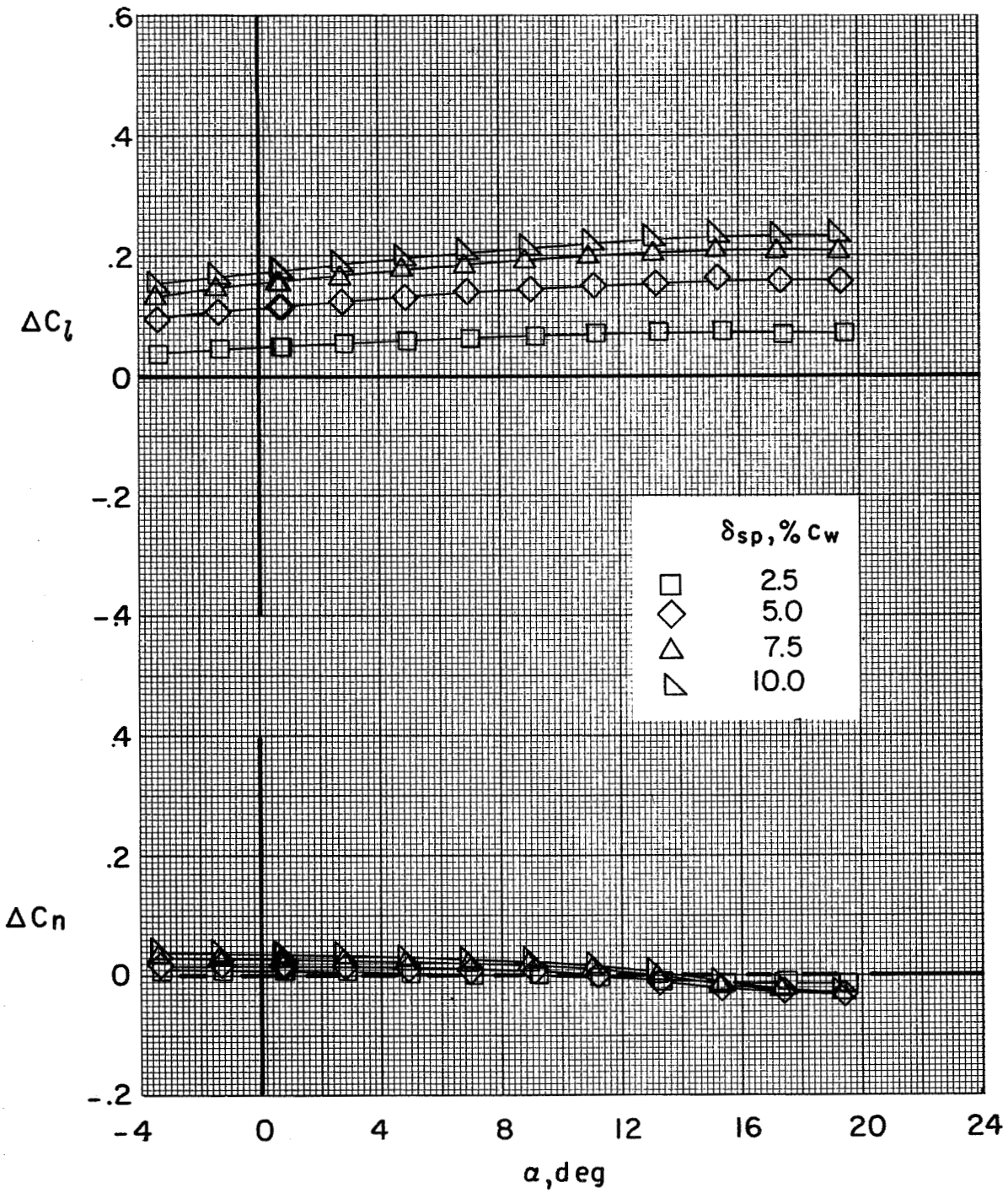

(b) Concluded.

Figure 72.- Continued.

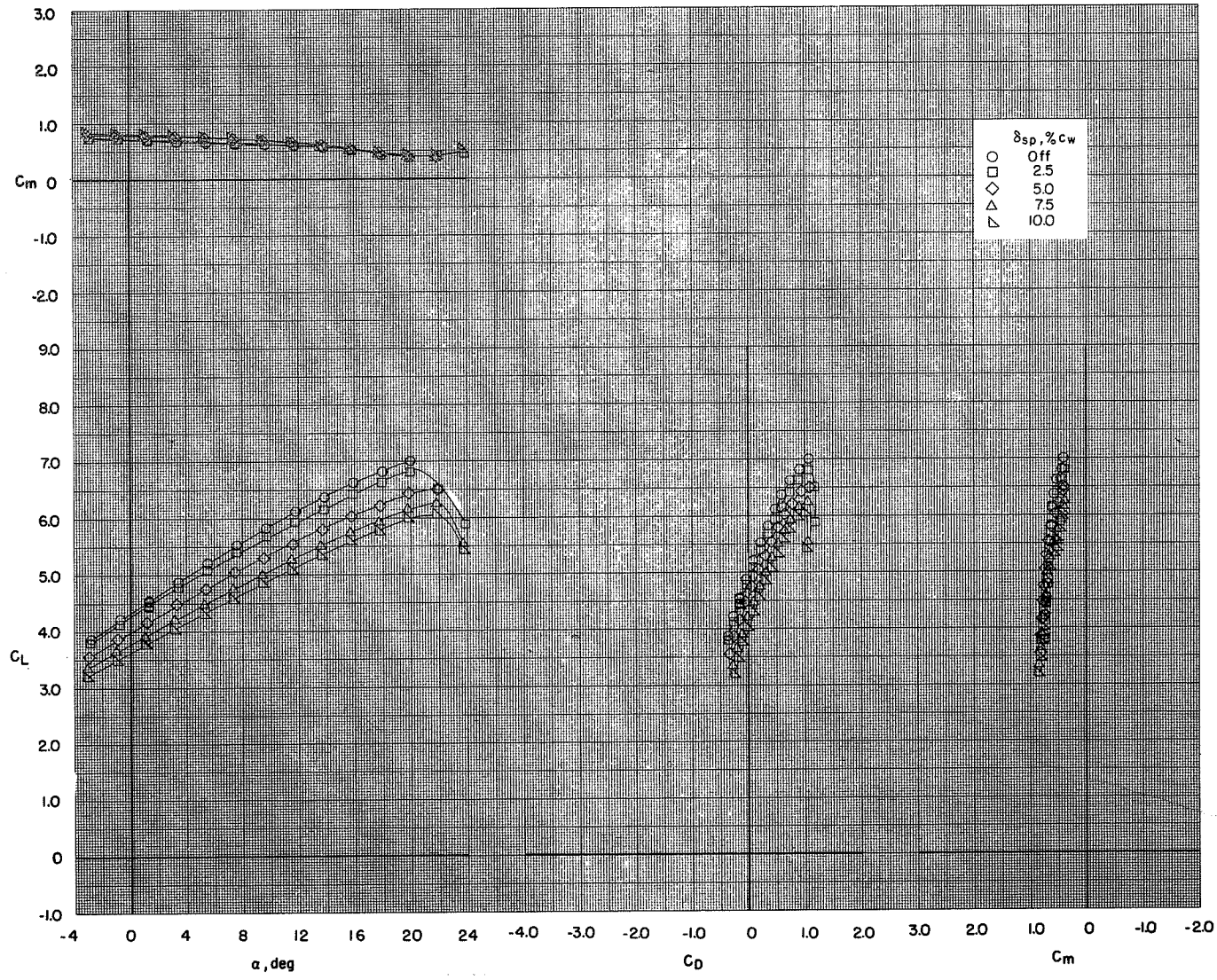

(c) $C_T = 3.04$.

Figure 72.- Continued.

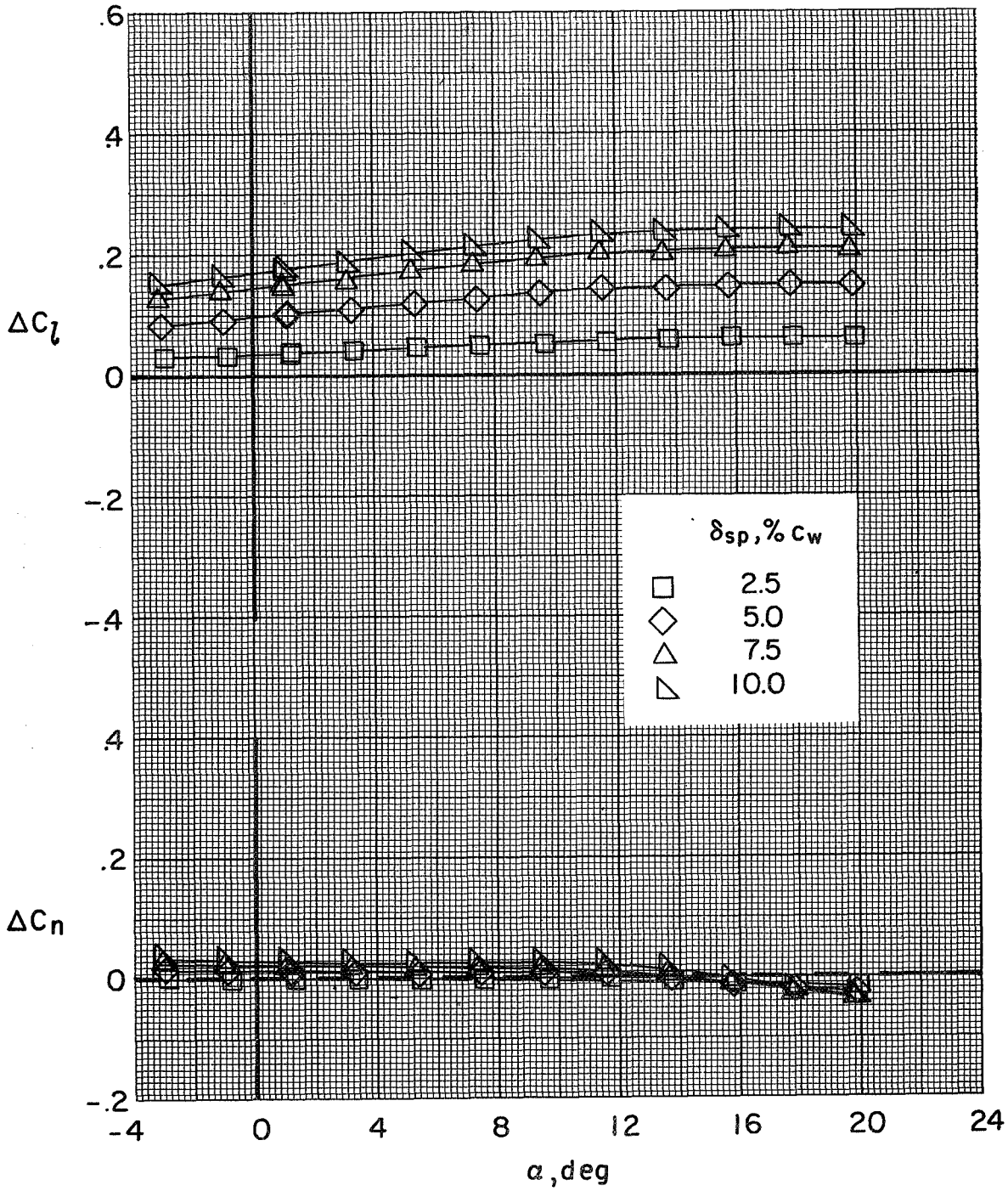

(c) Concluded.

Figure 72.- Concluded.

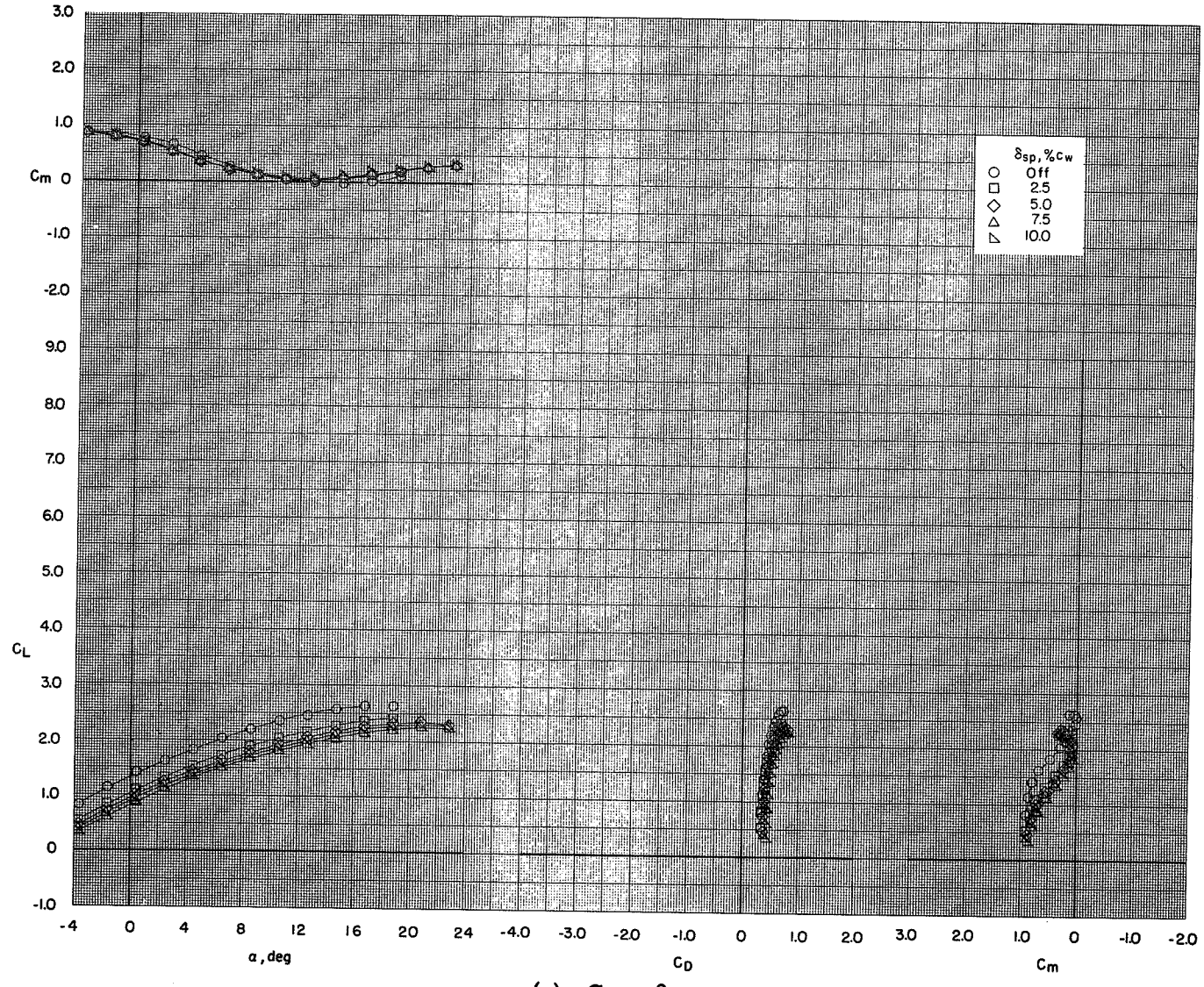

(a) $C_T = 0$.

Figure 73.- Effect of spoiler projection on the aerodynamic characteristics of the model with flaps deflected and leading-edge slat on. BPR 10.0; T-tail at 5^o; $\delta_f = 0^o/65^o/65^o$; $c_s = 25$ percent; $\delta_s = 50^o$; left inboard engine out.

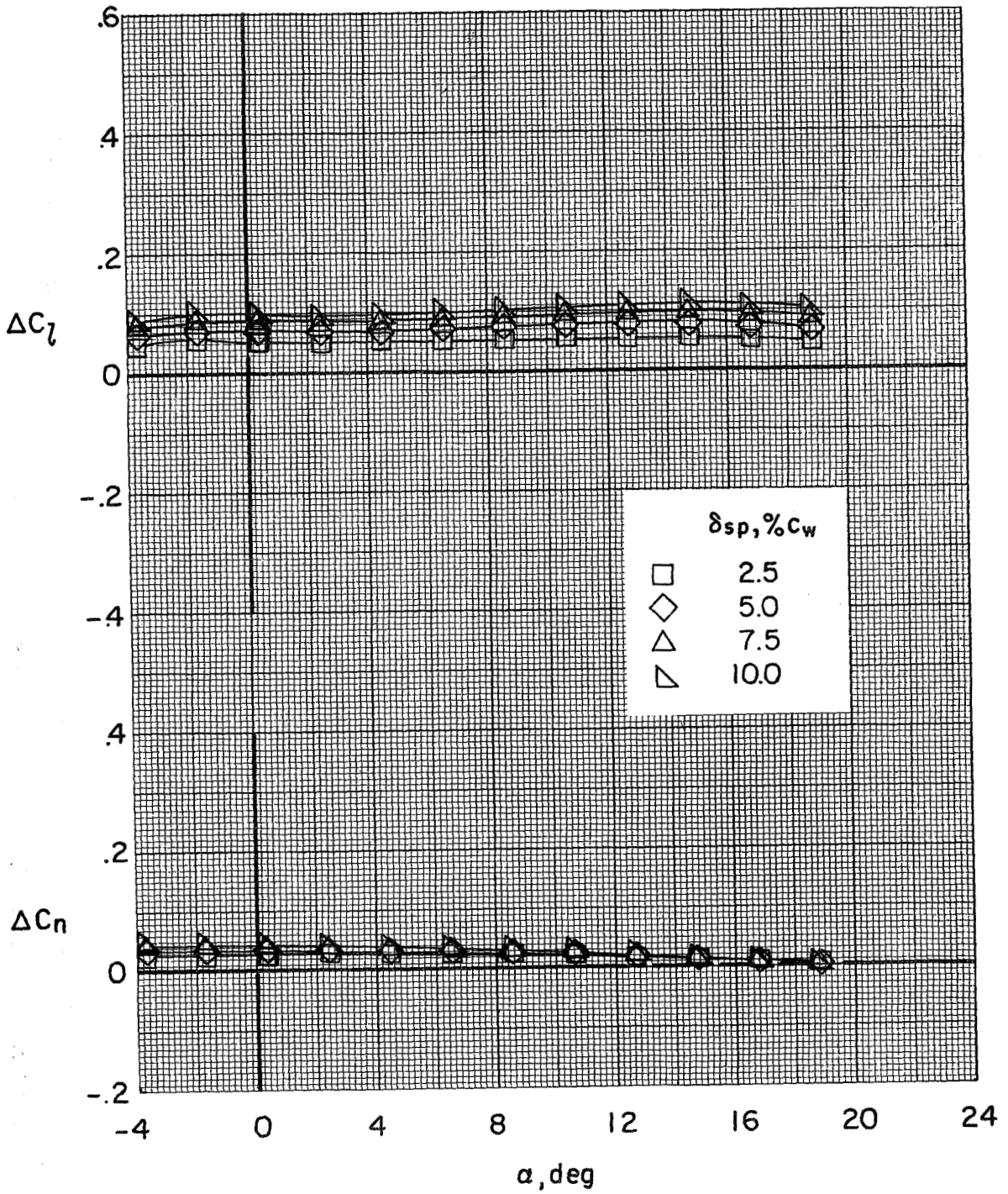

(a) Concluded.

Figure 73.- Continued.

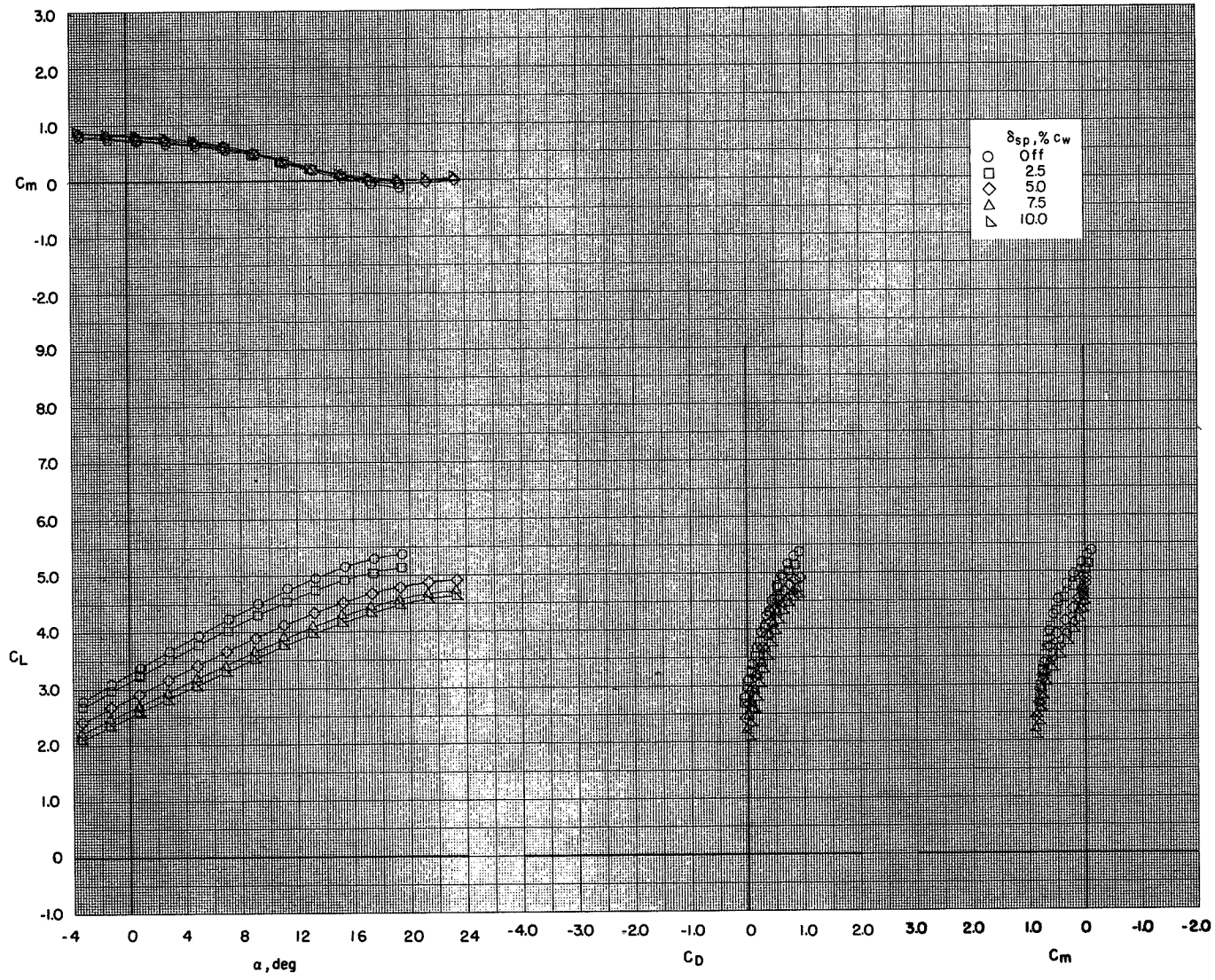

(b) $C_T = 1.69$.

Figure 73.- Continued.

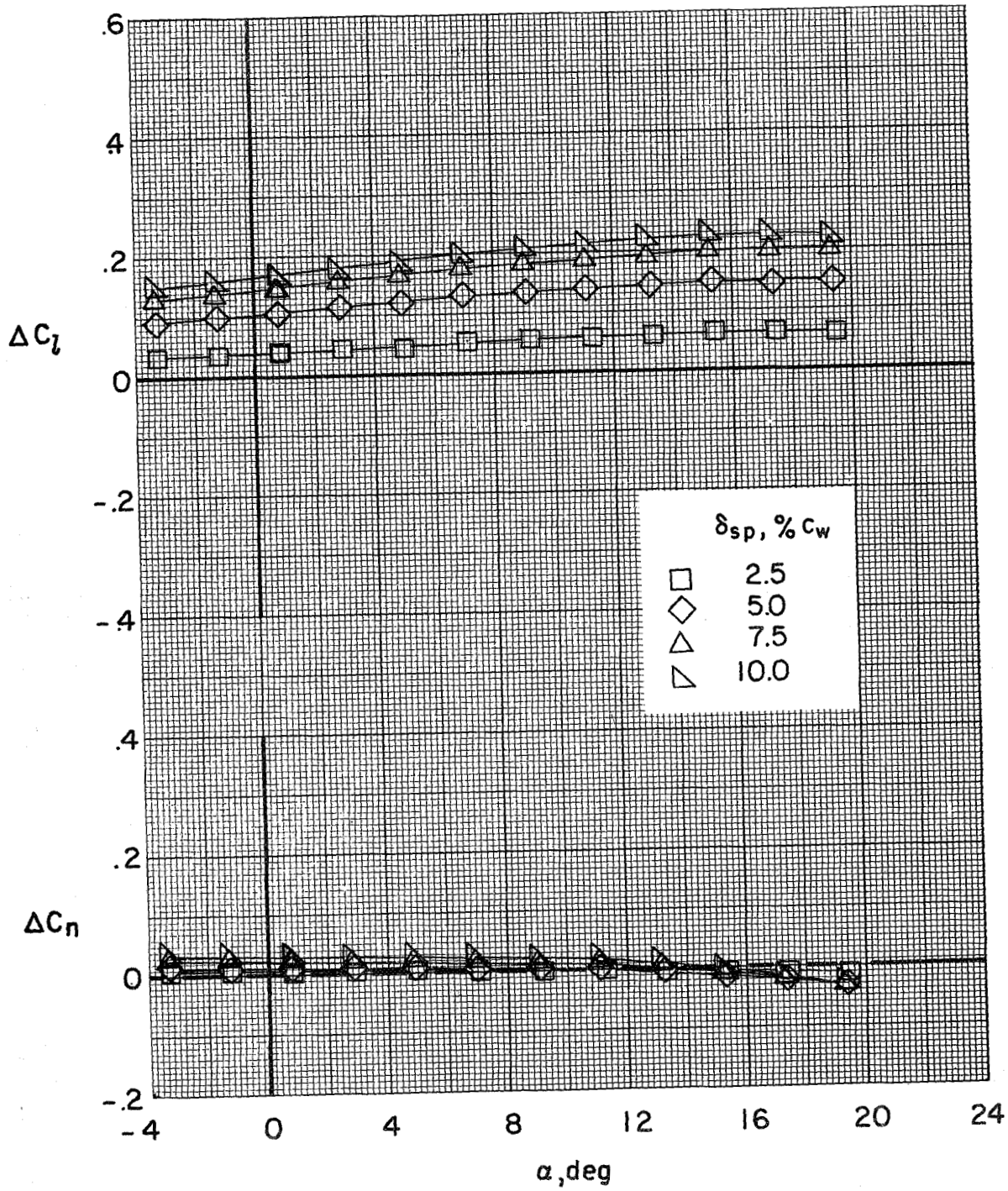

(b) Concluded.

Figure 73.- Continued.

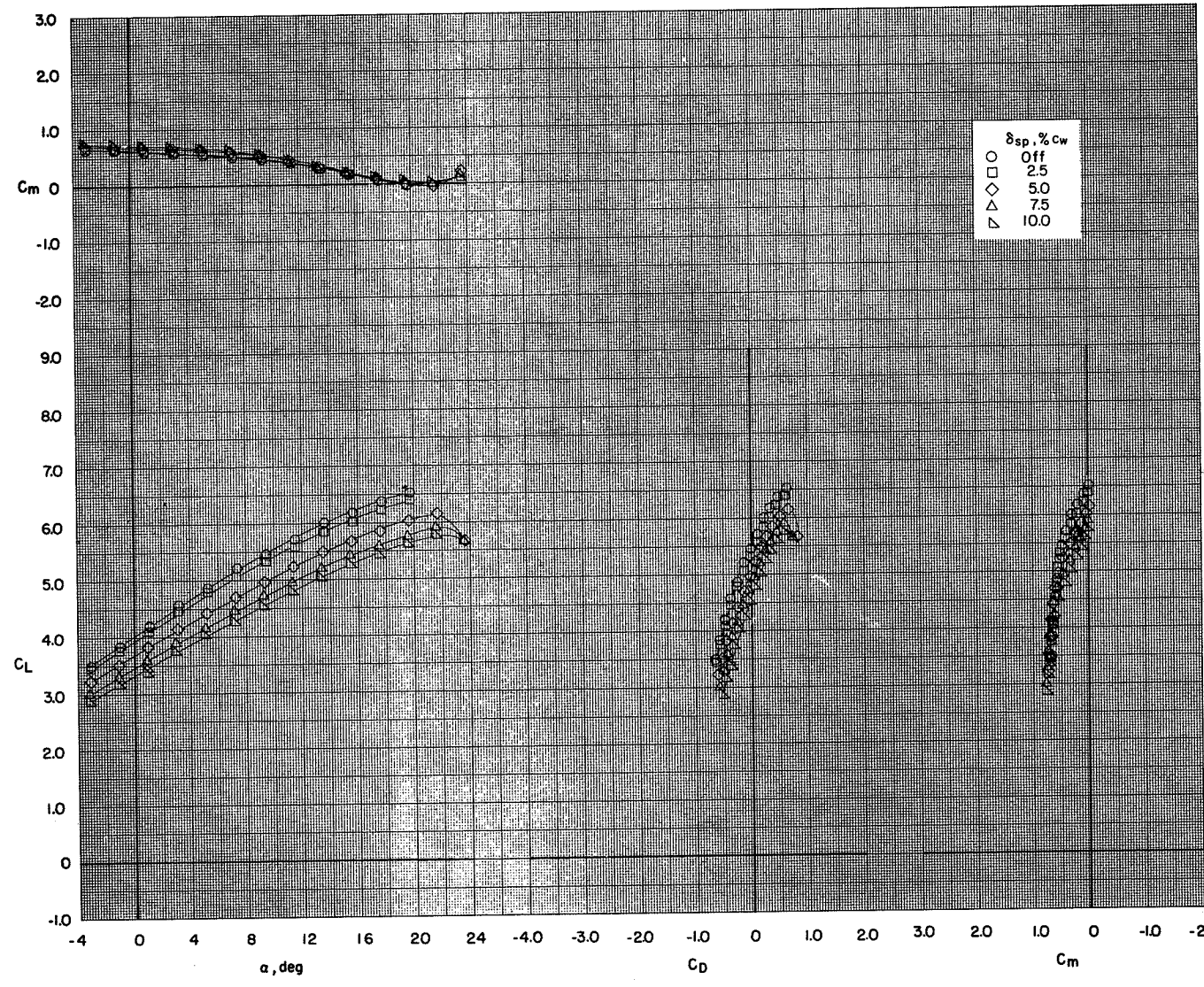

(c) $C_T = 3.04$.

Figure 73.- Continued.

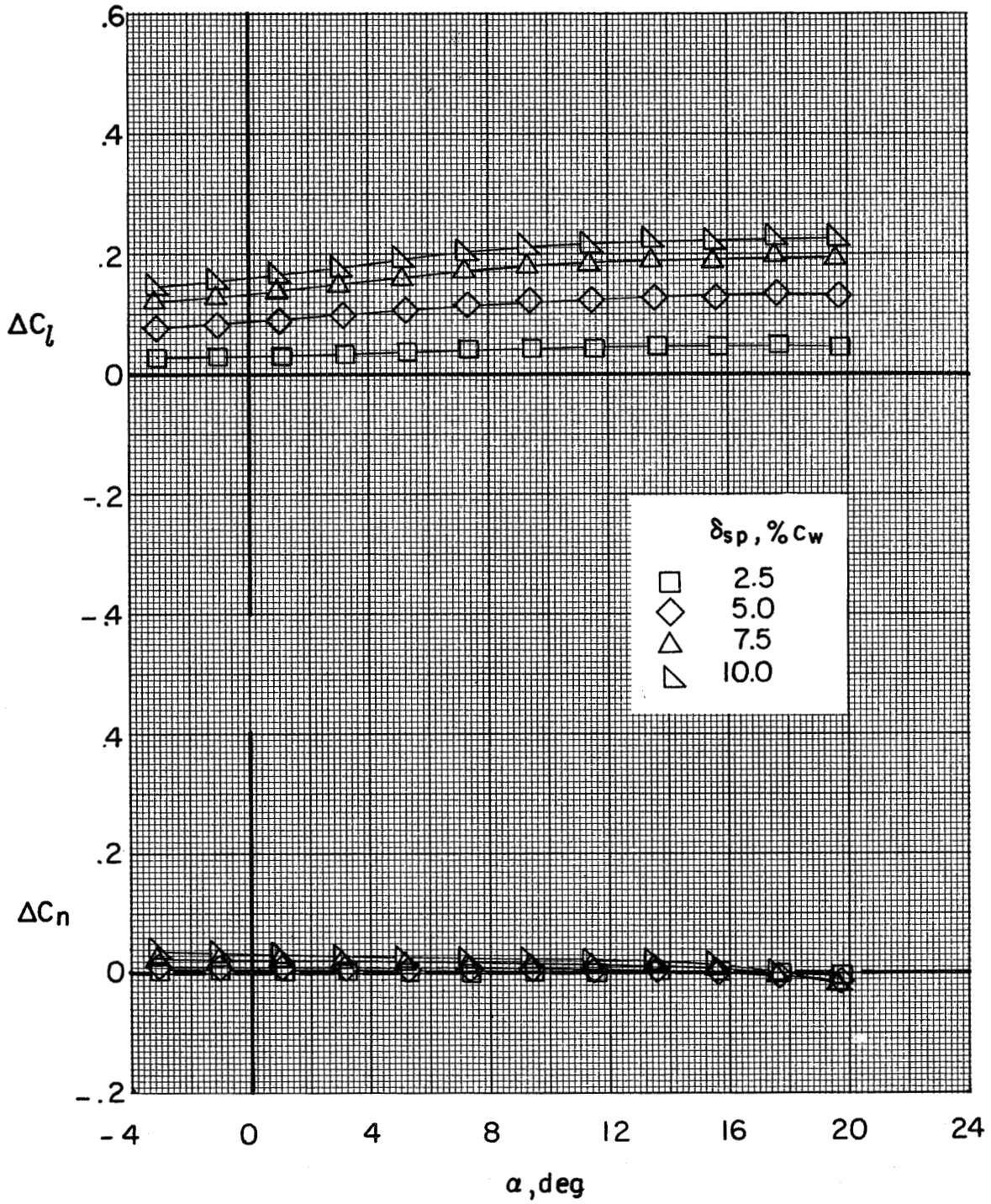

(c) Concluded.

Figure 73.- Concluded.

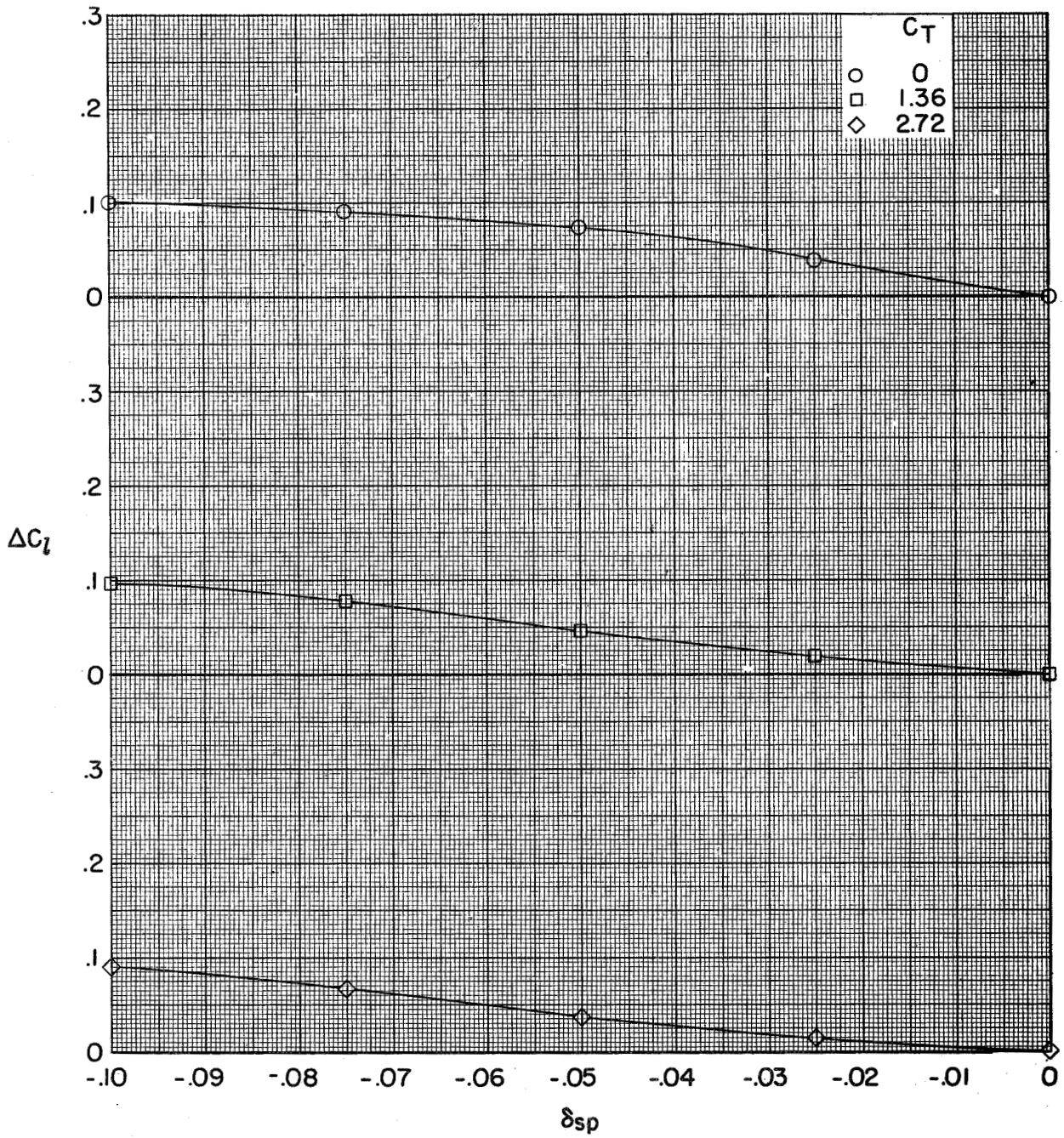

(a) Rolling-moment coefficient.

Figure 74.- Summary of lateral directional moments due to spoiler projection for the model with flaps deflected and leading-edge slat on. BPR 6.2; T-tail at 5^o; $\delta_f = 0^o/35^o/35^o$; c_s = 25 percent; $\delta_s = 50^o$; left outboard engine out.

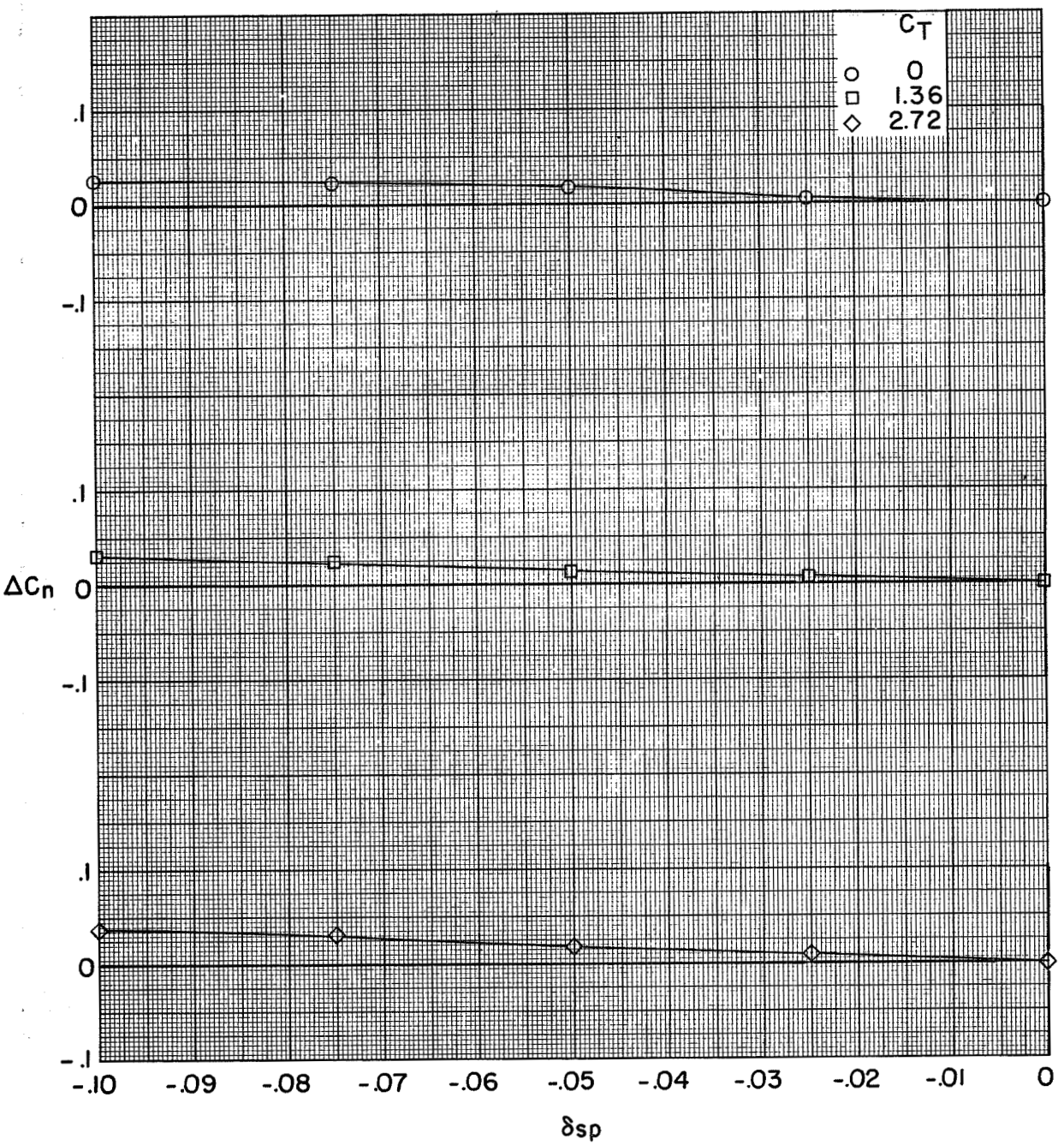

(b) Yawing-moment coefficient.

Figure 74.- Concluded.

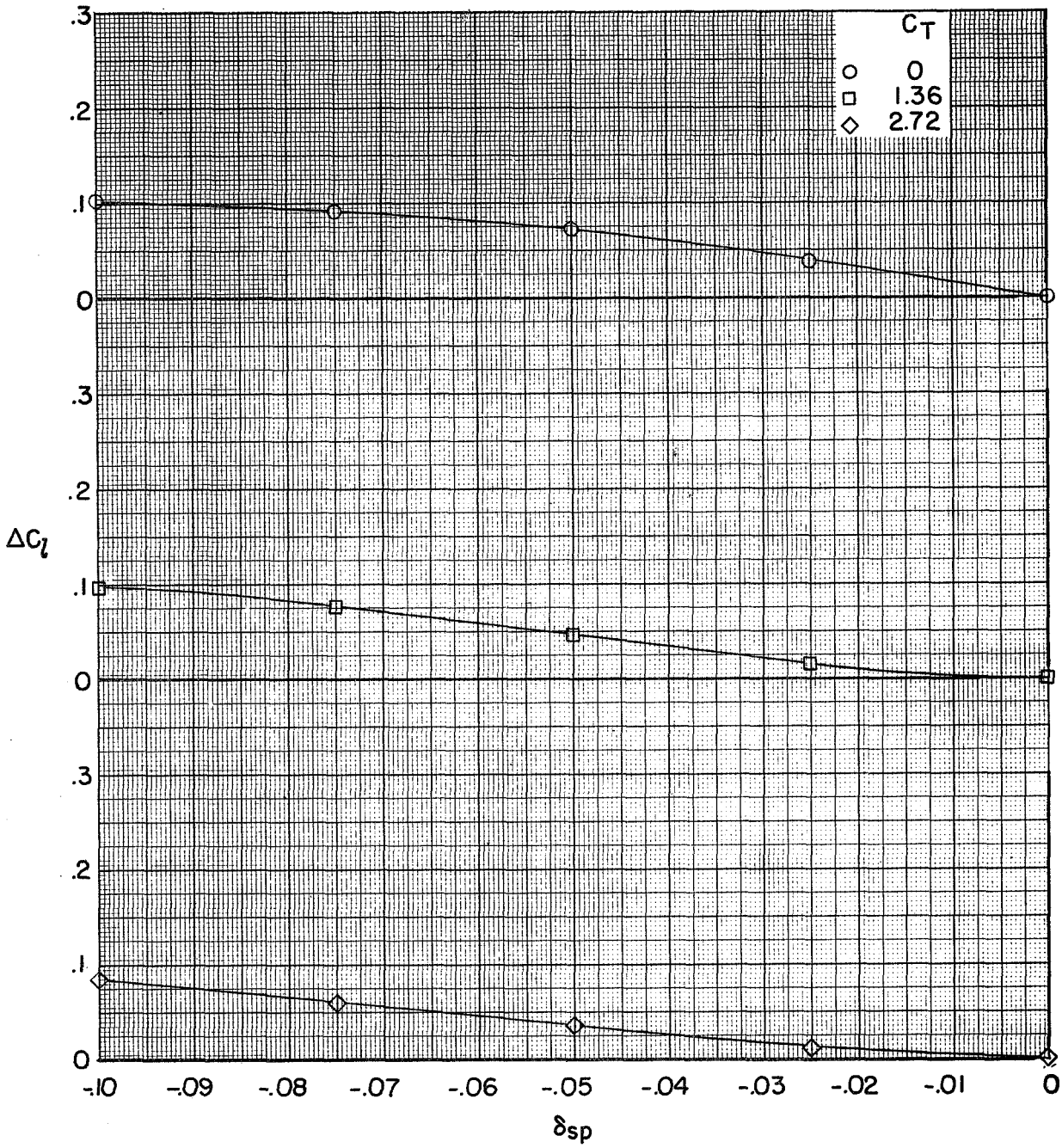

(a) Rolling-moment coefficient.

Figure 75.- Summary of lateral-directional moments due to spoiler projection for the model with flaps deflected and leading-edge slat on. BPR 6.2; T-tail at 5^o; $\delta_f = 0^o/35^o/35^o$; $c_s = 25$ percent; $\delta_s = 50^o$; left inboard engine out.

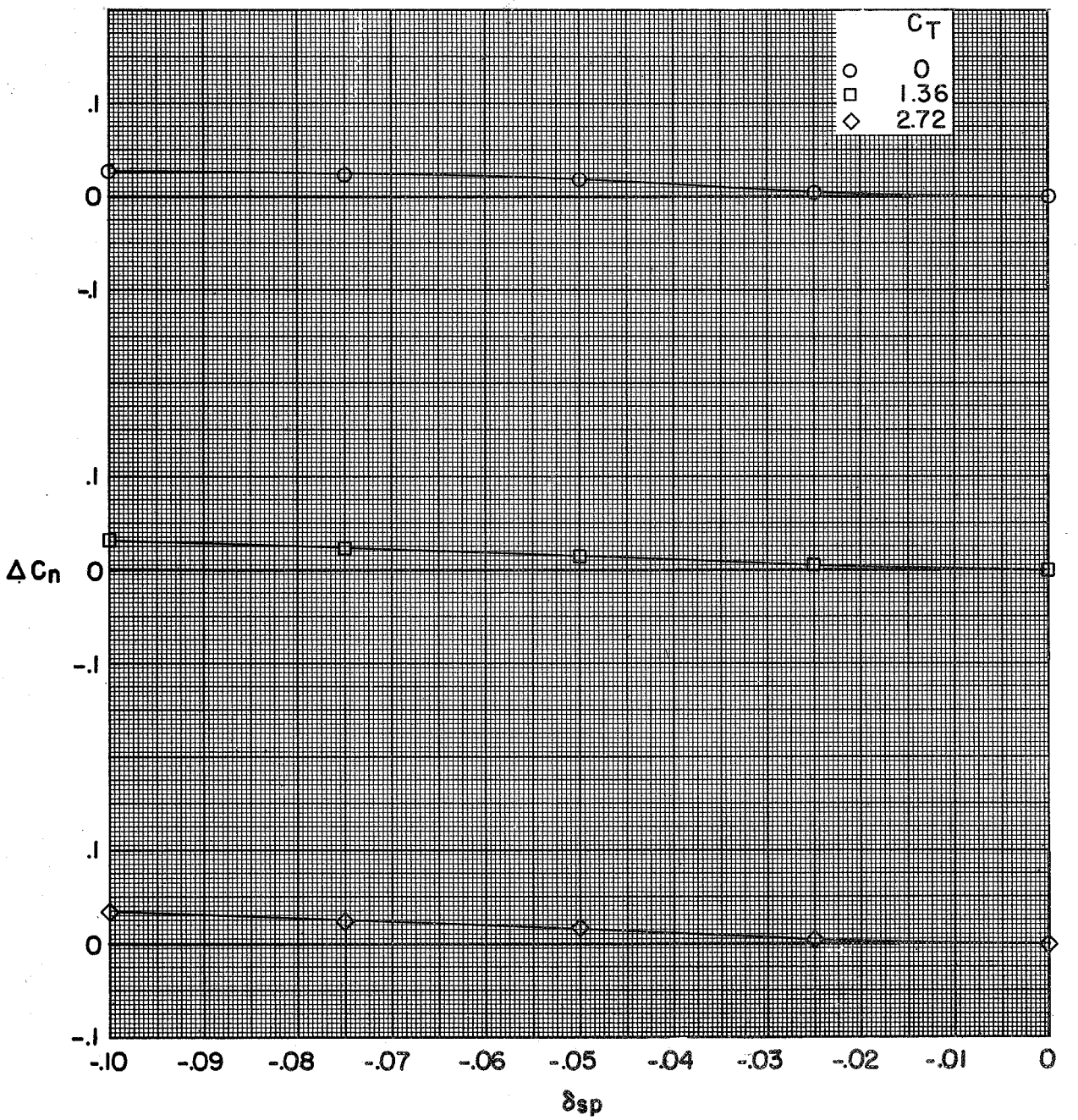

(b) Yawing-moment coefficient.

Figure 75.- Concluded.

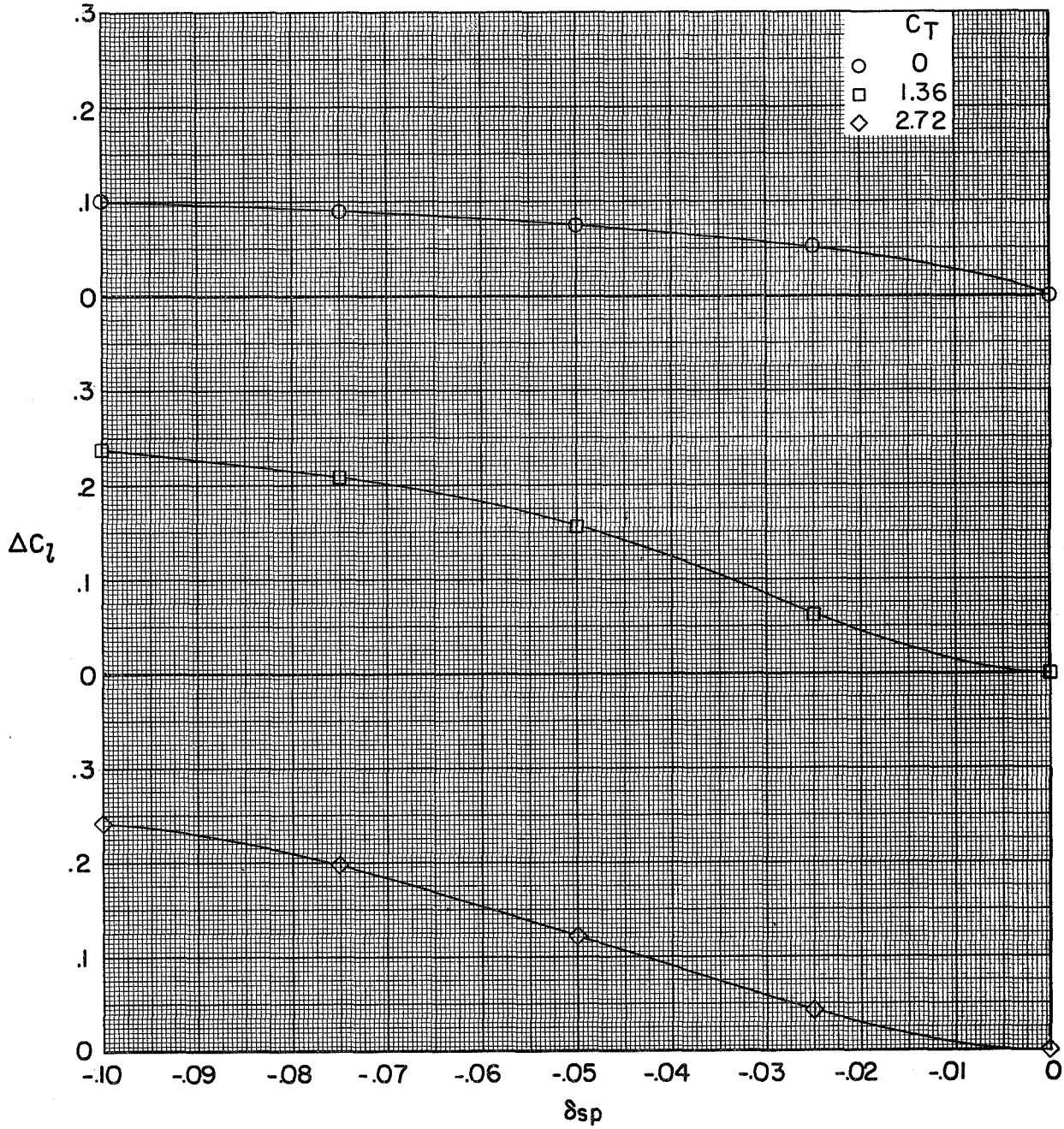

(a) Rolling-moment coefficient.

Figure 76.- Summary of lateral-directional moments due to spoiler projection for the model with flaps deflected and leading-edge slat on. BPR 6.2; T-tail at 5^o; $\delta_f = 0^o/65^o/65^o$; $c_s = 25$ percent; $\delta_s = 50^o$; left outboard engine out.

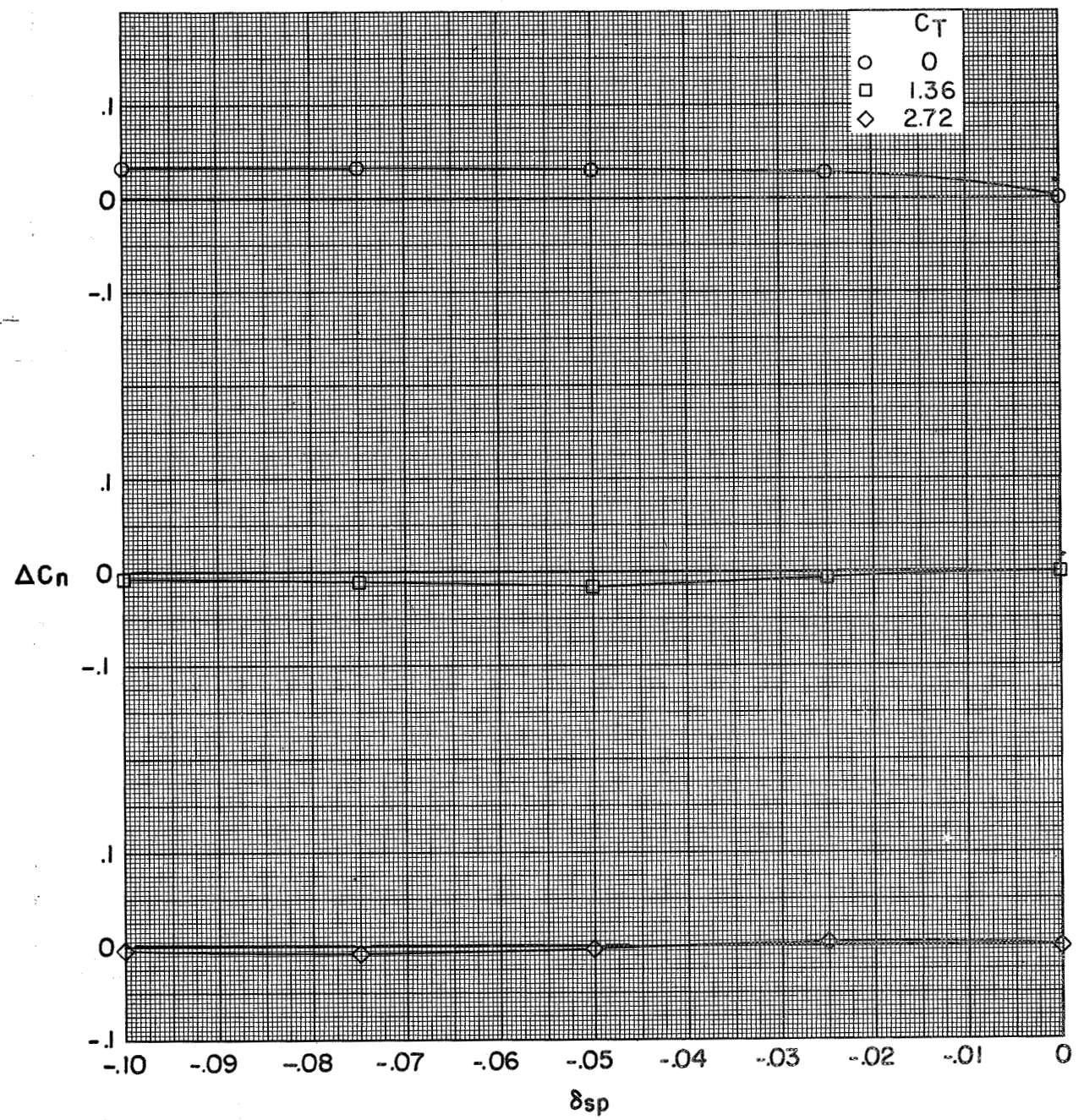

(b) Yawing-moment coefficient.

Figure 76.- Concluded.

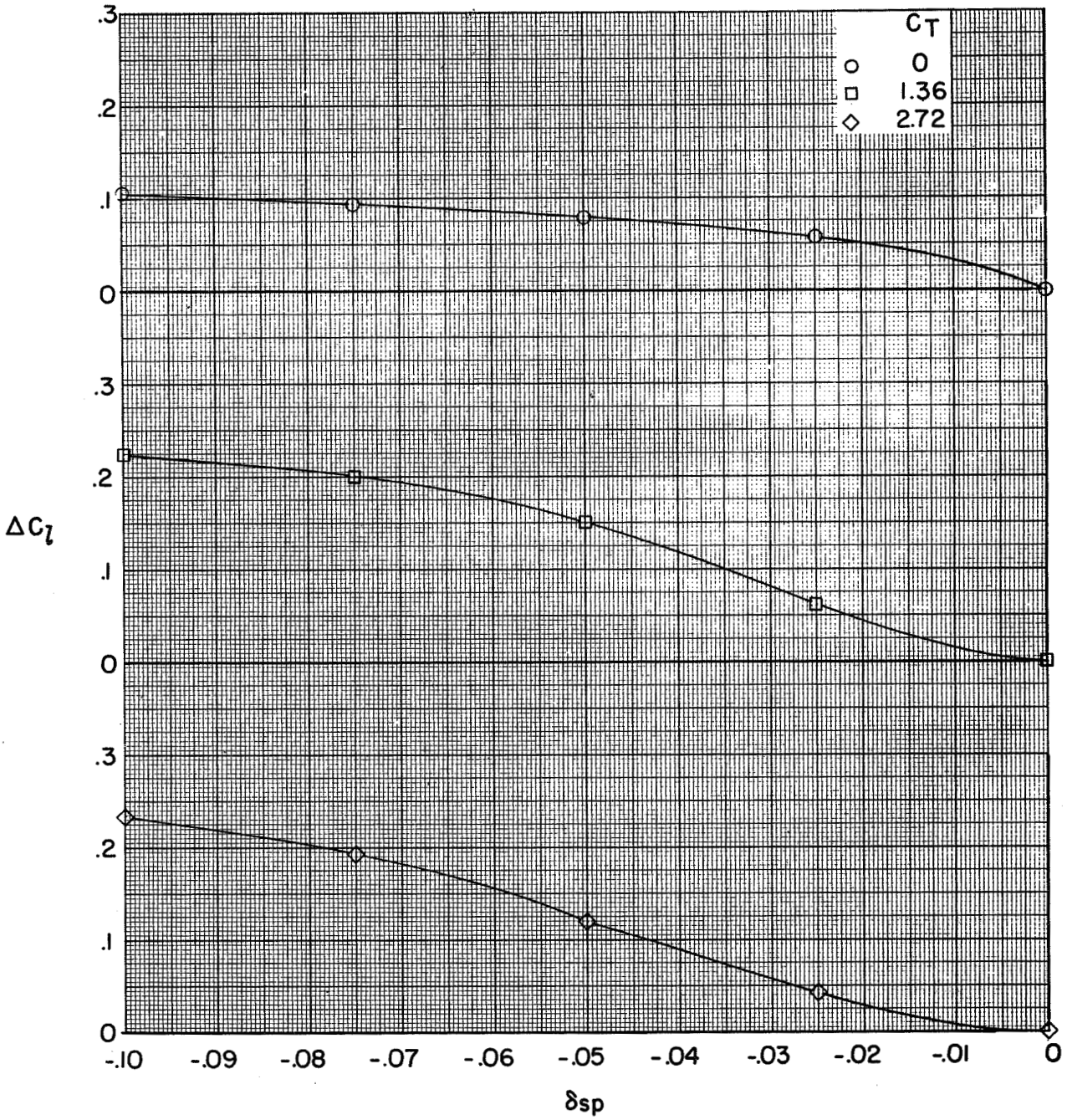

(a) Rolling-moment coefficient.

Figure 77.- Summary of lateral-directional moments due to spoiler projection for the model with flaps deflected and leading-edge slat on. BPR 6.2; T-tail at 5^o; $\delta_f = 0^o/65^o/65^o$; $c_s = 25$ percent; $\delta_s = 50^o$; left inboard engine out.

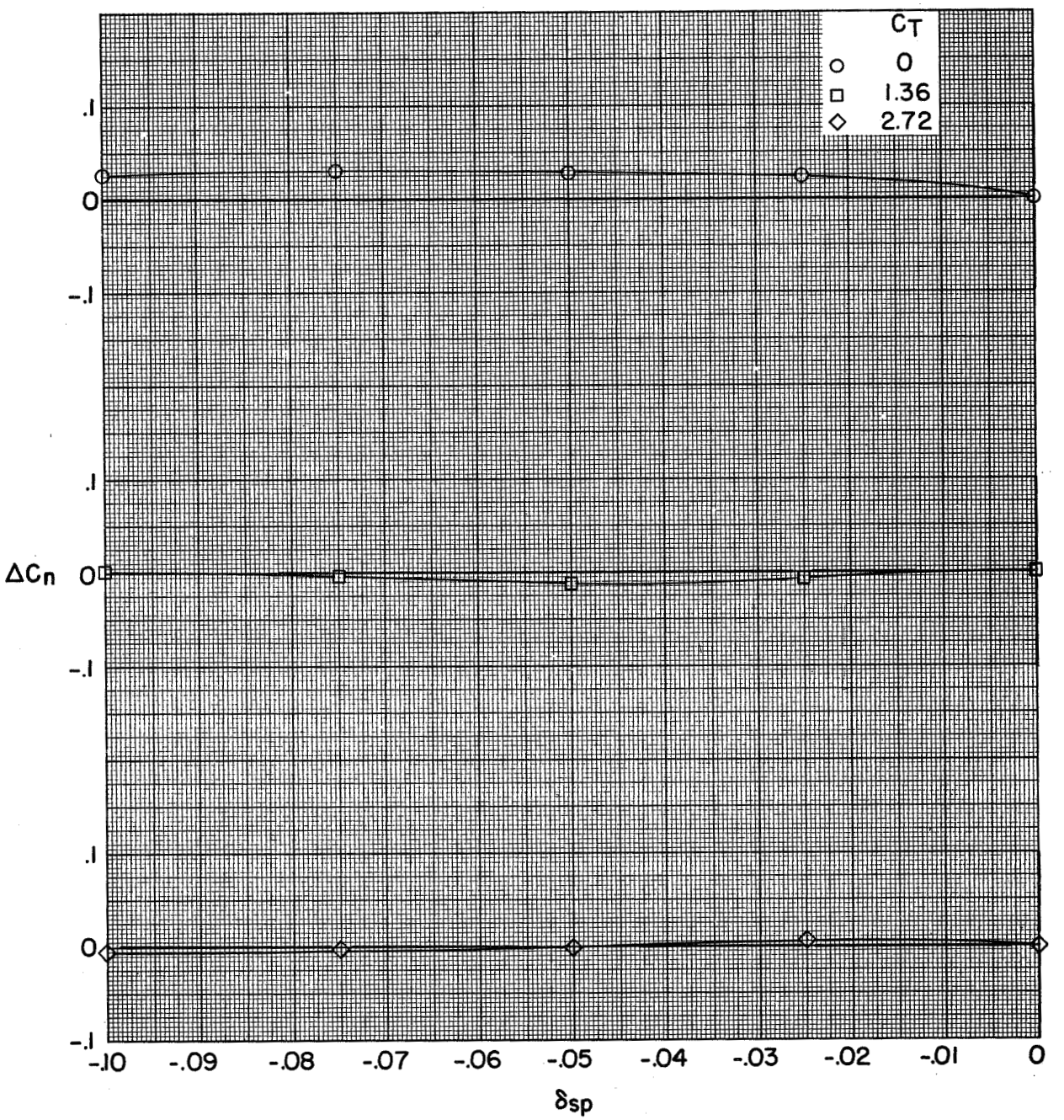

(b) Yawing-moment coefficient.

Figure 77.- Concluded.

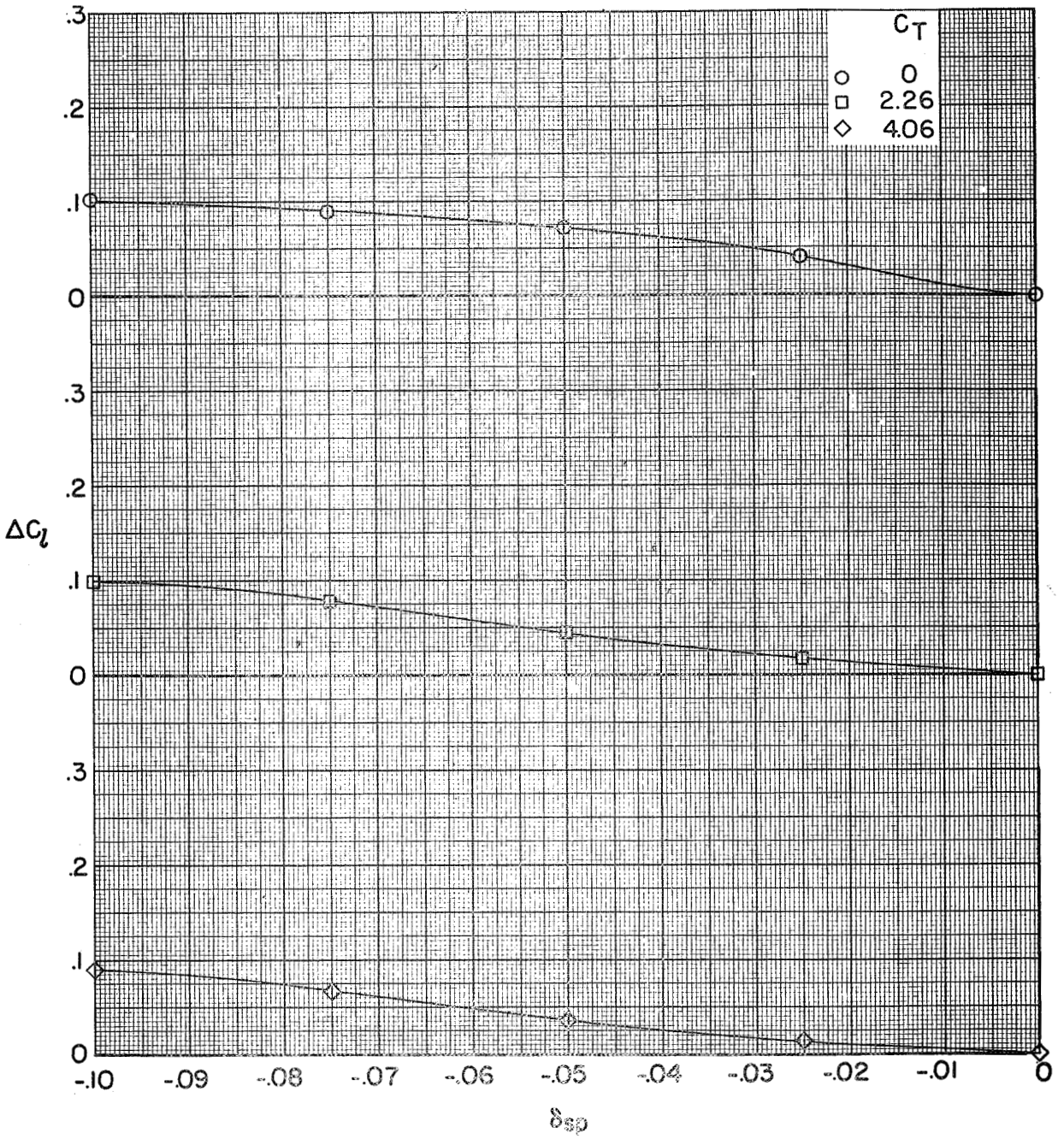

(a) Rolling-moment coefficient.

Figure 78.- Summary of lateral-directional moments due to spoiler projection for the model with flaps deflected and leading-edge slat on. BPR 10.0; T-tail at 5^o; $\delta_f = 0^o/35^o/35^o$; c_s = 25 percent; $\delta_s = 50^o$; symmetrical power.

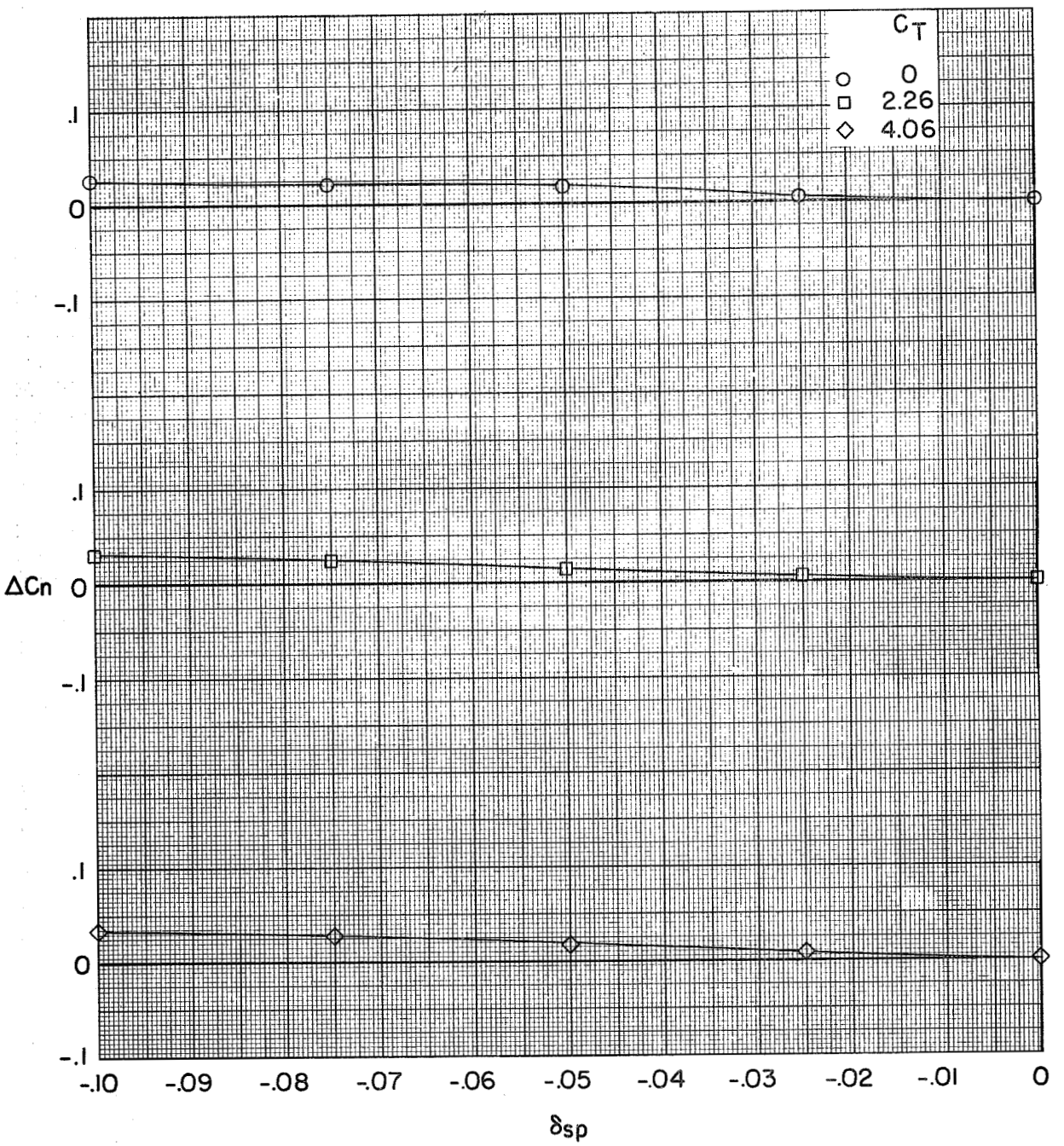

(b) Yawing-moment coefficient.

Figure 78.- Concluded.

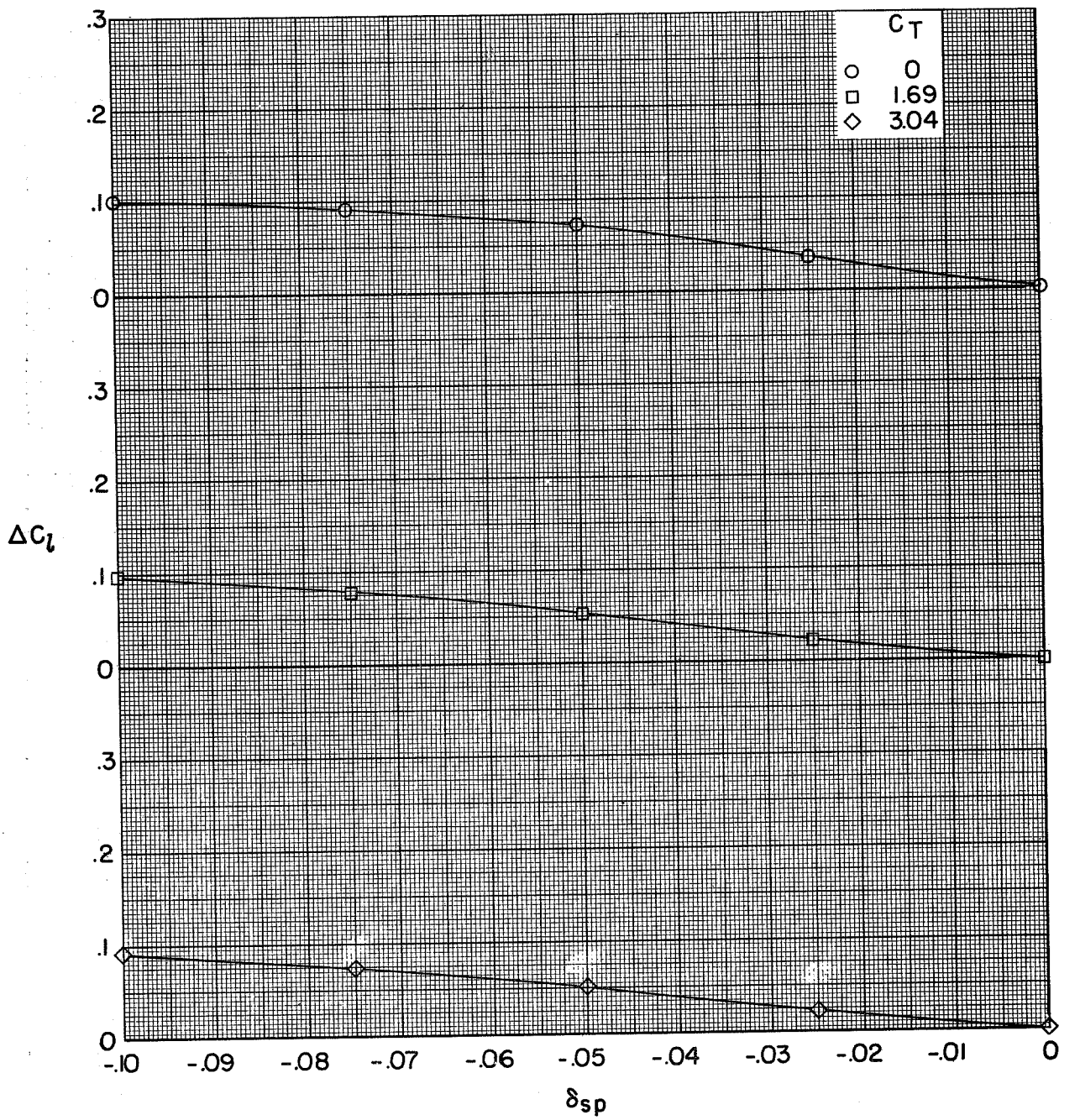

(a) Rolling-moment coefficient.

Figure 79.- Summary of lateral-directional moments due to spoiler projection for the model with flaps deflected and leading-edge slat on. BPR 10.0; T-tail at 5^o; $\delta_f = 0^o/35^o/35^o$; c_s = 25 percent; $\delta_s = 50^o$; left outboard engine out.

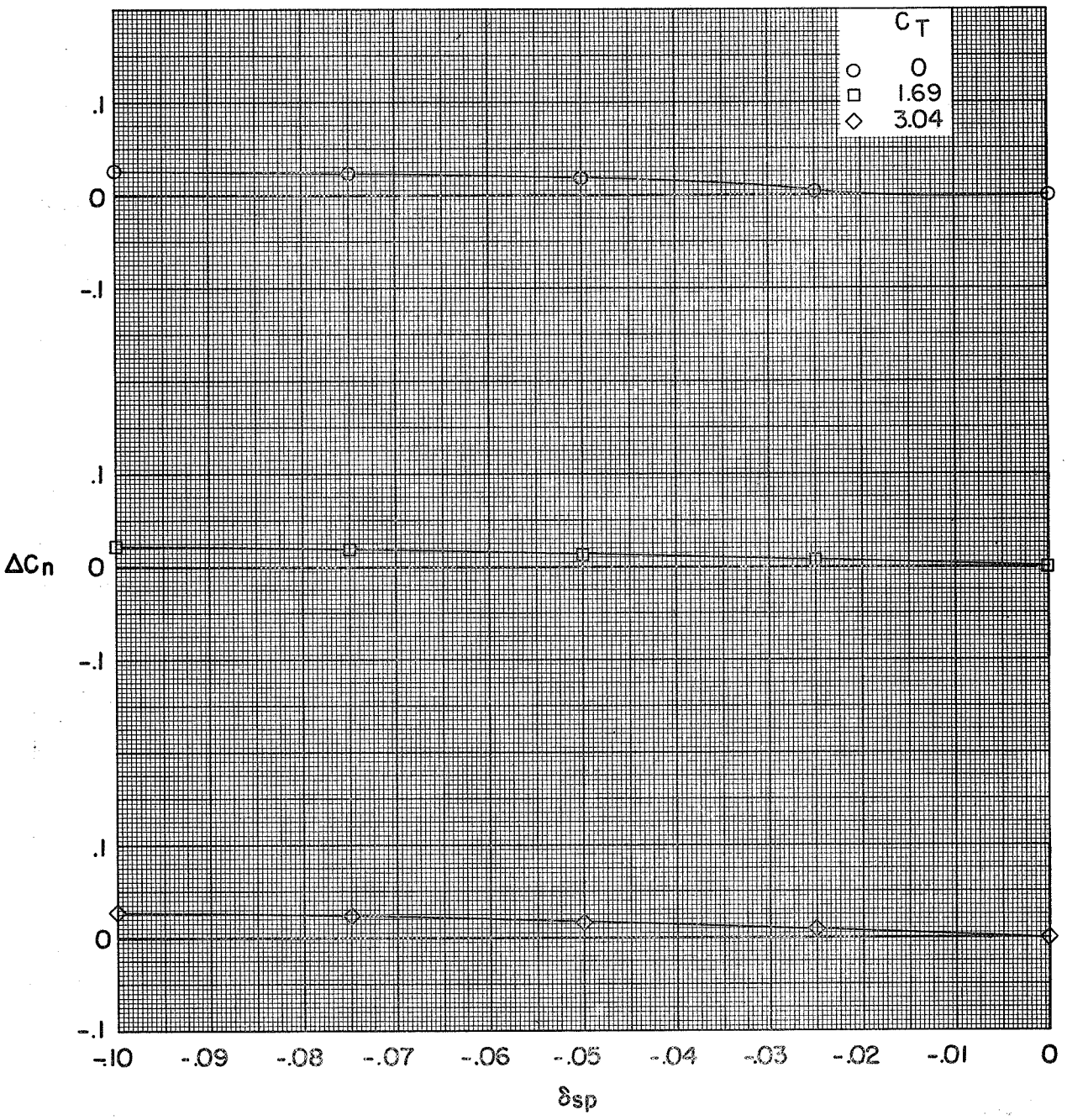

(b) Yawing-moment coefficient.

Figure 79.- Concluded.

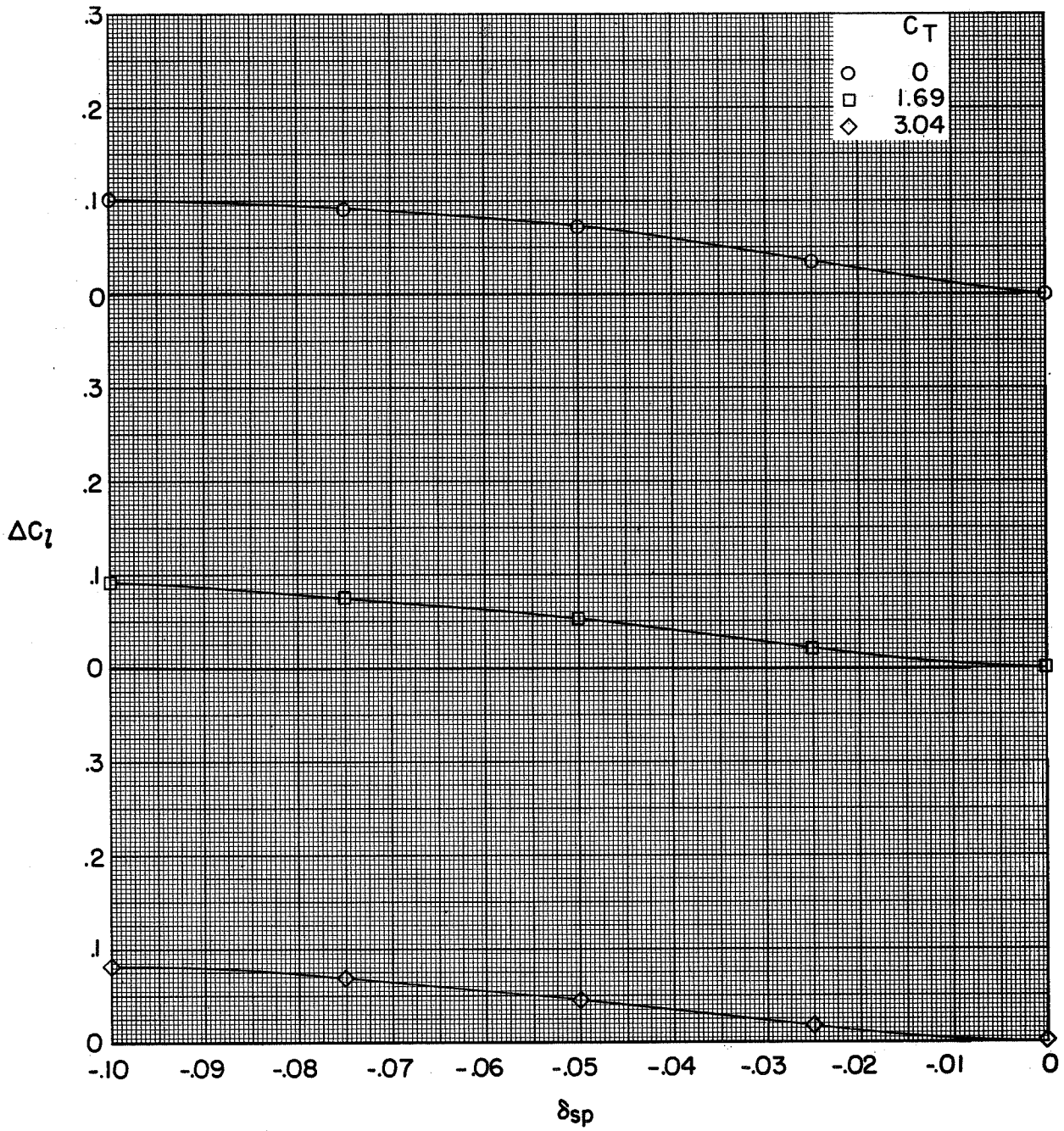

(a) Rolling-moment coefficient.

Figure 80.- Summary of lateral-directional moments due to spoiler projection for the model with flaps deflected and leading-edge slat on. BPR 10.0; T-tail at 5^o; $\delta_f = 0^o/35^o/35^o$; c_s = 25 percent; $\delta_s = 50^o$; left inboard engine out.

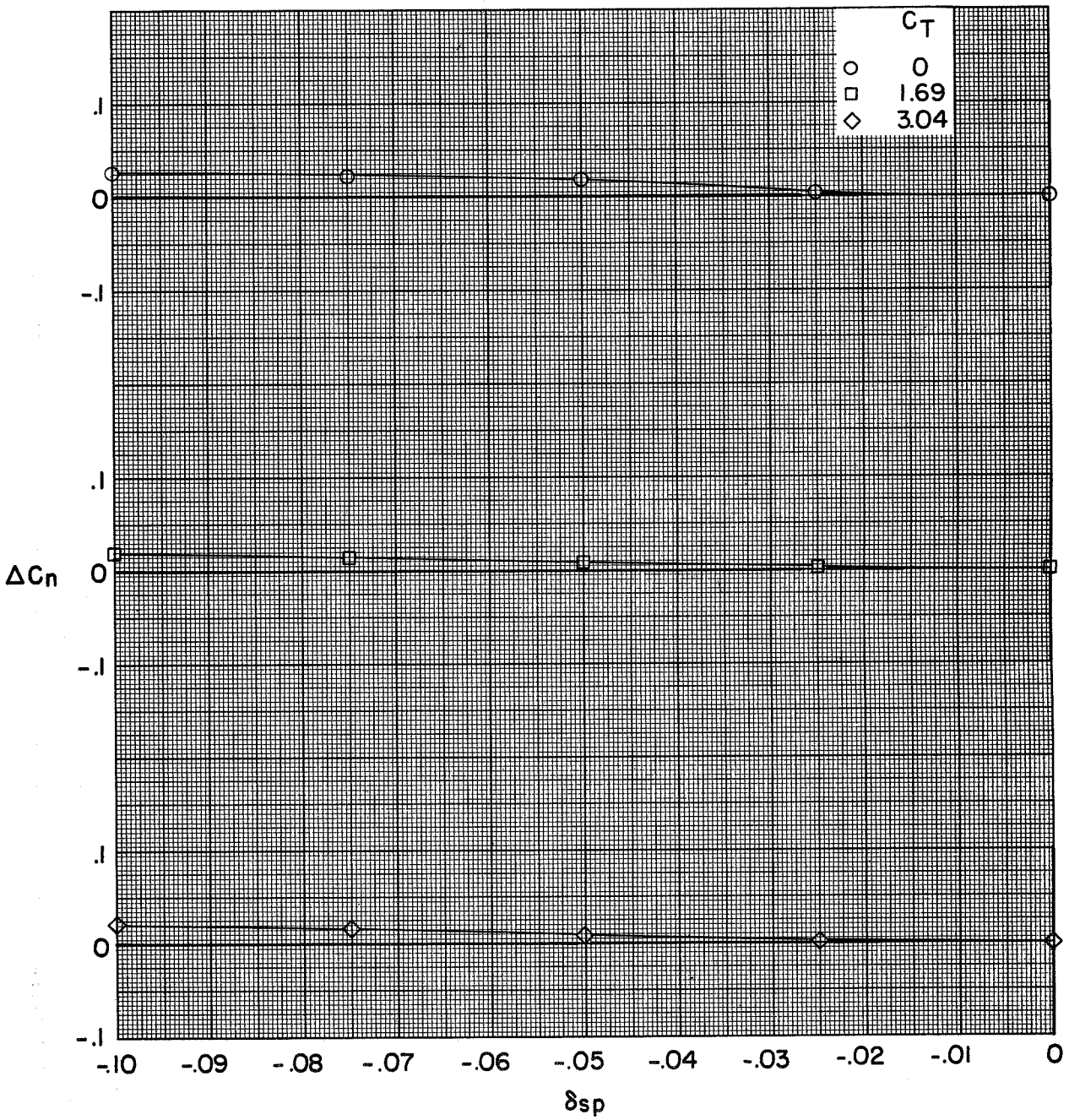

(b) Yawing-moment coefficient.

Figure 80.- Concluded.

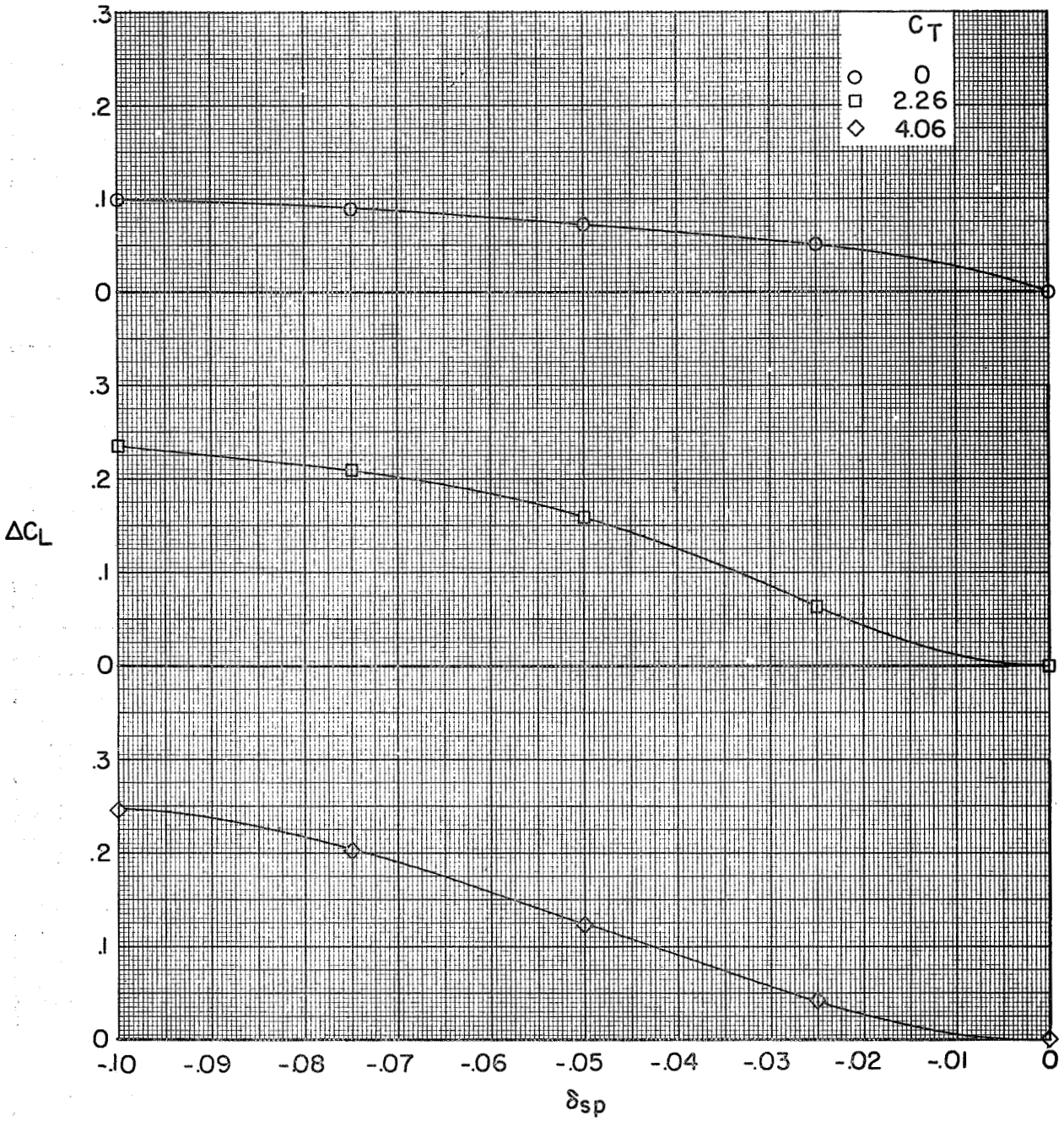

(a) Rolling-moment coefficient.

Figure 81.- Summary of lateral-directional moments due to spoiler projection for the model with flaps deflected and leading-edge slat on. BPR 10.0; T-tail at 5^o; $\delta_f = 0^o/65^o/65^o$; c_s = 25 percent; $\delta_s = 50^o$; symmetrical power.

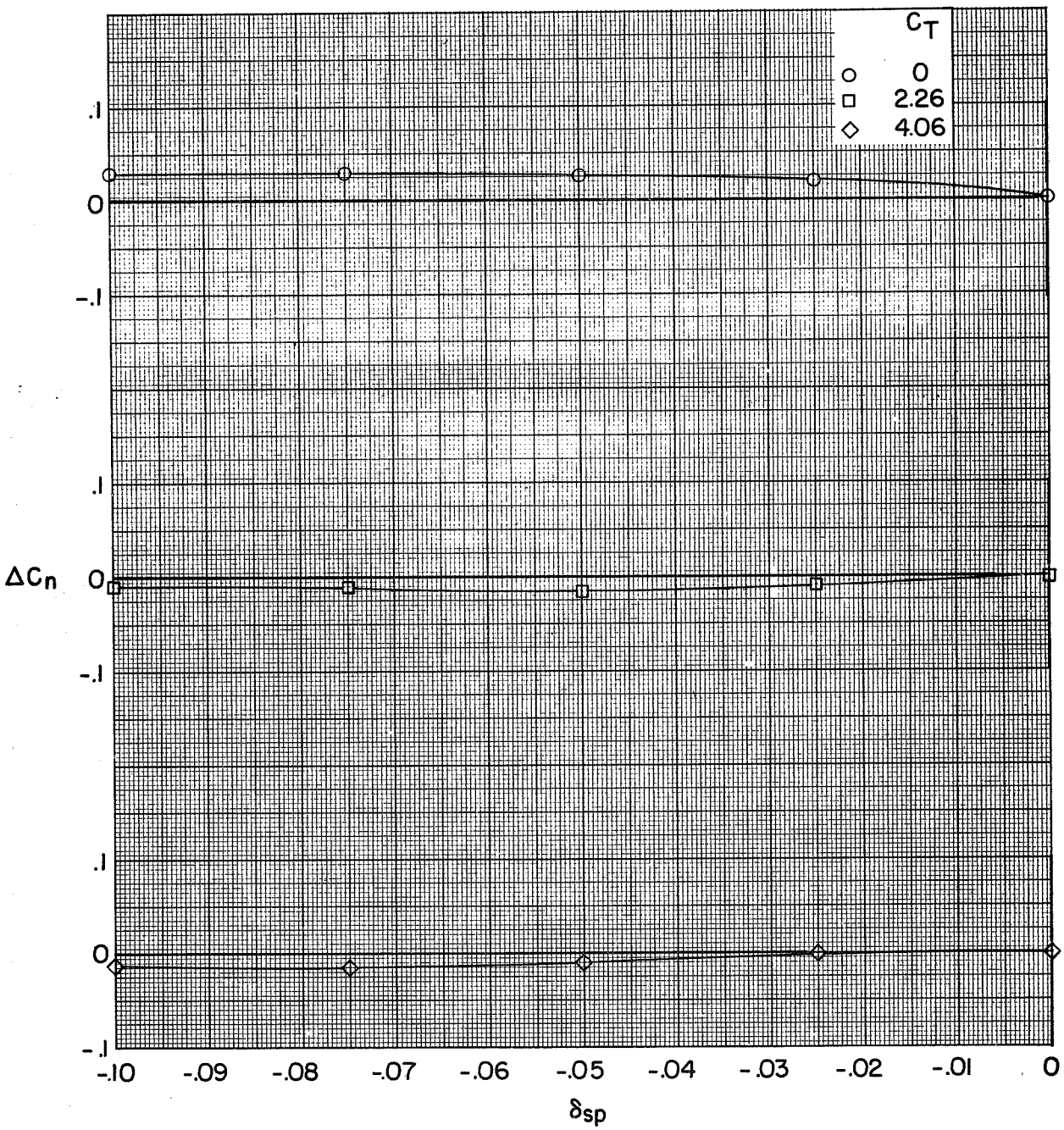

(b) Yawing-moment coefficient.

Figure 81.- Concluded.

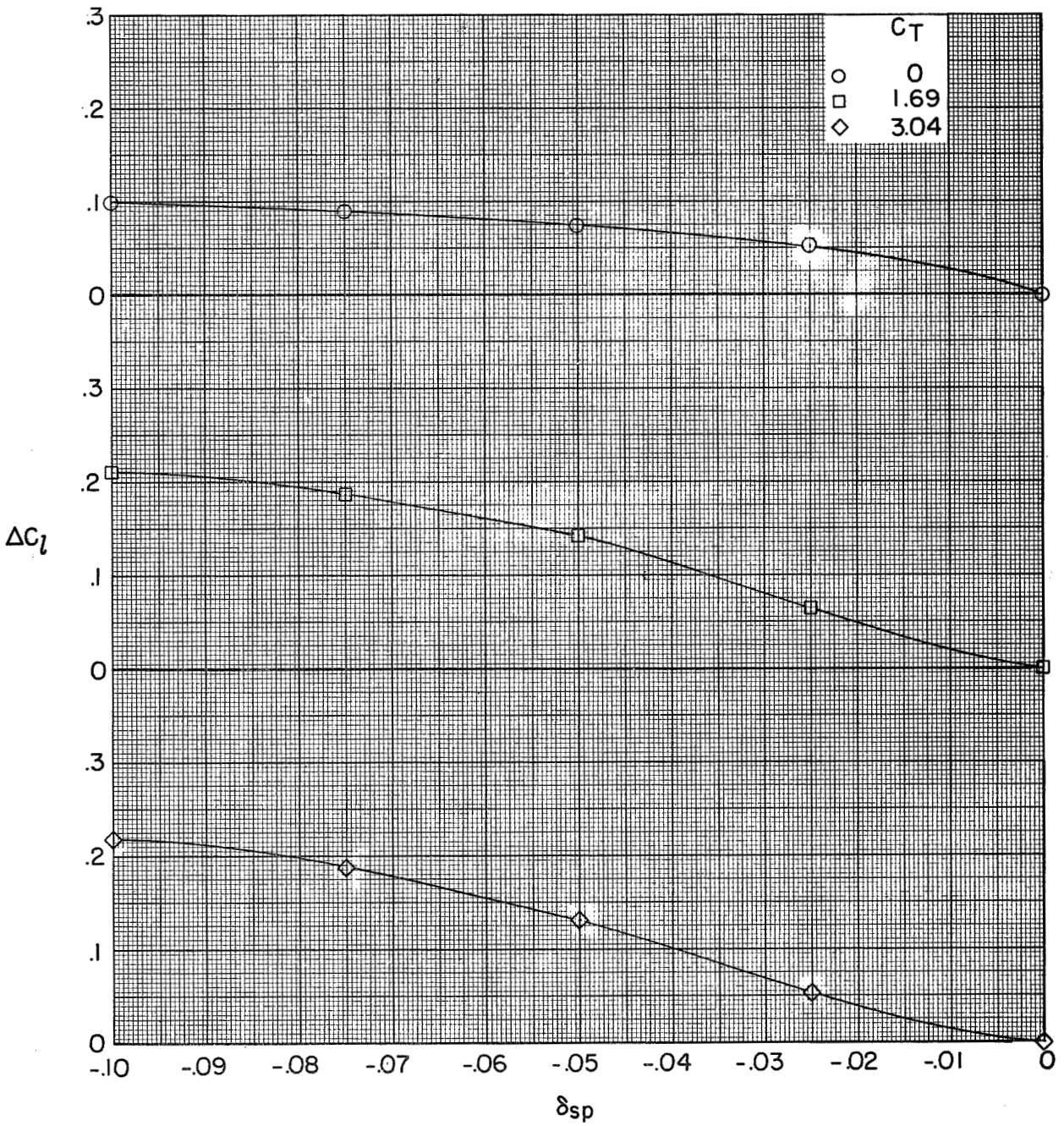

(a) Rolling-moment coefficient.

Figure 82.- Summary of lateral-directional moments due to spoiler projection for the model with flaps deflected and leading-edge slat on. BPR 10.0; T-tail at 5^o; $\delta_f = 0^o/65^o/65^o$; c_s = 25 percent; $\delta_s = 50^o$; left outboard engine out.

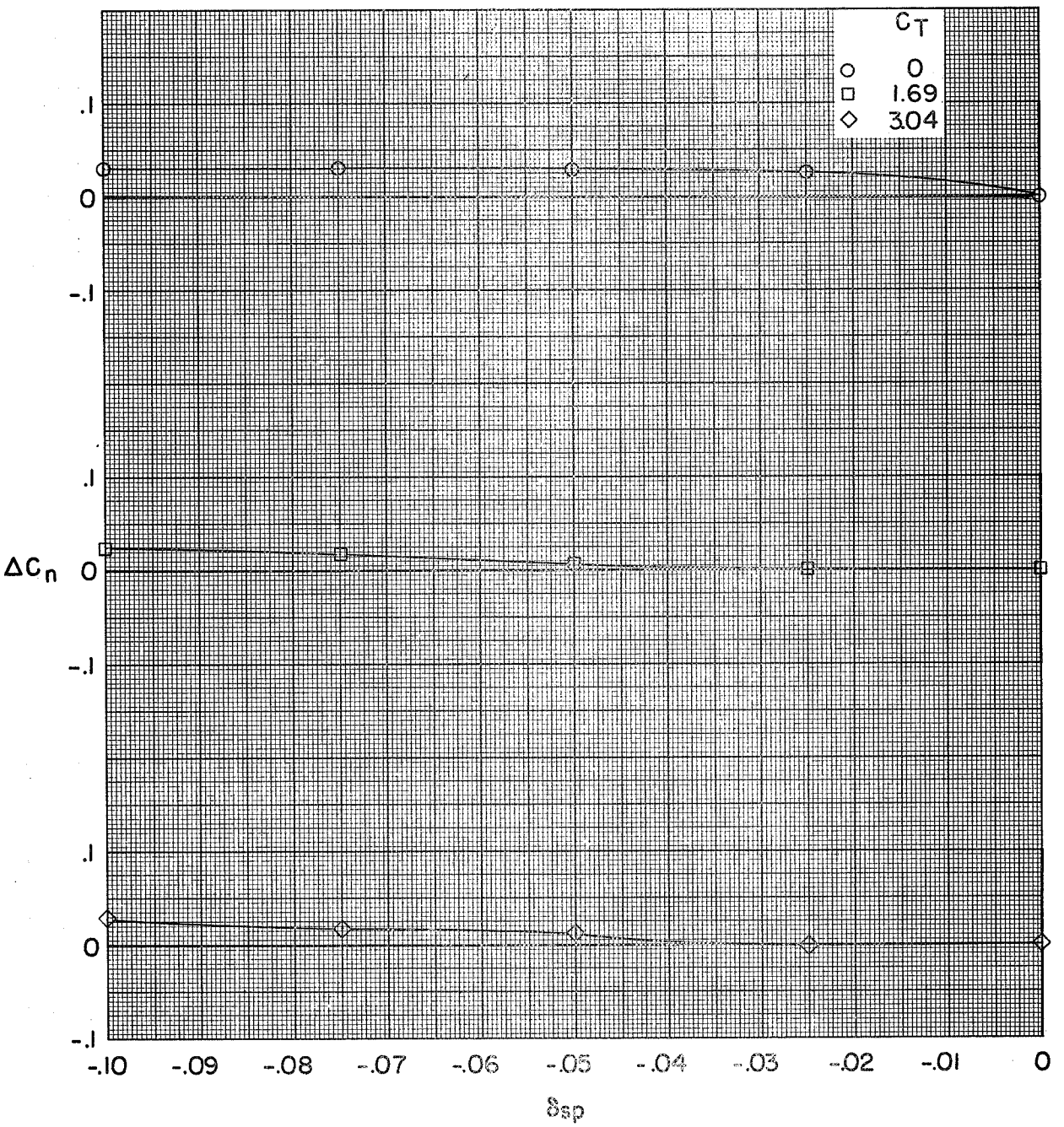

(b) Yawing-moment coefficient.

Figure 82.- Concluded.

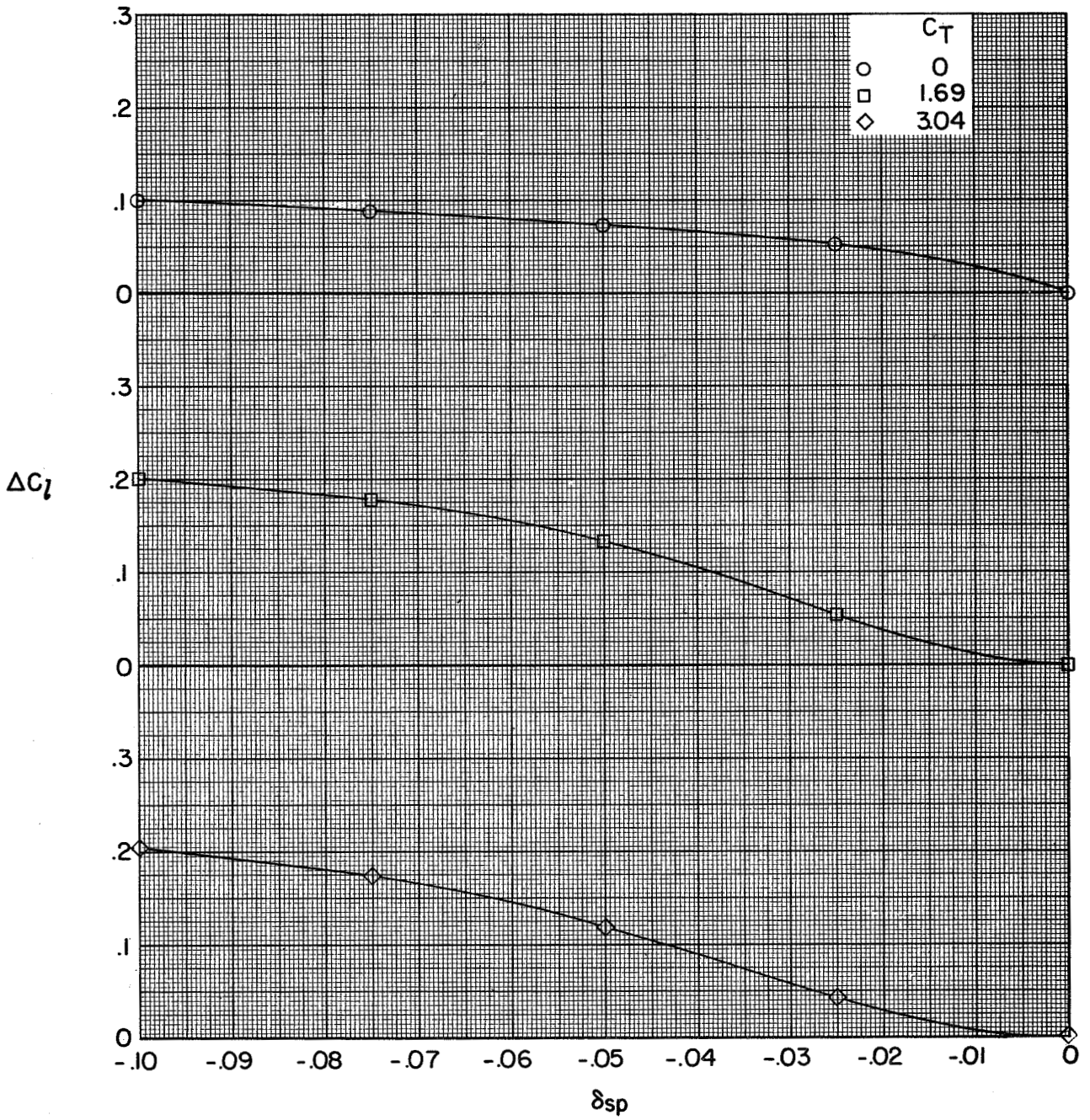

(a) Rolling-moment coefficient.

Figure 83.- Summary of lateral-directional moments due to spoiler projection for the model with flaps deflected and leading-edge slat on. BPR 10.0; T-tail at 5^o; $\delta_f = 0^o/65^o/65^o$; $c_s = 25$ percent; $\delta_s = 50^o$; left inboard engine out.

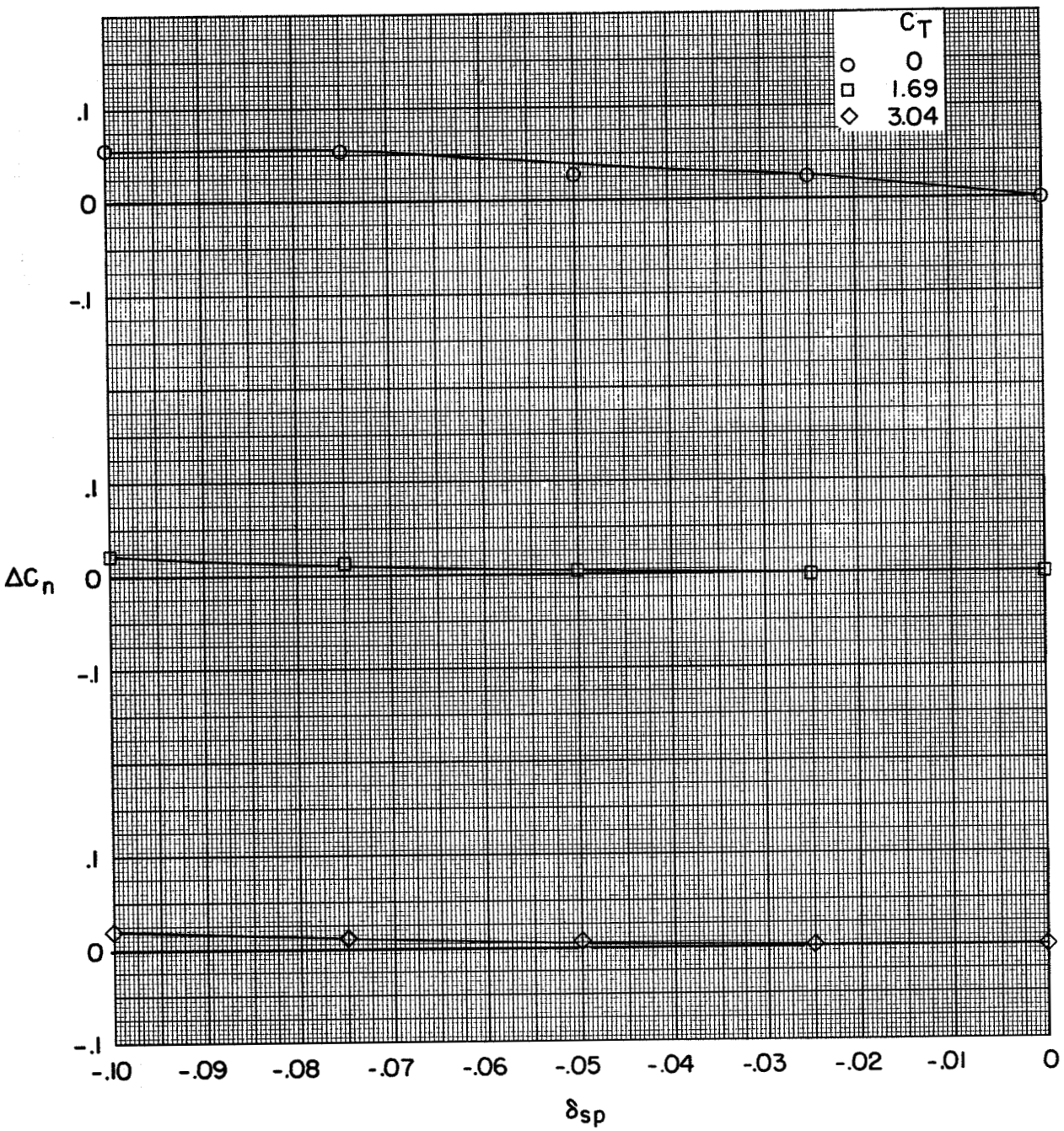

(b) Yawing-moment coefficient.

Figure 83.- Concluded.

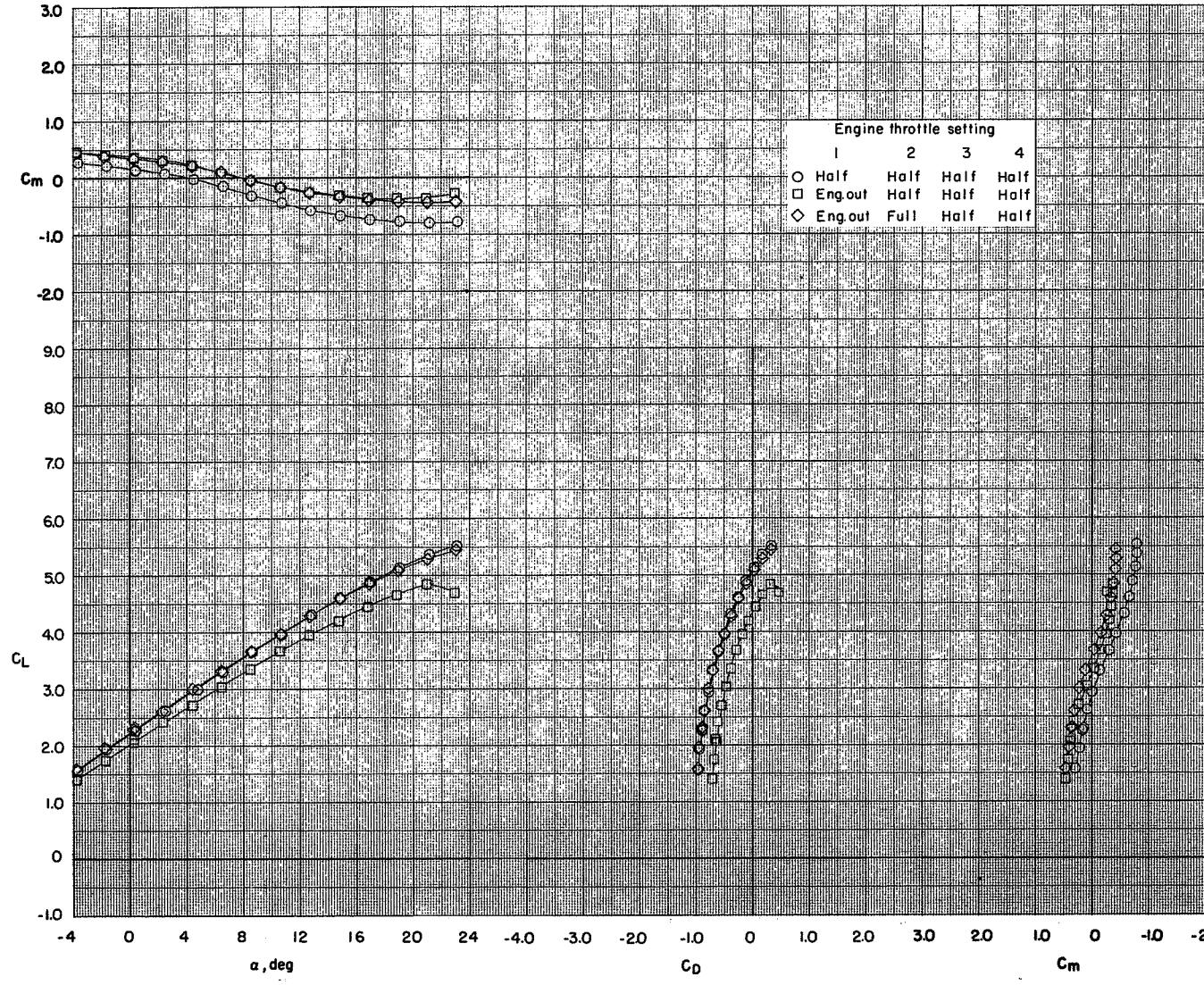

(a) Longitudinal characteristics.

Figure 84.- Effectiveness of a power recovery from the engine-out condition. BPR 6.2; T-tail at 5^{o}; $\delta_f = 0^{o}/35^{o}/35^{o}$; $c_s = 25$ percent; $\delta_s = 50^{o}$; $C_T \approx 2$; left outboard engine out.

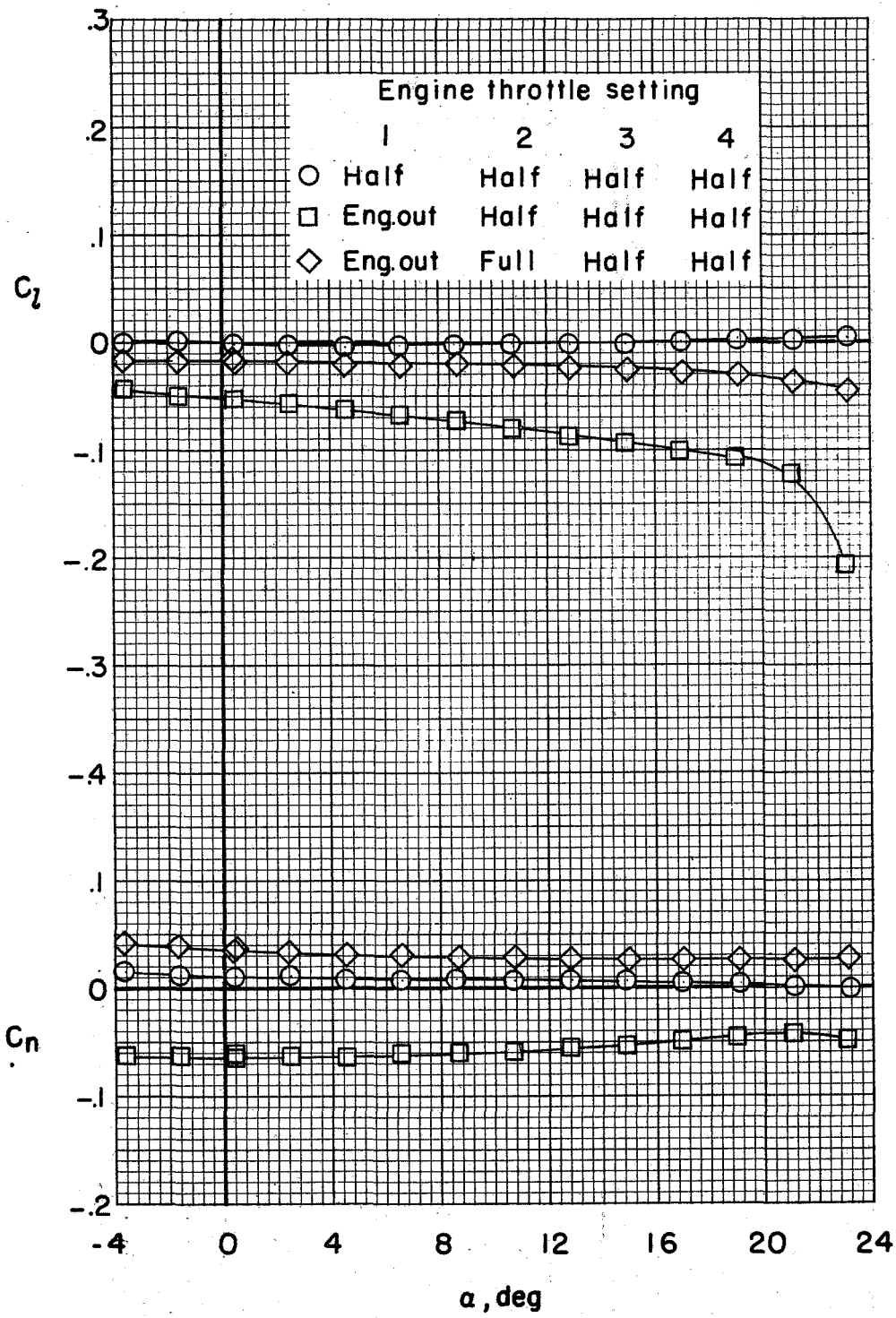

(b) Lateral-directional characteristics.

Figure 84.- Concluded.

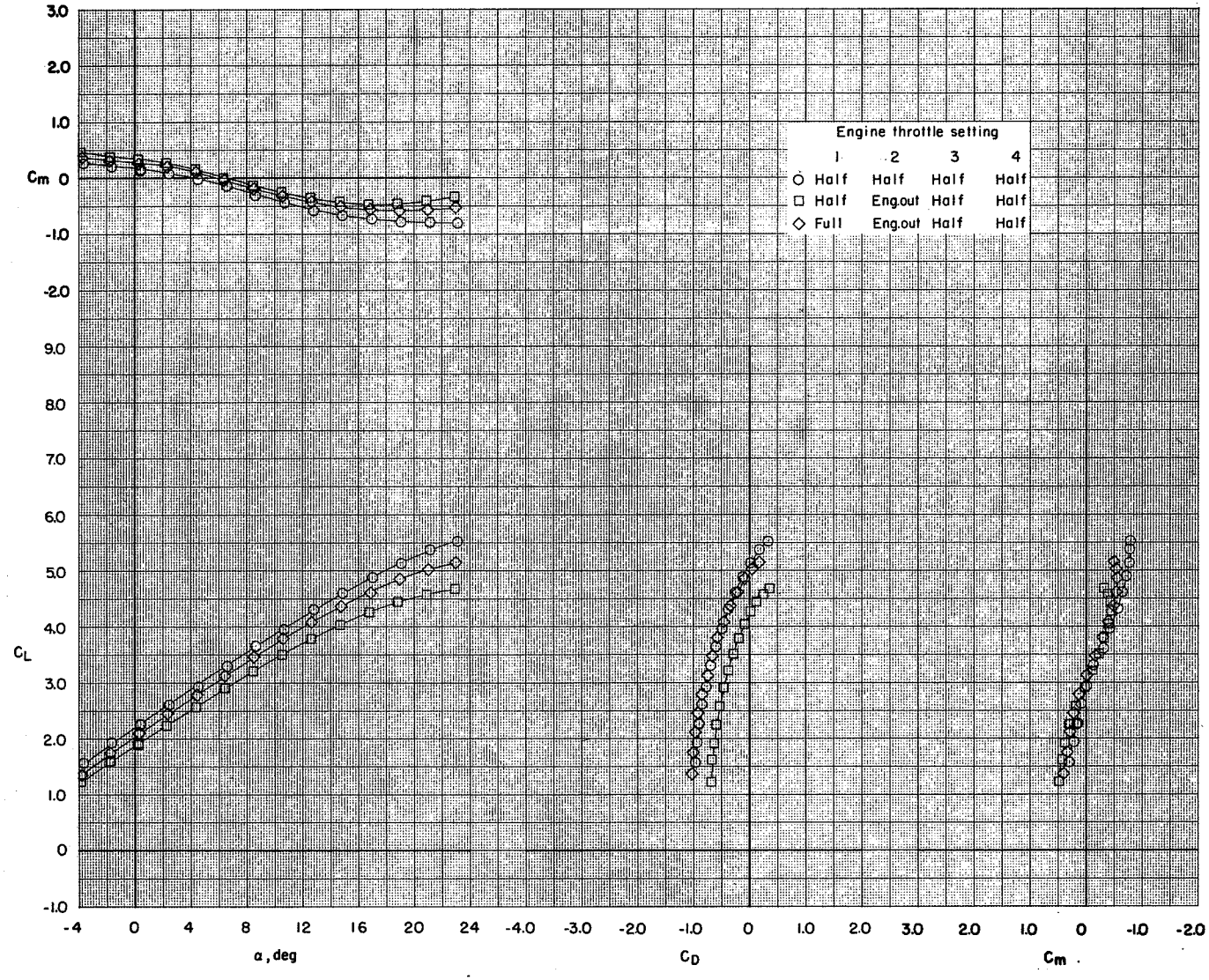

(a) Longitudinal characteristics.

Figure 85.- Effectiveness of a power recovery from the engine-out condition. BPR 6.2; T-tail at 5^{o}; $\delta_f = 0^{o}/35^{o}/35^{o}$; $c_S = 25$ percent; $\delta_S = 50^{o}$; $C_T \approx 2$; left inboard engine out.

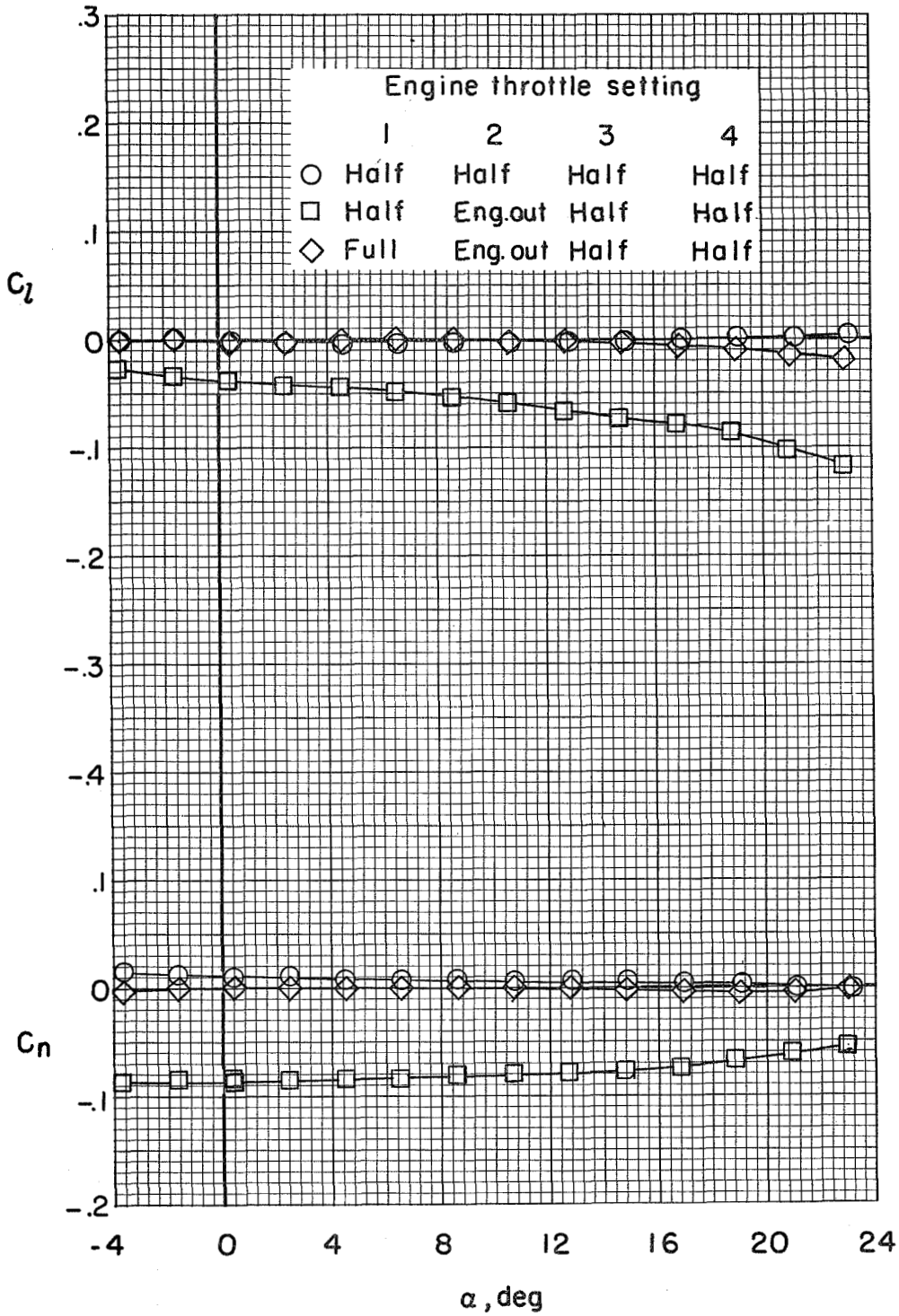

(b) Lateral-directional characteristics.

Figure 85.- Concluded.

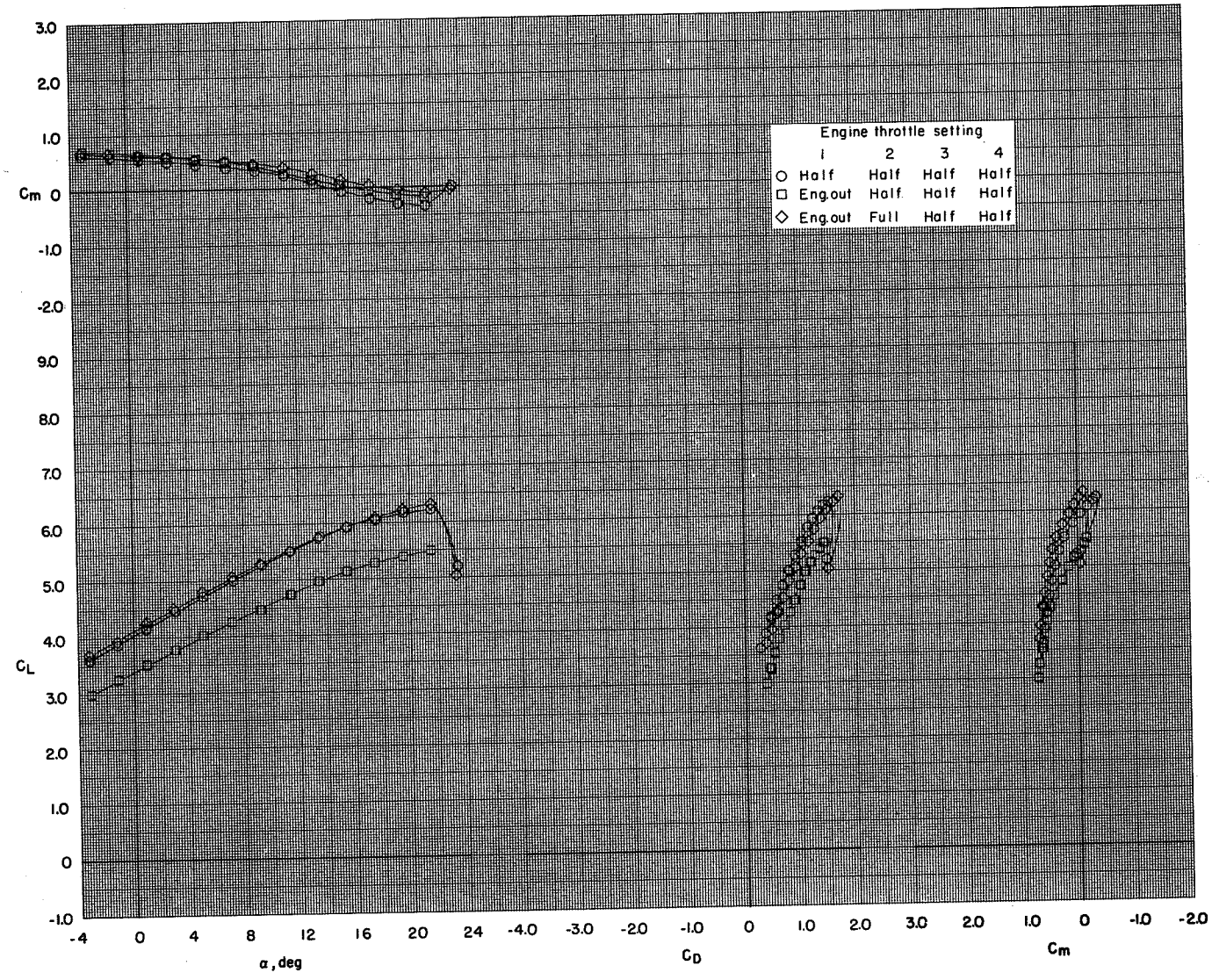

(a) Longitudinal characteristics.

Figure 86.- Effectiveness of a power recovery from the engine-out condition. BPR 6.2; T-tail at 5^{o}; $\delta_f = 0^{o}/65^{o}/65^{o}$; $c_s = 25$ percent; $\delta_s = 50^{o}$; $C_T \approx 2$; left outboard engine out.

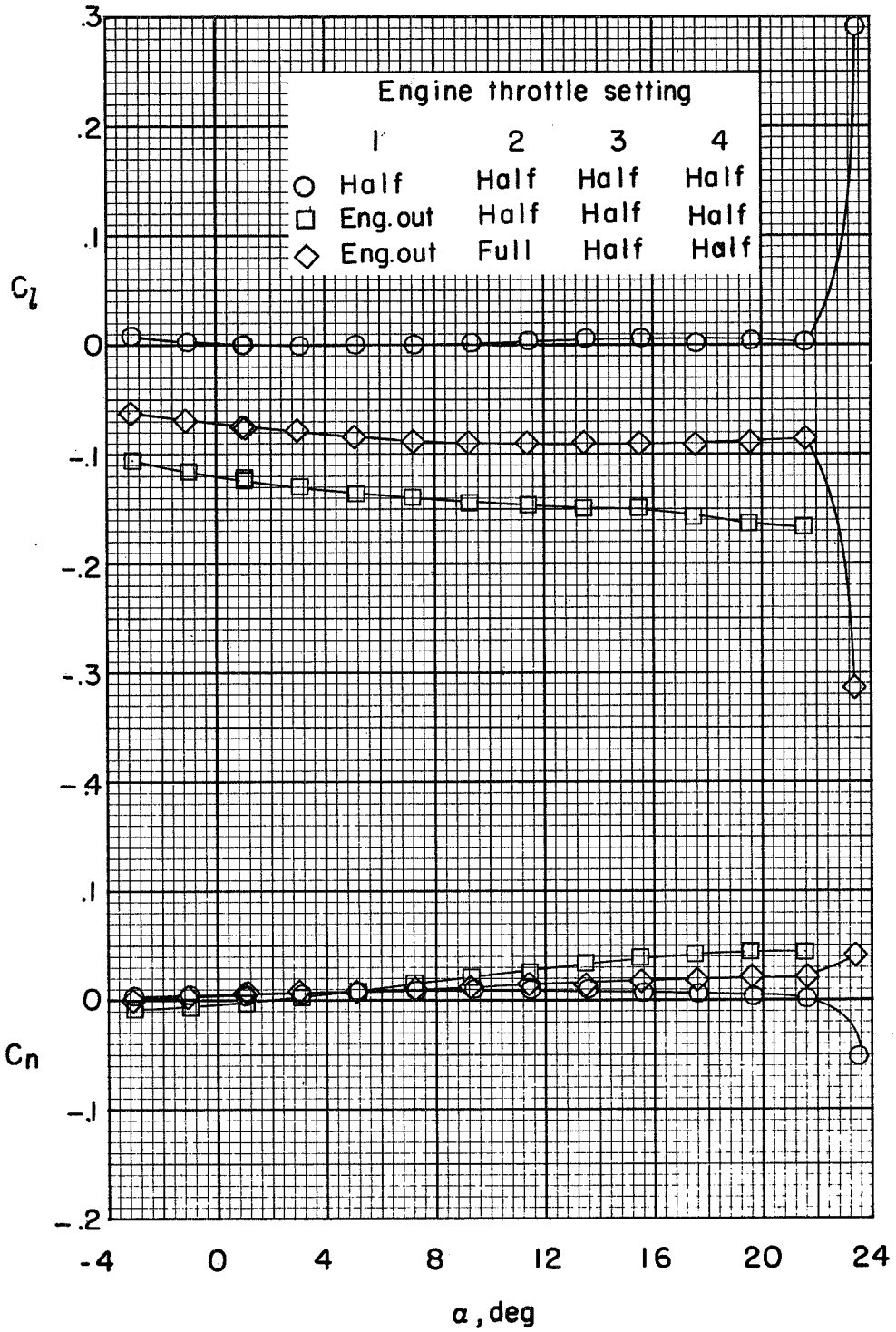

(b) Lateral-directional characteristics.

Figure 86.- Concluded.

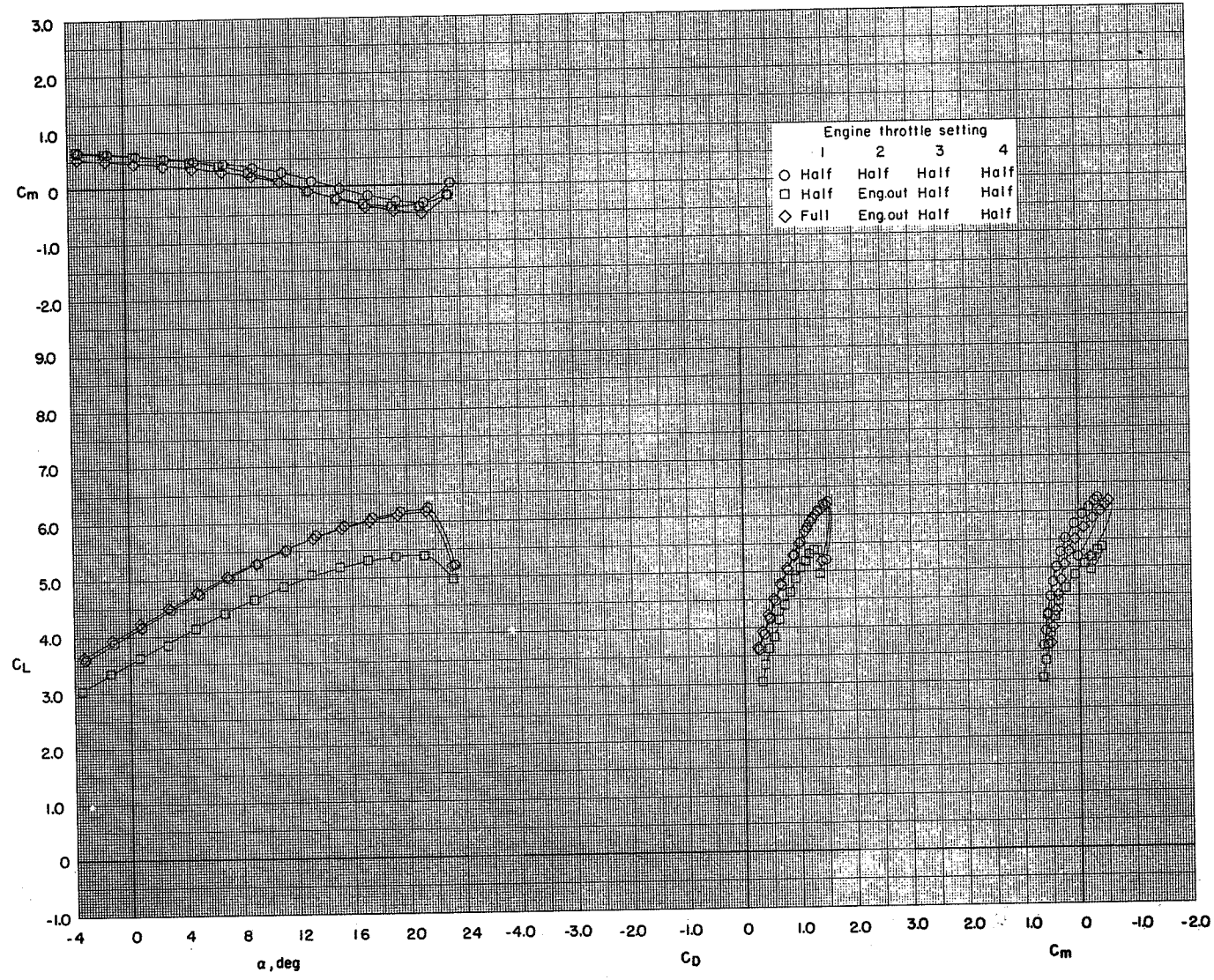

(a) Longitudinal characteristics.

Figure 87.- Effectiveness of a power recovery from the engine-out condition. BPR 6.2; T-tail at 5^{o}; $\delta_f = 0^{o}/65^{o}/65^{o}$; $c_s = 25$ percent; $\delta_s = 50^{o}$; $C_T \approx 2$; left inboard engine out.

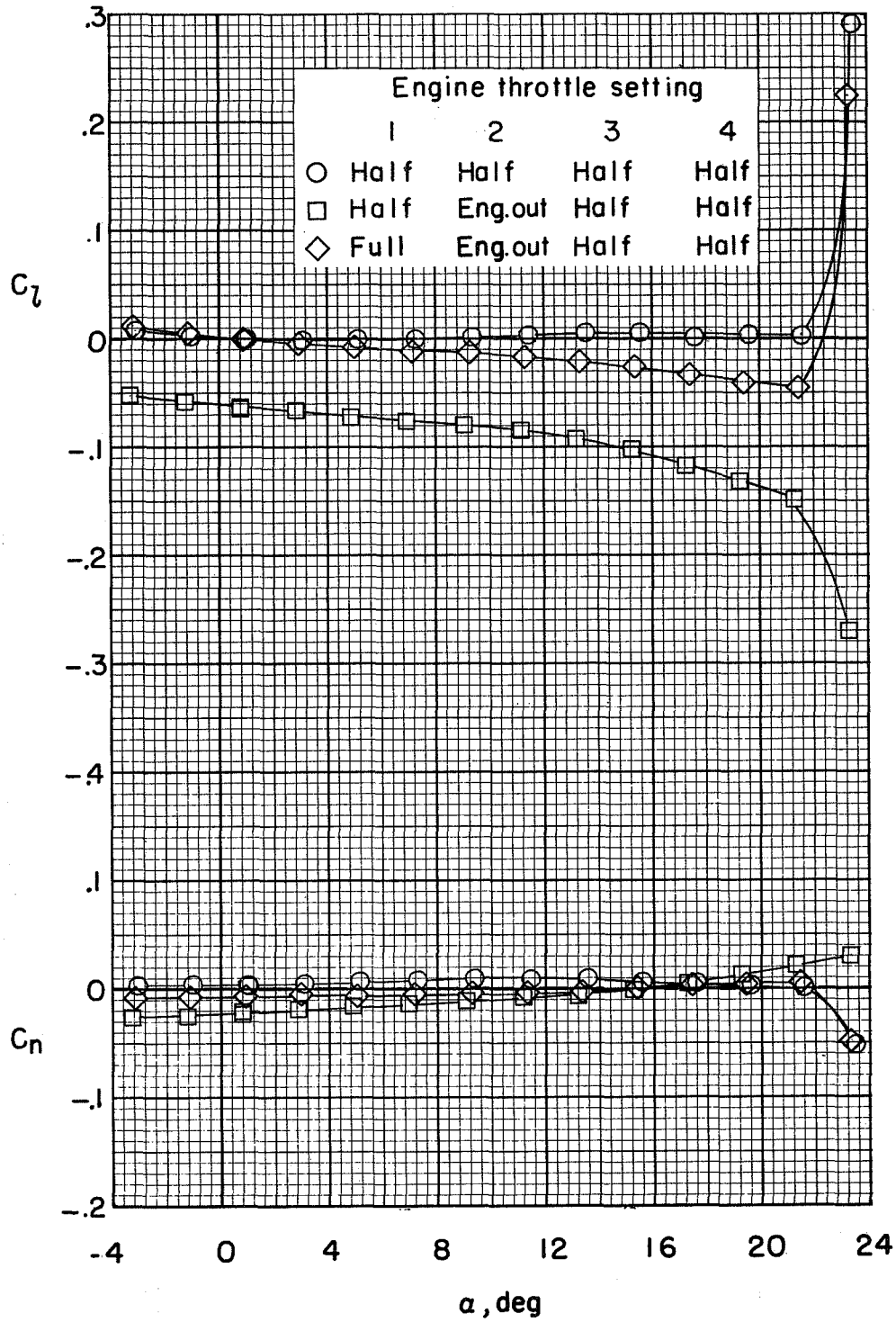

(b) Lateral-directional characteristics.

Figure 87.- Concluded.

*U.S. GOVERNMENT PRINTING OFFICE: 1975 - 635-275/43

NATIONAL AERONAUTICS AND SPACE ADMINISTRATION
WASHINGTON, D.C. 20546

OFFICIAL BUSINESS
PENALTY FOR PRIVATE USE $300

SPECIAL FOURTH-CLASS RATE BOOK

POSTAGE AND FEES PAID
NATIONAL AERONAUTICS AND SPACE ADMINISTRATION
451

U.S.MAIL

POSTMASTER: If Undeliverable (Section 158 Postal Manual) Do Not Return

"The aeronautical and space activities of the United States shall be conducted so as to contribute . . . to the expansion of human knowledge of phenomena in the atmosphere and space. The Administration shall provide for the widest practicable and appropriate dissemination of information concerning its activities and the results thereof."

—NATIONAL AERONAUTICS AND SPACE ACT OF 1958

NASA SCIENTIFIC AND TECHNICAL PUBLICATIONS

TECHNICAL REPORTS: Scientific and technical information considered important, complete, and a lasting contribution to existing knowledge.

TECHNICAL NOTES: Information less broad in scope but nevertheless of importance as a contribution to existing knowledge.

TECHNICAL MEMORANDUMS: Information receiving limited distribution because of preliminary data, security classification, or other reasons. Also includes conference proceedings with either limited or unlimited distribution.

CONTRACTOR REPORTS: Scientific and technical information generated under a NASA contract or grant and considered an important contribution to existing knowledge.

TECHNICAL TRANSLATIONS: Information published in a foreign language considered to merit NASA distribution in English.

SPECIAL PUBLICATIONS: Information derived from or of value to NASA activities. Publications include final reports of major projects, monographs, data compilations, handbooks, sourcebooks, and special bibliographies.

TECHNOLOGY UTILIZATION PUBLICATIONS: Information on technology used by NASA that may be of particular interest in commercial and other non-aerospace applications. Publications include Tech Briefs, Technology Utilization Reports and Technology Surveys.

Details on the availability of these publications may be obtained from:

SCIENTIFIC AND TECHNICAL INFORMATION OFFICE

NATIONAL AERONAUTICS AND SPACE ADMINISTRATION

Washington, D.C. 20546